Abstract and Applied Analysis

Mathematical and Computational Analyses of Flow and Transport Phenomena

Guest Editors: Shuyu Sun, Mohamed Fathy El-Amin, and Jianzhong Lin

Mathematical and Computational Analyses of Flow and Transport Phenomena

Abstract and Applied Analysis

Mathematical and Computational Analyses of Flow and Transport Phenomena

Guest Editors: Shuyu Sun, Mohamed Fathy El-Amin, and Jianzhong Lin

Editorial Board

Contents

Hindawi Publishing Corporation
Abstract and Applied Analysis
Volume 2014, Article ID 381619, 2 pages
http://dx.doi.org/10.1155/2014/381619

Editorial

Mathematical and Computational Analyses of Flow and Transport Phenomena

Shuyu Sun,[1] Mohamed Fathy El-Amin,[2] and Jianzhong Lin[3]

[1] *Computational Transport Phenomena Laboratory, King Abdullah University of Science and Technology, Thuwal 23955-6900, Saudi Arabia*
[2] *Department of Mathematics, Aswan University, Aswan 81528, Egypt*
[3] *Faculty of Engineering Zhejiang University, Zhejiang, China*

Correspondence should be addressed to Shuyu Sun; shuyu.sun@kaust.edu.sa

Received 7 April 2014; Accepted 7 April 2014; Published 8 May 2014

1. Introduction

In this special issue, a number of papers have been accepted for publication. The special issue concerns with theoretical investigation and mathematical analysis that are very important for all scientific, engineering, and environmental applications. From mathematical modeling to computational analysis and all the way to developing analytical and numerical solutions, studying solutions properties, and so forth, the theoretical, mathematical, and computational analyses are indispensable bases. Rapid progress has been seen in the analysis of flow and transport phenomena especially in the recent years because of the significance of flow and transport to science and engineering.

2. Overview of Work Presented in This Special Issue

The list of papers published in this issue covers a wide range of applications using different approaches and analyses, and it may be divided into five groups as follows.

The first group of papers consists of nine papers that address various issues in the area of particles/nanoparticles suspensions flow that are used in different applications. Z. You et al. have studied a long-term deep bed filtration in porous media with size exclusion particle capture mechanism in the paper entitled "*Exact solution for long-term size exclusion suspension-colloidal transport in porous media*." On the other hand, E. H. Aly and A. Ebaid have introduced a direct and effective approach to obtain the exact analytical solution for the nanoparticles-water flow over an isothermal stretching sheet with the effect of the slip model in the paper entitled "*Exact analytical solution for suction and injection flow with thermal enhancement of five nanofluids over an isothermal stretching sheet with effect of the slip model: a comparative study*." In another paper entitled "*The flow and heat transfer of a nanofluid past a stretching/shrinking sheet with a convective boundary condition*," S. Mansur and A. Ishak have studied the boundary layer flow of a nanofluid past a stretching/shrinking sheet with a convective boundary condition. Moreover, H. Qing and X. Mingliang have proposed a model of fundamental aspects of the Taylor-series expansion method of moment (TEMOM) to describe the aerosol population balance equation due to Brownian coagulation in the continuum regime in the paper entitled "*The fundamental aspects of TEMOM model for particle coagulation due to Brownian motion—part ii: in the continuum regime*." R. Wang has presented numerical investigations on particle trapping techniques by using intrinsic hydrodynamic effects in an expansion-contraction microfluidic device in the paper entitled "*Hydrodynamic trapping of particles in an expansion-contraction microfluidic device*." L.-Z. Huang and D.-M. Nie in the article entitled "*Lattice Boltzmann simulation of collision between 2D circular particles suspension in Couette flow*" simulated the collision between 2D circular particles suspension in Couette flow by using multiple relaxation time-based lattice Boltzmann and direct forcing/fictitious domain method. In the paper entitled "*Modeling and numerical*

analysis of the solid particle erosion in curved ducts," K. Sun et al. presented a modeling and computational study on particle erosion in curved ducts. In another paper, M. H. Alawi et al. have introduced a mathematical model to describe the fine-particles transport carried by a two-phase flow in a porous medium to describe the formation damage of asphalt-paved roads in the paper entitled "*Modeling and simulation of flow and formation damage of asphalt-paved roads*." Finally, F. Yuan and F. Gan have used the method of moments to predict the evolution of aerosol particles in the rainfall process in the paper entitled "*Evolution of aerosol particles in the rainfall process via method of moments*." In the paper entitled "*Direct numerical simulation of concentration and orientation distribution of fibers in a mixing layer*" by K. Zhou et al., the concentration and orientation of suspended fibers in a mixing layer are investigated numerically.

The second group is concerned with reservoir modeling and simulation. S. Borazjani et al. presented the paper entitled "*Exact solution for non-self-similar wave-interaction problem during two-phase four-component flow in porous media*." Analytical solutions for one-dimensional two-phase multicomponent flows in porous media describe processes of enhanced oil recovery, environmental flows of waste disposal, and contaminant propagation in subterranean reservoirs and water management in aquifers. In the paper entitled "*New scheme of finite difference heterogeneous multiscale method to solve saturated flow in porous media*," F. Chen and L. Ren have constructed a finite difference scheme, namely, the development of the finite difference heterogeneous multiscale method (FDHMM), for simulating saturated water flow in random porous media. J. Xu et al. in their paper "*A direct Eulerian GRP scheme for the prediction of gas-liquid two-phase flow in HTHP transient wells*" have introduced a dimensional splitting technique with Eulerian generalized Riemann problem (GRP) scheme to solve coupled system model of partial differential equations which concerns with the variation of the pressure and temperature, velocity, and density at different times and depths in high temperature-high pressure (HTHP) gas-liquid two-phase flow wells. In addition to flow simulation in reservoir, reservoir sedimentation is also considered in this issue. The basic factors influencing the density of sediments deposited in reservoirs are discussed, and uncertainties in reservoir sedimentation have been determined using the Delta method by F. Imanshoar et al. in the paper entitled "*Reservoir sedimentation based on uncertainty analysis*." Also, the paper of L. Gan and J. Xu, "*Retrofitting transportation network using a fuzzy random multiobjective bilevel model to hedge against seismic risk*," focuses on the problem of hedging against seismic risk through the retrofit of transportation systems in large-scale construction projects.

The third group, which consists of two papers, is concerned with some biological applications. In the first paper entitled "*A new method of moments for the bimodal particle system in the Stokes regime*," Y.-H. Liu and Z.-Q. Yin studied the particle system in the Stokes regime with a bimodal distribution. A. Y. Tang and N. Amin have reviewed some numerical approaches to solve fluid structure interaction problems in blood flow in the paper entitled "*Some numerical approaches to solve fluid structure interaction problems in blood flow*."

The fourth group focuses on some heat transfer in fluid flow problems. M. Goodarzi et al. have introduced a comparison study for the problem of natural convection heat transfer inside cavities and enclosures in the paper entitled "*Comparison of the finite volume and lattice Boltzmann methods for solving natural convection heat transfer problems inside cavities and enclosures*." In the paper entitled "*Revisiting Blasius flow by fixed point method,*" D. Xu et al. have used the fixed-point method to resolve the Blasius problem.

The last group is related to flow and transport applications in electronic devices. Numerical simulations for the melt flow under the influence of control devices in a T-type two-strand bloom caster tundish are presented by Z. He et al. in the paper entitled "*Numerical modeling of the fluid flow in continuous casting tundish with different control devices*." The fluid-driven efficiency of the micropump based on induced charge electroosmotic was studied numerically by K. Zhang et al. in the paper entitled "*Design of T-shaped micropump based on induced charge electroosmotic*."

3. Conclusions

This special issue presents and highlights new applications and new challenges in five different important research areas of flow and transport. This special issue is not intended to be an exhaustive collection nor a survey of all of the current trends in flow and transport research; many additional significant research areas of flow and transport still exist and remain to be explored, but multidisciplinary research effort is a clear trend.

Acknowledgments

The authors would like to thank the participants of the special issue for their inspiring contributions and the anonymous reviewers for their diligent work, which led to the high quality of the special issue. The lead guest editor S. Sun would like to acknowledge KAUST Faculty Baseline Research Fund (BRF) for supporting his research in flow and transport.

Shuyu Sun
Mohamed Fathy El-Amin
Jianzhong Lin

Hindawi Publishing Corporation
Abstract and Applied Analysis
Volume 2014, Article ID 731567, 13 pages
http://dx.doi.org/10.1155/2014/731567

Research Article

Exact Solution for Non-Self-Similar Wave-Interaction Problem during Two-Phase Four-Component Flow in Porous Media

S. Borazjani,[1] P. Bedrikovetsky,[1] and R. Farajzadeh[2,3]

[1] *Australian School of Petroleum, The University of Adelaide, SA 5005, Australia*
[2] *Shell Global Solutions International, Rijswijk, The Netherlands*
[3] *Delft University of Technology, The Netherlands*

Correspondence should be addressed to S. Borazjani; sara.borazjani@adelaide.edu.au

Received 6 September 2013; Revised 27 December 2013; Accepted 29 December 2013; Published 12 March 2014

Academic Editor: Shuyu Sun

Analytical solutions for one-dimensional two-phase multicomponent flows in porous media describe processes of enhanced oil recovery, environmental flows of waste disposal, and contaminant propagation in subterranean reservoirs and water management in aquifers. We derive the exact solution for 3×3 hyperbolic system of conservation laws that corresponds to two-phase four-component flow in porous media where sorption of the third component depends on its own concentration in water and also on the fourth component concentration. Using the potential function as an independent variable instead of time allows splitting the initial system to 2×2 system for concentrations and one scalar hyperbolic equation for phase saturation, which allows for full integration of non-self-similar problem with wave interactions.

1. Introduction

Exact self-similar solutions of Riemann problems for hyperbolic systems of conservation laws and non-self-similar solutions of hyperbolic wave interactions have been derived for various flows in gas dynamics, shallow waters, and chromatography (see monographs [1–8]). For flow in porous media, hyperbolic systems of conservation laws describe two-phase multicomponent displacement [9, 10]. Consider

$$\frac{\partial s}{\partial t} + \frac{\partial f(s,c)}{\partial x} = 0 \tag{1}$$

$$\frac{\partial (cs + a(c))}{\partial t} + \frac{\partial (cf(s,c))}{\partial x} = 0, \tag{2}$$

where s is the saturation (volumetric fraction) of aqueous phase and f is the water flux. Equation (1) is the mass balance for water and (2) is the mass balance for each component in the aqueous solution. Under the conditions of thermodynamic equilibrium, the concentrations of the components adsorbed on the solid phase (a_i) and dissolved in the aqueous phase (c_i) are governed by adsorption isotherms:

$$a = a(c), \qquad a = (a_1, a_2, \ldots, a_n), \qquad c = (c_1, c_2, \ldots, c_n). \tag{3}$$

Exact and semianalytical solutions of one-dimensional flow problems are widely used in stream-line simulation for flow prediction in three-dimensional natural reservoirs [10]. The sequence of concentration shocks in the one-dimensional analytical solution is important for interpretation of laboratory tests in two-phase multicomponent flow in natural reservoir cores.

The scalar hyperbolic equations (1) and (2), $n = 0$, correspond to displacement of oil by water [9, 10]. The $(n+1) \times (n+1)$ system (1) and (2) describes two-phase flow of oleic and aqueous phases with n components (such as polymer and different salts) that may adsorb and be dissolved in both phases. These flows are typical for so-called chemical enhanced oil recovery displacements, like injections of polymers or surfactants, and for numerous environmental flows [9, 10]. For polymer injection in oil reservoirs, $i = 1$ corresponds to polymer and $i = 2, 3, \ldots, n$ to different ions.

Therefore the system (1) and (2) is called the multicomponent polymer-flooding model [11, 12]. Besides, $(n-1)\times(n-1)$ hyperbolic system (1) and (2) describes two-phase n-component displacement, which is typical for so-called gas methods of enhanced oil recovery [9, 10, 13, 14]. The processes of hot water injection with phase transitions, secondary migration of hydrocarbons with consequent formation of petroleum accumulations, enhanced geothermal energy projects, and injections into aquifers are described by the above systems. The Riemann problems correspond to continuous injection of chemical solutions or gases into oil reservoirs; the solutions are self-similar [3, 9, 14]. The wave-interaction problems correspond to piece-wise-constant initial-boundary conditions, for which the solutions are non-self-similar [1, 10, 15–17]. The wave-interaction solutions describe injection of limited slugs (banks) of chemical solutions or gaseous solvents driven in the reservoirs by water or gas [9, 10].

Riemann problem (1) and (2) with $n = 1$ has been solved with applications to various injections of polymers [17, 18], carbonized water and surfactants [19, 20], and so forth. More complex self-similar solutions of (1) and (2) for $n = 2, 3$ were obtained by Barenblatt et al. [21] and Braginskaya and Entov [22] and later by Johansen et al. and Winther et al. [11, 12, 23–25]. Analogous solutions for gas injection and $n = 3, 4, \ldots$ have been obtained by Orr and others [9, 13, 26–31].

The system (1) and (2) describes two-phase multicomponent displacements in large scale approximation, where the dissipative effects of capillary pressure, diffusion, and thermodynamic nonequilibrium are negligible if they are compared with advective fluxes under the large length scale of the natural subterranean reservoirs. Travelling waves near to shock discontinuities in dissipative systems have been presented in [10, 32]. A semianalytical global solutions have been obtained by Geiger et al. [33] and Schmid et al. [34]; see also [16].

The particular case of so-called multicomponent polymer flooding is the dependency of the component sorption concentration of its own concentration only $a_i(c_1, c_2, \ldots, c_n) = a_i(c_i)$. Exact solutions of the Riemann problem for this case show that the concentration of each component performs the jump without shocks of other components (see the corresponding solution in the books [10, 21]). Therefore, in concentration profiles, the shocks are located in order of decrease of derivatives of the sorption functions. In the case of Henry isotherms $a_i(c_i) = \Gamma_i c_i$, the shocks are located in order of increase of Henry's sorption coefficients Γ_i.

The distinguished invariant feature of $(n + 1) \times (n + 1)$ conservation law systems for two-phase multicomponent flows in porous media with sorption and phase transitions equations (1) and (2) is its splitting into an $n \times n$ auxiliary system for concentrations $c_i(x, t)$ and a scalar hyperbolic equation for saturation $s(x, t)$ [35, 36]. This splitting explains the simple form of Riemann problem solutions for system (1) and (2) as compared with gas dynamics or chromatography [1, 2, 37].

The non-self-similar solution of system (1) and (2), $n = 2$, for slug injections has been considered by Fayers [17], where the qualitative behaviour of characteristic lines and shocks has been described. The exact solutions of system (1) and (2) for $n = 2$ and 3 have been obtained in [15] (see book [10] for detailed derivations, in which the sorption of component depends on its own concentration only $a_i = a_i(c_i)$, $i = 1, 2, \ldots$). Numerous interactions of different saturation-concentration shocks occur after the injection, resulting in appearance of moving zones with different combinations of components. However, after all interactions, different component slugs are separated from each other. As in the case of continuous injection, the slugs are finally positioned in the order of decreasing sorption isotherm derivatives (da_i/dc_i). It seems that this simplified case draws the line where the analytical solutions can be found from the analysis of system (1) and (2) directly. Consideration of cross-effects $a_i = a_i(c_1, c_2, \ldots, c_n)$ in sorption functions equation (3) introduces significant difficulties into wave analysis, and even the Riemann problem cannot be solved for any arbitrary case $n = 2$ (see [38], where the Riemann solutions have been obtained for several particular cases).

The splitting technique reduces number of equations in (1) and (2) by one, allowing for exact solutions in more complex multicomponent cases [35–40]. The Riemann problem with cross-effects for adsorption $a_i = a_i(c_1, c_2)$ has been solved in [39, 41, 42] for continuous polymer injection with varying salinity using the splitting method. In the current paper, the exact solution for non-self-similar problem of injection of polymer slug with varying salinity followed by water drive is obtained.

The structure of the text is as follows. The particular case of the general system (1) and (2) that is discussed in the current work is introduced in Section 2 along with physics assumptions and initial-boundary conditions for slug injection problem. The detailed description of the splitting procedure for the system is discussed along with formulation of initial and boundary conditions for the auxiliary system which is presented in Section 3. Section 4 contains derivation of the Riemann solution that corresponds to the first stage of the slug injection. The wave-interaction slug injection problem is solved in Section 5. Section 6 contains a simplified solution for the particular case where the initial chemical concentration is zero, which corresponds to the case of polymer slug injection. The paper is concluded by physical interpretation of the solution obtained for chemical slug injection with different water salinity into oilfield (Sections 7 and 8).

2. Formulation of the Problem

Let us discuss the displacement of oil by aqueous chemical solution with water drive accounting for different salinities of formation and injected waters. In the following text, the component $n = 1$ is called the polymer, and that $n = 2$ is called the salt. The assumptions of the mathematical model are as follows: both phases are incompressible, dispersion and capillary forces are neglected, there are two phases (oleic and aqueous phases) and two components dissolved in water (polymer and salt), water and oil phases are immiscible, chemical and salt concentrations in water are negligibly small and do not affect the volume of the aqueous phase,

the fractional flow of the aqueous phase is affected by concentration of the dissolved chemical, the fractional flow is independent of salt concentration, chemical and salt do not dissolve in oil, linear sorption for the polymer $a = \Gamma c$, Henry's sorption coefficient Γ is salinity-dependent, salt does not adsorb on the rock, and temperature is constant.

The system of governing equations consists of mass balance equations for aqueous phase, for dissolved and adsorbed chemical, and for dissolved salt [8, 9]:

$$\frac{\partial s}{\partial t} + \frac{\partial f(s,c)}{\partial x} = 0 \tag{4}$$

$$\frac{\partial (cs + a(c,\beta))}{\partial t} + \frac{\partial (cf(s,c))}{\partial x} = 0 \tag{5}$$

$$\frac{\partial (\beta s)}{\partial t} + \frac{\partial (\beta f(s,c))}{\partial x} = 0, \tag{6}$$

where s is the water saturation, f is the fractional flow function, a is the polymer sorption isotherm, and c and β are chemical and salt concentrations, respectively.

The fractional flow function (water flux) depends on the water saturation s and on the chemical concentration c. The typical S-shapes of fractional flow functions f under $c = \text{const}$ are shown in Figure 1. The fractional flow is a monotonically decreasing function of c. Sorption isotherms are linear for fixed salinity $a(c,\beta) = \Gamma(\beta)c$. The functions f and a are assumed to be bounded and smooth.

The system (4)–(6) is a hyperbolic 3×3 system of conservation laws with unknowns s, c, and β.

The displacement of oil by chemical slug corresponds to the following initial-boundary problem:

$$x = 0 \begin{cases} \beta = 0, & c = c_1, \quad s = s^L, \quad t < 1 \\ \beta = 0, & c = c_2, \quad s = s^L, \quad t > 1 \end{cases} \tag{7}$$

$$t = 0, \quad \beta = 1, \quad c = c_2, \quad s = s^R. \tag{8}$$

For $t < 1$, during continuous injection of chemical solution with different salinity, the solution of system (4)–(6) subject to initial-boundary conditions equations (7) and (8) coincides with the solution of the Riemann problem:

$$x = 0, \quad \beta = 0, \quad c = c_1, \quad s = s^L \tag{9}$$

$$t = 0, \quad \beta = 1, \quad c = c_2, \quad s = s^R. \tag{10}$$

The initial condition is denoted by R in Figure 1 and the boundary condition corresponding to injection of the slug is denoted as L.

Generally $c(x,0) = c_2 > 0$ is positive. Further in the text, the component with concentration c is called "chemical," while for the case of the absence of this component initially in the reservoir $c(x,0) = c_2 = 0$ we use the term "polymer."

The solution of the Riemann problem is self-similar: $s(x,t) = s(\xi)$, $c(x,t) = c(\xi)$, $\beta(x,t) = \beta(\xi)$, $\xi = x/t$ and it can be found in [37, 39, 40]. The solution of the problem (7) and (8) in the neighbourhood of the point $(0,1)$ in (x,t)-plane is also self-similar. The global solution of the system (4)–(6) subject to the initial-boundary conditions equations (7) and (8) is non-self-similar; it expresses the interactions between hyperbolic waves occurring from decays of Riemann discontinuities in points $(0,0)$ and $(0,1)$ in (x,t)-plane.

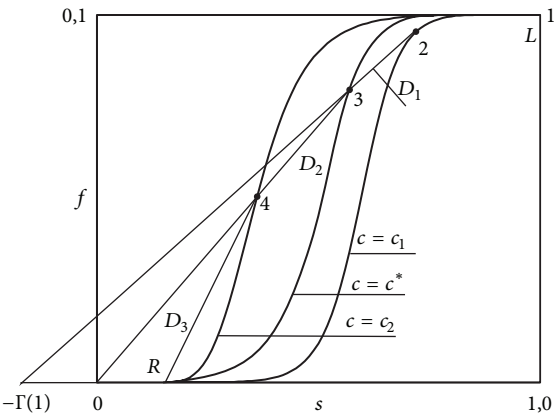

Figure 1: Fractional flow curves and Riemann problem solution, where c_1 is the slug concentration, c_2 is the initial concentration, and c^* is the intermediate concentration.

System of (4)–(6) subject to the initial and boundary conditions equations (9) and (10) is solved in Section 4 using the method so-called splitting procedure [35]. This procedure is explained in the next section.

3. Splitting Procedure

In the present section we briefly explain the splitting method for the solution of hyperbolic system of conservation laws equations (4)–(6).

3.1. Streamline/Potential Function and Auxiliary System. As it follows from divergent (conservation law) form of equation for mass balance for water (1) or (4), there does exist such a potential function $\varphi(x,t)$ that

$$\begin{aligned} s &= -\frac{\partial \varphi}{\partial x} \\ f &= \frac{\partial \varphi}{\partial t}; \end{aligned} \tag{11}$$

that is,

$$d\varphi = f dt - s dx, \tag{12}$$

$$\varphi(x,t) = \int_{0,0}^{x,t} f dt - s dx. \tag{13}$$

Equation (4) is merely the condition of equality of second derivatives of the potential φ as taken in different orders. It also expresses that the differential of the first order form equation (12) equals zero. The splitting procedure consists of changing the independent variables from (x,t) to (x,φ) in system (4)–(6). Figures 2 and 3 show the corresponding mapping [43, 44].

From fluid mechanics point of view, $\varphi(x,t)$ is a potential function, which equals the volume of fluid flowing through

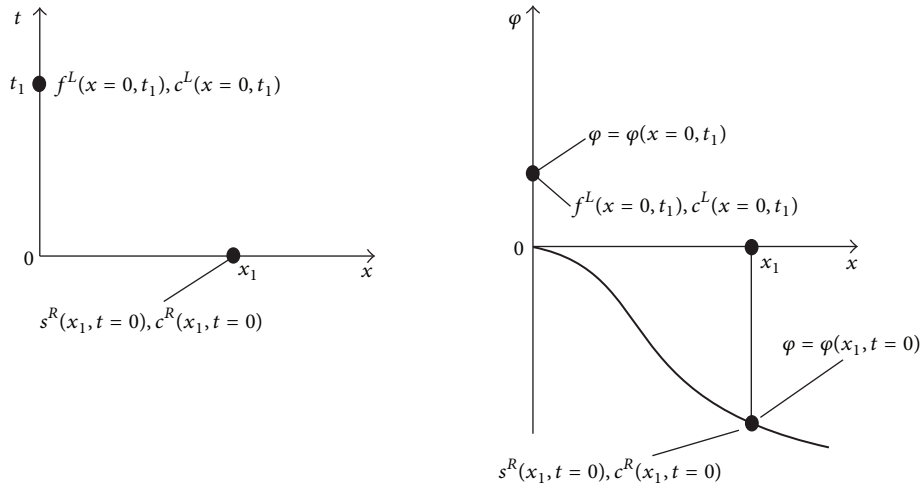

Figure 2: Introduction of potential function (Lagrangian coordinate) and mapping between independent variables.

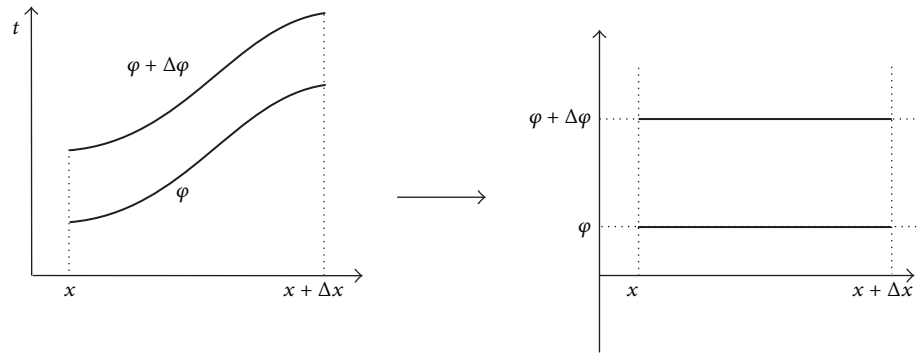

Figure 3: Derivation of mass balance equation in Eulerian and Lagrangian coordinate systems.

a trajectory connecting points $(0, 0)$ and (x, t). As it follows from (12), two streamlines in Figure 3 correspond to constant values of potential, that is, there is no flux through streamlines:

$$\varphi(x, t_2) - \varphi(x, t_1) = \int_{t_1}^{t_2} f(x, t)\, dt. \tag{14}$$

Equation (4) shows that the integral of (13) along the closed contour is equal to zero; that is, the volume of fluid flowing through a trajectory connecting points $(0, 0)$ and (x, t) is independent of trajectory and depends on end points only. The potential function equation (13) is determined in the way that one end of trajectory is fixed at point $(0, 0)$.

Let us derive the relationship between the elementary wave speeds of the system in (φ, x) coordinates and those of the large system in (t, x). Consider the trajectory $x = x_0(t)$ and its image $\varphi = \varphi_0(t)$ by the mapping equation (13):

$$\varphi_0(t) = \varphi(x_0(t), t). \tag{15}$$

Define the trajectory speeds as

$$D = \frac{dx}{dt}, \qquad V = \frac{dx}{d\varphi}. \tag{16}$$

Let us use x as a parameter for both curves $x = x_0(t)$ and $\varphi = \varphi_0(t)$. Taking derivation of both parts of (13) in x along trajectories and using speed definitions in (16), we obtain

$$\frac{1}{V} = \frac{f}{D} - s \tag{17}$$

from which follows the relationship between elementary wave speed in planes (x, t) and (x, φ):

$$D = \frac{f}{s + 1/V}. \tag{18}$$

For example, the eigenvalues of the system of equation in (t, x) plane λ_i and in (φ, x), Λ_i, are related by (Figure 4 [43, 44])

$$\Lambda_i(s, c) = \frac{f}{s + 1/\lambda_i}. \tag{19}$$

From now on, the independent variables (x, φ) are used in (4)–(6) instead of (x, t). Expressing the differential form dt from (12) as

$$dt = \frac{d\varphi}{f} + \frac{s\,dx}{f} \tag{20}$$

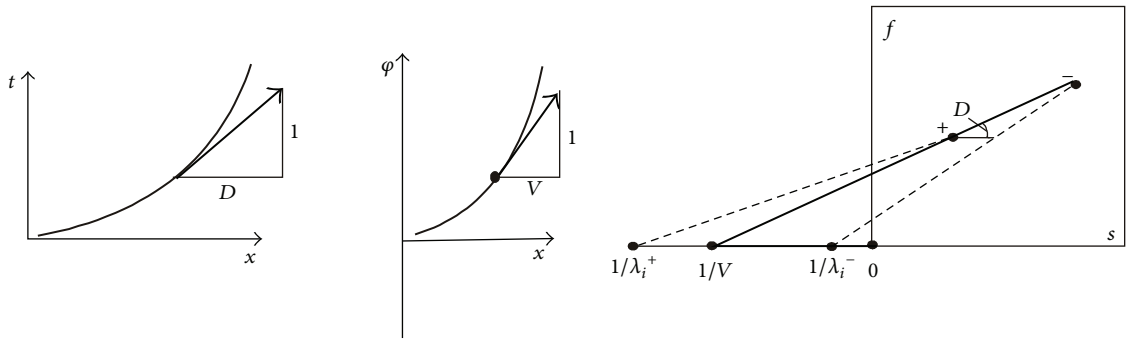

Figure 4: Speeds of a particle in Eulerian and Lagrangian coordinates.

and accounting for zero differential of the form dt

$$d^2t = 0 = \left[\frac{\partial}{\partial x}\left(\frac{1}{f}\right) - \frac{\partial}{\partial \varphi}\left(\frac{s}{f}\right)\right] dx d\varphi \tag{21}$$

we obtain the expression for (4) in coordinates (x, φ)

$$\frac{\partial (s/f)}{\partial \varphi} - \frac{\partial (1/f)}{\partial x} = 0. \tag{22}$$

So, (22) is the mass balance for water; that is, it is (4) rewritten in coordinates (x, φ).

Let us derive (5) in (x, φ) coordinates. The conservation laws for (5) in the integral form are

$$\oint_{\partial\Omega} (cf)\, dt - (cs + a)\, dx = 0, \tag{23}$$

where Ω is a closed domain $\Omega \subset R^2$, so the integral of (23) is taken over the closed contour.

Applying the definition of the potential function equation (13) into (23) yields

$$\oint_{\partial\Omega} c\,(f dt - s dx) - a dx = \oint_{\partial\Omega} c d\varphi - a dx = 0. \tag{24}$$

Tending the domain radius to zero and applying Green's theorem,

$$\frac{\partial a\,(c, \beta)}{\partial \varphi} + \frac{\partial c}{\partial x} = 0. \tag{25}$$

Now let us perform change of independent variables in (6) in (x, φ) coordinates as follows:

$$\iint \left(\frac{\partial (\beta s)}{\partial t} + \frac{\partial (\beta f\,(s, c))}{\partial x}\right) dx\, dt = \oint_{\partial\Omega} \beta s dx - \beta f\,(s, c)\, dt$$
$$= \oint \beta d\varphi = \iint \frac{\partial \beta}{\partial x} = 0. \tag{26}$$

Finally, the $(n + 1) \times (n + 1)$ system of conservation laws for two-phase n component chemical flooding in porous media with adsorption can be split into an $n \times n$ auxiliary system equations (25) and (26) and one independent lifting equation (22). The splitting is obtained from the change of independent variables (x, t) to (x, φ). This change of coordinates also transforms the water conservation law into the lifting equation. The solution of hyperbolic system (22), (25), and (26) consists of three steps: (1) solution of the auxiliary problem, (25), and (26) subject to initial and boundary conditions, (2) solution of the lifting equation, (22), and (3) determining time t for each point of the plane (x, φ) from (13).

The auxiliary system contains only equilibrium thermodynamic variables, while the initial system contains both hydrodynamic functions (phase's relative permeabilities and viscosities) and equilibrium thermodynamic variables.

The above splitting procedure is applied to the solution of displacement of oil by polymer slug with alternated salinity in the next section.

3.2. Formulation of the Splitting Problem for Two-Phase Flow with Polymers and Salt. Introducing new variables "density" F and "flux" U and applying the splitting technique, the 3×3 system (4)–(6) is transformed to the following form:

$$F = -\frac{s}{f}, \qquad U = \frac{1}{f} \tag{27}$$

$$\frac{\partial (F\,(U, c))}{\partial \varphi} + \frac{\partial (U)}{\partial x} = 0 \tag{28}$$

$$\frac{\partial a\,(c, \beta)}{\partial \varphi} + \frac{\partial c}{\partial x} = 0 \tag{29}$$

$$\frac{\partial \beta}{\partial x} = 0. \tag{30}$$

The auxiliary system equations (29) and (30) are independent of (28). The auxiliary system has thermodynamic nature since it contains only sorption function $a(c, \beta)$ and the unknowns are the component concentrations c and β. Equation (28) is the volume conservation for two immiscible phases. For the known auxiliary solution of (29) and (30), equation (28) is a scalar hyperbolic equation. Figure 5 shows the projection of the space of the large system into that of auxiliary system and the lifting procedure [43, 44].

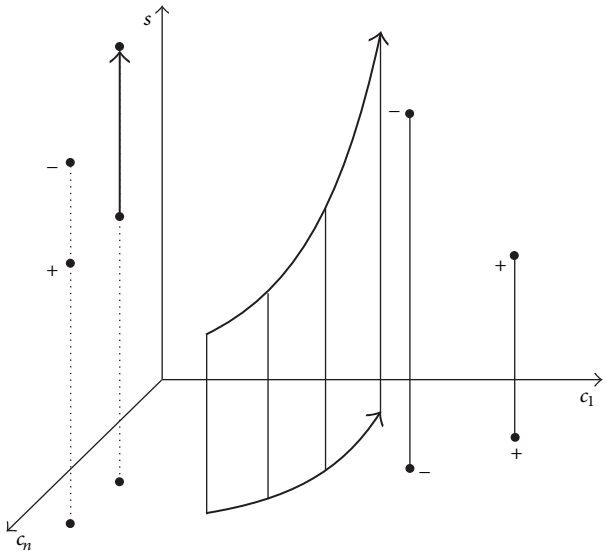

Figure 5: Projection of the space of the large system into that of auxiliary system and the lifting procedure using the solution of auxiliary system.

The boundary conditions for slug problem equation (7) are reformulated for coordinates (x, φ) as

$$x = 0 \begin{cases} \beta = 0, & c = c_1, \quad U = 1, \quad \varphi < 1 \\ \beta = 0, & c = c_2, \quad U = 1, \quad \varphi > 1. \end{cases} \tag{31}$$

Figure 2 shows how the initial and boundary conditions for the large system (4) and (6) are mapped into those for auxiliary system and the lifting equations (28)–(30).

The initial conditions for slug problem equation (8) are reformulated for coordinates (x, φ) as

$$\varphi = -\, s^R x, \quad \beta = 1, \quad c = c_2, \quad U = +\infty. \tag{32}$$

The solution of the Riemann problem for $\varphi < 1$ corresponds to the following initial and boundary conditions:

$$\begin{aligned} x = 0, \quad \beta = 0, \quad c = c_1, \quad U = 1 \\ \varphi = -s^R x, \quad \beta = 1, \quad c = c_2, \quad U = +\infty. \end{aligned} \tag{33}$$

4. Solution for the Riemann Problem

Let us discuss the solution of the problem equations (7) and (8) for $t < 1$, which is self-similar; that is, the boundary and initial conditions become (9) and (10).

The mass balance conditions on shocks which follow from the conservation law (Hugoniot-Rankine condition) form of the system (28)–(30) are

$$\sigma [U] = [F] \tag{34}$$

$$\sigma [c] = [a] \tag{35}$$

$$\sigma [\beta] = 0, \tag{36}$$

where σ is reciprocal to the shock velocity of (28)–(30). As salt and polymer concentration are connected by the thermodynamic equilibrium relationship $a(c, \beta)$, function a is discontinuous if c is discontinuous, so is β. Since F is a function of c and U, discontinuity of c and U yields discontinuity of F.

As it follows from equality (36), either $\sigma = 0$ or $[\beta] = 0$. From (34) and (35) it follows that if $\sigma = 0$, $[a] = 0$ and $[F] = 0$. If $[\beta] = 0$, from (35) and (36) it follows that $\sigma = [a]/[c]$ and $\sigma = [F]/[U]$; therefore it yields to $\sigma = [a]/[c] = [F]/[U]$. Finally from (34), if $[\beta] = 0$ and $[c] = 0$ this leads to $\sigma = [F]/[U]$.

The shock waves must obey the Lax evolutionary conditions [1–4, 9].

4.1. Solution for the Auxiliary System. The solution of auxiliary system is presented in Figure 6 by sequence of c-shock from point L into intermediate point and (c, β)-shock into point R. The corresponding formulae are as follows:

$$\begin{matrix} c(x, \varphi) \\ \beta(x, \varphi) \end{matrix} = \begin{cases} c_1, & \beta = 0, \quad \varphi > \Gamma(0)\, x \\ c^*, & \beta = 0, \quad 0 < \varphi < \Gamma(0)\, x \\ c_2, & \beta = 1, \quad -s^R x < \varphi < 0, \end{cases} \tag{37}$$

where the condition of continuity of function $a(c, \beta)$ on the shock with $\sigma = 0$, and (35) allows finding the intermediate concentration

$$c^* = \frac{\Gamma(1)}{\Gamma(0)} c_2. \tag{38}$$

4.2. Solution for the Lifting Equation. Figure 7 exhibits initial and boundary conditions for hydrodynamics lifting equation (28). Curves $F = F(U, c)$ are shown for constants $c = c_1$, $c = c_2$, and $c = c^*$; they are obtained from fractional flow curves $f = f(s, c)$ for the same constant values of concentration c. Point R corresponds to U tending to infinity and F tending to minus infinity, where the fractional flow f tends to zero. The tangent of the segment $(0, 0)$–(U, F) tends to $-s^R$.

The solution of lifting equation with known concentrations (37) is given by centred wave L–2, (c-U)-shock 2–>3, (β-c-U)-shock 3–>4, and U-shock 4–>R (Figure 7). The centred wave (L–2) is given by (39)

$$\frac{\varphi}{x} = \frac{\partial F\left(U^1, c_1\right)}{\partial U}. \tag{39}$$

Points 2 and 3 are determined by the condition of equality of U and c shock speeds:

$$\frac{\partial F\left(U_2, c_1\right)}{\partial U} = \frac{F_2\left(U_2, c_1\right) - F_3\left(U_3, c^*\right)}{U_2 - U_3} = \Gamma(0). \tag{40}$$

Point 4 is determined by condition of equality of the shock velocities c, β, and U:

$$F_3\left(U_3, c^*\right) = F_4\left(U_4, c_2\right) = 0. \tag{41}$$

Point 4 is connected to point R by U-shock:

$$\frac{F_4\left(U_4, c_2\right) - F_i\left(U_R, c_2\right)}{U_4 - U_i} = \frac{-s_4 f^R + s^R f_4}{f^R - f_4} = -s^R. \tag{42}$$

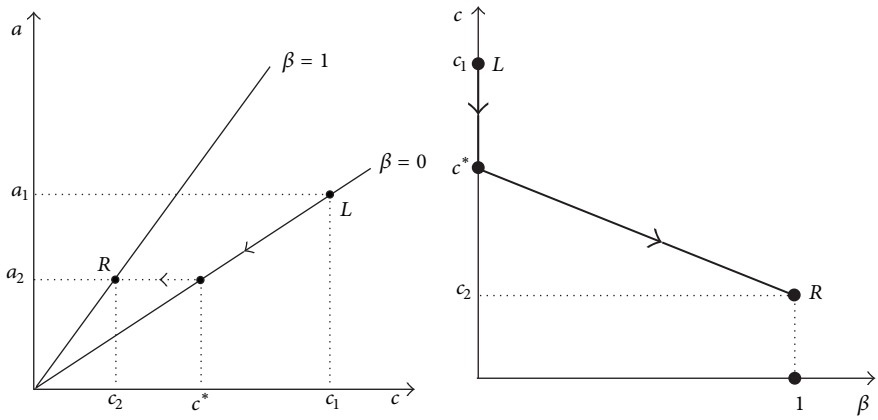

Figure 6: Solution of the auxiliary problem. (a) Adsorption isotherm for chemical for different water salinities and the Riemann problem solution; (b) Riemann problem solution on the plane of chemical concentration c and salinity β.

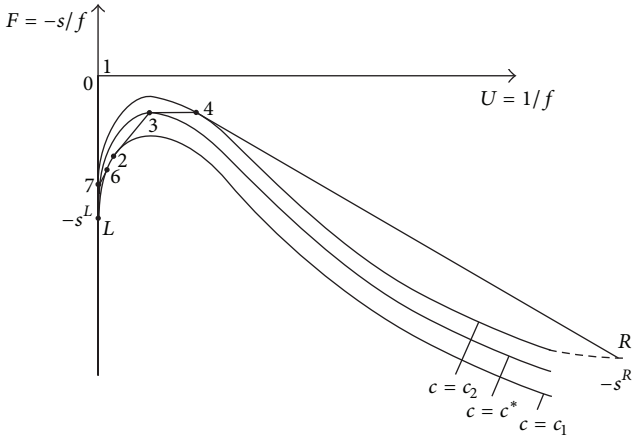

Figure 7: The image of the solution in (F-U) plane.

The solution of the Riemann problem equations (28)–(30) with free variables (x, φ) is given by the following formulae:

$$\begin{matrix} U(x,\varphi) \\ c(x,\varphi) \\ \beta(x,\varphi) \end{matrix} = \begin{cases} U^1\left(\dfrac{\varphi}{x}\right), & c_1, \quad \beta = 0, \quad \varphi > \Gamma(0)\, x \\ U_3, & c^*, \quad \beta = 0, \quad 0 < \varphi < \Gamma(0)\, x \\ U_4, & c_2, \quad \beta = 1, \quad -s^R x < \varphi < 0 \\ \infty, & c_2, \quad \beta = 1, \quad \varphi > -s^R x. \end{cases} \tag{43}$$

The expression $s = -UF(U, c)$ allows calculating saturation $s(x, \varphi)$:

$$\begin{matrix} s(x,\varphi) \\ c(x,\varphi) \\ \beta(x,\varphi) \end{matrix} = \begin{cases} s^1\left(\dfrac{\varphi}{x}\right), & c_1, \quad \beta = 0, \quad \varphi > \Gamma(0)\, x \\ s_3, & c^*, \quad \beta = 0, \quad 0 < \varphi < \Gamma(0)\, x \\ s_4, & c_2, \quad \beta = 1, \quad -s^R x < \varphi < 0 \\ s^R, & c_2, \quad \beta = 1, \quad \varphi < -s^R x. \end{cases} \tag{44}$$

Figure 8 shows the solution of the system (28)–(30) in (φ, x)-plane. For $\varphi < 1$, the solution is self-similar; the wave interaction occurs at $\varphi > 1$.

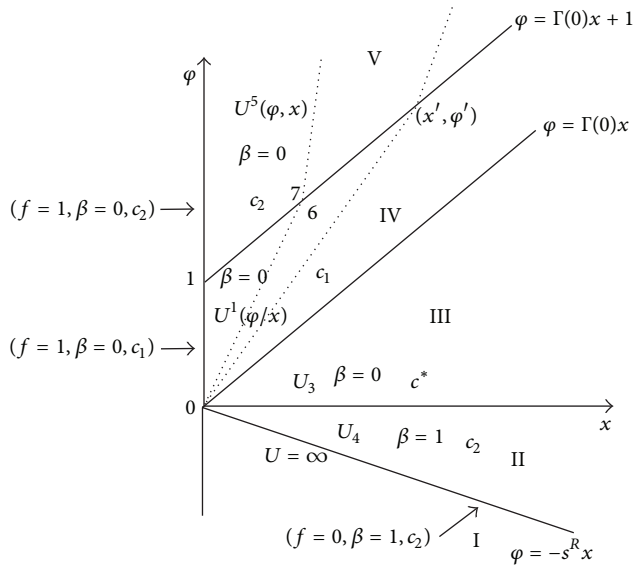

Figure 8: Solution of the auxiliary and lifting system for slug problem in (φ, x)-plane.

4.3. Inverse Mapping: Change of Variables from (φ, x) to (t, x). Time $t = t(x, \varphi)$ for solution is calculated from (12) along any path from point (x, φ) to point $(0, 0)$. The expression for time t in zone II is

$$t = \frac{1}{f_4}\int_0^{\varphi} d\varphi + \frac{s_4}{f_4}\int_0^{x} dx = \left(\frac{-s^R + s_4}{f_4}\right) x. \tag{45}$$

The expression for time t in zone III is

$$t = \frac{1}{f_3}\int_0^{\varphi} d\varphi + \frac{s_3}{f_3}\int_0^{x} dx = \frac{s_3}{f_3} x. \tag{46}$$

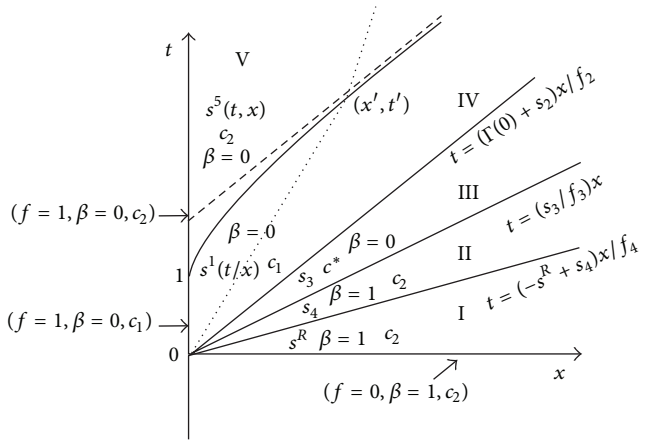

Figure 9: Non-self-similar solution of the problem for wave interactions in (x,t)-plane.

In zone IV, integral for calculation time, $t = \int_{0,0}^{x,\varphi}(d\varphi/f + sdx/f)$ is calculated along the characteristic in centred U-wave:

$$t = \frac{\varphi}{f\left(s^1(\varphi/x), c_1\right)} + \frac{s^1(\varphi/x)}{f\left(s^1(\varphi/x), c_1\right)}x. \tag{47}$$

Figure 9 shows the solution for the Riemann problem at $t < 1$; see Figure 10 for detailed description of the Riemann solution and profiles of unknown functions. Finally, the solution of the Riemann problem for the system (4)–(6) is

$$\begin{matrix} s(x,t) \\ c(x,t) \\ \beta(x,t) \end{matrix} = \begin{cases} s^1\left(\dfrac{t}{x}\right), & c_1, \quad \beta = 0, \quad t > \dfrac{\Gamma(0) + s_2}{f_2}x, \\ s_3, & c^*, \quad \beta = 0, \quad \dfrac{s_3}{f_3}x < t < \dfrac{\Gamma(0) + s_2}{f_2}x, \\ s_4, & c_2, \quad \beta = 1, \quad \dfrac{-s^R + s_4}{f_4}x < t < \dfrac{s_3}{f_3}x, \\ s^R, & c_2, \quad \beta = 1, \quad t < \dfrac{-s^R + s_4}{f_4}x. \end{cases} \tag{48}$$

5. Solution of the Slug Problem

Now let us solve the slug problem equations (31) and (32) for auxiliary system (29) and (30). The solution of Riemann problem at the point $(0,1)$ is given by c-shock with $c^- = c_2$ and $c^+ = c_1$ under constant β:

$$\begin{matrix} c(x,\varphi) \\ \beta(x,\varphi) \end{matrix} = \begin{cases} c_2, & \beta = 0, \quad \varphi > \Gamma(0)x + 1 \\ c_1, & \beta = 0, \quad \Gamma(0)x < \varphi < \Gamma(0)x + 1 \\ c^*, & \beta = 0, \quad 0 < \varphi < \Gamma(0)x \\ c_2, & \beta = 1, \quad -s^R x < \varphi < 0. \end{cases} \tag{49}$$

The solution of the auxiliary system is given by (49).

So, zone I in Figure 8 corresponds to initial conditions, the solution is given by point 4 in zone II, and point 3 holds in zone III. Centred waves equation (39) fills in zone IV. In zone V, $c = c_2$ and $\beta = 0$.

Now let us solve the lifting equation (28) with given $c(x,\varphi)$ and $\beta(x,\varphi)$.

The Hugoniot-Rankine condition for the rear slug front is

$$\frac{F\left(U^+, c_1\right) - F\left(U^-, c_2\right)}{U^+ - U^-} = \Gamma(0). \tag{50}$$

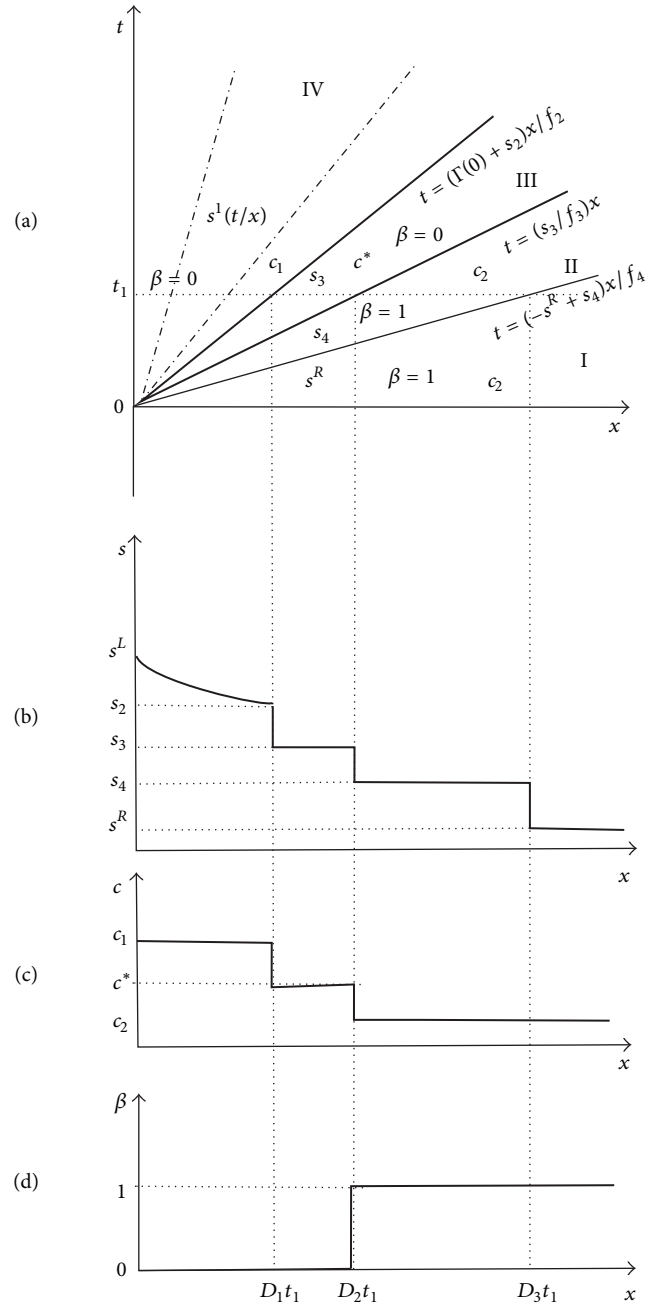

Figure 10: Solution of the Riemann problem: (a) trajectories of shock fronts and characteristic lines in (x,t)-plane; (b) saturation profile; (c) chemical concentration profile; (d) salinity profile.

U is constant along the characteristic lines behind the rear front

$$U_5(x,\varphi) = U^{-}\left(x',\varphi'\right), \tag{51}$$

where point (x',φ') is located on the rear front and is located on the same characteristic line with point (x,φ):

$$\frac{\varphi-\varphi'}{x-x'} = \frac{\partial F(U_5,c_1)}{\partial U}. \tag{52}$$

The solution of lifting equation $U(x,\varphi)$ is given by different formulae in zones I–V:

$$\begin{matrix} U(x,\varphi) \\ c(x,\varphi) \\ \beta(x,\varphi) \end{matrix} = \begin{cases} U_5(x,\varphi), & c_2, & \beta=0, & \varphi > \Gamma(0)\,x+1 \\ U^1\left(\dfrac{\varphi}{x}\right), & c_1, & \beta=0, & \Gamma(0)\,x<\varphi<\Gamma(0)\,x+1 \\ U_3, & c^*, & \beta=0, & 0<\varphi<\Gamma(0)\,x \\ U_4, & c_2, & \beta=1, & -s^R x<\varphi<0 \\ \infty, & c_2, & \beta=1, & \varphi>-s^R x, \end{cases} \tag{53}$$

where the equation for rear front of the chemical slug in the auxiliary plane is

$$\varphi = \Gamma(0)\,x+1. \tag{54}$$

Finally, the solution of auxiliary problem equation (53) allows calculating $t(x,\varphi)$ for zones I, II, ..., V. Let us start with determining time t along the rear front of the slug. The centred s-wave propagates ahead of the rear front

$$\frac{\varphi}{x} = \frac{f(s^+,c_1)-s^+f'(s^+,c_1)}{f'(s^+,c_1)}. \tag{55}$$

From (54), (55) follow the expression for $x_D(\varphi_D)$ in a parametric form:

$$x_D(s^+) = \frac{f'(s^+,c_1)}{f(s^+,c_1)-f'(s^+,c_1)(s^++\Gamma)} = \frac{f'(s^+,c_1)}{\Delta} \tag{56}$$

$$\begin{aligned} \varphi_D(s^+) &= \frac{f(s^+,c_1)-s^{1^+}f'(s^+,c_1)}{f(s^+,c_1)-f'(s^+,c_1)(s^++\Gamma)} \\ &= \frac{f(s^+,c_1)-s^{1^+}f'(s^+,c_1)}{\Delta}. \end{aligned} \tag{57}$$

Integration of the form (41) along the rear front gives

$$\begin{aligned} t_D &= \frac{\varphi}{f(s^+(\varphi,x),c_2)} + \frac{s^+(\varphi,x)}{f(s^+(\varphi,x),c_2)}x \\ t_D &= \frac{1}{f(s^+,c_1)-f'(s^+,c_1)\left(s^{1^+}+\Gamma\right)} = \frac{1}{\Delta}. \end{aligned} \tag{58}$$

Finally, the solution of the slug problem for the system (4)–(6) subject to initial and boundary conditions equations (7) and (8) is (Figure 9)

$$\begin{matrix} s(x,t) \\ c(x,t) \\ \beta(x,t) \end{matrix} = \begin{cases} s_5(t,x), & c_2, & \beta=0, & t>\dfrac{\Gamma(0)+s_5(t,x)}{f_5(s_5(t,x),c_2)}x+1 \\ s^1\left(\dfrac{t}{x}\right), & c_1, & \beta=0, & \dfrac{\Gamma(0)+s_2}{f_2}x<t<\dfrac{\Gamma(0)+s_5(t,x)}{f_5(s_5(t,x),c_2)}x+1 \\ s_3, & c^*, & \beta=0, & \dfrac{s_3}{f_3}x<t<\dfrac{\Gamma(0)+s_2}{f_2}x \\ s_4, & c_2, & \beta=1, & \dfrac{-s^R+s_4}{f_4}x<t<\dfrac{s_3}{f_3}x \\ s^R, & c_2, & \beta=1, & t<\dfrac{-s^R+s_4}{f_4}x. \end{cases} \tag{59}$$

Figure 11 presents trajectories of shock fronts in (x,t)-plane along with profiles of unknowns s, c, and β at typical moments.

Here the trajectory of the rear slug front $x_D = x_D(t)$ is given in a parametric form (Figure 12)

$$\begin{aligned} \frac{1}{x_D} &= s_B+\Gamma(0) \\ \frac{1}{t_D} &= f_A, \end{aligned} \tag{60}$$

where s_B is the abscissa of point B and f_A is the ordinate of point A (Figure 12). Equations (60) can be solved graphically. Straight line AB is a tangent to the fractional flow curve $c = c_1$, the tangent point in $s+$. The rear front position x_D is determined by the interval BC at the moment determined by AC.

6. Particular Case for the Polymer Absence in the Reservoir before the Injection

In reality, there is no chemical initially in the reservoir during the majority of chemical enhanced oil recovery applications; that is, $c(x,0) = 0$. For zero initial polymer concentration, the intermediate polymer concentration is equal to zero, so the points ahead and behind the β-shock coincide in planes (c,a) and (s,f). The particular simplified solution is (Figures 13 and 14)

$$\begin{matrix} s(x,t) \\ c(x,t) \\ \beta(x,t) \end{matrix} = \begin{cases} s_5(t,x), & c=0, & \beta=0, & t>\dfrac{\Gamma(0)+s_5(t,x)}{f_5(s_5(t,x),c_2)}x+1 \\ s^1\left(\dfrac{t}{x}\right), & c=c_1, & \beta=0, & \dfrac{\Gamma(0)+s_2}{f_2}x<t<\dfrac{\Gamma(0)+s_5(t,x)}{f_5(s_5(t,x),c_2)}x+1 \\ s_3, & c=0, & \beta=0, & \dfrac{s_3}{f_3}x<t<\dfrac{\Gamma(0)+s_2}{f_2}x \\ s_3, & c=0, & \beta=1, & \dfrac{-s^R+s_3}{f_3}x<t<\dfrac{s_3}{f_3}x \\ s^R, & c=0, & \beta=1, & t<\dfrac{-s^R+s_3}{f_3}x. \end{cases} \tag{61}$$

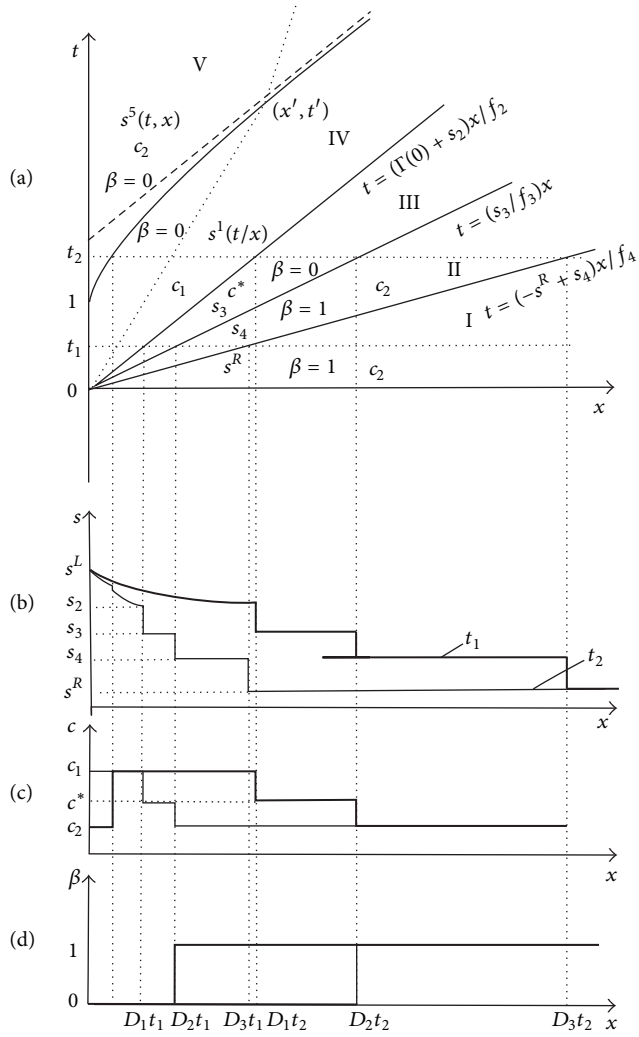

FIGURE 11: The solution of the slug injection problem: (a) trajectories of shock fronts and characteristic lines in (x, t)-plane; (b) saturation profile; (c) chemical concentration profile; (d) salinity profile.

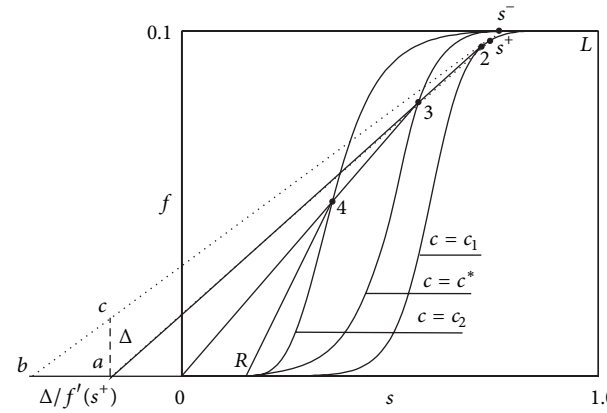

FIGURE 12: Solution of the lifting equation in (s, f)-plane.

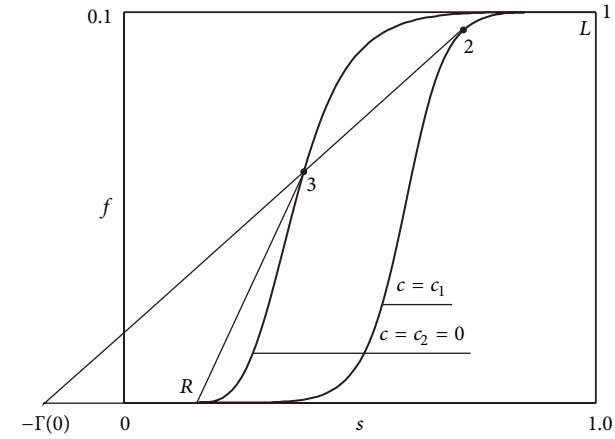

FIGURE 13: Solution of the lifting system in $(f\text{-}s)$ plane when $c_2 = 0$.

7. Fluid Mechanics Interpretation of the Solution

Following exact solution equations (4)–(9), let us describe structure of two-phase flow with chemical and salt additives during chemical slug injection.

During continuous injection $t < 1$, the solution of chemical slug injection coincides with that of continuous chemical injection. Initial conditions equation (10) is shown by point R that corresponds to low initial saturation and initial concentrations of chemical c_2 and of salt $\beta = 1$. The boundary condition at $x = 0$ corresponds to point L of injection of chemical solution with concentration c_1 and salinity $\beta = 0$. The path of Riemann problem solution in plane (s, f) consists of centred s-wave with injected chemical concentration and unity salinity, c-s-shock 2–>3, c, s, β-shock 3–>4, and s-shock 4–>R into initial point (Figure 1). Following nomenclature by Courant and Friedrichs [1] and Lake [9], the Riemann solution is L–2–>3–>4–>R. Shock 2–>3 in plane (c, β) is horizontal; shock 3–>4 is vertical (Figure 6(b)). Shock 2–>3 in plane (c, a) occurs along the sorption isotherm; shock 3–>4 is a horizontal jump from isotherm $c = c^*$ to that $c = c_2$ (Figure 7).

The trajectories of shocks 2–>3, 3–>4, and 4–> R are shown in Figure 7. Shock velocities are constant, so the trajectories are straight lines. Let us fix the position $x = 1$ of the raw of production wells. Before arrival of the front 4–> R at the moment $t = 1/D_3$, oil with fraction of water f^R and initial concentrations of chemical and salt is produced. After arrival of the front, water-oil mixture with water fraction f_4 and initial concentrations of chemical and salt is produced until the arrival of the 3–>4 front at the moment $t = 1/D_2$.

The corresponding profiles of saturation and concentrations are shown in Figure 10. The moment t_1 for profiles is fixed in Figure 10(a), allowing defining positions of all fronts in this moment. Corresponding profiles at that moment for saturation, chemical concentration, and salinity are shown in Figures 10(b), 10(c), and 10(d), respectively. The saturation profile consists of declining interval s^L–s_2 in s-wave, two oil-water banks s_3 and s_4, and the initial undisturbed zone s^R. The chemical concentration profile consists of injected value $c = c_1$ in s-wave, intermediate value c^* in s_3-bank, and initial

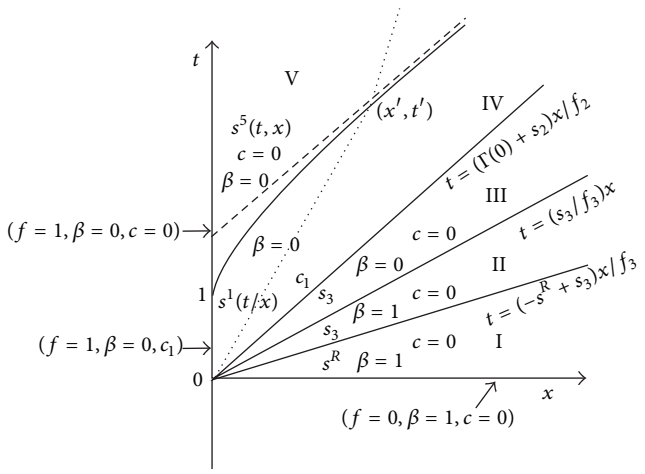

FIGURE 14: Non-self-similar solution of the problem for wave interactions in (x, t)-plane when $c_2 = 0$.

concentration c_2 in s_4-bank and in the initial zone. Salinity β-profile consists of injected value in zones IV and III and initial value in other zones.

Injection of water without chemical and with salinity $\beta = 0$ starts at the moment $t = 1$. The flow is not self-similar anymore. The front trajectories and profiles are shown in Figure 11. The solution for slug problem coincides with the solution for continuous injection ahead of the rear front $x_D(t)$. The profiles taken at the moment $t_1 < 1$ during continuous injection (Figure 11) coincide with those from Figure 10.

The propagation of the rear slug front from the beginning of water drive injection in the reservoir is shown in Figure 11(a). The rear front velocity decreases reaching the value of the forward front D_3 when time tends to infinity. The slug thickness increases and stabilises.

The profiles are shown in Figures 11(b), 11(c), and 11(d) for the moment after the beginning of slug injection $t_2 > 1$. Saturation decreases in a simple wave behind the rear slug front, jumps down on the front, decreases in centred s-wave in the slug, and is constant in zones II, II, and I. Chemical slug dissolution during the water drive injection is shown in Figure 11(c). There does occur the full concentration shock from zero behind the read slug front to the injected value in the slug. Further in the reservoir, there does appear a zone of intermediate chemical concentration c^* in the bank s_3. The concentration is equal to its initial value in banks s_4 and in the initial zone. So, dissolution of slug occurs in the initial water by formation of oil-water bank s_3 with lower chemical concentration. Salinity changes by full shock on the front between zones III and II.

8. Conclusions

Application of the splitting method to 3×3 conservation law system describing two-phase four-component flow in porous media allows drawing the following conclusions.

(1) The method of splitting between hydrodynamics and thermodynamics in system of two-phase multicomponent flow in porous media allows obtaining an exact solution for non-self-similar problem of displacement of oil by chemical slug with different water salinity for the case of linear polymer adsorption affected by water salinity.

(2) The solution consists of explicit formulae for water saturation and polymer and salt concentrations in the continuity domains and of implicit formulae for front trajectories.

(3) First integrals for front trajectories allow for graphical interpretation at the hodograph plane, yielding a graphical method for finding the front trajectories.

(4) For linear sorption isotherms, the solution depends on three fractional flow curves that correspond to initial reservoir state R, injected fluid L, and an intermediate curve for intermediate polymer concentration and injected salinity; the value for intermediate polymer concentration is the part of exact solution.

(5) For linear sorption isotherms, the only continuous wave is s-wave with constants c and β; concentrations c and β change only across the fronts by jumps; thus the solution of any problem with piece-wise constant initial and boundary conditions is reduced to interactions between s-waves and shocks.

(6) Introduction of salinity dependency for sorption of the chemical introduces the intermediate (c, β)-shock into the solution of the Riemann problem; this shock interacts with s-wave and concentration shocks in the solution of any problem with piece-wise constant initial and boundary conditions.

(7) The exact solution shows that the injected chemical slug dissolves in the connate reservoir water rather than in the chemical-free water injected after the slug.

Conflict of Interests

The authors declare that there is no conflict of interests regarding the publication of this paper.

Acknowledgments

Long-term cooperation in hyperbolic systems and fruitful discussions with Professors A. Shapiro (Technical University of Denmark), Y. Yortsos (University of Southern California), A. Roberts (University of Adelaide), A. Polyanin (Russian Academy of Sciences), M. Lurie, and V. Maron (Moscow Oil and Gas Gubkin University) are gratefully acknowledged. The reviewers are gratefully acknowledged for their critical comments yielding to significant improvement of the text.

References

[1] R. Courant and K. O. Friedrichs, *Supersonic Flow and Shock Waves*, Springer, New York, NY, USA, 1976.

[2] I. M. Gel'fand, "Some problems in the theory of quasi-linear equations," *Uspekhi Matematicheskikh Nauk*, vol. 14, no. 2, pp. 87–158, 1959.

[3] A. G. Kulikovskii, N. V. Pogorelov, and A. Yu. Semenov, *Mathematical Aspects of Numerical Solution of Hyperbolic Systems*, vol. 118, Chapman & Hall/CRC Press, Boca Raton, Fla, USA, 2001.

[4] B. L. Rozhdestvenski and N. N. Ianenko, *Systems of Quasilinear Equations and Their Application to the Dynamics of Gases*, vol. 55, American Mathematical Society, 1983.

[5] G. B. Whitham, *Linear and Nonlinear Waves*, vol. 42, John Wiley & Sons, Hoboken, NJ, USA, 2011.

[6] A. Kulikovskii and E. Sveshnikova, *Nonlinear Waves in Elastic Media*, CRC Press, Boca Raton, Fla, USA, 1995.

[7] J. D. Logan, *An Introduction to Nonlinear Partial Differential Equations*, vol. 93, John Wiley & Sons, Hobokon, NJ, USA, 2010.

[8] H. K. Rhee, R. Aris, and N. R. Amundson, *First-Order Partial Differential Equations: Theory and Application of Hyperbolic Systems of Quasilinear Equations*, Dover, New York, NY, USA, 2001.

[9] L. W. Lake, *Enhanced Oil Recovery*, Prentice Hall, Englewood Cliffs, NJ, USA, 1989.

[10] P. Bedrikovetsky, *Mathematical Theory of Oil and Gas Recovery: With Applications to Ex-USSR Oil and Gas Fields*, Kluwer Academic Publishers, Boston, Mass, USA, 1993.

[11] T. Johansen, A. Tveito, and R. Winther, "A Riemann solver for a two-phase multicomponent process," *SIAM Journal on Scientific and Statistical Computing*, vol. 10, no. 5, pp. 846–879, 1989.

[12] T. Johansen and R. Winther, "The Riemann problem for multicomponent polymer flooding," *SIAM Journal on Mathematical Analysis*, vol. 20, no. 4, pp. 908–929, 1989.

[13] R. Johns and F. M. Orr Jr., "Miscible gas displacement of multicomponent oils," *SPE Journal*, vol. 1, pp. 39–50, 1996.

[14] F. M. Orr Jr., *Theory of Gas Injection Processes*, Tie-Line Publications, Copenhagen, Denmark, 2007.

[15] P. Bedrikovetsky, "Displacement of oil by a chemical slug with water drive," *Journal of Fluid Dynamics*, vol. 3, pp. 102–111, 1982.

[16] V. G. Danilov and D. Mitrovic, "Smooth approximations of global in time solutions to scalar conservation laws," *Abstract and Applied Analysis*, vol. 2009, Article ID 350762, 26 pages, 2009.

[17] F. Fayers, "Some theoretical results concerning the displacement of a viscous oil by a hot fluid in a porous medium," *Journal of Fluid Mechanics*, vol. 13, pp. 65–76, 1962.

[18] E. L. Claridge and P. L. Bondor, "A graphical method for calculating linear displacement with mass transfer and continuously changing mobilities," *SPE Journal*, vol. 14, no. 6, pp. 609–618, 1974.

[19] G. J. Hirasaki, "Application of the theory of multicomponent, multiphase displacement to three-component, two-phase surfactant flooding," *SPE Journal*, vol. 21, no. 2, pp. 191–204, 1981.

[20] G. A. Pope, L. W. Lake, and F. G. Helfferich, "Cation exchange in chemical flooding—part 1: basic theory without dispersion," *SPE Journal*, vol. 18, no. 6, pp. 418–434, 1978.

[21] G. I. Barenblatt, V. M. Entov, and V. M. Ryzhik, *Theory of Fluid Flows through Natural Rocks*, Kluwer Academic Publishers, London, UK, 1989.

[22] G. S. Braginskaya and V. M. Entov, "Nonisothermal displacement of oil by a solution of an active additive," *Fluid Dynamics*, vol. 15, no. 6, pp. 873–880, 1980.

[23] O. Dahl, T. Johansen, A. Tveito, and R. Winther, "Mulicomponent chromatography in a two phase environment," *SIAM Journal on Applied Mathematics*, vol. 52, no. 1, pp. 65–104, 1992.

[24] T. Johansen, Y. Wang, F. M. Orr Jr., and B. Dindoruk, "Four-component gas/oil displacements in one dimension—part I: global triangular structure," *Transport in Porous Media*, vol. 61, no. 1, pp. 59–76, 2005.

[25] T. Johansen and R. Winther, "The solution of the Riemann problem for a hyperbolic system of conservation laws modeling polymer flooding," *SIAM Journal on Mathematical Analysis*, vol. 19, no. 3, pp. 541–566, 1988.

[26] P. Bedrikovetsky and M. Chumak, "Riemann problem for two-phase four-and morecomponent displacement (Ideal Mixtures)," in *Proceedings of the 3rd European Conference on the Mathematics of Oil Recovery*, 1992.

[27] V. Entov, F. Turetskaya, and D. Voskov, "On approximation of phase equilibria of multicomponent hydrocarbon mixtures and prediction of oil displacement by gas injection," in *Proceedings of the 8th European Conference on the Mathematics of Oil Recovery*, 2002.

[28] V. Entov and D. Voskov, "On oil displacement by gas injection," in *Proceedings of the 7th European Conference on the Mathematics of Oil Recovery*, 2000.

[29] R. T. Johns, B. Dindoruk, and F. M. Orr Jr., "Analytical theory of combined condensing/vaporizing gas drives," *SPE Advanced Technology Series*, vol. 1, no. 2, pp. 7–16, 1993.

[30] C. Wachmann, "A mathematical theory for the displacement of oil and water by alcohol," *Old SPE Journal*, vol. 4, pp. 250–266, 1964.

[31] A. Zick, "A combined condensing/vaporizing mechanism in the displacement of oil by enriched gases," in *Proceedings of the SPE Annual Technical Conference and Exhibition*, 1986.

[32] O. M. Alishaeva, V. M. Entov, and A. F. Zazovskii, "Structures of the conjugate saturation and concentration discontinuities in the displacement of oil by a solution of an active material," *Journal of Applied Mechanics and Technical Physics*, vol. 23, no. 5, pp. 675–682, 1982.

[33] S. Geiger, K. S. Schmid, and Y. Zaretskiy, "Mathematical analysis and numerical simulation of multi-phase multi-component flow in heterogeneous porous media," *Current Opinion in Colloid and Interface Science*, vol. 17, no. 3, pp. 147–155, 2012.

[34] K. S. Schmid, S. Geiger, and K. S. Sorbie, "Analytical solutions for co- and counter-current imbibition of sorbing, dispersive solutes in immiscible two-phase flow," in *Proceedings of the 12th European Conference on the Mathematics of Oil Recovery*, 2012.

[35] A. P. Pires, P. G. Bedrikovetsky, and A. A. Shapiro, "A splitting technique for analytical modelling of two-phase multicomponent flow in porous media," *Journal of Petroleum Science and Engineering*, vol. 51, no. 1-2, pp. 54–67, 2006.

[36] A. P. Pires, *Splitting between thermodynamics and hydrodynamics in the processes of enhanced oil recovery [Ph.D. thesis]*, Laboratory of Petroleum Exploration and Production, North Fluminense State University UENF, 2003.

[37] H.-K. Rhee, R. Aris, and N. R. Amundson, "On the theory of multicomponent chromatography," *Philosophical Transactions of the Royal Society A*, vol. 267, no. 1182, pp. 419–455, 1970.

[38] V. M. Entov and A. F. Zazovskii, "Displacement of oil by a solution of an active and a passive additive," *Fluid Dynamics*, vol. 17, no. 6, pp. 876–884, 1982.

[39] C. B. Cardoso, R. C. A. Silva, and A. P. Pires, "The role of adsorption isotherms on chemical-flooding oil recovery,"

in *Proceedings of the SPE Annual Technical Conference and Exhibition (ATCE '07)*, pp. 773–780, November 2007.

[40] B. Vicente, V. Priimenko, and A. Pires, "Streamlines simulation of polymer slugs injection in petroleum reservoirs," in *Proceedings of the SPE Latin America and Caribbean Petroleum Engineering Conference*, 2012.

[41] S. Oladyshkin and M. Panfilov, "Splitting the thermodynamlics and hydrodynamics in compositional gas-liquid flow through porous reservoirs," in *Proceedings of the 10th European Conference on the Mathematics of Oil Recovery*, 2006.

[42] P. M. Ribeiro and A. P. Pires, "The displacement of oil by polymer slugs considering adsorption effects," in *Proceedings of the SPE Annual Technical Conference and Exhibition (ATCE '08)*, pp. 851–865, September 2008.

[43] P. Bedrikovetski, A. Pires, and A. Shapiro, "Conservation law system for two-phase n-component flow in porous media: splitting between thermodynamics and hydrodynamics," in *Proceedings of the 10th International Congress on Hyperbolic Problems Theory*, 2004.

[44] A. Pires, P. Bedrikovetsky, and A. Shapiro, "Splitting between thermodynamics and hydrodynamics in compositional modelling," in *Proceedings of the 9th European Conference on the Mathematics of Oil Recovery*, 2004.

Hindawi Publishing Corporation
Abstract and Applied Analysis
Volume 2014, Article ID 367627, 6 pages
http://dx.doi.org/10.1155/2014/367627

Research Article

Reservoir Sedimentation Based on Uncertainty Analysis

Farhad Imanshoar,[1] Afshin Jahangirzadeh,[2] Hossein Basser,[2] Shatirah Akib,[2] Babak Kamali,[2] Mohammad Reza M. Tabatabaei,[3] and Masoud Kakouei[4]

[1] *Faculty of Civil Engineering, University of Tabriz, Tabriz, Iran*
[2] *Department of Civil Engineering, Faculty of Engineering, University of Malaya, 50603 Kuala Lumpur, Malaysia*
[3] *Faculty of Water and Environment Engineering, Power and Water University of Technology, Tehran, Iran*
[4] *Department of Computer Engineering, Faculty of Engineering, Payam Noor University, Astaneh Ashrafieh, Iran*

Correspondence should be addressed to Afshin Jahangirzadeh; afshin.jk@gmail.com

Received 16 September 2013; Revised 23 January 2014; Accepted 27 January 2014; Published 4 March 2014

Academic Editor: Mohamed Fathy El-Amin

Reservoir sedimentation can result in loss of much needed reservoir storage capacity, reducing the useful life of dams. Thus, sufficient sediment storage capacity should be provided for the reservoir design stage to ensure that sediment accumulation will not impair the functioning of the reservoir during the useful operational-economic life of the project. However, an important issue to consider when estimating reservoir sedimentation and accumulation is the uncertainty involved in reservoir sedimentation. In this paper, the basic factors influencing the density of sediments deposited in reservoirs are discussed, and uncertainties in reservoir sedimentation have been determined using the Delta method. Further, Kenny Reservoir in the White River Basin in northwestern Colorado was selected to determine the density of deposits in the reservoir and the coefficient of variation. The results of this investigation have indicated that by using the Delta method in the case of Kenny Reservoir, the uncertainty regarding accumulated sediment density, expressed by the coefficient of variation for a period of 50 years of reservoir operation, could be reduced to about 10%. Results of the Delta method suggest an applicable approach for dead storage planning via interfacing with uncertainties associated with reservoir sedimentation.

1. Introduction

Reservoir sedimentation is filling of the reservoir with sediment carried into the dam reservoir by streams [1]. Understanding the reservoir sedimentation process is of fundamental significance in hydrosystems engineering. Sediment inflow and deposition can affect the function of dam reservoirs. Therefore, it is of crucial importance to estimate the sedimentation rate and the period of time before sediment accumulation could interfere with the useful functioning of the reservoir. When designing a reservoir, sufficient sediment storage capacity should be taken into account so that sediment accumulation will not impair the function of the reservoir during the useful operational-economic life of the project [2].

Sedimentation process in a reservoir is quite complex because it is often influenced by several factors including hydrological fluctuations in water and sediment inflow, variation in sediment particle size, reservoir operation cycle, and physical controls such as size and shape of the reservoir [3, 4]. Other factors that may be important for some reservoirs are vegetation cover in upper reaches, turbulence and density currents, erosion of deposited sediments, and sluicing of sediment through the dam.

Once the volume of sediment inflow to a reservoir has been determined, effects of the sedimentation process over the life span and the daily operation of the reservoir must be evaluated. In the design of a reservoir, the mean annual sediment inflow, the efficacy of the reservoir in trapping sediment, the ultimate density of the deposited sediment, and the distribution of the sediment within the reservoir are among the most important factors that must be considered. Additional storage volume equal to the volume of the sediment expected to be deposited during the life of the reservoir is often included in the original design to prevent premature loss of storage capacity. The United States Bureau of Reclamation [2] suggests using a 100-year period of

economic analysis and sediment accumulation in a reservoir. Less than 100 years of sediment accumulation may also be suggested in cases where the economic analysis justifies lesser allocation. However, there is uncertainty associated with the factors involved in reservoir sedimentation. The sources of uncertainty can be generally classified into two main groups: first group is natural factors (the natural factors are related to natural happenings and conditions), which include meteoric factors, changes in watershed hydraulic characteristics, and natural disaster occurrences. Second group is unnatural factors (the unnatural factors are caused by human-induced activities) which include land-use changes and management strategies [3, 4].

On the whole, natural variability and model related uncertainties constantly have an effective role in accuracy of determining the amount of sediment deposition in the reservoir on a yearly basis, the accumulated sediment volume in the reservoir over the number of years of reservoir operation, and the time it takes for the accumulation of a certain amount of sediment in the reservoir (e.g., a fraction of the death capacity or a fraction of the total capacity of the reservoir) [3, 5, 6]. In this context, the response of the system to variable, uncertain inputs can be statistically quantified through uncertainty analysis [7].

Salas and Shin [3] analyzed the uncertainty of many factors involved in reservoir sedimentation. These factors, called "stochastic inputs," include those inputs associated with annual suspended and bed load sediment rating curves, those associated with the type of incoming sediment, those associated with the trap efficacy of a reservoir, and those associated with the variability of annual stream flow. Intrinsically, these inputs are of random phenomena [7, 8]. This type of variability is always associated with the factors involved in reservoir sedimentation and may not be controlled [3, 9].

This study focuses on identifying the basic factors influencing the density of sediments deposited in the reservoirs and determining uncertainties in reservoir sedimentation using the Delta method. A case study of Kenny Reservoir in the White River Basin in northwestern Colorado [3, 9] was designated to determine the density of deposits in the reservoir and the coefficient of variation. Thus, the present study is an attempt to ascertain the accuracy of determining the mean density of accumulated sediments after a certain period of time by calculating the coefficient of variation [9].

2. Factors Contributing to Reservoir Sedimentation

2.1. Natural Factors. Natural factors affecting reservoir sedimentation are those intrinsic aspects of the world's water hydrologic cycle and the rate of land surface change. These factors are meteoric factors (e.g., precipitation, snow, hail, and wind) [3], watershed topography and geology, vegetation cover, natural disasters (e.g., floods and droughts), and the hydraulic condition of the reservoir (e.g., the ratio of reservoir capacity to inflow volume, the shape of the reservoir, specifications of bottom outlets, the condition of reservoir operation, the trap efficiency of the reservoir, flow turbulence, and physical properties of inflow) [11].

Table 1: Sediment classification according to size.

Sediment type	Size range (mm)
Clay	<0.004
Silt	0.004 to 0.062
Sand	0.062 to 2

2.2. Unnatural (Human-Induced) Factors. Overexploitation of forests, destruction of grasslands, and land-use changes induced by human activities affect water resources and often intensify soil erosion which consequently increase reservoir sedimentation rates in different ways. Management strategies, as a human-related factor, can also directly affect the sedimentation process in reservoir dams. The main deficiencies in this field could be the propensity to store water from wet to dry seasons, the tendency to produce more hydropower energy without considering sedimentary aspects, incorrect design of water works, and shortcomings of operation manuals [11, 12].

3. Methods

3.1. Density of Deposited Sediments. Basic factors influencing the density of sediments deposited in a reservoir are (i) the reservoir operation and management, (ii) the texture and size of deposited sediment particles, and (iii) the compaction or consolidation rate of deposited sediments [2, 11]. Among these, the operational plan of the reservoir is probably the most significant factor [2, 3, 5]. Sediments deposited in a reservoir are subject to considerable drawdown with the result that the sediments may be exposed for long periods, and therefore undergo greater consolidation. On the other hand, reservoirs which operate under a fairly stable pool do not allow the deposits to dry out and consolidate as much. The size of the incoming sediment particles has a significant effect on density of deposits. Sediment deposits composed of silt and sand have higher densities than those in which clay predominates [2]. The classification of sediments according to size is proposed by the American Geophysical Union (Table 1).

Accumulation of new sediment deposits on top of previously deposited sediments often changes the density of earlier deposits. The consolidation process affects the average density over the estimated life of the reservoir, such as for a 100-year period. Therefore, the influence of reservoir operation is the most significant factor due to its effect on the amount of consolidation that can take place in the clay fraction of the deposited material when a reservoir is subject to considerable drawdown. Strand and Pemberton [10] classified reservoir operations (Table 2).

Abovementioned reservoir types for operation were assessed by engineering judgment. Selection of the proper reservoir operation can usually be made through the operation study prepared for the reservoir [10]. This concept

Table 2: Classification of reservoir operation [10].

No.	Reservoir operation
1	Sediment always submerged or nearly submerged
2	Normally moderate to considerable reservoir drawdown
3	Reservoir normally empty
4	Riverbed sediments

depends on hydraulic conditions of the intake and sediment trap coefficient of the reservoir. For example, for reservoir type 1, released water of dam is clear or near to clear; therefore the sediments are always submerged or nearly submerged while for reservoir type 4, running river flow passes the dam and, in other words, the released water is debris flow. The other two operations are judged in this manner.

The size of sediment particles entering the reservoir also affects the density, as shown by the variation in initial masses. Once the reservoir operation number has been assessed, the density of the sediment deposits can be estimated using (1) [2, 10]. Consider

$$W_0 = W_C P_C + W_m P_m + W_S P_S, \quad (1)$$

where W_0 is unit weight (kg/m^3), P_C, P_m, and P_S are the percentages of clay, silt, and sand in the inflowing sediment, respectively, and W_C, W_m, and W_S are coefficients of unit weight of clay, silt, and sand, respectively (Table 3) [2, 10].

Sediments accumulate in the reservoir in each of the T years of operation, and each year's deposit will have a different compaction time, which is significantly dependent on the type of reservoir operation and the size of the incoming sediment particles. Thus, density of sediments deposited during T years of reservoir operation can be estimated as an approximation of the integral of (2) [5, 13]:

$$W_T = W_0 + 0.4343K\left[\frac{T}{T-1}(\ln T) - 1\right], \quad T > 1, \quad (2)$$

where W_T is the average density after T years of operation, W_0 is the initial unit weight (density) derived from (1), and K is consolidation constant dependent on type of reservoir operation and sediment size distribution (Table 4). In practice, a weighted average of consolidation constants must be used for a mixture of sediment (3) [2, 5, 13]:

$$K_i = K_C P_C + K_m P_m + K_S P_S. \quad (3)$$

3.2. Analysis of Uncertainty of Reservoir Sedimentation. When designing hydrosystems, it is essential to take uncertainty into consideration since many influences are functionally related to a number of uncertain variables. For instance, as already noted, natural factors and unnatural factors result in a complex and uncertain procedure for reservoir sedimentation trend, and hence sediment density is subject to uncertainty. On the other hand, optimal design of reservoir geometry (dead storage and live storage) is a fundamental goal for hydraulic engineers.

Table 3: Initial unit weight of incoming sediments based on reservoir operation and type of sediments.

Operation type	Initial unit weight (kg/m^3)		
	Clay-W_C	Silt-W_m	Sand-W_S
1	416	1120	1550
2	561	1140	1550
3	641	1150	1550
4	961	1170	1550

Table 4: K values for incoming sediments based on reservoir operation and type of sediment [2].

Operation type	K values for SI units		
	Clay-K_C	Silt-K_m	Sand-K_S
1	256	91	0
2	135	29	0
3, 4	0	0	0

Several methods for uncertainty analysis have been developed and applied in water resources engineering. The most widely used methods are Monte Carlo Simulation (MCS) and first-order analysis (FOA) [3, 5]. The latter is based on linearization of the functional relationship which relates a dependent random variable and a set of independent random variables by Taylor series expansion. The FOA method has been applied to several water resource and environmental engineering problems including uncertainty [5, 6, 14]. For example, Tehrani et al. benefited from Latin Hypercube Sampling method to estimate accumulated reservoir sediment volume in Shahr-Chai Dam by FOA method and the sensitivity analysis showed that suspended sediment and bed load, followed by annual stream flow, were the most important factors influencing the accumulated reservoir sedimentation volume, for both the total period and the wet and dry time periods, and trap efficiency and percentage of sediments are the next most important [5]. Furthermore, Hall used FOA method to extend a fuzzy set theory and possibility theory for coastal hydraulics [14].

In MCS method, stochastic inputs are generated from their probability distributions and are then entered into empirical or analytical models of the underlying physical process involved in generating stochastic outputs. The generated outputs are then analyzed statistically to quantify the uncertainty of the output [15, 16]. Salas and Shin [3] analyzed the uncertainty of annual reservoir sedimentation volume (RSV) and accumulated reservoir sedimentation volume (ARSV) based on Monte Carlo Simulation (MCS) and Latin Hypercube Sampling (LHS). The procedures were applied to the case of Kenny Reservoir in the White River basin in Colorado. The results indicated that the variability of RSV may be described by a Gamma-2 distribution for which the coefficient of variation was of the order of 65% [3]. This rate of variation for determining annual reservoir sedimentation volume makes a serious challenge to design or manage the reservoir operation.

Although the abovementioned studies developed methodical outcomes in hydrosystem analysis especially in alluvial hydraulics uncertainties, in these researches the density of sediments which were deposited in the reservoir was assumed constant. The sediments, which accumulate in the reservoir by passing the time, will have a different compaction; therefore their density will change depending on variety of factors. Consequently, in this paper in order to develop former studies, it is aimed to focus on identifying the basic factors which affect the density of sediments deposited in the reservoirs. Also uncertainties in reservoir sediments density are determined using the Delta method.

3.3. Analysis of Uncertainty (Delta Method). First-order analysis of uncertainties, which is also known as the Delta method, is a rather straightforward and useful technique for the approximation of such uncertainties. This method is widely used in many fields of engineering due mainly to its ease of application to a wide variety of problems [17–19]. Mays stated that Delta method application is quite popular in many fields of engineering and, as a result, he developed a risk-based solution for storm sewers' design [17]. Imanshoar et al. used Delta method to study trophic state index (TSI) uncertainty and its variation for Miyun Reservoir in China. Their research showed that the average TSI number and its variation for mentioned reservoir oscillated between Mesotrophic to Eutrophic category [18]. Furthermore, Resende et al. applied Delta method to estimate the mapping, from uncertainty in discrete choice model parameters to uncertainty of profit outcomes, and they identified the estimated α-profit as a closed form function of design decision variables in computer science [19].

First-order analysis is often used to assess the uncertainty in a deterministic model formulation involving parameters which are uncertain (i.e., not known with certainty). First-order analysis specifically enables us to determine the mean and variance of a random variable which is functionally related to several other variables, some of which are random. Thus, using first-order analysis, the combined effect of uncertainty in a model formulation, and the use of uncertain parameters can be assessed [14, 17]. Consider a random variable y that is a function of k random variables (4) (multivariate case) [17]:

$$y = G\left(x_1, x_2, \ldots, x_j\right) = G\left(x_i\right), \quad i = 1 \sim j. \tag{4}$$

This function can be expressed as a deterministic equation such as the equation mentioned above, a rational formula or Manning's equation, or a complex model that must be solved on a computer. The objective is to treat a deterministic model that has uncertain inputs in order to determine the effect of the uncertain parameters $x_1, \ldots, x_k$ on the model output y. Equation (4) can be expressed as $y = G(x_i)$, where $x = x_1, x_2, \ldots, x_k$. Using a Taylor series expansion of k random variables, ignoring the second and higher order terms, we can obtain [17]

$$\mu_y \approx G\left(\overline{x}\right) + \sum_{i=1}^{j}\left(\frac{\partial G}{\partial x_i}\right)_{\overline{x}}\left(x_i - \overline{x}_i\right), \tag{5}$$

where μ_y refers to the mean value of y under the variation of x_i and the derivation $(\partial G/\partial x_i)_{\overline{x}}$ are the sensitivity coefficients that represent the rate of change of the function value $G(x_i)$ at $(x_i - \overline{x}_i)$. Assuming that the k random variables are independent, the variance of y can be approximated as [17]

$$\Omega_y^2 = \sum_{i=1}^{j}\left[\left(\frac{\partial G}{\partial x_i}\right)_{\overline{x}_i}^2\left(\frac{\overline{x}_i}{\mu_y}\right)^2\Omega_{x_i}^2\right]. \tag{6}$$

It is important to remember that all of the random parameters are assumed to follow a uniform distribution, so the mean and variance of each parameter can be calculated using mean $= (a + b)/2$ and variance $= (a - b)^2/12$, in which a and b are the lower and upper bounds, respectively (7). Consider

$$\Omega = \frac{\sigma}{\overline{\overline{X}}} = \frac{\sqrt{3}}{3}\left(\frac{b - a}{b + a}\right). \tag{7}$$

3.3.1. Uncertainty Analysis for Density of Sediments Deposited. Notwithstanding the advances made in understanding several factors involved in reservoir sedimentation, predicting the accumulation of sediment in a reservoir throughout the years after construction of the dam is still a complex problem in hydraulic engineering. As noted earlier, the volume of reservoir sedimentation depends, among other factors, on the quantity of sediment inflow, the percentage of sediment inflow trapped by the reservoir, and the specific weight of the deposited sediments considering the effect of compaction with time. The sediments entering a reservoir are generally a mixture of clay, silt, and sand. The fraction of each type of sediment, namely, P_C, P_m, and P_S (for clay, silt, and sand, resp.), vary from year to year. Thus, it would be impractical to determine such variable fractions from field measurements. Standard statistical analysis can offer a certain distribution function for predicting fractions of each sediment type. For instance, it may be assumed that such fractions are uniformly distributed with lower and upper bounds that are obtained from the measurements. Or the fractions of each type of sediments may be assumed to be independent. In this approach the percentages of clay, silt, and sand will have to be adjusted so that they add up to 100% [3].

Therefore, to determine the uncertainty associated with the type of incoming sediment and their effect on deposited sediment's density, (2) can be rewritten using (1) and (3) as follows:

$$\begin{aligned} W_T = {} & P_C\left\{W_C + 0.434K_C\left[\frac{T}{T-1}(\ln T) - 1\right]\right\} \\ & + P_m\left\{W_m + 0.434K_m\left[\frac{T}{T-1}(\ln T) - 1\right]\right\} \\ & + P_S\left\{W_S + 0.434K_S\left[\frac{T}{T-1}(\ln T) - 1\right]\right\}. \end{aligned} \tag{8}$$

Using (5) and (6), the variation coefficient of deposited sediments' density after T years of operation could be determined as follows:

$$\Omega_{W_T}^2 = \left(\frac{\partial W_T}{\partial P_C}\right)^2 \left(\frac{\partial \overline{P}_C}{\partial \mu_{W_T}}\right)^2 \Omega_{P_C}^2 + \left(\frac{\partial W_T}{\partial P_m}\right)^2 \left(\frac{\partial \overline{P}_m}{\partial \mu_{W_T}}\right)^2 \Omega_{P_S}^2 + \left(\frac{\partial W_T}{\partial P_S}\right)^2 \left(\frac{\partial \overline{P}_S}{\partial \mu_{W_T}}\right)^2 \Omega_{P_S}^2, \tag{9}$$

where Ω_{W_T} is the coefficient of variation of sediments' density after T years of operation, and Ω_{P_C}, Ω_{P_m}, and Ω_{P_S} are the variation coefficient of clay, silt, and sand percentage, respectively. Equation (9) can thus be rewritten as follows:

$$\Omega_{W_T}^2 = \left(W_C + 0.434K_C\left[\frac{T}{T-1}(\ln T) - 1\right]\right)^2 \left(\frac{\partial \overline{P}_C}{\partial \mu_{W_T}}\right)^2 \Omega_{P_C}^2 + \left(W_m + 0.434K_m\left[\frac{T}{T-1}(\ln T) - 1\right]\right)^2 \left(\frac{\partial \overline{P}_m}{\partial \mu_{W_T}}\right)^2 \Omega_{P_S}^2 + \left(W_S + 0.434K_S\left[\frac{T}{T-1}(\ln T) - 1\right]\right)^2 \left(\frac{\partial \overline{P}_S}{\partial \mu_{W_T}}\right)^2 \Omega_{P_S}^2. \tag{10}$$

4. Results and Discussion

4.1. Case Study (Kenny Reservoir). Uncertainty analysis of density of sediments deposited in reservoir after T years of operation as described earlier was applied to the Kenny Reservoir in the White River Basin in northwestern Colorado. Taylor Draw Dam was constructed in the early 1980's and created the Kenny Reservoir with a capacity of about 17×10^6 m^3, which has been in operation since 1984 [3, 20].

The mean density of sediments deposited after $T = 50$ years of operation and its coefficient of variation for Kenny Reservoir data was determined using the abovementioned method. The range of percentages of each type of sediment (i.e., P_C, P_m, and P_S for clay, silt, and sand, resp.) are independent because of their physical differences. It is important to mention that Tobin and Hollowed evaluated statistical distributions of each type of sediment and found them close to the uniform type, and therefore they assumed them to be uniformly distributed [3, 9]. Also, according to the reservoir hydraulic condition (permanent reservoir with long length) the sediments were always submerged. Also, the lower and upper bounds for each fraction were analyzed by Tobin and Hollowed using twenty samples of suspended sediment which were collected [3, 9] (Table 5).

It should be borne in mind that for each sample the percentages of clay, silt, and sand should add up to 100% ($P_C + P_m + P_S = 100\%$). The mean percentages of sediment accumulated (Table 5) can be summarized according to the type and the coefficient of variation using (9).

Assuming the sediments are always submerged or nearly submerged in Kenny Reservoir (using Table 6 and (8)), the mean density of sediments after $T = 50$ years of operation can be obtained as follows:

$$\mu_{w_T} = \frac{28.5}{100}\left\{416 + 0.4343 \times 256\left[\frac{50}{50-1}(\ln 50) - 1\right]\right\} + \frac{51}{100}\left\{1120 + 0.4343 \times 91\left[\frac{50}{50-1}(\ln 50) - 1\right]\right\} + \frac{28.5}{100}\{1500 + 0\} = 1065.42\ \text{kg/m}^3. \tag{11}$$

Table 5: Clay, silt, and sand percentages range.

Sediment type	Lower bound	Upper bound	Distribution
P_C (%)	16	41	Uniform
P_m (%)	39	63	Uniform
P_S (%)	14	43	Uniform

Table 6: Statistical properties of stochastic inputs for uncertainty analysis.

Sediment type	Mean	Standard deviation	Coefficient of variation
P_C (%)	28.5	7.216884	0.253224
P_m (%)	51	6.928197	0.135847
P_S (%)	28.5	8.37159	0.293740

Then, using Table 4 (reservoir type 1) and (10), coefficient of variation of sediments' density after $T = 50$ years of Kenny reservoir operation can be assessed as follows:

$$\Omega_{W_T}^2 = 0.0098 \longrightarrow \Omega_{W_T} = 0.099. \tag{12}$$

Hence, the accuracy in determining the mean density of sediments after $T = 50$ years of operation in this reservoir is ±9.9%. Further, the standard deviation of this parameter can be determined as follows:

$$\sigma_{W_T} = \mu_{W_T}\Omega_{W_T}. \tag{13}$$

Thus,

$$\sigma_{W_T} = 1065.42 \times 0.099 = 105.48\ \text{kgm}^{-3}, \tag{14}$$

where σ_{W_T} refers to the standard deviation of variable y (in this case $y = W_T$).

Results of this case study indicate that the mean density of sediments deposited after 50 years of operation in Kenny Reservoir is 1065.42 ± 105.48 (mean ± SD) kg/m^3 (14). Therefore, the accuracy of calculating the mean density of sediments deposited after the 50th year of operation and the needed volume for dead storage design is 9.9% (~10%).

5. Conclusion

Due to the wide range of uncertain parameters involved in the design procedure, predicting the deposition and accumulation of sediments in a reservoir is a complex problem,

one that has attracted the attention of hydraulic engineers and scientists for many decades. In this paper, the problem of analyzing and quantifying the uncertainty of mean density of sediments deposited in a reservoir and its compaction through the years of reservoir operation has been addressed.

Since in previous studies the density of sediments which were deposited in the reservoir were assumed constant, in this paper the former studies were developed by identifying the basic factors which affect the density of sediments deposited in the reservoirs. Also uncertainties in reservoir sediments density are determined using the Delta method.

For this purpose, the uncertainty of the input factors (stochastic inputs) was analyzed first. Then, using the Delta method, the uncertainty associated with the type of incoming sediments and their effect on density of sediments and its coefficient of variation were determined.

Results of this research indicate that the mean density of sediments deposited after 50 years of operation in Kenny Reservoir is 1065.42 ± 105.48 (mean $\pm$ SD) kg/m^3. Therefore, the accuracy of calculating the mean density of sediments deposited after the 50th year of operation and the needed volume for dead storage design is 10%. This user-friendly method can be applied to engineering practices to optimize dead storage planning via interfacing with uncertainties associated with reservoir sedimentation.

Conflict of Interests

The authors declare that there is no conflict of interests regarding the publication of this paper.

Acknowledgments

Financial support by the high impact research grants of the University of Malaya (UM.C/625/1/HIR/116, account number: J-16002-00-7383000-000000) and (UM.C/625/1/HIR/61, account number: H-16001-00-D000061) is gratefully acknowledged. Also authors would like to thank the partly support of IPPP grant, number PV058-2012A.

References

[1] F. Imanshoar, Y. Hassanzadeh, M. T. Aalami, and A. Danandehmehr, "Uncertainty analysis for determining density of deposits in dams' reservoirs," *Journal of Water and Soil Science*, vol. 23, pp. 27–38, 2013 (Persian).

[2] United States Bureau of Reclamation (USBR), *Design of Small Dams*, United States Bureau of Reclamation (USBR), Denver, Colo, USA, 3rd edition, 1987.

[3] J. D. Salas and H. Shin, "Uncertainty analysis of reservoir sedimentation," *Journal of Hydraulic Engineering*, vol. 125, no. 4, pp. 339–350, 1999.

[4] S. W. Fleming, A. Marsh Lavenue, A. H. Aly, and A. Adams, "Practical applications of spectral analysis of hydrologic time series," *Hydrological Processes*, vol. 16, no. 2, pp. 565–574, 2002.

[5] M. V. Tehrani, J. M. V. Samani, and M. Montaseri, "Uncertainty analysis of reservoir sedimentation using Latin Hypercube sampling and Harr's method: Shahar Chai Dam in Iran," *Journal of Hydrology New Zealand*, vol. 47, no. 1, pp. 25–42, 2008.

[6] Y. K. Tung and B. C. Yen, *Hydrosystems Engineering Uncertainty Analysis*, McGraw-Hill, New York, NY, USA, 2005.

[7] S. Franceschini and C. W. Tsai, "Assessment of uncertainty sources in water quality modeling in the Niagara River," *Advances in Water Resources*, vol. 33, no. 4, pp. 493–503, 2010.

[8] O. O. Osidele, W. Zeng, and M. B. Beck, "Coping with uncertainty: a case study in sediment transport and nutrient load analysis," *Journal of Water Resources Planning and Management*, vol. 129, no. 4, pp. 345–355, 2003.

[9] R. L. Tobin and C. P. Hollowed, "Water quality and sediment transport Characteristics in Kenney reservoir, White river basin," Northwestern Colorado Report, U.S. Geological Survey, Denver, Colo, USA, 1990.

[10] R. I. Strand and E. L. Pemberton, "Reservoir sedimentation," Technical Guideline for Bureau of Reclamation, U.S. Department of Interior Bureau of Reclamation, Denver, Colo, USA, 1982.

[11] G. L. Morris and J. Fan, *Reservoir Sedimentation Handbook: Design and Management of Dams, Reservoirs and Watersheds for Sustainable Use*, McGraw-Hill, New York, NY, USA, 1997.

[12] V. Jothiprakash and V. Garg, "Re-look to conventional techniques for trapping efficiency estimation of a reservoir," *International Journal of Sediment Research*, vol. 23, no. 1, pp. 76–84, 2008.

[13] C. R. Miller, *Determination of the Unit Weight of Sediment for Use in Sediment Volume Computations*, U.S. Department of Interior Bureau of Reclamation, Denver, Colo, USA, 1953.

[14] J. W. Hall, "Handling uncertainty in the hydroinformatic process," *Journal of Hydroinformatics*, vol. 5, pp. 215–232, 2003.

[15] J. D. Salas, *Analysis and Modelling of Hydrologic Time Series*, McGraw-Hill, New York, NY, USA, 1993.

[16] J. M. V. Samani, M. Tehrani, and M. Montaseri, "The evaluation of three methods of uncertainty (MCS, LHS and Harr) in dam reservoir sedimentation," *Journal of Engineering and Applied Sciences*, vol. 2, pp. 1074–1084, 2007.

[17] L. W. Mays, *Water Resources Engineering*, John Wiley & Sons, New York, NY, USA, 2nd edition, 2005.

[18] F. Imanshoar, Y. Hassanzadeh, and M. R. M. Tabatabai, "Analysis of trophic state uncertainty and its Variation: Miyun Reservoir, Beijing, China," in *Proceedings of the 1st International Conference on Dams & Hydropower (ICDHP '12)*, Tehran, Iran, February 2012.

[19] C. B. Resende, C. G. Heckmann, and J. J. Michalek, "Robust design for profit maximization under uncertainty of consumer choice model parameters using Delta method," in *Proceedings of the ASME, 2011 International Design Engineering Technical Conferences & Computers and Information in Engineering Conference*, Washington, DC, USA, 2011.

[20] H. L. Chen, *Stochastic characteristics of environmental and hydrologic time series [dissertation]*, Purdue University, Stillwater, Okla, USA, 1999.

Hindawi Publishing Corporation
Abstract and Applied Analysis
Volume 2014, Article ID 575298, 19 pages
http://dx.doi.org/10.1155/2014/575298

Research Article

New Scheme of Finite Difference Heterogeneous Multiscale Method to Solve Saturated Flow in Porous Media

Fulai Chen[1,2] and Li Ren[2]

[1] *Department of Mathematics, Xiangnan University, Chenzhou 423000, China*
[2] *Department of Soil and Water Sciences, China Agricultural University and Key Laboratory of Plant-Soil Interactions, MOE, Beijing 100094, China*

Correspondence should be addressed to Li Ren; renl@mx.cei.gov.cn

Received 4 October 2013; Accepted 16 January 2014; Published 2 March 2014

Academic Editor: Shuyu Sun

A new finite difference scheme, the development of the finite difference heterogeneous multiscale method (FDHMM), is constructed for simulating saturated water flow in random porous media. In the discretization framework of FDHMM, we follow some ideas from the multiscale finite element method and construct basic microscopic elliptic models. Tests on a variety of numerical experiments show that, in the case that only about a half of the information of the whole microstructure is used, the constructed scheme gives better accuracy at a much lower computational time than FDHMM for the problem of aquifer response to sudden change in reservoir level and gives comparable accuracy at a much lower computational time than FDHMM for the weak drawdown problem.

1. Introduction

Natural porous media exhibit a significant spatial variability in most attributes of hydrogeological interest. For instance, it is quite typical for hydraulic conductivity to vary orders of magnitude over distances [1]. The groundwater flow problems in heterogeneous porous media can be accurately solved by using conventional finite element method or finite difference method based on smaller scale, which leads to more computational cost. Discrete schemes obtained in this way are often by far too expensive to be solved directly. For the sake of the accuracy and efficiency, several different but related multiscale methods, such as the multiscale finite element method (MsFEM) [2, 3], the heterogeneous multiscale method (HMM) [4], and the numerical homogenization method [5], for problems with oscillating coefficients have been proposed to accommodate the fine-scale description directly. Here, we should also mention the work of Babuška in the 70s [6–8], which motivated these multiscale methods in an extent.

Multiscale solution methods are currently under active investigation for the simulation of subsurface flow in heterogeneous formations [9]. Ye et al. [10] applied MsFEM to simulate two- and three-dimensional saturated flow problems. Chen and Hou [11] proposed a mixed multiscale finite element method for elliptic problems with oscillating coefficients; they demonstrated the efficiency and accuracy of the proposed method for flow transport in a porous medium with a random log-normal relative permeability. He and Ren [12] presented the finite volume MsFEM for solving saturated flow in heterogeneous porous media. E et al. [13] took a systemic analysis of HMM for elliptic homogenization problems, where the error between the numerical solution of HMM and the solution of homogenized equation is estimated, and how to construct better approximation of the exact solution from the HMM solution is discussed. Ming and Zhang [14] applied HMM to the linear parabolic homogenization problem and discriminated different types of microscopic models. Ming and Yue [15] discussed the numerical performance of HMM including comparison with other methods. Yue and E [16] developed HMM for linear and nonlinear transport equations with multiscale velocity fields in heterogeneous porous media and focused on the problem where advection is dominant at the small scale.

Most of existing multiscale methods have been limited to the finite element method [17–19]. There are also widely

used finite difference flow and solute transport models in both the groundwater and oil industries. To handle multiscale problems with finite difference methods, based on the framework of HMM [4], Abdulle and E [20] proposed the finite difference heterogeneous multiscale method (FDHMM) for solving multiscale parabolic problems. This method includes a "heterogeneous" discretization which cares about the fine scale only on small representative region of the spatial domain. FDHMM has two components: a macroscopic scheme evolved on a coarse grid (the grid of interest) with unknown data recovered from the solutions of the microscopic model and a microscopic scheme, in which the original equation is solved on a sparse (heterogeneous) spatial domain. The similar idea can be found in [21]. Chen and Ren [22] applied FDHMM to Richards' equation; they found that FDHMM could effectively simulate the transient unsaturated flow in the specific soils. In the saturated flow case, we may precompute the macroscopic flux at a preprocessing step to save the computational time. In addition, Abdulle and E [20] studied the multiscale parabolic equation without the source sink term and considered the examples where the coefficients change according to the smooth function. For transient flow problem in heterogeneous porous media, the coefficients generally change in a random form; thus there is a need for more evaluation of the applicability of FDHMM.

Here, we propose a new scheme of FDHMM for simulating not only the steady saturated flow problem but also the transient saturated flow problem in geostatistical random porous media. The constructed scheme employs an idea presented by Ming and Zhang [14]; that is, the microscale parabolic model can be reduced to the microscopic elliptic model for the problem without oscillation propagation in time. Motivated by the construction of the multiscale finite element base functions [2, 3], in every control volume, we divide the microscopic elliptic model into two basic microscopic elliptic models and estimate the basic macroscopic flux by the solutions of these two basic microscopic elliptic models. The small scale information is then brought to the large scale through the approximation of basic macroscopic fluxes. These basic macroscopic fluxes are just calculated once at the preprocessing step and will be used in the subsequent computations. In general, governing coarse-grid equation and coupling the approach of the new scheme are the same as those of FDHMM by Abdulle and E. The main difference between the two methods is the microscopic scheme, in contrast to FDHMM by Abdulle and E, where the numerical fluxes are computed on the fly using localized and more resolved computations which means that FDHMM by Abdulle and E needs the macroscopic and microscopic evolution at every time step and the new scheme adopts the idea of MsFEM of Hou et al., by numerically precomputing a finite difference analogue of a multiscale shape function, which provides a fixed expression for the numerical basic flux in terms of the coarse variables. It means that the fine-scale information is coupled into the coarse scale by this finite difference analogue of a multiscale shape function. In addition, the new scheme incorporates ideas from Ming and Zhang [14] to transform the microscopic parabolic model to a microscopic elliptic model, which allows MsFEM ideas to be adopted in the computational scheme.

Our method is also analogous to the classical upscaling method, where the upscaled hydraulic conductivities are precomputed [23, 24]. Different from the classical upscaling method, the present method only precomputes the basic macroscopic fluxes. The estimation of the macroscopic fluxes, which contain both microscopic information of the medium property and useful information about the gradients of the solutions of microscopic elliptic models, is coupled into the course of solving the coarse equation, and it makes the constructed scheme put more emphasis on the interaction between the macro- and microscale behavior. On the other hand, in the new scheme, the fine-scale global flow solution is decomposed into a series of local microscopic problems; the computations of these basic microscale problems can be carried out sequentially; this obviously saves the computational time and the memory requirement, which may provide the proposed method with a possibility to solve large flow problems under restricted computational capabilities.

This paper is organized as follows. We firstly describe the flow problem and introduce the principle and the algorithm of the constructed scheme in detail. Numerical examples to illustrate the performance of the constructed scheme are arranged in Section 3. Some conclusions are given in Section 4.

2. New Scheme of FDHMM

2.1. Flow Problem. The transient saturated flow through a heterogeneous porous medium is governed by the parabolic partial differential equation

$$S_s(\mathbf{x})\frac{\partial \psi(\mathbf{x},t)}{\partial t} = \nabla\cdot\left[\mathbf{K}(\mathbf{x})\nabla\psi(\mathbf{x},t)\right] + R(\mathbf{x},t), \quad \text{in } \Omega\times(0,T), \tag{1}$$

where ψ is the hydraulic head, S_s is the specific storage coefficient, $\mathbf{K}$ is the hydraulic conductivity tensor, R is the source sink term, $\mathbf{x} = (x, y)$ is the spatial coordinate, t is the time variable, Ω is the study area, and T is the time domain.

2.2. Principle and Algorithm. The discretization in this study is the mesh-centered finite difference. To simplify the presentation of the constructed scheme, we assume that the solution domain Ω is a square and uniformly discretize it with a coarse $N\times N$ mesh. Let the Cartesian coordinates of this coarse mesh be represented by (x_i, y_j), $i, j = 1, \ldots, N+1$. $H = x_{i+1} - x_i = y_{j+1} - y_j$ denotes the coarse mesh size.

Notice that a macroscopic model is known to exist according to the homogenization theory, and the idea of the constructed scheme is to evolve a macroscopic model for the flux form of (1),

$$S_s(\mathbf{x})\frac{\partial \Psi(\mathbf{x},t)}{\partial t} = -\nabla\cdot F(\mathbf{x},t) + R(\mathbf{x},t), \quad \text{in } \Omega\times(0,T), \tag{2}$$

on a coarse mesh, where Ψ is the macroscopic state variable corresponding to ψ, that is, we have $\Psi = \psi$ at the coarse

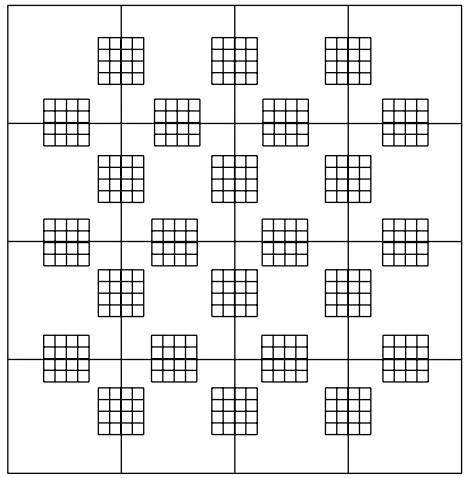

Figure 1: Illustration of the macroscopic and microscopic computational domains.

node (i, j), and F is the macroscopic flux. In fact, based on the principle of the flux balance, we can also deduce (2).

To solve (2), we firstly need to determine the macroscopic flux F. In the absence of explicit knowledge of F, our problem reduces to approximate the flux F; this will be done by locally solving a set of microscopic models. In Figure 1, we center a control volume at the midpoint of the line between any two coarse nodes except for two exterior nodes. Thus, there are four control volumes $I^{\delta}_{i\pm(1/2),j}$ and $I^{\delta}_{i,j\pm(1/2)}$ around every interior node (i, j) and these control volumes are centered at the points $(i \pm (1/2), j)$ and $(i, j \pm (1/2))$, respectively (see Figure 2). We assume that the control volume $I^{\delta}_{i\pm(1/2),j}$ is a square of size δ and discretize it into a fine $M \times M$ mesh, for which (ξ_k, η_l) denotes the coordinate of node (k, l), where $k, l = 1, \ldots, M+1$. $a = \xi_{k+1} - \xi_k = \eta_{l+1} - \eta_l$ denotes the fine mesh size. For ξ_k and η_l, we have

$$\begin{aligned} \xi_k &= \frac{H-\delta}{2} + (k-1)\frac{\delta}{M}, \\ \eta_l &= H - \frac{\delta}{2} + (l-1)\frac{\delta}{M}, \quad k, l = 1, \ldots, M+1. \end{aligned} \tag{3}$$

Similarly, (η_l, ξ_k) denotes the coordinate of the control volume $I^{\delta}_{i,j\pm(1/2)}$.

2.2.1. Basic Microscopic Elliptic Problems. To estimate the macroscopic flux, we need to solve a set of local microscale problems in the control volumes. Actually, the saturated hydraulic conductivity tensor $\mathbf{K}(\mathbf{x})$ in this study is only a function of the spatial position and does not oscillate in the temporal direction, and we only need the spatial homogenization of $\mathbf{K}(\mathbf{x})$ at the microscopic evolution. According to the conclusion of [14], in every control volume I^{δ}, we can only solve the following reduced elliptic equation:

$$\nabla \cdot \left[\mathbf{K}(\mathbf{x}) \nabla \psi(\mathbf{x})\right] = 0, \quad \text{in } I^{\delta}. \tag{4}$$

In every control volume I^{δ}, similar to the construction of the multiscale finite element base functions developed by Hou and Wu [2] and Hou et al. [3], we will solve two basic elliptic problems with the Dirichlet-Neumann boundary condition in which the Dirichlet boundary condition is used in one direction and no-flow boundary condition is used in the other direction. For $I^{\delta}_{i+(1/2),j}$ $(i, j = 1, 2, \ldots, N)$, the Dirichlet boundary condition is used in x-direction and no-flow boundary condition is used in y-direction, and vice versa for $I^{\delta}_{i,j+(1/2)}$ $(i, j = 1, 2, \ldots, N)$.

Set the head of the basic elliptic problem with no dimensional change. Let ϕ^1 and ϕ^2 be the solutions of these two basic elliptic problems, respectively. In $I^{\delta}_{i+(1/2),j}$, as shown in Figure 2, for the first basic elliptic problem, the head on the left side is 1, and that on the right side is 0, and vice versa for the second basic elliptic problem. Similarly, in $I^{\delta}_{i,j+(1/2)}$, for the first basic elliptic problem, the head on the bottom side is 1, and that on the top side is 0, and vice versa for the second basic elliptic problem. The cell problems are computed in parallel, and the number of the processors is reduced [16, 25]. To solve the basic elliptic problem, we considered employing the conventional finite difference method with multigrid over a fine mesh to solve the original equation. For implementing the multigrid algorithm, we use directly a numerical simulator MGD9V [26]. In fact, according to the above two basic elliptic problems, we have $\phi^1 + \phi^2 = 1$. Then, we only need to solve the first basic elliptic problem and obtain the solution ϕ^2 of the second basic elliptic problem in the course of computation according to $\phi^2 = 1 - \phi^1$.

2.2.2. Estimation of Basic Macroscopic Fluxes. After solving the basic elliptic problems, we estimate basic macroscopic fluxes based on the solutions of the basic elliptic problems. In $I^{\delta}_{i+(1/2),j}$, $F^{x_\alpha,\beta}_{i+(1/2),j}$ $(\alpha, \beta = 1, 2)$ denote, respectively, the basic macroscopic fluxes estimated by the solutions of two basic elliptic problems; we have

$$\begin{aligned} F^{x_\alpha,1}_{i+(1/2),j} &= -\frac{1}{\left|I^{\delta}_{i+(1/2),j}\right|} \int\int_{I^{\delta}_{i+(1/2),j}} K(\mathbf{x}) \frac{\partial \phi^\alpha}{\partial x} dx\, dy \\ &\approx -\frac{a^2}{\delta^2} \sum_{k=1}^{M}\sum_{l=1}^{M} K_{k+(1/2),l} \frac{\phi^\alpha_{k+1,l} - \phi^\alpha_{k,l}}{a}, \\ F^{x_\alpha,2}_{i+(1/2),j} &= -\frac{1}{\left|I^{\delta}_{i+(1/2),j}\right|} \int\int_{I^{\delta}_{i+(1/2),j}} \frac{y}{H} K(\mathbf{x}) \frac{\partial \phi^\alpha}{\partial x} dx\, dy \\ &\approx -\frac{a^2}{\delta^2} \sum_{k=1}^{M}\sum_{l=1}^{M} \frac{\eta_l}{H} K_{k+(1/2),l} \frac{\phi^\alpha_{k+1,l} - \phi^\alpha_{k,l}}{a}, \quad \alpha = 1, 2, \end{aligned} \tag{5}$$

where $K_{k+(1/2),l}$ is the geometric mean of $K_{k,l}$ and $K_{k+1,l}$. Similarly, in $I^{\delta}_{i,j+(1/2)}$,

$$F^{y_\alpha,1}_{i,j+(1/2)} = -\frac{1}{\left|I^{\delta}_{i,j+(1/2)}\right|} \int\int_{I^{\delta}_{i,j+(1/2)}} K(\mathbf{x}) \frac{\partial \phi^\alpha}{\partial y} dx\, dy$$

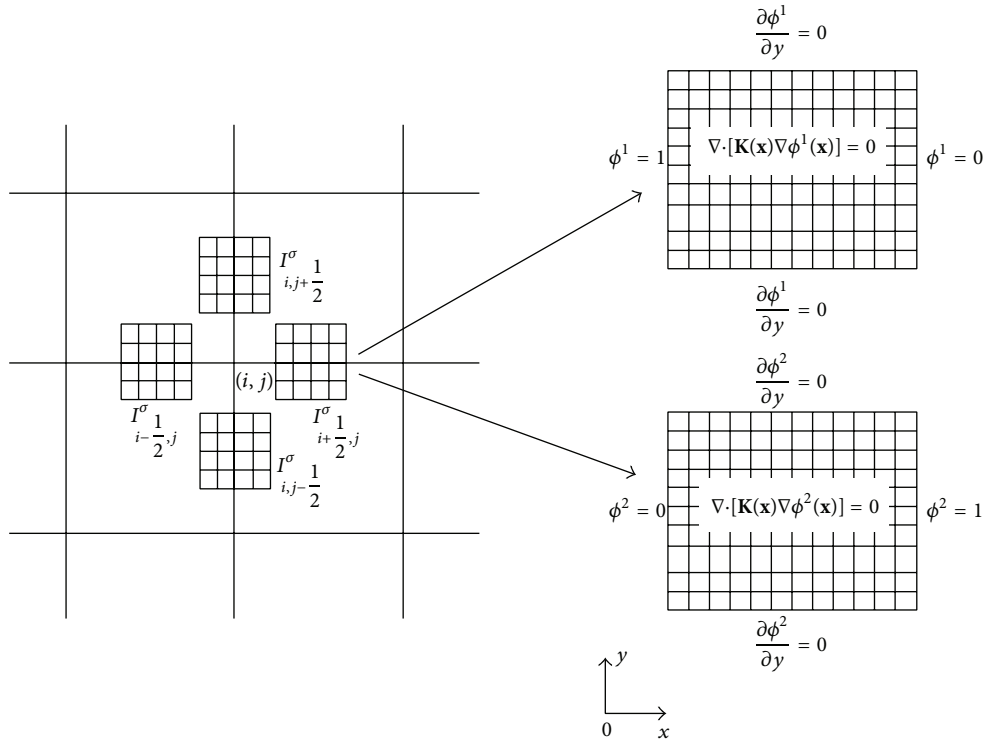

Figure 2: The control volumes at the coarse node (i, j) and two basic microscopic elliptic models for the control volume $I^{\delta}_{i+(1/2),j}$.

$$\approx -\frac{a^2}{\delta^2} \sum_{k=1}^{M} \sum_{l=1}^{M} K_{k,l+(1/2)} \frac{\phi^{\alpha}_{k,l+1} - \phi^{\alpha}_{k,l}}{a},$$

$$F^{y_\alpha,2}_{i,j+(1/2)} = -\frac{1}{\left| I^{\delta}_{i,j+(1/2)} \right|} \int \int_{I^{\delta}_{i,j+(1/2)}} \frac{x}{H} K(\mathbf{x}) \frac{\partial \phi^{\alpha}}{\partial y} dx\, dy$$

$$\approx -\frac{a^2}{\delta^2} \sum_{k=1}^{M} \sum_{l=1}^{M} \frac{\eta_k}{H} K_{k,l+(1/2)} \frac{\phi^{\alpha}_{k,l+1} - \phi^{\alpha}_{k,l}}{a}, \quad \alpha = 1, 2, \tag{6}$$

where $K_{k,l+(1/2)}$ is the geometric mean of $K_{k,l}$ and $K_{k,l+1}$.

2.2.3. Estimation of Macroscopic Fluxes. Based on the estimation of the basic macroscopic fluxes, we will estimate macroscopic fluxes. Let $\Psi^n_{i,j}$ be a coarse numerical solution of (2) at time t^n, to estimate the macroscopic flux F^n at time t^n; we will deal with it below.

We first solve a microscopic elliptic problem with the Dirichlet-Neumann boundary condition at every control volume I^{δ}. Head at the Dirichlet boundary of the control volume is calculated by bilinear interpolating functions.

For the control volume $I^{\delta}_{i+(1/2),j}$, heads at the left and right sides are

$$\psi^{n,\text{left},l}_{i+(1/2),j} = g_1(\eta_l) + \xi_1 \frac{g_2(\eta_l) - g_1(\eta_l)}{H},$$
$$\psi^{n,\text{right},l}_{i+(1/2),j} = g_1(\eta_l) + \xi_{M+1} \frac{g_2(\eta_l) - g_1(\eta_l)}{H}, \tag{7}$$

respectively, where

$$g_1(\eta_l) = \begin{cases} \frac{\eta_l}{H} \Psi_{i,j} + \left(1 - \frac{\eta_l}{H}\right) \Psi_{i,j-1}, & 1 \le l \le \frac{M}{2}, \\ \left(2 - \frac{\eta_l}{H}\right) \Psi_{i,j} + \left(\frac{\eta_l}{H} - 1\right) \Psi_{i,j+1}, & \frac{M}{2} < l \le M, \end{cases}$$

$$g_2(\eta_l) = \begin{cases} \frac{\eta_l}{H} \Psi_{i+1,j} + \left(1 - \frac{\eta_l}{H}\right) \Psi_{i+1,j-1}, & 1 \le l \le \frac{M}{2}, \\ \left(2 - \frac{\eta_l}{H}\right) \Psi_{i+1,j} + \left(\frac{\eta_l}{H} - 1\right) \Psi_{i+1,j+1}, & \frac{M}{2} < l \le M. \end{cases} \tag{8}$$

Thus, $\psi^{n,l}$, the solution of the microscopic elliptic problem in $I^{\delta}_{i+(1/2),j}$, is obtained over the control volume $I^{\delta}_{i+(1/2),j}$ via the linear combination of ϕ^1 and ϕ^2, which are the solutions of two corresponding basic elliptic problems, respectively, and then we have

$$\psi^{n,l} = \psi^{n,\text{left},l}_{i+(1/2),j} \phi^1 + \psi^{n,\text{right},l}_{i+(1/2),j} \phi^2, \quad l = 1, \ldots, M+1. \tag{9}$$

Similarly, in $I^{\delta}_{i,j+(1/2)}$, heads at the bottom and top sides are

$$\psi^{n,\text{bottom},l}_{i,j+(1/2)} = g_3(\eta_l) + \xi_1 \frac{g_4(\eta_l) - g_3(\eta_l)}{H},$$
$$\psi^{n,\text{top},l}_{i,j+(1/2)} = g_3(\eta_l) + \xi_{M+1} \frac{g_4(\eta_l) - g_3(\eta_l)}{H}, \tag{10}$$

respectively, where

$$g_3(\eta_l) = \begin{cases} \frac{\eta_l}{H}\Psi_{i,j} + \left(1 - \frac{\eta_l}{H}\right)\Psi_{i-1,j}, & 1 \le l \le \frac{M}{2}, \\ \left(2 - \frac{\eta_l}{H}\right)\Psi_{i,j} + \left(\frac{\eta_l}{H} - 1\right)\Psi_{i+1,j}, & \frac{M}{2} < l \le M, \end{cases}$$

$$g_4(\eta_l) = \begin{cases} \frac{\eta_l}{H}\Psi_{i,j+1} + \left(1 - \frac{\eta_l}{H}\right)\Psi_{i-1,j+1}, & 1 \le l \le \frac{M}{2}, \\ \left(2 - \frac{\eta_l}{H}\right)\Psi_{i,j+1} + \left(\frac{\eta_l}{H} - 1\right)\Psi_{i+1,j+1}, & \frac{M}{2} < l \le M. \end{cases} \tag{11}$$

The solution of the microscopic elliptic problem in this control volume is

$$\psi^{n,l} = \psi^{n,\text{bottom},l}_{i,j+(1/2)}\phi^1 + \psi^{n,\text{top},l}_{i,j+(1/2)}\phi^2, \quad l = 1, \ldots, M+1. \tag{12}$$

Like the assumption in [27], we assume that the situation investigated in this study is for locally isotropic conductivity and also assume the hydraulic conductivity tensor with principal axes oriented in the direction of the principal statistical anisotropy axes of the local parameters. It means that the conductivity tensor for a locally heterogeneous medium is

$$\mathbf{K} = \begin{pmatrix} K(\mathbf{x}) & 0 \\ 0 & K(\mathbf{x}) \end{pmatrix}. \tag{13}$$

By applying the above assumption, we derive the macroscopic flux F^n,

$$\begin{aligned} F^n &= -\frac{1}{|I^\delta|}\int\int_{I^\delta} \mathbf{K}(\mathbf{x})\nabla\psi(\mathbf{x}, t^n)\, d\mathbf{x} \\ &= -\frac{1}{|I^\delta|}\int\int_{I^\delta} \begin{pmatrix} K(\mathbf{x}) & 0 \\ 0 & K(\mathbf{x}) \end{pmatrix} \begin{pmatrix} \frac{\partial\psi^n}{\partial x} \\ \frac{\partial\psi^n}{\partial y} \end{pmatrix} dx\, dy \\ &= -\frac{1}{|I^\delta|}\int\int_{I^\delta} \begin{pmatrix} K(\mathbf{x})\frac{\partial\psi^n}{\partial x} \\ K(\mathbf{x})\frac{\partial\psi^n}{\partial y} \end{pmatrix} dx\, dy = \begin{pmatrix} F^{n,x} \\ F^{n,y} \end{pmatrix}, \end{aligned} \tag{14}$$

where $F^{n,x}$ and $F^{n,y}$ are estimated macroscopic fluxes in x-direction and y-direction at time t^n, respectively. For the control volume $I^\delta_{i+(1/2),j}$, together with (3), (5), (7), (9), and (14), we have

$$\begin{aligned} F^{n,x}_{i+(1/2),j} &= -\frac{1}{\left|I^\delta_{i+(1/2),j}\right|}\int\int_{I^\delta_{i+(1/2),j}} K(\mathbf{x})\frac{\partial\psi^n}{\partial x}dx\, dy \\ &\approx -\frac{a^2}{\delta^2}\sum_{k=1}^{M}\sum_{l=1}^{M} K_{k+(1/2),l}\frac{\psi^{n,l}_{k+1,l} - \psi^{n,l}_{k,l}}{a} \\ &= -\frac{a^2}{\delta^2}\sum_{k=1}^{M}\sum_{l=1}^{M} K_{k+(1/2),l}\left(\psi^{n,\text{left},l}_{i+(1/2),j}\frac{\phi^1_{k+1,l} - \phi^1_{k,l}}{a} + \psi^{n,\text{right},l}_{i+(1/2),j}\frac{\phi^2_{k+1,l} - \phi^2_{k,l}}{a}\right) \\ &\approx \left[\frac{H-\delta}{4H}\left(2\Psi^n_{i+1,j} + \Psi^n_{i+1,j-1} - \Psi^n_{i+1,j+1}\right) + \frac{H+\delta}{4H}\left(2\Psi^n_{i,j} + \Psi^n_{i,j-1} - \Psi^n_{i,j+1}\right)\right]F^{x_1,1}_{i+(1/2),j} \\ &+ \left[\frac{H-\delta}{4H}\left(-\Psi^n_{i+1,j-1} + \Psi^n_{i+1,j+1}\right) + \frac{H+\delta}{4H}\left(-\Psi^n_{i,j-1} + \Psi^n_{i,j+1}\right)\right]F^{x_1,2}_{i+(1/2),j} \\ &+ \left[\frac{H+\delta}{4H}\left(2\Psi^n_{i+1,j} + \Psi^n_{i+1,j-1} - \Psi^n_{i+1,j+1}\right) + \frac{H-\delta}{4H}\left(2\Psi^n_{i,j} + \Psi^n_{i,j-1} - \Psi^n_{i,j+1}\right)\right]F^{x_2,1}_{i+(1/2),j} \\ &+ \left[\frac{H+\delta}{4H}\left(-\Psi^n_{i+1,j-1} + \Psi^n_{i+1,j+1}\right) + \frac{H-\delta}{4H}\left(-\Psi^n_{i,j-1} + \Psi^n_{i,j+1}\right)\right]F^{x_2,2}_{i+(1/2),j}. \end{aligned} \tag{15}$$

Similarly, for $I^\delta_{i,j+(1/2)}$, we have

$$\begin{aligned} F^{n,y}_{i,j+(1/2)} &\approx \left[\frac{H-\delta}{4H}\left(2\Psi^n_{i,j+1} + \Psi^n_{i-1,j+1} - \Psi^n_{i+1,j+1}\right) + \frac{H+\delta}{4H}\left(2\Psi^n_{i,j} + \Psi^n_{i-1,j} - \Psi^n_{i+1,j}\right)\right]F^{y_1,1}_{i,j+(1/2)} \\ &+ \left[\frac{H-\delta}{4H}\left(-\Psi^n_{i-1,j+1} + \Psi^n_{i+1,j+1}\right) + \frac{H+\delta}{4H}\left(-\Psi^n_{i-1,j} + \Psi^n_{i+1,j}\right)\right]F^{y_1,2}_{i,j+(1/2)} \\ &+ \left[\frac{H+\delta}{4H}\left(2\Psi^n_{i,j+1} + \Psi^n_{i-1,j+1} - \Psi^n_{i+1,j+1}\right) + \frac{H-\delta}{4H}\left(2\Psi^n_{i,j} + \Psi^n_{i-1,j} - \Psi^n_{i+1,j}\right)\right]F^{y_2,1}_{i,j+(1/2)} \\ &+ \left[\frac{H+\delta}{4H}\left(-\Psi^n_{i-1,j+1} + \Psi^n_{i+1,j+1}\right) + \frac{H-\delta}{4H}\left(-\Psi^n_{i-1,j} + \Psi^n_{i+1,j}\right)\right]F^{y_2,2}_{i,j+(1/2)}. \end{aligned} \tag{16}$$

2.2.4. Macroscopic Evolution. Let Δt be a time step size, where $\Delta t = t^{n+1} - t^n$. The macroscopic evolution on the coarse mesh is now done via the approximation of (2), and here we use

the Crank-Nicolson method to construct the fully discretized version of (2),

$$\frac{S_{si,j}}{\Delta t}\left(\Psi_{i,j}^{n+1}-\Psi_{i,j}^{n}\right) = -\frac{1}{2H}\left(F_{i+(1/2),j}^{n+1,x}-F_{i-(1/2),j}^{n+1,x}+F_{i,j+(1/2)}^{n+1,y}-F_{i,j-(1/2)}^{n+1,y}\right) - \frac{1}{2H}\left(F_{i+(1/2),j}^{n,x}-F_{i-(1/2),j}^{n,x}+F_{i,j+(1/2)}^{n,y}-F_{i,j-(1/2)}^{n,y}\right)+R_{i,j}^{n}. \tag{17}$$

Combining (15), (16), and (17) yields

$$\begin{aligned}\frac{S_{si,j}}{\Delta t}\left(\Psi_{i,j}^{n+1}-\Psi_{i,j}^{n}\right) &= \left(c_1\Psi_{i-1,j-1}^{n+1}+c_2\Psi_{i,j-1}^{n+1}+c_3\Psi_{i+1,j-1}^{n+1}+c_4\Psi_{i-1,j}^{n+1}+c_5\Psi_{i,j}^{n+1}+c_6\Psi_{i+1,j}^{n+1}+c_7\Psi_{i-1,j+1}^{n+1}+c_8\Psi_{i,j+1}^{n+1}+c_9\Psi_{i+1,j+1}^{n+1}\right)\\ &+\left(c_1\Psi_{i-1,j-1}^{n}+c_2\Psi_{i,j-1}^{n}+c_3\Psi_{i+1,j-1}^{n}+c_4\Psi_{i-1,j}^{n}+c_5\Psi_{i,j}^{n}+c_6\Psi_{i+1,j}^{n}+c_7\Psi_{i-1,j+1}^{n}+c_8\Psi_{i,j+1}^{n}+c_9\Psi_{i+1,j+1}^{n}\right)+R_{i,j}^{n},\end{aligned} \tag{18}$$

where

$$\begin{aligned}c_1 = &-\frac{1}{8H^2}\times\left[(H+\delta)\left(-F_{i-(1/2),j}^{x_1,1}+F_{i-(1/2),j}^{x_1,2}-F_{i,j-(1/2)}^{y_1,1}+F_{i,j-(1/2)}^{y_1,2}\right)+(H-\delta)\left(-F_{i-(1/2),j}^{x_2,1}+F_{i-(1/2),j}^{x_2,2}-F_{i,j-(1/2)}^{y_2,1}+F_{i,j-(1/2)}^{y_2,2}\right)\right],\\ c_2 = &-\frac{1}{8H^2}\left[(H+\delta)\left(F_{i+(1/2),j}^{x_1,1}-F_{i+(1/2),j}^{x_1,2}-F_{i-(1/2),j}^{x_2,1}+F_{i-(1/2),j}^{x_2,2}-2F_{i,j-(1/2)}^{y_1,1}\right)+(H-\delta)\left(F_{i+(1/2),j}^{x_2,1}-F_{i+(1/2),j}^{x_2,2}-F_{i-(1/2),j}^{x_1,1}+F_{i-(1/2),j}^{x_1,2}-2F_{i,j-(1/2)}^{y_2,1}\right)\right],\\ c_3 = &-\frac{1}{8H^2}\left[(H+\delta)\left(F_{i+(1/2),j}^{x_2,1}-F_{i+(1/2),j}^{x_2,2}+F_{i,j-(1/2)}^{y_1,1}-F_{i,j-(1/2)}^{y_1,2}\right)+(H-\delta)\left(F_{i+(1/2),j}^{x_1,1}-F_{i+(1/2),j}^{x_1,2}+F_{i,j-(1/2)}^{y_2,1}-F_{i,j-(1/2)}^{y_2,2}\right)\right],\\ c_4 = &-\frac{1}{8H^2}\left[(H+\delta)\left(F_{i,j+(1/2)}^{y_1,1}-F_{i,j+(1/2)}^{y_1,2}-2F_{i-(1/2),j}^{x_1,1}-F_{i,j-(1/2)}^{y_1,1}+F_{i,j-(1/2)}^{y_2,2}\right)+(H-\delta)\left(F_{i,j+(1/2)}^{y_2,1}-F_{i,j+(1/2)}^{y_2,2}-2F_{i-(1/2),j}^{x_2,1}+F_{i,j-(1/2)}^{y_1,2}\right)\right],\\ c_5 = &-\frac{1}{8H^2}\left[(H+\delta)\left(2F_{i+(1/2),j}^{x_1,1}+2F_{i,j+(1/2)}^{y_1,1}-2F_{i-(1/2),j}^{x_2,1}-2F_{i,j-(1/2)}^{y_2,1}\right)+(H-\delta)\left(2F_{i+(1/2),j}^{x_2,1}+2F_{i,j+(1/2)}^{y_2,1}-2F_{i-(1/2),j}^{x_1,1}-2F_{i,j-(1/2)}^{y_1,1}\right)\right],\\ c_6 = &-\frac{1}{8H^2}\left[(H+\delta)\left(2F_{i+(1/2),j}^{x_2,1}-F_{i,j+(1/2)}^{y_1,1}+F_{i,j+(1/2)}^{y_1,2}+F_{i,j-(1/2)}^{y_2,1}-F_{i,j-(1/2)}^{y_2,2}\right)+(H-\delta)\left(2F_{i+(1/2),j}^{x_1,1}-F_{i,j+(1/2)}^{y_2,1}+F_{i,j+(1/2)}^{y_2,2}-F_{i,j-(1/2)}^{y_1,2}\right)\right],\\ c_7 = &-\frac{1}{8H^2}\left[(H+\delta)\left(F_{i,j+(1/2)}^{y_2,1}-F_{i,j+(1/2)}^{y_2,2}+F_{i-(1/2),j}^{x_1,1}-F_{i-(1/2),j}^{x_1,2}\right)+(H-\delta)\left(F_{i,j+(1/2)}^{y_1,1}-F_{i,j+(1/2)}^{y_1,2}+F_{i-(1/2),j}^{x_2,1}-F_{i-(1/2),j}^{x_2,2}\right)\right],\\ c_8 = &-\frac{1}{8H^2}\left[(H+\delta)\left(-F_{i+(1/2),j}^{x_1,1}+F_{i+(1/2),j}^{x_1,2}+2F_{i,j+(1/2)}^{y_2,1}+F_{i-(1/2),j}^{x_2,1}-F_{i-(1/2),j}^{x_2,2}\right)+(H-\delta)\left(-F_{i+(1/2),j}^{x_2,1}+F_{i+(1/2),j}^{x_2,2}+2F_{i,j+(1/2)}^{y_1,1}+F_{i+(1/2),j}^{x_1,1}-F_{i-(1/2),j}^{x_1,2}\right)\right],\\ c_9 = &-\frac{1}{8H^2}\left[(H+\delta)\left(-F_{i+(1/2),j}^{x_2,1}+F_{i+(1/2),j}^{x_2,2}+F_{i,j+(1/2)}^{y_2,1}+F_{i,j+(1/2)}^{y_2,2}\right)+(H-\delta)\left(-F_{i+(1/2),j}^{x_1,1}+F_{i+(1/2),j}^{x_1,2}-F_{i,j+(1/2)}^{y_1,1}+F_{i,j+(1/2)}^{y_1,2}\right)\right].\end{aligned} \tag{19}$$

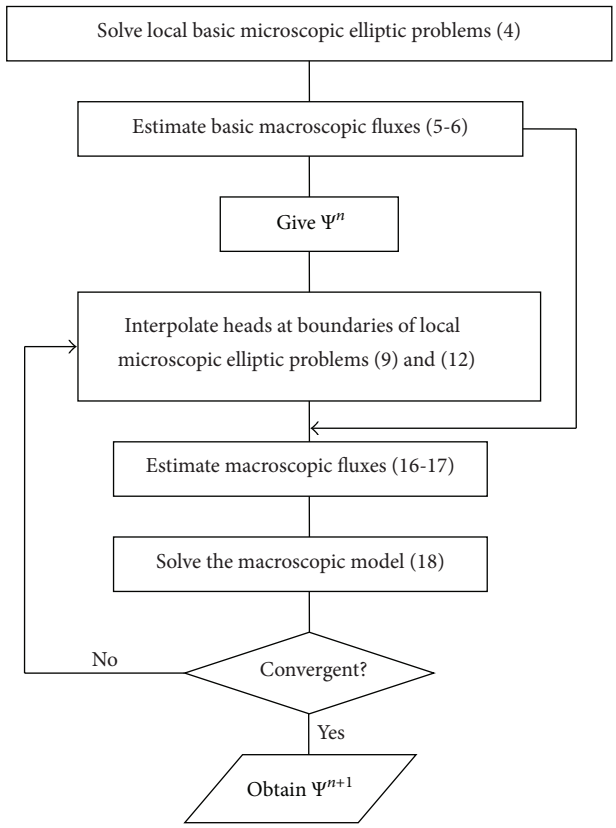

Figure 3: Flow chart of the new scheme at a time step.

Then, we solve the following equation at the coarse mesh by using MGD9V [26]:

$$\begin{aligned}
&-c_1\Psi^{n+1}_{i-1,j-1}-c_2\Psi^{n+1}_{i,j-1}-c_3\Psi^{n+1}_{i+1,j-1}-c_4\Psi^{n+1}_{i-1,j}\\
&\quad+\left(\frac{S_{si,j}}{\Delta t}-c_5\right)\Psi^{n+1}_{i,j}-c_6\Psi^{n+1}_{i+1,j}-c_7\Psi^{n+1}_{i-1,j+1}\\
&\quad-c_8\Psi^{n+1}_{i,j+1}-c_9\Psi^{n+1}_{i+1,j+1}\\
&=c_1\Psi^{n}_{i-1,j-1}+c_2\Psi^{n}_{i,j-1}+c_3\Psi^{n}_{i+1,j-1}+c_4\Psi^{n}_{i-1,j}\\
&\quad+\left(\frac{S_{si,j}}{\Delta t}+c_5\right)\Psi^{n}_{i,j}+c_6\Psi^{n}_{i+1,j}+c_7\Psi^{n}_{i-1,j+1}+c_8\Psi^{n}_{i,j+1}\\
&\quad+c_9\Psi^{n}_{i+1,j+1}+R^{n}_{i,j}.
\end{aligned}\tag{20}$$

Thus, the algorithm is completed. The solution procedure at a time step is illustrated in Figure 3. We also give a summary which only includes the relevant discrete equations necessary to implement the proposed method. Firstly, the basic elliptic problems (4) are solved. Then, basic macroscopic fluxes (5) and (6) are estimated, and the coefficients (19) are calculated. The above steps are finished at the preprocessing step. Finally, the macroscopic discrete equations (20) are evolved.

The algorithm described above is easy to extend to the steady flow problem in heterogeneous porous media. Under the condition of the steady flow, the left-hand side of (1) equals zero. Correspondingly, the left-hand side of macroscopic (2) equals zero. The remainder will similarly be completed; then we have

$$\begin{aligned}
&c_1\Psi_{i-1,j-1}+c_2\Psi_{i,j-1}+c_3\Psi_{i+1,j-1}+c_4\Psi_{i-1,j}+c_5\Psi_{i,j}\\
&\quad+c_6\Psi_{i+1,j}+c_7\Psi_{i-1,j+1}+c_8\Psi_{i,j+1}+c_9\Psi_{i+1,j+1}=-\frac{1}{2}R_{i,j}.
\end{aligned}\tag{21}$$

Although FDHMM proposed by Abdulle and E [20] works for the transient problem, it is also easy to extend to the steady problem. The given coarse- and fine-grid equations of FDHMM are elliptic equations in the steady condition. The iteration scheme of FDHMM is similar to that of the new scheme, and the solutions of both methods are the same.

The locally hydraulic conductivity (13) is assumed to be isotropic, but the macroscopic conductivity may be anisotropic or a full tensor because the final macroscopic scheme (18) is a nine-spot one. The algorithm may also be extended to general quadrilateral mesh; the method is similar to [28].

3. Evaluation of Numerical Accuracy

All porous media in nature are heterogeneous. The heterogeneity in this study comes from the hydraulic conductivity. As the standard deviation of logarithmic hydraulic conductivity increases, the heterogeneity increases. The random conductivity field is generated by the Turning Band method [29], in which the hydraulic conductivity is assumed to be locally isotropic. In this study, we used four saturated groundwater flow examples, including two steady flow examples and two transient flow examples, to show the main advantages of the constructed scheme. Also, influences of different factors are examined, such as conductivity fields with high variability as well as different correlation structures, the flow rate of the pumping well, and the size of the local microscale model, on the accuracy of the constructed scheme.

3.1. Implementation. The algorithm has been implemented in a FORTRAN code. Because it is difficult to construct interesting multiscale problem with an exact solution, people often compare the coarse scale solution obtained by the multiscale method with a computed reference solution obtained on the fine scale. We have employed the conventional finite difference method with multigrid over a fine mesh to solve the original equation and refer to this solution as the "exact" solution.

As a measure of the error, we take the relative L_2 norm and the relative maximum norm

$$\begin{aligned}
\mathrm{eer}_2&=\left[\frac{\sum_{i=1}^{N'}\left(\Psi_i-\Psi\left(\mathbf{x}_i\right)\right)^2}{\sum_{i=1}^{N'}\left(\Psi\left(\mathbf{x}_i\right)\right)^2}\right]^{1/2},\\
\mathrm{eer}_\infty&=\frac{\max_{i=1,\ldots,N'}\left|\Psi_i-\Psi\left(\mathbf{x}_i\right)\right|}{\max_{i=1,\ldots,N'}\left|\Psi\left(\mathbf{x}_i\right)\right|},
\end{aligned}\tag{22}$$

respectively, where N' is the total number of nodes on the coarse mesh, Ψ_i denotes the coarse solution at the coarse node

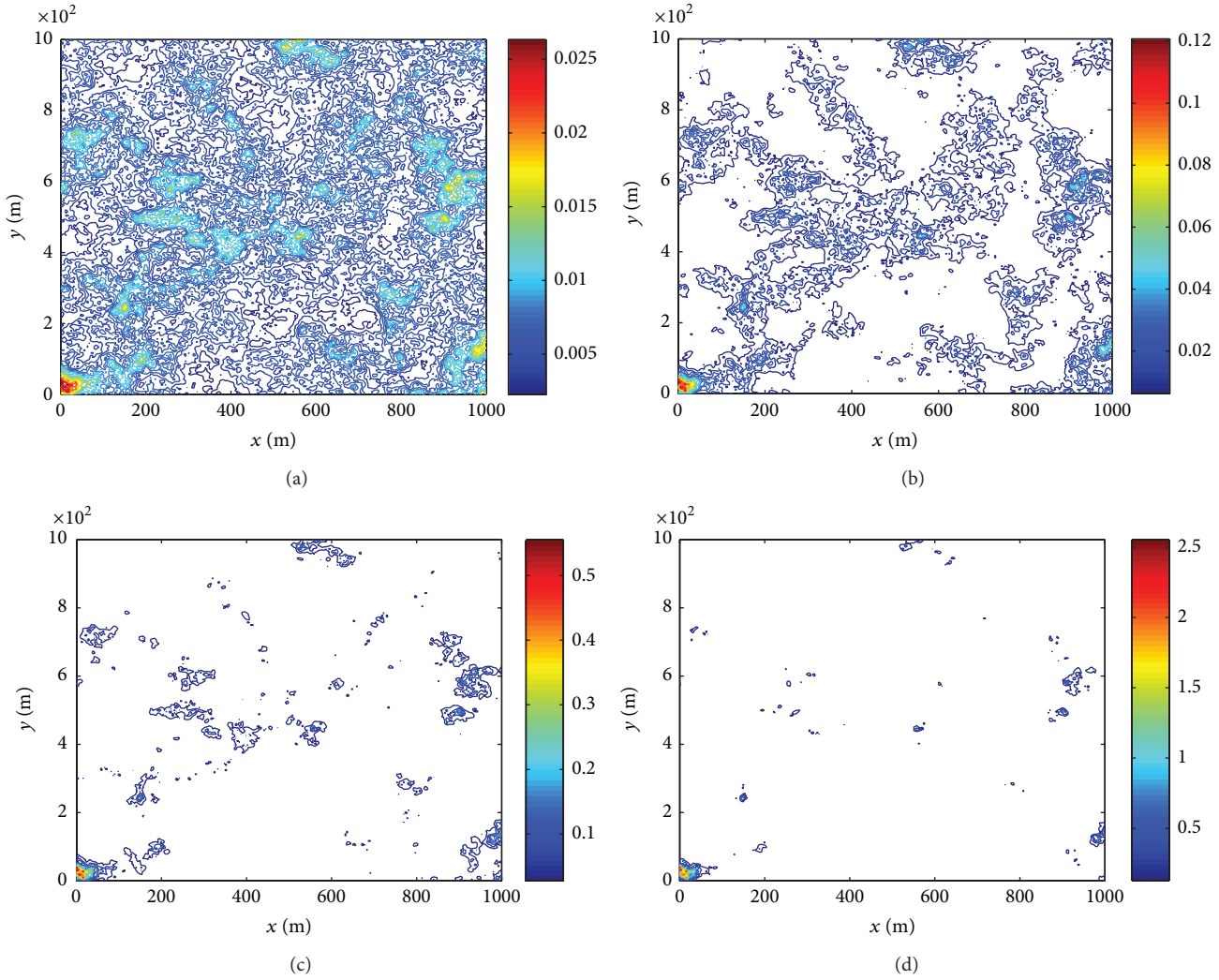

FIGURE 4: A realization of the random saturated conductivity fields of different standard deviations under $\lambda_x = \lambda_y = 100$ m: (a) $\sigma_{\ln K} = 0.5$, (b) $\sigma_{\ln K} = 1.0$, (c) $\sigma_{\ln K} = 1.5$, and (d) $\sigma_{\ln K} = 2.0$.

$\mathbf{x}_i$, and $\Psi(\mathbf{x}_i)$ denotes the "exact" solution projected on the coarse mesh; that is, $\Psi(\mathbf{x}_i) = \psi(\mathbf{x}_i)$ at the coarse node. Here, $\psi(\mathbf{x})$ is the "exact" solution.

In all test examples, the study domain Ω is a rectangle covering 1 km × 1 km with the point $(0, 0)$ as the origin. A uniform finite difference mesh is constructed by dividing Ω into an $N \times N$ mesh. The fine mesh is a 256×256 mesh, and the "exact" solution and the random hydraulic conductivity field are obtained on this mesh. The coarse mesh is a 16×16 mesh and the coarse solution is obtained by using the multiscale method on this mesh.

3.2. Steady Flow Problems with Isotropic and Anisotropic Microstructure. We impose the Dirichlet-Neumann boundary condition for the test steady flow problem. The left and right sides of boundary are Dirichlet boundaries. Head on the left is 20 m, and that on the right side is 10 m. The top and bottom sides are impermeable boundaries. To start the computation using the new scheme, we need to choose the size of the control volume δ. In this study, δ is chosen to be equal to a half of the coarse mesh size, which means that we only use about 50% of the total data at the small scale; that is, $\delta = (1/2)H$. Every control volume I^{δ} is uniformly divided into an 8×8 mesh such that its mesh size equals the size of the fine mesh.

Four conductivity fields with isotropic correlation microstructure are first applied. Correlation lengths of these conductivity fields are $\lambda_x = \lambda_y = 10$ m, $\lambda_x = \lambda_y = 20$ m, $\lambda_x = \lambda_y = 40$ m, and $\lambda_x = \lambda_y = 100$ m, respectively. We assume that the geometric mean of hydraulic conductivity is $\overline{K} = 0.006$ m/min. Under $\sigma_{\ln K} = 0.5, 1.0, 1.5, 2.0$, where $\sigma_{\ln K}$ is the standard deviation of logarithmic hydraulic conductivity, these four conductivity fields vary by about one, three, five, and six orders of magnitude, respectively. A realization of the random conductivity fields with $\lambda_x = \lambda_y = 100$ m and $\sigma_{\ln K} = 0.5, 1.0, 1.5, 2.0$ is plotted in Figure 4. Figure 5 plots the errors of the solutions of the constructed scheme for different correlation lengths at

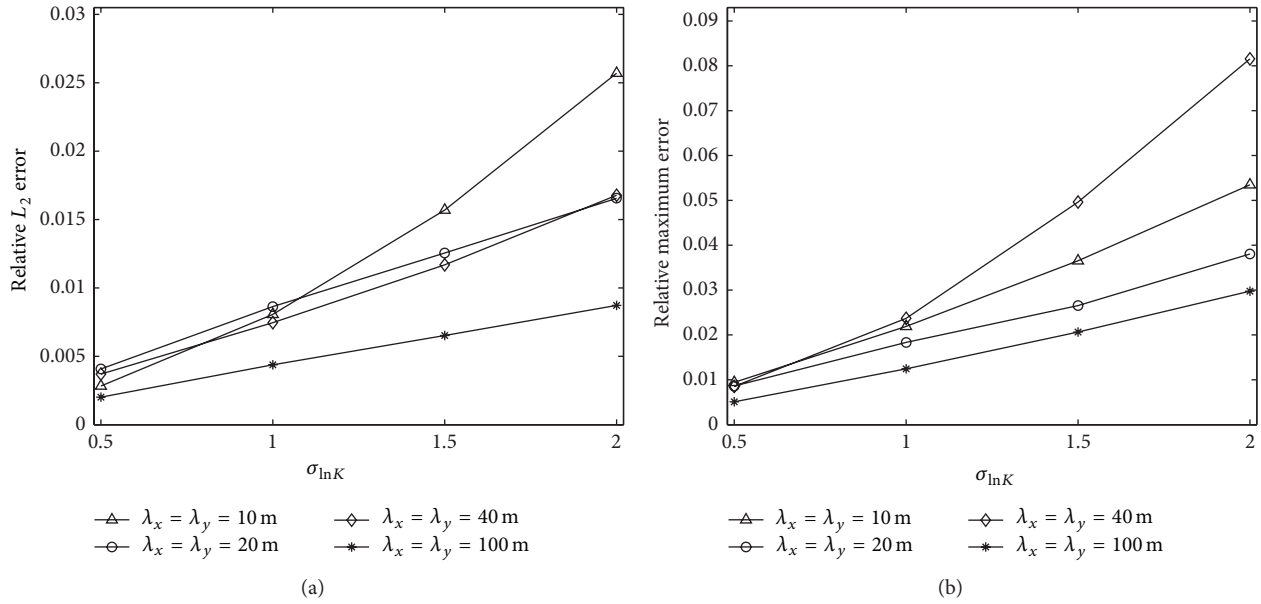

FIGURE 5: Relative (a) L_2 and (b) maximum errors between the fine-scale model and the new scheme for the steady flow problem with isotropic correlation microstructure.

$\sigma_{\ln K} = 0.5, 1.0, 1.5, 2.0$. It illustrates that the larger standard deviation of logarithmic hydraulic conductivity leads to the less accurate results. Furthermore, at the case with $\lambda_x = \lambda_y = 10$ m and $\sigma_{\ln K} = 2.5$, in which the conductivity field varies by about nine orders of magnitude, the new scheme is even not convergent, although it works for other correlation scales for the same logarithmic conductivity variance. The reason may be that conductivities of highly heterogeneous systems are highly discontinuous, which makes the direct application of the algorithm infeasible. It may also indicate that the standard deviation of logarithmic hydraulic conductivity plays an important role in the accuracy of the new scheme. At the same time, when $\sigma_{\ln K} = 0.5$, the results obtained under different correlation lengths have about the same accuracy and the correlation length of conductivity field shows no significant effect on the accuracy of the new scheme. It is noted that the correlation length is even larger than the size of the control volume in the case with $\lambda_x = \lambda_y = 100$ m. The heads in section $y = 500$ m obtained from the fine-scale model on the fine mesh and the constructed scheme on the coarse mesh for the case with $\lambda_x = \lambda_y = 100$ m and $\sigma_{\ln K} = 0.5, 1.0, 1.5, 2.0$ are depicted in Figure 6, and we observe that the solution obtained by the constructed scheme on a coarse mesh is able to approximate the exact solution. The above discussion indicates that the new scheme gives a reasonable accuracy for the test steady flow examples with isotropic correlation microstructure.

Convergence should be a necessary condition for the new scheme as a good numerical method. Here, we only consider the conductivity field with $\lambda_x = \lambda_y = 100$ m. Fixing $\delta = (1/2)H$, Figure 7 plotted the relative errors for coarse meshes with 4×4, 8×8, 16×16, and 32×32 elements under four cases that $\sigma_{\ln K} = 0.5, 1.0, 1.5, 2.0$, respectively. The errors monotonically decrease as the total number of coarse elements increases and tend to zero, which means that the new scheme solution converges as the coarse grid is refined.

Next, we turn to consider three conductivity fields with anisotropic correlation microstructure. Fixing y-direction correlation length $\lambda_y = 10$ m, x-direction correlation lengths of these conductivity fields are $\lambda_x = 20$ m, $\lambda_x = 40$ m, and $\lambda_x = 100$ m, respectively. Assume that $\overline{K} = 0.006$ m/min. Under $\sigma_{\ln K} = 0.5, 1.0, 1.5, 2.0$, these three conductivity fields vary by over one, three, five, and seven orders of magnitude, respectively. The results of the constructed scheme for different correlation lengths at $\sigma_{\ln K} = 0.5, 1.0, 1.5, 2.0$ are depicted in Figure 8. As in the previous example, the standard deviation of logarithmic hydraulic conductivity shows significant effect on the accuracy of the new scheme. The errors obviously increase with $\sigma_{\ln K}$ increasing. Compared to the standard deviation, the correlation length of conductivity field has relatively little influence on the accuracy of the new scheme. The maximum error in Figure 8 is attained at the case with $\lambda_x = 100$, $\lambda_y = 10$ m, and $\sigma_{\ln K} = 2.0$, and the relative L_2 and maximum errors of the solution of the constructed scheme are 2.28% and 5.88%, respectively. Similar to the isotropic case, the new scheme also gives a reasonable accuracy for the test steady flow examples with anisotropic correlation microstructure.

3.3. Aquifer Response to Sudden Change in Reservoir Level. We design this transient test example based on the example in [30]. Consider the confined aquifer in the study area. Initial head is equal to 20 m everywhere in the aquifer. We wish to simulate changes in head through time if, at $t = 0$, we suddenly drop the water level in the reservoir on four sides of the study area from 20 m to 10 m. The specific storage coefficient and the thickness of the aquifer are 2.0×10^{-4} m^{-1}

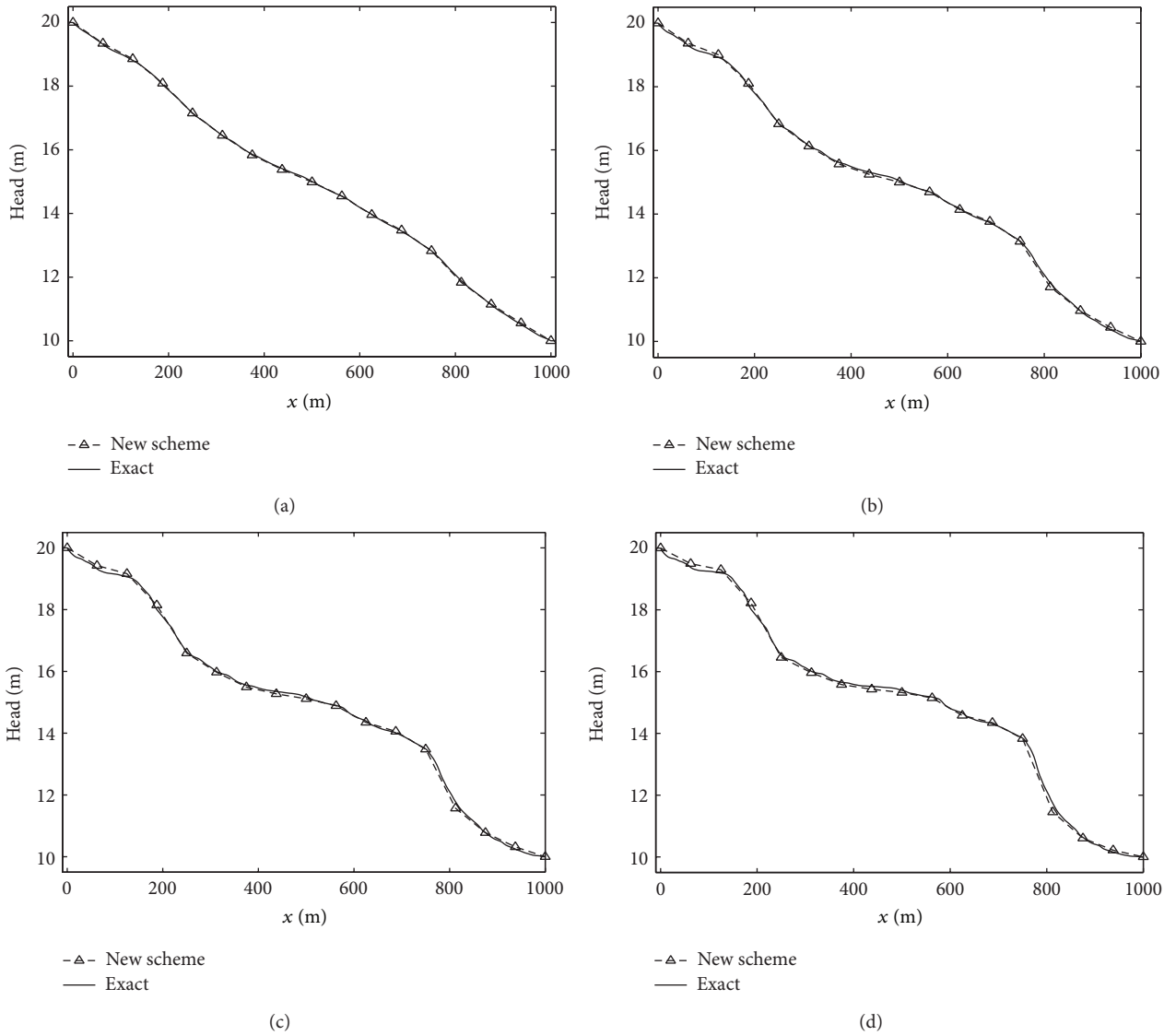

Figure 6: Exact solution and the coarse solution of the new scheme in section $y = 500$ m for the steady flow problem under isotropic correlation microstructure with different standard deviations: (a) $\sigma_{\ln K} = 0.5$, (b) $\sigma_{\ln K} = 1.0$, (c) $\sigma_{\ln K} = 1.5$, and (d) $\sigma_{\ln K} = 2.0$.

and 10 m, respectively. To generate the random hydraulic conductivity field, we assume that $\overline{K}$ is 0.003 m/min, the standard deviation of $\ln K$ is 1.5, and the correlation structure of the conductivity is anisotropic with $\lambda_x = 40$ m and $\lambda_y = 10$ m. Conductivity K in this random field varies by over five orders of magnitude. Fix a time step size $\Delta t = 5$ min and the study time 8000 min.

At first, accuracies and efficiencies of the constructed scheme and FDHMM are compared. Let the size of the control volume $\delta = (1/2)H$, and the control volume I^δ is uniformly divided into an 8×8 mesh. The computational results of different multiscale schemes at times = 500, 1000, 2000, 4000, 5000, 6000, and 8000 min are plotted in Figure 9. Figure 9 indicates that the new scheme seems to be more accurate than FDHMM. After $t = 1000$ min, eer_2 and eer_∞ of the solution of the constructed scheme monotonically decrease from 2.06% to 0.32% and from 7.37% to 0.95%, respectively, while those of FDHMM fluctuate in the intervals 2.71%~6.60% and 6.13%~15.40%, respectively. The reason leading to the difference between the results obtained by the constructed scheme and obtained by FDHMM may be the different approaches of estimating the macroscopic flux. Compared with FDHMM in which the approximation of the macroscopic flux is determined before the coarse equation is solved, for the constructed scheme, the computation of the macroscopic flux is coupled into the course of solving the coarse equation. Thus, a quasistationary state of the computed macroscopic flux is approached in the global domain for the constructed scheme and in the local domain for FDHMM, and it may make the constructed scheme give better accuracy than FDHMM for this test problem. We plot the heads in the whole study domain at times $t = 1000$ and 5000 min obtained from the fine-scale model on the fine mesh and two multiscale methods on the coarse mesh (Figure 10). We observe that

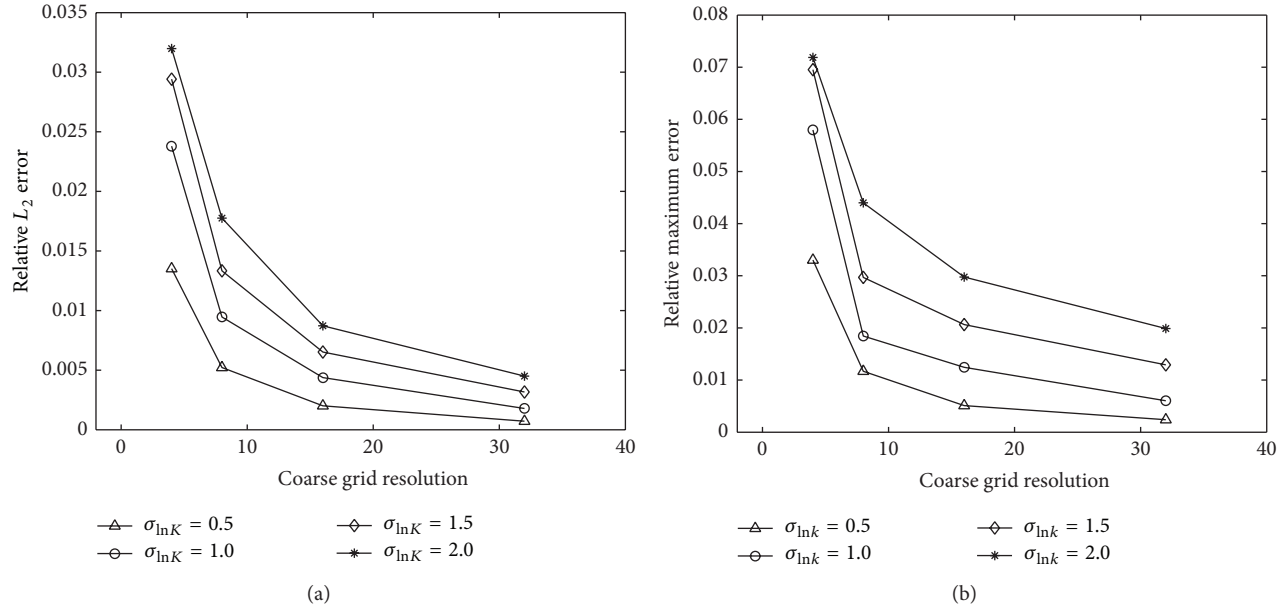

FIGURE 7: Relative (a) L_2 and (b) maximum errors of the solution of the new scheme for coarse grids with 4×4, 8×8, 16×16, and 32×32 elements.

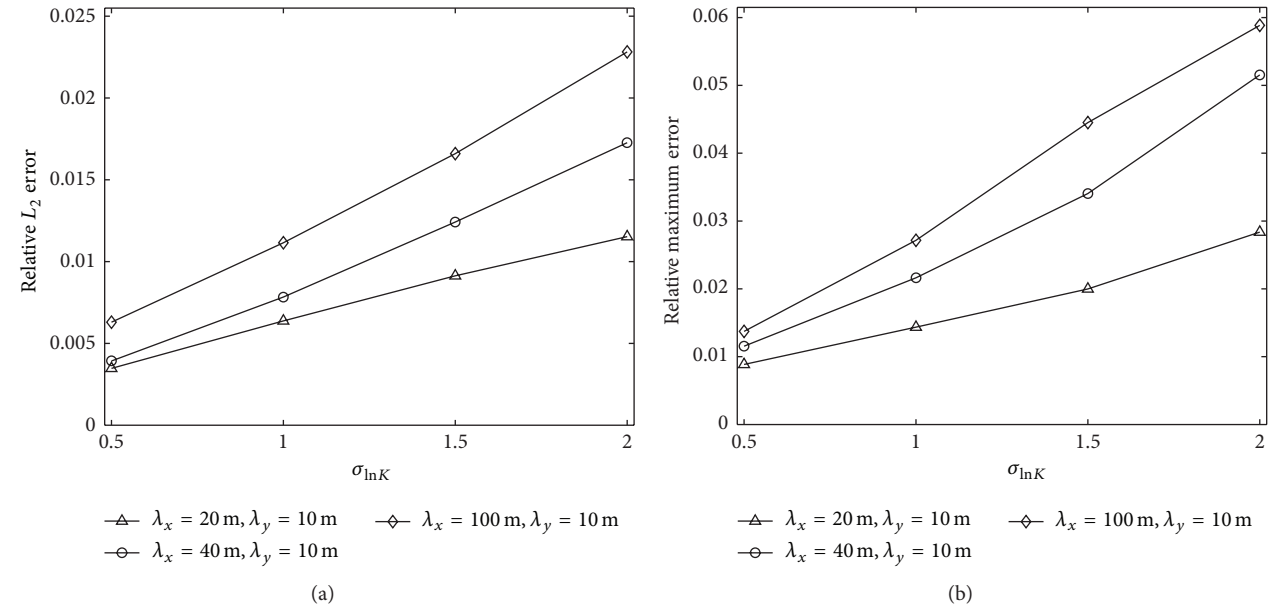

FIGURE 8: Relative (a) L_2 and (b) maximum errors between the fine-scale model and the new scheme for the steady flow problem with anisotropic correlation microstructure.

the heads obtained by the new scheme on a coarse mesh can satisfyingly approximate the "exact" heads, and FDHMM underestimates the heads at the coarse nodes.

The results were obtained on a computer running Windows XP with 2.66 GHz processor, 2 megabytes of cache, and 512 megabytes of RAM. For this test example, memory requirements using the conventional finite difference method, the constructed scheme, and FDHMM are about 27.7, 4.3, and 4.3 megabytes, respectively; CPU times using the three methods are about 12.1 min, 0.1 min, and 7.2 min, respectively. Compared with the computational cost of the conventional finite difference method, in our test example, the present new can save about 84.5% memory and about 99.2% CPU time, and FDHMM can save about 84.5% memory and about 40.5% CPU time. We need to solve $4N(N-1)$ basic microscopic elliptic problems in the constructed scheme. In fact, the computations of these basic microscale problems can be carried out sequentially, and, at a time,

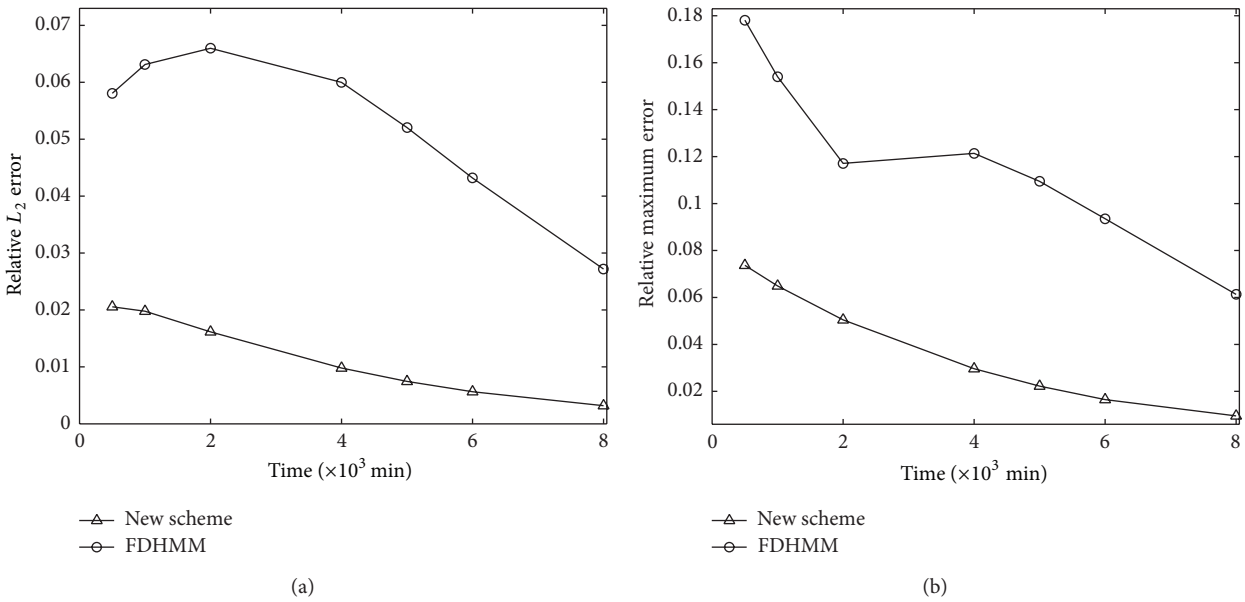

Figure 9: Relative (a) L_2 and (b) maximum errors between exact and two coarse solutions for aquifer response to sudden change in reservoir level.

we only need to solve two basic microscale problems (one for $I^{\delta}_{i+(1/2),j}$ and the other for $I^{\delta}_{i,j+(1/2)}$). When $\delta = (1/2)H$, every basic microscale problem has $(M+1)^2$ unknowns; the degrees of freedom of these basic microscale problems are $2(M+1)^2$. Added $(N+1)^2$ degrees of freedom of the macroscopic scheme, the total degrees of freedom of the new scheme are $2(M+1)^2 + (N+1)^2$. Similarly, the total degrees of freedom of FDHMM are also $2(M+1)^2 + (N+1)^2$, and degrees of freedom of the full fine scheme are $(2NM+1)^2$. Thus, both the constructed scheme and FDHMM can obviously save the memory requirement. The first saving in computational time in two multiscale schemes is achieved by reducing the computation of the fine mesh on the whole domain. The fine-scale global flow solution is decomposed into a series of local microscopic problems, and this greatly saves the computational time. However, local microscopic models of the new scheme only need to be solved once at the preprocessing step, while those of FDHMM need to be solved at every time step. Thus, the constructed scheme needs much less CPU time than FDHMM.

Next, we discuss the effects of different cell sizes on the accuracy of the constructed scheme. In a coarse 16×16 mesh, the coarse mesh size H equals 1000/16 m; we change the size of the control volume and let $\delta = (1/2)H, (3/4)H, H, (5/4)H$ in turn. To obtain the same size as the full fine mesh size, these control volumes are uniformly divided into 8×8, 12×12, 16×16, and 20×20 meshes in turn. The results obtained by the constructed scheme under different control volume sizes at times = 500, 1000, 2000, 4000, 5000, 6000, and 8000 min are depicted in Figure 11. We observe that the cases with $\delta = (3/4)H$, $\delta = H$, and $\delta = (5/4)H$ have about the same accuracy, and the case with $\delta = (1/2)H$ has a less accuracy. This is likely because, at three cases with $\delta = (3/4)H$, $\delta = H$, and $\delta = (5/4)H$, the main microstructural information is efficiently captured by the control volume. It may indicate that the control volume size shows no significant effect on the accuracy of the constructed scheme when it is chosen to be near the coarse mesh size.

3.4. Steady and Transient Flow Problems with Weak Well Drawdown. In this section, we first consider the steady flow problem with well drawdown in heterogeneous porous media. Similar to the examples discussed in [10, 31], we impose the following fixed head and no flux boundary conditions for the test example: heads on the left and right sides are 10 m and top and bottom sides are impermeable boundaries. In addition, a pumping well with the constant flow rate Q is located at the point (500 m, 500 m), and we let $Q = 0.12\,\mathrm{m}^3/\mathrm{min}$, $0.24\,\mathrm{m}^3/\mathrm{min}$, $0.36\,\mathrm{m}^3/\mathrm{min}$, and $0.48\,\mathrm{m}^3/\mathrm{min}$, respectively. The aquifer is 10 m thick. We also choose $\delta = (1/2)H$ and uniformly divide every control volume I^{δ} into an 8×8 mesh such that its mesh size equals the size of the fine mesh.

Four conductivity fields with $\sigma_{\ln K} = 0.5, 1.0, 1.5, 2.0$ are considered. Assume that the geometric mean of hydraulic conductivity is $\overline{K} = 0.018\,\mathrm{m/min}$ and the anisotropic correlation microstructure with $\lambda_x = 40$, $\lambda_y = 10$ m. The errors of the results obtained by the constructed scheme under different well flow rates at $\sigma_{\ln K} = 0.5, 1.0, 1.5, 2.0$ are plotted in Figure 12. Different from the examples of Section 3.2, the standard deviation of logarithmic hydraulic conductivity shows no significant effect on the accuracy of the new scheme. For example, given $Q = 0.12\,\mathrm{m}^3/\mathrm{min}$, when $\sigma_{\ln K} = 0.5, 1.0, 1.5, 2.0$, relative L_2 errors of the solution of the new scheme are about 0.15%, 0.15%, 0.17%, and 0.20%, respectively, and relative maximum errors of the solution

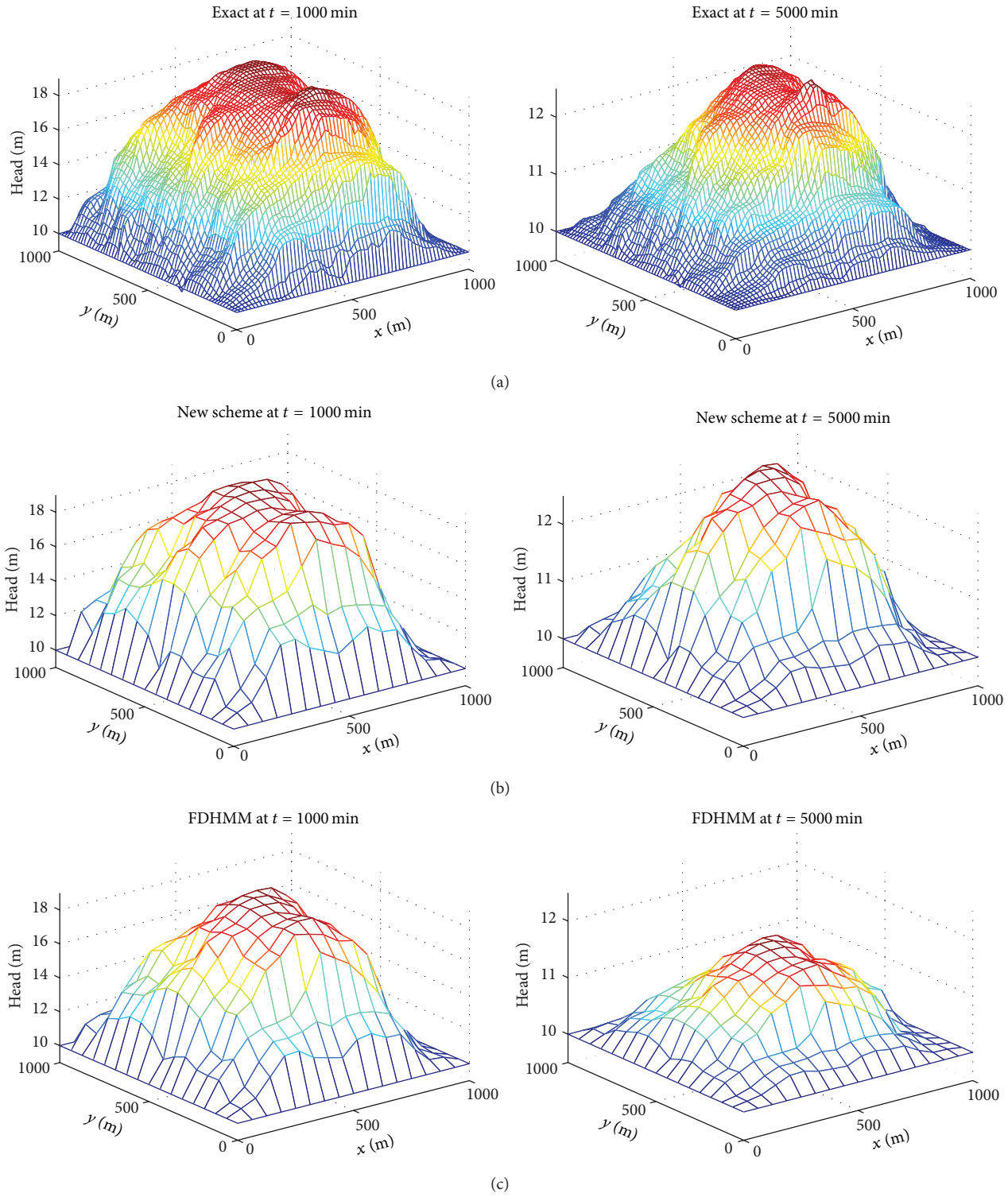

FIGURE 10: Exact solution (top), the coarse solutions of the new scheme (middle), and FDHMM (bottom) at times t = 1000 min (left) and 5000 min (right) for aquifer response to sudden change in reservoir level.

of the new scheme are 2.52%, 2.29%, 2.17%, and 2.00%, respectively. The important factor affecting the accuracy of the new scheme is the flow rate of the pumping well. The larger the flow rate of pumping well is, the larger the resulting errors are. Setting $\sigma_{\ln K}$ = 1.0, Figure 13 plots the heads in section y = 500 m obtained from the fine-scale model on the fine mesh and the constructed scheme on the coarse mesh for the cases Q = 0.12, 0.24, 0.36, 0.48 m^3/min. There are larger errors of the results of the constructed scheme near point (500 m, 500 m), which are caused by the pumping well

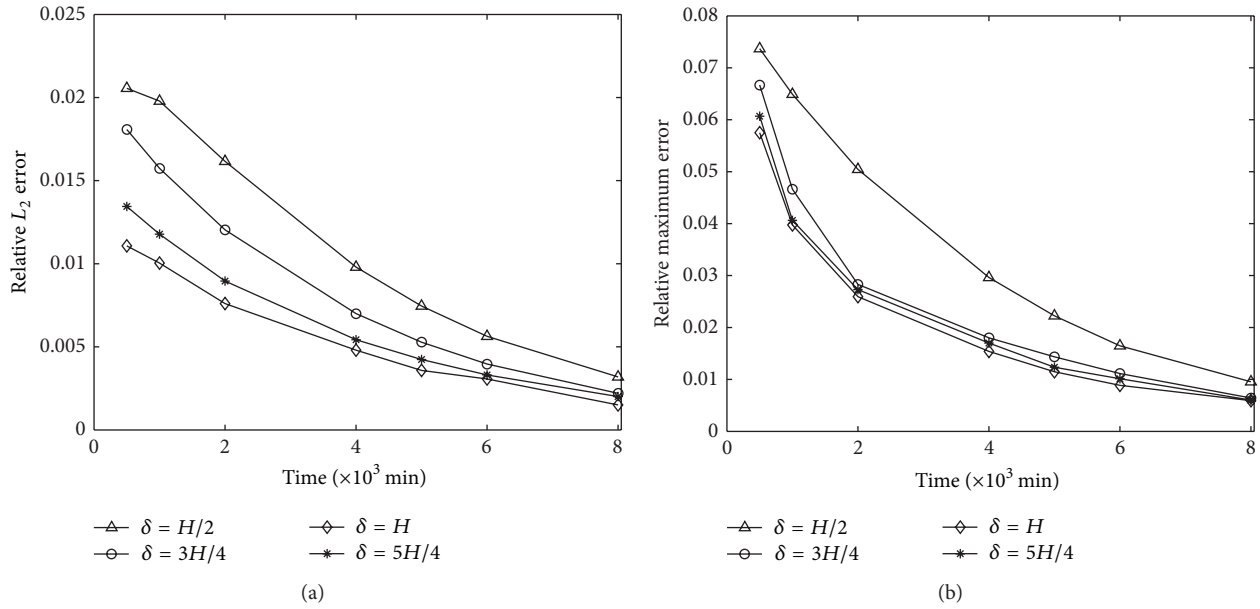

Figure 11: Relative (a) L_2 and (b) maximum errors between the fine-scale model and the new scheme under different cell sizes for aquifer response to sudden change in reservoir level.

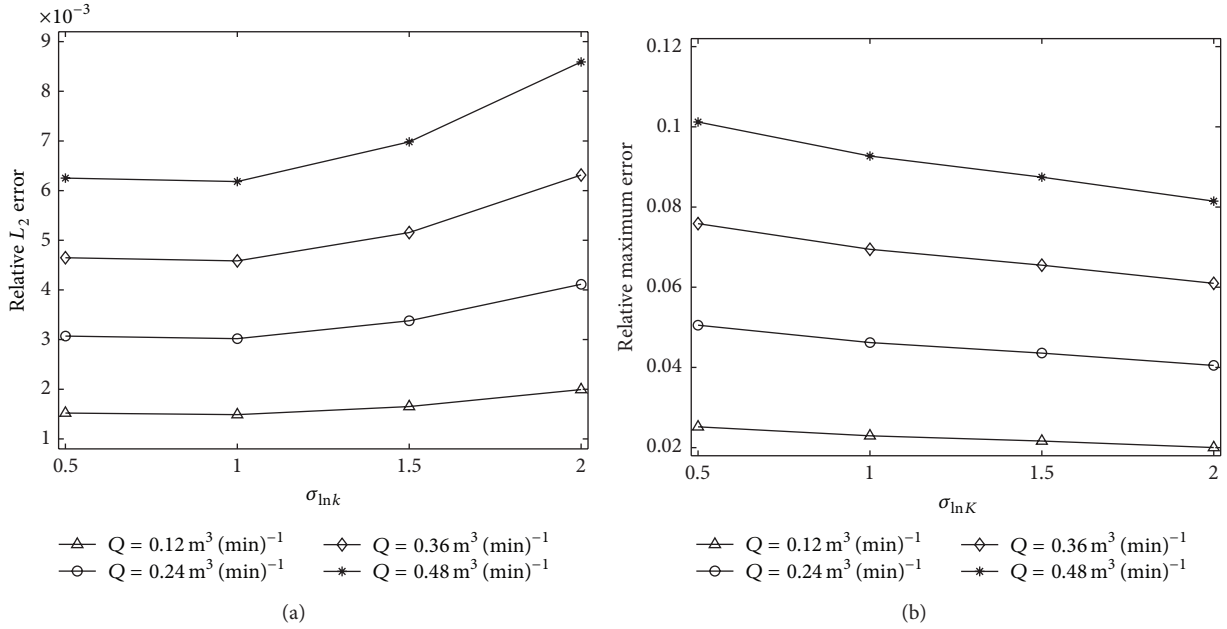

Figure 12: Relative (a) L_2 and (b) maximum errors between the fine-scale model and the new scheme for the steady flow problem with well drawdown.

at this point. This is likely because heads near the well vary nonlinearly with distance to the well, which cannot be well described by the constructed scheme. On the other hand, the problem of the well singularity may be related to the chosen scale. If we choose a coarse 32×32 mesh and $\delta = (1/2)H$ and resolve this well drawdown problem. When $\sigma_{\ln K} = 1.0$, in Figure 14, we replot the curves shown in Figure 13. We observe that the accuracy of the new scheme was improved markedly.

Next, we consider the transient well drawdown problem in heterogeneous porous media. Boundaries of the study area are Dirichlet types. Heads on four sides are all 10 m. Initial pressure head is also 10 m everywhere in the aquifer. The specific storage coefficient is $2.0 \times 10^{-4}\,\mathrm{m}^{-1}$ and the aquifer is 10 m thick. There is a pumping well at the point (500 m, 500 m). The well has the constant flow rate of $0.24\,\mathrm{m}^3/\mathrm{min}$ and is pumped for 1600 min in the problem. The time step is 1 min for every method. This test example is analogous to

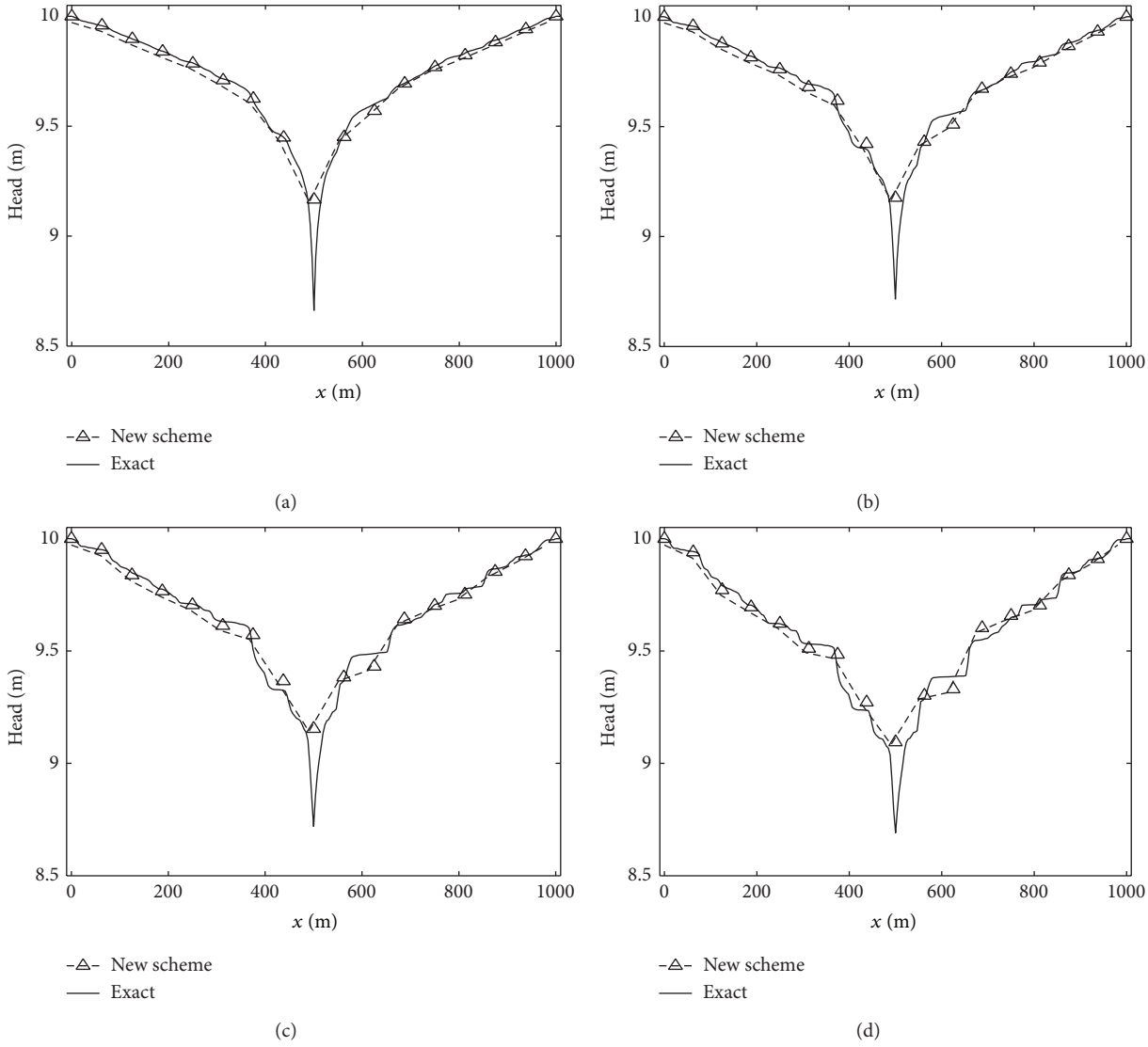

Figure 13: Exact solution and the coarse solution of the new scheme in section $y = 500$ m for the steady well drawdown problem under different well flow rates: (a) $Q = 0.12$, (b) $Q = 0.24$, (c) $Q = 0.36$, and (d) $Q = 0.48$ $(\mathrm{m}^3(\mathrm{min})^{-1})$.

the examples used in [10, 31]. The statistical parameters used to describe random conductivity field are $\overline{K} = 0.018$ m/min, $\sigma_{\ln K} = 1.0$, $\lambda_x = 40$ m, and $\lambda_y = 10$ m. This random conductivity field varies by over three orders of magnitude.

Similar to Section 3.3, we compare accuracies and efficiencies of the constructed scheme and FDHMM. The control volume I^{δ} has a size of $(1/2)H$ and is uniformly divided into an 8×8 mesh. We plot the computational results of different multiscale schemes at times = 100, 200, 400, 800, 1000, 1200, and 1600 min (Figure 15). The constructed scheme gives a little more accuracy than FDHMM. Over the whole simulating time, eer_2 and eer_∞ of the solution of the new scheme are less than 0.26% and 4.15%, respectively, and those of FDHMM are less than 0.38% and 5.44%, respectively. Figure 16 shows the heads at times $t = 200$ and 1000 min in section $y = 500$ m obtained from the fine-scale model on the fine mesh and two multiscale methods on the coarse mesh. We observe that the solutions obtained by both the constructed scheme and FDHMM on a coarse mesh are able to satisfyingly approximate the exact solution except of the well singularity. Near the well singularity, the results obtained by both multiscale methods are in rough agreement with those obtained by the fine-scale model, and the heads are overestimated to be about 0.45 m and 0.50 m by the constructed scheme and FDHMM at the well singularity, respectively, at $t = 200$ min. This fact may imply that, although a quasibalance state of the macroscopic flux is achieved in the global domain for the constructed scheme versus in the local domain for FDHMM, this advantage of the constructed scheme is not obvious for the well drawdown problem.

Computational costs of the three methods in this test example are similar to those in the test example discussed in

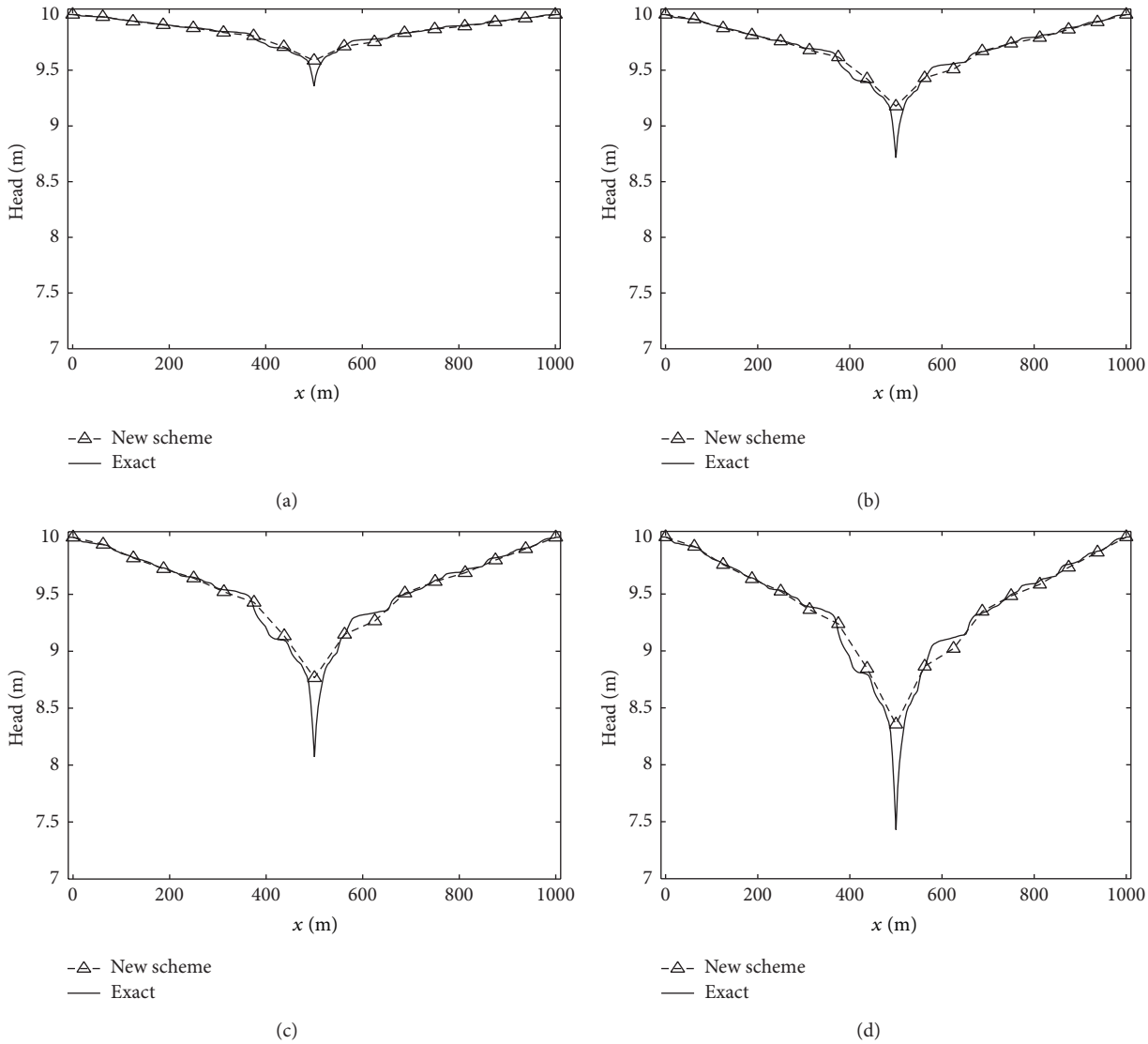

FIGURE 14: Exact solution and the coarse solution of the new scheme at the coarse 32×32 mesh in section $y = 500$ m under different well flow rates: (a) $Q = 0.12$, (b) $Q = 0.24$, (c) $Q = 0.36$, and (d) $Q = 0.48$ $(\mathrm{m}^3(\mathrm{min})^{-1})$.

Section 3.3 and are omitted in this section. This is followed by a discussion of effects of different cell sizes on the accuracy of the constructed scheme. As described in Section 3.3, in a coarse 16×16 mesh, the control volumes are chosen to have sizes of $\delta = (1/2)H, (3/4)H, H, (5/4)H$ and are uniformly divided into 8×8, 12×12, 16×16, and 20×20 meshes in turn. Plotted in Figure 17 are the calculated results of the constructed scheme under different control volume sizes at times $t = 100, 200, 400, 800, 1000, 1200,$ and 1600 min. It indicates that four cases give a reasonable accuracy in eer_2 and eer_∞. We observe that the results for $\delta = H$ are the best, the results for $\delta = (3/4)H$ are less accurate than those for $\delta = H$, the results for $\delta = (5/4)H$ are less accurate than those for $\delta = (3/4)H$, and the results for $\delta = (1/2)H$ are the worst. The results obtained under three cases with $\delta = (3/4)H, H, (5/4)H$ are very similar. Thus, the control volume size may be chosen to be near the size of the coarse mesh for the sake of the accuracy of the constructed scheme. In addition, under the cases with $\delta = (1/2)H$ and $\delta = (3/4)H$, we only use about 50% and 75% of the information of the whole microstructure, respectively. This flexibility of choosing the size of the control volume means that the constructed scheme may be applied to the flow problem for which the microstructure cannot be completely found beforehand.

4. Conclusion

A new scheme of the finite difference heterogeneous multiscale method, which puts more emphasis on the interaction between the macro- and microscale behaviors, has been presented for solving saturated water flow problems in random porous media. The macroscopic iteration formulas of steady and transient flow problems have been explicitly deduced. By

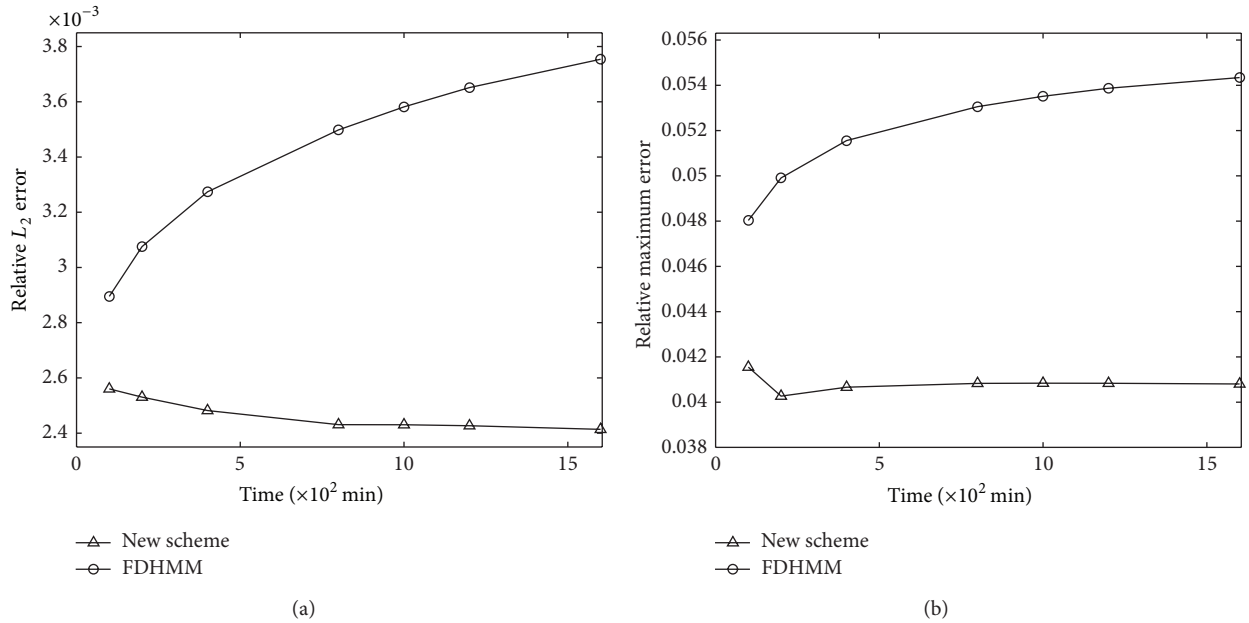

FIGURE 15: Relative (a) L_2 and (b) maximum errors between exact and two coarse solutions for the transient flow problem with weak well drawdown.

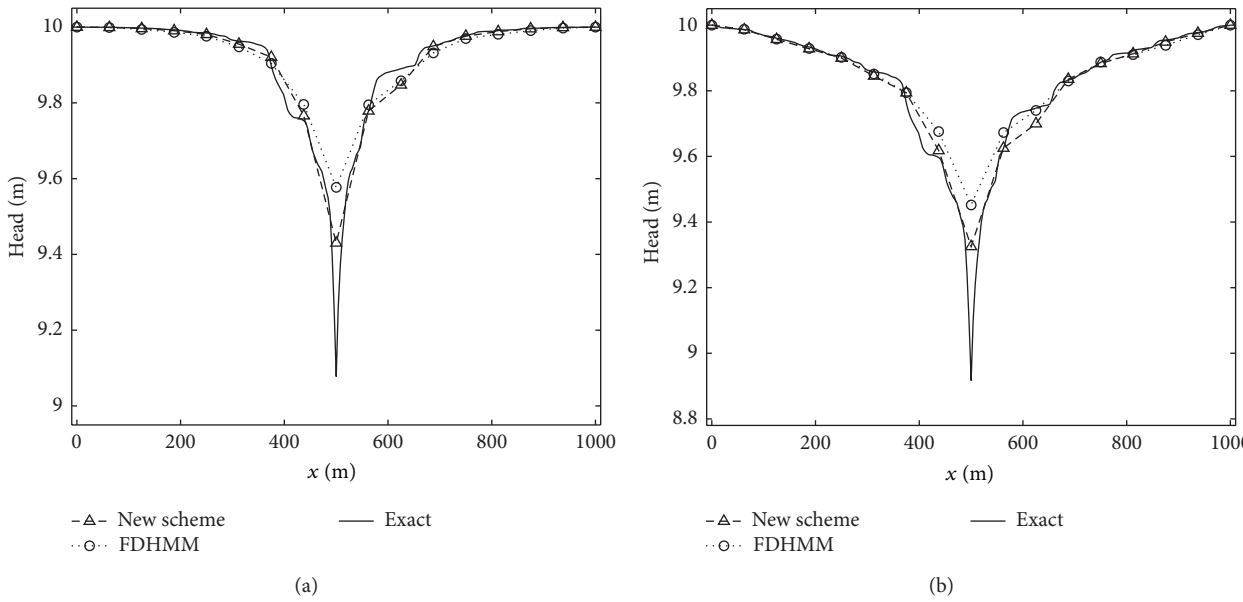

FIGURE 16: Exact solution and two coarse solutions at times (a) $t = 200$ min and (b) 1000 min in section $y = 500$ m for the transient flow problem with weak well drawdown.

solving basic microscopic elliptic problems and estimating basic macroscopic fluxes, it is subtly brought to the large scale for microscale information of the medium property and useful information about the gradients of the solutions of basic microscopic elliptic models. For the transient flow problem, different from that FDHMM needs the macroscopic and microscopic evolution at every time step, the constructed scheme implements the microscopic evolution at the preprocessing step and only needs the macroscopic evolution at every time step, which offers substantial saving in the computational cost. The constructed scheme saves about 58.7% CPU time compared to FDHMM for aquifer response to sudden change in reservoir level on the case $\delta = (1/2)H$. Different numerical examples, including two steady flow problems and two transient flow problems subject to Dirichlet-Neumann boundary type, are applied to test the efficiency and accuracy of the constructed scheme. We have considered seven correlation lengths and four standard deviations of the hydraulic conductivity field for steady flow problems with isotropic and anisotropic microstructure and

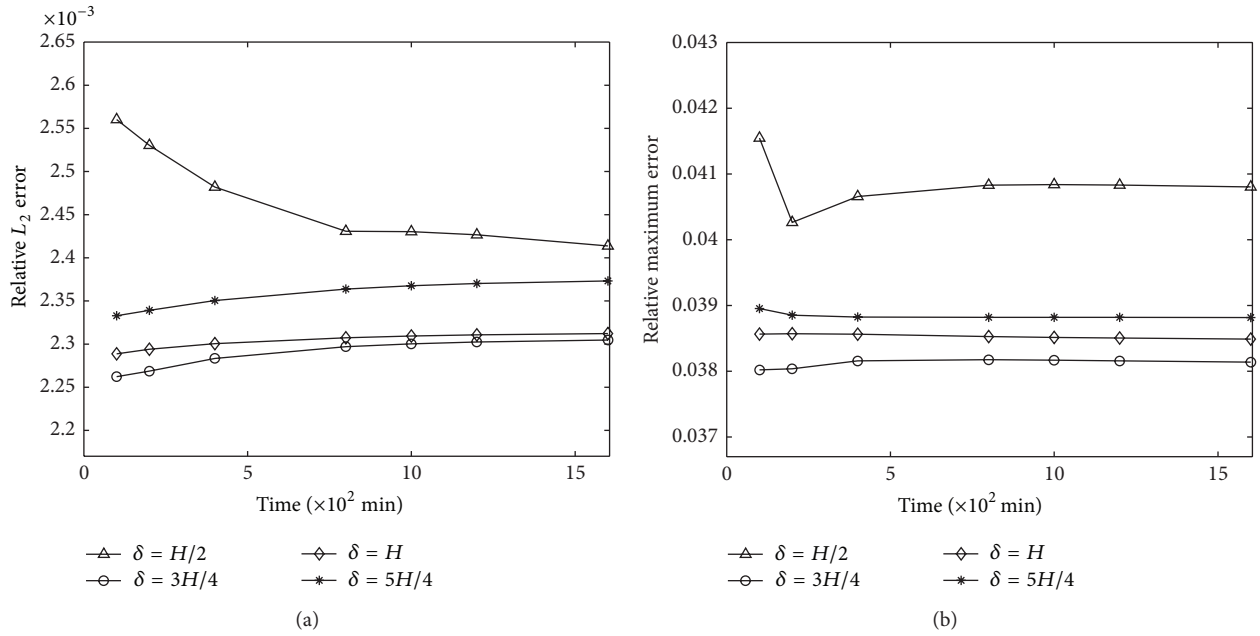

FIGURE 17: Relative (a) L_2 and (b) maximum errors between the fine-scale model and the new scheme under different cell sizes for the transient flow problem with weak well drawdown.

considered four flow rates of the pumping well and four standard deviations of the hydraulic conductivity field for the steady flow problem with well drawdown. In every transient flow problem, we have also considered four sizes of the control volume. The numerical experiments demonstrate that the constructed scheme gives a better accuracy than FDHMM for aquifer response to sudden change in reservoir level and gives a comparable accuracy to FDHMM for the weak well drawdown problem. The numerical experiments also indicate that the constructed scheme can efficiently capture the macroscale behavior of the solution on a coarse mesh for the steady and transient flow problems without well drawdown, and the scheme can approximately handle the weak well drawdown problem. The well singularity is related to the chosen scale. We may refine the coarse mesh size to improve the accuracy of the solution to the well drawdown problem. The standard deviation of logarithmic hydraulic conductivity field plays an important role in the accuracy of the constructed scheme. The larger the standard deviation is, the less accurate the results are. The spatial correlation length of random conductivity field has relatively little influence on the accuracy of the constructed scheme. To obtain a reasonable accuracy, the size of the control volume may be chosen to be near or to be equal to the coarse mesh size or other suitable size if necessary. This flexibility of choosing the size of the control volume means that the constructed scheme can be not only applied to the flow problem for which the microstructure is completely found but may be also applied to the flow problem for which the microstructure is only partly found beforehand.

This study is limited to two-dimensional saturated flow through heterogeneous porous media. We also plan to extend this scheme to solve unsaturated water flow problems with heterogeneity which would be more difficult to simulate.

Conflict of Interests

The authors declare that there is no conflict of interests regarding the publication of this paper.

Acknowledgments

This work was supported by the Natural Science Foundation of China (51039007), the Natural Science Foundation of Hunan Province (13JJ3120), and the Construct Program of the Key Discipline in Hunan Province.

References

[1] B. B. Dykaar and P. K. Kitanidis, "Determination of the effective hydraulic conductivity for heterogeneous porous media using a numerical spectral approach 2: results," *Water Resources Research*, vol. 28, no. 4, pp. 1167–1178, 1992.

[2] T. Y. Hou and X.-H. Wu, "A multiscale finite element method for elliptic problems in composite materials and porous media," *Journal of Computational Physics*, vol. 134, no. 1, pp. 169–189, 1997.

[3] T. Y. Hou, X.-H. Wu, and Z. Cai, "Convergence of a multiscale finite element method for elliptic problems with rapidly oscillating coefficients," *Mathematics of Computation*, vol. 68, no. 227, pp. 913–943, 1999.

[4] W. E and B. Engquist, "The heterogeneous multiscale methods," *Communications in Mathematical Sciences*, vol. 1, no. 1, pp. 87–132, 2003.

[5] Y. Efendiev and A. Pankov, "Numerical homogenization of nonlinear random parabolic operators," *Multiscale Modeling & Simulation*, vol. 2, no. 2, pp. 237–268, 2004.

[6] I. Babuška, "Solution of interface problems by homogenization. I," *SIAM Journal on Mathematical Analysis*, vol. 7, no. 5, pp. 603–634, 1976.

[7] I. Babuška, "Homogenization and its application. Mathematical and computational problems," in *Numerical Solution of Partial Differential Equations. III*, B. Hubbard, Ed., pp. 89–116, Academic Press, New York, NY, USA, 1976.

[8] I. Babuška, "Solution of interface problems by homogenization. III," *SIAM Journal on Mathematical Analysis*, vol. 8, no. 6, pp. 923–937, 1977.

[9] L. J. Durlofsky, Y. Efendiev, and V. Ginting, "An adaptive local-global multiscale finite volume element method for two-phase flow simulations," *Advances in Water Resources*, vol. 30, no. 3, pp. 576–588, 2007.

[10] S. Ye, Y. Xue, and C. Xie, "Application of the multiscale finite element method to flow in heterogeneous porous media," *Water Resources Research*, vol. 40, Article ID W09202, 2004.

[11] Z. Chen and T. Y. Hou, "A mixed multiscale finite element method for elliptic problems with oscillating coefficients," *Mathematics of Computation*, vol. 72, no. 242, pp. 541–576, 2003.

[12] X. He and L. Ren, "Finite volume multiscale finite element method for solving the groundwater flow problems in heterogeneous porous media," *Water Resources Research*, vol. 41, no. 10, Article ID W10417, 2005.

[13] W. E, P. Ming, and P. Zhang, "Analysis of the heterogeneous multiscale method for elliptic homogenization problems," *Journal of the American Mathematical Society*, vol. 18, no. 1, pp. 121–156, 2005.

[14] P. Ming and P. Zhang, "Analysis of the heterogeneous multiscale method for parabolic homogenization problems," *Mathematics of Computation*, vol. 76, no. 257, pp. 153–177, 2007.

[15] P. Ming and X. Yue, "Numerical methods for multiscale elliptic problems," *Journal of Computational Physics*, vol. 214, no. 1, pp. 421–445, 2006.

[16] X. Yue and W. E, "Numerical methods for multiscale transport equations and application to two-phase porous media flow," *Journal of Computational Physics*, vol. 210, no. 2, pp. 656–675, 2005.

[17] F. Rotersa, P. Eisenlohra, L. Hantcherlia et al., "Overview of constitutive laws, kinematics, homogenization and multi-scalemethods in crystal plasticity finite-element modeling: theory, experiments, applications," *Acta Materialia*, vol. 58, pp. 1152–1211, 2010.

[18] J. Principe, R. Codina, and F. Henke, "The dissipative structure of variational multiscale methods for incompressible flows," *Computer Methods in Applied Mechanics and Engineering*, vol. 199, no. 13–16, pp. 791–801, 2010.

[19] V. John and A. Kindl, "Numerical studies of finite element variational multiscale methods for turbulent flow simulations," *Computer Methods in Applied Mechanics and Engineering*, vol. 199, no. 13–16, pp. 841–852, 2010.

[20] A. Abdulle and W. E, "Finite difference heterogeneous multi-scale method for homogenization problems," *Journal of Computational Physics*, vol. 191, no. 1, pp. 18–39, 2003.

[21] W. E, B. Engquist, and Z. Huang, "Heterogeneous multiscale method: a general methodology for multiscale modeling," *Physical Review B*, vol. 67, Article ID 092101, 2003.

[22] F. Chen and L. Ren, "Application of the finite difference heterogeneous multiscale method to the Richards' equation," *Water Resources Research*, vol. 44, Article ID W07413, 2008.

[23] X. Wen and J. J. Gomez-Hernandez, "Upscaling hydraulic conductivities in heterogeneous media: an overview," *Journal of Hydrology*, vol. 183, no. 1-2.

[24] P. Renard and G. de Marsily, "Calculating equivalent permeability: a review," *Advances in Water Resources*, vol. 20, no. 5-6, pp. 253–278, 1997.

[25] R. Du and P. Ming, "Heterogeneous multiscale finite element method with novel numerical integration schemes," *Communications in Mathematical Sciences*, vol. 8, pp. 797–1091, 2010.

[26] P. M. de Zeeuw, "Matrix-dependent prolongations and restrictions in a blackbox multigrid solver," *Journal of Computational and Applied Mathematics*, vol. 33, no. 1, pp. 1–27, 1990.

[27] L. W. Gelhar and C. L. Axness, "Three-dimensional stochastic analysis of macrodispersion in aquifers," *Water Resources Research*, vol. 19, no. 1, pp. 161–180, 1983.

[28] H. Cao and X. Yue, "The discrete finite volume method on quadrilateral mesh," *Journal of Suzhou University*, vol. 10, pp. 6–10, 2005.

[29] A. Mantoglou and J. L. Wilson, "The turning bands method for simulation of random fields using line generation by a spectral method," *Water Resources Research*, vol. 18, no. 5, pp. 1379–1394, 1982.

[30] H. F. Wang and M. P. Anderson, *Introduction to Groundwater Modeling: Finite Difference and Finite Element Methods*, W. H. Free-Man and Company, San Francisco, Calif, USA, 1982.

[31] X. He and L. Ren, "A modified multiscale finite element method for well-driven flow problems in heterogeneous porous media," *Journal of Hydrology*, vol. 329, no. 3-4, pp. 674–684, 2006.

Hindawi Publishing Corporation
Abstract and Applied Analysis
Volume 2014, Article ID 549189, 8 pages
http://dx.doi.org/10.1155/2014/549189

Review Article

Some Numerical Approaches to Solve Fluid Structure Interaction Problems in Blood Flow

Aik Ying Tang and Norsarahaida Amin

Department of Mathematical Sciences, Faculty of Science, Universiti Teknologi Malaysia UTM, 81310 Johor Bahru, Johor Darul Takzim, Malaysia

Correspondence should be addressed to Norsarahaida Amin; norsarahaida@utm.my

Received 4 October 2013; Accepted 12 January 2014; Published 23 February 2014

Academic Editor: Mohamed Fathy El-Amin

Some numerical approaches to solve fluid structure interaction problems in blood flow are reviewed. Fluid structure interaction is the interaction between a deformable structure with either an internal or external flow. A discussion on why the compliant artery associated with fluid structure interaction should be taken into consideration in favor of the rigid wall model being included. However, only the Newtonian model of blood is assumed, while various structure models which include, amongst others, generalized string models and linearly viscoelastic Koiter shell model that give a more realistic representation of the vessel walls compared to the rigid structure are presented. Since there exists a strong added mass effect due to the comparable densities of blood and the vessel wall, the numerical approaches to overcome the added mass effect are discussed according to the partitioned and monolithic classifications, where the deficiencies of each approach are highlighted. Improved numerical methods which are more stable and offer less computational cost such as the semi-implicit, kinematic splitting, and the geometrical multiscale approach are summarized, and, finally, an appropriate structure and numerical scheme to tackle fluid structure interaction problems are proposed.

1. Introduction

Fluid structure interaction is defined as the interaction between deformable structures with an internal or surrounding fluid flow. Such deformation can either be stable or oscillatory. Problems involving fluid structure interaction are classified into the one-way problem which occurs when the movement of the structure controls the motion of fluid but the fluid's motion does not influence the structure, or the two-way fluid structure interaction problem when the movement of the structure influences the motion of the fluid and vice versa [1].

Fluid structure interaction is more often considered in modelling biofluids because the interaction between the blood and vessel wall is of great clinical interest, for example, in studying cardiovascular diseases which are a major cause of death in developed countries [2].

The interaction between blood flow and vessel wall is often neglected because the coupled fluid and solid equations are complicated and difficult to solve [3]. Earlier numerical models used to predict blood flow are based on rigid geometries [4] in which only the arterial lumen needs to be reconstructed and discretized, yielding results that are reasonably accurate and can be obtained in a relatively short time [5]. However, there are still further considerations to be taken into account such as the elastic nature and stresses on the arterial wall that play crucial roles in arterial disease, as well as the material property alterations with the development of the atherosclerotic lesion [6].

Numerous studies had been carried out to compare the effect of the rigid and compliant wall on blood flow. Lee and Xu [7] indicated that the axial velocities at the center being of a rigid wall are higher compared to the ones in the compliant model. Mass conservation theory is utilized to explain such phenomena as the internal fluid pressure exerted on the vessel wall pushes the vessel wall outward consistently and slows the fluid flow due to the flow area expansion. Rigid wall simulation of blood flow through arteries also overpredicts the wall shears stress. These findings showed that incorporating fluid structure interaction has significant effects on blood

flow characteristics [2, 7]. Siogkas et al. [5] considered a rigid wall assumption and fluid structure interaction simulations of blood flow in the arterial segments. They concluded that the computational time for the simulation of fluid structure interaction is longer than that of the rigid wall assumption. It was found that the required time for the simulation is 30–40 minutes in the case of rigid wall but takes almost 5 hours in the compliant vessel.

Fluid structure interaction describes the wave propagation in arteries driven by the pulsatile blood flow. From the theoretical point of view, such problems are complex and challenging due to the high nonlinearity of the problem. Not only the fluid equation exhibits nonlinearity, the structure displacement modifies the fluid domain which generates geometrical nonlinearities as well [8].

The generalized string model had been utilized as the structure of blood flow in compliant vessels and arteries [9–15]. Causin et al. [16] explained that the generalized string model is a structural model derived from the theory of linear elasticity for a cylindrical tube with small thickness. The reference configuration is a cylindrical surface of the base circle radius R that is supposed to move in radially, neglecting the longitudinal and angular displacements. Nobile and Vergara [15] pointed out that the generalized string model neglects bending as well. According to Čanić et al. [17–20], there are no analytical results which are able to prove the well posedness of fluid structure interaction problems without assuming the structure model that includes the higher order derivative terms, capturing the viscoelastic behavior, or the terms describing bending rigidity. In hemodynamics, there exists a strong added mass effect issue in which the fluid and structure have comparable densities. If the structure density is higher than the fluid density, such as in aeroelasticity, the added mass effect is negligible. Various structural models are discussed in Section 2.

Numerical approaches of fluid structure interaction which are discussed in Section 3 can be broadly classified into two: the partitioned approach and the monolithic approach. Partitioned approach can be further subdivided into the loosely and strongly coupled algorithms [20–27]. In hemodynamics, the use of explicit partitioned algorithm turns out to be problematic where stability is concerned, particularly due to the added mass effect. In addition, the implicit partitioned algorithms are also affected by the added mass effect in terms of convergence. Special treatment of the interface conditions needs to be considered [8, 16, 28–30]. To date, it seems that only the monolithic and implicit schemes are applicable in blood flow simulation involving fluid structure interaction. However, they are costly in terms of computational cost, computational time, and memory requirement [9–11, 31–33]. In Section 4, the improved numerical methods which are stable but with low computational time are summarized.

2. Fluid Structure Interaction Problem Formulation

Fluid structure interaction problem can be divided into three parts: fluid problem, structure problem, and coupling condition. The model discussed here is based on the work of [9, 10]. Consider the flow of an incompressible, viscous Newtonian fluid in a two-dimensional symmetric channel with thin and deformable walls in Figure 1.

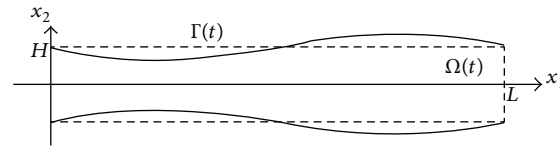

Figure 1: Sketch of flow region [9, 10].

2.1. The Fluid Problem. Let x_1 and x_2 denote the horizontal and vertical coordinates, respectively. Assume that the fluid domain is supplanted by a symmetry boundary condition at the axis of symmetry. The fluid domain is denoted by $\Omega(t)$, where

$$\Omega(t) = \left\{(x_1, x_2) \in R^2 \mid x_1 \in (0, L),\ x_2 \in \left(0, H + \eta(x_1, t)\right)\right\} \tag{1}$$

with the lateral (top) boundary condition

$$\Gamma(t) = \left\{(x_1, x_2) \in R^2 \mid x_1 \in (0, L),\ x_2 = \left(0, H + \eta(x_1, t)\right)\right\}. \tag{2}$$

The fluid flow is governed by the Navier-Stokes equations:

$$\rho_f \left(\frac{\partial \mathbf{u}}{\partial t} + \mathbf{u} \cdot \nabla \mathbf{u}\right) = \nabla \cdot \boldsymbol{\sigma}, \qquad \nabla \cdot \mathbf{u} = 0, \quad \text{in } \Omega(t) \text{ for } t \in (0, T), \tag{3}$$

where $\mathbf{u} = (u_1, u_2)$ is the fluid velocity, p is the fluid pressure, ρ_f is the fluid density, and $\boldsymbol{\sigma}$ is the fluid stress tensor. The fluid is assumed as Newtonian so that the fluid stress tensor is given by $\boldsymbol{\sigma} = -p\mathbf{I} + 2\mu\mathbf{D}(\mathbf{u})$, where μ is the fluid viscosity and $\mathbf{D}(\mathbf{u})$ is the rate-of-strain tensor $\mathbf{D}(\mathbf{u}) = ((\nabla \mathbf{u}) + (\nabla \mathbf{u})^T)/2$.

Blood is known as a suspension of red blood cells, white blood cells, and platelets in plasma. Although blood is not a Newtonian fluid, it is well accepted that, in medium-to-large arteries, the Newtonian assumption is acceptable. The non-Newtonian nature due to the particular rheology is relevant to the small arteries and capillaries where the diameter of the arteries and the size of the cell are comparable [18, 35]. For a critical review on blood flow, one can refer to [36] where the blood rheology, blood viscosity models, and conditions are listed. In this paper, only Newtonian fluid will be considered as in [9–11, 33].

2.2. The Structure Problem. Since the fluid structure interaction problem is complicated, the simplified model is used whenever possible. Previous studies indicated that the simplified mathematical model presenting the major physical characteristics is reasonable. A common set of simplifying models includes the use of two-dimensional models instead of the more realistic three-dimensional ones, cylindrical geometry

of a section of an artery without branching, neglecting the viscoelastic term and the bending rigidity, and even a further reduction to one-dimensional models. The two-dimensional and three-dimensional models are rather complex while the one-dimensional models suffer from a serious drawback as they are not closed and oversimplifying the viscous fluid [18–20].

Recent studies on the two-dimensional models with some simplification assumptions include that of Nobile and Vergara [15]. They assumed that the structure behaves as a membrane which implies that the structure is a thin elastic shell with no bending, whose thickness is neglected and which can be described by a two-dimensional manifold. A simple inertia-algebraic membrane model which considers small deformation is considered. The structure equation with initial conditions is as follows:

$$\begin{aligned} \rho_s h_s \frac{\partial^2 \eta}{\partial t^2} + \beta\eta &= f_s \quad \text{in } (0,T)\times\Gamma^0, \\ \eta\big|_{t=0} &= \eta_0 \quad \text{in } \Gamma^0, \\ \left.\frac{\partial \eta}{\partial t}\right|_{t=0} &= \eta_v \quad \text{in } \Gamma^0, \end{aligned} \tag{4}$$

where η_0, η_v are initial conditions. If in the particular case $\rho_s = 0$, it is known as the algebraic model.

Nobile [37] proposed a generalised string model derived from a cylindrical configuration. Let

$$\Gamma = \{(r,\theta,z) : r = R_0, 0 \le z \le L, 0 \le \theta < 2\pi\} \tag{5}$$

be the cylindrical reference surface of radius R_0, while the longitudinal and angular displacement are neglected; thus the radial displacement $\eta_r = \eta_r(t,\theta,z)$ is given by

$$\rho_s h_s \frac{\partial^2 \eta_r}{\partial t^2} - kGh\frac{\partial^2 \eta_r}{\partial z^2} + \frac{Eh}{1-\nu^2}\frac{\eta_r}{R_0^2} - \gamma\frac{\partial^3 \eta_r}{\partial z^2 \partial t} = f(t,\theta,z), \tag{6}$$

where $kGh(\partial^2\eta_r/\partial z^2)$ account for shear deformation while $\gamma(\partial^3\eta_r/\partial z^2\partial t)$ introduced the viscoelastic behaviour. By neglecting the viscoelastic terms and the term of second derivatives in z, the resulting equation (7) is so-called independent ring model

$$\rho_s h_s \frac{\partial^2 \eta_r}{\partial t^2} + \frac{Eh}{1-\nu^2}\frac{\eta_r}{R_0^2} = p - p_{\text{ext}}. \tag{7}$$

Further simplification by neglecting the inertia term will result in the simple algebraic equation

$$\frac{Eh}{1-\nu^2}\frac{\eta_r}{R_0^2} = p - p_{\text{ext}}. \tag{8}$$

Generalised string model had been widely used as the structure of blood flow in compliant vessels and arteries [12–16, 32]. It is derived from the theory of linear elasticity for a cylindrical tube with small thickness. The reference configuration is a cylindrical surface of the base circle radius R that is supposed to move in radially, the longitudinal and angular displacements being neglected [16]. Causin et al. [16] suggested that the results will be more qualitative in the present example of a nonnegligible second-order term.

Guidoboni et al. [9, 10] proposed the generalized string model which includes the elastic and viscoelastic behavior. $\Gamma(t)$ is assumed as a linearly viscoelastic thin shell, undergoing only transversal displacement $\eta = \eta(x,t)$:

$$\rho_s h_s \frac{\partial^2 \eta}{\partial t^2} + C_0\eta - C_1\frac{\partial^2 \eta}{\partial x_1^2} + D_0\frac{\partial \eta}{\partial t} - D_1\frac{\partial^3 \eta}{\partial t \partial x_1^2} = f_2 \quad \text{on } (0,L)\times(0,T). \tag{9}$$

Čanić et al. [18–20] stated that there are no analytical results which are able to prove the well posedness of fluid structure interaction problems without assuming the structure model that includes the higher order derivative terms capturing the viscoelastic behavior or with the terms describing bending rigidity. They explained that the bending rigidity of the vessels walls which are being neglected might mean oversimplifying the physics. Thus, their motivation was to derive the Koiter shell equations in cylindrical coordinate. The linearly viscoelastic cylindrical Koiter shell model is given as

$$\begin{aligned} \rho_w h\frac{\partial^2 \eta_r}{\partial t^2} + C_0\eta_r - C_1\frac{\partial^2 \eta_r}{\partial z^2} + C_2\frac{\partial^4 \eta_r}{\partial z^4} \\ + D_0\frac{\partial \eta}{\partial x} - D_1\frac{\partial^3 \eta_r}{\partial t \partial z^2} + D_2\frac{\partial^5 \eta_r}{\partial t \partial z^4} = f_r. \end{aligned} \tag{10}$$

There are two interesting features: bending rigidity plays a nonnegligible role in the ε^2 approximation of the original problem, and the fluid viscous dissipation imparts long-term viscoelastic memory effects on the motion of the arterial walls.

2.3. The Coupling Condition. The coupling condition between both fluid and structure is

$$u_1 = 0, \qquad u_2 = \frac{\partial \eta}{\partial t} \quad \text{on } \Gamma(t) \text{ for } t \in (0,T). \tag{11}$$

The initial and boundary conditions for fluid velocity $\mathbf{u}$ and the structure displacement η are prescribed as

$$\begin{aligned} \mathbf{u} = 0, \qquad \eta = 0, \qquad \frac{\partial \eta}{\partial t} = 0, \\ \eta(0,t) = 0, \qquad \eta(L,t) = 0. \end{aligned} \tag{12}$$

3. Numerical Approaches for Fluid Structure Interaction Problems

In this paper, the numerical approaches in solving fluid structure interaction problems are classified into two: namely, the partitioned and the monolithic approach [20–24, 26]. Other numerical approaches such as the conforming and nonconforming mesh associated with the immersed boundary

method in solving fluid structure interactions have been reviewed in [27].

Partitioned approach treats the fluid and structure problems as two computational fields which can be solved using two distinct solvers. The interface conditions between the fluid and structure are solved through loosely or strongly coupled algorithms [20–24, 26, 27]. Figure 2 shows that loosely coupled algorithms are known as explicit algorithms while strongly coupled algorithms are known as implicit algorithms.

Partitioned approach is based on the successive solution of three subproblems and allows one to reuse the existing codes. Monolithic approach treats the fluid and structure as a single system. In other words, flow and structure problem is solved with a single code. The interfacial conditions are implicit in the solution procedure. The solution procedures of the monolithic and partitioned approach are illustrated in Figure 3 where S^f and S^s denote the fluid and structure solution, respectively [21, 23, 27].

3.1. Partitioned Approach. According to Sieber [34], information in loosely coupling algorithms will be exchanged between the solvers only once per time step. This implies that the fluid and structure should be in equilibrium. Then the data can be exchanged only if both fluid and structure variables are constant within each time step. Before starting the iterations process, all materials, fluid properties parameters, fluid and structure variables, time step, and the convergence criteria should be initialized. However, convergence problems might increase due to the nature of explicit coupling algorithms. Thus the choice of time-step size was restricted and it was not suitable for large structural deformations problems. Figure 4 shows the comparison in terms of stability, generality, and programming efforts for both couplings.

Andersson and Ahl [26] summarized some issues about loosely and strongly coupled algorithms. For loosely coupled algorithms, instability issue increases with decreasing the mass density ratio. Besides, the decrease in time-step size further increases the instability, known as the artificial added mass effect. Errors in the predictions along with the added mass effect caused the incorrect coupling forces that led to the instability. For strongly coupled algorithms, it was more stable for low mass density ratio. On the other hand, due to more subiterations, the computational time increases when the ratio is reduced.

Deparis et al. [38] stated that standard loosely coupling algorithms solved the fluid, geometry, and the interface explicitly and the structure implicitly. The computational cost was cheap but unstable especially when the structure was light. Several suggestions had been made to overcome the stability issues. Nobile and Vergara [29] proposed Robin interface conditions to be enforced to solve fluid and structure subproblems. Burman and Fernández [28] proposed a stabilized explicit coupling for fluid structure interaction based on Nitsche's scheme. Numerical simulation of fluid structure interaction problems involving a viscous compressible fluid and elastic structure was considered. The explicit coupling scheme without correction had given a stable approximation with poor accuracy. High order accuracy was achieved after a few correction iterations and the results were comparable to that with implicit scheme solution [28].

It has also been suggested that the geometry and interface coupling should be treated implicitly [18]. Vierendeels et al. [39] proposed a coupling method for strongly coupled fluid structure interaction problems with partitioned solvers. They solved the reduced order models for fluid and structure problem and a small number of coupling iterations. Commercial CFD software package Fluent 6.2 was used as the fluid solver and Abaqus 6.5 was used as the structural solver. This coupling method showed a satisfactory convergence behavior. Thus, it can be summarized that the explicit partitioned algorithms are not suitable for problems in hemodynamics. It was proved to be problematic with the stability issues as the added mass effect of the fluid on the structure [16, 25, 29]. Implicit partitioned algorithms were also affected by the added mass effect as they converge slowly. Special treatments of the interface conditions had to be considered.

3.2. Monolithic Approach. Deficiencies in the partitioned method had motivated the investigation on monolithic methods [21]. Hron and Turek [40] and Hron and Mádlík [41] stated that the monolithic approach which treated the problem as a single continuum with coupling automatically takes care of the internal interface. This gets rid of the problematic interface treatment when the fluid and structure are solved separately. The results computed using monolithic approaches were ten times more accurate, but the computational cost was three to four times higher than those of the partitioned methods as stated in Michler et al. [21].

Heil [22] explained that if the fluid is incompressible or the problem is steady, the solution of a large system of coupled nonlinear algebraic equations is needed. The solution of a nonlinear system by Newton's method was utilized since it yielded a powerful and rapidly converging scheme. However, repeated assembly of the Jacobian matrix and the solutions associated with the linear systems for Newton corrections contributed to the increase in computational cost. Thus they developed an efficient preconditioning technique that allows the rapid iterative solution instead of applying the Newton method as in [20].

Heil et al. [20] studied the fluid structure interaction in collapsible channel with monolithic and partitioned approaches. Both approaches were competitive in the test case involving steady problems. In unsteady problems, strongly coupled partitioned solvers suffered from severe convergence problems and an under-relaxation parameter needs to be applied in stabilizing the solution procedure. Monolithic solvers become more essential in unsteady problems but required an efficient precondition for the large problems, particularly in three-dimensional problems [20].

Razzaq et al. [42, 43] presented numerical simulation of fluid structure interaction in hemodynamics with monolithic approach. They restricted the research on two-dimensional models which allow the systematic tests of the proposed methods. The corresponding monolithic treatment of the fluid structure interaction problems suggested that a stable

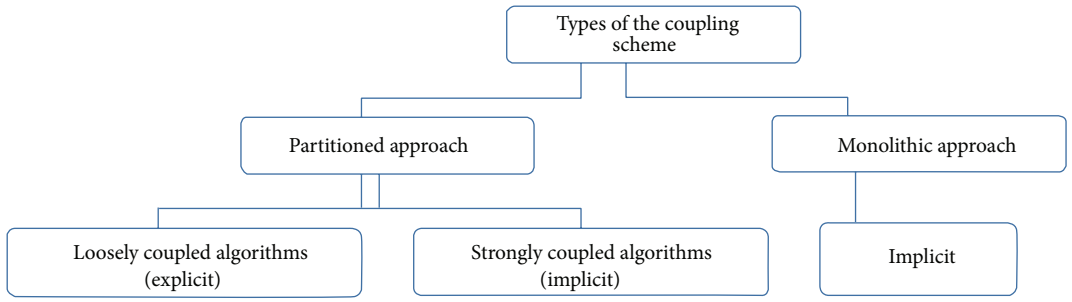

Figure 2: Coupling schemes in solving fluid structure interaction problems.

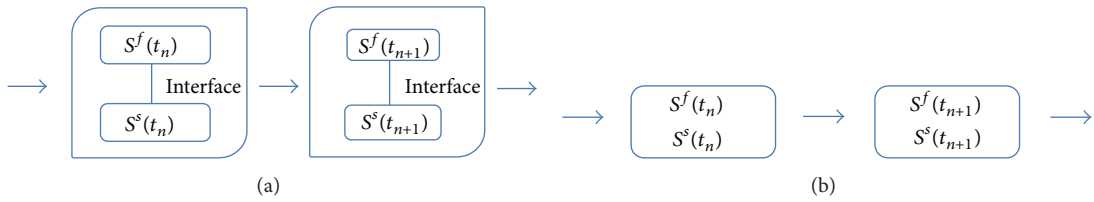

Figure 3: Schematic of (a) partitioned approach and (b) monolithic approach [27].

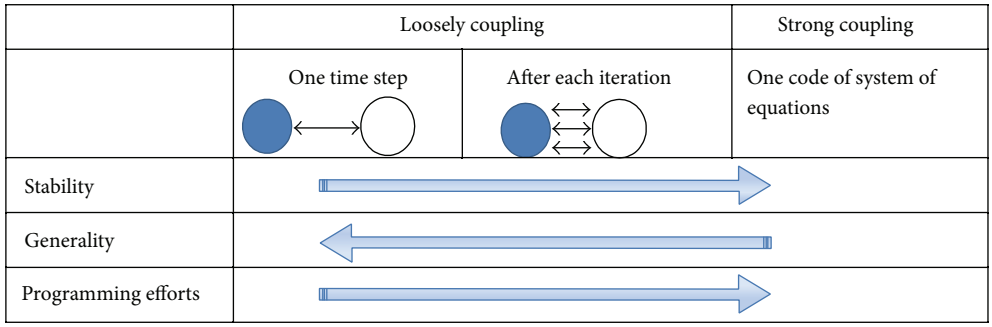

Figure 4: Comparing between loosely and strongly coupling algorithms [34].

second-order time stepping scheme as well as the same finite elements for fluid and structure should be utilized. Hron and Turek [40] and Hron and Mádlík [41] applied different types of discretization in space and time. They solved the simplified two-dimensional examples with finite element and Crank-Nicolson for the space and time discretization, respectively. The resulting nonlinear algebraic system was solved by an approximate Newton's method. The results obtained had high accuracy and robustness.

4. Improved Numerical Methods

Although stability and accuracy of partitioned approach can be improved through prediction techniques, their error remains larger than monolithic solutions [20, 21]. To date, monolithic and implicit schemes seem to be applicable in fluid structure interactions in blood flow. However, subiterations that are performed at each time step increase the computational time and computational costs [9, 10, 30–33]. Several approaches based on the coupling algorithms had been proposed in recent research works, such as the semi-implicit, kinematic splitting algorithm, and the geometrical multiscale approach.

4.1. Semi-Implicit Approach. Fernández et al. [30, 31] proposed a semi-implicit scheme to solve the numerical simulation of fluid structure interaction problems involving strong added mass effect, particularly in hemodynamics. The idea of the semi-implicit scheme was to treat the added mass effect implicitly while other contributions such as geometrical nonlinearities, viscous, and convective effects are solved explicitly. Such explicit-implicit splitting can be naturally performed using a Chorin-Temam projection scheme in the fluid. The authors claimed that this scheme was numerically stable, given in theoretical and numerical evidence for a wide range of physical and discrete parameters.

However, Astorino et al. [44] stated that the scheme proposed in [30, 31] had computing limitations such that

(i) it was assumed that the fluid problem is to be solved with a projection scheme;

(ii) the energy was not perfectly balanced. Astorino et al. [44] then modified the scheme in [30, 31] by treating the explicit part of the coupling with Nitsche-based mortaring. The authors claimed that their scheme was independent of the added mass effect.

Badia et al. [8] proposed a similar previous semi-implicit approach which was based on the inexact block-LU factorization of the linear system. The linear system was obtained after the space-time discretization and linearization of the fluid structure interaction problems. The idea presented was to decouple the fluid velocity computation of the strongly coupled fluid structure system. Only pressure and structure unknowns were involved, with the advantage of reducing the computational costs and maintaining stability. Since the pressure was still coupled to the structure, the stability of the scheme was independent of the added mass effect.

4.2. Kinematic Splitting Algorithm. Guidoboni et al. [9, 10, 33] proposed a new version of the loosely coupled-type algorithm. The algorithm which is known as the kinematically coupled scheme is aligned with the crucial role of the kinematic condition for the proposed algorithm. This scheme applied the hypothesis that the arterial wall was modelled as a thin shell so that such scheme does not suffer from instabilities related to the high nonlinear interfacial coupling between the flow and structure. The idea of the kinematically coupled scheme was presented as follows.

(1) Use operator splitting for time-discretization.

(2) No iterations between the fluid and structure subproblems were required.

(3) Impose the kinematic condition in strong form in order to maintain the tight link between fluid and structure in each sub-problem.

(4) The fluid stress at the interface did not have to be computed explicitly.

Kinematically coupled scheme splits the structure into two parts: the hydrodynamic load exerted by the fluid on the structure and the purely elastic part without the hydrodynamic load. The hydrodynamic part, consisting of the fluid stress acting on the interface and the viscoelastic terms, is treated together with the fluid. By adding the hydrodynamic part of the structure equation to the fluid equation and by utilizing the kinematic interface condition, they deal with the inertia of both fluid and structure at the same time, thereby getting around the difficulty associated with the added mass effect. The elastic part was treated separately and this enabled the use of a wide range of structural models [9, 10].

Guidoboni et al. [9, 10] considered the incompressible, viscous Newtonian fluid in a two-dimensional channel with thin, deformable walls in the generalized string model. Time discretization via Lie's operator splitting was applied through the scheme. Since the operator splitting was developed only for the first-order formulation, the kinematic boundary condition was applied into the structure equation to transform the second-order formulation to the first-order formulation. The overall structure of the scheme was to solve the four subproblems with different numerical schemes. Existing fluid and structure solvers can be used as "black boxes." Numerical results of kinematically coupled scheme showed excellent agreement with those obtained using an implicit scheme [9, 10].

Bukač et al. [11] extended the work of [9, 10] by replacing the generalized string model with linearly viscoelastic cylindrical Koiter shell model. The authors tried to capture the radial and longitudinal displacement of the linearly viscoelastic Koiter shell for the underlying fluid structure interaction problem. In addition, they aimed to increase the accuracy of kinematically coupled scheme with the modified Lie's scheme. The modified scheme was named as kinematically coupled β-scheme. The results were comparable with the monolithic scheme in [8]. Such a scheme was modular and easy to implement and had low computational cost.

The idea of kinematic splitting algorithm inspired Lukáčová-Medviďová et al. [45] to propose a similar technique to solve the fluid structure interaction problems of non-Newtonian fluids. Lukáčová-Medviďová et al. [45] claimed that their approach was more general than [9, 10, 33] because they allowed the use of second-order splitting method and non-Newtonian rheology. They applied implicit backward Euler discretization to the fluid and second-order Newmark scheme for the structure. The results were conditionally stable.

4.3. Geometrical Multiscale Approach. Formaggia et al. [13, 32] mentioned that although the coupling algorithm for fluid structure interaction should be implicit, it is difficult to simulate large regions. The simulation of three-dimensional fluid structure interaction suffered a pressure wave that had been generated and reflected at the flow section. Thus, geometrical multiscale approach was proposed by coupling the detailed three-dimensional fluid structure interaction model with a one-dimensional reduced model as shown in Figure 5. They applied an implicit coupling on the three-dimensional fluid structure interaction problem and the Lax-Wendroff scheme on the one-dimensional model. The explicit numerical algorithm was proposed for the geometrical multiscale coupling. Formaggia et al. [13, 32] attempted to eliminate the spurious reflection at the flow section through geometrical multiscale approach by implying one-dimensional reduced model as the absorbing boundary condition. The results showed that the pressure wave is quite well absorbed by the one-dimensional model.

Janela et al. [46] stated that as the flow is driven by a pressure pulse generated by a constant pressure, the vessel inflates initially near the inflow boundary. The motion propagates along the vessel until it reaches the outflow section and is reflected back. Such issue can be solved through geometrical multiscale approach as proposed by [32]. Janela et al. [47] proposed several absorbing boundary conditions in order to cope with the spurious reflection. The numerical approximation of three-dimensional and one-dimensional coupling was performed through a staggered algorithm, iterating the three-dimensional fluid structure interaction and one-dimensional model. The coupling can be performed implicitly, comprising subiterations at each time

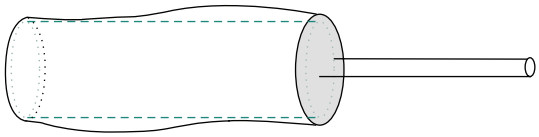

Figure 5: Three-dimensional and one-dimensional coupling model.

step or explicitly, with no subiterations at each time step. The proposed linear absorbing boundary conditions had been proven to be effective in absorbing the pressure wave.

Both Formaggia et al. [32] and Janela et al. [46, 47] mentioned that the homogenous boundary condition will lead to energy decay property. Standard homogenous boundary condition introduces the spurious reflections of the pressure wave which will cause the structure to continue oscillating. Proper boundary conditions should be chosen in order to cope with the reflection issues caused by the three-dimensional fluid structure interaction.

5. Conclusion

Fluid structure interaction needs to be included in models of blood flow as blood interacts mechanically with the vessel wall. It is suggested that the linearly viscoelastic Koiter shell model should be adopted to model the structure of the vessel wall since it takes into account the elastic and viscoelastic behavior with bending rigidity.

The main issue in the fluid structure interaction model of blood flow model is on how to get rid of the added mass effect so that the numerical solution will be stable and the computational cost is low. The monolithic scheme has been the most commonly used approach, but it is expensive in terms of computational cost and memory requirement. To get around this problem, various ways to improve on the partitioned approach have been sought.

Classical partitioned approach considers a problem separately as fluid, structure, and interface. Problem arises when the interface is solved separately. In the kinematically coupled scheme, which is a loosely coupled partitioned-type algorithm, an operator splitting is applied instead of the problem being split into the fluid and structure subproblems. Such splitting algorithm offers the flexibility of applying any suitable numerical methods in solving each subproblem. As the computational cost is measured according to the number of iterations, the computational cost of the kinematically coupled scheme is lower, with the results obtained being as accurate as those obtained from the implicit schemes.

Conflict of Interests

The authors declare that there is no conflict of interests regarding the publication of this paper.

Acknowledgment

Financial supports provided by Vot 03H34 and Vot 01G31, Research University Grant Scheme, Universiti Teknologi Malaysia, are gratefully acknowledged.

References

[1] K. J. Paik, *Simulation of fluid-structure interaction for surface ships with linear/nonlinear deformations [Ph.D. thesis]*, University of Iowa, 2010, http://ir.uiowa.edu/etd/569.

[2] Z. Mortazavinia, A. Zare, and A. Mehdizadeh, "Effects of renal artery stenosis on realistic model of abdominal aorta and renal arteries incorporating fluid-structure interaction and pulsatile non-Newtonian blood flow," *Applied Mathematics and Mechanics*, vol. 33, no. 2, pp. 165–176, 2012.

[3] W. Zhang, C. Herrera, S. N. Atluri, and G. S. Kassab, "Effect of surrounding tissue on vessel fluid and solid mechanics," *Journal of Biomechanical Engineering*, vol. 126, no. 6, pp. 760–769, 2004.

[4] V. Kanyanta, A. Ivankovic, and A. Karac, "Validation of a fluid-structure interaction numerical model for predicting flow transients in arteries," *Journal of Biomechanics*, vol. 42, no. 11, pp. 1705–1712, 2009.

[5] P. K. Siogkas, A. I. Sakellarios, T. P. Exarchos et al., "Blood flow in arterial segments: rigid vs. deformable walls simulations," *Journal of the Serbian Society for Computational Mechanics*, vol. 5, no. 1, pp. 69–77, 2011.

[6] M. H. Friedman, R. Krams, and K. B. Chandran, "Flow interactions with cells and tissues: cardiovascular flows and fluid-structure interactions: sixth international bio-fluid mechanics symposium and workshop, March 28–30, 2008, Pasadena, California," *Annals of Biomedical Engineering*, vol. 38, no. 3, pp. 1178–1187, 2010.

[7] K. W. Lee and X. Y. Xu, "Modelling of flow and wall behaviour in a mildly stenosed tube," *Medical Engineering and Physics*, vol. 24, no. 9, pp. 575–586, 2002.

[8] S. Badia, A. Quaini, and A. Quarteroni, "Splitting methods based on algebraic factorization for fluid-structure interaction," *SIAM Journal on Scientific Computing*, vol. 30, no. 4, pp. 1778–1805, 2008.

[9] G. Guidoboni, R. Glowinski, N. Cavallini, S. Čanić, and S. Lapin, "A kinematically coupled time-splitting scheme for fluid-structure interaction in blood flow," *Applied Mathematics Letters*, vol. 22, no. 5, pp. 684–688, 2009.

[10] G. Guidoboni, R. Glowinski, N. Cavallini, and S. Čanić, "Stable loosely-coupled-type algorithm for fluid-structure interaction in blood flow," *Journal of Computational Physics*, vol. 228, no. 18, pp. 6916–6937, 2009.

[11] M. Bukač, S. Čanić, R. Glowinski, J. Tambača, and A. Quaini, "Fluid-structure interaction in blood flow capturing non-zero longitudinal structure displacement," *Journal of Computational Physics*, vol. 235, pp. 515–541, 2013.

[12] A. Quarteroni and L. Formaggia, "Mathematical modelling and numerical simulation of the cardiovascular system," in *Modelling of Living Systems*, vol. 12 of *Handbook of Numerical Analysis*, pp. 3–127, North-Holland, Amsterdam, The Netherlands, 2004.

[13] L. Formaggia, J. F. Gerbeau, F. Nobile, and A. Quarteroni, "On the coupling of 3D and 1D Navier-Stokes equations for flow problems in compliant vessels," *Computer Methods in Applied Mechanics and Engineering*, vol. 191, no. 6-7, pp. 561–582, 2001.

[14] L. Formaggia, D. Lamponi, and A. Quarteroni, "One-dimensional models for blood flow in arteries," *Journal of Engineering Mathematics*, vol. 47, no. 3-4, pp. 251–276, 2003.

[15] F. Nobile and C. Vergara, "An effective fluid-structure interaction formulation for vascular dynamics by generalized Robin conditions," *SIAM Journal on Scientific Computing*, vol. 30, no. 2, pp. 731–763, 2008.

[16] P. Causin, J. F. Gerbeau, and F. Nobile, "Added-mass effect in the design of partitioned algorithms for fluid-structure problems," *Computer Methods in Applied Mechanics and Engineering*, vol. 194, no. 42–44, pp. 4506–4527, 2005.

[17] S. Čanić, A. Mikelić, and J. Tambača, "A two-dimensional effective model describing fluid-structure interaction in blood flow: analysis, simulation and experimental validation," *Comptes Rendus*, vol. 333, no. 12, pp. 867–883, 2005.

[18] S. Čanić, J. Tambača, G. Guidoboni, A. Mikelić, C. J. Hartley, and D. Rosenstrauch, "Modeling viscoelastic behavior of arterial walls and their interaction with pulsatile blood flow," *SIAM Journal on Applied Mathematics*, vol. 67, no. 1, pp. 164–193, 2006.

[19] S. Čanić, C. J. Hartley, D. Rosenstrauch, J. Tambaca, G. Guidoboni, and A. Mikelic, "Blood flow in compliant arteries: an effective viscoelastic reduced model, numerics, and experimental validation," *Annals of Biomedical Engineering*, vol. 34, no. 4, pp. 575–575, 2006.

[20] M. Heil, A. L. Hazel, and J. Boyle, "Solvers for large-displacement fluid-structure interaction problems: segregated versus monolithic approaches," *Computational Mechanics*, vol. 43, no. 1, pp. 91–101, 2008.

[21] C. Michler, S. J. Hulshoff, E. H. van Brummelen, and R. de Borst, "A monolithic approach to fluid-structure interaction," *Computers and Fluids*, vol. 33, no. 5-6, pp. 839–848, 2004.

[22] M. Heil, "An efficient solver for the fully coupled solution of large-displacement fluid-structure interaction problems," *Computer Methods in Applied Mechanics and Engineering*, vol. 193, no. 1-2, pp. 1–23, 2004.

[23] J. Degroote, P. Bruggeman, R. Haelterman, and J. Vierendeels, "Stability of a coupling technique for partitioned solvers in FSI applications," *Computers and Structures*, vol. 86, no. 23-24, pp. 2224–2234, 2008.

[24] J. Degroote, R. Haelterman, S. Annerel, P. Bruggeman, and J. Vierendeels, "Performance of partitioned procedures in fluid-structure interaction," *Computers and Structures*, vol. 88, no. 7-8, pp. 446–457, 2010.

[25] S. R. Idelsohn, F. Del Pin, R. Rossi, and E. Oñate, "Fluid-structure interaction problems with strong added-mass effect," *International Journal for Numerical Methods in Engineering*, vol. 80, no. 10, pp. 1261–1294, 2009.

[26] C. Andersson and D. Ahl, *Fluid structure interaction—evaluation of two coupling techniques [M.S. thesis]*, School of Information Science, Computer and Electrical Engineering Halmstad University, 2011.

[27] G. Hou, J. Wang, and A. Layton, "Numerical methods for fluid-structure interaction—a review," *Communications in Computational Physics*, vol. 12, no. 2, pp. 337–377, 2012.

[28] E. Burman and M. A. Fernández, "Stabilized explicit coupling for fluid-structure interaction using Nitsche's method," *Comptes Rendus Mathématique*, vol. 345, no. 8, pp. 467–472, 2007.

[29] F. Nobile and C. Vergara, "Partitioned algorithms for fluid-structure interaction problems in haemodynamics," *Milan Journal of Mathematics*, vol. 80, no. 2, pp. 443–467, 2012.

[30] M. A. Fernández, J.-F. Gerbeau, and C. Grandmont, "A projection algorithm for fluid-structure interaction problems with strong added-mass effect," *Comptes Rendus Mathématique*, vol. 342, no. 4, pp. 279–284, 2006.

[31] M. A. Fernández, J.-F. Gerbeau, and C. Grandmont, "A projection semi-implicit scheme for the coupling of an elastic structure with an incompressible fluid," *International Journal for Numerical Methods in Engineering*, vol. 69, no. 4, pp. 794–821, 2007.

[32] L. Formaggia, A. Moura, and F. Nobile, "On the stability of the coupling of 3D and 1D fluid-structure interaction models for blood flow simulations," *ESAIM: Mathematical Modelling and Numerical Analysis*, vol. 41, no. 4, pp. 743–769, 2007.

[33] G. Guidoboni, R. Glowinski, S. Čanić, N. Cavallini, and M. Bukac, "Modeling of free boundary flows with applications to blood flow," in *Proceedings of the IV European Conference on Computational Mechanics (ECCM '10)*, Paris, France, 2010.

[34] M. S. G. Sieber, *Numerical simulation of fluid-structure interaction using loose coupling methods [Ph.D. thesis]*, Technical University Darmstadt, Darmstadt, Germany, 2001.

[35] S. Čanić, D. Lamponi, A. Mikelić, and J. Tambača, "Self-consistent effective equations modeling blood flow in medium-to-large compliant arteries," *Multiscale Modeling & Simulation*, vol. 3, no. 3, pp. 559–596, 2005.

[36] F. Yilmaz and M. Y. Gundogdu, "A critical review on blood flow in large arteries; relevance to blood rheology, viscosity models, and physiologic conditions," *Korea Australia Rheology Journal*, vol. 20, no. 4, pp. 197–211, 2008.

[37] F. Nobile, *Numerical approximation of fluid-structure interaction problems with application to haemodynamics [Ph.D. thesis]*, EPFL, Lausanne, Switzerland, 2001.

[38] S. Deparis, M. A. Fernández, and L. Formaggia, "Acceleration of a fixed point algorithm for fluid-structure interaction using transpiration conditions," *ESAIM: Mathematical Modelling and Numerical Analysis*, vol. 37, no. 4, pp. 601–616, 2003.

[39] J. Vierendeels, L. Lanoye, J. Degroote, and P. Verdonck, "Implicit coupling of partitioned fluid-structure interaction problems with reduced order models," *Computers and Structures*, vol. 85, no. 11–14, pp. 970–976, 2007.

[40] J. Hron and S. Turek, "A monolithic FEM/multigrid solver for an ALE formulation of fluid-structure interaction with applications in biomechanics," in *Fluid-Structure Interaction*, vol. 53 of *Lecture Notes in Computational Science and Engineering*, pp. 146–170, Springer, Berlin, Germany, 2006.

[41] J. Hron and M. Mádlík, "Fluid-structure interaction with applications in biomechanics," *Nonlinear Analysis: Real World Applications*, vol. 8, no. 5, pp. 1431–1458, 2007.

[42] M. Razzaq, S. Turek, J. Hron et al., *Numerical Simulation and Benchmarking of Fluid Structure Interaction with Application to Hemodynamics*, Technical University, Fakultät für Mathematik, 2009.

[43] M. Razzaq, S. Turek, J. Hron et al., *Numerical Simulation of Fluid Structure Interaction with Application to Aneurysm Hemodynamics*, Technical University, Fakultät für Mathematik, 2009.

[44] M. Astorino, F. Chouly, and M. A. Fernández, "An added-mass free semi-implicit coupling scheme for fluid-structure interaction," *Comptes Rendus Mathématique*, vol. 347, no. 1-2, pp. 99–104, 2009.

[45] M. Lukáčová-Medviďová, G. Rusnáková, and A. Hundertmark-Zaušková, "Kinematic splitting algorithm for fluid-structure interaction in hemodynamics," *Computer Methods in Applied Mechanics and Engineering*, vol. 265, pp. 83–106, 2013.

[46] J. Janela, A. Moura, and A. Sequeira, "A 3D non-Newtonian fluid-structure interaction model for blood flow in arteries," *Journal of Computational and Applied Mathematics*, vol. 234, no. 9, pp. 2783–2791, 2010.

[47] J. Janela, A. Moura, and A. Sequeira, "Absorbing boundary conditions for a 3D non-Newtonian fluid-structure interaction model for blood flow in arteries," *International Journal of Engineering Science*, vol. 48, no. 11, pp. 1332–1349, 2010.

Hindawi Publishing Corporation
Abstract and Applied Analysis
Volume 2014, Article ID 762184, 15 pages
http://dx.doi.org/10.1155/2014/762184

Research Article

Comparison of the Finite Volume and Lattice Boltzmann Methods for Solving Natural Convection Heat Transfer Problems inside Cavities and Enclosures

M. Goodarzi,[1] M. R. Safaei,[2] A. Karimipour,[3] K. Hooman,[4] M. Dahari,[2] S. N. Kazi,[2] and E. Sadeghinezhad[2]

[1] *Department of Software Engineering, Faculty of Computer Science & Information Technology, University of Malaya, 50603 Kuala Lumpur, Malaysia*
[2] *Department of Mechanical Engineering, Faculty of Engineering, University of Malaya, 50603 Kuala Lumpur, Malaysia*
[3] *Department of Mechanical Engineering, Najafabad Branch, Islamic Azad University, Isfahan, Iran*
[4] *School of Mechanical and Mining Engineering, The University of Queensland, St Lucia, Brisbane, QLD 4072, Australia*

Correspondence should be addressed to M. R. Safaei; cfd_safaei@yahoo.com

Received 28 September 2013; Revised 22 November 2013; Accepted 24 November 2013; Published 9 February 2014

Academic Editor: Mohamed Fathy El-Amin

Different numerical methods have been implemented to simulate internal natural convection heat transfer and also to identify the most accurate and efficient one. A laterally heated square enclosure, filled with air, was studied. A FORTRAN code based on the lattice Boltzmann method (LBM) was developed for this purpose. The finite difference method was applied to discretize the LBM equations. Furthermore, for comparison purpose, the commercially available CFD package FLUENT, which uses finite volume Method (FVM), was also used to simulate the same problem. Different discretization schemes, being the first order upwind, second order upwind, power law, and QUICK, were used with the finite volume solver where the SIMPLE and SIMPLEC algorithms linked the velocity-pressure terms. The results were also compared with existing experimental and numerical data. It was observed that the finite volume method requires less CPU usage time and yields more accurate results compared to the LBM. It has been noted that the 1st order upwind/SIMPLEC combination converges comparatively quickly with a very high accuracy especially at the boundaries. Interestingly, all variants of FVM discretization/pressure-velocity linking methods lead to almost the same number of iterations to converge but higher-order schemes ask for longer iterations.

1. Introduction

Studying heat transfer and fluid flow using computational methods is easier [1], safer [2], and much less costly [3] compared to experimental techniques. There are a large number of problems which can be simulated with great accuracy to replicate experiments with high resolutions [4]. There are currently a range of approaches with the potential to serve in modeling heat transfer and fluid flows, such as the finite difference method (FDM), finite element method (FEM), finite volume method (FVM), lattice boltzmann method (LBM), boundary elements method (BEM), molecular dynamics simulation, and direct simulation Monte Carlo. The most widely employed approaches in the field of thermofluids are the first four [5]. However, application of FDM can be difficult when complex geometries are involved [6]. The FEM schemes can be intricate for solving conservative equations, while the nonstandard FEMs have low computational efficiency [7]. Application of FVM is difficult and complex to cases with complex moving boundaries [8]. LBM is a compressible model for ideal gases and can theoretically always simulate the compressible Navier-Stokes equations. With the Chapman-Enskog expansion [9], LBM can simulate incompressible flow for low Mach numbers ($Ma < 0.15$) albeit at the expense of a compressibility error [10, 11]. Besides, regular square grids used with LBM make it very hard to extend the simulation to curved boundaries [12]. All in all, the accuracy of all these numerical approaches is dependent

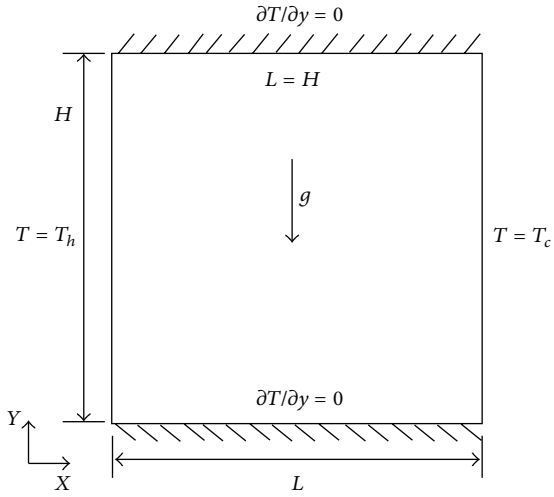

Figure 1: Schematic of analyzed configuration.

on the problem configuration, discretization scheme, and numerical algorithm used [5]. As such, an important question to answer is about finding the best approach to solve a certain problem subject to computational efficiency and accuracy as the most important constrains. Along these lines, Rouboa and Monteiro [13] investigated the heat transfer phenomenon during cast solidification in a complicated configuration by FVM and FDM. A comparison between the numerical results and experimental ones indicated that both discretization approaches produced good outcome, with FVM being slightly better as it uses more information than FDM to capture spatial temperature variations. Despite recent progress in computing power and techniques, the literature review indicates a lack of comprehensive studies on selecting the ideal means of analyzing internal heat transfer and fluid flow problems. In particular, an optimal solution technique and procedure to simulate internal natural convection are yet to be presented. To fill this gap in the literature, laminar natural convection heat transfer of air inside a laterally heated square enclosure is investigated using both FVM and LBM. The simulation results were compared against those from the literature. Particular attention was given to different discretization techniques as well as pressure-velocity linking approaches to find the best method for simulating internal free convection problems.

2. Governing Equations

2.1. Finite Volume Method. Continuity, momentum, and energy equations were employed for flow analysis in a system depicted by Figure 1. Density was computed by invoking the Boussinesq approximation for $\Delta T < 30^{\circ}\mathrm{C}$ [14]. The governing equations are written as follows [15].

Continuity equation:

$$\frac{\partial u}{\partial x} + \frac{\partial v}{\partial y} = 0. \tag{1}$$

Momentum equations in X and Y directions:

$$u\frac{\partial u}{\partial x} + v\frac{\partial u}{\partial y} = \frac{-1}{\rho}\frac{\partial p}{\partial x} + \frac{\mu}{\rho}\left(\frac{\partial^2 u}{\partial x^2} + \frac{\partial^2 u}{\partial y^2}\right),$$

$$u\frac{\partial v}{\partial x} + v\frac{\partial v}{\partial y} = \frac{-1}{\rho}\frac{\partial p}{\partial y} + \frac{\mu}{\rho}\left(\frac{\partial^2 v}{\partial x^2} + \frac{\partial^2 v}{\partial y^2}\right) + \beta g\left(T - T_c\right). \tag{2}$$

Energy equation:

$$u\frac{\partial T}{\partial x} + v\frac{\partial T}{\partial y} = \frac{k}{\rho C_p}\left(\frac{\partial^2 T}{\partial x^2} + \frac{\partial^2 T}{\partial y^2}\right). \tag{3}$$

2.2. Lattice Boltzmann Method. The hydrodynamic and thermal Boltzmann equations with using density-momentum and internal energy distribution functions (double population) are as follows [16, 17]:

$$\frac{\partial f_i}{\partial t} + c_{i\alpha}\frac{\partial f_i}{\partial x_\alpha} = \Omega\left(f\right) = -\frac{1}{\tau_f}\left(f_i - f_i^e\right),$$

$$\frac{\partial g_i}{\partial t} + c_{i\alpha}\frac{\partial g_i}{\partial x_\alpha} = \Omega\left(g_i\right) - f_i Z_i = 0.5|\mathbf{c} - \mathbf{u}|^2\Omega\left(f_i\right) - f_i Z_i$$

$$= -\frac{g_i - g_i^e}{\tau_g} - f_i Z_i. \tag{4}$$

Double population LBM model (TLBM) uses two separated distribution functions f and g for hydrodynamic and thermal fields, respectively. This model is the latest one among different presented models of thermal LBMs. In addition, it shows more accuracy and stability during the solution process. As LBM solution process naturally tends to divergence having a stable approach like TLBM helps the convergence. Microscopic velocities for a D2Q9 lattice model are [12]

$$\mathbf{c}_i = \left(\cos\frac{i-1}{2}\pi, \sin\frac{i-1}{2}\pi\right), \quad i = 1, 2, 3, 4,$$

$$\mathbf{c}_i = \sqrt{2}\left(\cos\left[\frac{(i-5)}{2}\pi + \frac{\pi}{4}\right], \sin\left[\frac{(i-5)}{2}\pi + \frac{\pi}{4}\right]\right), \quad i = 5, 6, 7, 8, \tag{5}$$

$$\mathbf{c}_0 = (0, 0).$$

Heat dissipation and hydrodynamic and thermal equilibrium distribution functions are given by

$$Z_i = \left(c_{i\alpha} - u_\alpha\right)\left[\frac{\delta u_\alpha}{\delta t} + c_{i\alpha}\frac{\partial u_\alpha}{\partial x_\alpha}\right],$$

$$f_i^e = \omega_i\rho\left[1 + 3\left(\mathbf{c}_i \cdot \mathbf{u}\right) + \frac{9\left(\mathbf{c}_i \cdot \mathbf{u}\right)^2}{2} - \frac{3\mathbf{u}^2}{2}\right], \quad i = 0, 1, \ldots, 8,$$

$$\omega_0 = \frac{4}{9}, \qquad \omega_{1,2,3,4} = \frac{1}{9}, \qquad \omega_{5,6,7,8} = \frac{1}{36},$$

$$
\begin{aligned}
g_0^e &= -\frac{2}{3}\rho e\mathbf{u}^2,\\
g_{1,2,3,4}^e &= \frac{1}{9}\rho e\left[1.5 + 1.5\left(\mathbf{c}_{1,2,3,4}\cdot\mathbf{u}\right)\right.\\
&\qquad \left. + 4.5\left(\mathbf{c}_{1,2,3,4}\cdot\mathbf{u}\right)^2 - 1.5\mathbf{u}^2\right],\\
g_{5,6,7,8}^e &= \frac{1}{36}\rho e\left[3 + 6\left(\mathbf{c}_{5,6,7,8}\cdot\mathbf{u}\right)\right.\\
&\qquad \left. + 4.5\left(\mathbf{c}_{5,6,7,8}\cdot\mathbf{u}\right)^2 - 1.5\mathbf{u}^2\right],
\end{aligned}
\tag{6}
$$

where $\rho e = \rho RT$ and ω is the weight function. Equation (4) in discretized forms [18] reads

$$
\begin{aligned}
&f_i\left(\mathbf{x}+\mathbf{c}_i\Delta t, t+\Delta t\right) - f_i\left(\mathbf{x},t\right)\\
&\quad = -\frac{\Delta t}{2\tau_f}\left[f_i\left(\mathbf{x}+\mathbf{c}_i\Delta t, t+\Delta t\right) - f_i^e\left(\mathbf{x}+\mathbf{c}_i\Delta t, t+\Delta t\right)\right]\\
&\qquad -\frac{\Delta t}{2\tau_f}\left[f_i\left(\mathbf{x},t\right) - f_i^e\left(\mathbf{x},t\right)\right],\\
&g_i\left(\mathbf{x}+\mathbf{c}_i\Delta t, t+\Delta t\right) - g_i\left(\mathbf{x},t\right)\\
&\quad = -\frac{\Delta t}{2\tau_g}\left[g_i\left(\mathbf{x}+\mathbf{c}_i\Delta t, t+\Delta t\right) - g_i^e\left(\mathbf{x}+\mathbf{c}_i\Delta t, t+\Delta t\right)\right]\\
&\qquad -\frac{\Delta t}{2} f_i\left(\mathbf{x}+\mathbf{c}_i\Delta t, t+\Delta t\right) Z_i\left(\mathbf{x}+\mathbf{c}_i\Delta t, t+\Delta t\right)\\
&\qquad -\frac{\Delta t}{2\tau_g}\left[g_i\left(\mathbf{x},t\right) - g_i^e\left(\mathbf{x},t\right)\right] - \frac{\Delta t}{2} f_i\left(\mathbf{x},t\right) Z_i\left(\mathbf{x},t\right).
\end{aligned}
\tag{7}
$$

The two last equations are implicit. Thus, the new functions $\widetilde{f}_i$ and $\widetilde{g}_i$ are developed to address this problem:

$$
\widetilde{f}_i = f_i + \frac{\Delta t}{2\tau_f}\left(f_i - f_i^e\right), \tag{8}
$$

$$
\widetilde{g}_i = g_i + \frac{\Delta t}{2\tau_g}\left(g_i - g_i^e\right) + \frac{\Delta t}{2} f_i Z_i. \tag{9}
$$

Collision and streaming steps of LBM are simulated by applying (7)–(9) as follows:

$$
\begin{aligned}
&\widetilde{f}_i\left(\mathbf{x}+\mathbf{c}_i\Delta t, t+\Delta t\right) - \widetilde{f}_i\left(\mathbf{x},t\right)\\
&\quad = -\frac{\Delta t}{\tau_f + 0.5\Delta t}\left[\widetilde{f}_i\left(\mathbf{x},t\right) - f_i^e\left(\mathbf{x},t\right)\right],\\
&\widetilde{g}_i\left(\mathbf{x}+\mathbf{c}_i\Delta t, t+\Delta t\right) - \widetilde{g}_i\left(\mathbf{x},t\right)\\
&\quad = -\frac{\Delta t}{\tau_g + 0.5\Delta t}\left[\widetilde{g}_i\left(\mathbf{x},t\right) - g_i^e\left(\mathbf{x},t\right)\right] - \frac{\tau_g\Delta t}{\tau_g + 0.5\Delta t} f_i Z_i.
\end{aligned}
\tag{10}
$$

Finally, the hydrodynamic and thermal variables can be obtained as

$$
\begin{aligned}
\rho &= \sum_i \widetilde{f}_i,\\
\rho\mathbf{u} &= \sum_i \mathbf{c}_i\widetilde{f}_i,\\
\rho e = \rho RT &= \sum_i \widetilde{g}_i - \frac{\Delta t}{2}\sum_i f_i Z_i.
\end{aligned}
\tag{11}
$$

3. Boundary Conditions

Figure 1 illustrates a schematic of the configuration analyzed in the present study along with the boundary conditions.

The nonequilibrium bounce-back model is used to simulate the no-slip boundary condition on the walls in LBM. This model improves accuracy compared to the usual bounce-back boundary condition and satisfies the zero mass flow rates at nodes on the wall. The collision occurs on the nodes located at the solid-fluid boundaries and distribution functions are reflected in a suitable direction, satisfying the equilibrium conditions [19].

The macroscopic boundary conditions for the present study are

$$
\begin{aligned}
&T = T_h \quad u = v = 0 \quad 0 < y < 1 \quad x = 0,\\
&T = T_c \quad u = v = 0 \quad 0 < y < 1 \quad x = 1,\\
&\frac{\partial T}{\partial y} = 0 \quad u = v = 0 \quad 0 < x < 1 \quad y = 0,\\
&\frac{\partial T}{\partial y} = 0 \quad u = v = 0 \quad 0 < x < 1 \quad y = 1.
\end{aligned}
\tag{12}
$$

4. Numerical Procedure

Our FVM solver uses the implicit line-by-line tridiagonal matrix algorithm [20, 21] to linearize the system of algebraic equations. First order upwind [22], second order upwind [23], power law [24], and Quadratic Upstream Interpolation for Convective Kinetics (QUICK) [25] schemes were applied in different trails to solve the same problem while the Semi-Implicit Method for Pressure-Linked Equations (SIMPLE) [26, 27] and SIMPLE-Consistent (SIMPLEC) [28, 29] procedures were selected for pressure-velocity coupling. The convergence criterion, maximum absolute error in each dependent variable, was set at 10^{-7}.

In LBM, the zero values for $U(x, y)$, $V(x, y)$, and $T(x, y)$ are applied as the initial conditions. However, to avoid problems in estimating the macroscopic variables in (12), the initial fluid density is set to unity. LBM dimensionless numbers Re, Ra, and Pr are defined identical to those of classical Navier-Stokes equations. However, the macroscopic numerical value should be calculated beforehand. For example, for Pr, one has the kinematics viscosity and thermal diffusivity determined in LBM as $\nu = \tau_f RT$ and $\alpha = 2\tau_g RT$, where τ_f and τ_g are hydrodynamic and thermal relaxation times and R is the gas constant. The Prandtl number can

then be written as $\Pr = \upsilon/\alpha = \tau_f RT/2\tau_g RT = \tau_f/2\tau_g$. For $\mathrm{Ra} = \mathrm{GrPr} = g\beta\Delta T H^3/\upsilon\alpha$ the values of υ and α are now known based on relaxation times, while the numerical values of g, β, H, ΔT are predetermined and fixed.

4.1. Gravity Effects in LBM. The Boussinesq approximation was used as $\rho = \overline{\rho}[1 - \beta(T - \overline{T})]$ to give buoyancy force per unit mass defined as $\mathbf{G} = \beta\mathbf{g}(T - \overline{T})$ and $f = G\cdot(c - u)f^e/RT$. Hence, the discretized Boltzmann equation is written as

$$\partial_t f_i + (\mathbf{c}_i \cdot \nabla) f_i = -\frac{f_i - f_i^e}{\tau_f} + \frac{\mathbf{G}\cdot(\mathbf{c}_i - \mathbf{u})}{RT} f_i^e,$$

$$\widetilde{f}_i(\mathbf{x} + \mathbf{c}_i\Delta t, t + \Delta t) - \widetilde{f}_i(\mathbf{x}, t) = -\frac{\Delta t}{\tau_f + 0.5\Delta t}\left[\widetilde{f}_i - f_i^e\right] + \frac{\Delta t\tau_f}{\tau_f + 0.5\Delta t}\frac{3G\left(c_{iy} - v\right)}{c^2} f_i^e. \tag{13}$$

Applying (8) and taking into consideration the effects of gravity, one has

$$\rho = \sum_i \widetilde{f}_i, \qquad u = \left(\frac{1}{\rho}\right)\sum_i \widetilde{f}_i c_{ix}, \qquad v = \left(\frac{1}{\rho}\right)\sum_i \widetilde{f}_i c_{iy} + \frac{\Delta t}{2}G, \tag{14}$$

while for thermal macroscopic variables (11) is applied.

4.2. Deriving Navier-Stokes Equations from LBM. In order to derive Navier-Stokes equations from the incompressible lattice Boltzmann equation by using Chapman-Enskog expansion the discretized form of Boltzmann equation can be written as

$$f_i(\mathbf{x} + \mathbf{c}_i\Delta t, t + \Delta t) - f_i(\mathbf{x}, t) = -\frac{f_i(\mathbf{x}, t) - f_i^e(\mathbf{x}, t)}{\tau_f}. \tag{15}$$

With $Kn = \varepsilon$ as a small (perturbation) variable, the Chapman-Enskog expansion for f_α and ∂_t reads

$$f_i = \sum_{n=0}^{\infty}\varepsilon^n f_i^{(n)} = f_i^{(0)} + \left[\varepsilon f_i^{(1)} + \varepsilon^2 f_i^{(2)} + \cdots\right] = f_i^{(\mathrm{eq})} + \left[f_i^{(n\mathrm{eq})}\right], \qquad \partial_t = \sum_{n=0}^{\infty}\varepsilon^n\partial_{t_n} = \partial_{t_0} + \varepsilon\partial_{t_1} + \cdots. \tag{16}$$

None of the nonequilibrium parts of the above equations should be used for estimating the macroscopic properties ρ and $\rho\mathbf{u}$:

$$\sum_i \varepsilon^n f_i^{(n)} = 0 \quad \forall n > 0, \qquad \sum_i \mathbf{c}_i\varepsilon^n f_i^{(n)} = 0 \quad \forall n > 0. \tag{17}$$

Using these equations together with Tailor expansion of Boltzmann equation around Δt, the terms which are smaller than (Δt) dropped, and then substitute into (15), we have

$$\left[\partial_{t_0} + \mathbf{c}_i\cdot\nabla\right] f_i^{(0)} = -\frac{f_i^{(1)}}{\tau_f}, \qquad \partial_{t_1} f_i^{(0)} + \left(1 - \frac{1}{2\tau_f}\right)\left[\partial_{t_0} + \mathbf{c}_i\cdot\nabla\right] f_i^{(1)} = -\frac{f_i^{(2)}}{\tau_f}. \tag{18}$$

Macroscopic density and velocity variables can be achieved by applying the first and second order of moments, leading to

$$\partial_t\sum_i f_i^{(0)} + \nabla\cdot\left(\sum_i \mathbf{c}_i f_i^{(0)}\right) = 0, \qquad \partial_t\left(\sum_i \mathbf{c}_i f_i^{(0)}\right) + \nabla\cdot\left[\Pi^{(0)} + \Delta t\left(1 - \frac{1}{2\tau_f}\right)\Pi^{(1)}\right] = O\left(\Delta t^2\right), \tag{19}$$

where

$$\Pi^{(0)} \equiv \sum_i \mathbf{c}_i\mathbf{c}_i f_i^{(0)}, \qquad \Pi^{(1)} \equiv \sum_i \mathbf{c}_i\mathbf{c}_i f_i^{(1)}. \tag{20}$$

Amount of $f_i^{(0)}$ is determined by using $f_i^e = \omega_i\rho[1 + 3(\mathbf{c}_i\cdot\mathbf{u}) + (9(\mathbf{c}_i\cdot\mathbf{u})^2/2) - (3\mathbf{u}^2/2)]$ and then using the zero and first order of moments of (18) together with $f_i^{(0)}$:

$$\partial_{t_0}\rho + \nabla\cdot(\rho\mathbf{u}) = 0, \qquad \partial_{t_1}\rho = 0, \qquad \partial_{t_0}(\rho\mathbf{u}) + \nabla\cdot(\rho\mathbf{u}\mathbf{u}) + \nabla\left(\rho c_s^2\right) = 0, \qquad \partial_{t_1}\rho + \nabla\cdot\left(2\upsilon\rho S - \Delta t\left(\tau_f - 0.5\right)\nabla\cdot(\rho\mathbf{u}\mathbf{u}\mathbf{u})\right) = 0, \tag{21}$$

where

$$S = \frac{\nabla\mathbf{u} + (\nabla\mathbf{u})^T}{2}, \qquad \upsilon = \frac{\left(2\tau_f - 1\right)\Delta t}{6}. \tag{22}$$

Finally, making use of $\nabla\cdot\mathbf{u} = 0, \nabla\rho = 0$ at incompressible limit and ignoring the term $\nabla\cdot(\rho\mathbf{u}\mathbf{u}\mathbf{u})$ in (21), continuity and momentum equations are recovered. In addition, the thermal energy equation would be recovered in a similar way; see [30, 31] for more details.

5. Grid Independence

Structured nonuniform grid distributions were applied for FVM simulations with a grid cluster near the walls to capture sharp velocity and temperature gradients. For LBM simulations structured grids based on D2Q9 lattice are applied.

Table 1: Grid independence tests (FVM and QUICK/SIMPLEC).

Number of grids	15987	31974	47961	63948	Experimental value [32]
Maximum X-velocity	0.001	0.001	0.0012	0.0012	—
Dimensionless temperature at the middle of the cavity	0.460	0.465	0.489	0.493	0.51

Table 2: Grid independence tests (LBM).

Number of grids	10000	32400	48400	67600	84100	Experimental value [32]
Maximum X-velocity	0.0004	0.0008	0.0010	0.0010	0.00103	—
Dimensionless temperature at the middle of the cavity	0.430	0.449	0.463	0.471	0.475	0.51

Table 3: Thermophysical properties of air [33].

ρ	C_p	μ	k	β	Gr	Pr	Ra
1.127	1007	1.9114×10^{-5}	0.0271	0.006092	2.662×10^{5}	0.71	1.890×10^{5}

Extensive grid independence checks were performed, as indicated by Tables 1 and 2, to observe that a grid with 47961 and 67600 cells for all FVM solvers and LBM, respectively, leads to mesh-independent results.

6. Results

Our numerical results, from different solvers, were compared with benchmark experimental data from Krane and Jessee [32] as well as the numerical predictions of Khanafer et al. [34], Oztop and Abu-Nada [35], and Bakhshan and Emrani [33]. The main dimensionless parameters were the Rayleigh and Prandtl numbers, which are constant at 1.89×10^5 and 0.71, respectively. The fluid thermophysical properties, as well as dimensionless numbers, are shown in Table 3.

For Pr = 0.71 and Ra = 1.89×10^5, the dimensionless temperature and vertical velocity profiles at midheight are plotted in Figures 2 and 3 and contrasted with the results from [32–35]. These figures illustrate a superior adaptation between the present simulation results using the FVM and LBM models and those of [32–35] works. Although previous research shows that, for complicated turbulent fluid flow problems, the QUICK/SIMPLEC is the most accurate choice [33], Figures 2(a) and 3(a) indicate that for laminar internal convection heat transfer problems there is no dramatic difference among the studied discretization approaches. However, it is obvious from Figures 2 and 3 that the FVM results are more accurate than those of LBM. This could be attributed to the compressible nature of LBM [36, 37], which creates a compressibility error for incompressible flows [12]. Among the discretization/pressure-velocity linking approaches examined, 1st order upwind/SIMPLEC has the closest results to experimental benchmark data, especially for the temperature contours in the range $0.20 \leq X \leq 0.80$. With vertical velocity distribution, however, the difference among FVM approaches is quite negligible. Nevertheless, the fact that the accuracy and stability of the convective terms comprise a contrasting pair is a general perception in the field of computational heat transfer. For instance, the first order upwind scheme is entirely stable even with strong false diffusion [38], while the second or third order schemes like QUICK are conditionally stable [25].

Table 4 successfully compares our numerical results with those available in the literature under similar conditions and geometry over a range of Ra values with Pr = 0.7. Slight discrepancies are observed in this table between some of the present work results and those of [34, 39–42] because of the differences between the employed discretization methods, as well as mesh generation types, as one would expect.

Table 5 provides the comparison of number of iterations and required CPU usage time for the different discretization methods considered here. As seen, LBM may take 4-5 times longer to converge and 8-9 times more iterations compared to FVM. There are two reasons for this. The first one is attributed to the way LBM handles heat transfer. Although in the present work the appropriate internal energy distribution function, g, [43] was used to obtain the temperature field, this model even tends to diverge. Furthermore, with LBM modeling the corners ask for a large number of fine grids near the corners. These two matters cause the LBM solutions to be comparatively more time consuming.

According to Table 5, the number of iterations for all FVM discretization method/pressure-velocity linking approaches is nearly equal. In this case, the difference between the QUICK/SIMPLEC method that necessitates the largest number of iterations and the lowest one (power law/SIMPLE) is only 79 iterations, that is, a 5.2% difference. With respect to CPU usage time, these proportions are to some extent different. For example, when comparing the most time consuming method (QUICK/SIMPLEC) with the 1st order upwind/SIMPLEC approach, this time disparity is about 4.94%, while the number of iterations differs by only 1.65%. As expected, higher-order accurate schemes are more time consuming.

The effects of the solution method, discretization scheme, and pressure/velocity coupling approach on the streamlines and X-velocity are illustrated by Figures 4 and 5. Two elliptical vortexes generally appear at the center of the cavity as a predominant feature of buoyancy-induced flow in a laterally heated square enclosure. In this context, the 1st order upwind scheme has the most precise results among

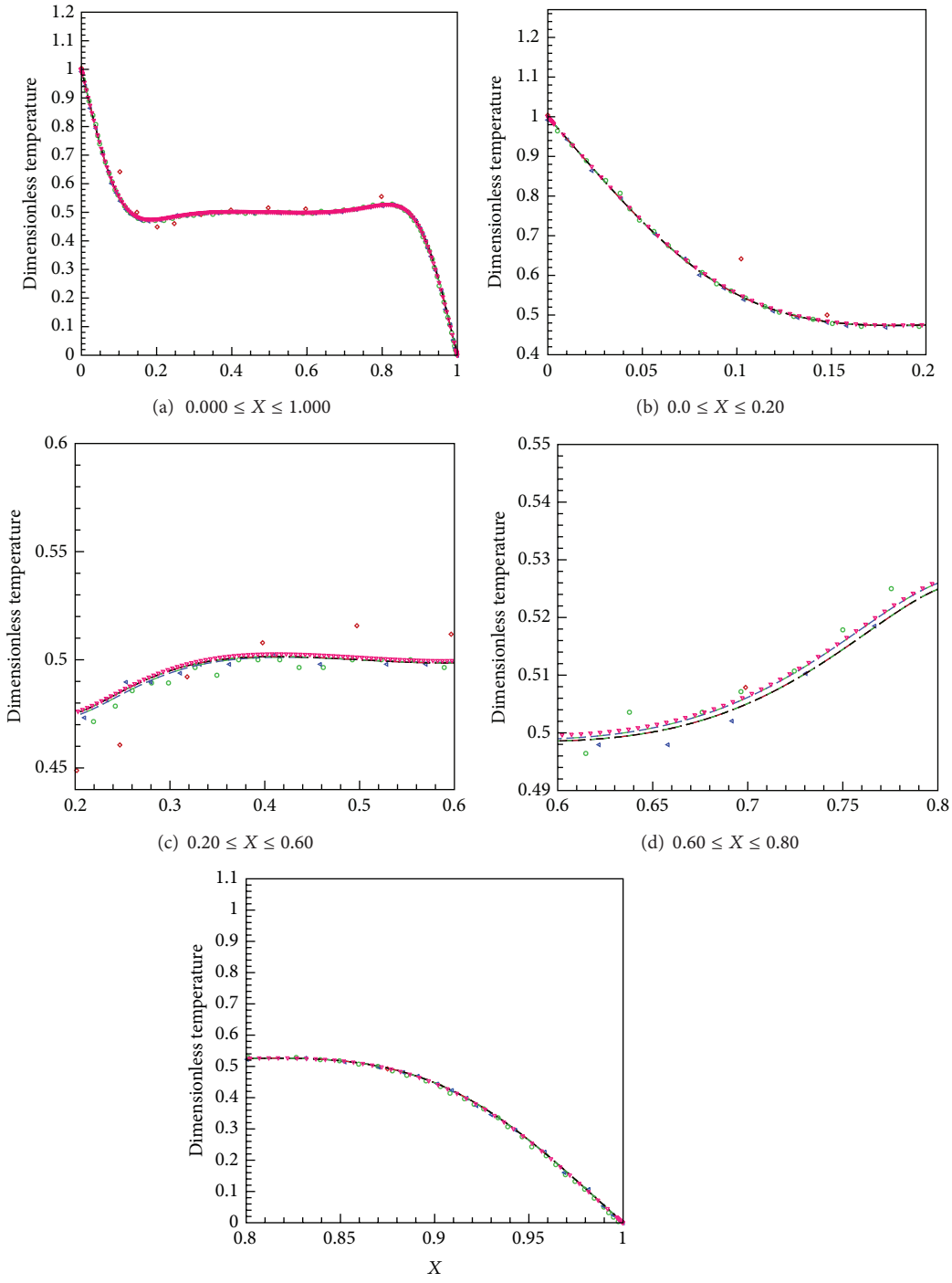

Figure 2: Dimensionless temperature representation at midheight.

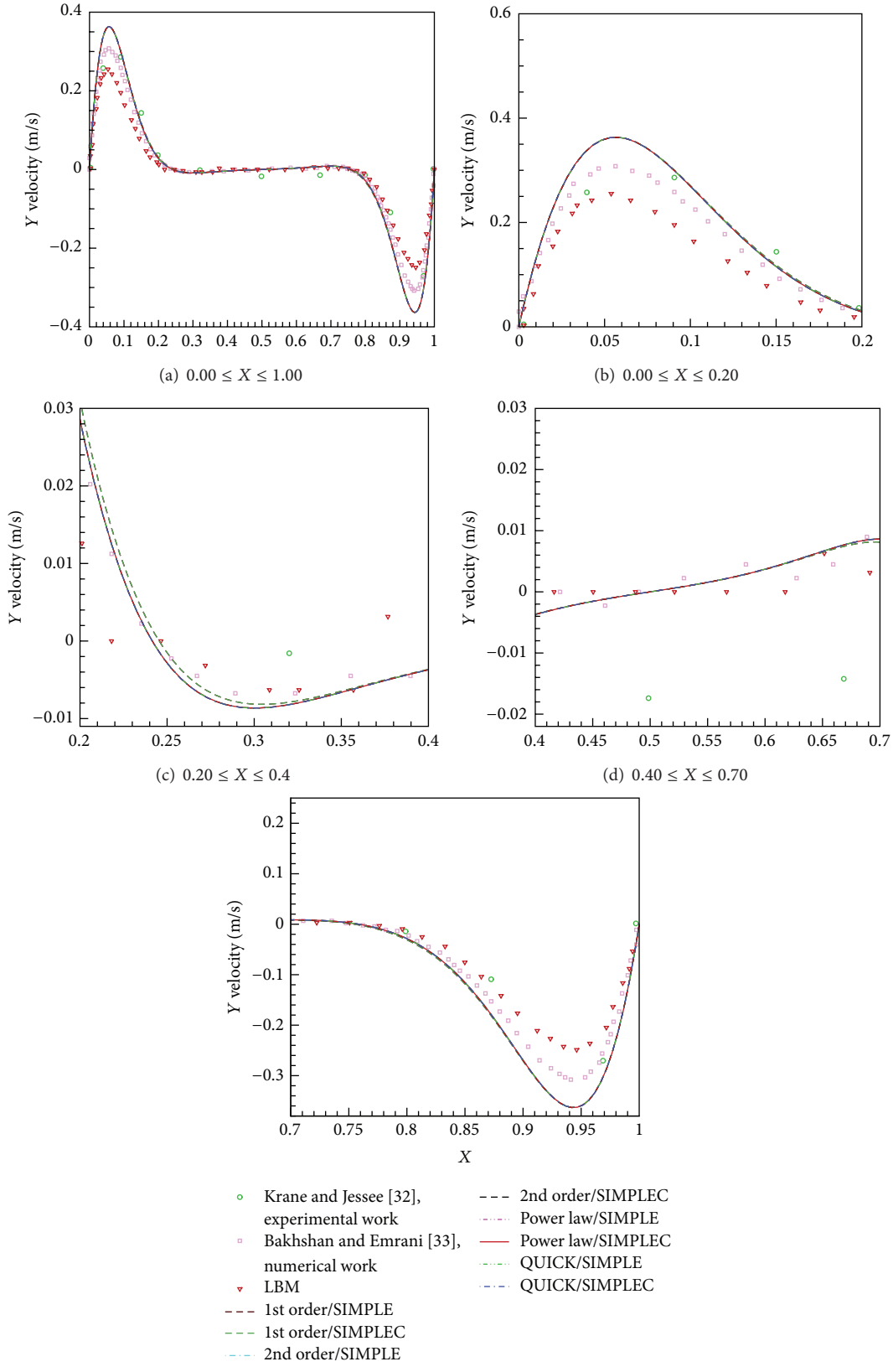

(a) $0.00 \le X \le 1.00$

(b) $0.00 \le X \le 0.20$

(c) $0.20 \le X \le 0.4$

(d) $0.40 \le X \le 0.70$

(e) $0.70 \le X \le 1.00$

Figure 3: Vertical velocity profile at midheight.

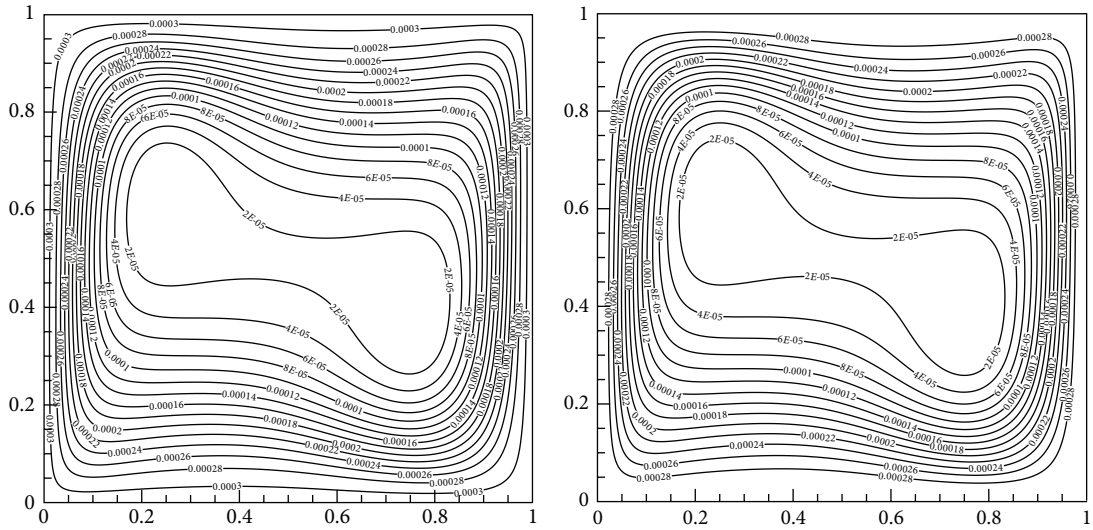

(a) 1st order upwind/SIMPLE

(b) 2nd order upwind/SIMPLE

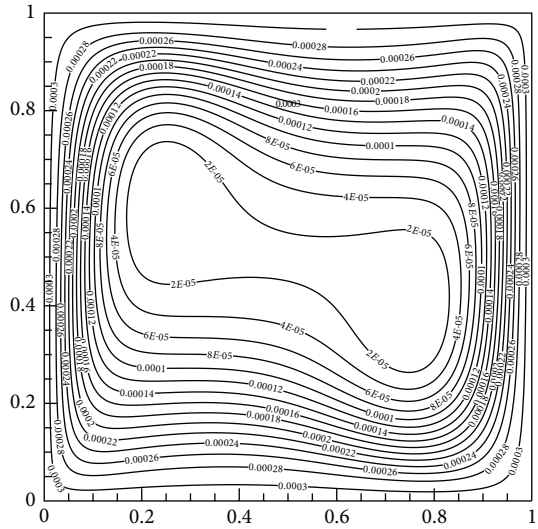

(c) 1st order upwind/SIMPLEC

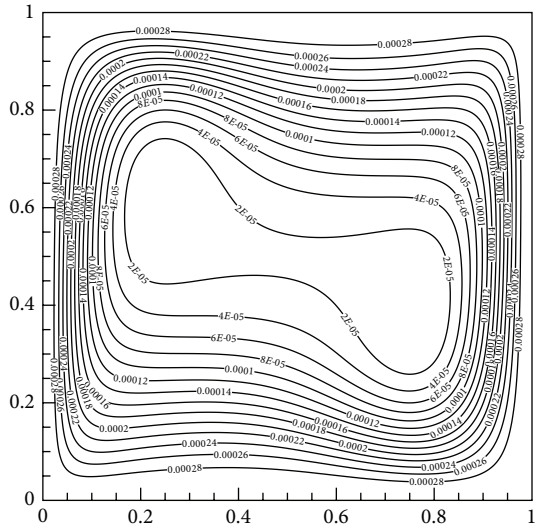

(d) 2nd order upwind/SIMPLEC

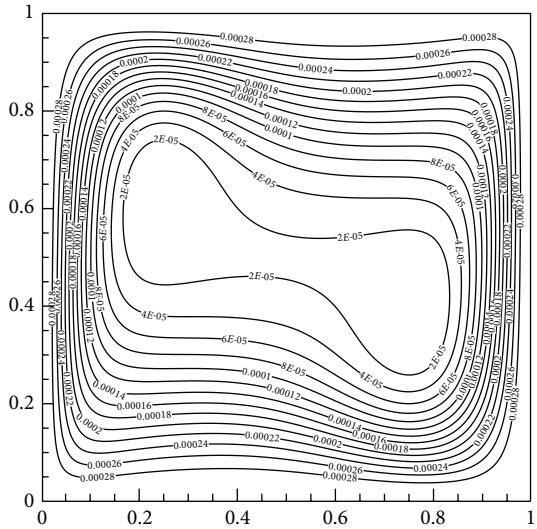

(e) Power law/SIMPLE

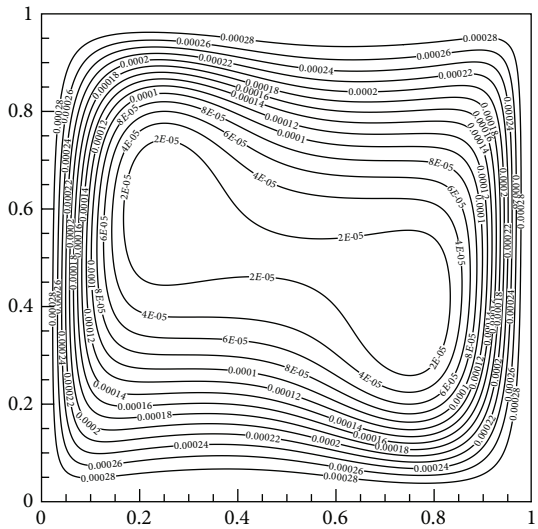

(f) QUICK/SIMPLE

Figure 4: Continued.

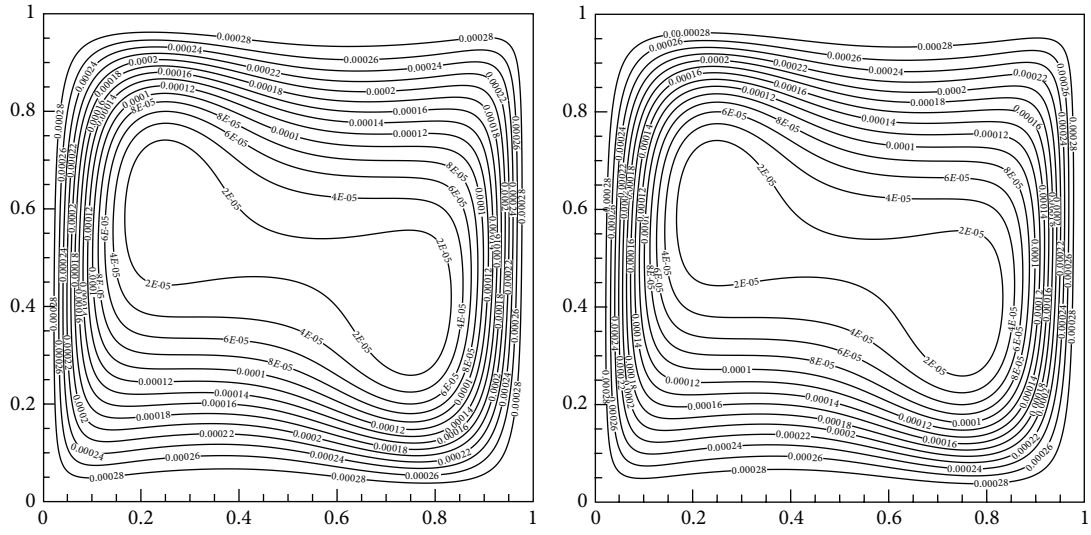

(g) Power law/SIMPLEC (h) QUICK/SIMPLEC

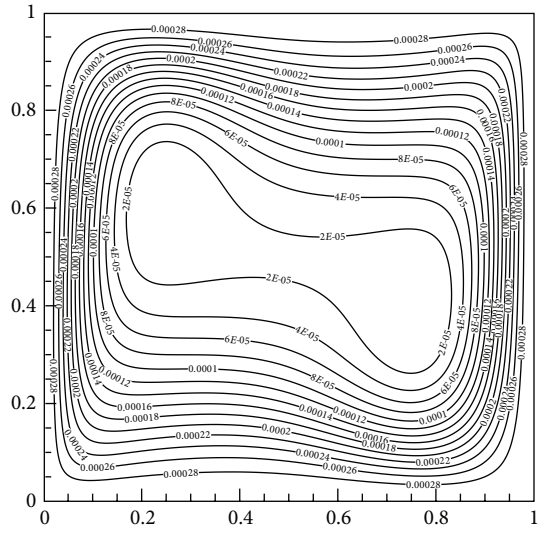

(i) LBM

Figure 4: Streamlines contours.

Table 4: Comparison of the average Nusselt number along the hot wall with those in the literature.

	$Ra = 10^3$	$Ra = 10^4$	$Ra = 10^5$	$Ra = 10^6$
Khanafer et al. [34], FVM	1.118	2.245	4.522	8.826
Barakos et al. [39], FVM	1.114	2.245	4.510	8.806
Markatos and Pericleous [40], FDM	1.108	2.201	4.430	8.754
de Vahl Davis [41], FDM	1.118	2.243	4.519	8.799
Fusegi et al. [42], 3-D FDM	1.105	2.302	4.646	9.012
1st upwind/SIMPLE	1.115	2.233	4.508	8.756
1st upwind/SIMPLEC	1.120	2.242	4.516	8.795
2nd upwind/SIMPLE	1.116	2.236	4.465	8.761
2nd upwind/SIMPLEC	1.119	2.240	4.489	8.799
Power law/SIMPLE	1.115	2.235	4.465	8.754
Power law/SIMPLEC	1.116	2.238	4.475	8.765
QUICK/SIMPLE	1.119	2.242	4.502	8.786
QUICK/SIMPLEC	1.113	2.230	4.479	8.757
LBM	1.108	2.210	4.456	8.756

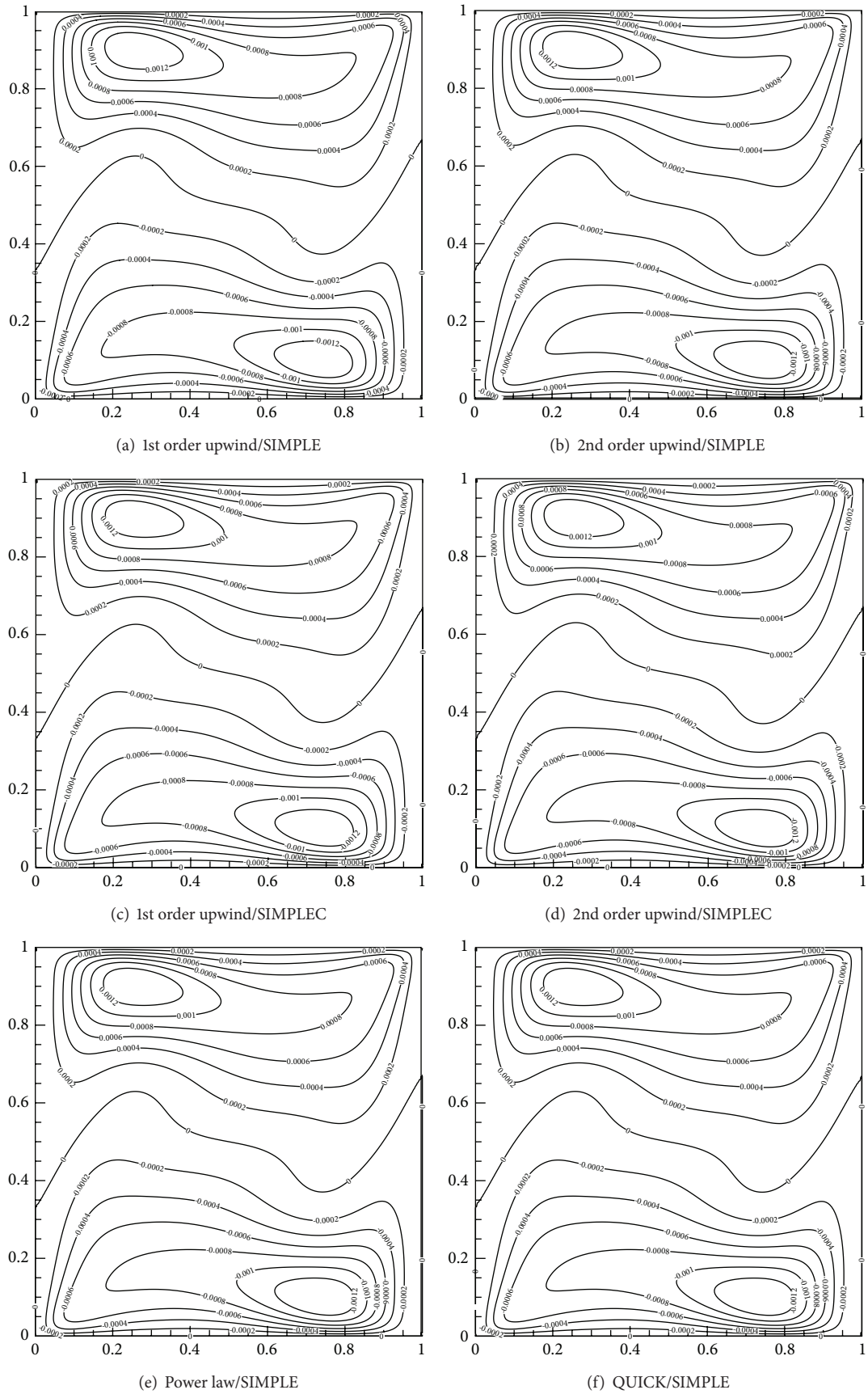

(a) 1st order upwind/SIMPLE

(b) 2nd order upwind/SIMPLE

(c) 1st order upwind/SIMPLEC

(d) 2nd order upwind/SIMPLEC

(e) Power law/SIMPLE

(f) QUICK/SIMPLE

Figure 5: Continued.

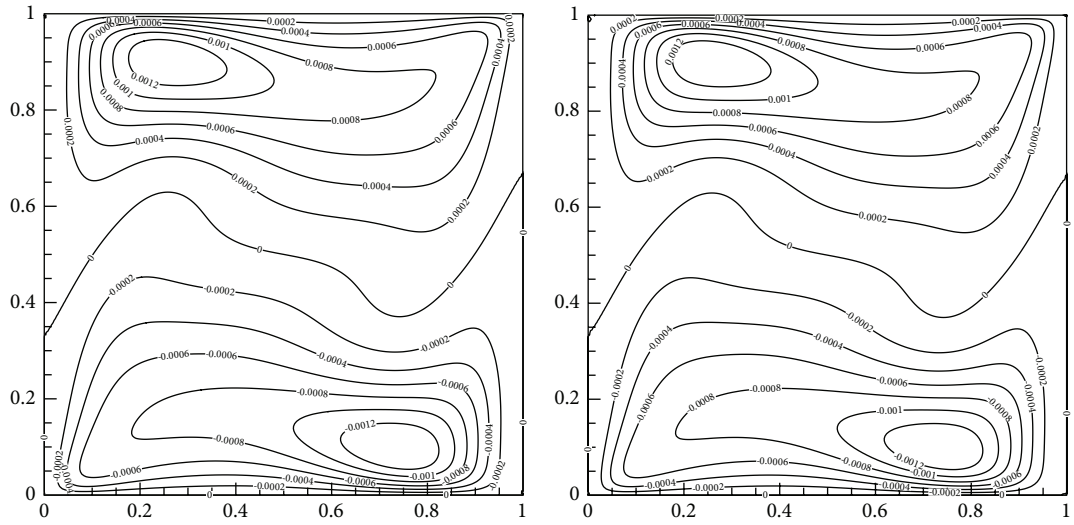

(g) Power law/SIMPLEC (h) QUICK/SIMPLEC

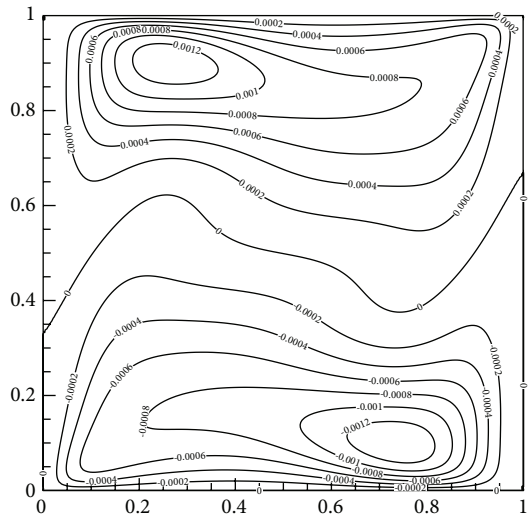

(i) LBM

Figure 5: X-velocity contours.

Table 5: Number of iterations and solving time for different discretization method.

Type of method	Case number	Discretization method/pressure-velocity linking approach	Number of iterations	Solving time (s)
Finite volume method	1	1st upwind/SIMPLE	1571	482
	2	1st upwind/SIMPLEC	1572	486
	3	2nd upwind/SIMPLE	1597	502
	4	2nd upwind/SIMPLEC	1598	509
	5	Power law/SIMPLE	1520	469
	6	Power law/SIMPLEC	1521	474
	7	QUICK/SIMPLE	1598	510
	8	QUICK/SIMPLEC	1599	519
Lattice Boltzmann method	1	Well-known finite difference method	47507	3360

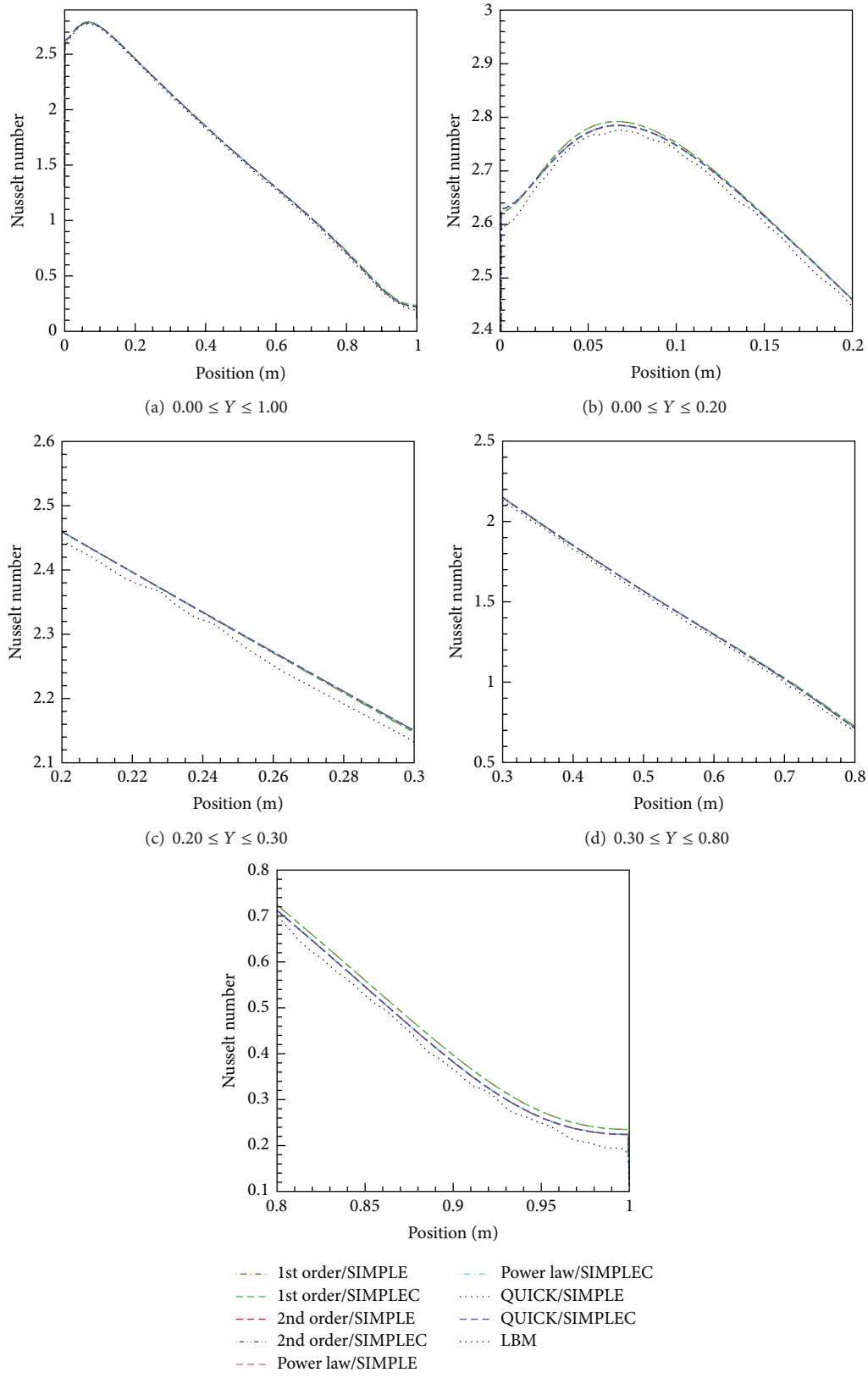

(a) $0.00 \le Y \le 1.00$

(b) $0.00 \le Y \le 0.20$

(c) $0.20 \le Y \le 0.30$

(d) $0.30 \le Y \le 0.80$

(e) $0.80 \le Y \le 1.00$

Figure 6: Nusselt number profile at hot wall.

the studied discretization schemes, especially in the northwest and southeast sides of the enclosure. Regarding the pressure/velocity coupling approaches, the maximum stream function values for the SIMPLE and SIMPLEC approaches are 0.0003 and 0.0003066, respectively, translating into 2.2% difference while the CPU usage time difference is only 4 s. For LBM, the value of stream function is 0.000278.

For the velocity contours in the X direction Figure 5 shows that the U-velocity contours have cross-diagonal similarity towards the $Y = X$ axis. Thus, all the methods analyzed present comparable results with no obvious difference.

Figure 6 demonstrates the local Nusselt number distributions along the left hot wall. For all discretization schemes, the Nusselt number is high near the bottom of the left wall (because of extreme temperature variations) and declines towards the top of the wall. The comparison between different solvers reveals that the 1st order upwind scheme predicts the maximum Nusselt number while LBM leads to the lowest one with some fluctuations along the hot wall. Interestingly, LBM uses about 40% more grids in that region compared to FVM ones.

7. Conclusions

Numerical tests using the finite volume and lattice Boltzmann methods with various discretization schemes and pressure-velocity linking algorithms were conducted to obtain the optimum discretization/linking approaches to address the internal convective heat transfer problems. The flow and temperature fields, as well as number of iterations and solving time, were evaluated.

The significant observations made in this study are summarized as follows.

(1) The finite volume method results are more accurate compared to those of LBM, especially at the corners.

(2) LBM needs a 4-5-fold CPU usage time and 8-9 times more iterations compared to the finite volume method to solve the problem considered here.

(3) Among the studied discretization/pressure-velocity linking algorithms, the 1st order upwind/SIMPLEC provides the most precise results against experimental benchmark data, especially in the boundary layers.

(4) The numbers of iterations for all FVM discretization/pressure-velocity linking methods are nearly equal.

(5) The higher-order accurate schemes are more time consuming.

One, however, notes that the above observations are valid within the limits of the parameters and problem considered in this study and could not be generalized to other cases without further investigations.

Nomenclature

x, y: Cartesian coordinates (m)
f: Density-momentum distribution function
H, L: Enclosure height and width (m)
Gr: Grashof number ($g\beta\Delta TL^3\upsilon^{-2}$)
$\vec{g}$: Gravitational acceleration (m s^2)
Z: Heat dissipation
g: Internal energy distribution function
c: Microscopic velocity vector
Pr: Prandtl number ($\upsilon\,\alpha^{-1}$)
P: Pressure (N m^2)
Ra: Rayleigh number (Gr Pr)
C_p: Specific heat capacity (J kg^1 K^1)
T, t: Temperature, time (K), (S)
k: Thermal conductivity (W m^{-1} K^{-1})
$u = (u, v)$: Velocities vector and its components in X and Y directions (m s^1).

Greek Symbols

μ: Dynamic viscosity (Pa S)
ρ: Density (kg m^3)
τ_g: Internal energy relaxation times
ν: Kinematics viscosity (m^2 s^1)
τ_f: Momentum relaxation times
β: Thermal expansion coefficient (K^1)
α: Thermal diffusivity, x-y direction components (m^2 s^1).

Subscripts

c: Cold wall
e: Equilibrium distribution function
h: Hot wall
i: Lattice velocity direction.

Conflict of Interests

The authors declare that there is no conflict of interests regarding the publication of this paper.

Acknowledgments

The authors gratefully acknowledge the High Impact Research Grant UM.C/HIR/MOHE/ENG/23, UMRG Grant RP012C-13AET and the University of Malaya, Malaysia, for support in conducting this research work.

References

[1] F. S. Mirhashemi and S. H. Hashemabadi, "Experimental and CFD study of wall effects on orderly stacked cylindrical particles heat transfer in a tube channel," *International Communications in Heat and Mass Transfer*, vol. 39, no. 3, pp. 449–455, 2012.

[2] C. Bellecci, P. Gaudio, I. Lupelli et al., "Loss of vacuum accident (LOVA): comparison of computational fluid dynamics (CFD) flow velocities against experimental data for the model

validation," *Fusion Engineering and Design*, vol. 86, no. 4-5, pp. 330–340, 2011.

[3] M. Selmi, M. J. Al-Khawaja, and A. Marafia, "Validation of CFD simulation for flat plate solar energy collector," *Renewable Energy*, vol. 33, no. 3, pp. 383–387, 2008.

[4] A. G. Dixon, G. Walls, H. Stanness, M. Nijemeisland, and E. H. Stitt, "Experimental validation of high Reynolds number CFD simulations of heat transfer in a pilot-scale fixed bed tube," *Chemical Engineering Journal*, vol. 200, pp. 344–356, 2012.

[5] Z. Zhang and X. Zhang, "Direct simulation of low-re flow around a square cylinder by numerical manifold method for Navier-Stokes equations," *Journal of Applied Mathematics*, vol. 2012, Article ID 465972, 14 pages, 2012.

[6] J. Nordström, J. Gong, E. van der Weide, and M. Svärd, "A stable and conservative high order multi-block method for the compressible Navier-Stokes equations," *Journal of Computational Physics*, vol. 228, no. 24, pp. 9020–9035, 2009.

[7] Z. Chen and L. Zhang, "A stabilized mixed finite element method for single-phase compressible flow," *Journal of Applied Mathematics*, vol. 2011, Article ID 129724, 2011.

[8] S. Boivin, F. Cayré, and J. Hérard, "A finite volume method to solve the Navier-Stokes equations for incompressible flows on unstructured meshes," *International Journal of Thermal Sciences*, vol. 39, no. 8, pp. 806–821, 2000.

[9] X. Liu, H. Liu, and Y. Liu, "Simulation of magnetorheological fluids based on Lattice Boltzmann method with double meshes," *Journal of Applied Mathematics*, vol. 2012, Article ID 567208, 16 pages, 2012.

[10] A. A. Mohamad, *Lattice Boltzmann Method: Fundamentals and Engineering Applications with Computer Codes*, Springer, 2011.

[11] Y. Shi, T. S. Zhao, and Z. L. Guo, "Lattice Boltzmann method for incompressible flows with large pressure gradients," *Physical Review E*, vol. 73, no. 2, Article ID 026704, 2006.

[12] A. Karimipour, A. H. Nezhad, A. D'Orazio, and E. Shirani, "The effects of inclination angle and prandtl number on the mixed convection in the inclined lid driven cavity using lattice boltzmann method," *Journal of Theoretical and Applied Mechanics*, vol. 51, no. 2, pp. 447–462, 2013.

[13] A. Rouboa and E. Monteiro, "Heat transfer in multi-block grid during solidification: performance of finite differences and finite volume methods," *Journal of Materials Processing Technology*, vol. 204, no. 1–3, pp. 451–458, 2008.

[14] A. Karimipour, M. Afrand, M. Akbari, and M. R. Safaei, "Simulation of fluid flow and heat transfer in the inclined enclosure," in *Proceedings of the World Academy of Science, Engineering and Technology*, World Academy of Science, Engineering and Technology, 2012.

[15] F. Garoosi, G. Bagheri, and F. Talebi, "Numerical simulation of natural convection of nanofluids in a square cavity with several pairs of heaters and coolers (HACs) inside," *International Journal of Heat and Mass Transfer*, vol. 67, pp. 362–376, 2013.

[16] H. Bararnia, K. Hooman, and D. D. Ganji, "Natural convection in a nanofluids-filled portioned cavity: the lattice-boltzmann method," *Numerical Heat Transfer A*, vol. 59, no. 6, pp. 487–502, 2011.

[17] G. Imani, M. Maerefat, and K. Hooman, "Lattice Boltzmann simulation of conjugate heat transfer from multiple heated obstacles mounted in a walled parallel plate channel," *Numerical Heat Transfer A*, vol. 62, no. 10, pp. 798–821, 2012.

[18] Z. Tian, C. Zou, H. J. Liu, Z. H. Liu, Z. L. Guo, and C. G. Zheng, "Thermal lattice boltzmann model with viscous heat dissipation in the incompressible limit," *International Journal of Modern Physics C*, vol. 17, no. 8, pp. 1131–1139, 2006.

[19] Q. Zou and X. He, "On pressure and velocity boundary conditions for the lattice Boltzmann BGK model," *Physics of Fluids*, vol. 9, no. 6, pp. 1591–1596, 1997.

[20] S. V. Patankar, *Numerical Heat Transfer and Fluid Flow*, Taylor & Francis, 1980.

[21] M. R. Safaei, B. Rahmanian, and M. Goodarzi, "Numerical study of laminar mixed convection heat transfer of power-law non-Newtonian fluids in square enclosures by finite volume method," *International Journal of Physical Sciences*, vol. 6, no. 33, pp. 7456–7470, 2011.

[22] M. R. Safaei, H. R. Goshayeshi, B. S. Razavi, and M. Goodarzi, "Numerical investigation of laminar and turbulent mixed convection in a shallow water-filled enclosure by various turbulence methods," *Scientific Research and Essays*, vol. 6, no. 22, pp. 4826–4838, 2011.

[23] M. Goodarzi, M. R. Safaei, K. Vafai et al., "Investigation of nanofluid mixed convection in a shallow cavity using a two-phase mixture model," *International Journal of Thermal Sciences*, vol. 75, pp. 204–220, 2014.

[24] S. S. Mousavi and K. Hooman, "Heat and fluid flow in entrance region of a channel with staggered baffles," *Energy Conversion and Management*, vol. 47, no. 15-16, pp. 2011–2019, 2006.

[25] W. Q. Tao, Y. L. He, Z. Y. Li, and Z. G. Qu, "Some recent advances in finite volume approach and their applications in the study of heat transfer enhancement," *International Journal of Thermal Sciences*, vol. 44, no. 7, pp. 623–643, 2005.

[26] P. Forooghi and K. Hooman, "Numerical study of turbulent convection in inclined pipes with significant buoyancy influence," *International Journal of Heat and Mass Transfer*, vol. 61, no. 1, pp. 310–322, 2013.

[27] M. R. Safaei, M. Goodarzi, and M. Mohammadi, "Numerical modeling of turbulence mixed convection heat transfer in air filled enclosures by finite volume method," *International Journal of Multiphysics*, vol. 5, no. 4, pp. 307–324, 2011.

[28] H. Goshayeshi, M. R. Safaei, and Y. Maghmoumi, "Numerical simulation of unsteady turbulent and laminar mixed convection in rectangular enclosure with hot upper moving wall by finite volume method," in *Proceedings of the 6th International Chemical Engineering Congress and Exhibition (IChEC '09)*, Kish Island, Iran, 2009.

[29] N. Lancial, F. Beaubert, S. Harmand, and G. Rolland, "Effects of a turbulent wall jet on heat transfer over a non-confined backward-facing step," *International Journal of Heat and Fluid Flow*, vol. 44, pp. 336–347, 2013.

[30] S. Hou, Q. Zou, S. Chen, G. Doolen, and A. C. Cogley, "Simulation of cavity flow by the lattice Boltzmann method," *Journal of Computational Physics*, vol. 118, no. 2, pp. 329–347, 1995.

[31] A. D'Orazio, C. Arrighetti, and S. Succi, *Kinetic Scheme for Fluid Flows with Heat Transfer*, University of Rome "La Sapienza", Roma, Italy, 2003.

[32] R. Krane and J. Jessee, "Some detailed field measurements for a natural convection flow in a vertical square enclosure," in *Proceedings of the 1st ASME-JSME Thermal Engineering Joint Conference*, pp. 323–329, 1983.

[33] Y. Bakhshan and S. H. Emrani, "Investigating the behavior of nanofluids in a rectangular enclosure in order to enhance the heat transfer coefficient," *Journal of Basic and Applied Scientific Research and Essays*, vol. 3, no. 1, pp. 976–986, 2013.

[34] K. Khanafer, K. Vafai, and M. Lightstone, "Buoyancy-driven heat transfer enhancement in a two-dimensional enclosure utilizing nanofluids," *International Journal of Heat and Mass Transfer*, vol. 46, no. 19, pp. 3639–3653, 2003.

[35] H. F. Oztop and E. Abu-Nada, "Numerical study of natural convection in partially heated rectangular enclosures filled with nanofluids," *International Journal of Heat and Fluid Flow*, vol. 29, no. 5, pp. 1326–1336, 2008.

[36] J. M. Buick and C. A. Created, "Gravity in a lattice Boltzmann model," *Physical Review E*, vol. 61, no. 5 A, pp. 5307–5320, 2000.

[37] X. He and L. Luo, "Lattice Boltzmann model for the incompressible Navier-Stokes equation," *Journal of Statistical Physics*, vol. 88, no. 3-4, pp. 927–944, 1997.

[38] W. Tao, *Recent Advances in Computational Heat Transfer*, Science Press, Beijing, China, 2000.

[39] G. Barakos, E. Mitsoulis, and D. Assimacopoulos, "Natural convection flow in a square cavity revisited: laminar and turbulent models with wall functions," *International Journal for Numerical Methods in Fluids*, vol. 18, no. 7, pp. 695–719, 1994.

[40] N. C. Markatos and K. A. Pericleous, "Laminar and turbulent natural convection in an enclosed cavity," *International Journal of Heat and Mass Transfer*, vol. 27, no. 5, pp. 755–772, 1984.

[41] G. de Vahl Davis, "Natural convection of air in a square cavity: a bench mark numerical solution," *International Journal for Numerical Methods in Fluids*, vol. 3, no. 3, pp. 249–264, 1983.

[42] T. Fusegi, J. M. Hyun, K. Kuwahara, and B. Farouk, "A numerical study of three-dimensional natural convection in a differentially heated cubical enclosure," *International Journal of Heat and Mass Transfer*, vol. 34, no. 6, pp. 1543–1557, 1991.

[43] A. Karimipour, A. H. Nezhad, A. D'Orazio, and E. Shirani, "Investigation of the gravity effects on the mixed convection heat transfer in a microchannel using lattice Boltzmann method," *International Journal of Thermal Sciences*, vol. 54, pp. 142–152, 2012.

Hindawi Publishing Corporation
Abstract and Applied Analysis
Volume 2014, Article ID 505890, 24 pages
http://dx.doi.org/10.1155/2014/505890

Research Article

Retrofitting Transportation Network Using a Fuzzy Random Multiobjective Bilevel Model to Hedge against Seismic Risk

Lu Gan[1,2] and Jiuping Xu[2,3]

[1] *Urban and Rural Development College, Sichuan Agricultural University, Dujiangyan 611830, China*
[2] *Uncertainty Decision-Making Laboratory, Sichuan University, Chengdu 610064, China*
[3] *State Key laboratory of Hydraulics and Mountain River Engineering, Sichuan University, Chengdu 610064, China*

Correspondence should be addressed to Jiuping Xu; xujiuping@scu.edu.cn

Received 28 August 2013; Revised 14 October 2013; Accepted 14 October 2013; Published 12 January 2014

Academic Editor: Mohamed Fathy El-Amin

This paper focuses on the problem of hedging against seismic risk through the retrofit of transportation systems in large-scale construction projects (LSCP). A fuzzy random multiobjective bilevel programming model is formulated with the objectives of the retrofit costs and the benefits on two separate levels. After establishing the model, a fuzzy random variable transformation approach and fuzzy variable approximation decomposition are used to deal with the uncertainty. An approximation decomposition-based multi-objective AGLNPSO is developed to solve the model. The results of a case study validate the efficiency of the proposed approach.

1. Introduction

Transportation networks play a very important role in both urban and rural areas, as well as in industrial sites such as large-scale construction sites. Liu et al. [1] stated that transportation networks are critical infrastructure and their smooth operation is important for maintaining the normal functions of society. However, disasters, especially earthquakes, cause not only tremendous economic losses and social chaos but also enormous damage to infrastructure (e.g., 2008 Wenchuan Earthquake, 2010 Chile Earthquake, and 2011 Japan Earthquake). Thus, as Liu et al. [1] pointed out, seismic risk control should also consider the effect that damaged or destroyed transportation networks have on the effectiveness of postdisaster rescue and repair activities and the associated socioeconomic losses. Under a seismic risk threat, retrofit decisions are considered to be an effective protective measure and can have a significant impact on these systems [1–3]. Therefore, promoting retrofit decisions for transportation networks is necessary to hedge against seismic risk.

The research in this area has mainly focused on the retrofitting of bridges for transportation networks [4–6]. Werner et al. [2] extended seismic retrofits to highway systems. Afterwards, Liu et al. [1] established a two-stage stochastic programming model for retrofit decisions for transportation network protection. This previous research, however, has primarily focused on urban transportation, but it is essential that transportation networks in large-scale construction projects (LSCP) also be considered. As a critical infrastructure, the smooth operation of these networks is important for maintaining the normal progress of these projects. Therefore, it is necessary to control the seismic risk for LSCP transportation networks to mitigate losses. When considering LSCP transportation network retrofits, there are significant challenges. First, these transportation systems have not only permanent links and temporary links to consider but must also assess the critical links (i.e., bridge, tunnel, etc.) and the noncritical links. Secondly, the retrofit decision making environment is a mutual environment involving an investor who pays for the retrofit and an administrator who controls the transportation systems. Thirdly, a consideration of the environmental costs for the investor has increasingly become necessary for social and economic development. Lastly, a majority of the previous research has assumed that seismic damage is classified into five categories and there is a set of discrete probabilities

associated with each of the five damage categories. In practice, however, the situation is often not that simple, and the description of the possible result of seismic damage is vague and uncertain. In this case, this needs to be qualified with a vague perception of a crisp but unobservable random variable. Hence, due to the complexity of assessing the seismic risk to property, seismic damage is subject to uncertainty with both fuzziness and randomness, that is, fuzzy random in nature. More recently, since Kwakernaak [7] proposed the concept of the fuzzy random variable, considerable research has been done, which has allowed for its application in many areas [7–13]. Unfortunately, there has been little research which has discussed a mixture of fuzziness and randomness in a transportation network retrofit problem. Therefore, the uncertainty with hybrid fuzziness and randomness induced by the seismic damage risk to property needs to be further studied and elaborated.

The fuzzy random variable was proposed by Kwakernaak [7] who regarded it as "random variables whose values are not real, but fuzzy numbers." From another view, Puri and Ralescu [14] and Klement et al. [15] regarded a fuzzy random variable as a random fuzzy set. Fuzzy random variables represent a well-formalized concept which has underlain many recent probabilistic and statistical studies involving data obtained from a random experiment when these data are assumed to be fuzzy set valued [16]. Therefore, in a transportation network retrofit problem, the description of seismic damage is considered a fuzzy random variable, that is, a discrete distribution variable with a vague perception (i.e., triangular fuzzy number). Several research works have demonstrated how these fuzzy random coefficients can be converted into crisp values. Usually, at first, the fuzzy random variables are transformed into fuzzy numbers using the fuzzy expected values [17] or transformed into (α_1, σ)-level trapezoidal fuzzy variables through an approach proposed in Xu and Liu [12]. Then, these fuzzy numbers are transformed into deterministic values using their expected value [18] or (α, β)-satisfactory solution to the programming is determined using fuzzy coefficients [12]. In this case, based on the properties of the fuzzy random seismic damage in this study, the theorem and the proof presented in Xu and Liu [12] are adjusted to allow for a discrete random distribution to obtain the equivalent fuzzy bilevel programming model. Then, using the theorem proposed by Zhang et al. [19], decomposition is used on these fuzzy variables to derive an approximate solution to the model.

Under these emerging challenges, this paper formulates a fuzzy random multiobjective bilevel programming model for a transportation network retrofit decision to hedge against seismic risk in an LSCP. The distinctions in the link types allow for the recognition of the retrofit and reconstruction costs. The investor and the administrator are the decision-makers on two separate levels. Retrofit costs which include the environmental costs and the retrofit benefits are the two objectives of the investor, and the retrofit benefits are the objective of the administrator. In order to describe the hybrid uncertainty of possible seismic damage, fuzzy random variables are introduced in the programming model, the use of which has been applied in many areas [10, 18]. To cope with the proposed fuzzy random multiobjective bilevel programming model, a transformation approach is used to obtain an equivalent fuzzy bilevel programming model. This approach transforms the fuzzy random variables in the model into fuzzy variables which are similar to trapezoidal fuzzy variables. Then, decomposition is utilized on these fuzzy variables using a fuzzy number decomposition theorem [19]. To solve the model, an approximation decomposition-based multiobjective AGLNPSO is developed in this paper. Through the decomposition of the fuzzy variables, the models are successively solved until termination, and the approximation solutions are obtained. The multiobjective AGLNPSO is a combination of the Pareto Archived Evolution Strategy (PAES) [20] and the AGLNPSO [21] which is developed by incorporating an adaptive particle swarm optimization (APSO) [22] with a GNLPSO [23] and a multiple objectives particle swarm optimization (MOPSO) [24].

This study contributes to the literature by adopting the work of Liu et al. [1] to an LSCP and describing the complex uncertain seismic damage scenario using fuzzy random variables. Bilevel decisions involving the investor and the administrator, distinctions between the various link types, and the specification of the retrofit decisions into several ranks according to the seismic damage scenario provide a more reasonable and practical description of the problem. The consideration of the environmental costs in the transportation network in an LSCP enhances the focus for management. To the best of our knowledge, an integrated approach to deal with fuzzy random variables has not been previously comprehensively studied. The approximation decomposition-based multiobjective AGLNPSO is developed as a useful tool to solve the problem, in which both the bilevel and multiobjective environments are considered.

The remainder of this paper is as follows. The problem description, the fuzzy random multiobjective bilevel programming model, the transformation approach, and the approximation decomposition are given in Section 2. An approximation decomposition-based multiobjective AGLNPSO is developed in Section 3. A case study is presented in Section 4. Finally, advantages, limitations, and possible future extensions of this work are presented in Section 5.

2. Modeling

In this section, the concepts for the LSCP transportation network, the bilevel decision framework, the environmental costs, and the fuzzy random seismic damage scenario are introduced. A multiobjective bilevel programming model for the problem considering fuzziness and randomness is established. See in the following the notations used to describe the model.

Index

a: Link in transportation network, $a \in A$

b: Node in transportation network, $b \in B$

v: Variable environment cost, $v \in V$

f: Fixed environmental cost, $f \in F$

i: Retrofit output, $i \in I$

j: Retrofit activity, $j \in J$

k: Origin-destination pair considered as commodity, $k \in \{1, \ldots, K\}$.

Variables

$m_a = \begin{cases} 1, & \text{Permanent link} \\ 0, & \text{Temporary link} \end{cases}$

$n_a = \begin{cases} 1, & \text{Critical link} \\ 0, & \text{Noncritical link} \end{cases}$

c_{va}^{p}: Increased variable retrofit costs for permanent link by basic rank (i.e., rank 1)

c_{va}^{t}: Variable retrofit costs for temporary link by basic rank (i.e., rank 1)

c_{fi}^{p}: Increased fixed retrofit costs for permanent link

c_{fi}^{t}: Fixed retrofit costs for temporary link

ρ: Weight of environmental costs

ce_{v}^{p}: Increased variable environmental costs for permanent link by basic rank (i.e., rank 1)

ce_{v}^{t}: Variable environmental costs for temporary link by basic rank (i.e., rank 1)

ce_{f}^{f}: Fixed environmental costs

pe_{jv}^{v}: Percent of activity cost center j in variable environment cost v

pe_{if}^{f}: Percent of output i in fixed environment cost f

ce_{j}^{c}: Variable environmental costs of activity cost center j

am_j: Cost of driver at activity cost center j

ra_j: Driver rate at activity cost center j

am_{ij}: Cost of driver for output i in activity cost center j

C: Retrofit costs including environmental costs

Q: Retrofit benefits

$\widetilde{\widetilde{\xi}}_a$: Preretrofit link damage state for link a

$\widetilde{\widetilde{\Xi}}_a$: Postretrofit link damage state for link a

cr_{va}^{p}: Increased variable reconstruction cost for permanent link by basic rank (i.e., rank 1)

cr_{va}^{t}: Variable reconstruction cost for temporary link by basic rank (i.e., rank 1)

cr_{fi}^{p}: Increased fixed reconstruction cost for permanent link

cr_{fi}^{t}: Fixed reconstruction cost for temporary link

γ: Weight coefficient conversion time to monetary value

ti_{a}^{0}: Free flow travel time and link a

α: Coefficient of BPR function

fl_a: The total flow on link a

ca_{a}': Practical capacity of link a is set at 90% of the design capacity

β: BPR function coefficient

ca_b: Capacity of node b

W: Node-commodity adjacency matrix

M: Link-commodity adjacency matrix.

Decision Variables

$$u_a : \in \{0, 1, 2, 3, 4, 5\}, \quad \forall a \in A$$
$$x_k : \leq 0, \quad \forall k = 1, \ldots, K. \tag{1}$$

2.1. LSCP Transportation Network. The LSCP transportation network is composed of an internal road system and an external road system and is always built based on the existing links around the site which are connected with the newly built links according to transportation need. There are two types of links (i.e., permanent links and temporary links) which vary considerably in terms of quality. In addition, according to the different functions, the links are divided into critical links and noncritical links. Critical links are those which have vital transport functions such as bridges and tunnels and which should be preferentially taken into account [1]. The retrofit decisions for the different link types vary. That is, the links being considered for the retrofit are either considered to be permanent or critical. The retrofit and reconstruction costs for the temporary links are lower than those for the permanent links. Further, the retrofit decision is specific with 0 (i.e., no retrofit) and there are several ranks according to the seismic damage scenarios.

2.2. Bilevel Decision Framework. In this paper, the seismic hazard retrofit decision for an LSCP transportation network involves two participants (i.e., the investor who pays for the retrofit and the administrator who controls the transportation). Therefore, these two participants are the decision-makers on two levels, both of whom successively make the retrofit decisions. The investor on upper level decides which retrofit rank should be taken for each link within the range and, therefore, the two objectives on this level are the retrofit costs including the environmental costs and the retrofit benefits. The administrator decides on the commodity flow (i.e., the transportation network flow once seismic damage has occurred) on the lower level according to the decision results of the upper level. On this level, the retrofit benefits are the primary objective. In this paper, the retrofit benefits are quantified as reconstruction and travel delay cost savings. The investor on the upper level affects the decisions of the administrator on lower level, but does not fully control them. The administrator makes their decision autonomously based on the scope of the decision of the upper level.

2.3. Environmental Costs. In recent years, more attention has been paid to environmental problems as these have begun to seriously affect both local communities and the economy. Thus, it is essential to consider the environmental costs in

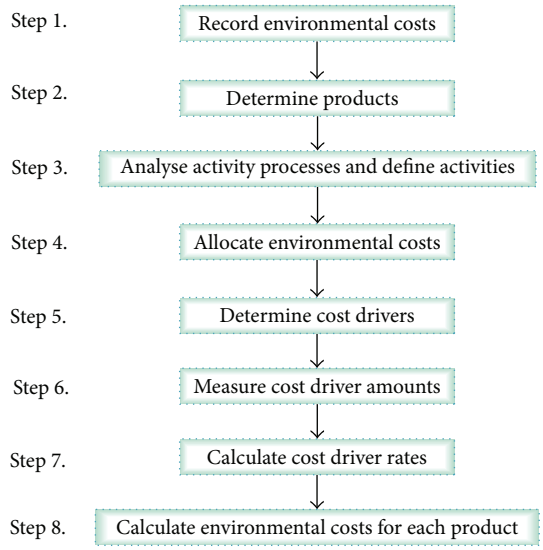

Figure 1: Obtain environmental costs for retrofitting transportation network in LSCP based on ABC.

the LSCP. In addition, as environmental costs affect the overall project cost, it is necessary to effectively record and calculate environmental costs in the LSCP. Generally, many environmental costs are not usually tracked systematically or attributed to the related processes and outputs but are simply summed and added to total cost [25]. The fact that environmental costs are not fully recorded often leads to distorted calculations [25]. Activity based costing (ABC) is an effective method to record and calculate environmental costs [26]. Cooper provided a comprehensive discussion of ABC [27–30], following the pioneering work of [31, 32]. This method treats activities as accounting objects, and identifies and measures the amount of activities using cost drivers.

The environmental costs for retrofitting LSCP transportation networks based on the ABC are as shown in Figure 1. As can be seen, the environmental costs are fully recorded according to the environmental cost categories proposed in [25]. Note that some environmental cost categories are related to the work processes, and others are not. Then, all the outputs involved in retrofitting the LSCP transportation network are determined and an analysis of the activity processes and a definition of the activities are prepared to determine the environmental costs. Every activity corresponds to an activity cost center. Jasch [25] proposed that the costs should be more precisely allocated to cost centers. Therefore, environmental costs are either directly allocated to each activity cost center or systematically traced to the responsible environmental media. Of course, if those costs are attributed to outputs directly (i.e., they are not related to the work processes), it is not necessary to allocate them to activity cost centers. Then, the cost drivers for the activity cost centers are determined and the cost driver amounts measured to calculate the cost driver rates. Finally, the environmental costs of each output are determined.

Therefore, by using a complete recording method, distortion in the environmental costs can be avoided and through this precise allocation it is easier to effectively manage these costs as it is possible to systematically trace them to the related processes and outputs.

2.4. Fuzzy Random Seismic Damage Scenario. To better understand the concepts for the fuzzy random seismic damage scenario, this subsection gives some basic knowledge for the definition and properties of the fuzzy random variables. After Zadeh [33] proposed the concept of fuzzy sets, many scholars have usually tied fuzziness to randomness as possible random outcomes have to be described using fuzzy sets. To describe this fuzziness and randomness, Kwakernaak [7] proposed the concept of fuzzy random variables in 1978. Kruse and Meyer [17] then worked on an expanded version of a similar model. In addition, Puri and Ralescu [14] and Klement et al. [15] also defined fuzzy random variables from other angles. In this paper, the fuzzy random variables are defined in the real number set. This makes the above definitions equivalent [34]. Here, the definition proposed by [14] is utilized.

In the following, $\mathbb{R}$ is denoted as the set of all real numbers, $\mathscr{F}_c(\mathbb{R})$ is denoted as the set of all fuzzy variables, and $\mathscr{K}_c(\mathbb{R})$ is denoted as all of the nonempty bounded close intervals.

Definition 1 (see [14]). In a given probability space $(\Omega, \mathscr{A}, \Pr)$, a mapping $\tilde{\tilde{\xi}} : \Omega \to \mathscr{F}_c(\mathbb{R})$ is called a fuzzy random variable in $(\Omega, \mathscr{A}, \Pr)$; if $\alpha \in (0, 1]$, the set-valued function $\tilde{\tilde{\xi}}_\alpha : \Omega \to \mathscr{K}_c(\mathbb{R})$,

$$\begin{aligned}\tilde{\tilde{\xi}}_\alpha(\omega) &= \left(\tilde{\tilde{\xi}}(\omega)\right)_\alpha \\ &= \left\{x \mid x \in \mathbb{R}, \mu_{\tilde{\tilde{\xi}}(\omega)}(x) \geq \alpha\right\}, \quad \forall \omega \in \Omega,\end{aligned} \tag{2}$$

is $\mathscr{F}$ measurable.

Definition 2 (see [35]). If $\tilde{\tilde{\xi}}_1, \tilde{\tilde{\xi}}_2, \ldots, \tilde{\tilde{\xi}}_n$ are fuzzy random variables defined in the probability space on $(\Omega, \mathscr{A}, \Pr)$, then $\tilde{\tilde{\xi}} = (\tilde{\tilde{\xi}}_1, \tilde{\tilde{\xi}}_2, \ldots, \tilde{\tilde{\xi}}_n)$ is called fuzzy random vector.

Lemma 3 (see [36]). *Let $\tilde{\tilde{\xi}} = (\tilde{\tilde{\xi}}_1, \tilde{\tilde{\xi}}_2, \ldots, \tilde{\tilde{\xi}}_n)$ be a fuzzy random vector, and let f be a continuous function from $\mathbb{R}^m$ to $\mathbb{R}$. Then $f(\tilde{\tilde{\xi}})$ is a fuzzy random variable.*

Definition 4 (see [14]). In a given probability space $(\Omega, \mathscr{A}, \Pr)$, if $\omega \in \Omega$, $\alpha \in [0, 1]$, the mapping $\omega \mapsto (\tilde{\tilde{\xi}})^-_\alpha(\omega)$ and $\omega \mapsto (\tilde{\tilde{\xi}})^+_\alpha(\omega)$ are integrable; then $\tilde{\tilde{\xi}}$ is called the integrated bounded fuzzy random variable on the probability space $(\Omega, \mathscr{A}, \Pr)$.

Definition 5 (see [14]). Let $\tilde{\tilde{\xi}}$ be an integrated bounded fuzzy random variable on the probability space $(\Omega, \mathscr{A}, \Pr)$; the

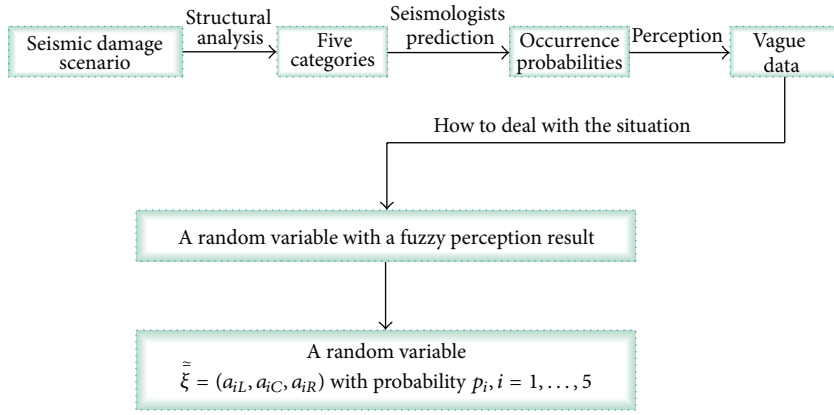

Figure 2: Fuzzy random seismic damage scenario.

expected value $E(\tilde{\tilde{\xi}})$ of $\tilde{\tilde{\xi}}$ is defined as the only fuzzy set in $\mathbb{R}$; for all $\alpha \in [0,1]$, it satisfies

$$E\left(\tilde{\tilde{\xi}}\right)_\alpha = \int_\Omega \tilde{\tilde{\xi}}_\alpha dp = \left\{ \int_\Omega f(\omega)\, dp(\omega) : f \in L^1(P), \; f(\omega) \in \tilde{\tilde{\xi}}_\alpha(\omega) \text{ a.s. } [P] \right\}, \tag{3}$$

where $\int_\Omega \tilde{\tilde{\xi}}_\alpha dp$ is the Aumann integral of $\tilde{\tilde{\xi}}_\alpha$ about P and $L^1(P)$ denote all of the integrable function $f : \Omega \to \mathbb{R}$ about the probability measure P.

Lemma 6 (see [37]). *Let $(\Omega, \mathscr{A}, \mathrm{Pr})$ be complete probability space; $\tilde{\tilde{\xi}} : \Omega \to \mathscr{F}_c(\mathbb{R})$ is an integrated bounded fuzzy random variable. Then for all $\alpha \in [0,1]$, the α-set of $E(\tilde{\tilde{\xi}})$ is the compact convex interval as follows:*

$$E\left(\tilde{\tilde{\xi}}\right)_\alpha = \left[\left(E\left(\tilde{\tilde{\xi}}\right)\right)_\alpha^-, \left(E\left(\tilde{\tilde{\xi}}\right)\right)_\alpha^+\right] = \left[\int_\Omega \left(\tilde{\tilde{\xi}}(\omega)\right)_\alpha^- dp(\omega), \left(\tilde{\tilde{\xi}}(\omega)\right)_\alpha^+ dp(\omega)\right]. \tag{4}$$

Lemma 7. *Let $(\Omega, \mathscr{A}, \mathrm{Pr})$ be complete probability space; $\tilde{\tilde{\xi}}_1, \tilde{\tilde{\xi}}_2$ are integrated bounded fuzzy random variables on $(\Omega, \mathscr{A}, \mathrm{Pr})$, $\lambda, \gamma \in \mathbb{R}$, and then*

$$E\left(\lambda\tilde{\tilde{\xi}}_1 + \gamma\tilde{\tilde{\xi}}_2\right) = \lambda E\left(\tilde{\tilde{\xi}}_1\right) + \gamma E\left(\tilde{\tilde{\xi}}_2\right). \tag{5}$$

For the fuzzy random seismic damage scenario, according to [1], advanced structural analysis can lead to a probabilistic assessment of the structural damage for a given earthquake, in terms of a set of discrete probabilities associated with each of the five damage categories. Seismologists also have made predictions as to the probabilities of various earthquake occurrences. These two sets of probabilistic estimations from earthquake-structural engineers and seismologists can be combined to prepare the damage prediction [1]. For the convenience of discussion, seismic damage to a structure (i.e., LSCP transportation network) is usually classified into five categories ranging from no damage to complete collapse. However, a description of the perception result for seismic damage is a category which is vague. In this case, a vague perception of a crisp but unobservable random variable is used as in the following:

$$\tilde{\tilde{\xi}} = (a_{iL}, a_{iC}, a_{iR}) \quad \text{with probability } p_i,\ i = 1, \ldots, 5. \tag{6}$$

Therefore, the seismic damage scenario can be viewed as a fuzzy random variable, which has a similar sense to the minor automobile collision damage outlined in [10]. See Figure 2 for a detailed description.

An example can be used to explain how to use the fuzzy random variable and to describe the uncertainty in a seismic damage scenario. Suppose that there is a link $a \in A$ in an LSCP transportation network. Seismic damage perception has five categories 1, 2, 3, 4, and 5 ranging from no damage to complete collapse and seismic damage randomly emerges with a certain probability. On the other hand, the description of the perception result is vague with values such as "about 1" and "about 3." These denote the fuzzy sets and can be conveniently described using triangular fuzzy sets, as shown in Figure 3. Here it is assumed that the probabilities for the five categories are 0.1, 0.2, 0.3, 0.3, and 0.1, so the seismic damage scenario can be seen as a fuzzy random variable as in (7) and as shown in Figure 3. It should be mentioned that one damage scenario has different meanings for the different damage ranks (i.e., its membership is different for each different damage rank). Similar examples can be found in [10]. Consider

$$\tilde{\tilde{\xi}}_a = \begin{cases} (0,1,2) & \text{with probability } 0.1 \\ (1,2,3) & \text{with probability } 0.2 \\ (2,3,4) & \text{with probability } 0.3 \\ (3,4,5) & \text{with probability } 0.3 \\ (4,5,6) & \text{with probability } 0.1. \end{cases} \tag{7}$$

It should be noted that the same category may have different possibilities for different links.

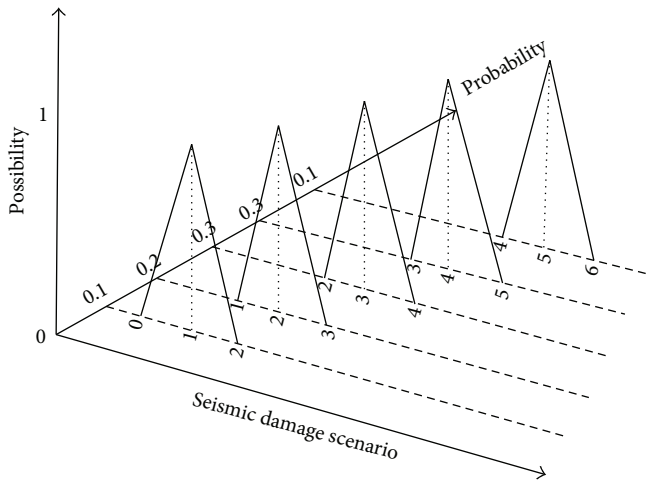

Figure 3: Value of seismic damage scenario.

2.5. Model Formulation. Denote a transportation network as $G(B, A)$, where B is the set of nodes and A is the set of network links. The decision variable on the upper level is $u_a \in \{0, 1, 2, 3, 4, 5\}$, which means that a decision has been done for link a to be retrofitted at rank u_a, $a \in A$. For each commodity $k \in \{1, \ldots, K\}$, $x_k \in R_+$ is the commodity flow (i.e., the decision variable on the lower level), and $ca_b \in R_+$ is the capacity of node b. Denote fl_a as the total flow on link a (i.e., $fl_a = Mx$, for all $a \in A$). To model the retrofit decision with seismic risk in this paper, the assumptions are as follows.

(1) The LSCP transportation network is composed of internal road systems and external road systems and has two types of links, permanent and temporary. In addition, two types of links are designated as critical or noncritical links.

(2) The links under retrofit consideration are those which are either permanent or critical.

(3) The retrofit activity process is the same for both permanent and temporary links.

(4) In the retrofit, the variable environmental and reconstruction costs for the temporary links are considered of less importance than the permanent links.

(5) The retrofit costs and the retrofit decision have a linear relationship which can be easily relaxed without changing the structure of the proposed model, as long as the data are available to support a more detailed analysis.

(6) The variable environmental costs and the retrofit decision have a linear relationship which can be easily relaxed without changing the structure of the proposed model, as long as the data are available to support a more detailed analysis.

(7) Origin-destination pairs (i.e., commodities) are determined in advance.

(8) Traffic flow can be controlled to achieve system equilibrium [1].

(9) The preretrofit link damage state is defined as the seismic damage scenario minus the retrofit decision u_a developed from [1].

(10) Reconstruction costs have a linear function with the postretrofit damage state which can be easily relaxed without changing the structure of the proposed model.

2.5.1. Upper-Level Programming. The investor on the upper level makes a decision as to whether there should be a retrofit for each link a in the transportation network and what rank the retrofit should be. The decision needs to fully consider the link types (i.e., permanent and temporary, critical and noncritical).

Objective Functions. One objective on the upper level is to minimize the retrofit costs, which include the environmental costs. In this paper, from a systems view, the retrofit costs are added directly to the objective function, which differs from [1]. The investor aims to minimize costs through their decision. Based on this assumption, the retrofit costs can be calculated using the sum of the variable and fixed costs for all links in the network. The retrofit costs for the temporary links are lower than the permanent links. In order to distinguish link types, 0-1 variables are introduced. m_a with 1 indicates a permanent link and is 0 otherwise; n_a with 1 indicates a critical link and is 0 otherwise. Therefore, the retrofit costs can be denoted as $\sum_{a\in A}(m_a \vee n_a)((c^t_{va} + m_a c^p_{va})u_a + (c^t_{fi} + m_a c^p_{fi}))$. Here, $\vee$ is defined as max, namely, $\max[m_a, n_a]$.

Based on the ABC described above and the assumptions, $\sum_{a\in A}(m_a \vee n_a)(ce^t_v + ce^p_v)u_a$ is the variable environment cost v and ce^f_f denotes the fixed environmental cost f. Through an analysis of the activity processes, the activity definitions, and the cost allocations, $ce^c_j = \sum_{v\in V} pe^v_{jv} \sum_{a\in A}(m_a \vee n_a)(ce^t_v + ce^p_v)u_a$ is the variable environmental costs of activity cost center j and $\sum_{f\in F} pe^f_{if} ce_f$ is the fixed environmental costs of output i. After determining the cost drivers for the activity cost centers and measuring the cost driver amounts, $ra_j = ce^c_j/am_j$ is the cost driver rate for activity cost center j. The variable environmental costs for output i are $\sum_{j\in J} ra_j am_{ij}$. After this, the environmental costs can then be presented as $\sum_{i\in I}(\sum_{j\in J}(\sum_{v\in V} pe^v_{jv} \sum_{a\in A}(m_a \vee n_a)(ce^t_v + ce^p_v)u_a/am_j)am_{ij} + \sum_{f\in F} pe^f_{if} ce^f_f)$. Thus, the objective can be described as

$$
\begin{aligned}
C(u) = {} & \sum_{a\in A}(m_a \vee n_a) \\
& \times \left(\left(c^t_{va} + m_a c^p_{va}\right)u_a + \left(c^t_{fi} + m_a c^p_{fi}\right)\right) \\
& + \rho \sum_{i\in I}\left(\sum_{j\in J}\frac{\sum_{v\in V} pe^v_{jv}\sum_{a\in A}(m_a \vee n_a)(ce^t_v + ce^p_v)u_a}{am_j}\right. \\
& \left. \times am_{ij} + \sum_{f\in F} pe^f_{if} ce^f_f\right).
\end{aligned} \tag{8}
$$

Here, ρ denotes the weight of the environmental costs and is determined by the investor.

The maximization of the retrofit benefit is another upper-level objective. The decision result of the lower-level is denoted $Q(x, \tilde{\tilde{\xi}})$ and quantified as savings in reconstruction and travel delay costs. u is the vector of u_a, $a \in A$, and $\tilde{\tilde{\xi}}$ is the vector of $\tilde{\tilde{\xi}}_a$, $a \in A$. This can be described as

$$Q\left(x, \tilde{\tilde{\xi}}\right). \tag{9}$$

Here, maximizing the retrofit benefit while minimizing reconstruction costs and travel time delay is denoted as $Q(u, \tilde{\tilde{\xi}})$, which will be described in detail in the objective for the lower level.

Logical Constraints. To describe the discrete decision variables for practical sense, the constraints in the following are presented:

$$u_a \in \{0, 1, 2, 3, 4, 5\}, \quad \forall a \in A. \tag{10}$$

The objective functions and constraints above make up the upper-level programming with lower-level programming as in the following:

$$\begin{aligned}
&\min\left(C(u), Q\left(x, \tilde{\tilde{\xi}}\right)\right) \\
&= \left(\sum_{a\in A}(m_a \vee n_a)\left(\left(c_{va}^t + m_a c_{va}^p\right)u_a + \left(c_{fi}^t + m_a c_{fi}^p\right)\right)\right. \\
&\quad + \rho\sum_{i\in I}\left(\sum_{j\in J}\frac{\sum_{v\in V} pe_{jv}^v \sum_{a\in A}(m_a \vee n_a)(ce_v^t + ce_v^p)u_a}{am_j} \times am_{ij} + \sum_{f\in F} pe_{if}^f ce_f^f\right), \\
&\quad \left.Q\left(x, \tilde{\tilde{\xi}}\right)\right) \\
&\text{s.t.} \begin{cases} u_a \in \{0, 1, 2, 3, 4, 5\}, & \forall a \in A \\ \text{lower-level programming.} \end{cases}
\end{aligned} \tag{11}$$

2.5.2. Lower-Level Programming. The administrator on the lower level decides on the commodity flow x_k. In transportation network literature, the flow between each origin-destination pair is often considered as one commodity. Different commodities represent travel between different origin-destination pairs. x_k is used to express the flow of k commodity. This optimal commodity flow decision seeks to achieve optimal retrofit benefits under a postretrofit state once an earthquake event has occurred and seismic damage sustained. First, it is necessary to introduce the postretrofit damage state before describing in detail the lower-level programming.

Postretrofit Damage State. A fuzzy random vector $\tilde{\tilde{\Xi}}$ is introduced to describe the damage to the link once an earthquake has occurred after the retrofit, which has been developed from [1]. Here, $\tilde{\tilde{\Xi}}$ is the vector for $\tilde{\tilde{\Xi}}_a$ $a \in A$. Assume that if a link is retrofitted at any rank, its damaged state (i.e., postretrofit damaged state in the earthquake) is denoted as a seismic damage scenario (i.e., preretrofit link damage state) minus the retrofit rank. Here, for demonstration, a negative postretrofit damaged state is not considered, so the negative state is treated as 0 indicating that the link will be intact. The relationship between the preretrofit link damage state $\tilde{\tilde{\xi}}_a$, the retrofit decision u_a, and the postretrofit damage state $\tilde{\tilde{\Xi}}_a(\tilde{\tilde{\xi}}_a, u)$ is described as in the following:

$$\tilde{\tilde{\Xi}}_a\left(\tilde{\tilde{\xi}}_a, u_a\right) = \left[\tilde{\tilde{\xi}}_a - u_a\right]_+, \quad \forall a \in A. \tag{12}$$

For any scenario, the postretrofit damaged state of link a can describe the current damaged state of link a in an earthquake after a retrofit. Based on the above, the discussion for the lower-level programming is as follows.

Objective Function. Retrofit benefits are the objective of the administrator. They are only quantified as savings in the minimization of reconstruction and travel delay costs [1]. To maximize benefits is to minimize costs. According to this assumption, the reconstruction costs can be presented as $\sum_{a\in A}(m_a \vee n_a)((cr_{va}^t + m_a cr_{va}^p)\tilde{\tilde{\Xi}}_a + (cr_{fi}^t + m_a cr_{fi}^p))$. This is calculated using the sum of the variable and fixed costs for all the links in the network when links are damaged in an earthquake and need to be reconstructed. Travel delay costs are the total travel time of all the links in the network. The travel time of each link is the product of link travel time and link flow. The link travel time depends on the link flow. Their relationship is usually described using a nondecreasing function such as the bureau of public roads (BPR) function [1]. The BPR function is in the form of $ti_a^0(1 + \alpha(fl_a/ca_a')^\beta)$. Where ti_a^0 and fl_a are free flow travel time and flow for link a, respectively, ca_a' is the "practical capacity" of link a and is set to be 90% of the design capacity. Thus, the travel delay costs of a can be denoted as $ti_a^0(1 + \alpha(fl_a/ca_a')^\beta)fl_a$. The objective function is presented as shown below:

$$\begin{aligned}
Q\left(x, \tilde{\tilde{\xi}}\right) = \sum_{a\in A}\left(\left(m_a \vee n_a\right)\left(\left(cr_{va}^t + m_a cr_{va}^p\right)\tilde{\tilde{\Xi}}_a + \left(cr_{fi}^t + m_a cr_{fi}^p\right)\right)\right. \\
\left. + \gamma ti_a^0\left(1 + \alpha\left(\frac{fl_a}{ca_a'}\right)^\beta\right)fl_a\right),
\end{aligned} \tag{13}$$

where γ is a weight coefficient converting the time to a monetary value, α, β are coefficients of the BPR function, and $\tilde{\tilde{\Xi}}_a$ is as $[\tilde{\tilde{\xi}}_a - u_a]_+$.

Node Capacity Constraint. Logistics in large scale postdisaster relief is very important [38]. Therefore, once an earthquake event occurs, a working transportation network for disaster relief and the LSCP are critically important, so the nodes in the network should be fully functioning. Therefore, the node capacity should be at capacity. The constraint is to keep transport in accordance with the flow and the capacity of node b as shown in the following:

$$Wx = ca_b, \quad \forall b \in B, \tag{14}$$

where W represents the node-commodity adjacency matrix. x is the commodity flow vector for $x_k, k \in K$. $ca_b \in R_+$ is the capacity of node b.

Flow Equation Constraint. The total flow on each link a is the sum of all flows of all commodity k that contains a and is obtained using the link commodity adjacency matrix and the commodity flow vector x as in the following:

$$fl_a = Mx, \quad \forall a \in A. \tag{15}$$

Damaged Link Flow Constraint. This constraint restricts the link flow when a link is damaged by the earthquake as in (16). This constraint is applied to the postretrofit damaged state and the "practical capacity" of link a, which is set at 90% of the design capacity:

$$fl_a \le \left(1 - \frac{\tilde{\tilde{\Xi}}_a}{5}\right) ca'_a, \quad \forall a \in A, \tag{16}$$

where fl_a is obtained in (15).

Logical Constraints. In order to describe the nonnegative variables in the model, the constraints in the following are presented:

$$x_k \ge 0, \quad \forall k = 1, \ldots, K. \tag{17}$$

The objective function and constraints above compose the lower-level programming as in the following:

$$Q\left(x, \tilde{\tilde{\xi}}\right) := \min \sum_{a \in A} \left((m_a \vee n_a) \left(\left(cr^t_{va} + m_a cr^p_{va} \right) \tilde{\tilde{\Xi}}_a + \left(cr^t_{fi} + m_a cr^p_{fi} \right) \right) + \gamma ti^0_a \left(1 + \alpha \left(\frac{fl_a}{ca'_a} \right)^{\beta} \right) fl_a \right)$$

$$\text{s.t.} \begin{cases} Wx = ca_b, & \forall b \in B, \\ fl_a = Mx, & \forall a \in A, \\ fl_a \le \left(1 - \dfrac{\tilde{\tilde{\Xi}}_a}{5}\right) ca'_a, & \forall a \in A, \\ x_k \ge 0, & \forall k = 1, \ldots, K. \end{cases} \tag{18}$$

2.5.3. Fuzzy Random Multiobjective Bilevel Programming Model. The complete multiobjective bilevel programming model under a fuzzy random environment is formulated based on the previous discussion as in the following model:

$$\min \left(C(u), Q\left(x, \tilde{\tilde{\xi}}\right) \right) = \left(\sum_{a \in A} (m_a \vee n_a) \left(\left(c^t_{va} + m_a c^p_{va} \right) u_a + \left(c^t_{fi} + m_a c^p_{fi} \right) \right) + \rho \sum_{i \in I} \left(\sum_{j \in J} \frac{\sum_{v \in V} pe^v_{jv} \sum_{a \in A} (m_a \vee n_a) \left(ce^t_v + ce^p_v \right) u_a}{am_j} \times am_{ij} + \sum_{f \in F} pe^f_{if} ce^f_f \right), Q\left(x, \tilde{\tilde{\xi}}\right) \right)$$

$$\text{s.t.} \begin{cases} u_a \in \{0, 1, 2, 3, 4, 5\}, & \forall a \in A, \\ Q\left(x, \tilde{\tilde{\xi}}\right) := \min \sum_{a \in A} \left((m_a \vee n_a) \left(\left(cr^t_{va} + m_a cr^p_{va} \right) \tilde{\tilde{\Xi}}_a + \left(cr^t_{fi} + m_a cr^p_{fi} \right) \right) + \gamma ti^0_a \left(1 + \alpha \left(\dfrac{fl_a}{ca'_a} \right)^{\beta} \right) fl_a \right) \\ \quad \text{s.t.} \begin{cases} Wx = ca_b, & \forall b \in B, \\ fl_a = Mx, & \forall a \in A, \\ fl_a \le \left(1 - \dfrac{\tilde{\tilde{\Xi}}_a}{5}\right) ca'_a, & \forall a \in A, \\ x_k \ge 0, & \forall k = 1, \ldots, K. \end{cases} \end{cases} \tag{19}$$

2.6. Transformation Approach for Fuzzy Random Variables. In this subsection, some basic knowledge for the fuzzy random variables is stated.

Definition 8 (see [33]). Given a domain U, if $\widetilde{A}$ is a fuzzy set on U, then for any $x \in U$, see the following:

$$\mu_{\widetilde{A}} : U \longrightarrow [0, 1], \qquad x \longrightarrow \mu_{\widetilde{A}}(x), \tag{20}$$

where $\mu_{\widetilde{A}}$ is called a membership function of x with respect to $\widetilde{A}$ and $\mu_{\widetilde{A}}$ denoted the grade to each point in U with a real number in the interval $[0, 1]$ that represents the grade of membership of x in $\widetilde{A}$. $\widetilde{A}$ is called a fuzzy set and described as follows:

$$\widetilde{A} = \left\{ (x, \mu_{\widetilde{A}}(x)) \mid x \in U \right\}. \tag{21}$$

Definition 9 (see [33]). Let there be a domain U. Let $\widetilde{A}$ be a fuzzy set which is defined on U. If α is possibility level and $0 \le \alpha \le 1$, $\widetilde{A}_\alpha$ consists of all elements whose degrees of membership in $\widetilde{A}$ are greater than or equal to α as in the following:

$$\widetilde{A}_\alpha = \{x \in U \mid \mu_{\widetilde{A}}(x) \ge \alpha\}; \tag{22}$$

then $\widetilde{A}_\alpha$ is called the α-level set of fuzzy set $\widetilde{A}$.

Definition 10 (see [39]). Let Θ be a nonempty set, and let $P(\Theta)$ be the power set of Θ. For each $A \subseteq P(\Theta)$, there is nonnegative number $\mathrm{Pos}\{A\}$, called its possibility, such that

(1) $\mathrm{Pos}(\emptyset) = 0$ and $\mathrm{Pos}(\Theta) = 1$,

(2) $\mathrm{Pos}(\bigcup_k A_k) = \sup_k \mathrm{Pos}(A_k)$ for any arbitrary collection $\{A_k\}$ in $P(\Theta)$.

The triple $(\Theta, P(\Theta), \mathrm{Pos})$ is called a possibility space. The function Pos is referred to as a possibility measure.

Definition 11 (see [40]). A fuzzy variable is defined as a function from the possibility space $(\Theta, P(\Theta), \mathrm{Pos})$ to the real number $\mathbb{R}$.

Definition 12. Let ε be a discrete random variable defined on a probability space $(\Omega, \mathscr{A}, \mathrm{Pr})$ with the discrete distribution $P_\varepsilon(x) = P\{x = x_n\}$, $n = 1, 2, \ldots$, and let θ be any given probability level and $0 \le \theta \le \max P_\varepsilon(x)$. ε_θ consists of all elements whose value of $P_\varepsilon(x)$ for ε is greater than or equal to θ as the following:

$$\varepsilon_\theta = \{x \in \mathbb{R} \mid P_\varepsilon(x) \ge \theta\}; \tag{23}$$

then ε_θ is called the θ-level set of random variable ε.

As stated in Section 2.4, the definition proposed by [14] is used in this paper. Although there are many properties and transformation approaches for the fuzzy random variable, to conveniently convert programming with fuzzy random coefficients into crisp values, Xu and Liu [12] proposed a theorem which could transform fuzzy random variables into fuzzy variables similar to trapezoidal fuzzy numbers. In this paper, this theorem and proof are adjusted to a discrete random distribution with fluctuating lower, central, and upper parameters for the fuzzy properties and extended bounds of possibility for the fuzzy variable.

Theorem 13. *Let*

$$\widetilde{\widetilde{\xi}} = \begin{cases} (a_{1L}, a_{1C}, a_{1R}) & \text{with probability } p_1 \\ \vdots & \vdots \\ (a_{iL}, a_{iC}, a_{iR}) & \text{with probability } p_i \\ \vdots & \vdots \\ (a_{IL}, a_{IC}, a_{IR}) & \text{with probability } p_I \end{cases} \tag{24}$$

be a fuzzy random variable, which has discrete random distribution with fluctuating lower, central, and upper parameter for fuzzy property. The discrete distribution is $P_\psi(x)$. δ is any given probability level of random variable; η is any given possibility level of fuzzy variable; then the fuzzy random variable can be transformed into a (δ, η)-level trapezoidal fuzzy variable.

Proof. Let

$$\widetilde{\widetilde{\xi}} = \begin{cases} (a_{1L}, a_{1C}, a_{1R}) & \text{with probability } p_1 \\ \vdots & \vdots \\ (a_{iL}, a_{iC}, a_{iR}) & \text{with probability } p_i \\ \vdots & \vdots \\ (a_{IL}, a_{IC}, a_{IR}) & \text{with probability } p_I \end{cases} \tag{25}$$

be a fuzzy random variable, which has discrete random distribution with fluctuating lower, central, and upper parameter for fuzzy property. The discrete distribution is $P_\psi(x)$. According to Definition 8, the δ-level sets (or δ-cuts) of the discrete random variable ψ can be denoted as follows:

$$\psi_\delta = \left[\psi_\delta^L, \psi_\delta^R\right] = \left\{x \in \mathbb{R} \mid P_\psi(x) \ge \delta\right\}. \tag{26}$$

Here, $\psi_\delta^L = \min\{x \in \mathbb{R} \mid P_\psi(x) \ge \delta\}$ and $\psi_\delta^R = \max\{x \in \mathbb{R} \mid P_\psi(x) \ge \delta\}$. The parameter $\delta \in [0, \max P_\psi(x)]$ here reflects the optimism degree for decision-maker. These intervals indicate where the range of the data lies at the probability level δ. Note that ψ_δ is crisp set.

Let $X = \{x_\omega = \psi(\omega) \in \mathbb{R} \mid P_\psi(\psi(\omega)) \ge \delta, \omega \in \Omega\}$; it is not hard to prove that $X = [\psi_\delta^L, \psi_\delta^R] = \psi_\delta$; namely, $\min X = \psi_\delta^L$ and $\max X = \psi_\delta^R$. In other words, ψ_δ^L is the minimum value that ψ achieves with probability δ; ψ_δ^R is the maximum value that ψ achieves with probability δ. Therefore, the δ-level fuzzy random variable $\widetilde{\widetilde{\xi}}_\delta$ can be defined as

$$\widetilde{\widetilde{\xi}}_\delta = \begin{cases} \psi_\delta^L = \left(a_{(\delta,L)}^L, a_{(\delta,C)}^L, a_{(\delta,R)}^L\right) & \text{with probability } p_\delta^L \\ \vdots & \vdots \\ \psi_\delta^R = \left(a_{(\delta,L)}^R, a_{(\delta,C)}^R, a_{(\delta,R)}^R\right) & \text{with probability } p_\delta^R. \end{cases} \tag{27}$$

It can also be denoted as follows:

$$\begin{aligned} \widetilde{\widetilde{\xi}}_\delta = \Big\{&\widetilde{\xi}_\delta(\omega) = \left(a_{(\delta,L)}(\omega), a_{(\delta,C)}(\omega), a_{(\delta,R)}(\omega)\right) \\ &\text{with probability } p(\omega) \mid x_\omega \in X, \omega \in \Omega\Big\}, \end{aligned} \tag{28}$$

where $\widetilde{\xi}_\delta(\omega)$ is a fuzzy variable. The variable $\widetilde{\widetilde{\xi}}_\delta$ can be expressed in another form as $\widetilde{\widetilde{\xi}}_\delta = \bigcup_{\omega\in\Omega} \widetilde{\xi}_\delta(\omega) = \widetilde{\xi}_\delta(\Omega)$; here $\widetilde{\xi}_\delta(\omega)(\omega \in \Omega)$ are fuzzy variables. So the fuzzy random variable $\widetilde{\widetilde{\xi}}$ is transformed into a group of fuzzy variables $\widetilde{\xi}_\delta(\omega)(\omega \in \Omega)$, which is denoted as $\widetilde{\xi}_\delta(\Omega)$. On the basis of the concept on fuzzy variable η-level sets (or η-cuts). The parameter $0 \le \eta \le 1$ let

$$\begin{aligned} \widetilde{\xi}_{(\delta,\eta)}(\omega) &= \left[\xi_{(\delta,\eta)}^L(\omega), \xi_{(\delta,\eta)}^R(\omega)\right] \\ &= \left\{x \in U \mid \mu_{\widetilde{\xi}_\delta(\omega)}(x) \ge \eta\right\}; \end{aligned} \tag{29}$$

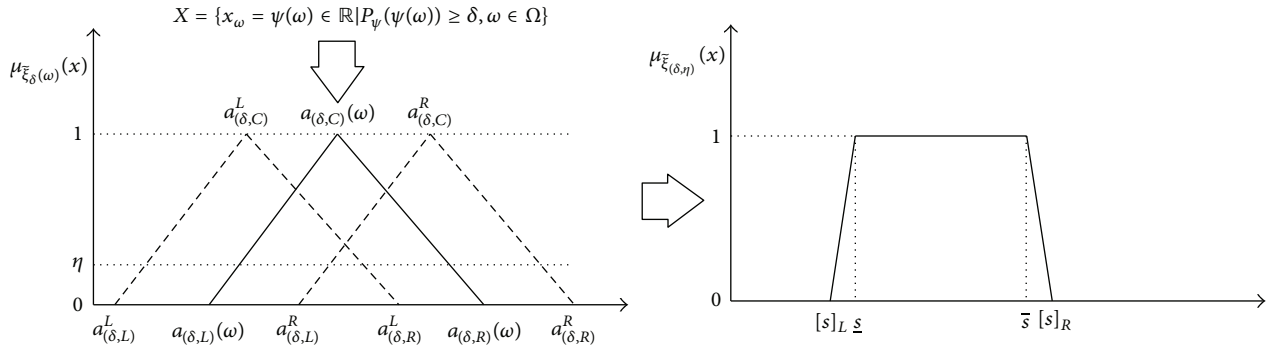

Figure 4: The transformation process from fuzzy random variable $\tilde{\tilde{\xi}}$ to (δ, η)-level trapezoidal fuzzy variable $\tilde{\tilde{\xi}}_{(\delta,\eta)}$.

then the η-level sets (or η cuts) of $\tilde{\xi}_\delta(\Omega)$ are defined as follows:

$$\begin{aligned}&\tilde{\xi}_{(\delta,\eta)}(\Omega)\\&= \left\{\tilde{\xi}_{(\delta,\eta)}(\omega) = \left[\xi^L_{(\delta,\eta)}(\omega), \xi^R_{(\delta,\eta)}(\omega)\right] \mid \omega \in \Omega\right\};\end{aligned} \tag{30}$$

here, $\xi^L_{(\delta,\eta)}(\omega) = \inf \mu^{-1}_{\tilde{\xi}_\delta(\omega)}(\eta)$, $\xi^R_{(\delta,\eta)}(\omega) = \sup \mu^{-1}_{\tilde{\xi}_\delta(\omega)}(\eta)$, $\omega \in \Omega$. Inspired by the fuzzy expected value of fuzzy random variable proposed by [10], it can be got as follows:

$$\begin{aligned}a_{(\delta,L)} &= \sum_\omega p(\omega)\, a_{(\delta,L)}(\omega),\\ a_{(\delta,R)} &= \sum_\omega p(\omega)\, a_{(\delta,R)}(\omega),\\ \xi^L_{(\delta,\eta)} &= \sum_\omega p(\omega)\, \xi^L_{(\delta,\eta)}(\omega),\\ \xi^R_{(\delta,\eta)} &= \sum_\omega p(\omega)\, \xi^R_{(\delta,\eta)}(\omega).\end{aligned} \tag{31}$$

Consequently, $\tilde{\tilde{\xi}}$ can be transformed into $\tilde{\xi}_{(\delta,\eta)}$ by the δ-cuts and η-cuts. See Figure 4.

Where $0 \leq \eta \leq 1$ and $\delta \in [0, \max P_\psi(x)]$, let $a_{(\delta,L)} = [s]_L$, $a_{(\delta,R)} = [s]_R$, $\xi^L_{(\delta,\eta)} = \underline{s}$, and $\xi^R_{(\delta,\eta)} = \overline{s}$; then the fuzzy random variable $\tilde{\tilde{\xi}}$ can be transformed into the (δ, η)-level trapezoidal fuzzy variable $\tilde{\xi}_{(\delta,\eta)}$ by the following equation:

$$\tilde{\tilde{\xi}} \longrightarrow \tilde{\xi}_{(\delta,\eta)} = \left([s]_L, \underline{s}, \overline{s}, [s]_R\right). \tag{32}$$

The parameters δ and η both reflect optimism degree of the decision-maker. Thus, the fuzzy random variable $\tilde{\tilde{\xi}}$ is transformed into a fuzzy variable which is a trapezoidal fuzzy number with the membership function $\mu_{\tilde{\xi}_{(\delta,\eta)}(x)}$. The value of $\mu_{\tilde{\xi}_{(\delta,\eta)}(x)}$ at $x \in [[s]_L, [s]_R]$ is considered subjectively to be 1 as below:

$$\mu_{\tilde{\xi}_{(\delta,\eta)(x)}} = \begin{cases}1 & \text{if } \underline{s} \leq x < \overline{s},\\ \dfrac{x - [s]_L}{\underline{s} - [m]_L} & \text{if } [s]_L \leq x < \underline{s},\\ \dfrac{[s]_R - x}{[s]_R - \overline{s}} & \text{if } \overline{s} \leq x < [s]_R,\\ 0 & \text{if } x < [s]_L, x > [s]_R.\end{cases} \tag{33}$$

Theorem 13 is proved. □

Through Theorem 13, the fuzzy random seismic damage scenario, namely, $\tilde{\tilde{\xi}}$, can be transformed into (δ, η)-level trapezoidal fuzzy variables $\tilde{\xi}_{(\delta,\eta)}$ and model (19) can be transformed into the following fuzzy multiobjective bilevel programming model:

$$\begin{aligned}&\min\left(C(u), Q\left(x, \tilde{\xi}_{(\delta,\eta)}\right)\right)\\&= \left(\sum_{a\in A}(m_a \vee n_a)\left(\left(c^t_{va} + m_a c^p_{va}\right)u_a + \left(c^t_{fi} + m_a c^p_{fi}\right)\right)\right.\\&\quad + \rho\sum_{i\in I}\left(\sum_{j\in J}\frac{\sum_{v\in V} pe^v_{jv}\sum_{a\in A}(m_a \vee n_a)\left(ce^t_v + ce^p_v\right)u_a}{am_j}\right.\\&\qquad \left.\left.\times am_{ij} + \sum_{f\in F} pe^f_{if} ce^f_f\right), Q\left(x, \tilde{\xi}_{(\delta,\eta)}\right)\right)\end{aligned}$$

$$\text{s.t.}\begin{cases}u_a \in \{0,1,2,3,4,5\}, \quad \forall a \in A,\\ Q\left(x, \tilde{\xi}_{(\delta,\eta)}\right)\\ \quad := \min\sum_{a\in A}\left((m_a \vee n_a)\left(\left(cr^t_{va} + m_a cr^p_{va}\right)\right.\right.\\ \qquad\qquad \times\left[\left(\tilde{\xi}_{(\eta,\delta)}\right)_a - u_a\right]_+\\ \qquad\qquad \left.\left.+\left(cr^t_{fi} + m_a cr^p_{fi}\right)\right)\right.\\ \qquad\qquad \left.+\gamma ti^0_a\left(1 + \alpha\left(\frac{fl_a}{ca'_a}\right)^\beta\right)fl_a\right)\\ \text{s.t.}\begin{cases}Wx = ca_b,\\ \quad \forall b \in B,\\ fl_a = Mx,\\ \quad \forall a \in A,\\ fl_a \leq \left(1 - \dfrac{\left[\left(\tilde{\xi}_{(\eta,\delta)}\right)_a - u_a\right]_+}{5}\right)ca'_a,\\ \qquad\qquad \forall a \in A,\\ x_k \geq 0,\\ \forall k = 1, \ldots, K.\end{cases}\end{cases} \tag{34}$$

2.7. Approximation Decomposition of Fuzzy Variables. In model (34), $\tilde{\tilde{\xi}}$ are coefficients, which when transformed to $\tilde{\xi}_{(\delta,\eta)}$ are fuzzy variables and so can be regarded as fuzzy numbers. Thus, an approximation decomposition method for fuzzy multiobjective linear bilevel programming model is introduced. This method is as in Zhang et al. [19] solution for fuzzy multiobjective bilevel programming, but with some further development done on the fuzzy multiobjective multifollower partial cooperative bilevel programming as outlined in [41].

Definition 14 (see [19]). A fuzzy number $\tilde{a}$ is defined as a fuzzy set on $\mathbb{R}$, whose membership function $\mu_{\tilde{a}}$ satisfies the following conditions.

(1) $\mu_{\tilde{a}}$ is a mapping from $\mathbb{R}$ to the closed interval $[0,1]$.

(2) It is normal; that is, there exists $x \in \mathbb{R}$ such that $\mu_{\tilde{a}}(x) = 1$.

(3) For any $\lambda \in (0,1]$, $a_\lambda = \{x; \mu_{\tilde{a}}(x) \geq \lambda\}$ is a closed interval, denoted by $[a_\lambda^L, a_\lambda^R]$.

Let $\mathcal{F}(\mathbb{R})$ be the set of all fuzzy numbers. By decomposition theorem of fuzzy sets [19], we have

$$\tilde{a} = \bigcup_{\lambda\in[0,1]} \lambda \left[a_\lambda^L, a_\lambda^R\right], \tag{35}$$

for every $\tilde{a} \in \mathcal{F}(\mathbb{R})$.

From Theorems 17 and 18 in research of Zhang et al. [19], the optimal solution for the model can be determined by solving the equivalent crisp multiobjective bilevel programming model as shown below:

$$\begin{aligned}
&\min\left(C(u), Q\left(x, \xi_\lambda^{L(R)}\right)\right) \\
&= \Bigg(\sum_{a\in A}(m_a \vee n_a)\left(\left(c_{va}^t + m_a c_{va}^p\right)u_a + \left(c_{fi}^t + m_a c_{fi}^p\right)\right) \\
&\quad + \rho\sum_{i\in I}\left(\sum_{j\in J}\frac{\sum_{v\in V} pe_{jv}^v \sum_{a\in A}(m_a \vee n_a)\left(ce_v^t + ce_v^p\right)u_a}{am_j} \times am_{ij} + \sum_{f\in F} pe_{if}^f ce_f^f\right), \\
&\quad \left(Q\left(x, \xi_\lambda^L\right), Q\left(x, \xi_\lambda^R\right)\right)\Bigg)
\end{aligned}$$

$$\text{s.t.}\begin{cases}
u_a \in \{0,1,2,3,4,5\}, \quad \forall a \in A, \\
Q\left(x, \xi_\lambda^{L(R)}\right) \\
\quad = \left(Q\left(x, \xi_\lambda^L\right), Q\left(x, \xi_\lambda^R\right)\right) \\
\quad := \min\Bigg(\displaystyle\sum_{a\in A}\Bigg((m_a \vee n_a)\left(\left(cr_{va}^t + m_a cr_{va}^p\right) \times \left[\left(\xi_a\right)_\lambda^L - u_a\right]_+ + \left(cr_{fi}^t + m_a cr_{fi}^p\right)\right) \\
\qquad + \gamma ti_a^0\left(1 + \alpha\left(\dfrac{fl_a}{ca_a'}\right)^\beta\right) fl_a\Bigg), \\
\qquad \displaystyle\sum_{a\in A}\Bigg((m_a \vee n_a)\left(\left(cr_{va}^t + m_a cr_{va}^p\right) \times \left[\left(\xi_a\right)_\lambda^R - u_a\right]_+ + \left(cr_{fi}^t + m_a cr_{fi}^p\right)\right) \\
\qquad + \gamma ti_a^0\left(1 + \alpha\left(\dfrac{fl_a}{ca_a'}\right)^\beta\right) fl_a\Bigg)\Bigg)
\end{cases}$$

$$\text{s.t.}\begin{cases}
Wx = ca_b, \\
\quad \forall b \in B, \\
fl_a = Mx, \\
\quad \forall a \in A, \\
fl_a \leq \left(1 - \dfrac{\left[\left(\xi_a\right)_\lambda^L - u_a\right]_+}{5}\right) ca_a', \\
\qquad \forall a \in A, \\
fl_a \leq \left(1 - \dfrac{\left[\left(\xi_a\right)_\lambda^R - u_a\right]_+}{5}\right) ca_a', \\
\qquad \forall a \in A, \\
x_k \geq 0, \\
\forall k = 1, \ldots, K.
\end{cases} \tag{36}$$

After transforming the fuzzy random seismic damage scenario $\tilde{\tilde{\xi}}$ into (δ,η)-level trapezoidal fuzzy variable $\tilde{\xi}_{(\delta,\eta)}$, an approximation progress of (δ,η)-level trapezoidal fuzzy variable $\tilde{\xi}_{(\delta,\eta)}$ is conducted until termination. During the approximation progress iterations, model (36) is solved within a series of λ valued by a decomposition of the interval $[0,1]$ into equal subintervals.

3. An Approximation Decomposition-Based Multiobjective AGLNPSO

Bilevel programming problem is NP-hard, which loosely means that it cannot in general be solved with a polynomial time algorithm [42] and it is difficult to find numerical solutions [43]. Many methods have been proposed to solve these problems, such as the branch-and-bound methods [44, 45], the descent method [46], and the penalty function method [47]. In addition, heuristic algorithms [48] and evolutionary computation [49] have also been proposed to obtain a numerical optimal solution or numerical efficient

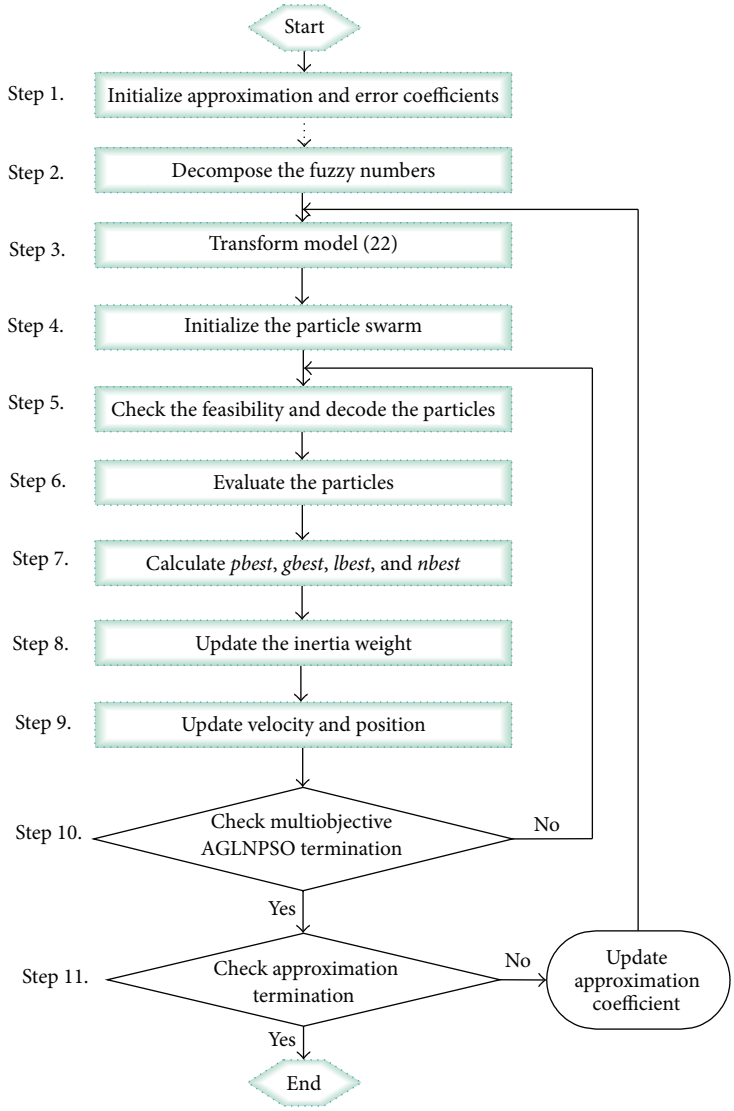

Figure 5: Overall procedure of the proposed method.

solution. PSO has been adopted for dealing with multiobjective optimization problems and has been found to be very successful, in addition to heuristics [50]. Therefore, with these considerations, the PSO is the approach adopted in this study. An approximation decomposition-based multiobjective AGLNPSO made up of approximation decomposition [19], PAES [20], AGLNPSO [21], and MOPSO [24] is proposed to solve the problem. Of course, this proposed algorithm may not be the best; however, it can assist in obtaining an effective solution, which is demonstrated in the analysis of the case problem. In the future, in order to get even better solutions more effectively, alternative approaches and algorithms (e.g., other exact approaches, (meta)heuristics, evolutionary algorithms, etc.) will be explored for comparison.

3.1. Overall Procedure for the Proposed Algorithm. The procedure for the proposed algorithm is presented as follows; see Figure 5.

Step 1. Initialize approximation coefficient $l = 1$, which is used to generate cut sets for the fuzzy numbers in model (36) and the error coefficient ϵ.

Step 2. Decompose interval $[0, 1]$ into 2^{l-1} equal subintervals with $(2^{l-1} + 1)$ nodes λ_i $(i = 0, \ldots, 2^{l-1})$, which are arranged in the order $0 = \lambda_0 < \lambda_1 < \cdots < \lambda_{2^{l-1}} = 1$.

Step 3. Transform model (34) into a series of models for model (36) with l.

Step 4. Initialize the parameters: swarm_size, iteration_max, the range of velocity and position for the variables, the personal best position acceleration constant, the global best position acceleration constant, the local best position acceleration constant, the near neighbor best acceleration constant, and the inertia weight_max. Then, initialize the velocities and positions of the particle-represented solutions.

Step 5. Check the feasibility and decode the particles.

Step 6. Solve the lower-level programming with the feasible solutions of the upper level to determine the optimal objective value. Calculate the two objectives on the upper level to evaluate every particle.

Step 7. Calculate the *pbest*, *gbest*, *lbest*, and *nbest* using the multiobjective method. Restore the Pareto optimal solutions (i.e., the (global) elite individuals), lower-level programming solutions, and objective values of upper level and lower level.

Step 8. Update the inertia weight for each iteration.

Step 9. Update the velocity and position of each particle.

Step 10. Check the multiobjective AGLNPSO termination. If the stopping criterion (i.e., iteration_max) is met, then end the multiobjective AGLNPSO procedure to obtain the optimal solution $(u, x)_{2^l}$ and go to Step 10; otherwise, go to Step 5.

Step 11. Check the approximation termination. If a stabilization of the Pareto optimal solution is achieved, then the Pareto optimal solution for the complete multiobjective bilevel programming model under fuzzy random environments is obtained, and it terminates. Otherwise, $l = l + 1$; go back to Step 3.

Here, the set convergence is proposed in this paper to describe the stabilization of the Pareto optimal solution, which is defined as ϖ and expressed as follows:

$$\begin{aligned} &m \in M, \qquad n \in N, \qquad \chi = 0. \\ &\text{If traversal } M \text{ for any } m \text{ there is} \\ &n = m, \quad n \in N; \text{ then } \chi = \chi + 1, \\ &\varpi = \frac{\chi}{|M|}. \end{aligned} \tag{37}$$

That is to say, if $\varpi \geq \epsilon$, the Pareto optimal solution set is stable and the approximation termination is achieved.

The details for the multiobjective AGLNPSO are described as follows and the notations used are shown.

s: Particle index, $s = 1, \ldots, S$

τ: Iteration index, $\tau = 1, \ldots, T$

h: Dimension index, $h = 1, \ldots, H$

u_r: Uniform random number in the interval $[0, 1]$

$w(\tau)$: Inertia weight in the τth iteration

$w^{\max}$: Maximum inertia weight value

$w^{\min}$: Minimum inertia weight value

$\omega_{sh}(\tau)$: Velocity of the sth particle at the hth dimension in the τth iteration

$\theta_{sh}(\tau)$: Position of the sth particle at the hth dimension in the τth iteration

$\theta^0_{sh}(\tau)$: Position for temporary and noncritical link of the sth particle at the hth dimension in the τth iteration

ψ_{sh}: Personal best position of the sth particle at the hth dimension

ψ_{gh}: Global best position of the sth particle at the hth dimension

ψ^L_{sh}: Local best position of the sth particle at the hth dimension

ψ^N_{sh}: Near neighbor best position of the sth particle at the hth dimension

c_p: Personal best position acceleration constant

c_g: Global best position acceleration constant

c_l: Local best position acceleration constant

c_n: Near neighbor best position acceleration constant

$\omega^{\max}$: Maximum velocity value

$\omega^{\min}$: Minimum velocity value

$\theta^{\max}$: Maximum position value

$\theta^{\min}$: Minimum position value

Θ_s: Vector position of the sth particle $[\theta_{s1}, \theta_{s2}, \ldots, \theta_{sH}]$

Ω_s: Vector velocity of the sth particle $[\omega_{s1}, \omega_{s2}, \ldots, \omega_{sH}]$

R_s: The sth set of solutions

c: The current solution randomly selected one from the nondominated solutions

c^N: New generated solution.

3.2. Solution Representation. In this paper, the particle-represented solution is A dimensions of retrofit rank u_a within $[0, 1, 2, 3, 4, 5]$ (i.e., $a \in A$) for all links in the LSCP transportation network.

3.3. Particle Swarm Initialization. Initialize S particles as a swarm; generate the sth particle with random position Θ_s in the range $\{0, 1, 2, 3, 4, 5\}$. Randomly generate velocity for each particle in the range $\{-5, -4, -3, -2, -1, 0, 1, 2, 3, 4, 5\}$. Set the iteration $\tau = 1$. Set swarm_size S, iteration_max T, personal best position acceleration constant c_p, global best position acceleration constant c_g, local best position acceleration constant c_l, near neighbor best position acceleration constant c_n, inertia weight_max $w^{\max}$, and inertia weight_min $w^{\min}$.

3.4. Feasibility Checking and Decoding Method. Since the links to be considered for retrofit are either permanent or critical, check and adjust the position of the temporary and noncritical links to 0. Then, the particle-represented solution can be directly decoded into a solution for the problem as shown in Figure 6.

3.5. Particle Evaluation. For $s = 1, \ldots, S$, set $\Theta_s(\tau)$ into the solution R_s that is u in the upper-level programming and put u into the lower-level programming to determine the optimal solution x and the optimal objective $Q(x)$. Calculate another objective for the upper-level programming $C(u)$.

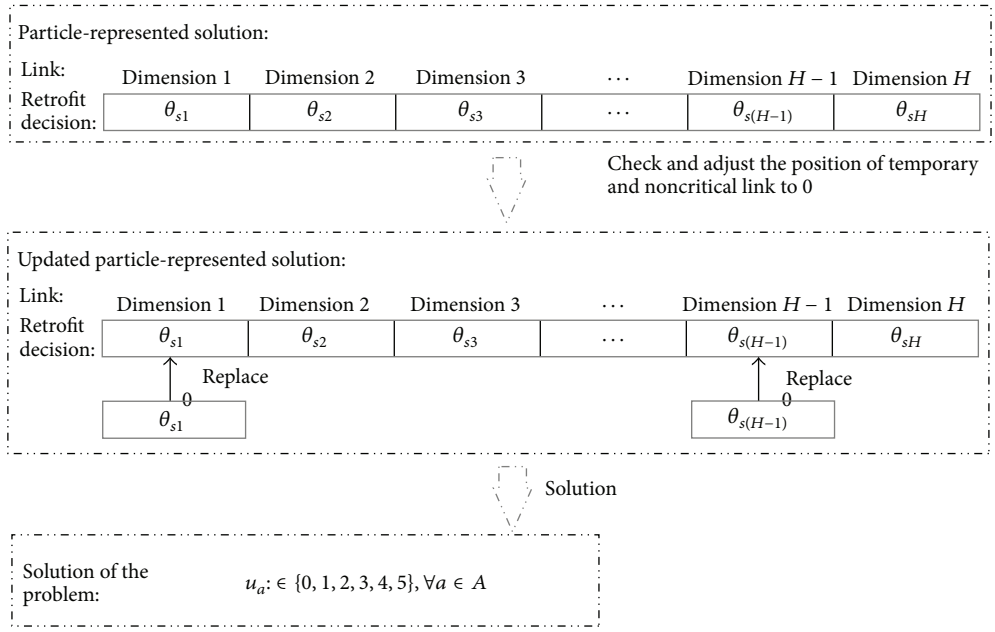

Figure 6: Transformation from the particle-represented to the problem solution.

3.6. Multiobjective Method. The multiobjective method is made up of the PAES procedure and the test procedure, and selection is introduced to calculate *pbest*, *gbest*, *lbest*, and *nbest*. This method uses a truncated archive to store the elite individuals (i.e., nondominated solutions), which is used to separate the objective function space into hypercubes, each of which has a score based on its density. Selection of the best is then based on a roulette wheel selection to select the best hypercube first and then uniformly choose a solution. Note that the initialized solution is regarded as the *pbest* and the nondominated solution of each particle at the 1th iteration. When the iteration updates, the updated solution and the nondominated solutions are used to calculate the *pbest* by the method. After the *pbest* has been confirmed at each iteration, the *pbest* nondominated solutions for all particles are considered with the *gbest* nondominated solutions (i.e., there is no *gbest* nondominated solution at initialization) to calculate the *gbest* by the method. Similar to the *gbest*, among all the *pbest* nondominated solutions from K neighbors of the sth particle and *lbest* nondominated solutions, set the *lbest* is also set using this method. For each particle on each dimension, set $\psi_{sh}^N = \psi_{oh}^N$ that maximizes $(Z(\Theta_s) - Z(\Psi_o))/(\theta_{sh} - \psi_{oh})$ to get *nbest*, $o \in S \setminus s$. Here, the maximization process uses the multiobjective method for the calculation of the *gbest* and *lbest* above. The details for the PAES procedure, test procedure, and selection procedure are outlined similarly for the *pbest*, *gbest*, *lbest*, and *nbest* next and in Procedures 1 and 2, where c is the current solution randomly selected from the nondominated solutions. Note that c is randomly selected from the *pbest* nondominated solutions to calculate the *gbest* at the 1th iteration.

Selection

Step 1. Divide 10 by the number of particles in each hypercube to get its score.

Step 2. Apply roulette wheel selection to hypercube according to their scores and select a hypercube.

Step 3. Uniformly choose a member of that hypercube.

Therefore, the *gbest* nondominated solutions at the Tth are the final solutions of the problem.

3.7. Inertia Weight Updating. Update the inertia weight for iteration τ using the following equations:

$$\overline{\omega} = \frac{\sum_{s=1}^{S}\sum_{h=1}^{H}|\omega_{sh}|}{S \cdot H},$$

$$\omega^* = \begin{cases} \left(1 - \dfrac{1.8\tau}{T}\right)\omega^{\max}, & 0 \le \tau \le \dfrac{T}{2}, \\ \left(0.2 - \dfrac{0.2\tau}{T}\right)\omega^{\max}, & \dfrac{T}{2} \le \tau \le T, \end{cases}$$

$$\Delta w = \frac{(\omega^* - \overline{\omega})}{\omega^{\max}}\left(w^{\max} - w^{\min}\right), \tag{38}$$

$$w = w + \Delta w,$$

$$w = w^{\max} \quad \text{if } w > w^{\max},$$

$$w = w^{\min} \quad \text{if } w > w^{\min}.$$

generate a new solution c^N
  if (c dominates c^N)
    discard c^N
  else if (c^N dominates c)
    replace c with c^N and add c^N to the archive
  else if (c^N is dominated by any member of the archive)
    discard c^N
  else if (c^N dominates any member of the archive)
    replace it with c^N and add c^N to the archive and all other members
    dominated by c^N are discarded
  else
    apply test procedure to c, c^N and the archive to determine which
    becomes the new current solution and whether to add c^N to the archive
until a termination criterion has been reached, return to the beginning

Procedure 1: PAES.

if the archive is not full
  add c^N to the archive
  if (c^N is in a less crowded region of the archive than c)
    accept c^N as the new current solution
  else
    maintain c as the current solution
else if (c^N is in a less crowded region of the archive than any other member on the archive)
    add c^N to the archive, and remove a member of the archive from the most crowded region
  if (c^N is in a less crowded region of the archive than c)
    accept c^N as the new current solution
  else
    maintain c as the current solution
  else
    don't add c^N to the archive

Procedure 2: Test.

3.8. Velocity and Position Updating. Update the velocity and the position of each sth particle using the following equations:

$$\omega_{sh}(\tau+1) = w(\tau)\,\omega_{sh}(\tau) + c_p u_r\left(\psi_{sh} - \theta_{sh}(\tau)\right) + c_g u_r\left(\psi_{gh} - \theta_{sh}(\tau)\right) + c_l u_r\left(\psi_{sh}^L - \theta_{sh}(\tau)\right),$$

$$\theta_{sh}(\tau+1) = \theta_{sh}(\tau) + \omega_{sh}(\tau+1).$$

If $\theta_{sh}(\tau+1) > \theta^{\max}$,

then set $\theta_{sh}(\tau+1) = \theta^{\max}$ $\omega_{sh}(\tau+1) = 0$.

If $\theta_{sh}(\tau+1) < \theta^{\min}$,

then set $\theta_{sh}(\tau+1) = \theta^{\min}$ $\omega_{sh}(\tau+1) = 0$. (39)

4. A Case Study

In this section, computational experiments were carried out on a large-scale water conservancy and hydropower construction project. Through the illustrative example on the data set adopted from the case problem, the proposed approach is validated and the efficiency of the algorithm is tested.

4.1. Presentation of Case Problem. The XLD hydropower station LSCP is in XLD gorge section of the JS river located in LB county of SC province and YS county of YN province, an area which is earthquake prone. The Yingjiang, Wenchuan, and Panzhihua-Huili earthquakes all seriously affected the local area. Therefore, it is critical that the LSCP risks be controlled, especially in the transportation network. Therefore, the proposed approach is suitable for use on the transportation network at the XLD hydropower LSCP.

The transportation network in the project has an internal road network and an external road network. The internal road network is composed of more than 20 major trunk roads and these roads form a solid network located on the left and right banks. There is a temporary traffic bridge upstream and a permanent traffic bridge downstream. The external road network is composed of several secondary roads used for automobiles, which begins at the project dam and terminates at the PED railway station. In order to apply

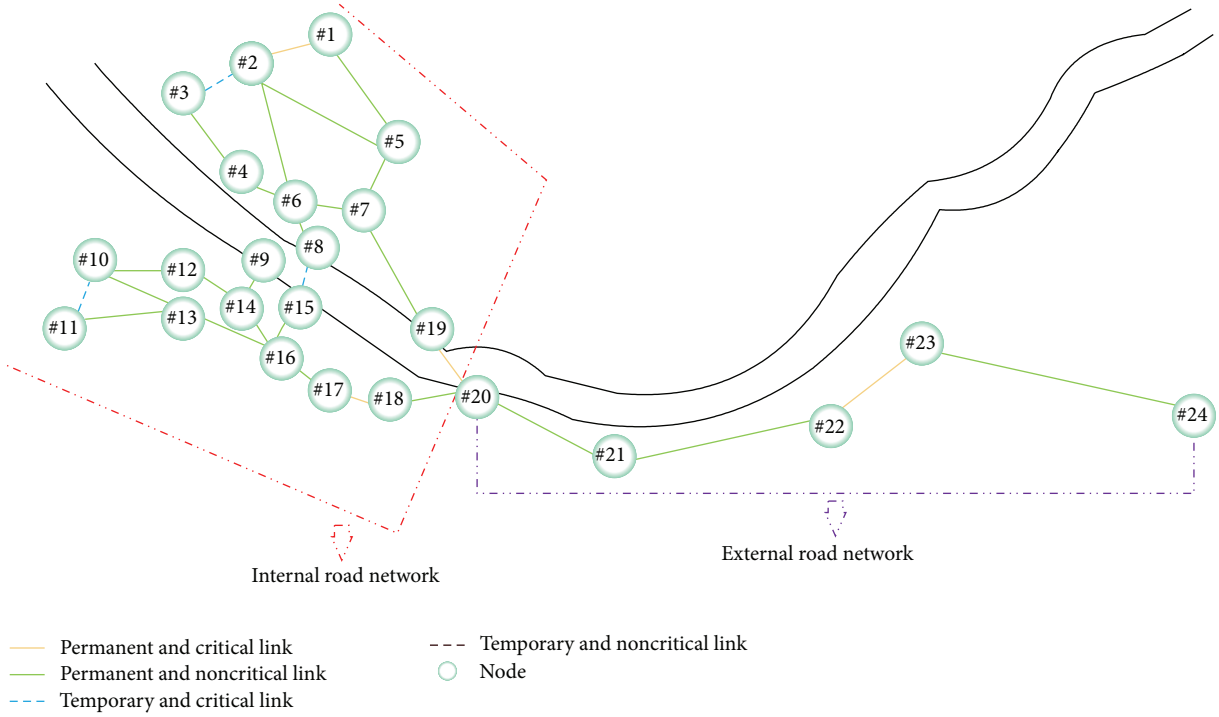

Figure 7: Simplified transportation network illustration in XLD hydropower LSCP.

the proposed approach more conveniently, adjacent roads of the same type have been combined and the concrete shapes of the roads have been ignored. A simplified transportation network illustration is shown in Figure 7 which distinguishes the permanent and temporary, critical and noncritical nature of each road according to the practical location of the transportation network. The illustration has 24 nodes and 18 and 29 links. There are 12 commodities in total, which represent travel between different origin-destination pairs. The 16 nodes in these commodities have certain capacities (unit: number of vehicles (n)) and others have no capacity. Tables 1 and 2 give the detailed data.

For each link in the transportation network, there is a free flow travel time t_a^0 (unit: hour (h)), a "practical capacity" for the link c_a' (unit: number of vehicles (n)), which is set to be 90% of the design capacity [1], and a fuzzy random seismic damage scenario $\tilde{\tilde{\xi}}_a$. The corresponding data for this case problem are stated in Table 3. It should be noted that the probabilities assigned to the fuzzy numbers for the fuzzy random numbers $\tilde{\tilde{\xi}}_a$ in Table 3 were obtained through a statistical analysis of the historical data in the area.

In the case problem, there are 2 outputs—the retrofit of permanent (i.e., $i = 1$) and temporary (i.e., $i = 2$) links. The activity process and activities for the retrofit are the same for both types of links. Activities (i.e., $j = 1, \ldots, 10$) are as (1) breaking pavement, (2) digging grooves, (3) laying pipes, (4) backfilling grooves, (5) strengthening earth-rock, (6) evening roadbeds, (7) digging gutters, (8) building kerbstones, (9) constructing bases, (10) constructing pavements. Every activity corresponds to an activity cost center. According to [25], 5 environmental media can be determined in the retrofit work: (1) air and climate, (2) waste water, (3) waste, (4) soil and ground water, (5) noise and vibration. Environmental cost categories are recorded as in [25].

Table 1: Travel of the commodities.

Commodity k	Travel of commodity
$1'$	#24 → #23 → #22 → #21 → #20
$2'$	#20 → #21 → #22 → #23 → #24
$3'$	#20 → #19 → #7 → #5 → #2
$4'$	#2 → #5 → #7 → #19 → #20
$5'$	#6 → #7 → #19 → #20
$6'$	#20 → #19 → #7 → #6
$7'$	#20 → #18 → #17 → #16 → #13
$8'$	#13 → #16 → #17 → #18 → #20
$9'$	#20 → #18 → #17 → #16 → #14
$10'$	#14 → #16 → #17 → #18 → #20
$11'$	#20 → #18 → #17 → #16 → #15
$12'$	#15 → #16 → #17 → #18 → #20

(1) Waste and emission treatment: depreciation for related equipment; maintenance, operating materials and services; related personnel; fees, taxes, and charges; insurance for environmental liabilities.

(2) Prevention and environmental management: external services for environmental management and personnel for general environmental management activities.

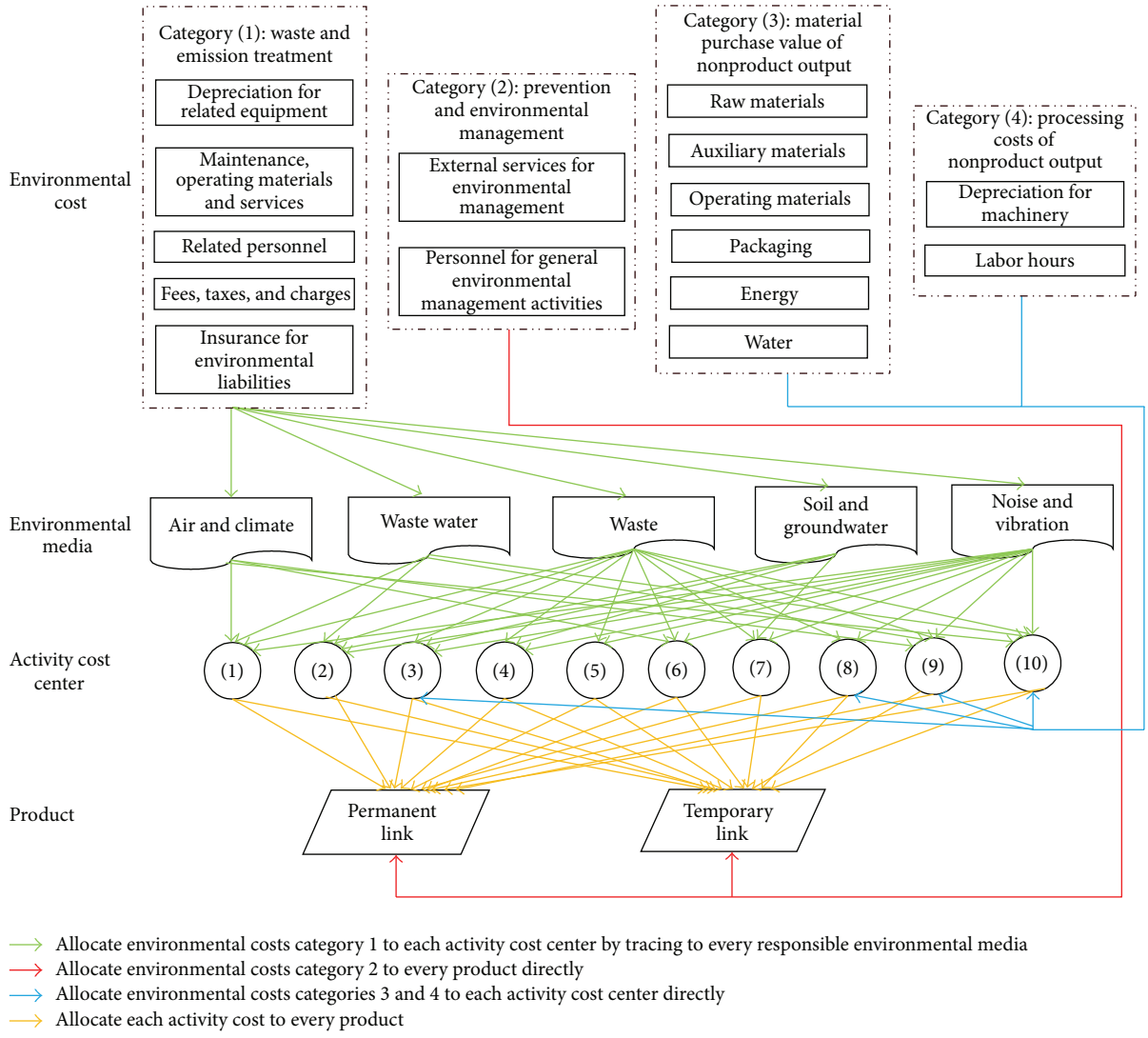

Figure 8: Allocate environmental costs of retrofit work.

Table 2: Capacity of node.

Node b	#24	#23	#22	#21	#20	#19	#7	#5	#2	#6	#18	#17	#16	#13	#14	#15
Capacity ca_b (n)	51	51	51	51	149	49	49	22	22	25	49	49	49	16	18	15

(3) Material purchase value of nonproduct output: raw materials; auxiliary materials; operating materials; packaging; energy; and water.

(4) Processing costs of nonproduct output: depreciation for machinery and labor hours.

Since categories 1, 3, and 4 are variable costs (i.e., $v = 1, 2, 3$), category 2 is fixed costs (i.e., $f = 1$); they are recoded as (unit: ¥) $[ce_1^p, ce_2^p, ce_3^p] = [11800, 5764, 2216]$, $[ce_1^t, ce_2^t, ce_3^t] = [73870, 8665, 3365]$, and $ce_1^f = 36538$. Based on the descriptions above, the environmental costs of the retrofit are allocated as shown in Figure 8.

Based on the practice of the case problem and Figure 8, the percentage output for the fixed environmental costs 1 is $[pe_1^f, pe_2^f] = [90.8\%, 9.2\%]$. To calculate the final environmental costs for each output, the corresponding data for the activity cost centers $j = 1, \ldots, 10$ is used as in Table 4. The percentage of j in the variable environmental cost categories is denoted as $[pe_{j1}^v, pe_{j2}^v, pe_{j3}^v]$. am_j denotes the cost driver amount in j and $[am_{1j}, am_{2j}]$ denotes the cost driver amount of outputs in j.

In addition, the corresponding cost data for the retrofit and reconstruction are shown in Table 5. The values for the other model parameters are as follows: $\delta = 0.2$, $\eta = 0.6$, $\rho = 1$, $\alpha = 0.25$, $\beta = 2$, and $\gamma = 1$.

4.2. Case Solution. The developed algorithm was adopted using MATLAB 7.0 on an Inter Core 2, 2.00 GHz clock

Table 3: Free flow travel time ti_a^0, practical capacity ca_a', and fuzzy random seismic damage scenario $\tilde{\tilde{\xi}}_a$ of each link.

Link a	Corresponding nodes b	Free flow travel time ti_a^0 (h)	Practical capacity ca_a' (n)	Fuzzy random seismic damage scenario $\tilde{\tilde{\xi}}_a$
1	#1, #2	0.10	72	$\tilde{\tilde{\xi}}_1 =$ {(0, 1, 2) with probability 13.7%; (1, 2, 3) with probability 18.9%; (2, 3, 4) with probability 25.8%; (3, 4, 5) with probability 16.9%; (4, 5, 6) with probability 24.7%}
2	#2, #3	0.08	75	$\tilde{\tilde{\xi}}_2 =$ {(0, 1, 2) with probability 7.8%; (1, 2, 3) with probability 15.2%; (2, 3, 4) with probability 23.4%; (3, 4, 5) with probability 29.5%; (4, 5, 6) with probability 24.1%}
3 4 5 6 7 8 9 10 11	#1, #5 #2, #5 #2, #6 #3, #4 #4, #6 #6, #7 #5, #7 #6, #8 #7, #19	0.25	87	$\tilde{\tilde{\xi}}_3$ $\tilde{\tilde{\xi}}_4$ $\tilde{\tilde{\xi}}_5$ $\tilde{\tilde{\xi}}_6$ $\tilde{\tilde{\xi}}_7 =$ {(0, 1, 2) with probability 11.5%; (1, 2, 3) with probability 8.9%; (2, 3, 4) with probability 32.8%; (3, 4, 5) with probability 27.4%; (4, 5, 6) with probability 19.4%} $\tilde{\tilde{\xi}}_8$ $\tilde{\tilde{\xi}}_9$ $\tilde{\tilde{\xi}}_{10}$ $\tilde{\tilde{\xi}}_{11}$
12	#19, #20	0.10	101	$\tilde{\tilde{\xi}}_{12} =$ {(0, 1, 2) with probability 8.6%; (1, 2, 3) with probability 20.3%; (2, 3, 4) with probability 28.6%; (3, 4, 5) with probability 21.5%; (4, 5, 6) with probability 21.1%}
13	#10, #11	0.05	96	$\tilde{\tilde{\xi}}_{13} =$ {(0, 1, 2) with probability 6.5%; (1, 2, 3) with probability 17.2%; (2, 3, 4) with probability 13.7%; (3, 4, 5) with probability 27.2%; (4, 5, 6) with probability 35.4%}
14 15 16 17 18 19 20 21 23 25	#1, #5 #12, #14 #14, #16 #9, #14 #11, #13 #13, #16 #10, #13 #15, #16 #16, #17 #18, #20	0.30	90	$\tilde{\tilde{\xi}}_{14}$ $\tilde{\tilde{\xi}}_{15}$ $\tilde{\tilde{\xi}}_{16}$ $\tilde{\tilde{\xi}}_{17}$ $\tilde{\tilde{\xi}}_{18} =$ {(0, 1, 2) with probability 12.8%; (1, 2, 3) with probability 20.3%; (2, 3, 4) with probability 16.5%; (3, 4, 5) with probability 31.2%; (4, 5, 6) with probability 19.2%} $\tilde{\tilde{\xi}}_{19}$ $\tilde{\tilde{\xi}}_{20}$ $\tilde{\tilde{\xi}}_{21}$ $\tilde{\tilde{\xi}}_{23}$ $\tilde{\tilde{\xi}}_{25}$

Table 3: Continued.

Link a	Corresponding nodes b	Free flow travel time ti_a^0 (h)	Practical capacity ca_a' (n)	Fuzzy random seismic damage scenario $\tilde{\tilde{\xi}}_a$
22	#8, #15	0.09	89	$\tilde{\tilde{\xi}}_{22} =$ {(0, 1, 2) with probability 7.4%; (1, 2, 3) with probability 19.4%; (2, 3, 4) with probability 21.6%; (3, 4, 5) with probability 23.8%; (4, 5, 6) with probability 27.8%}
24	#17, #18	0.10	84	$\tilde{\tilde{\xi}}_{24} =$ {(0, 1, 2) with probability 23.2%; (1, 2, 3) with probability 9.1%; (2, 3, 4) with probability 20.8%; (3, 4, 5) with probability 21.6%; (4, 5, 6) with probability 25.3%}
26 27 29	#20, #21 #21, #22 #23, #24	0.40	126	$\tilde{\tilde{\xi}}_{26}$ $\tilde{\tilde{\xi}}_{27} =$ $\tilde{\tilde{\xi}}_{29}$ {(0, 1, 2) with probability 16.6%; (1, 2, 3) with probability 23.2%; (2, 3, 4) with probability 7.9%; (3, 4, 5) with probability 30.1%; (4, 5, 6) with probability 22.2%}
28	#22, #23	0.15	96	$\tilde{\tilde{\xi}}_{28} =$ {(0, 1, 2) with probability 14.7%; (1, 2, 3) with probability 121.3%; (2, 3, 4) with probability 10.8%; (3, 4, 5) with probability 28.1%; (4, 5, 6) with probability 25.1%}

Table 4: Corresponding data of activity cost centers.

Activity cost center j	pe_{j1}^v	pe_{j2}^v	pe_{j3}^v	am_j	am_{1j}	am_{2j}
1	15.6%	0.0%	0.0%	426.30 m^2	408.10 m^2	18.20 m^2
2	6.7%	0.0%	0.0%	9.74 m^3	9.32 m^3	0.42 m^3
3	6.7%	25.0%	25.0%	60.90 m	58.30 m	2.60 m
4	6.7%	0.0%	0.0%	3.35 m^3	3.21 m^3	0.14 m^3
5	5.4%	0.0%	0.0%	25.58 m^3	24.49 m^3	1.09 m^3
6	15.6%	0.0%	0.0%	426.30 m^2	408.10 m^2	18.20 m^2
7	6.7%	0.0%	0.0%	0.61 m^3	0.58 m^3	0.03 m^3
8	5.4%	25.0%	25.0%	60.90 m	58.30 m	2.60 m
9	15.6%	25.0%	25.0%	426.30 m^2	408.1 m^2	18.20 m^2
10	15.6%	25.0%	25.0%	426.30 m^2	408.10 m^2	18.20 m^2

pulse with 2048 MB memory. The algorithmic parameters for the case problem were set as follows: error coefficient $\epsilon = 0.9$, swarm_size $S = 20$, iteration_max $T = 100$, inertia weight_max $w^{\max} = 0.9$, inertia weight_min $w^{\min} = 0.1$, personal best position acceleration constant $c_p = 0.5$, global best position acceleration constant $c_g = 0.5$, local best position acceleration constant $c_l = 0.2$, and near neighbor best acceleration constant $c_n = 0.1$.

After 8 iterations of the approximation decomposition, the approximation termination was achieved within 36 minutes on an average of 10 runs, which is time acceptable. The optimal solutions are shown in Tables 6 and 7. For all the Pareto optimal solutions on the upper level, the corresponding solutions on the lower level are the same. Table 6 shows a Pareto optimal solution set with 45 solutions on the upper level, where only 10 of the set are enumerated for convenience of expression. The investor is able to choose their preferred plan from the set. If they feel that the retrofit costs including environmental costs C are more important, they would choose the minimum costs plan and vice versa. Since there are fuzzy numbers in model (36), it cannot state crisp optimal objective values in final decision results. However, they are easy to be transformed into equivalent crisp forms by many fuzzy theories and it will not effect the decision.

Table 5: Cost data of retrofit and reconstruction.

Item	Cost (¥)
Increased variable retrofit costs for permanent link by basic rank (i.e., rank 1) c_{va}^{p}	16732
Variable retrofit costs for temporary link by basic rank (i.e., rank 1) c_{va}^{t}	30528
Increased fixed retrofit costs for permanent link c_{fi}^{p}	14525
Fixed retrofit costs for temporary link c_{fi}^{t}	28637
Increased variable reconstruction cost for permanent link by basic rank (i.e., rank 1) cr_{va}^{p}	107052
Variable reconstruction cost for temporary link by basic rank (i.e., rank 1) cr_{va}^{t}	98063
Increased fixed reconstruction cost for permanent link cr_{fi}^{p}	69894
Fixed reconstruction cost for temporary link cr_{fi}^{t}	50183

4.3. Analytic Results of the Proposed Approach

(1) Worthiness of Modeling and Solutions. Fuzzy random programming approach explicitly considers the entire range of uncertain scenarios and thus is more conforming to reality for hedging better against uncertainty. Although it increases the complexity of modeling, the model is well transformed orienting computer implementation. In addition, the computing complexity of the model is not greater than that of the stochastic programming approach used in [1]. Therefore, the extra effort on modeling and solving fuzzy random bilevel programming is worthwhile.

The multiobjective method is introduced to determine the Pareto optimal solution set for the upper level and provides more effective and nondominated alternatives for the decision-maker. Compared with the weight-sum method for multiobjective in [19], the solutions in this paper have more reference value for the decision-maker and reflect the users' preference requirements. Therefore, it is more worthwhile.

(2) Efficiency of Algorithm. This paper compares GA, an usually used metaheuristics algorithm, and the developed algorithm in this study. The merit of GA is its strong evolutionary process to find an optimal solution by the operation of crossover, mutation, and selection. However, the randomly generated initial generation at the algorithms' beginning affects the solution quality because of the bad gene inherited from the parent generation. Moreover, the searching capability is reduced as GA does not rely on gradient or derivative information. In the developed algorithm, the particle-represented solutions closely connect the particles of PSO and the solutions to the problem. The hybrid particle-updating mechanism successfully enhances the searching capability. The developed algorithm is a useful tool for the solution to the problem. In contrast to the previous papers, such as [19, 21], both the bilevel and multiobjective environments are considered in this paper.

For multiobjective optimization, the definition of quality is substantially more complex than for single-objective optimization problems. Figure 9 shows the iterative results of Pareto optimal solutions in 8 iterations. Note that in each iteration of approximation decomposition, these fuzzy numbers in model (36) are decomposed into crisp forms. Therefore, the objective values can be evaluated. For further expression of the efficiency of the convergence, three metrics of performance are studied. Table 8 shows the metrics of performance for Pareto optimal sets proposed in [51] and the set convergence of Pareto optimal sets in 8 iterations after 10 runs.

(3) Efficiency of Algorithm Parameters. Since the search space for the problem is so large and the computing process is time-consuming, it is necessary to choose reasonable algorithm parameters. Table 9 shows the comparison results of different swarm_size (i.e., S) and iteration_max (i.e., T) on average computing time and iterations after 10 runs. Looking into Table 9, when $S = 10$, the program could not obtain results in more than 3600 s and more than 10 iterations with both $T = 100$ and $T = 200$. This is the same when $S = 50$ with the lower iterations. When $S = 20$ and $T = 200$, the process is more time-consuming than the current algorithm parameters. Therefore, the current ones are considered suitable.

5. Conclusions

This paper studies retrofit decision for transportation network of LSCP to hedge against seismic risk. On the consideration of the emerged challenges in the problem, using distinctions of various link types, bilevel decision, environmental costs, and fuzzy random seismic damage scenario, a fuzzy random multiobjective bilevel programming model is set up. A transforming approach is in use to obtain equivalent fuzzy bilevel programming model. Then, decomposition is utilized to these fuzzy variables by decomposition theorem of fuzzy number. An approximation decomposition-based multiobjective AGLNPSO is developed to solve the problem. A case study is presented as an illustrative example of this problem. The results validate the worthiness of modeling and solutions and test the efficiency of the algorithm and parameters.

The contributions of this paper to literature are as the follows. (1) This study adopts the work of [1] to the filed of LSCP. Bilevel decision involves, with the investor and the administer, distinctions of various link types, and retrofit decision specified into several ranks according to the seismic damage scenario provides more reasonable and practical description of the problem. (2) Although there are many works on environmental cost, such as [25, 26], few papers consider it in transportation network in LSCP. Thus it enhances the focus points of management aims of the problem. (3) This paper uses fuzzy random seismic damage scenario to describe the hybrid uncertain situation. To the best of our knowledge, it has never been done before. (4) The approximation decomposition-based multiobjective AGLNPSO is developed as one of the useful tools to solve

Table 6: Pareto optimal solution set on the upperlevel.

Solution u_a		1^*	2^*	3^*	4^*	5^*	6^*	7^*	8^*	9^*	10^*	.....
	1	3	3	3	3	4	4	2	1	3	3	.....
	2	4	3	4	3	4	4	1	5	2	4	.....
	3	2	4	2	3	2	1	2	1	5	2	.....
	4	2	2	3	3	5	1	3	3	1	3	.....
	5	4	3	3	1	4	4	1	5	3	4	.....
	6	3	4	3	3	5	2	5	3	3	3	.....
	7	4	3	3	3	3	5	1	1	2	3	.....
	8	2	3	2	3	1	1	3	4	3	3	.....
	9	3	4	3	2	5	1	2	4	4	3	.....
	10	3	3	3	2	3	3	4	1	3	2	.....
	11	2	2	2	2	3	3	2	1	1	2	.....
	12	3	3	4	2	2	3	3	4	2	4	.....
	13	3	3	3	1	5	3	4	4	2	3	.....
	14	4	3	4	1	1	5	3	2	3	3	.....
Link a	15	2	2	1	1	2	1	2	1	3	2	.....
	16	3	2	3	3	3	3	3	4	1	3	.....
	17	3	2	3	2	2	4	3	2	2	3	.....
	18	3	2	3	3	3	4	4	1	1	3	.....
	19	3	3	2	5	1	2	5	1	3	2	.....
	20	2	3	2	2	2	2	2	2	4	3	.....
	21	2	4	2	5	1	1	4	3	5	4	.....
	22	3	3	3	5	4	1	4	3	4	2	.....
	23	2	3	2	5	2	1	2	2	3	2	.....
	24	2	2	3	4	1	2	3	4	2	2	.....
	25	3	2	3	2	3	3	1	5	2	3	.....
	26	2	2	2	3	1	1	3	1	1	2	.....
	27	4	3	4	1	3	4	3	3	2	3	.....
	28	3	2	3	3	3	5	2	3	1	3	.....
	29	4	4	4	5	4	5	2	5	3	4	.....

Table 7: Optimal solutions on the lowerlevel.

Commodity k	$1'$	$2'$	$3'$	$4'$	$5'$	$6'$	$7'$	$8'$	$9'$	$10'$	$11'$	$12'$
Flow of commodity x_k (n/h)	25.50	25.50	12.00	12.00	12.50	12.50	8.00	8.00	9.00	9.00	7.50	7.50

Table 8: Metrics of performance and set convergence for Pareto optimal sets.

Iteration	The average distance	The distribution	The extent	The set convergence
1	0.0812	0.5623	5.0088	—
2	0.0630	0.4615	5.7706	Iteration 1–2: 0.5610
3	0.1364	0.8600	6.8594	Iteration 2–3: 0.6765
4	0.1223	0.5250	6.3147	Iteration 3–4: 0.7632
5	0.1502	0.6820	6.7538	Iteration 4–5: 0.8750
6	0.2835	0.9600	6.6417	Iteration 5–6: 0.8571
7	0.0973	0.5289	5.4451	Iteration 6–7: 0.5712
8	0.1300	0.8635	6.6424	Iteration 7–8: 0.9143

Table 9: Comparison of different algorithm parameters.

	$S = 10$		$S = 20$		$S = 50$	
	$T = 100$	$T = 200$	$T = 100$	$T = 200$	$T = 100$	$T = 200$
Computing time (s)	≥3600	≥3600	2160	3480	≥3600	≥3600
Iterations	≥16	≥12	8	6	≥4	≥3

this problem. In contrast to the previous papers, such as [19, 21], both the bilevel and multiobjective environments are considered in this paper.

There are three areas suggested for future research. First, more cost categories need to be investigated and the detailed relationships between the retrofit decision and the costs should be outlined to ensure the model is as practical as possible. Secondly, to determine better, more effective solutions with lower memory and computing time requirements, alternative approaches and algorithms (e.g., other exact approaches, (meta)heuristics, evolutionary algorithms, etc.) could be used to make comparisons. Finally, consideration of other behavior assumptions, such as the travelers learning or user equilibrium, may change the structure of the problem. Each of these areas is very important and equally worthy of our concern.

Conflict of Interests

The authors declare no conflict of interests.

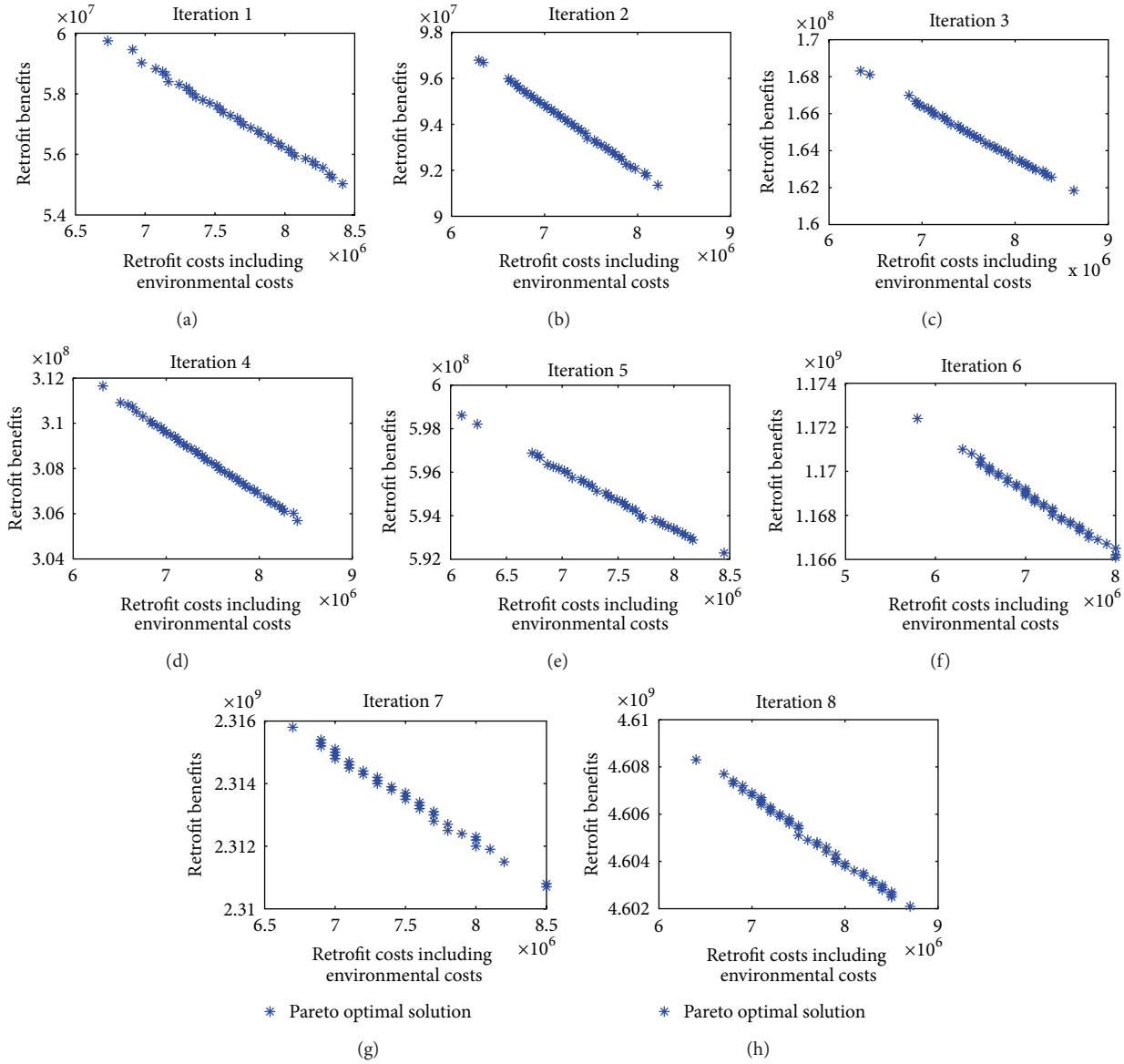

Figure 9: Iterative results of Pareto optimal solutions in 8 iterations.

Acknowledgments

This research was supported by the Key Program of NSFC (Grant no. 70831005), "985" Program of Sichuan University "Innovative Research Base for Economic Development and Management," and the Research Foundation of Ministry of Education for the Doctoral Program of Higher Education of China (Grant no. 20130181110063).

References

[1] C. Liu, Y. Fan, and F. Ordóñez, "A two-stage stochastic programming model for transportation network protection," *Computers and Operations Research*, vol. 36, no. 5, pp. 1582–1590, 2009.

[2] S. D. Werner, C. E. Taylor, J. E. Moore, and J. S. Walton, *Seismic Retrofitting Manuals for Highway Systems, Volume I, Seismic Risk Analysis of Highway Systems, and Technical Report for Volume I*, Multidisciplinary Center for Earthquake Engineering Research, Buffalo, NY, USA, 1999.

[3] J. Sohn, T. J. Kim, G. J. D. Hewings, J. S. Lee, and S.-G. Jang, "Retrofit priority of transport network links under an earthquake," *Journal of Urban Planning and Development*, vol. 129, no. 4, pp. 195–210, 2003.

[4] M. J. N. Priestley, F. Seible, and G. F. Calvi, *Seismic Design and Retrofit of Bridges*, John Wiley & Sons, New York, NY, USA, 1996.

[5] M. Shinozuka, Y. Murachi, X. Dong, Y. Zhou, and M. J. Orlikowski, "Effect of seismic retrofit of bridges on transportation networks," *Earthquake Engineering and Engineering Vibration*, vol. 2, no. 2, pp. 169–179, 2003.

[6] Y. Zhou, S. Banerjee, and M. Shinozuka, "Socio-economic effect of seismic retrofit of bridges for highway transportation networks: a pilot study," *Structure and Infrastructure Engineering*, vol. 6, no. 1-2, pp. 145–157, 2010.

[7] H. Kwakernaak, "Fuzzy random variables-I. Definitions and theorems," *Information Sciences*, vol. 15, no. 1, pp. 1–29, 1978.

[8] R. Zhao, W. Tang, and C. Wang, "Fuzzy random renewal process and renewal reward process," *Fuzzy Optimization and Decision Making*, vol. 6, no. 3, pp. 279–295, 2007.

[9] W. Fei, "A generalization of bihari's inequality and fuzzy random differential equations with non-Lipschitz coefficients," *International Journal of Uncertainty, Fuzziness and Knowlege-Based Systems*, vol. 15, no. 4, pp. 425–439, 2007.

[10] A. F. Shapiro, "Fuzzy random variables," *Insurance*, vol. 44, no. 2, pp. 307–314, 2009.

[11] Y. K. Liu and J. Gao, "The independence of fuzzy variables with applications to fuzzy random optimization," *International Journal of Uncertainty, Fuzziness and Knowlege-Based Systems*, vol. 15, supplement 2, pp. 1–20, 2007.

[12] J. P. Xu and Y. G. Liu, "Multi-objective decision making model under fuzzy random environment and its application to inventory problems," *Information Sciences*, vol. 178, no. 14, pp. 2899–2914, 2008.

[13] J. Xu and Z. Zhang, "A fuzzy random resource-constrained scheduling model with multiple projects and its application to a working procedure in a large-scale water conservancy and hydropower construction project," *Journal of Scheduling*, vol. 15, no. 2, pp. 253–272, 2012.

[14] M. L. Puri and D. A. Ralescu, "Fuzzy random variables," *Journal of Mathematical Analysis and Applications*, vol. 114, no. 2, pp. 409–422, 1986.

[15] E. P. Klement, M. L. Puri, and D. A. Ralescu, "Limit theorems for fuzzy random variables," *Proceedings of The Royal Society of London A*, vol. 407, no. 1832, pp. 171–182, 1986.

[16] M. Á. Gil, M. López-Díaz, and D. A. Ralescu, "Overview on the development of fuzzy random variables," *Fuzzy Sets and Systems*, vol. 157, no. 19, pp. 2546–2557, 2006.

[17] R. Kruse and K. D. Meyer, *Statistics with Vague Data*, D. Reidel Publishing, Dordrecht, The Netherlands, 1987.

[18] J. Xu, F. Yan, and S. Li, "Vehicle routing optimization with soft time windows in a fuzzy random environment," *Transportation Research E*, vol. 47, no. 6, pp. 1075–1091, 2011.

[19] G. Zhang, J. Lu, and T. Dillon, "Decentralized multi-objective bilevel decision making with fuzzy demands," *Knowledge-Based Systems*, vol. 20, no. 5, pp. 495–507, 2007.

[20] J. D. Knowles and D. W. Corne, "Approximating the nondominated front using the pareto archived evolution strategy," *Evolutionary Computation*, vol. 8, no. 2, pp. 149–172, 2000.

[21] T. J. Ai, *Particle Swarm Optimization for Generalized Vehicle Routing Problem [Doctoral Dissertation]*, Asian Institute of Technology, Thailand, 2008.

[22] G. Ueno, K. Yasuda, and N. Iwasaki, "Robust adaptive particle swarm optimization," in *Proceedings of the IEEE International Conference on Systems, Man, Cybernetics*, pp. 3915–3920, October 2005.

[23] T. J. Ai and V. Kachitvichyanukul, "A particle swarm optimization for the vehicle routing problem with simultaneous pickup and delivery," *Computers and Operations Research*, vol. 36, no. 5, pp. 1693–1702, 2009.

[24] C. A. C. Coello and M. S. Lechunga, "MOPSO: a proposal for multiple objective particle swarm optimization," in *Proceedings of the IEEE Word Congress on Computational Intelligence*, 2002.

[25] C. Jasch, "The use of environmental management accounting (EMA) for identifying environmental costs," *Journal of Cleaner Production*, vol. 11, no. 6, pp. 667–676, 2003.

[26] X. Xiao, *Theory of Environment Cost*, China Financial & Economic Publishing House, Beijing, China, 2002.

[27] R. Cooper, "The rise of activity-based costing part one: what is an activity-based cost system?" *Journal of Cost Management*, vol. 2, pp. 45–54, 1988.

[28] R. Cooper, "The rise of activity-based costing part two: when do I need an activity-based cost system?" *Journal of Cost Management*, vol. 2, pp. 41–48, 1988.

[29] R. Cooper, "The rise of activity-based costing part three: how many cost drivers do you need, and how do you select them?" *Journal of Cost Management*, vol. 2, pp. 34–46, 1989.

[30] R. Cooper, "The rise of activity-based costing part four: what do activity-based cost systems look like?" *Journal of Cost Management*, vol. 3, pp. 34–46, 1989.

[31] R. S. Kaplan, "Measuring manufacturing performance: a new challenge for managerial accounting research," *The Accounting Review*, vol. 58, pp. 686–705, 1983.

[32] R. S. Kaplan, "Yesterday's accounting undermines production," *Harvard Business Review*, pp. 95–101, 1984.

[33] L. A. Zadeh, "Fuzzy sets," *Information and Control*, vol. 8, no. 3, pp. 338–353, 1965.

[34] V. Krätschmer, "A unified approach to fuzzy random variables," *Fuzzy Sets and Systems*, vol. 123, no. 1, pp. 1–9, 2001.

[35] J. Li, J. Xu, and M. Gen, "A class of multiobjective linear programming model with fuzzy random coefficients," *Mathematical and Computer Modelling*, vol. 44, no. 11-12, pp. 1097–1113, 2006.

[36] Y.-K. Liu and B. Liu, "Fuzzy random variables: a scalar expected value operator," *Fuzzy Optimization and Decision Making*, vol. 2, no. 2, pp. 143–160, 2003.

[37] M. López-Díaz and M. A. Gil, "The λ-average value and the fuzzy expectation of a fuzzy random variable," *Fuzzy Sets and Systems*, vol. 99, no. 3, pp. 347–352, 1998.

[38] L. Özdamar and O. Demir, "A hierarchical clustering and routing procedure for large scale disaster relief logistics planning," *Transportation Research E*, vol. 48, no. 3, pp. 591–602, 2012.

[39] D. Dubois and H. Prade, *Possibility Theory: An Approach to Computerized Processing of Uncertainty*, Plenum Press, New York, NY, USA, 1988.

[40] S. Nahmias, "Fuzzy variables," *Fuzzy Sets and Systems*, vol. 1, no. 2, pp. 97–110, 1978.

[41] G. Zhang, J. Lu, and Y. Gao, "An algorithm for fuzzy multi-objective multi-follower partial cooperative bilevel programming," *Journal of Intelligent and Fuzzy Systems*, vol. 19, no. 4-5, pp. 303–319, 2008.

[42] J. F. Bard, "Some properties of the bilevel programming problem," *Journal of Optimization Theory and Applications*, vol. 68, no. 2, pp. 371–378, 1991.

[43] L. Yao and J. Xu, "A class of expected value bilevel programming problems with random coefficients based on rough approximation and its application to a production-inventory system," *Abstract and Applied Analysis*, vol. 2013, Article ID 312527, 12 pages, 2013.

[44] J. F. Bard and J. E. Falk, "An explicit solution to the multi-level programming problem," *Computers and Operations Research*, vol. 9, no. 1, pp. 77–100, 1982.

[45] J. Fortuny-Amat and B. McCarl, "A representation and economic interpretation of a two-level programming problem," *Journal of the Operational Research Society*, vol. 32, no. 9, pp. 783–792, 1981.

[46] L. Vicente, G. Savard, and J. Júdice, "Descent approaches for quadratic bilevel programming," *Journal of Optimization Theory and Applications*, vol. 81, no. 2, pp. 379–399, 1994.

[47] L. M. Case, *An l_1 Penalty Function Approach to the Nonlinear Bilevel Programming Problem [Ph.D. thesis]*, University of Waterloo, Ottawa, Canada, 1999.

[48] B. Lucio, C. Massimiliano, and G. Stefano, "A bilevel flow model for hazmat transportation network design," *Transportation Research C*, vol. 17, no. 2, pp. 175–196, 2009.

[49] Y. Gao, G. Zhang, J. Lu, and H.-M. Wee, "Particle swarm optimization for bi-level pricing problems in supply chains," *Journal of Global Optimization*, vol. 51, no. 2, pp. 245–254, 2011.

[50] L. Cagnina, S. Esquivel, and C. A. C. Coello, "A particle swarm optimizer for multi-objective optimization," *Journal of Computer Science and Technology*, vol. 5, no. 4, pp. 204–210, 2005.

[51] E. Zitzler, K. Deb, and L. Thiele, "Comparison of multiobjective evolutionary algorithms: empirical results," *Evolutionary Computation*, vol. 8, no. 2, pp. 173–195, 2000.

Hindawi Publishing Corporation
Abstract and Applied Analysis
Volume 2014, Article ID 953151, 9 pages
http://dx.doi.org/10.1155/2014/953151

Research Article

Revisiting Blasius Flow by Fixed Point Method

Ding Xu,[1] Jinglei Xu,[2] and Gongnan Xie[3]

[1] *State Key Laboratory for Strength and Vibration of Mechanical Structures, School of Aerospace, Xi'an Jiaotong University, No. 28, Xianning West Road, Xi'an 710049, China*
[2] *School of Jet Propulsion, Beijing University of Aeronautics and Astronautics, Xueyuan Road, No. 37, Beijing 100191, China*
[3] *School of Mechanical Engineering, Northwestern Polytechnical University, Xi'an, Shaanxi 710072, China*

Correspondence should be addressed to Jinglei Xu; xujl@buaa.edu.cn

Received 28 October 2013; Revised 7 December 2013; Accepted 7 December 2013; Published 12 January 2014

Academic Editor: Mohamed Fathy El-Amin

The well-known Blasius flow is governed by a third-order nonlinear ordinary differential equation with two-point boundary value. Specially, one of the boundary conditions is asymptotically assigned on the first derivative at infinity, which is the main challenge on handling this problem. Through introducing two transformations not only for independent variable bur also for function, the difficulty originated from the semi-infinite interval and asymptotic boundary condition is overcome. The deduced nonlinear differential equation is subsequently investigated with the fixed point method, so the original complex nonlinear equation is replaced by a series of integrable linear equations. Meanwhile, in order to improve the convergence and stability of iteration procedure, a sequence of relaxation factors is introduced in the framework of fixed point method and determined by the steepest descent seeking algorithm in a convenient manner.

1. Introduction

The Navier-Stokes equations are the fundamental governing equations of fluid flow. Usually, this set of nonlinear partial differential equations has no general solution, and analytical solutions are very rare only for some simple fluid flows. However, in some certain flows, the Navier-Stokes equations may be reduced to a set of nonlinear ordinary differential equations under a similarity transform [1, 2]. These similarity solutions could not only provide some physical significance to the complex Navier-Stokes equations but also act as a benchmarking for numerical method. The well-known Blasius flow [3–5] is possibly the simplest example among these similarity solutions. It describes the idealized incompressible laminar flow past an semi-infinite flat plate at high Reynolds numbers, which is mathematically a third-order nonlinear two-point boundary value problem:

$$\mathscr{A}_f[f] = 2f''' + ff'' = 0, \tag{1}$$

subject to the boundary conditions:

$$f(0) = 0, \qquad f'(0) = 0, \qquad \lim_{\eta\to\infty} f'(\eta) = 1, \tag{2}$$

where the prime denotes differentiation to the variable η and $f(\eta)$ is the nondimensional stream function related to the stream function $\psi(x, y)$ as follows:

$$\psi(x, y) = f(\eta)\sqrt{\nu x U_\infty}. \tag{3}$$

$\eta = y\sqrt{U_\infty/(\nu x)}$ is the similarity variable, where U_∞ is the free stream velocity, ν is the kinematic viscosity coefficient, and x and y are the two independent coordinates. The two velocity components are then determined:

$$u = \frac{\partial\psi}{\partial y} = U_\infty f'(\eta),$$
$$v = -\frac{\partial\psi}{\partial x} = \frac{1}{2}\left[\eta f'(\eta) - f(\eta)\right]\cdot\sqrt{\frac{\nu U_\infty}{x}}. \tag{4}$$

According to (1) and (2) the solution is defined on a semi-infinite interval $\eta \geq 0$, and one of the boundary conditions is asymptotically assigned on the first derivative of function at infinity, which are the main challenges on solving the

Blasius flow. The solution to this problem has the following asymptotic property [6, 7]:

$$f \sim \frac{f''(0)\eta^2}{2}, \quad \text{as } \eta \longrightarrow 0,$$
$$f \sim \eta + B, \quad \text{as } \eta \longrightarrow \infty, \tag{5}$$

where B is a constant and the benchmarking value provided by Boyd [6, 7] is $B = -1.720787657520503$.

As known, no simple closed-form solution to the Blasius problem is available, despite the simple form and such a long history of it since 1908 [3]. Much attention has been paid to this problem. Blasius [3] himself firstly investigated this problem by the perturbation method and obtained an approximate solution by matching a power series solution for small η to an asymptotic expansion for large η. However, this procedure may be improper because of somewhat restricted radius of convergence in the first power series [8]. Later, this problem was handled by Bender et al. [9] with δ-expansion in a smart manner. The approximate solutions were obtained by He [10], Liao [11, 12], and Turkyilmazoglu [13–16] with the variational iteration method, homotopy analysis method, and homotopy perturbation method, respectively. Wang [17] also investigated this problem by the Adomian decomposition method. Meantime, there are a lot of numerical methods emerging to handle the Blasius problem including, but not limited to, shooting method, finite differences method, and spectral method [18–31]. A vast bibliography of numerical methods has developed for this problem, so a full account of them is out of the scope of this paper, and readers are suggested to refer to the review articles [6, 7]. It is noted that the existing numerical methods usually integrate this problem over a finite interval $\eta \in [0, \eta_\infty]$, although the Blasius problem is originally defined on the semi-infinite interval $\eta \in [0, +\infty)$. Thus the value of η_∞ should be chosen sufficiently large to assure the accuracy of the asymptotical boundary condition at infinity. However, the appropriate value η_∞ could not be determined beforehand, so usually the trial-and-error approach is involved, and some different values should be tried to find the appropriate η_∞ to satisfy the demanded accuracy.

In order to exactly assure the boundary conditions (2) and obtain a uniformly valid solution on the semi-infinite interval $\eta \in [0, +\infty)$, two transformations not only for the independent variable η but also for function $f(\eta)$ are introduced in this paper. The transformed nonlinear differential equation is subsequently investigated with the fixed point method (FPM) [33], which transforms the nonlinear differential equation into a series of integrable linear differential equations. Hence, an approximate semianalytical solution to the Blasius problem is finally obtained, which is valid on the whole domain and can satisfy the asymptotic property automatically. Meantime, in order to improve the convergence and stability of iteration procedure, a sequence of relaxation factors is introduced in the framework of FPM, which are determined by the steepest descent seeking algorithm. Thus, the accuracy of this approximate solution could be improved step by step in a convenient manner.

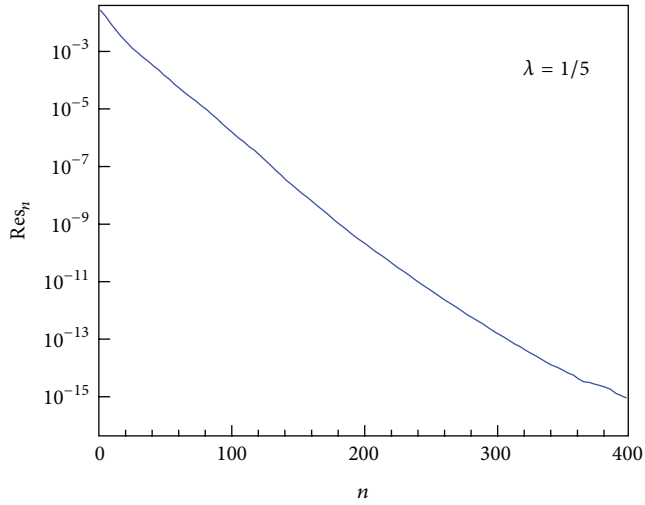

Figure 1: The convergence history of Res_n ($\lambda = 1/5$).

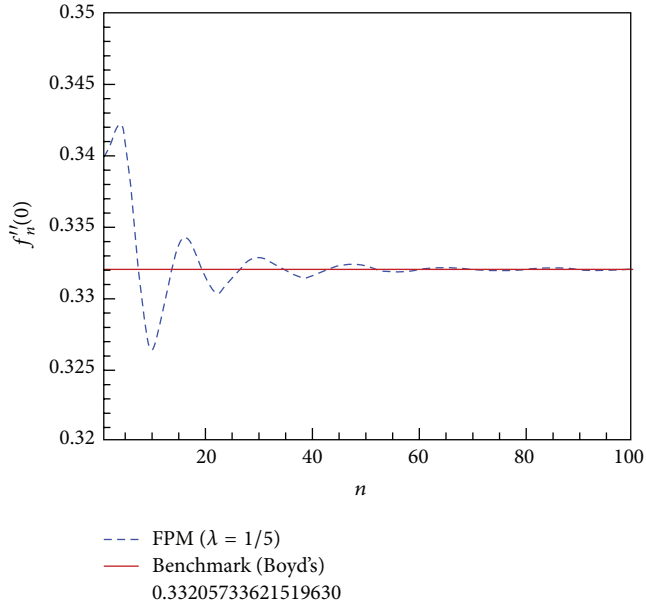

Figure 2: The convergence history of $f_n''(0)$ ($\lambda = 1/5$).

2. Revisiting the Blasius Equation by Fixed Point Method

2.1. Transformations. As mentioned in Section 1, the main challenge on handling the Blasius problem originates from the semi-infinite interval $\eta \in [0, +\infty)$ and the asymptotic boundary condition $\lim_{\eta \to \infty} f'(\eta) = 1$. In order to overcome these difficulties, two transformations are introduced for independent variable η and function $f(\eta)$, respectively,

$$z = \frac{(\lambda\eta - 1)}{(\lambda\eta + 1)},$$
$$g(z) = \frac{\lambda(f - \eta)}{(1 + \lambda\eta)}, \tag{6}$$

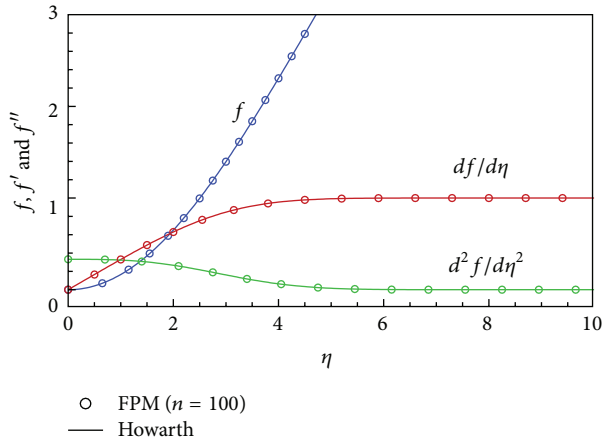

FIGURE 3: Comparison of FPM result ($\lambda = 1/5$, $n = 100$) with Howarth's numerical result.

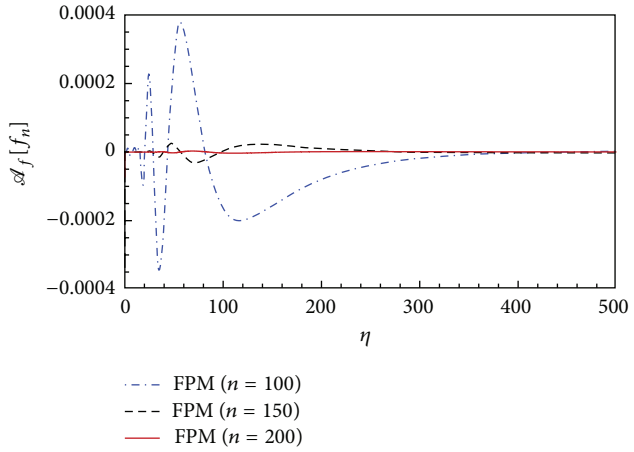

FIGURE 4: The residual error function $\mathscr{A}_f[f_n] = 2f_n''' + f_n f_n''$ ($\lambda = 1/5$).

where λ (>0) is a free parameter. $1/\lambda$ stands for the length dimension and its physical meaning is related to the scale of boundary layer thickness. The influence of λ on the solution will be discussed in detail in Section 3.2.

Hence, the original Blasius equation becomes

$$\mathscr{A}_g[g] = \lambda^2(1-z)^3 g''' + \left[1 - 3\lambda^2(1-z)^2 + z + 2g\right] g'' = 0, \tag{7}$$

with the following boundary conditions:

$$g(-1) = 0, \qquad g'(-1) = -\frac{1}{2}, \qquad g(1) = 0, \tag{8}$$

where the prime denotes differentiation to the new variable z. It is clear that the semi-infinite interval $\eta \in [0, +\infty)$ is mapped to the bounded interval $-1 \le z \le 1$, and the original asymptotic boundary condition $\lim_{\eta\to\infty} f'(\eta) = 1$ becomes

$$g(1) = \lim_{\eta\to\infty} \frac{\lambda(f-\eta)}{1+\lambda\eta} = \lim_{\eta\to\infty} \frac{\lambda\left[f'(\eta) - 1\right]}{\lambda} = 0, \tag{9}$$

which is beneficial to the acquirement of the valid solution in the whole domain.

2.2. The Idea of Fixed Point Method (FPM). The fixed point, a fundamental concept in functional analysis [34], has been widely adopted in studying the existence and uniqueness of solutions by pure mathematicians. Recently, the fixed point concept has been used to handle nonlinear differential equations, and the fixed point method (FPM) has been proposed to obtain the explicit approximate analytical solution to the nonlinear differential equation [33].

To outline the idea of FPM, let us consider the following nonlinear differential equation:

$$\begin{aligned} \mathscr{A}[u] &= 0, \\ \mathscr{B}_+[u] &= 0, \end{aligned} \tag{10}$$

where $\mathscr{A}[\cdot]$ is a nonlinear operator and u is an unknown function. Here, $\mathscr{B}_+[u] = 0$ is the boundary condition and/or initial condition for u.

$\mathscr{T}[\cdot]$ is a contractive map:

$$\mathscr{T}[u] = u - \varpi \cdot \mathscr{L}_C^{-1}[\mathscr{A}[u]], \tag{11}$$

where $\mathscr{L}_C[\cdot]$ is a linear continuous bijective operator, named as the linear characteristic operator of the nonlinear operator $\mathscr{A}[\cdot]$ and $\mathscr{L}_C^{-1}[\cdot]$ is the inverse operator of $\mathscr{L}_C[\cdot]$. ϖ is a real nonzero free parameter, named as the relaxation factor, which could improve the convergence and stability of iteration procedure. The optimal value ϖ is usually dependent on the problem to be solved [33]. Then, a solution sequence $\{u_n | n = 0, 1, 2, 3, \ldots\}$ can be obtained from the following iteration procedure:

$$u_{n+1} = \mathscr{T}[u_n] = u_n - \varpi_{n+1} \cdot \mathscr{L}_C^{-1}[\mathscr{A}[u_n]], \quad \mathscr{B}_+[u_{n+1}] = 0 \qquad n = 0, 1, 2, \ldots \tag{12}$$

$$\Longleftrightarrow \mathscr{L}_C[u_{n+1}] = \mathscr{L}_C[u_n] - \varpi_{n+1} \cdot \mathscr{A}[u_n], \quad \mathscr{B}_+[u_{n+1}] = 0 \qquad n = 0, 1, 2, \ldots. \tag{13}$$

If the convergence of the solution sequence $\{u_n | n = 0, 1, 2, 3, \ldots\}$ is ensured, it is clear that the limit value u^* is exactly the zero point of the original nonlinear operator $\mathscr{A}[\cdot]$:

$$\begin{aligned} \mathscr{A}[u^*] &= 0, \\ \mathscr{B}_+[u^*] &= 0, \end{aligned} \tag{14}$$

and u^* is also named as a fixed point of the contractive map $\mathscr{T}[u]$.

In [33], only one relaxation factor ϖ is introduced and determined by the so-called ϖ-curves in a heuristic manner. Here, a sequence of relaxation factors $\{\varpi_n | n = 1, 2, 3, \ldots\}$ is introduced in (12), which will be decided according to the steepest descent seeking algorithm in the following Section 2.3.

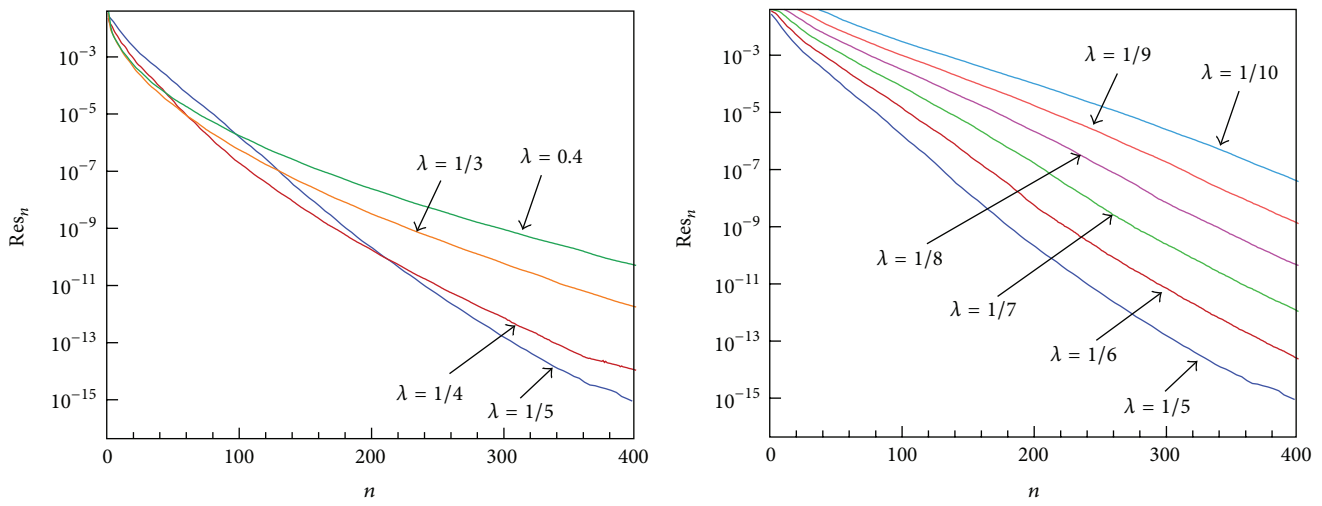

(a) Comparison among $\lambda = 0.4$, $\lambda = 1/3$, $\lambda = 1/4$, and $\lambda = 1/5$

(b) Comparison among $\lambda = 1/5$, $\lambda = 1/6$, $\lambda = 1/7$, $\lambda = 1/8$, $\lambda = 1/9$, and $\lambda = 1/10$

Figure 5: The influence of λ value on the square residual error Res_n.

Table 1: Comparison of $f''(0)$ between FPM ($\lambda = 1/5$) and others.

n	Present (FPM) $f_n''(0)$	Fazio [31]	Zhang and Chen [32]	Boyd [6, 7] (Benchmark)
1	0.3399132521631			
25	0.3314634706964			
50	0.3322299008614			
100	0.3320852976636			
150	0.3320560696476			
200	0.3320572413724	0.3320575595	0.33205733621	0.33205733621519630
250	0.3320573781489			
300	0.3320573415043			
400	0.3320573362780			
600	0.3320573362198			
800	0.3320573362153			

2.3. The Steepest Descent Seeking Algorithm (SDS). As mentioned in Section 2.2, the relaxation factor $\{\varpi_n | n = 1, 2, 3, \ldots\}$ could improve the convergence and stability of iteration procedure, and usually the optimal value of relaxation factor is dependent on the problem to be solved. Here, an algorithm, named as the steepest descent seeking algorithm (SDS), is adopted to determine the optimal value of the relaxation factor.

Let Res_n denote the square residual error of the aforementioned iteration procedure in (13):

$$\begin{aligned} \mathrm{Res}_n &= \mathrm{Res}_n(\varpi_1, \varpi_2, \ldots \varpi_n) \\ &= \int_\Omega \left(\mathscr{A}[u_n]\right)^2 d\Omega, \quad n = 1, 2, 3, \ldots, \end{aligned} \tag{15}$$

where Ω is the definition domain of the variable and Res_n is a kind of global residual error and can evaluate the accuracy of the approximation u_n. Then it is suggested that the optimal value of relaxation factor $\varpi_{n,\mathrm{opt}}$ corresponds to the value ϖ_n such that Res_n obtains the minimum value $\min(\mathrm{Res}_n)$. For example, when $n = 1$, the square residual error $\mathrm{Res}_1(\varpi_1)$ is a function of ϖ_1 only and thus the optimal value $\varpi_{1,\mathrm{opt}}$ can be obtained by solving the nonlinear algebraic equation:

$$\frac{d\mathrm{Res}_1}{d\varpi_1} = 0. \tag{16}$$

When $n = 2$, the square residual error $\mathrm{Res}_2(\varpi_1, \varpi_2)$ is dependent on ϖ_1 and ϖ_2. Because the optimal value $\varpi_{1,\mathrm{opt}}$ is known from the previous step, the optimal value $\varpi_{2,\mathrm{opt}}$ is governed by the following nonlinear algebraic equation:

$$\frac{d\mathrm{Res}_2}{d\varpi_2} = 0. \tag{17}$$

Similarly, for the nth-higher order, the square residual error Res_n actually contains an unknown relaxation factor

Table 2: Comparison of f between FPM ($\lambda = 1/5$) and Howarth.

η	f			
	FPM			Howarth [21]
	$n = 50$	$n = 200$	$n = 800$	
0	0.	0.	0.	0
0.2	0.006644529362447	0.006640995986591	0.006640999714597	0.00664
0.4	0.02657431250127	0.02655986911996	0.02655988401799	0.02656
0.6	0.05976777037563	0.05973460409079	0.05973463749804	0.05974
0.8	0.1061682229933	0.1061081617252	0.1061082208390	0.10611
1.0	0.1656669946990	0.1655716339700	0.1655717257893	0.16557
1.2	0.2380877115384	0.2379485860317	0.2379487172889	0.23795
1.4	0.3231726092163	0.3229813967422	0.3229815738295	0.32298
1.6	0.4205717973682	0.4203205366053	0.4203207655016	0.42032
1.8	0.5298364510983	0.5295177515398	0.5295180377438	0.52952
2	0.6504167979655	0.6500240214585	0.6500243699353	0.65003
3	1.397637112752	1.396807516637	1.396808230870	1.39682
4	2.307039632340	2.305745294404	2.305746418462	2.30576
5	3.284986166454	3.283272129531	3.283273665156	3.28329
6	4.281691879364	4.279618989982	4.279620922514	4.27964
7	5.281627551984	5.279236492841	5.279238811029	5.27926
8	6.281851614090	6.279210729689	6.279213431346	6.27923
10	8.282182252512	8.279208870686	8.279212342934	/
15	13.284515240195	13.27920694573	13.279212342479	/
20	18.283646215099	18.27920502276	18.279212342479	/

Table 3: Comparison of f' between FPM ($\lambda = 1/5$) and Howarth.

η	f'			
	FPM			Howarth [21]
	$n = 50$	$n = 200$	$n = 800$	
0	0.	0.	0.	0
0.2	0.06644347995228	0.06640775477474	0.06640779209625	0.06641
0.4	0.1328378289536	0.1327640864649	0.1327641607610	0.13277
0.6	0.1990509318305	0.1989371417431	0.1989372524222	0.19894
0.8	0.2648643497350	0.2647089925007	0.2647091387231	0.26471
1.0	0.3299775414929	0.3297798506391	0.3297800312497	0.32979
1.2	0.3940157297864	0.3937758909492	0.3937761044339	0.39378
1.4	0.4565422496657	0.4562615202332	0.4562617647051	0.45627
1.6	0.5170757864638	0.5167565112060	0.5167567844226	0.51676
1.8	0.5751123265865	0.5747578444754	0.5747581438894	0.57477
2	0.6301509546266	0.6297654136655	0.6297657365024	0.62977
3	0.8465117311855	0.8460440464746	0.8460444436580	0.84605
4	0.9559675373580	0.9555178143322	0.9555182298107	0.95552
5	0.9919283302451	0.9915414951870	0.9915419001644	0.99155
6	0.9993091537696	0.9989724827440	0.9989728724358	0.99898
7	1.000215077512	0.9999212208137	0.9999216041479	0.99992
8	1.000195058002	0.9999958903313	0.9999962745353	1.00000
10	1.000231913519	0.9999996129000	0.9999999980154	/
15	1.000224523350	0.9999996133026	1.000000000000	/
20	0.9997789079310	0.9999996166005	1.000000000000	/

Table 4: Comparison of f'' between FPM ($\lambda = 1/5$) and Howarth.

η	f'' FPM $n = 50$	FPM $n = 200$	FPM $n = 800$	Howarth [21]
0	0.3322299008614	0.3320572413724	0.33205733621526	0.33206
0.2	0.3321681255428	0.3319836510534	0.33198383711462	0.33199
0.4	0.3316651431123	0.3314696606323	0.33146984420144	0.33147
0.6	0.3302835149673	0.3300789475208	0.33007912757428	0.33008
0.8	0.3275995678839	0.3273890950354	0.32738927014924	0.32739
1.0	0.3232190113859	0.3230069482211	0.32300711668693	0.32301
1.2	0.3167975457228	0.3165890310990	0.31658919106110	0.31659
1.4	0.3080647180157	0.3078652421801	0.30786539179016	0.30787
1.6	0.2968484699253	0.2966633238744	0.29666346145571	0.29667
1.8	0.2830971363448	0.2829308930580	0.28293101725975	0.28293
2	0.2668953087923	0.2667514357803	0.26675154569727	0.26675
3	0.1613836232798	0.1613602778747	0.16136031954088	0.16136
4	0.06418469140538	0.06423412147661	0.064234121091696	0.06424
5	0.01584093436570	0.01590681516643	0.015906798685320	0.01591
6	$2.367987742194e-3$	$2.402051505611e-3$	$2.4020398437568e-3$	0.00240
7	$1.526040209602e-4$	$2.201705391867e-4$	$2.201689552708e-4$	0.00022
8	$-9.161215077567e-4$	$1.223887615942e-5$	$1.224092624324e-5$	0.00001
10	$1.667970449293e-4$	$9.650715210973e-9$	$8.442915877193e-9$	/
15	$2.499528919705e-4$	$-1.207941083287e-10$	$1.426848065722e-17$	/
20	$1.244076430614e-4$	$1.815564827202e-9$	$4.736242910970e-18$	/

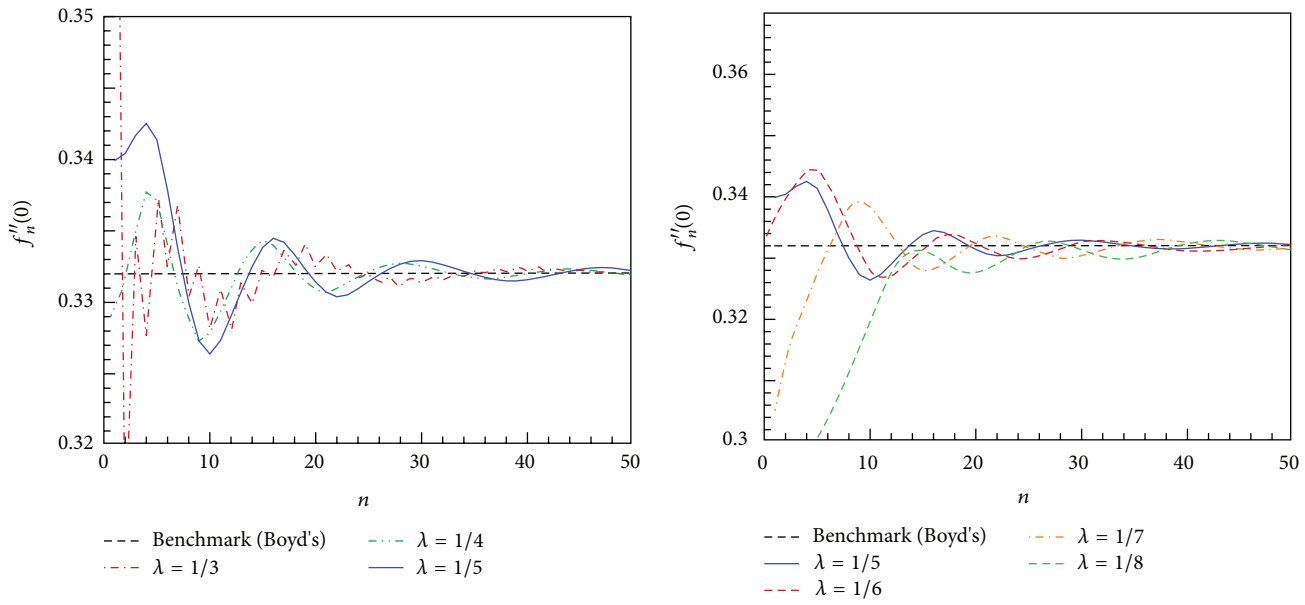

(a) Comparison among $\lambda = 1/3$, $\lambda = 1/4$, and $\lambda = 1/5$

(b) Comparison among $\lambda = 1/5$, $\lambda = 1/6$, $\lambda = 1/7$, and $\lambda = 1/8$

Figure 6: The influence of λ value on the convergence of $f_n''(0)$.

ω_n only, so the optimal value $\omega_{n,\text{opt}}$ is determined by the following nonlinear algebraic equation:

$$\frac{d\text{Res}_n}{d\omega_n} = 0. \tag{18}$$

The name of the steepest descent seeking algorithm just comes from the aforementioned approach; that is, every optimal value $\omega_{n,\text{opt}}$ is sought to minimize the corresponding square residual error Res_n. According to this approach, only one nonlinear algebraic equation should be solved in every iteration step, and the elements of the sequence $\{\omega_n | n = 1, 2, 3, \ldots\}$ are obtained sequentially and separately.

2.4. Iteration Procedure. Now, for (7), let us choose the linear characteristic operator:

$$\mathscr{L}_C[g] = \frac{d^3 g}{dz^3} = g''', \tag{19}$$

and construct an iteration procedure as follows:

$$\mathscr{L}_C\left[g_{n+1}\right] = \mathscr{L}_C\left[g_n\right] - \varpi_{n+1}\cdot \mathscr{A}_g\left[g_n\right],$$
$$g_{n+1}(-1) = 0, \quad g'_{n+1}(-1) = -\frac{1}{2}, \quad g_{n+1}(1) = 0, \quad n = 0, 1, 2\ldots \tag{20}$$

$$\Longleftrightarrow \quad \begin{aligned} &g'''_{n+1} = g'''_n - \varpi_{n+1}\left\{\lambda^2(1-z)^3 g'''_n + \left[1 - 3\lambda^2(1-z)^2 + z + 2g_n\right] g''_n\right\}, \\ &g_{n+1}(-1) = 0, \quad g'_{n+1}(-1) = -\frac{1}{2}, \quad g_{n+1}(1) = 0, \quad n = 0, 1, 2\ldots. \end{aligned} \tag{21}$$

The initial guess g_0 is conveniently chosen as

$$g_0 = \frac{\left(z^2 - 1\right)}{4}, \tag{22}$$

which satisfies the following equation:

$$\begin{aligned} &\mathscr{L}_C\left[g_0\right] = 0, \\ &g_0(-1) = 0, \qquad g'_0(-1) = -\frac{1}{2}, \qquad g_0(1) = 0. \end{aligned} \tag{23}$$

3. Result and Discussion

3.1. Results as λ=1/5. Before the acquirement of approximate solution according to the iteration procedure (21), the free parameter λ should be determined. It is found that the iteration procedure converges rapidly when the value of $1/\lambda$ takes the scale of boundary layer thickness. Here, the value of λ is firstly set to $\lambda = 1/5$ and the influence of λ value on the solution will be studied in Section 3.2.

In order to demonstrate FPM, the procedure to obtain the first-order approximation $g_1(z)$ is given here in detail. Firstly, the governing equation for $g_1(z)$ is deduced according to (21):

$$\begin{aligned} &g'''_1 = -\frac{\varpi_1}{100}\left(19 + 62z + 19z^2\right), \\ &g_1(-1) = 0, \qquad g'_1(-1) = -\frac{1}{2}, \qquad g_1(1) = 0. \end{aligned} \tag{24}$$

Then the first order approximation $g_1(z)$ takes the following form:

$$\begin{aligned} g_1(z) = {} & \frac{73\varpi_1}{6000} - \frac{1}{4} + \frac{209\varpi_1}{6000}z + \left(\frac{1}{4} + \frac{41\varpi_1}{3000}\right)z^2 \\ & - \frac{19\varpi_1}{600}z^3 - \frac{31\varpi_1}{1200}z^4 - \frac{19\varpi_1}{6000}z^5. \end{aligned} \tag{25}$$

It is clear that the first-order approximation $g_1(z)$ in (25) is dependent on the relaxation factor ϖ_1, whose optimal value could be determined by the steepest descent seeking algorithm (SDS) as mentioned in Section 2.3. Here, the square residual error Res_n of the original equation (1) is introduced:

$$\mathrm{Res}_n = \int_0^{+\infty}\left(\mathscr{A}_f\left[f_n\right]\right)^2 d\eta = \int_{-1}^{+1}\frac{(1-z)^2}{8\lambda}\left(\mathscr{A}_g\left[g_n\right]\right)^2 dz. \tag{26}$$

Then, the square residual error of $f_1(\eta)$ is as follows:

$$\begin{aligned} \mathrm{Res}_1\left(\varpi_1\right) = {} & 0.06590476 - 0.02813884\varpi_1 + 0.004530836\varpi_1^2 \\ & + 2.330415\times 10^{-4}\varpi_1^3 + 5.251947\times 10^{-6}\varpi_1^4, \end{aligned} \tag{27}$$

and the optimal value $\varpi_{1,\mathrm{opt}}$ and the minimum of Res_1 are

$$\varpi_{1,\mathrm{opt}} = 2.560515, \qquad \min\left(\mathrm{Res}_1\right) = 0.02769798. \tag{28}$$

Hence, the first-order approximation $g_1(z)$ is finally determined:

$$\begin{aligned} g_1(z) = {} & -0.2188471 + 0.08919127z + 0.2849937z^2 \\ & - 0.08108297z^3 - 0.06614663z^4 - 0.008108297z^5. \end{aligned} \tag{29}$$

For the higher-order approximation $g_n(z)$, the procedure is similar, and an explicit semianalytical solution could be deduced by the symbolic computation software, such as MAXIMA, MAPLE and MATHEMATICA.

In consideration of the transformation (6), the corresponding approximate solution $f_n(\eta)$ to the original Blasius equations (1) and (2) is

$$f_n(\eta) = g_n(z)\cdot\left(\eta + \frac{1}{\lambda}\right) + \eta, \quad z = \frac{(\lambda\eta - 1)}{(\lambda\eta + 1)}. \tag{30}$$

The convergence history of the square residual error Res_n is illustrated in Figure 1, which clearly shows that Res_n is gradually reduced during the iteration procedure, so the accuracy of the approximate solution could be improved step by step to any possibility.

The second derivative $f''(0)$ is a measure of the shear stress on the plate and plays a critical role in the Blasius problem [4, 5]. The relationship between $f''_n(0)$ and $g''_n(-1)$ can be deduced as follows:

$$f''_n(0) = 4\lambda g''_n(-1). \tag{31}$$

The convergence history of $f''_n(0)$ is displayed in Figure 2, which shows that the difference between the approximation $f''_n(0)$ and Boyd's [6, 7] benchmarking result $f''(0) = 0.33205733621519630$ decreases during the iteration procedure. Meanwhile, the comparison between the present result

Table 5: The asymptotic property of f for large positive η ($\lambda = 1/5$, $n = 800$).

η	$f - \eta$	$B = \lim_{\eta\to\infty}(f-\eta)$ (Benchmark) [6, 7]
5	−1.716726334844	
6	−1.720379077486	
7	−1.720761188971	
8	−1.720786568654	
9	−1.720787629355	
10	−1.720787657066	
11	−1.720787657516	−1.720787657520503
12	−1.720787657520	
13	−1.720787657521	
14	−1.720787657521	
15	−1.720787657521	
20	−1.720787657521	
25	−1.720787657521	
30	−1.720787657521	

and others given in [6, 7, 31, 32] is tabulated in Table 1, which shows that $f_n''(0)$ is the same as Boyd's benchmarking result within 7 significant digits when $n \geq 300$ and within 12 significant digits when $n \geq 800$.

The approximate semianalytical solutions and the well-known Howarth's [32] accurate numerical result of $f(\eta)$, $f'(\eta)$, and $f''(\eta)$ are compared in Figure 3 and simultaneously tabulated in Tables 2–4, which shows that the present result obtained by FPM is of high accuracy.

The residual error function $\mathscr{A}_f[f_n] = 2f_n''' + f_n f_n''$ is plotted in Figure 4, which also reveals that the error of approximate solutions gradually decreases during the iteration procedure. Moreover, the present approximate solutions are uniformly valid in the whole region.

Based on the asymptotic property of $f(\eta)$ given in (5), we obtain

$$B = \lim_{\eta\to\infty}(f-\eta). \tag{32}$$

The approximate value of B could be obtained as follows:

$$B \approx f_n(\eta) - \eta, \quad \text{for large } \eta. \tag{33}$$

The comparison between the approximate value of B obtained by FPM ($n = 800$, $\lambda = 1/5$) and the benchmarking result $B = -1.720787657520503$ provided by Boyd [6, 7] is given in Table 5, which shows that the present result is the same as Boyd's benchmarking result within 7 significant digits when $\eta \geq 9$ and within 13 significant digits when $\eta \geq 13$.

3.2. The Influence of λ Value on the Solution. It is clear that $1/\lambda$ takes the length dimension in consideration of transformation (6). In order to investigate the influence of λ value on the solution, some different λ values are considered in the following calculations, and the comparison of Res_n at different λ values is displayed in Figures 5(a) and 5(b). It is found that all Res_n corresponding to different λ values are gradually reduced during the iteration procedure, and Res_n based on $\lambda = 1/5$ converges more rapidly than others. What is the physical meaning of λ? Let us try to find the answer from the Prandtl's boundary layer theory [5].

According to Prandtl's boundary layer theory, the effect of viscosity is mainly confined to the boundary layer such that $\eta < \delta$, and the outer flow ($\eta > \delta$) could be considered as inviscid flow. From Table 3, the thickness of the boundary layer is just about $\delta \approx 5$, where $u/U_\infty = f' \approx 0.99$. Now, the physical meaning of λ becomes clear. $1/\lambda$ has the same scale of boundary layer thickness δ. In consideration of transformation (6), the region $-1 \leq z \leq 1$ is divided into two equal parts, and the viscous flow ($\eta < \delta \approx 5$) and inviscid flow ($\eta > \delta \approx 5$) correspond to $-1 \leq z < 0$ and $0 < z < 1$, respectively. Although this determination of λ is in a heuristic manner, it is fortunate that the solution is quite insensitive to λ so long as $1/\lambda$ is of the same order-of-magnitude as $\delta \approx 5$. The influence of λ on the convergence of $f_n''(0)$ is given in Figures 6(a) and 6(b), which also reveals that the limit values of $f_n''(0)$ with different λ values agree well with each other. Hence, the selection of λ is nonessential to the final solution.

4. Conclusion

In this paper, the well-known Blasius flow is revisited by the fixed point method (FPM). In order to overcome the difficulties originated from the semi-infinite interval and asymptotic boundary condition, two transformations are introduced for not only the independent variable but also the dependent variable. Under these transformations, all the boundary conditions are exactly assured for every order approximate solution. In the meanwhile, a free scale parameter λ is introduced in the transformation, and its physical meaning is related to the thickness of the boundary layer. Moreover, a sequence of relaxation factors $\{\omega_n | n = 1, 2, 3, \ldots\}$ is introduced to improve the convergence and stability during iteration procedure, and its elements are obtained in a convenient manner by the steepest descent seeking algorithm. Finally, the comparison of the present results with other scholars' numerical results, especially with the benchmarking results provided by Boyd, shows that FPM is an effective and accurate approach to obtain the semianalytical solution to nonlinear problems.

Nomenclature

U_∞: Free stream velocity, m/s
u: x-components of the velocity, m/s
v: y-components of the velocity, m/s
$\psi(x, y)$: Stream function, m^2/s
$f(\eta)$: Nondimensional stream function
ν: Kinematic viscosity coefficient, m^2/s.

Conflict of Interests

The authors declare that there is no conflict of interests regarding the publication of this paper.

Acknowledgments

The work is supported by the National Natural Science Foundation of China (Approval no. 11102150) and the Fundamental Research Funds for the Central Universities.

References

[1] C. Y. Wang, "Exact solutions of the unsteady navier-stokes equations," *Applied Mechanics Reviews*, vol. 42, no. 11, pp. S269–S282, 1989.

[2] C. Y. Wang, "Exact solutions of the steady-state Navier-Stokes equations," *Annual Review of Fluid Mechanics*, vol. 23, no. 1, pp. 159–177, 1991.

[3] H. Blasius, "Grenzschichten in flüssigkeiten mit kleiner reibung," *Zeitschrift für Angewandte Mathematik und Physik*, vol. 56, pp. 1–37, 1908.

[4] F. M. White, *Viscous Fluid Flow*, McGraw-Hill, New York, NY, USA, 1991.

[5] H. Schlichting and K. Gersten, *Boundary-Layer Theory*, Springer, 2000.

[6] J. P. Boyd, "The Blasius function in the complex plane," *Experimental Mathematics*, vol. 8, no. 4, pp. 381–394, 1999.

[7] J. P. Boyd, "The Blasius function: Computations before computers, the value of tricks, undergraduate projects and open research problems," *SIAM Review*, vol. 50, no. 4, pp. 791–804, 2008.

[8] H. Weyl, "On the differential equations of the simplest boundary-layer problems," *Annals of Mathematics*, vol. 43, pp. 381–407, 1942.

[9] C. M. Bender, K. A. Milton, S. S. Pinsky, and L. M. Simmons Jr., "A new perturbative approach to nonlinear problems," *Journal of Mathematical Physics*, vol. 30, no. 7, pp. 1447–1455, 1989.

[10] J. He, "Approximate analytical solution of blasius' equation," *Communications in Nonlinear Science and Numerical Simulation*, vol. 4, no. 1, pp. 75–78, 1999.

[11] S.-J. Liao, "An explicit, totally analytic approximate solution for Blasius' viscous flow problems," *International Journal of Non-Linear Mechanics*, vol. 34, no. 4, pp. 759–778, 1999.

[12] S.-J. Liao, "A uniformly valid analytic solution of two-dimensional viscous flow over a semi-infinite flat plate," *Journal of Fluid Mechanics*, vol. 385, pp. 101–128, 1999.

[13] M. Turkyilmazoglu, "A homotopy treatment of analytic solution for some boundary layer flows," *International Journal of Nonlinear Sciences and Numerical Simulation*, vol. 10, no. 7, pp. 885–889, 2009.

[14] M. Turkyilmazoglu, "An optimal variational iteration method," *Applied Mathematics Letters*, vol. 24, no. 5, pp. 762–765, 2011.

[15] M. Turkyilmazoglu, "An analytic shooting-like approach for the solution of nonlinear boundary value problems," *Mathematical and Computer Modelling*, vol. 53, no. 9-10, pp. 1748–1755, 2011.

[16] M. Turkyilmazoglu, "Convergence of the homotopy perturbation method," *International Journal of Nonlinear Sciences and Numerical Simulation*, vol. 12, no. 1-8, pp. 9–14, 2011.

[17] L. Wang, "A new algorithm for solving classical Blasius equation," *Applied Mathematics and Computation*, vol. 157, pp. 1–9, 2004.

[18] T. M. Shih and H. J. Huang, "Numerical method for solving nonlinear ordinary and partial differential equations for boundary-layer flows," *Numerical Heat Transfer*, vol. 4, no. 2, pp. 159–178, 1981.

[19] T. M. Shih, "A method to solve two-point boundary-value problems in boundary-layer flows or flames," *Numerical Heat Transfer*, vol. 2, pp. 177–191, 1979.

[20] S. Goldstein, "Concerning some solutions of the boundary layer equations in hydrodynamics," *Mathematical Proceedings of the Cambridge Philosophical Society*, vol. 26, no. 1, pp. 1–30, 1930.

[21] L. Howarth, "On the solution of the laminar boundary layer equations, proceedings of the royal society of London," *Series A-Mathematical and Physical Sciences*, vol. 164, pp. 547–579, 1938.

[22] T. Cebeci and H. B. Keller, "Shooting and parallel shooting methods for solving the Falkner-Skan boundary-layer equation," *Journal of Computational Physics*, vol. 7, no. 2, pp. 289–300, 1971.

[23] R. Fazio, "The Blasius problem formulated as a free boundary value problem," *Acta Mechanica*, vol. 95, no. 1–4, pp. 1–7, 1992.

[24] I. K. Khabibrakhmanov and D. Summers, "The use of generalized Laguerre polynomials in spectral methods for nonlinear differential equations," *Computers and Mathematics with Applications*, vol. 36, no. 2, pp. 65–70, 1998.

[25] A. A. Salama, "Higher-order method for solving free boundary-value problems," *Numerical Heat Transfer, Part B*, vol. 45, no. 4, pp. 385–394, 2004.

[26] R. Cortell, "Numerical solutions of the classical Blasius flat-plate problem," *Applied Mathematics and Computation*, vol. 170, no. 1, pp. 706–710, 2005.

[27] A. A. Salama and A. A. Mansour, "Fourth-order finite-difference method for third-order boundary-value problems," *Numerical Heat Transfer, Part B*, vol. 47, no. 4, pp. 383–401, 2005.

[28] R. Fazio, "Numerical transformation methods: blasius problem and its variants," *Applied Mathematics and Computation*, vol. 215, no. 4, pp. 1513–1521, 2009.

[29] F. Auteri and L. Quartapelle, "Galerkin-laguerre spectral solution of self-similar boundary layer problems," *Communications in Computational Physics*, vol. 12, pp. 1329–1358, 2012.

[30] R. Fazio, "Scaling invariance and the iterative transformation method for a class of parabolic moving boundary problems," *International Journal of Non-Linear Mechanics*, vol. 50, pp. 136–140, 2013.

[31] R. Fazio, "Blasius problem and Falkner-Skan model: töpfer's algorithm and its extension," *Computers & Fluids*, vol. 73, pp. 202–209, 2013.

[32] J. Zhang and B. Chen, "An iterative method for solving the Falkner-Skan equation," *Applied Mathematics and Computation*, vol. 210, no. 1, pp. 215–222, 2009.

[33] D. Xu and X. Guo, "Fixed point analytical method for nonlinear differential equations," *Journal of Computational and Nonlinear Dynamics*, vol. 8, no. 1, 9 pages, 2013.

[34] E. Zeidler, *Nonlinear Functional Analysis and Its Applications, I: Fixed-Point Theorems*, Springer, 1986.

Hindawi Publishing Corporation
Abstract and Applied Analysis
Volume 2013, Article ID 680693, 9 pages
http://dx.doi.org/10.1155/2013/680693

Research Article

Exact Solution for Long-Term Size Exclusion Suspension-Colloidal Transport in Porous Media

Z. You,[1] P. Bedrikovetsky,[1] and L. Kuzmina[2]

[1] *Australian School of Petroleum, The University of Adelaide, Adelaide, SA 5005, Australia*
[2] *National Research University Higher School of Economics, 20 Myasnitskaya Ulitsa, Moscow 101000, Russia*

Correspondence should be addressed to Z. You; zhenjiang.you@adelaide.edu.au

Received 3 September 2013; Accepted 26 November 2013

Academic Editor: Shuyu Sun

Long-term deep bed filtration in porous media with size exclusion particle capture mechanism is studied. For monodispersed suspension and transport in porous media with distributed pore sizes, the microstochastic model allows for upscaling and the exact solution is derived for the obtained macroscale equation system. Results show that transient pore size distribution and nonlinear relation between the filtration coefficient and captured particle concentration during suspension filtration and retention are the main features of long-term deep bed filtration, which generalises the classical deep bed filtration model and its latter modifications. Furthermore, the exact solution demonstrates earlier breakthrough and lower breakthrough concentration for larger particles. Among all the pores with different sizes, the ones with intermediate sizes (between the minimum pore size and the particle size) vanish first. Total concentration of all the pores smaller than the particles turns to zero asymptotically when time tends to infinity, which corresponds to complete plugging of smaller pores.

1. Introduction

Transport, filtration, and subsequent retention of suspended particles and colloids in porous media are common phenomena in nature and in many industrial applications. In petroleum industry, migration of fine particles in low consolidated natural rocks during production of heavy oils leads to significant productivity decline [1–4]. Invasion of drilling fluid into oil and gas reservoirs results in well impairment and formation damage due to particle straining in thin pores [5–7]. Flow of suspensions and colloids in porous media with particle retention by matrix is also important for filtering of water and industrial liquid or gas fluid streams [8–10], enhanced bioremediation [11, 12], particle accumulation in the streambed sediments [13], propagation of biocolloids (bacteria viruses and protozoan parasites) in aquifers, surface water and wastewater treatment, and so forth [14–20].

A thorough understanding and reliable prediction of particle transport and retention by mathematical modelling are critical to the planning and design of abovementioned industrial and environmental processes. Up to date, considerable research has been devoted to the description of transport and retention behaviour of suspensions in porous media, as well as their effects on the alteration of the formation rock (a number of reviews are available in the literature; see [21–29]). In spite of all these works, the mechanisms of suspension transport and capture in porous media are still incompletely understood and quantified.

The classical suspension-colloidal deep bed filtration (DBF) theory is the most commonly used approach for predicting particle transport behaviour and the consequent media alterations [3, 8, 9, 14, 15]. The classical DBF model includes two equations for particle population balance and capture kinetics, respectively [21, 30]. Several forms of filtration coefficient as function of retained particle concentration for different capture mechanisms and the resultant analytical solutions have been reported in the literature [21, 31]. However, the reported mismatch between the modelled and measured particle DBF data makes it necessary to examine the fundamental principles of the classical model for suspension transport in porous media, including its upscaling from micro- to macroscale and possible model generalisations [32–34].

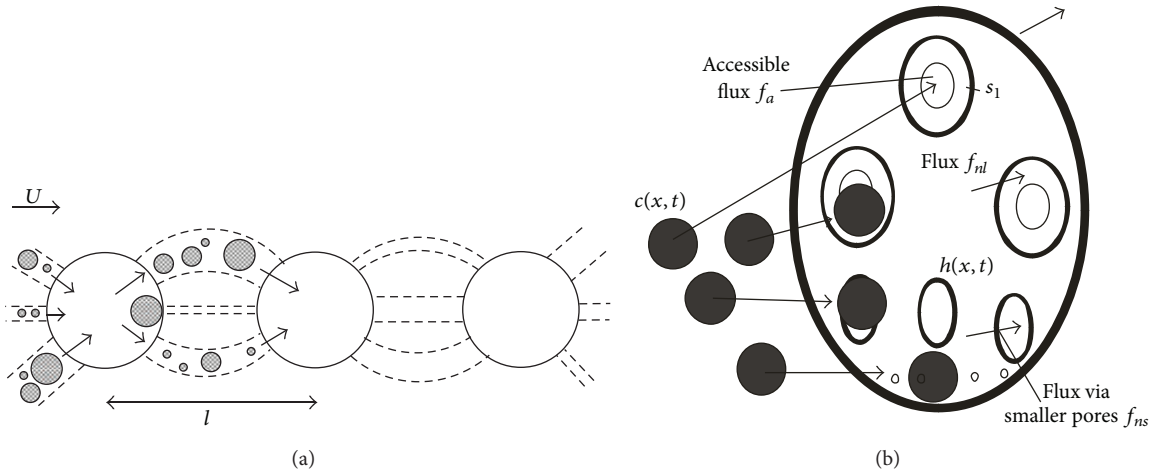

Figure 1: Geometric model of parallel capillary bundles with mixing chambers: (a) bundles of parallel capillaries alternated by mixing chambers; (b) cross section of the capillary bungle with size-excluded particles.

Sharma and Yortsos [35–37] derived a new population balance model, accounting for variation of pore and particle size distributions due to several particle capture mechanisms. It is assumed that the particle population moves at the average flow velocity of the carrier fluid, and the whole porous space is accessible to particles. The particles smaller than the pores pass without straining; while the particles larger than the pores are size-excluded in the medium. Particularly, these assumptions lead to independent deep bed filtration of polydispersed particles under the low retention conditions.

Introduction of accessibility and flux reduction factors into the population balance equations describes simultaneous flow of suspension in accessible pores and flow of particle-free water in inaccessible fraction of porous space; it also results in the particle speed that differs from the carrier water velocity [32, 38, 39]. A linearised model describes deep bed filtration under the short-time injection; the concentration decays with time exponentially due to retention [14, 15, 21, 23]. The analytical model for long-time injection does not account for accessibility and flux reduction factors [38, 39].

In the present paper, an exact solution for long-term deep bed filtration accounting for accessibility and flux reduction factors is derived. Being downscaled, the solution exhibits the transient development of the pore size distribution due to particle size exclusion. The macroscale equations result in nonlinear retained-particle-concentration dependencies for filtration coefficient as well as the accessibility and flux reduction factors, which generalise the classical DBF model.

The structure of this paper is as follows. Section 2 presents the microscale system of governing equations with varying pore and particle size distributions. The upscaling of the micromodel for monodispersed suspension is briefly derived in Section 3. The analytical solution of the upscaled equations with expressions for suspended and captured particle concentrations during long-term injection is derived in Section 4. The concentration profiles and histories as obtained from the exact solution along with constitutive relations of the upscaled model are presented and discussed in Section 5. Finally, Section 6 presents the conclusions of the study.

2. Microstochastic Model for Suspension Transport in Porous Media

The geometric model of porous media for size exclusion suspension-colloidal transport is a bundle of parallel tubes intercalated by the mixing chambers (Figure 1(a)). Size exclusion flow in any arbitrary 3D domain occurs with particle motion in "thicker" pore and capture in "thinner" pore throat. The parallel-tube-mixing-chamber model (PTMC) separates flow from capture: the capture occurs at the exit of mixing chambers at entrances of thinner pores, while the motion occurs in larger parallel capillaries (Figure 1(b)). The phenomenological parameters and functions used in the stochastic model are described briefly in this section. For more details, refer to [32].

The number of pores per unit cross-sectional area of porous media is defined by the pore concentration function

$$h(x,t) = \int_0^\infty H\left(r_p, x, t\right) dr_p, \tag{1}$$

which is the integral of pore concentration distribution function $H(r_p, x, t)$ in terms of the pore radius r_p. In the similar manner, the overall concentration of suspended particles in porous media results from the integration of concentration of these particles in r_s for all particle sizes

$$c(x,t) = \int_0^\infty C\left(r_s, x, t\right) dr_s, \tag{2}$$

where $C(r_s, x, t)$ is the concentration distribution function of suspended particles. The total concentration of retained particles is also obtained by integration in particle size

$$\sigma(x,t) = \int_0^\infty \Sigma\left(r_s, x, t\right) dr_s, \tag{3}$$

where $\Sigma(r_s, x, t)$ is the concentration distribution function of retained particles.

The porosity is the total cross-sectional area of all pores per unit cross-sectional area of porous media

$$\phi[H] = \int_0^\infty s_1(r_p) H(r_p, x, t)\, dr_p, \tag{4}$$

where $s_1(r_p) = \pi r_p^2$ is the cross-sectional area of a single pore with radius r_p. The accessible fraction of the total porosity can be obtained by integrating the cross-sectional area of large pores only ($r_p > r_s$),

$$\phi_a[H, r_s] = \int_{r_s}^\infty s_1(r_p) H(r_p, x, t)\, dr_p, \tag{5}$$

due to the fact that only the pores with sizes larger than r_s are accessible to these particles.

The conductance in a single pore follows from the steady state Poiseuille flow in circular capillary [40], expressed as $k_1(r_p) = \pi r_p^4/8$. Comparison with Darcy's law leads to the following formula for permeability:

$$k[H] = \int_0^\infty k_1(r_p) H(r_p, x, t)\, dr_p. \tag{6}$$

The fractions of accessible and inaccessible fluxes are defined as the accessible and inaccessible fractional flow functions, respectively. The total flux of flow is the sum of the flux via accessible larger pores and that via inaccessible smaller pores, for any given particle size r_s. According to Darcy's law, the accessible fractional flow function can be calculated as fraction of accessible permeability

$$f_a[H, r_s] = \frac{1}{k} \int_{r_s}^\infty k_1(r_p) H(r_p, x, t)\, dr_p; \tag{7}$$

thus, the inaccessible fractional flow function is

$$f_{ns}[H, r_s] = 1 - f_a[H, r_s] = \frac{1}{k} \int_0^{r_s} k_1(r_p) H(r_p, x, t)\, dr_p. \tag{8}$$

The system of governing equations for suspension transport in porous media consists of the mass balance equation for particles and the kinetic equations for particle retention and pore plugging.

First, the conservation law for suspended and retained particles results in the advective-capture equation for suspended and retained concentrations in the following form:

$$\frac{\partial}{\partial t}\{\phi_a[H, r_s] C(r_s, x, t) + \Sigma(r_s, x, t)\} + U\frac{\partial}{\partial x}\{C(r_s, x, t) f_a[H, r_s]\} = 0. \tag{9}$$

Second, particle capture kinetics is obtained from the assumption that particle accumulation in the pores with given sizes is proportional to the particle flux through these pores:

$$\frac{\partial \Sigma(r_s, x, t)}{\partial t} = \frac{UC(r_s, x, t) f_a[H, r_s]}{lk[H]} \times \int_0^{r_s} k_1(r_p) H(r_p, x, t)\, dr_p. \tag{10}$$

The proportionality coefficient is equal to the capture probability per unit length of particle trajectory. The length parameter l is the distance between mixing chambers in the PTMC model [32, 41].

Third, under the assumption of complete plugging, one retained particle plugs one pore and vice versa. It allows deriving the following kinetic equation for pore concentration decrease due to particle size exclusion:

$$\frac{\partial H(r_p, x, t)}{\partial t} = -\frac{k_1(r_p)}{k} UH(r_p, x, t) \times \int_0^{r_s} C(r_s, x, t) f_a[H, r_s]\, dr_s. \tag{11}$$

The system of three governing equations (9)–(11) determines the suspended and retained particle concentration distributions along with the pore concentration distribution, C, Σ, and H. This completes the stochastic model for suspension transport in porous media with distributed pore and particle sizes.

In the next section, the microscale system of governing equations for suspension transport in porous media will be applied to the flow of monodispersed suspension, in which case the upscale equation system is derived and the analytical solution is obtained in macroscale.

3. Upscaling for Transport of Monodispersed Suspension

In the case of monodispersed suspension transport in porous media with arbitrary pore size distribution, the particle concentration distribution function can be expressed using the Dirac delta function δ: $C(r_s, x, t) = c(x, t)\delta(r_s - r_{s0})$, where r_{s0} is the particle size. Substitution of $C(r_s, x, t)$ into system (9)–(11) and integration in terms of r_s in (9) and (10) and r_p in (11) result in the following governing equations in macroscale:

$$\frac{\partial}{\partial t}\{\phi_a[H] c(x, t) + \sigma(x, t)\} + U\frac{\partial}{\partial x}\{c(x, t) f_a[H]\} = 0, \tag{12}$$

$$\frac{\partial \sigma(x, t)}{\partial t} = \frac{1}{l} f_a f_{ns}[H] c(x, t) U, \tag{13}$$

$$\frac{\partial h(x, t)}{\partial t} = -Uc(x, t) f_a f_{ns}[H] \equiv -l\frac{\partial \sigma(x, t)}{\partial t}. \tag{14}$$

Equation (14) indicates the conservation of the sum of volumetric concentrations of vacant pores and retained particles, $h/l + \sigma = h_0/l + \sigma_0$, which is exactly the mathematical form for the condition of complete pore plugging.

An implicit analytical solution for pore concentration distribution function $H(r_p, x, t)$ is derived with the uniform initial condition for H [32]: $t = 0 : H(r_p, x, t) = H_0(r_p)$. In this case, the solution $H(r_p, x, t)$ is equivalent to the solution

of an ordinary-differential-integral equation $H(r_p, y)$

$$H\left(r_p, y\right) = H_0\left(r_p\right) e^{-k_1 y}; \quad y = 0: \; H = H_0\left(r_p\right), \tag{15}$$

where the auxiliary function $y(h)$ is implicitly determined from the following problem as an inverse function [32]:

$$h\left(y\right) = \int_0^\infty H_0\left(r_p\right) e^{-k_1 y} dr_p; \quad y = 0: \; h = h_0. \tag{16}$$

The final form of governing equations for the transport of monosize particle suspension is obtained from the system (12)–(14) and the solution for pore concentration distribution function (15)-(16). Introduction of the dimensionless parameters $X = x/L$, $T = Ut/L\phi_0$, $C = c/c^0$, $S = \sigma/c^0\phi_0$, $\Lambda = Lf_a f_{ns}/l$, and $s = \phi_a/\phi_0$ leads to the following dimensionless form of governing equations:

$$\frac{\partial}{\partial T}\left\{s\left(S\right)C + S\right\} + \frac{\partial}{\partial X}\left\{Cf_a\left(S\right)\right\} = 0, \tag{17}$$

$$\frac{\partial S}{\partial T} = \Lambda\left(S\right)C. \tag{18}$$

The initial and boundary conditions for constant injection of suspension into clean porous media are $T = 0 : C = S = 0$; $X = 0 : C = 1$.

The system of (17)-(18), a type of the first-order hyperbolic system [42], contains functions of saturation, accessible fractional flow, and filtration, all of which depend on retained particle concentration in porous media. The analytical solution to the system (17)-(18) subject to the initial and boundary conditions will be presented in the next section.

4. Analytical Solution for Long-Term Monodispersed Suspension Transport

Derivation of the analytical solution starts from expressing the suspension concentration C from kinetic equation (18) in the following form:

$$C = \frac{1}{\Lambda\left(S\right)}\frac{\partial S}{\partial T}. \tag{19}$$

An auxiliary function $F(S)$ is introduced such that $C = \partial F(S)/\partial T$. Substitution into (19) leads to

$$F\left(S\right) = \int_0^S \frac{1}{\Lambda\left(u\right)} du. \tag{20}$$

Mass balance equation (17) is rewritten as

$$\frac{\partial}{\partial T}\left(s\left(S\right)\frac{\partial F\left(S\right)}{\partial T} + S\right) + \frac{\partial}{\partial X}\left(\frac{\partial F\left(S\right)}{\partial T} f_a\left(S\right)\right) = 0. \tag{21}$$

Rearranging the second term on the left side of (21)

$$\begin{aligned}\frac{\partial}{\partial X}\left(\frac{\partial F\left(S\right)}{\partial T} f_a\left(S\right)\right) &= \frac{\partial}{\partial X}\left(\frac{\partial F\left(S\right)}{\partial S}\frac{\partial S}{\partial T} f_a\left(S\right)\right) \\ &= \frac{\partial}{\partial X}\frac{\partial}{\partial T}\left(\int_0^S \frac{\partial F}{\partial S}\left(u\right) f_a\left(u\right) du\right) \\ &= \frac{\partial}{\partial T}\left(\frac{\partial F\left(S\right)}{\partial X} f_a\left(S\right)\right)\end{aligned} \tag{22}$$

and integrating (21) in terms of T result in

$$s\left(S\right)\frac{\partial F\left(S\right)}{\partial T} + S + \frac{\partial F\left(S\right)}{\partial X} f_a\left(S\right) = g\left(X\right), \tag{23}$$

where the function $g(X) = 0$ can be determined from the initial condition.

The first-order hyperbolic equation (23) has the characteristic lines satisfying the following equation:

$$\frac{dT}{dX} = \frac{s\left(S\right)}{f_a\left(S\right)}. \tag{24}$$

The first-order PDE (23) is degenerated to the first-order ODE along the characteristic lines (24)

$$\frac{dF\left(S\right)}{dX} = -\frac{S}{f_a\left(S\right)}. \tag{25}$$

From the boundary condition $C(0, T) = 1 = \partial F(S)/\partial T$, we have $X = 0 : F(S) = T$. Therefore, $F(S(0, T_0)) = T_0$ at arbitrary moment, T_0. This provides the solution for the initial retained particle concentration $S(0, T_0)$ at the moment T_0

$$\int_0^{S(0,T_0)} \frac{1}{\Lambda\left(S\right)} dS = T_0. \tag{26}$$

Subsequently, we obtain the retained particle concentration profile $S(X, T)$ by integration of the ODE (25) as follows:

$$\int_{S(X,T)}^{S(0,T_0)} \frac{f_a\left(S\right)}{S\Lambda\left(S\right)} dS = X. \tag{27}$$

Finally, the suspended particle concentration $C(X, T)$ is calculated from (19) by using the results of retained concentration profile $S(X, T)$ from (27)

$$C\left(X, T\right) = \frac{1}{\Lambda\left(S\right)}\frac{\partial S\left(X, T\right)}{\partial T}. \tag{28}$$

So far, the exact solution for long-term transport of monodispersed suspension in porous media has been derived. Application of the proposed model to a synthetic medium will be demonstrated in the next section.

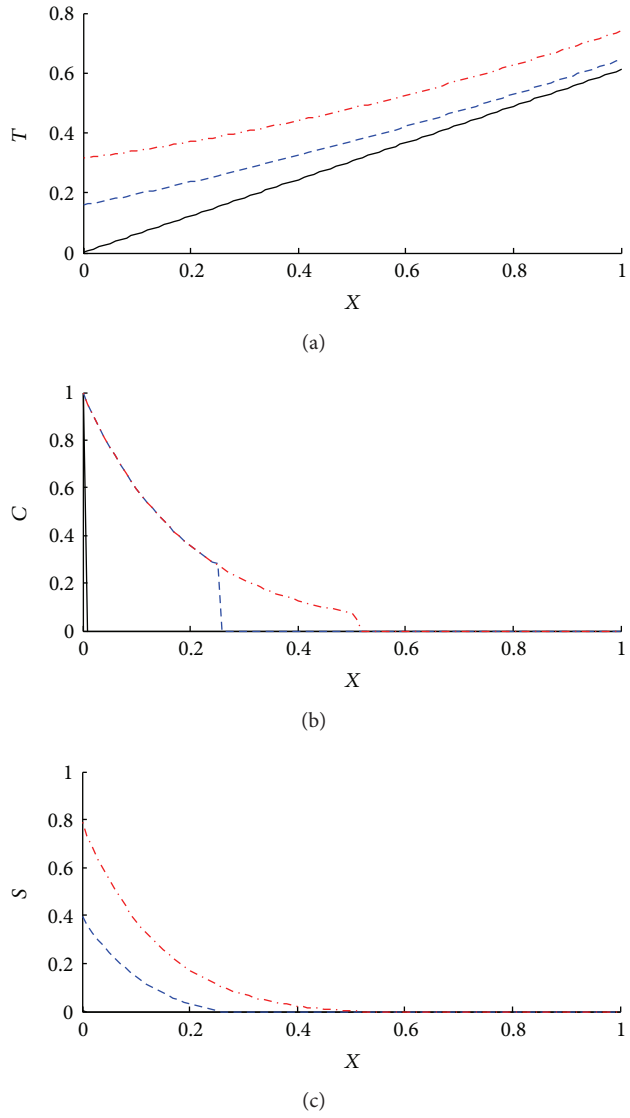

Figure 2: The exact solution for 1D deep bed filtration long-term injection problem: (a) characteristic lines and the concentration front in (X,T)-plane; (b) shock front in the suspended concentration profile; (c) continuous retention concentration profile.

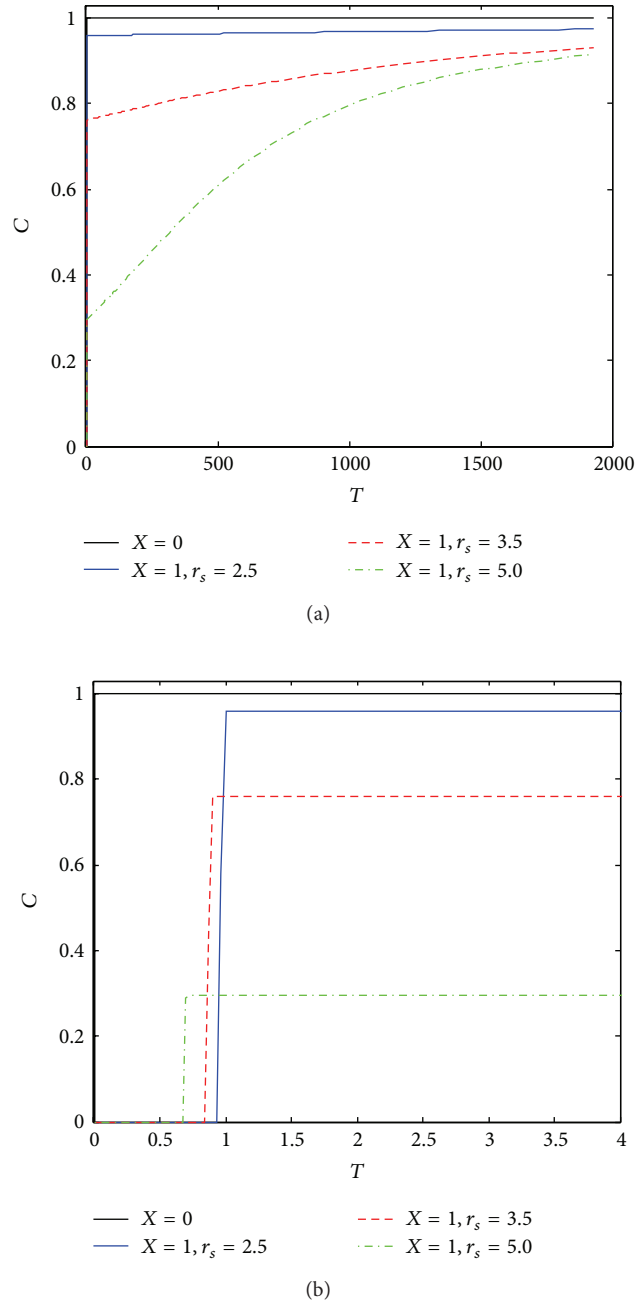

Figure 3: Suspended particle concentration at the core inlet and outlet: (a) full time scale history; (b) zoom-in at the early stage.

5. Results and Discussions

In this section, the analytical solution derived in Section 4 is applied to a synthetic example of porous medium. The solution behaviour is analysed in detail.

Let us start from the structure of the flow pattern, shown in Figure 2. At the beginning of the suspension injection (black curves in Figure 2), the suspended particle concentration C drops from unity to zero at $X = 0$ and the retained particle concentration S is zero everywhere, according to the initial and boundary conditions. Both the saturation s and the fractional flow function f_a are constant; therefore, the characteristic curve is straight line at $T = 0$ based on (24). When the time $T > 0$, the concentration front starts propagating from inlet $X = 0$ along the core. In Figure 2, the blue dashed curves present an early stage and the red dash-dot curves correspond to a later moment. It is shown that particle concentrations C and S decrease along the distance X behind the concentration front while remain zero ahead of the front. The characteristic curve deviates from straight line when $T > 0$. The larger the time, the higher the nonlinearity.

Consider the porous medium with a log-normal pore size distribution, with the mean pore radius 4 μm and the

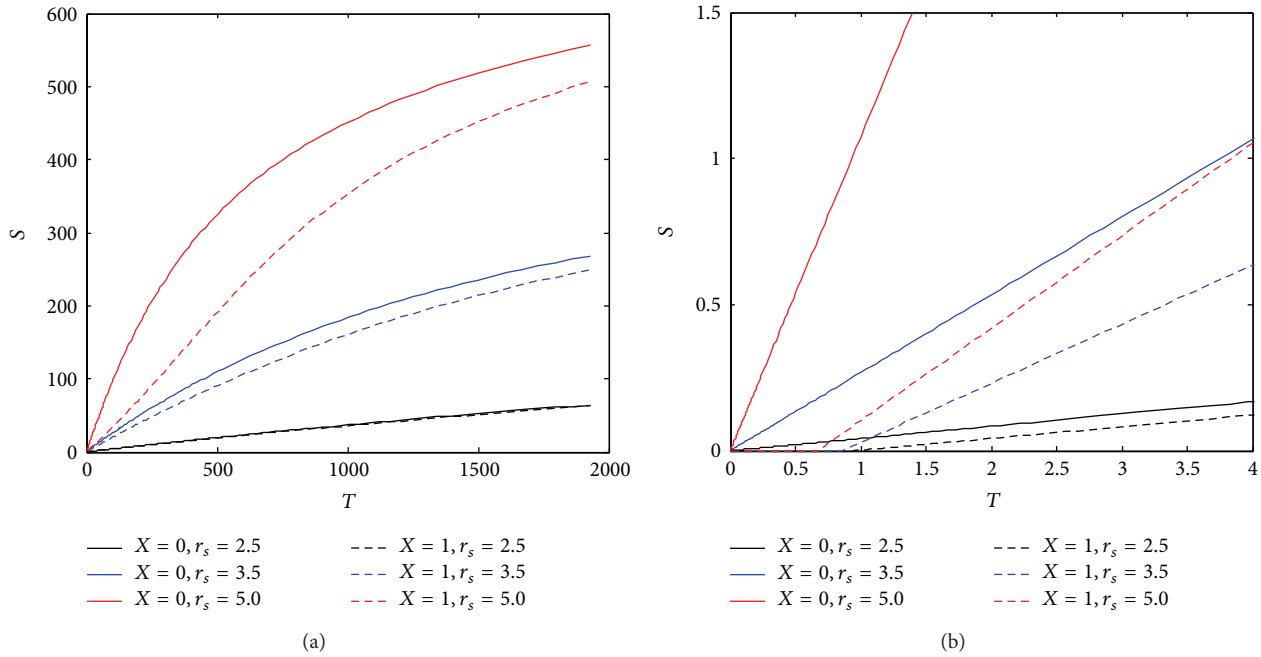

FIGURE 4: Captured particle concentration at the inlet and outlet: (a) full time scale history; (b) zoom in at the early stage.

standard deviation 2 μm. Three monodispersed suspensions are injected into the medium separately, with particle sizes 2.5, 3.5, and 5.0 μm, respectively. Suspended particle concentration profiles $C(X,T)$ are calculated from the analytical solution derived in Section 4. Figure 3(a) shows the inlet concentration $C(0,T)$ and outlet concentrations for different particle sizes $C(1,T)$ in full scale. Figure 3(b) focuses on the early stage around the breakthrough moment. It is found that particle breakthrough occurs at $T < 1$ pvi; the increase of particle size results in earlier breakthrough but lower breakthrough concentration. After breakthrough, there is a plateau of outlet concentration at small time (Figure 3(b)); then $C(1,T)$ increases gradually and approaches unity asymptotically at large time (Figure 3(a)).

The retained particle concentration profile S is presented in Figure 4. The profiles $S(0,T)$ at the inlet and $S(1,T)$ at the outlet for three particle sizes are illustrated in Figure 4(a); while the zoom in at early stage is in Figure 4(b) for comparison. Particle retention at the inlet starts from $T = 0$, increasing linearly with time at the early stage (Figure 4(b)). Compared to the deposition profile $S(0,T)$ at the inlet, the profile $S(1,T)$ at the outlet exhibits a delay (Figure 4(b)) due to the time required for particle travelling from inlet to outlet. The larger the particle size, the smaller the delay, indicating the earlier breakthrough for large particles, which agrees with the results shown in Figure 3. In the long time span (Figure 4(a)), the retained particle concentration increases nonlinearly with time and asymptotically approaches the maximum, which is equal to the overall concentration of pores smaller than the particle.

Figure 5 compares the evolution of the pore concentration distribution for different particle sizes. At $T = 0$, $H = H_0(r_p)$ for all three particle sizes (black curves in Figures 5(a)–5(c)). When $T > 0$, $H(r_p, X, T)$ decreases with time for smaller pores ($r_p < r_s$) due to particle size exclusion; while H keeps intact for $r_p > r_s$, which means larger pores are always accessible to the particles. The pores with intermediate sizes between the minimum pore size and the particle size vanish faster with time than the smaller pores. It is because the accessible suspension flux via intermediate pores is higher than that via small pores, which leads to the larger capture rate in intermediate pores. Finally, all the pores smaller than the particle size will disappear when the time tends to infinity, which corresponds to the full plugging of small pores by the particles.

In Figure 6, the nonlinear relationship between the filtration coefficient and the retained particle concentration is presented for different particle sizes. For the same value of retained particle concentration, the larger particle size leads to the larger filtration coefficient. With the particle size fixed, the higher retention concentration causes the filtration function to deviate from the linearity, where the low retention assumption is no longer valid [41].

Fractional flow function curve obtained from PTMC model is given in Figure 7. The increase of particle size results in the decrease of both accessible porosity and accessible flow fraction. The convex shape of the curve implies that the ratio of f_a/s increases with particle size, which corresponds to the rise of propagation speed of concentration front. It is in agreement with the results presented in Figures 3 and 4.

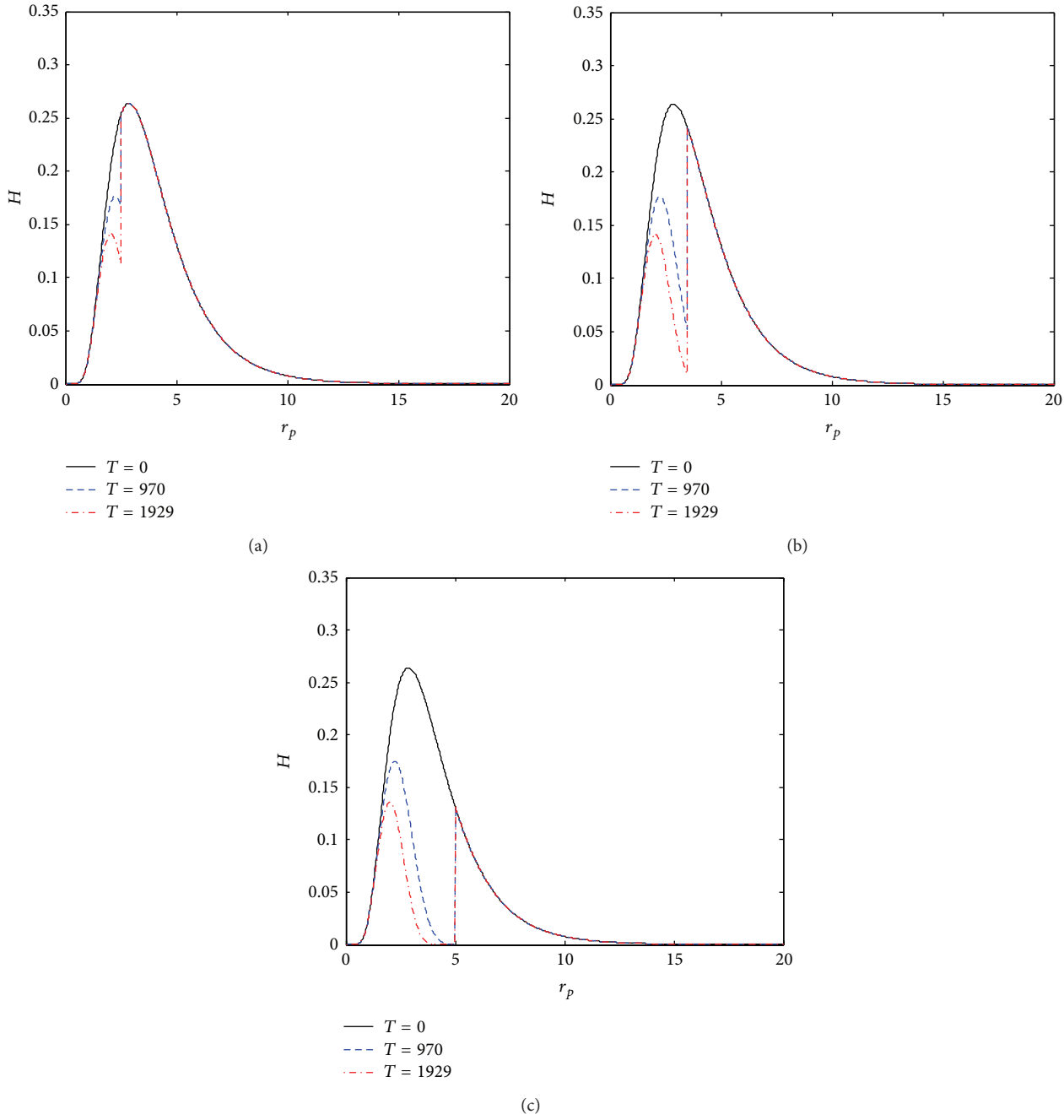

Figure 5: Evolution of the pore size distribution for different sizes of injected particles: (a) $r_s = 2.5\,\mu$m; (b) $r_s = 3.5\,\mu$m; (c) $r_s = 5.0\,\mu$m.

The geometrical model of parallel capillaries intercalated by mixing chambers adopted in the current work, results in connective set of pores for any arbitrary particle size $r_s > 0$. However, this is not the case for the real geometry of porous space. The pores smaller than the threshold value do not form an infinite cluster. The threshold effect is described by the percolation model of porous media [43–45]. Percolation description of porous space with corresponding calculations of accessibility and flux reduction factors will significantly change the form of fractional flow curve [32] and affect the solution.

The majority of deep bed filtration processes in the nature and in industry do not long as far as asymptotic stabilisation without capture. Nevertheless, these processes last longer than short-term periods of linear deep bed filtration with constant filtration coefficient [41]. The linear deep bed filtration corresponds to the case of invariant pore size distribution. This is an asymptotic case where the concentration of retained particles is negligibly smaller than the number of initial vacant pores. More exactly, the linear solution is the zero term in asymptotic expansion. The expansion could correspond to small injected concentration,

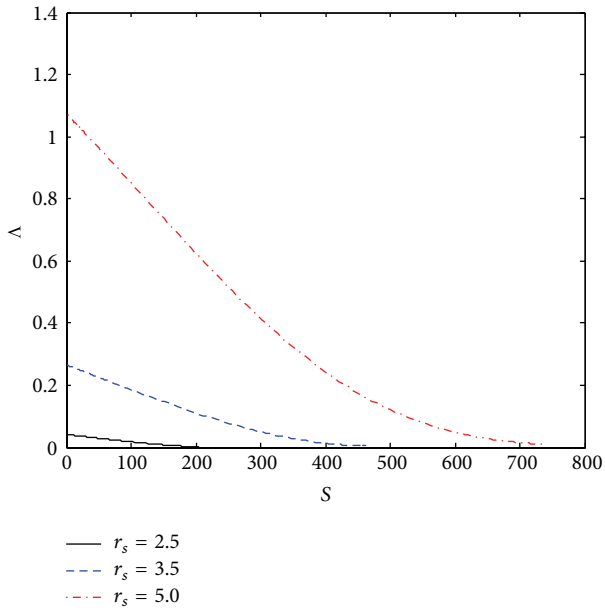

Figure 6: Filtration coefficient as function of captured particle concentration.

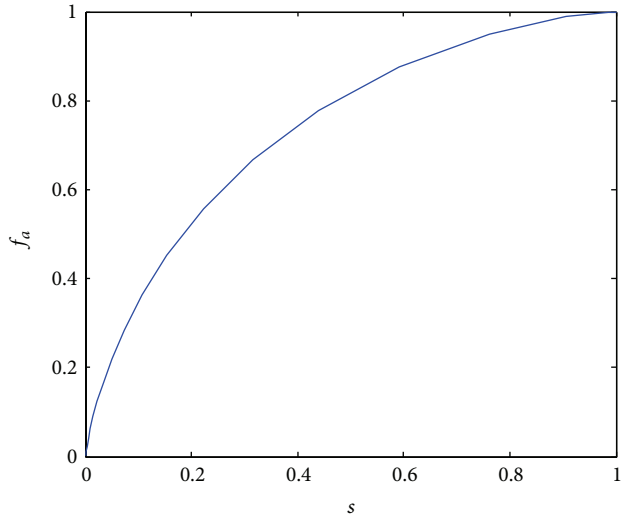

Figure 7: Fractional flow function for accessible flow.

or small filtration coefficient, or small times. Asymptotic solution including first term of the expansion would provide more detailed description of the intermediate stage of deep bed filtration. It is expected that the effect of full plugging of intermediate size pores (Figure 5) would be captured by the first term of asymptotic expansion.

6. Conclusions

Derivation of the exact solution for long-term deep bed filtration with accessibility and flux reduction allows drawing the following conclusions.

The exact solution of the upscaled problem allows for downscaling, exhibiting the dynamics for pore size distributions during the continuous particle straining.

The exact solution exhibits preferential plugging of pores with sizes equal to or below the injected particle size. The pores with radius equal to the injected particle radius disappear first. Then the smaller pores start to disappear in the sequence of their sizes. The radius interval of disappearing sizes increases with time. The lower bound of the interval turns to zero asymptotically when time tends to infinity, which corresponds to complete plugging of pores smaller than the particle size.

The larger the injected particles, the faster the breakthrough and the lower the breakthrough concentration. However, the breakthrough concentrations of all size particles tend to one with time tending to infinity, which corresponds to complete plugging of smaller pores and capture-free transport via the larger pores.

The above are the consequences of the geometric porous space model with parallel tubes, which also results in the convex fractional flow function.

Acknowledgments

The authors thank Professor Alexander Shapiro (Technical University of Denmark) for long-term cooperation on stochastic modelling of deep bed filtration. Especial thanks are due to Drs. Alex Badalyan and Themis Carageorgos (ASP) for the firm support and encouragement. The privilege of scientific contacts with Professor Y. Osipov (Moscow Civil Engineering University) and discussions of asymptotical nonlinear analysis are gratefully acknowledged.

References

[1] G. I. Barenblatt, V. M. Entov, and V. M. Ryzhik, *Theory of Fluid Flows Through Natural Rocks*, Kluwer Academic, Dordrecht, The Netherlands, 1990.

[2] P. Bedrikovetsky, *Mathematical Theory of Oil and Gas Recovery: With Applications to Ex-USSR Oil and Gas Fields*, Kluwer Academic, Dordrecht, The Netherlands, 1993.

[3] K. C. Khilar and H. S. Fogler, *Migrations of Fines in Porous Media*, Kluwer Academic, Dordrecht, The Netherlands, 1998.

[4] F. Civan, *Reservoir Formation Damage: Fundamentals, Modeling, Assessment, and Mitigation*, Gulf Professional, Amsterdam, The Netherlands, 2nd edition, 2007.

[5] J. M. Schembre and A. R. Kovscek, "Mechanism of formation damage at elevated temperature," *Journal of Energy Resources Technology, Transactions of the ASME*, vol. 127, no. 3, pp. 171–180, 2005.

[6] F. Civan, "Non-isothermal permeability impairment by fines migration and deposition in porous media including dispersive transport," *Transport in Porous Media*, vol. 85, no. 1, pp. 233–258, 2010.

[7] Z. You, A. Badalyan, and P. Bedrikovetsky, "Size-exclusion colloidal transport in porous media-stochastic modeling and experimental study," *SPE Journal*, vol. 18, pp. 620–633, 2013.

[8] D. C. Mays and J. R. Hunt, "Hydrodynamic aspects of particle clogging in porous media," *Environmental Science and Technology*, vol. 39, no. 2, pp. 577–584, 2005.

[9] D. C. Mays and J. R. Hunt, "Hydrodynamic and chemical factors in clogging by montmorillonite in porous media," *Environmental Science and Technology*, vol. 41, no. 16, pp. 5666–5671, 2007.

[10] C. Tien and B. V. Ramarao, *Granular Filtration of Aerosols and Hydrosols*, Elsevier, Amsterdam, The Netherlands, 2nd edition, 2007.

[11] P. Baveye, P. Vandevivere, B. L. Hoyle, P. C. DeLeo, and D. Sanchez De Lozada, "Environmental impact and mechanisms of the biological clogging of saturated soils and aquifer materials," *Critical Reviews in Environmental Science and Technology*, vol. 28, no. 2, pp. 123–191, 1998.

[12] M. Vidali, "Bioremediation. An overview," *Pure and Applied Chemistry*, vol. 73, no. 7, pp. 1163–1172, 2001.

[13] A. I. Packman and J. S. MacKay, "Interplay of stream-subsurface exchange, clay particle deposition, and streambed evolution," *Water Resources Research*, vol. 39, no. 4, pp. ESG41–ESG49, 2003.

[14] K.-M. Yao, M. T. Habibian, and C. R. O'Melia, "Water and waste water filtration: concepts and applications," *Environmental Science and Technology*, vol. 5, no. 11, pp. 1105–1112, 1971.

[15] M. Elimelech, X. Jia, J. Gregory, and R. Williams, *Particle Deposition and Aggregation: Measurement, Modelling and Simulation*, Butterworth-Heinemann, Oxford, UK, 1995.

[16] W. J. Weiss, E. J. Bouwer, R. Aboytes et al., "Riverbank filtration for control of microorganisms: results from field monitoring," *Water Research*, vol. 39, no. 10, pp. 1990–2001, 2005.

[17] N. Tufenkji, D. R. Dixon, R. Considine, and C. J. Drummond, "Multi-scale Cryptosporidium/sand interactions in water treatment," *Water Research*, vol. 40, no. 18, pp. 3315–3331, 2006.

[18] J. Y. Shin, R. F. Spinette, and C. R. O'Melia, "Stoichiometry of coagulation revisited," *Environmental Science and Technology*, vol. 42, no. 7, pp. 2582–2589, 2008.

[19] S. Torkzaban, J. Wan, T. K. Tokunaga, and S. A. Bradford, "Impacts of bridging complexation on the transport of surface-modified nanoparticles in saturated sand," *Journal of Contaminant Hydrology*, vol. 136-137, pp. 86–95, 2012.

[20] S. A. Bradford, S. Torkzaban, and A. Shapiro, "A theoretical analysis of colloid attachment and straining in chemically heterogeneous porous media," *Langmuir*, vol. 29, pp. 6944–6952, 2013.

[21] J. P. Herzig, D. M. Leclerc, and P. Legoff, "Flow of suspensions through porous media—application to deep filtration," *Industrial and Engineering Chemistry*, vol. 62, no. 5, pp. 8–35, 1970.

[22] L. M. McDowell-Boyer, J. R. Hunt, and N. Sitar, "Particle transport through porous media," *Water Resources Research*, vol. 22, no. 13, pp. 1901–1921, 1986.

[23] J. N. Ryan and M. Elimelech, "Colloid mobilization and transport in groundwater," *Colloids and Surfaces A*, vol. 107, pp. 1–56, 1996.

[24] J. F. Schijven and S. M. Hassanizadeh, "Removal of viruses by soil passage: overview of modeling, processes, and parameters," *Critical Reviews in Environmental Science and Technology*, vol. 30, no. 1, pp. 49–127, 2000.

[25] T. K. Sen and K. C. Khilar, "Review on subsurface colloids and colloid-associated contaminant transport in saturated porous media," *Advances in Colloid and Interface Science*, vol. 119, no. 2-3, pp. 71–96, 2006.

[26] S. A. Bradford and S. Torkzaban, "Colloid transport and retention in unsaturated porous media: a review of interface-, collector-, and pore-scale processes and models," *Vadose Zone Journal*, vol. 7, no. 2, pp. 667–681, 2008.

[27] J. S. Chang, S. Vigneswaran, J. K. Kandasamy, and L. J. Tsai, "Effect of pore size and particle size distribution on granular bed filtration and microfiltration," *Separation Science and Technology*, vol. 43, no. 7, pp. 1771–1784, 2008.

[28] D. Lin, X. Tian, F. Wu, and B. Xing, "Fate and transport of engineered nanomaterials in the environment," *Journal of Environmental Quality*, vol. 39, no. 6, pp. 1896–1908, 2010.

[29] T. K. Sen, "Processes in pathogenic biocolloidal contaminants transport in saturated and unsaturated porous media: a review," *Water, Air, and Soil Pollution*, vol. 216, no. 1–4, pp. 239–256, 2011.

[30] A. C. Payatakes, R. Rajagopalan, and C. Tien, "Application of porous media models to the study of deep bed filtration," *The Canadian Journal of Chemical Engineering*, vol. 52, pp. 722–731, 1974.

[31] F. Kuhnen, K. Barmettler, S. Bhattacharjee, M. Elimelech, and R. Kretzschmar, "Transport of iron oxide colloids in packed quartz sand media: monolayer and multilayer deposition," *Journal of Colloid and Interface Science*, vol. 231, no. 1, pp. 32–41, 2000.

[32] P. Bedrikovetsky, "Upscaling of stochastic micro model for suspension transport in porous media," *Transport in Porous Media*, vol. 75, no. 3, pp. 335–369, 2008.

[33] A. A. Shapiro and P. G. Bedrikovetsky, "Elliptic random-walk equation for suspension and tracer transport in porous media," *Physica A*, vol. 387, no. 24, pp. 5963–5978, 2008.

[34] A. A. Shapiro and P. G. Bedrikovetsky, "A stochastic theory for deep bed filtration accounting for dispersion and size distributions," *Physica A*, vol. 389, no. 13, pp. 2473–2494, 2010.

[35] M. M. Sharma and Y. C. Yortsos, "Transport of particulate suspensions in porous media: model formulation," *AIChE Journal*, vol. 33, no. 10, pp. 1636–1643, 1987.

[36] M. M. Sharma and Y. C. Yortsos, "Network model for deep bed filtration processes," *AIChE Journal*, vol. 33, no. 10, pp. 1644–1653, 1987.

[37] M. M. Sharma and Y. C. Yortsos, "Fines migration in porous media," *AIChE Journal*, vol. 33, no. 10, pp. 1654–1662, 1987.

[38] A. Santos and P. Bedrikovetsky, "A stochastic model for particulate suspension flow in porous media," *Transport in Porous Media*, vol. 62, no. 1, pp. 23–53, 2006.

[39] A. A. Shapiro, P. G. Bedrikovetsky, A. Santos, and O. O. Medvedev, "A stochastic model for filtration of particulate suspensions with incomplete pore plugging," *Transport in Porous Media*, vol. 67, no. 1, pp. 135–164, 2007.

[40] L. D. Landau and E. M. Lifshitz, *Fluid Mechanics*, Pergamon Press, Oxford, UK, 2nd edition, 1987.

[41] P. Chalk, N. Gooding, S. Hutten, Z. You, and P. Bedrikovetsky, "Pore size distribution from challenge coreflood testing by colloidal flow," *Chemical Engineering Research and Design*, vol. 90, no. 1, pp. 63–77, 2012.

[42] A. P. Pires and P. G. Bedrikovetsky, "First-order hyperbolic systems of quasilinear equations: systems of conservation laws of gas dynamic type," in *Handbook of NonlInear Partial Differential Equations*, A. D. Polyanin and V. F. Zaitzev, Eds., pp. 1607–1620, Chapman & Hall, Boca Raton, Fla, USA, 2nd edition, 2012.

[43] V. I. Selyakov and V. V. Kadet, *Percolation Models for Transport in Porous Media with Applications to Reservoir Engineering*, Kluwer Academic, Dordrecht, The Netherlands, 1996.

[44] H. Yuan, A. Shapiro, Z. You, and A. Badalyan, "Estimating filtration coefficients for straining from percolation and random walk theories," *Chemical Engineering Journal*, vol. 210, pp. 63–73, 2012.

[45] H. Yuan, Z. You, A. Shapiro, and P. Bedrikovetsky, "Improved population balance model for straining-dominant deep bed filtration using network calculations," *Chemical Engineering Journal*, vol. 226, pp. 227–237, 2013.

Hindawi Publishing Corporation
Abstract and Applied Analysis
Volume 2013, Article ID 490123, 6 pages
http://dx.doi.org/10.1155/2013/490123

Research Article

The Fundamental Aspects of TEMOM Model for Particle Coagulation due to Brownian Motion—Part II: In the Continuum Regime

He Qing and Xie Mingliang

State Key Laboratory of Coal Combustion, Huazhong University of Science and Technology, Wuhan 430074, China

Correspondence should be addressed to Xie Mingliang; mlxie@mail.hust.edu.cn

Received 24 August 2013; Revised 13 November 2013; Accepted 3 December 2013

Academic Editor: Shuyu Sun

The fundamental aspects of the Taylor-series expansion method of moment (TEMOM) model proposed to model the aerosol population balance equation due to Brownian coagulation in the continuum regime is shown in this study, such as the choice of the expansion point u, the relationship between asymptotic behavior and analytical solution, and the error of the high-order moment equations. All these analyses will contribute to the buildup of the theoretical system of the TEMOM model.

1. Introduction

The population balance equations (PBE) are used to describe the evolution process of aerosol particles in a wide range of physical, chemical, and environmental subjects, such as nucleation, coagulation, diffusion, convection, and so on. When the Brownian coagulation plays a dominant role in such cases where aerosol particles at a high concentration are concerned or where suspended particles have evolved for a long time [1], the PBE for a monovariants system can be written as [2]

$$\frac{\partial n(v,t)}{\partial t} = \frac{1}{2}\int_0^v \beta(v_1, v-v_1)\, n(v_1,t)\, n(v-v_1,t)\, dv_1 - \int_0^\infty \beta(v_1,v)\, n(v,t)\, n(v_1,t)\, dv_1, \quad (1)$$

in which $n(v,t)$ is the number density concentrations of the particles with volume from v to $v+dv$ at time t, $\beta(v,v_1)$ is the collision frequency function between particles with volumes v and v_1.

Because of its strong nonlinear partial integral-differential structure, the direct solution is very complicated and only a limited number of analytical solutions exist for simple coagulation kernel [3]. So several methods are proposed to solve this equation numerically, such as the sectional method (SM) [4], the Monte Carlo method (MCM) [5], and the method of moment (MM) [6]. With lower computational cost compared to the SM and MCM, the moment method has been widely used and become a powerful tool for investigating evolution processes of aerosol particles [7, 8].

By multiplying v^k both the sides of (1) then integrating over the entire particle size distribution (PSD) [9], the growth rate of the particle moment can be obtained as follows:

$$\frac{dM_k}{dt} = \frac{1}{2}\iint_0^\infty \left[(v+v_1)^k - v^k - v_1^k\right] \times \beta(v,v_1)\, n(v,t)\, n(v_1,t)\, dv\, dv_1, \quad (k=0,1,2,\ldots), \quad (2)$$

where the moment M_k is defined as

$$M_k = \int_0^\infty v^k n(v)\, dv. \quad (3)$$

One main difficulty of the moment method is the closure of the moment equations. There exist several methods to overcome this bottleneck, including but not limited to the quadrature method of moment (QMOM) [10], the direct quadrature

method of moment (DQMOM) [11], and the Taylor-series expansion method of moment (TEMOM) [3, 12].

It should be pointed out that the TEMOM has no prior assumption for the PSD using the Taylor-series expansion to achieve the closure and is considered as a promising approach to approximate the PBE for its relative simplicity of implementation and high accuracy [13]. Based on TEMOM model, the important information about the PSD, namely, the particle number density, particle mass, and geometric standard deviation, can be obtained for Brownian coagulation over the entire size regimes, and its results have a great agreement with other moment methods [3, 12–16]. But in these works, some fundamental problems are not clarified, for example, why the expansion point u is set to be M_1/M_0 instead of other formulas; why the Taylor-series are truncated just at the first three terms; and what about the errors estimation of the present TEMOM model. In the present study, mainly as a methodological introduction, we would like to demonstrate the theoretical analysis to answer these questions for Brownian coagulation in the continuum regime.

2. Brief Review of TEMOM Model and Its Solutions in the Continuum Regime

At the initial time, the particle size maybe small in the free molecule regime. As time advances, the particle volume will grow due to coagulation between particles, and the particle size will transform to the near continuum regime via the transition regime and finally will tend to the continuum regime [17]. Therefore, the characteristic of particle evolution in the continuum regime is important to understand the coagulation mechanism. The collision frequency function β in the continuum regime is

$$\beta = B_2\left(\frac{1}{v^{1/3}} + \frac{1}{v_1^{1/3}}\right)\left(v^{1/3} + v_1^{1/3}\right), \tag{4}$$

where the constant $B_2 = 3k_BT/2\mu$, k_B is the Boltzmann's constant, T is temperature, and μ is gas viscosity. Substituting (4) into (2), a set of moment equations including integral and fractional moments can be obtained. Using a Taylor-series expansion at $v = u = M_1/M_0$ for v^k, the fractional moments can be approximated by the combination of integral moments as follows:

$$\begin{aligned} v^k &= u^k + u^{k-1}k\,(v-u) \\ &\quad + \frac{u^{k-2}k\,(k-1)}{2}(v-u)^2 \\ &\quad + \frac{u^{k-3}k\,(k-1)\,(k-2)}{3!}(v-u)^3 + \cdots; \end{aligned} \tag{5}$$

then the closure of the moment equations will be achieved automatically without any prior assumption about the particle size spectrum. The minimum number of moments for closing the equations is the first three-order moments M_0, M_1, and M_2, which represents or are proportional to the total particle number concentration, and the total particle mass concentration, the total scattering light, respectively. According to the results derived by Yu et al. [3] and Xie and Wang [18], the equations can be rearranged as follows:

$$\begin{aligned} \frac{dM_0}{dt} &= \frac{B_2\left(2M_C^2 - 13M_C - 151\right)M_0^2}{81}, \\ \frac{dM_1}{dt} &= 0, \\ \frac{dM_2}{dt} &= -\frac{2B_2\left(2M_C^2 - 13M_C - 151\right)M_1^2}{81}, \end{aligned} \tag{6}$$

where the dimensionless moment M_C is defined as

$$M_C = \frac{M_0M_2}{M_1^2}. \tag{7}$$

It is clear that M_1 remains constant due to the rigorous mass conservation requirement, and its initial conditions can be noted as M_{00}, M_{20}, and $M_{C0} = M_{00}M_{20}/M_1^2$. Equations in (6) are a set of ordinary differential equations and can be solved directly. The main process is described briefly as follows. Because of the same structures of the first and the third equations in (6), the following relationship can be obtained:

$$\frac{dM_2}{dM_0} = \frac{-2M_1^2}{M_0^2}. \tag{8}$$

This equation can be dissolved directly as follows:

$$M_2 = \frac{2M_1^2}{M_0} + C_1M_1^2, \qquad C_1 = \frac{M_{20}}{M_1^2} - \frac{2}{M_{00}}, \tag{9}$$

where C_1 is the integration constant, and the dimensionless moment M_C can be expressed as

$$M_C = 2 + M_0C_1. \tag{10}$$

Then substituting (10) into the first formula in (6), the relationship between M_0 and t can be obtained:

$$\begin{aligned} &5\ln M_0 + \frac{169}{C_1M_0} - \frac{5}{2}\ln\left|169 + 5C_1M_0 - 2C_1^2M_0^2\right| \\ &\quad - \frac{701}{9\sqrt{17}}\operatorname{arctanh}\frac{\left|4C_1M_0 - 5\right|}{9\sqrt{17}} = \frac{13^4B_2}{3^4C_1}t + C_2, \\ &C_2 = 5\ln M_{00} + \frac{169}{C_1M_{00}} - \frac{5}{2}\ln\left|169 + 5C_1M_{00} - 2C_1^2M_{00}^2\right| \\ &\quad - \frac{701}{9\sqrt{17}}\operatorname{arctanh}\frac{\left|4C_1M_{00} - 5\right|}{9\sqrt{17}}, \end{aligned} \tag{11}$$

in which C_2 is the integration constant. Then the second moment M_2 and dimensionless particle moment M_C can be calculated by (9) and (10), respectively. As time advances, M_0 tends to zero due to coagulation; (11) can be simplified with some limit operation as

$$\lim_{M_0 \to 0}\frac{1}{M_0} = \lim_{t \to \infty}\frac{169B_2}{81}t, \tag{12}$$

which is consistent with the asymptotic analysis shown by Xie et al. [18, 19].

3. The Choice of Expansion Point u

In the TEMOM model, the choice of the expansion point at $u = M_1/M_0$ is not arbitrary. Some researchers think that the expansion for the characteristic size should take account of dispersion in the size spectrum and that is best done by using the well-known log-normal based expression $u = M_0^{-3/2} M_1^2 M_2^{-1/2}$ in a second order closure formalism [6]. Using the expansion point, the corresponding moment equations based on TEMOM in the continuum regime are rewritten as

$$\begin{aligned}
&\frac{dM_0}{dt} \\
&= -\frac{B_2 M_0^2 \left(-2M_C^4 + 17M_C^{5/2} - 4M_C^2 - 35M_C + 35M_C^{1/2} + 151\right)}{81}, \\
&\frac{dM_1}{dt} = 0, \\
&\frac{dM_2}{dt} \\
&= -\frac{2B_2 M_1^2 \left(2M_C^4 - 8M_C^{5/2} - 5M_C^2 - 145M_C - 8M_C^{1/2} + 2\right)}{81M_C}.
\end{aligned} \tag{13}$$

The detailed derivation is provided in the appendix. The comparison of numerical results between (6) and (13) is shown in Figure 1. And the initial conditions are selected as lognormal distribution: $M_{00} = 1$; $M_1 = 1$; $M_{20} = 4/3$. The results show that the relative errors are small, and the two sets of equations are equivalent approximately. However, this selection results in more complicated moment equations. In fact, for any expression, when it is operated using the Taylor expansion technique, the selection of the expansion point is not unique. In mathematics, we only need to make sure in the targeted range than the Taylor-series expansion is convergent, and the final constructed moment equations are simple in the form. From this viewpoint, the selection of $u = M_0^{-3/2} M_1^2 M_2^{-1/2}$ cannot be considered to be prior to the selection of $u = M_1/M_0$.

4. The High-Order Moment Equations

The accuracy of the TEMOM model largely depends on the truncation errors of Taylor-series expansion. One method to determine the truncated errors is comparing the results of different TEMOM models, for example, the first three-moment model, the first four-moment model, the first five-moment model, and so forth. Similar to the derivation of the first three moment equations, v^k is expanded at $v = u$ and truncated at the first four terms as

$$\begin{aligned}
v^k = {} & u^k + u^{k-1} k (v-u) \\
& + \frac{u^{k-2} k (k-1)}{2} (v-u)^2 \\
& + \frac{u^{k-3} k (k-1)(k-2)}{3!} (v-u)^3 + \cdots;
\end{aligned} \tag{14}$$

then the closed first four-moment equations can be obtained as follows:

$$\begin{aligned}
\frac{dM_0}{dt} = {} & \frac{B_2}{6561} \left(\frac{70M_0^6 M_3^2}{M_1^6} - \frac{636M_0^5 M_3 M_2}{M_1^5} \right. \\
& + \frac{1440M_0^4 M_2^2}{M_1^4} + \frac{1225M_0^4 M_3}{M_1^3} \\
& \left. - \frac{5160M_0^3 M_2}{M_1^2} - 10061M_0^2 \right), \\
\frac{dM_1}{dt} = {} & 0, \\
\frac{dM_2}{dt} = {} & \frac{B_2}{6561} \left(\frac{-32M_0^4 M_3^2}{M_1^4} + \frac{408M_0^3 M_3 M_2}{M_1^3} \right. \\
& - \frac{1260M_0^2 M_2^2}{M_1^2} - \frac{344M_0^2 M_3}{M_1} \\
& \left. + 3570M_0 M_2 + 23902M_1^2 \right), \\
\frac{dM_3}{dt} = {} & \frac{B_2}{2187} \left(\frac{76M_0^3 M_3^2}{M_1^3} - \frac{348M_0^2 M_3 M_2}{M_1^2} \right. \\
& + 925M_3 M_0 + \frac{36M_0 M_2^2}{M_1} \\
& \left. + 25791M_1 M_2 - \frac{236M_1^3}{M_0} \right);
\end{aligned} \tag{15}$$

with the same process, the closed first five-moment equations are

$$\begin{aligned}
&\frac{dM_0}{dt} \\
&= \frac{B_2 M_0^2}{59049 M_1^8} \\
&\quad \times \left(-59049M_1^8 + 8520M_0^4 M_4 M_2 M_1^2 \right. \\
&\qquad - 11550M_0^3 M_4 M_1^4 \\
&\qquad - 45474M_0^3 M_3 M_2 M_1^3 + 60060M_0^2 M_3 M_1^5 \\
&\qquad - 128700M_0 M_2 M_1^6 - 3745M_0^5 M_4 M_3 M_1 \\
&\qquad + 51480M_0^2 M_2^2 M_1^4 + 350M_0^6 M_4^2 \\
&\qquad \left. + 10010M_0^4 M_3^2 M_1^2 \right), \\
&\frac{dM_1}{dt} = 0,
\end{aligned}$$

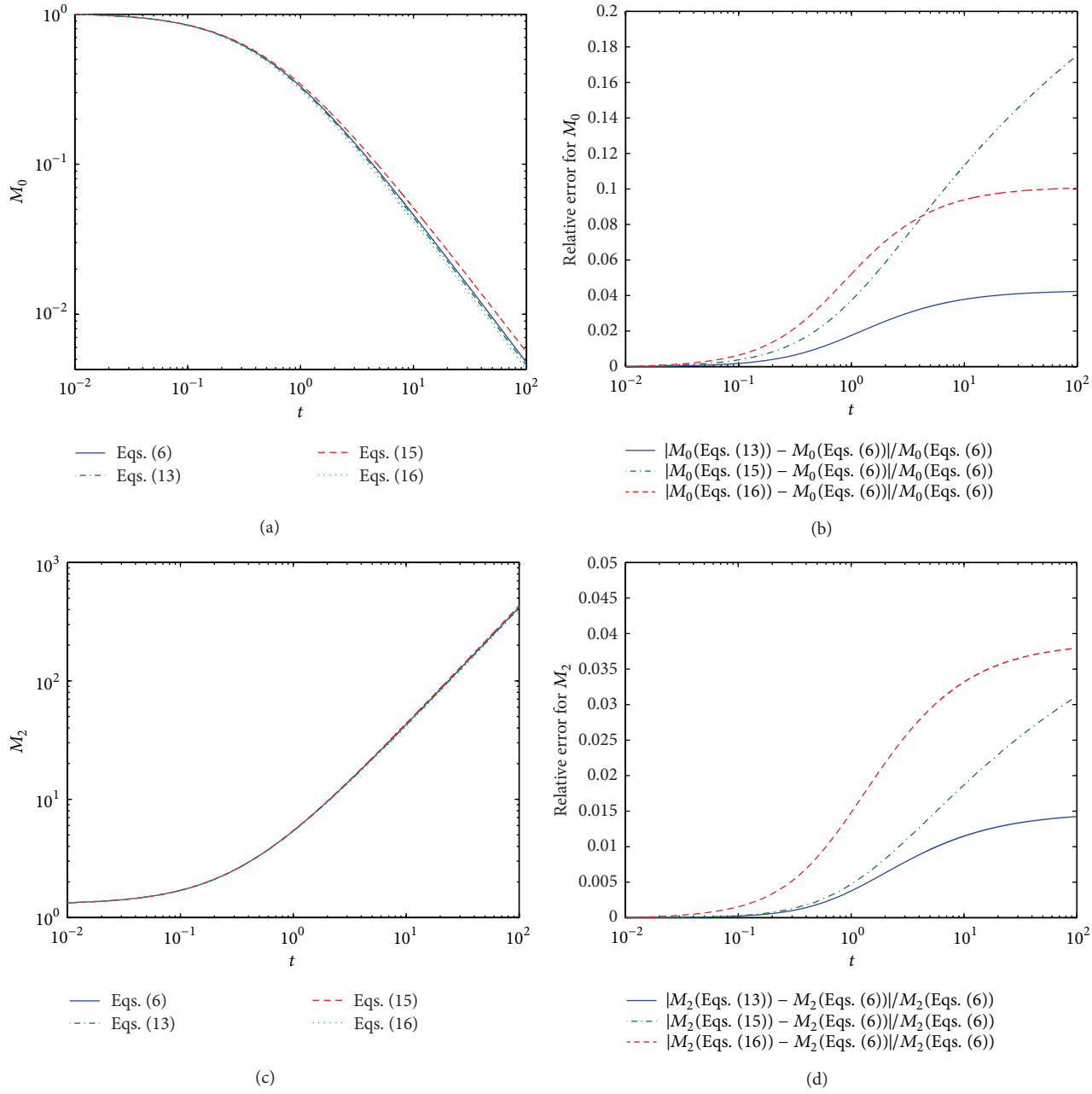

FIGURE 1: The comparison of numerical results among (6), (13), (15), and (16) with the initial condition $M_{00} = 1$, $M_1 = 1$, and $M_{20} = 4/3$; (a) the numerical results of M_0; (b) the relative errors for M_0; (c) the numerical results of M_2; (d) the relative errors for M_2.

$$\begin{aligned}
\frac{dM_2}{dt} &= \frac{-2B_2}{59049M_1^6} \\
&\times \left(-525M_0^3M_4M_1^4 - 8160M_0^3M_3M_2M_1^3 \right. \\
&+ 4080M_0^2M_3M_1^5 \\
&- 22050M_0M_2M_1^6 - 106299M_1^8 \\
&+ 12600M_0^2M_2^2M_1^4 \\
&+ 1280M_0^4M_3^2M_1^2 + 35M_0^6M_4^2 \\
&+ 1365M_0^4M_4M_2M_1^2 \\
&\left. -424M_0^5M_4M_3M_1\right), \\
\frac{dM_3}{dt} &= \frac{B_2}{19683M_1^5} \\
&\times \left(-1105M_0^4M_4M_3M_1 + 915M_0^3M_4M_2M_1^2\right.
\end{aligned}$$

$$
\begin{aligned}
&- 930M_0^2M_4M_1^4 \\
&- 9870M_0^2M_3M_2M_1^3 + 13584M_0M_3M_1^5 \\
&+ 226458M_2M_1^6 \\
&+ 3150M_0M_2^2M_1^4 + 3920M_0^3M_3^2M_1^2 \\
&+74M_0^5M_4^2\Big),
\end{aligned}
$$

$$
\begin{aligned}
\frac{dM_4}{dt} &= \frac{-2B_2}{59049M_1^4M_0^2} \\
&\times \Big(695M_0^6M_4^2 - 2905M_0^5M_4M_3M_1 \\
&+ 8340M_0^4M_4M_2M_1^2 \\
&- 16545M_0^3M_4M_1^4 + 14430M_0^3M_3M_2M_1^3 \\
&+ 22770M_0M_2M_1^6 - 481344M_0^2M_3M_1^5 \\
&- 360297M_0^2M_2^2M_1^4 - 7020M_1^8 \\
&-4810M_0^4M_3^2M_1^2\Big).
\end{aligned} \tag{16}
$$

The comparison of numerical results among (5), (14), and (15) are also shown in Figure 1. The results show that the relative errors are small, and the three sets of equations can be considered equivalent nearly. Since the complexity of moment equations increases rapidly with the increasing number of reserved items but with little differences in the numerical results, we usually prefer using the first three-moment model proposed originally by Yu et al. [3].

5. Conclusion

Without a prior assumption for the shape of particle size distribution, the TEMOM has been considered as a promising method to model the aerosol population balance equation. In this study, the fundamental problems of the TEMOM model in the continuum regime due to Brownian coagulation are clarified, such as the choice of the expansion point u and the error of the high-order moment equations. It benefits the understanding of PBE and TEMOM model.

Appendix

With the same process as Yu et al. [3] shown, we can get the first three-moment equations as follows:

$$
\begin{aligned}
\frac{dM_0}{dt} &= -B_2\left(M_{1/3}M_{-1/3} + M_0^2\right), \\
\frac{dM_1}{dt} &= 0, \\
\frac{dM_2}{dt} &= 2B_2\left(M_{4/3}M_{-2/3} + M_1^2\right).
\end{aligned} \tag{A.1}
$$

Then using (3) and (5), the fractional moments can be approximated by the combination of the first three integral moments, for example, the $M_{1/3}$ is

$$
\begin{aligned}
M_{-1/3} &= \frac{1}{9u^{7/3}}\left(2M_2 - 7uM_1 + 14u^2M_0\right), \\
M_{1/3} &= \frac{1}{9u^{5/3}}\left(-M_2 + 5uM_1 + 5u^2M_0\right) \\
M_{2/3} &= \frac{1}{9u^{4/3}}\left(-M_2 + 8uM_1 + 2u^2M_0\right), \\
M_{4/3} &= \frac{1}{9u^{2/3}}\left(2M_2 + 8uM_1 - u^2M_0\right).
\end{aligned} \tag{A.2}
$$

Now replacing all the fractional moments by the integral moments (i.e., M_0, M_1, and M_2) in (A.2) and substituting $u = M_1^2/(M_0^{3/2}M_2^{1/2})$ and $M_C = M_0M_2/M_1^2$ into (A.1), (13) is obtained.

Acknowledgments

The authors should appreciate the useful discussion and suggestion from Dr. Yu Mingzhou at China Jiliang University. This work is supported by the National Natural Science Foundation of China with Grant nos. 50806023 and 50721005, the Fundamental Research Funds for the Central Universities (Project no. 2013TS078), and the Program of Introducing Talents of Discipline to Universities ("111" Project no. B06019), China.

References

[1] S. H. Park, K. W. Lee, E. Otto, and H. Fissan, "The log-normal size distribution theory of Brownian aerosol coagulation for the entire particle size range. Part I: analytical solution using the harmonic mean coagulation kernel," *Journal of Aerosol Science*, vol. 30, no. 1, pp. 3–16, 1999.

[2] S. K. Friedlander, *Smoke, Dust, and Haze: Fundamentals of Aerosol Dynamics*, Oxford University Press, London, UK, 2nd edition, 2000.

[3] M. Z. Yu, J. Z. Lin, and T. L. Chan, "A new moment method for solving the coagulation equation for particles in Brownian motion," *Aerosol Science and Technology*, vol. 42, no. 9, pp. 705–713, 2008.

[4] S. S. Talukdar and M. T. Swihart, "Aerosol dynamics modeling of silicon nanoparticle formation during silane pyrolysis: a comparison of three solution methods," *Journal of Aerosol Science*, vol. 35, no. 7, pp. 889–908, 2004.

[5] N. M. Morgan, C. G. Wells, M. J. Goodson, M. Kraft, and W. Wagner, "A new numerical approach for the simulation of the growth of inorganic nanoparticles," *Journal of Computational Physics*, vol. 211, no. 2, pp. 638–658, 2006.

[6] S. E. Pratsinis, "Simultaneous nucleation, condensation, and coagulation in aerosol reactors," *Journal of Colloid And Interface Science*, vol. 124, no. 2, pp. 416–427, 1988.

[7] E. Otto, F. Stratmann, H. Fissan, S. Vemury, and S. E. Pratsinis, "39 P 17 Brownian coagulation in the transition regime II: a comparison of two modelling approaches," *Journal of Aerosol Science*, vol. 24, no. 1, pp. S535–S536, 1993.

[8] M.-Z. Yu, J.-Z. Lin, and T.-L. Chan, "Effect of precursor loading on non-spherical TiO_2 nanoparticle synthesis in a diffusion flame reactor," *Chemical Engineering Science*, vol. 63, no. 9, pp. 2317–2329, 2008.

[9] R. R. Upadhyay and O. A. Ezekoye, "Evaluation of the 1-point quadrature approximation in QMOM for combined aerosol growth laws," *Journal of Aerosol Science*, vol. 34, no. 12, pp. 1665–1683, 2003.

[10] R. McGraw, "Description of aerosol dynamics by the quadrature method of moments," *Aerosol Science and Technology*, vol. 27, no. 2, pp. 255–265, 1997.

[11] R. O. Fox, *Computational Models for Turbulent Reacting Flows*, Cambridge University Press, Cambridge, UK, 2003.

[12] M. Z. Yu and J. Z. Lin, "Taylor-expansion moment method for agglomerate coagulation due to Brownian motion in the entire size regime," *Journal of Aerosol Science*, vol. 40, no. 6, pp. 549–562, 2009.

[13] M. Z. Yu and J. Z. Lin, "Solution of the agglomerate Brownian coagulation using Taylor-expansion moment method," *Journal of Colloid and Interface Science*, vol. 336, no. 1, pp. 142–149, 2009.

[14] M. Z. Yu and J. Z. Lin, "Binary homogeneous nucleation and growth of water-sulfuric acid nanoparticles using a TEMOM model," *International Journal of Heat and Mass Transfer*, vol. 53, no. 4, pp. 635–644, 2010.

[15] M. Z. Yu, J. Z. Lin, H. H. Jin, and Y. Jiang, "The verification of the Taylor-expansion moment method for the nanoparticle coagulation in the entire size regime due to Brownian motion," *Journal of Nanoparticle Research*, vol. 13, no. 5, pp. 2007–2020, 2011.

[16] M. L. Xie, M. Z. Yu, and L. P. Wang, "A TEMOM model to simulate nanoparticle growth in the temporal mixing layer due to Brownian coagulation," *Journal of Aerosol Science*, vol. 54, pp. 32–48, 2012.

[17] E. Otto, H. Fissan, S. H. Park, and K. W. Lee, "The log-normal size distribution theory of Brownian aerosol coagulation for the entire particle size range. Part II: analytical solution using Dahneke's coagulation kernel," *Journal of Aerosol Science*, vol. 30, no. 1, pp. 17–34, 1999.

[18] M. L. Xie and L. P. Wang, "Asymptotic solution of population balance equation based on TEMOM model," *Chemical Engineering Science*, vol. 94, pp. 79–83, 2013.

[19] M. L. Xie and Q. He, "Analytical solution of TEMOM model for particle coagulation due to Brownian motion," *Journal of Aerosol Science*, vol. 66, pp. 24–30, 2013.

Hindawi Publishing Corporation
Abstract and Applied Analysis
Volume 2013, Article ID 496243, 6 pages
http://dx.doi.org/10.1155/2013/496243

Research Article

Hydrodynamic Trapping of Particles in an Expansion-Contraction Microfluidic Device

Ruijin Wang[1,2]

[1] *Zhejiang University of Science and Technology, Hangzhou 310023, China*
[2] *Centre of Smart Interface, Technische Universität Darmstadt, 24878 Darmstadt, Germany*

Correspondence should be addressed to Ruijin Wang; wrj5188@163.com

Received 8 September 2013; Accepted 8 November 2013

Academic Editor: Jianzhong Lin

Manipulation and sorting of particles utilizing microfluidic phenomena have been a hot spot in recent years. Here, we present numerical investigations on particle trapping techniques by using intrinsic hydrodynamic effects in an expansion-contraction microfluidic device. One emphasis is on the underlying fluid dynamical mechanisms causing cross-streamlines migration of the particles in shear and vortical flows. The results show us that the expansion-contraction geometric structure is beneficial to particle trapping according to its size. Particle Reynolds number and aspect ratio of the channel will influence the trapping efficiency greatly because the force balance between inertial lift and vortex drag forces is the intrinsic reason. Especially, obvious inline particles contribution presented when the particle Reynolds number being unit. In addition, we selected three particle sizes (2, 7, and 15 μm) to examine the trapping efficiency.

1. Introduction

Microfluidics has greatly interested many researchers in recent years, and has been widely used in the areas of nanomaterials preparation, pharmaceutical analysis, protein engineering, and so on [1–4]. Manipulation and sorting particles suspended in microflow are often applied to biomedical area. Separating targeted particles from the detect solution is an important process. Not a few techniques such as membrane filtration, fluorescence, or magnetic particle sorting were developed in recent years, and they have a wide range of applications [5–7]. However, microfluidic-based devices introduce several advantages, such as higher efficiency, lower sample buffer consumption, fine spatial resolution, and lower cost [8]. In addition, microfluidic-based device can trap particles based on their intrinsic physical characteristics. Hydrodynamic manipulation of particles in an expansion-contraction microfluidic device is a passive method by harnessing microchannel geometrical effects and nonlinear hydrodynamic forces and needs not any application of external force leading to a complicated device structure.

Passive methods used to trapping particles by exerting hydrodynamic force are arising in microfluidic devices. The main approaches are the cross-stream migration of suspended particles in confined flows and microvortical flow. The microvortex generated in sudden expansion is of great importance for particle manipulation. Researchers have gained some beneficial research results [9–11] in the theoretical analysis and experimental investigations on the formation of vortices in different microchannel configurations. Jiang et al. [9] numerically investigated the flow field under various inlet flow rates and cavity structures and then systematically studied the flow features of the vortex and Dean flow in this channel by LBM. Bălan et al. [10] investigated the dynamics of the vortices generated in the vicinity of Y- and T-microbifurcations with one occluded branch. The velocity distribution and streamlines were obtained through the experiments and numerical simulations. Karimi et al. [11] concentrated their study on the dynamical mechanisms of cross stream migration particles in shear and vortical flows. Tsai et al. [12–14] found that Reynolds number and aspect ratio are both influential factors for flow patterns in a suddenly expansion microchannel. Park et al. [15] developed a kind of microfluidic method for focusing on microparticles through the combined use of inertial lift forces and turbulent secondary flows in a patterned microchannel. Furthermore,

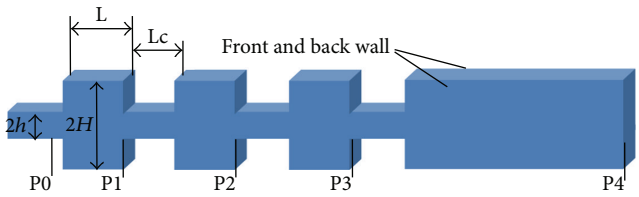

Figure 1: Geometric model of the expansion-contraction microfluidic device.

some particles trapping applications of the microvortices in an expansion-contraction microchannel have been presented in recent years [16, 17]. According to their research work, in the contraction part, particles flow under the balance of shear-gradient lift force and wall effect lift force. When the particles move into the expansion part, wall effect lift force disappears and the shear-gradient lift force leads particles to the vortex formed in the orifice. Lee's group [18, 19] demonstrated a blood plasma separation scheme by employing the unilateral contraction-expansion array microchannel with a low aspect ratio. Small particles are driven predominantly by Dean drag force while the larger ones are lifted by the inertial force and stay close to their previous positions, leading to the isolation of different size particles. The inlet flow rate should be appropriately controlled to avoid particles migration into the vortex in the orificial under a high flow rate.

In the present research, microvortex in the expansion-contraction microchannel is numerically studied in order to understand the particle migration mechanism. The particles distribution and equilibrium position will vary with the change of inlet flow rate and geometry dimensions. Moreover, the research object is also to gain an insight into what condition being beneficial to the particle trapping efficiency for varying particle sizes and to supply the design foundations of such a microfluidic device.

2. Problem Description

2.1. Geometric Model and Parameter Settings. The microdevice under investigation is presented in Figure 1. There are 3 orifices in order to separate the varying particle size distinctly. The distance from inlet to the first orifice is 2000 μm, and the width of channel and orifice is 200 and 800 μm (with another being 400), respectively. The spacing distance between 2 orifices is 500 μm. The depth of the entire device is set to be 200 μm. The dimension of the orifice is 800×800 μm. Inlet is injected with deionized water with polystyrene microspheres being at the size of 2, 7, and 15 μm (corresponding to the size of platelet, red blood cell and white blood cell). The outlet for drainage is long enough off the last orifice, so we are able to obtain distinct separation in terms of particle size. Full-developed velocity profile is set at inlet, while the outflow is set at the outlet. The reference atmospheric pressure is given at the inlet, and the no-slip condition is used at the walls.

The settings of carried fluid properties: the viscosity, density, specific heat, and thermal conductivity of continuous phase are 1.003 g/m·s, 0.9982 g/cm^3, 4180 J/kg·K, and 0.6 W/m·K, respectively. Density and specific heat of polystyrene microspheres are 1.055 g/cm^3 and 1300 J/kg·K.

2.2. Numerical Model. The numerical model includes the continuity equation, Navier-Stokes equation which is still valid in current microchannel flow, and continuity equation for volume fraction

$$\nabla \cdot V = 0,$$
$$\rho \left[\frac{\partial V}{\partial t} + (V \cdot \nabla) V \right] = -\nabla p + \mu \nabla^2 V, \tag{1}$$

where p is the pressure, μ is the dynamic viscosity, and ρ is the density,

The particle continuity is derived from Buongiorno [20]. In our simulation, it is considered to be a dilute mixture (about 0.5% wt). Brownian diffusion can be regarded as the only slip mechanism for particle transport at low Reynolds number in microflow. They are incorporated into the particle transport equation as follows:

$$\frac{\partial \alpha_p}{\partial t} + V \cdot \nabla \alpha_p = \nabla \cdot \left(D_B \nabla \alpha_p \right), \tag{2}$$

where α_p denotes the particle volume fraction. Brownian diffusion is described by the terms on the right hand side. D_B is Brownian diffusion coefficient. The coefficients read as

$$D_B = \frac{k_B T}{3\pi \mu_b d_p}, \tag{3}$$

where k_B denotes Boltzmann's constant, μ_b the viscosity of carried fluid, and d_p the particle diameter. The bulk fluid (carried fluid) is set to be zero.

There is still a lack of accurate theoretical models for the prediction of the viscosity the fluid containing particles. Normally, empirical laws [21] to predict the viscosity are

$$\mu_n = \mu_b \left(1 + 18.8 \alpha_p \right). \tag{4}$$

2.3. Method Validation. In order to verify the availability of the numerical model, we simulated numerically the flow with particles in a circular capillary. The particles distributions are shown in Figure 2. The equilibrium position is about 0.6 radius, being in good agreement with the theoretical results. We confirm the availability of our numerical model for the particle-laden microflow.

3. Results and Discussion

3.1. Particle Trapping Mechanism. When particles are suspended in the carried fluid, the particle behavior is affected by the inertial and viscous forces occurring in the interaction with fluid. According to a number of theoretical analyses, the inertial migration phenomenon can be explained by a shear-gradient-induced lift force that causes particles to migrate away from the axis of pipe and a wall-effect-induced lift force that repels particles away from a pipe wall [22, 23]. This was proved to be right by our simulation results in Figure 2. In the

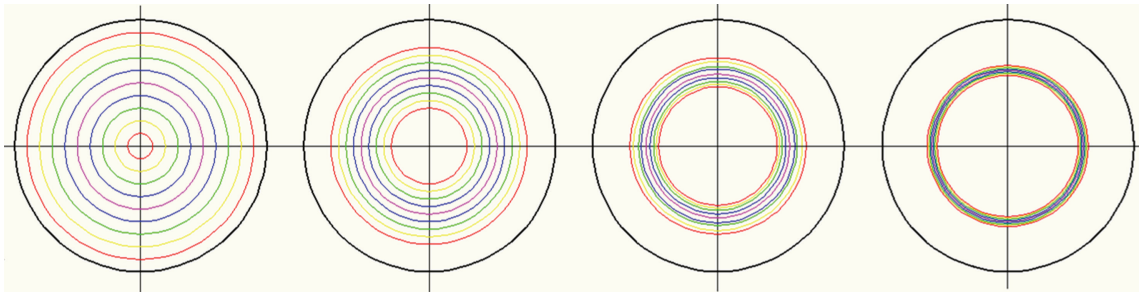

Figure 2: The contour lines of particle concentration in varying position of capillary. (a) 500 μm downstream, (b) 1000 μm downstream, (c) 2000 μm downstream, and (d) 4000 μm downstream.

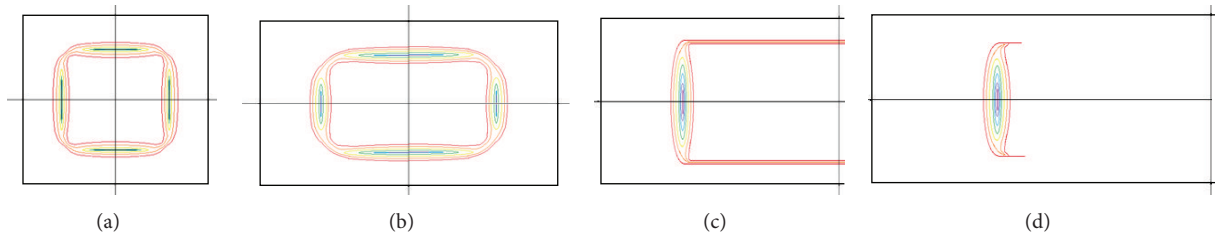

Figure 3: The contour line of particle concentration in varying aspect ratio (AR): (a) AR = 1, (b) AR = 2, (c) AR = 3, and (d) AR = 4.

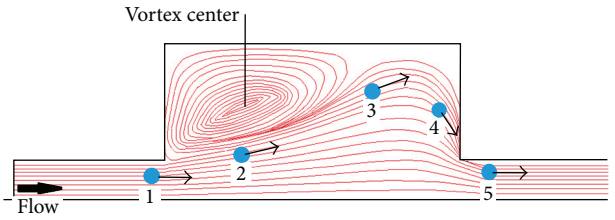

Figure 4: Microvortex structure and particle movement in an orifice.

case of square ducts, particles were concentrated near four walls (top, bottom, left, and right) [24]. We also simulated manifold geometries with varying aspect ratio (AR), and the results were shown in Figure 3. Numerical results show us that the particles distribution in almost in two lines when the aspect ratio is larger than 3 (see Figures 3(c) and 3(d)). This is the basis of hydrodynamic manipulation of particles in an expansion-contraction microfluidic device.

The channel geometry of multiorifices pattern (expansion-contraction structure) was designed so as to transform the particle distribution in a cross section of a straight channel and subsequently concentrate particles close to both side walls of channel. The mechanism of particle enrichment is based on the vortex flow due to the suddenly expansion channel, as shown in Figure 4. In this case, the wall-effect-induced lift forces are weakened compared to the shear-gradient-induced lift force; the reason is probably the long distance from the main stream to the side walls. The majority of particles can be focused near sidewalls as long as they pass through a series of contraction/expansion channels. The mechanism of particle migration induced by solely inertial lift forces cannot explain the dissimilarity for various particle sizes, because the size-based particle separation in a multiorifices microchannel is driven by a combination of two fluid-mechanical forces: inertial lift force and the momentum change over certain time interval is equivalent to inertial force. Inertial forces consist of two parts: inertial lift force and momentum-change-induced inertial force. The inertial lift force is caused by the lateral pressure gradient exerted on a particle, and the momentum-change-induced inertial force can be calculated by an equation. According to the momentum change over a certain time interval which is equivalent to inertial force, the particle migration velocity under consideration of the lateral migration driven by the inertial force can be obtained [25] by

$$U_d = \frac{\rho_p d^2 U^2}{18\mu D_h}. \tag{5}$$

Therefore, important dimensionless parameter named particle Reynolds number should be defined, because we are able to estimate the fluid dynamic phenomenon of particle flowing through a microchannel by using it. It is defined as the ratio of the inertial lift force and momentum-change-induced inertial force as

$$\mathrm{Re}_p = \frac{U_m d^2}{\nu D_h}. \tag{6}$$

Here, d is the particle diameter, D_h is the hydraulic diameter of the channel, U_m is the maximum flow velocity in the channel, and ν is the kinematic viscosity of the carried liquid,

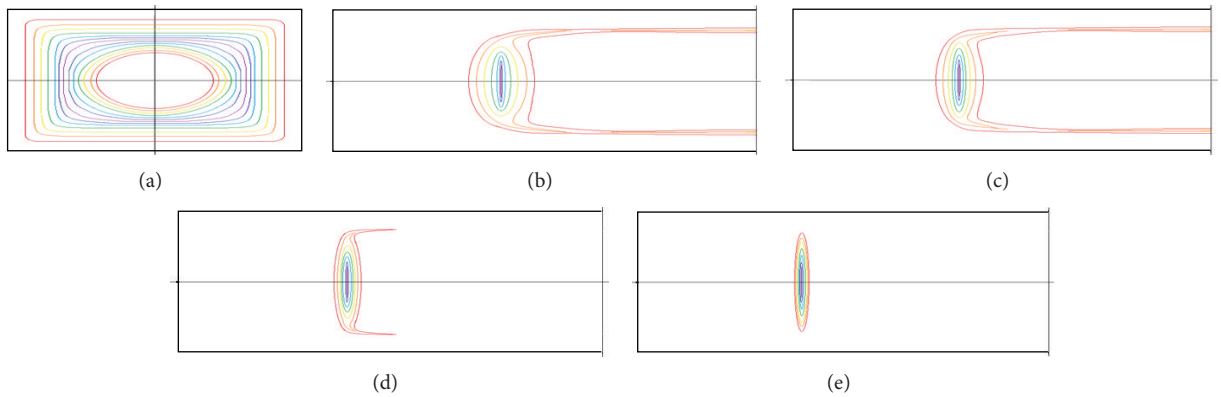

Figure 5: The contour line of particle concentration in varying position of our device: (a) position P0, (b) position P1, (c) position P2, (d) position P3, and (e) position P4.

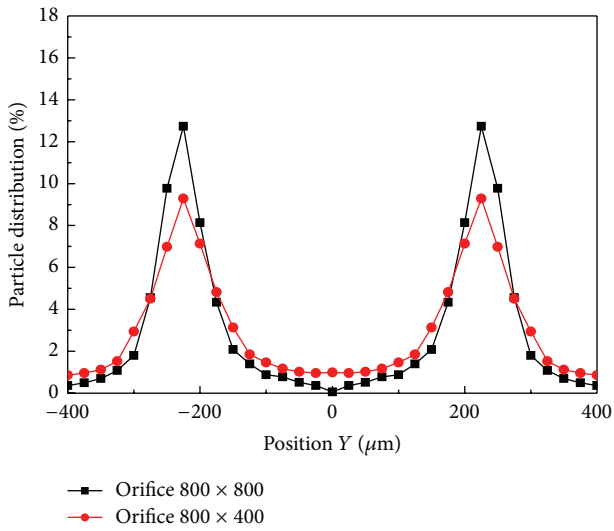

Figure 6: Trapping efficiency comparison between two kinds of orifices.

μ is the dynamic viscosity. For Re_p bigger than 1, the inertial force becomes a dominant parameter for driving the lateral migration of particles transverse to fluid streamlines. In contrast, in the case of Re_p less than 1, the particle behavior is strongly promoted to follow the flow pattern by a viscous drag force acting on the particle surface.

3.2. Numerical Results and Discussions. The channel geometry influences the particle trapping efficiency obviously. The main influence factors are aspect ratio, orifice number, and orifice structure. Figure 3 showed us that the aspect ratio affects the particle distribution obviously. Fortunately, the AR value of normal microfluidic device made of PDMS (polydimethylsiloxane) is bigger than 3. However, orifice number will also influence the trapping efficiency. Figure 5 shows us the contour lines of particle concentration in varying position of our device. Figure 5(a) is near the inlet but well developed, most of the particles were not trapped, and the particles distribution is almost identical over the entire section. At the end of first, second, and third orifices, the width of particle distribution decreases obviously in turn, and the particles near front and back wall fast disappeared. Near the channel end (outlet), the particles distribution appears to be two narrow lines. We also numerically simulated two orifice structures, and the comparison of their particle distributions (defined as the local population of particles to the total population of particles) was illustrated in Figure 6. Obviously the particles distribution lines in 800 × 400 μm orifice are not so narrow as those in 800 × 800 μm orifice. The reason should be that the particles trajectory will not be influenced by the microvortex in 800 × 400 μm orifice so greatly as that in 800 × 800 μm orifice. We can see in Figure 4 that the streamlines should be flat near the region from expansion to contraction when the orifice width decreased, and the particle movement at position 3 will not be so steep that the outward migration velocity is decreased.

Equation (5) indicated that the flow rate is of great importance to the particle trapping. Our simulations were carried out for various flow rates ranging from 50 to 1000 μL/min, with relevant Reynolds number being about 8–160. To the particle size of 2, 7, and 15 μm, particle Reynolds numbers are calculated to be 0.02–0.41, 0.24–4.82, and 1.13–20.1, respectively. Figure 7 shows us the particle contributions in flow rates being 100, 200, and 500 μL/min, respectively, and the particle size is 7 μm. We can see that the trapping efficiency was better under the flow rate being 200 μL/min than that of 100 μL/min flow rate, and (5) indicated also that the lateral migration velocity (meaning of trapping efficiency) increased with the increasing of the flow velocity. However, almost all the particles concentrated near the center line of the channel, and the trapping efficiency closed to zero when the flow rate is very great. This can be explained as follows: when the flow velocity is great enough, the vortex center drifted right (see in Figure 4) and occupied almost the entire orifice, and therefore the streamlines in main channel will close to straight lines and the lateral migration of particles transverse to fluid streamlines decreased. In fact, Re_p can express the trapping efficiency, because we know that when Re_p is bigger than one, the inertial force becomes a dominant parameter

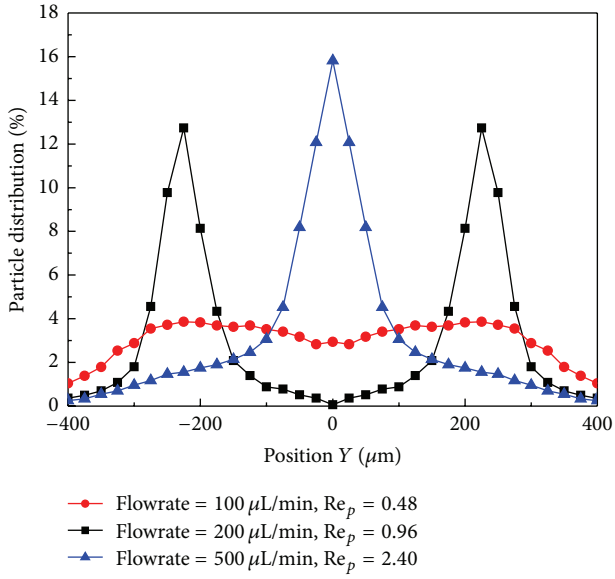

FIGURE 7: Particle contribution in various flow rates (with particle size being 7 μm).

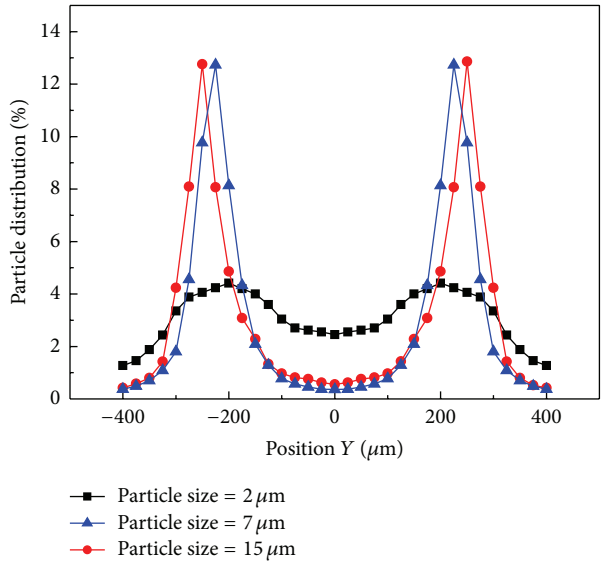

FIGURE 8: Trapping efficiency comparison of three particle sizes.

for driving the lateral migration of particle transverse to fluid streamlines. In contrast, in the case of Re_p less than one, the particle behavior is strongly promoted to follow the flow pattern by a viscous drag force acting on the particle surface.

Particle size is another important factor to influence particle trapping efficiency. We simulated 3 sizes of particles 2, 7, and 15 μm, and the particle concentrations are 100, 25, and $5 \times 10^3/\mu$L, respectively. In order to acquire relatively better trapping efficiency, the corresponding flow rate is 1000, 200, and 50 μL/min. The particle Reynolds numbers can be calculated using (6), and they are 0.41, 0.98, and 1.13, respectively. Although the particle Reynolds number is only 0.41 to particle size 2 μm, the flow rate is somewhat greater (1000 μL/min). The numerical results are shown in Figure 8. The particle distribution for particle sizes 7 and 15 μm showed us good trapping efficiency. Notice that the distribution center of particles with size of 7 μm is about 230 μm and that of particle with size of 15 μm is a little bigger (240 μm). However, the distribution center of particle with size of 2 μm is less than 210 μm. This result agrees with many published results. In addition, the numerical results verified once again that particle Reynolds number can predict the particle trapping efficiency.

4. Conclusions

After numerical simulations being carried out for various particle sizes under various flow rates in various orifices structures, the following conclusions can be drawn.

(1) multiorifices structure is beneficial to particle trapping.

(2) Aspect ratio of square channel influences the particle distribution greatly. When aspect ratio is bigger than 3, particle distribution appears to be two-lines structure, and loop line structure for less than 2 aspect ratios.

(3) Particle Reynolds number is of great importance to particle trapping. When Re_p is bigger than one, the inertial force is dominant and enhanced the lateral migration of particle transverse to fluid streamlines. In contrast, in the case of Re_p less than one, the particle is to follow the flow pattern by a viscous drag force on the particle surface.

Conflict of Interests

The author declares that there is no conflict of interests regarding the publication of this paper.

Acknowledgment

The author acknowledges the support from the Natural Science Foundation of Zhejiang Province China (LY12A02007).

References

[1] F. B. Bao and J. Z. Lin, "Linear stability analysis for various forms of one-dimensional Burnett equations," *International Journal of Nonlinear Sciences and Numerical Simulation*, vol. 6, no. 3, pp. 295–303, 2005.

[2] F. B. Bao, J. Z. Lin, and X. Shi, "Burnett simulation of flow and heat transfer in micro Couette flow using second-order slip conditions," *Heat and Mass Transfer*, vol. 43, no. 6, pp. 559–566, 2007.

[3] F. B. Bao and J. Z. Lin, "Burnett simulation of gas flow and heat transfer in micro Poiseuille flow," *International Journal of Heat and Mass Transfer*, vol. 51, no. 15-16, pp. 4139–4144, 2008.

[4] F. B. Bao and J. Z. Lin, "Burnett simulations of gas flow in microchannels," *Fluid Dynamics Research*, vol. 40, no. 9, pp. 679–694, 2008.

[5] J. R. SooHoo, J. K. Herr, J. M. Ramsey, and G. M. Walker, "Microfluidic cytometer for the characterization of cell lysis," *Analytical Chemistry*, vol. 84, no. 5, pp. 2195–2203, 2012.

[6] J. H. Kang, S. Krause, H. Tobin, A. Mammoto, M. Kanapathipillai, and D. E. Ingber, "A combined micromagnetic-microfluidic device for rapid capture and culture of rare circulating tumor cells," *Lab on a Chip*, no. 12, pp. 2175–2182, 2012.

[7] H. S. Moon, K. Kwon, K. A. Hyun et al., "Spatially gradated segregation and recovery of circulating tumor cells from peripheral blood of cancer patients," *Biomicrofluidics*, vol. 7, no. 3, Article ID 034109, 2013.

[8] A. A. S. Bhagat, H. Bow, H. W. Hou, S. J. Tan, J. Han, and C. T. Lim, "Microfluidics for cell separation," *Medical and Biological Engineering and Computing*, vol. 48, no. 10, pp. 999–1014, 2010.

[9] D. Jiang, D. K. Sun, N. Xiang, K. Chen, H. Yi, and Z. Ni, "Lattice Boltzmann numerical simulation and experimental research of dynamic flow in an expansion-contraction microchannel," *Biomicroflidics*, vol. 7, no. 3, Article ID 034113, 2013.

[10] C. C. M. Bălan, D. Broboană, and C. Bălan, "Lattice Boltzmann numerical simulation and experimental research of dynamic flow in an expansion-contraction microchannel," *Microfluidics and Nanofluidics*, vol. 13, no. 5, pp. 819–827, 2012.

[11] A. Karimi, S. Yazdi, and A. M. Ardekani, "Hydrodynamic mechanisms of cell and particle trapping in microfluidics," *Biomicrofluidics*, vol. 7, no. 2, Article ID 021501, 2013.

[12] C. H. Tsai, H. T. Chen, Y. N. Wang, C. Lin, and L. Fu, "Capabilities and limitations of 2-dimensional and 3-dimensional numerical methods in modeling the fluid flow in sudden expansion microchannels," *Microfluidics and Nanofluidics*, vol. 3, no. 1, pp. 13–18, 2007.

[13] C. H. Tsai, C. P. Yeh, C. H. Lin, R. Yang, and L. Fu, "Formation of recirculation zones in a sudden expansion microchannel with a rectangular block structure over a wide Reynolds number range," *Microfluidics and Nanofluidics*, vol. 12, no. 1–4, pp. 213–220, 2012.

[14] C. H. Tsai, C. H. Lin, L. M. Fu, and H. C. Chen, "High-performance microfluidic rectifier based on sudden expansion channel with embedded block structure," *Biomicrofluidics*, vol. 6, no. 2, Article ID 024108, 2012.

[15] J. S. Park, S. H. Song, and H. Jung, "Continuous focusing of microparticles using inertial lift force and vorticity via multi-orifice microfluidic channels," *Lab on a Chip*, vol. 9, no. 7, pp. 939–948, 2009.

[16] A. J. MacH, J. H. Kim, A. Arshi, S. C. Hur, and D. Di Carlo, "Automated cellular sample preparation using a centrifuge-on-a-chip," *Lab on a Chip*, vol. 11, no. 17, pp. 2827–2834, 2011.

[17] S. C. Hur, A. J. Mach, and D. Di Carlo, "High-throughput size-based rare cell enrichment using microscale vortices," *Biomicrofluidics*, vol. 5, no. 2, Article ID 022206, 2011.

[18] M. G. Lee, S. Choi, and H. J. Kim, "Inertial blood plasma separation in a contraction-expansion array microchannel," *Applied Physics Letters*, vol. 98, pp. 253702–253712, 2011.

[19] M. G. Lee, S. Choi, and J. K. Park, "Inertial separation in a contraction-expansion array microchannel," *Journal of Chromatography A*, vol. 1218, no. 27, pp. 4138–4143, 2011.

[20] J. Buongiorno, "Convective transport in nanofluids," *Journal of Heat Transfer*, vol. 128, no. 3, pp. 240–250, 2006.

[21] S. M. S. Murshed, S. H. Tan, and N. T. Nguyen, "Temperature dependence of interfacial properties and viscosity of nanofluids for droplet-based microfluidics," *Journal of Physics D*, vol. 41, no. 8, Article ID 085502, 2008.

[22] J. P. Matas, J. F. Morris, and E. Guazzelli, "Inertial migration of rigid spherical particles in Poiseuille flow," *Journal of Fluid Mechanics*, vol. 515, pp. 171–195, 2004.

[23] L. Zeng, S. Balachandar, and P. J. Fischer, "Wall-induced forces on a rigid sphere at finite Reynolds number," *Journal of Fluid Mechanics*, vol. 536, pp. 1–25, 2005.

[24] B. Chun and A. J. C. Ladd, "Inertial migration of neutrally buoyant particles in a square duct: an investigation of multiple equilibrium positions," *Physics of Fluids*, vol. 18, no. 3, Article ID 031704, 2006.

[25] J. S. Park and H. Jung, "Multiorifice flow fractionation: continuous size-based separation of microspheres using a series of contraction/expansion microchannels," *Analytical Chemistry*, vol. 81, no. 20, pp. 8280–8288, 2009.

Hindawi Publishing Corporation
Abstract and Applied Analysis
Volume 2013, Article ID 171732, 7 pages
http://dx.doi.org/10.1155/2013/171732

Research Article

A Direct Eulerian GRP Scheme for the Prediction of Gas-Liquid Two-Phase Flow in HTHP Transient Wells

Jiuping Xu,[1] Min Luo,[1,2] Jiancheng Hu,[1,2] Shize Wang,[3] Bin Qi,[3] and Zhiguo Qiao[3]

[1] *Uncertainty Decision-Making Laboratory, Sichuan University, Chengdu 610064, China*
[2] *College of Mathematics, Chengdu University of Information Technology, Chengdu 610225, China*
[3] *Research School of Engineering Technology, China Petroleum and Chemical Corporation, Deyang 618000, China*

Correspondence should be addressed to Jiuping Xu; xujiuping@scu.edu.cn

Received 10 September 2013; Accepted 17 October 2013

Academic Editor: Mohamed Fathy El-Amin

A coupled system model of partial differential equations is presented in this paper, which concerns the variation of the pressure and temperature, velocity, and density at different times and depths in high temperature-high pressure (HTHP) gas-liquid two-phase flow wells. A new dimensional splitting technique with Eulerian generalized riemann problem (GRP) scheme is applied to solve this set of conservation equations, where Riemann invariants are introduced as the main ingredient to resolve the generalized Riemann problem. The basic data of "X well" (HTHP well), 7100 m deep, located in Southwest China, is used for the case history calculations. Curve graphs of pressures and temperatures along the depth of the well are plotted at different times. The comparison with the results of Lax Friedrichs (LxF) method shows that the calculating results are more fitting to the values of real measurement and the new method is of high accuracy.

1. Introduction

The prediction of pressure and temperature of transient gas-liquid flow in a wellbore is important but difficult for well completion test because they are characterized by the dependence of pressure, density, velocity, and other flow parameters on both time and space. As for pressure prediction research, there exist empirical formulas, such as those given by Beggs and Brill [1], Mukherjee and Brill [2, 3], and so on. Different researchers such as Hurlburt and Hanratty [4] and Cazarez-Candia and Vásquez-Cruz [5] have proposed mechanistic models, assuming that flow is under steady-state conditions; other researchers such as Taitel et al. [6]; Ouyang and Aziz [7] have proposed unsteady-state gas-liquid two-phase flow models. Fontanilla and Aziz [8] and Ali [9] presented two simultaneous ordinary differential equations for estimating the steam pressure and quality and solved these equations by using the fourth-order Runge-Kutta method. However, those models can only predict the pressure profiles but not the temperature profiles and ignored their interdependence.

Concerning both pressure and temperature in HTHP wells, Wu et al. have presented a coupled system model of differential equations in [10], but this model only considered the single phase flow statement. In this paper, we build a set of coupled partial differential equations of pressure, temperature, density, and velocity in HTHP gas-liquid two-phase flow wells on the base of the model which was build by Xu et al. in [11]. The numerical model, which accords with the actual situation of the well, allows for the change of oblique angle,different heat transfer medium in annular and the depth of the physical properties of the formation.

We found an algorithm solving model with generalized Riemann problem (GRP) scheme, which is an analytic extension of the Godunov scheme in [12] and originally designed by Li and Chen in [13] for the shallow water equations. A direct and simple derivation of the Eulerian generalized Riemann problem scheme is presented to get the integration in time of the conservation laws. Riemann invariants are applied in order to resolve the singularity at the jump discontinuity. The approach has the advantage that the contact discontinuity in each local wave pattern is always fixed with speed zero, while the rarefaction and the shock waves are located on either side. Since the extension of this scheme to multidimensional cases is obtained using

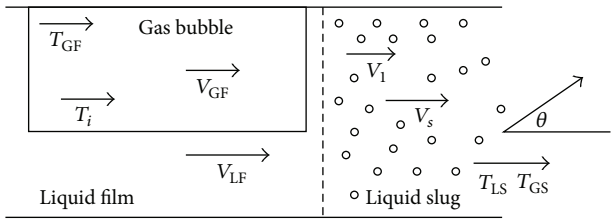

Figure 1: The two-phase flow.

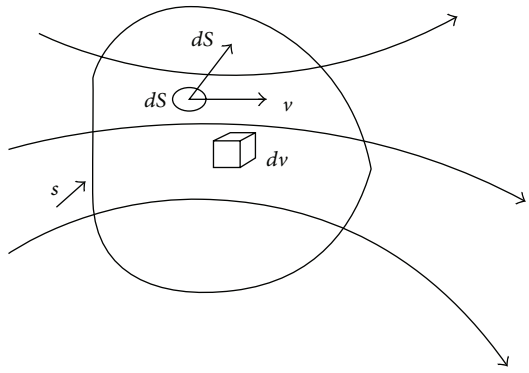

Figure 2: Control volume 1.

the dimensional splitting technique, getting the integration in time of the conservation laws is more direct and simple.

In this paper, we use GRP method for solving this problem and get more accurate prediction of pressure and temperature compared with those obtained from the existing correlations such as LxF method in [11]. The basic data for the calculation are from X well, 7100 m of depth in Southwest China. The curves of the gas pressure and temperature along the depth of the well are plotted. The results can provide a technical reliance for the process of designing well tests in HTHP gas-liquid wells and a dynamic analysis of production from wells.

2. Model Formulation

Considering the two-phase flow system shown in Figure 1, the mixture density and velocity are related to the in situ liquid volume fraction (holdup), H, as follows:

$$\begin{aligned} \rho_m &= \rho_l H + \rho_g (1 - H) \\ v_m &= v_l H + v_g (1 - H) \\ u_m &= u_l H + u_g (1 - H). \end{aligned} \tag{1}$$

2.1. Mass Balance. Consider the flow model shown in Figure 2. According to the fluid moves through the fixed control volume depicted by John and Anderson in [14], we have

$$\iint_S \rho_m v_m ds = -\frac{\partial}{\partial t} \iiint_v \rho_m dv_m. \tag{2}$$

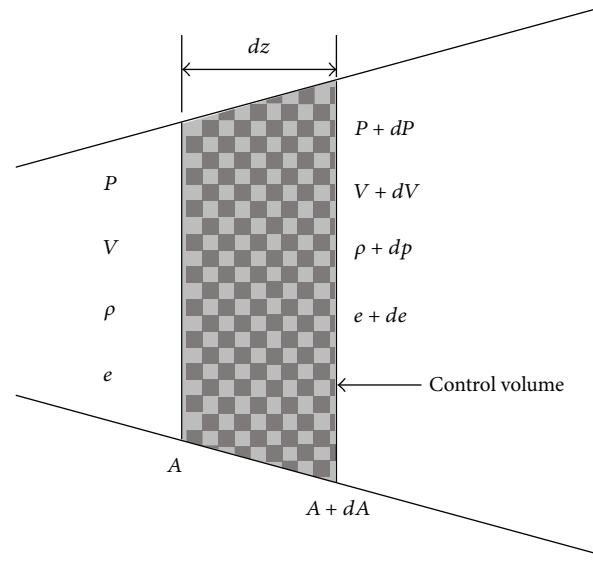

Figure 3: Control volume 2.

Under transient conditions, applied to the control volume in Figure 3, in the limit as dz becomes very small, the volume and surface integral in (2) becomes

$$\begin{aligned} \frac{\partial}{\partial t} \iiint_v \rho_m dv &= \frac{\partial}{\partial t} (\rho_m A dz) \\ \iint_S \rho_m v_m ds &= \rho_m v_m dv_m + \rho_m A dv_m + A v_m d\rho_m \\ &= d(\rho_m v_m A). \end{aligned} \tag{3}$$

Substituting (3) into (2), we get the mass balance equation:

$$\frac{\partial \rho_m}{\partial t} + \frac{\partial (\rho_m v_m)}{\partial z} = 0. \tag{4}$$

2.2. Momentum Balance. As shown in Figure 4, the integral form of the z component the momentum equation can be written as follows with the external forces:

$$\begin{aligned} &\frac{\partial}{\partial t} \iiint_v \rho_m u_m dV + \iint_S (\rho_m u_m v_m) \cdot dS \\ &\quad = -\iint_S (PdS)\, dz - \rho_m g \cos\theta A dz - \frac{\lambda \rho_m v_m^2}{2d} A dz, \end{aligned} \tag{5}$$

where $\rho_m g \cos\theta A dz$ is the force of gravity, $(\lambda \rho_m v^2 A/2) dz$ is the shear stress, and

$$\begin{aligned} \frac{\partial}{\partial t} \iiint_v \rho_m u_m dV &= \frac{\partial}{\partial t} (\rho_m v_m A dz) \\ \iint_S (\rho_m u_m v_m) \cdot dS &= -\rho_m v_m^2 A \\ &\quad + (\rho_m + d\rho_m)(v_m + dv_m)^2 (A + dA) \\ -\iint_S (PdS)_z &= -PA + (P + dP)(A + dA) - 2P\left(\frac{dA}{2}\right). \end{aligned} \tag{6}$$

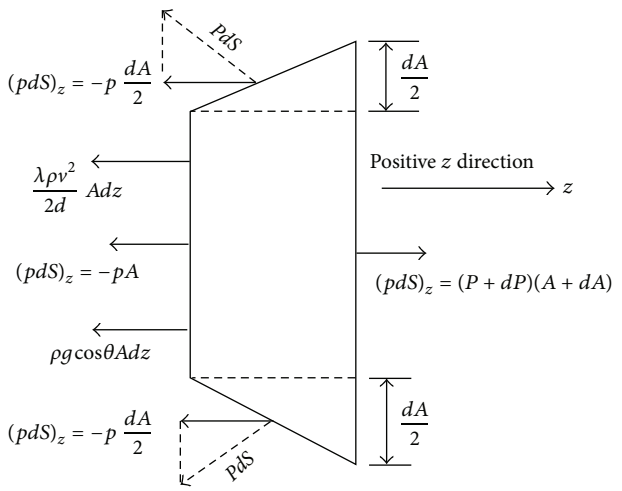

Figure 4: Control volume 3.

Substituting (6) into (5), we obtain momentum balance equation:

$$\frac{\partial}{\partial t}\left(\rho_m v_m\right) + \frac{\partial}{\partial z}\left(P + \rho_m v_m^2\right) = -\rho_m g\cos\theta - \frac{\lambda\rho_m v_m^2}{2d}. \quad (7)$$

2.3. Energy Balance. For the transient flow, it leads directly to the energy equation in terms of temperature. As shown in Figure 5, we should consider the heat transmission within wellbore and from wellbore to formation as transient.

According to the energy balance law, the heat variation flowing on control volume that is equal to the combination heat of inflow and outflow, and the heat transferring to the second dimension, we get the energy balance equation of transient flow:

$$\begin{aligned}&\left(wC_pT\right)z - \left(wC_pT\right)(z+dz) - 2\pi r_{to}U_{to}\left(T - T_r\right)dz \\ &\quad = \frac{\partial\left(\rho_m C_p T\right)}{\partial t}Adz,\end{aligned} \quad (8)$$

where $T_r = (K_e T_{ei} + r_{to}U_{to}T_e T_{\mathrm{wbD}})/(K_e + r_{to}U_{to}T_{\mathrm{wbD}})$ and $w = \rho_m v_m A$. Equation (8) equals the following equation:

$$\frac{\partial\left(\rho_m v_m T\right)}{\partial z} + \frac{\partial\left(\rho_m T\right)}{\partial t} = \frac{2\pi K_e r_{to}U_{to}\left(T_{ei} - T\right)}{C_P\left(K_e + r_{to}U_{to}T_{\mathrm{wbD}}\right)}. \quad (9)$$

Finally, we obtain the coupled system model of partial differential equations:

$$\begin{aligned}&\frac{\partial\rho_m}{\partial t} + \frac{\partial\left(\rho_m v_m\right)}{\partial z} = 0,\\ &\frac{\partial\left(\rho_m v_m\right)}{\partial t} + \frac{\partial\left(P + \rho_m v_m^2\right)}{\partial z} = -\rho_m g\cos\theta - \frac{\lambda}{2d},\\ &\frac{\partial\left(\rho_m T\right)}{\partial t} + \frac{\partial\left(\rho_m v_m T\right)}{\partial z} = \frac{2\pi K_e r_{to}U_{to}\left(T_{ei} - T\right)}{C_P\left(K_e + r_{to}U_{to}T_{\mathrm{wbD}}\right)},\\ &\rho_m = \frac{MP\gamma_g}{ZRT},\\ &\left(P, T, \rho_m, v_m\right) = \left(P_0, T_0, \rho_{m0}, v_{m0}\right) \quad t = 0,\ z = 0.\end{aligned} \quad (10)$$

3. Format Construction

We unify the conservation equations (4), (7), and (9) which are also included in (10) into the following formation:

$$\begin{aligned}&\frac{\partial A_m}{\partial t} + \frac{\partial B_m}{\partial z} = C_m, \quad m = 1, 2, 3,\\ &U = \begin{cases}A_1 = \rho_m\\ A_2 = \rho_m v_m\\ A_3 = 0,\end{cases} \qquad F(U) = \begin{cases}B_1 = \rho_m v_m\\ B_2 = P + \rho_m v_m^2\\ B_3 = \rho_m v_m T,\end{cases}\\ &S(U) = \begin{cases}C_1 = 0\\ C_2 = -\rho_m g\cos\theta - \dfrac{\lambda}{2d}\\ C_3 = \dfrac{2\pi K_e r_{to}U_{to}\left(T_{ei} - T\right)}{C_P\left(K_e + r_{to}U_{to}T_{\mathrm{wbD}}\right)}.\end{cases}\end{aligned} \quad (11)$$

We define the equally spaced grid points, the interface points, and the cells as

$$z_j = j\Delta z, \qquad z_{j+1/2} = \frac{z_j + z_{j+1}}{2}, \qquad C_j = \left[z_{j-1/2}, z_{j+1/2}\right]. \quad (12)$$

We assume that the data at time $t = t_n$ are piecewise linear with a slope σ_j^n and we have $U(z, t_n) = U_j^n + \sigma_j^n(z - z_j)$, $z \in (z_{j-1/2}, z_{j+1/2})$.

The second-order Godunov scheme for (11) takes the following form: $U_j^{n+1} = U_j^n - (\Delta t/\Delta x)(F(U_{j+1/2}^{n+1/2}) - F(U_{j-1/2}^{n+1/2}))$, where $U_{j+1/2}^{n+1/2}$ is the midpoint value or the value of U at the cell interface $(z_{j+1/2}, t_n)$ with accuracy of second order. More specifically, the mid-point value $U_{j+1/2}^{n+1/2}$ is computed with the formulas $U_{j+1/2}^{n+1} = U_{j+1/2}^n + (\Delta t/2)\left(\partial U/\partial t\right)_{j+1/2}^n$ and $U_{j+1/2}^n = R^A(0; U_{j+1/2,-}^n, U_{j+1/2,+}^n)$. Also, $R^A((z - z_{j+1/2})/(t - t_n); U_{j+1/2,-}^n, U_{j+1/2,+}^n)$ is the solution of the Riemann problem centered at $(z_{j+1/2}, t_n)$. Moreover, $U_{j+1/2,-}^n$ and $U_{j+1/2,+}^n$ are the limiting values of initial data $U(z, t_n)$ on both sides of $(z_{j+1/2}, t_n)$. We present a direct and simple derivation of the Eulerian geralized Riemann problem (GRP) scheme and apply Riemann invariants in order to resolve the singularity at the jump discontinuity.

The local wave configuration is usually piecewise smooth and consists of rarefaction waves, shocks, and contact discontinuities. As the general rarefaction waves are considered, the initial data can be regarded as a perturbation of the Riemann initial data U_L and U_R.

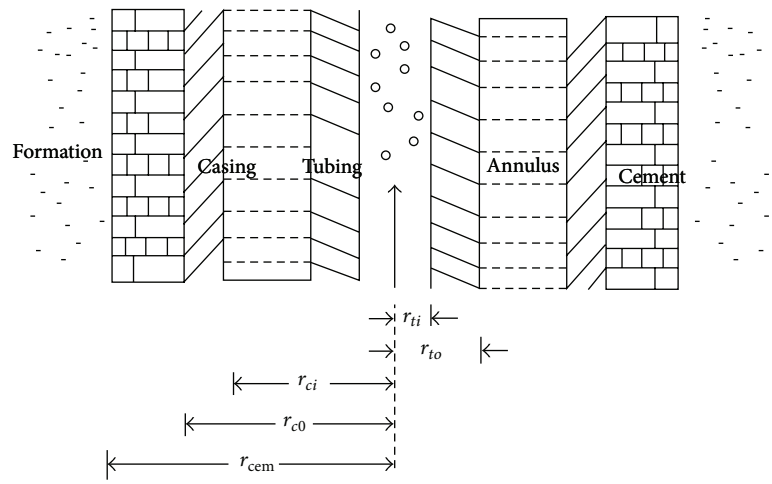

FIGURE 5: The radial transfer of heat.

The GRP scheme assumes piecewise linear data for the flow variables, which leads to the generalized Riemann problem for (11) subject to the initial data:

$$U(z,0) = \begin{cases} U_L + zU_L', & z < 0 \\ U_R + zU_R', & z > 0, \end{cases} \tag{13}$$

where U_L, U_R, U_L', and U_R' are constant vectors.

The initial structure of the solution is determined by the associated Riemann solution, denoted by $\lim_{t\to 0} U(\lambda t, t) = R^A(\lambda; U_L, U_R)$, $\lambda = x/t$.

4. Solving Process

Step 1. Set the step length. In this paper,

$$h = 1\ (\mathrm{m}), \qquad \tau = 60\ (\mathrm{s}). \tag{14}$$

Step 2. Obtain each point's inclination: $\theta_j = \theta_{j-1} + (\theta_{j'} - \theta_{j'-1})h/\Delta s_{j'-1}$.

Step 3. The in situ liquid volume fraction (holdup) in (1) can be calculated from

$$H(\theta_j) = \frac{0.98 E_l^{0.4846}}{Fr^{0.0868}} \times \left\{ 1 + (1 - E_l) \ln \left[\frac{4.7 N_{vl}^{0.1244}}{E_l^{0.8692} Fr^{0.5056}} \right] \times \left[\sin(1.8\theta_j) - \frac{1}{3}\sin^3(1.8\theta_j) \right] \right\}. \tag{15}$$

Step 4. Calculate the following parameters by Liao and Feng in [15]:

$$U_{to} = \left(\frac{r_{to}}{r_{ti} h_r} + \frac{r_{to} \ln(r_{to}/r_{ti})}{r_{ti} h_r} + \frac{1}{h_c + h_r} + \frac{r_{to} \ln(r_{c0}/r_{ci})}{r_{\mathrm{cas}}} + \frac{r_{to} \ln(r_h/r_{c0})}{r_{\mathrm{cem}}} \right)^{-1},$$

$$T_{\mathrm{wbD}} = \frac{2\pi K_e (T_{ei} - T_{\mathrm{wb}})}{\sum_{j=1}^{m} (Q_{j-1} - Q_j)}. \tag{16}$$

Step 5. For piecewise given initial data $U^n(z) = U_j^n + \sigma_j^n (z - z_j)$, $z \in (z_{j-1/2}, z_{j+1/2})$, we solve the Riemann problem for (11) to define the Riemann solution $U_{j+1/2}^n = R(0; U_j^n + (\Delta z/2)\sigma_j^n, U_{j+1}^n - (\Delta z/2)\sigma_{j+1}^n)$, which is the same as the classical Godunov scheme and the Riemann solver in [16] is used in the solution.

Step 6. Determine $(\partial U/\partial t)_{j+1/2}^n$ and evaluate the new cell averages U_j^{n+1}. We apply monotonic algorithm slope limiters to suppress the local oscillations near discontinuities. We use parameter $\alpha = 1.9$ in $\sigma_j^{n+1} = \min\mathrm{mod}(\alpha(U_j^{n+1} - U_{j-1}^{n+1})/\Delta z, \sigma_j^{n+1,-}, \alpha(U_{j+1}^{n+1} - U_j^{n+1})/\Delta z)$, where $U_{j+1/2}^{n+1,-} = U_{j+1/2}^n + \Delta z(\partial U/\partial z)_{j+1/2}^n$ and $\sigma_j^{n+1,-} = (1/\Delta z)(\Delta U)_j^{n+1,-} = (1/\Delta z)(U_{j+1/2}^{n+1,-} - U_{j-1/2}^{n+1,-})$.

5. Results and Discussion

In this simulation, we study a pipe in X well located in Sichuan Basin, Southwest China. All the needed parameters are given in [17] as follows: fluid density is 1000 kg/m^3; depth of the well is 7100 m; friction coefficient is 1.2; ground temperature is 160°C; ground thermal conductivity parameter is 2.06; ground temperature gradient is 0.0218°C/m. Parameters of pipes are given in Table 1. Inclination, azimuth, and vertical depth are given in Table 2.

Through the simulation, we use GRP method to calculate the prediction of pressure and temperature of the oil in the pipe and draw a sensitive analysis for the results. We compare the results of pressure and temperature calculated for the well head at 1200 s by GRP and LxF scheme with the measurement results, which also shows that GRP scheme is more accurate

Table 1: Parameters of pipes.

Diameter	Thickness	Weight	Expansion	Coefficient	Young	Modulus
88.9	9.53	18.9	0.0000115	215	0.3	1400
88.9	7.34	15.18	0.0000115	215	0.3	750
88.9	6.45	13.69	0.0000115	215	0.3	4200
73	7.82	12.8	0.0000115	215	0.3	600
73	5.51	9.52	0.0000115	215	0.3	150

Table 2: Parameters of azimuth, inclination, and vertical depth.

Number	Measured	Inclination	Azimuth	Vertical depth
1	0	0	120.33	0
2	303	1.97	121.2	302.87
3	600	1.93	120.28	599.73
4	899	0.75	126.57	898.59
5	1206	1.25	124.9	1205.45
6	1505	1.04	124.62	1504.32
7	1800	0.49	123.75	1799.18
8	2105	2.49	125.27	2104.04
9	2401	1.27	123.13	2399.91
10	2669	2.44	120.12	2667.79
11	3021	0.14	127.39	3019.63
12	3299	1.18	122.60	3297.50
13	3605	2.05	123.25	3603.36
14	3901	0.16	121.45	3899.22
15	4183	2.92	121.24	4181.09
16	4492	2.73	129.22	4489.95
17	4816.07	1.98	121.61	4813.87
18	5099.07	2.74	129.93	5096.74
19	5394.07	0.13	120.46	5391.61
20	5706.07	0.63	129.59	5703.47
21	5983.07	2.09	120.14	5980.34
22	6302.07	2.69	122.91	6299.19
23	6597.07	2.45	129.41	6594.06
24	6911.12	0.15	124.88	6907.96

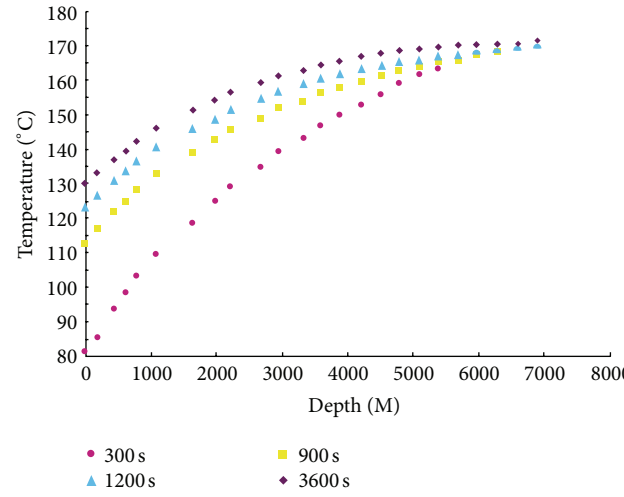

Figure 6: Temperature distribution at different depths.

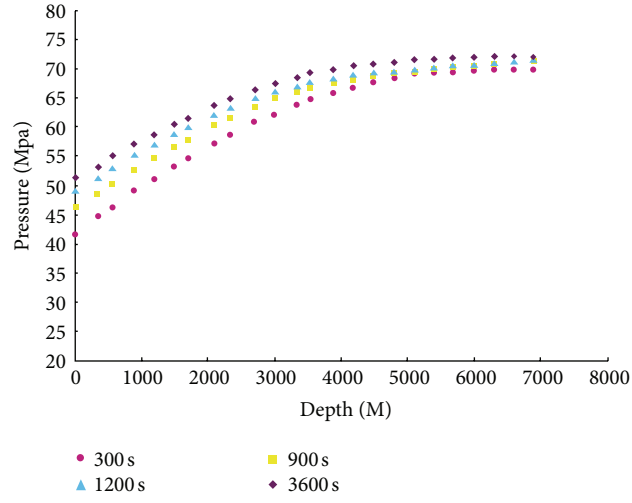

Figure 7: Pressure distribution at different depths.

in the real calculation. We obtain series of results contained in tables and figures and analyze these results as follows.

When the bottom pressure is 70 MPa, temperatures are plotted in Figure 6 at different depths and shown in detail in Table 3. When the output keeps constant, the temperature increases with the increasing depth of the well and when the depth fixed, the temperature increases with the increasing time. In addition, it can be seen from the figure that the temperature changes quickly in the early stage but stabilizes over time, especially after 1200 s.

It is established that, when depth is constant, the pressure shown in Figure 7 and Table 4 increased with an increase of the time. When the output keeps constant, the pressure increased with the increasing depth of the well. This is because, with time increasing, the flow increases and then the frictional heat leads to an increase in the pressure. It can also be seen that the pressure changes quickly in the early stage but stabilizes over time.

As shown in Table 5, for the comparative results of the well head temperature at 1200 s, the relative error between the calculation results and the measurement results of GRP scheme method is 5.12% and by LxF method is 6.70%, while the relative error between the results in pressure predition at

Table 3: Temperature at different depths on 300 s, 900 s, 1200 s, and 3600 s.

Depth	Time			
	300 s	900 s	1200 s	3600 s
0	81.22	115.29	124.19	132.27
300	85.45	121.38	127.55	133.34
600	92.67	125.54	131.76	136.56
900	95.54	129.48	134.96	138.87
1200	101.16	133.77	137.58	141.94
1500	106.49	136.66	140.77	143.15
1800	111.76	140.67	143.23	145.17
2100	116.98	143.54	146.29	147.39
2400	121.86	145.66	148.49	149.14
2700	126.89	148.45	150.78	151.93
3000	131.55	151.78	152.99	153.85
3300	136.85	153.74	154.86	155.91
3600	140.88	154.02	154.46	157.87
3900	144.67	157.12	158.73	159.45
4200	148.25	159.34	160.87	161.88
4500	152.74	161.53	161.65	162.65
4800	155.77	162.55	162.72	163.45
5100	159.75	163.42	163.49	164.56
5400	162.36	164.56	164.87	165.24
5700	164.32	165.74	165.45	166.57
6000	166.36	166.56	167.67	167.97
6300	167.91	168.77	168.87	169.65
6600	168.23	169.45	169.57	169.81
6900	170.24	170.56	171.78	171.52

Table 4: Pressure at different depths on 300 s, 900 s, 1200 s, and 3600 s.

Depth	Time			
	300 s	900 s	1200 s	3600 s
0	42.55	46.62	50.24	51.34
300	43.23	47.53	50.64	52.67
600	44.86	48.71	50.46	53.47
900	45.87	49.13	51.41	54.69
1200	46.73	50.43	52.32	54.79
1500	48.46	51.24	53.36	55.53
1800	49.43	52.43	54.47	56.12
2100	50.34	53.83	55.42	57.37
2400	51.96	56.92	54.37	57.85
2700	53.53	57.22	55.45	58.97
3000	54.44	58.46	56.78	59.34
3300	55.24	59.97	57.47	60.95
3600	56.76	59.94	58.95	61.22
3900	57.33	60.98	59.04	62.29
4200	58.93	61.22	60.29	63.33
4500	59.34	62.45	61.24	64.48
4800	60.89	63.43	62.23	64.33
5100	61.56	64.19	63.22	64.78
5400	63.35	65.24	64.18	65.34
5700	64.69	65.45	65.12	66.34
6000	65.45	66.79	66.15	67.56
6300	66.99	67.49	67.11	67.47
6600	67.46	68.52	68.22	68.58
6900	69.28	69.46	69.92	69.55

the same time calculated by GRP scheme method is 8.81% and by LxF method is 9.73%, which shows that the distribution prediction of the two-phase flow is more accurate in actual calculation by GRP scheme method.

6. Conclusion

In this paper, considering the variation of pressure, temperature, velocity; and density at different times and depths in gas-liquid two-phase flow, we present a system model of partial differential equations according to mass, momentum, and energy. We establish an algorithm solving model with a new difference method with a direct Eulerian GRP scheme which is proven to be efficient for the numerical implementation in this paper. The basic data of the X well (HTHP well), 7100 m deep in Sichuan Basin, Southwest China, was used for case history calculations, and a sensitivity analysis is completed for the model. The gas-liquid's pressure and temperature curves along the depth of the well are plotted, and the curves intuitively reflect the flow law and the characteristics of heat transfer in formation. The results can provide the technical reliance for the process of designing well tests in high temperature-high pressure gas-liquid two-phase flow wells and dynamic analysis of production. Furthermore, the works in this paper can raise safety and reliability of deep completion test and will yield notable economic and social benefits and avoid or lessen accidents caused by improper technical design.

Table 5: Comparative results of the well head at 1200 s.

Well-head	Temperature	Pressure
Measurement results	180.65	76.10
Results by GRP method (relative error)	171.78 (5.12%)	69.92 (8.81%)
Results by LxF method (relative error)	169.30 (6.70%)	69.36 (9.73%)

Nomenclature

A: A total length of conduit (m^2)
C_J: Joule-Thompson coefficient (K/pa)
C_p: Heat capacity (J/kg·K)
D: A hydraulic diameter (m)
G: Acceleration constant of gravity (m/s^2)
K_e: Formation conductivity (J/m·K)
P: Pressure (KPa)
r_D: Dimensionless radius
r_{to}: Outer radius of conduit (m)
T: Temperature (K)
t_D: Dimensionless time

T_e: Temperature of the stratum (K)
T_{wb}: Wellbore temperature (K)
T_{wbD}: Dimensionless wellbore temperature (K)
T_r: Temperature of the second surface (K)
T_{ei}: Initial temperature of formation (K)
U_{to}: Overall-heat-transfer coefficient (W/m·K)
V: Velocity (m/s)
Z: A total length of conduit (m)
z: The distance coordinate in the direction along the conduit
h_c: Heat transfer coefficient for natural convection based on outside tubing surface and the temperature difference between outside tubing and inside casing surface
h_r: Heat transfer coefficient for radiation based on the outside tubing surface and the temperature difference between the outside tubing and inside casing surface
K_{cas}: Thermal conductivity of the casing material at the average casing temperature
K_{cem}: Thermal conductivity of the cement at the average cement temperature and pressure
λ : The friction coefficient, dimensionless
γ_g: Euler constant 1.781
ρ : Density (kg/m^3)
θ : Inclination angle flow conduit.

Conflict of Interests

The authors declare that there is no conflict of interests regarding the publication of this paper.

Acknowledgments

This research was supported by the Key Program of NSFC (Grant no. 70831005) and the Key Project of China Petroleum and Chemical Corporation (Grant no. GJ-73-0706).

References

[1] H. D. Beggs and J. R. Brill, "A study of two-phase flow in inclined pipes," *Journal of Petroleum Technology*, vol. 25, pp. 607–617, 1973.

[2] H. Mukherjee and J. P. Brill, "Liquid holdup correlations for inclined two-phase flow," *Journal of Petroleum Technology*, vol. 35, no. 5, pp. 1003–1008, 1983.

[3] H. Mukherjee and J. P. Brill, "Empirical equations to predict flow patterns in two-phase inclined flow," *International Journal of Multiphase Flow*, vol. 11, no. 3, pp. 299–315, 1985.

[4] E. T. Hurlburt and T. J. Hanratty, "Prediction of the transition from stratified to slug and plug flow for long pipes," *International Journal of Multiphase Flow*, vol. 28, no. 5, pp. 707–729, 2002.

[5] O. Cazarez-Candia and M. A. Vásquez-Cruz, "Prediction of pressure, temperature, and velocity distribution of two-phase flow in oil wells," *Journal of Petroleum Science and Engineering*, vol. 46, no. 3, pp. 195–208, 2005.

[6] Y. Taitel, O. Shoham, and J. P. Brill, "Simplified transient solution and simulation of two-phase flow in pipelines," *Chemical Engineering Science*, vol. 44, no. 6, pp. 1353–1359, 1989.

[7] L.-B. Ouyang and K. Aziz, "Transient gas-liquid two-phase flow in pipes with radial influx or efflux," *Journal of Petroleum Science and Engineering*, vol. 30, no. 3-4, pp. 167–179, 2001.

[8] J. P. Fontanilla and K. Aziz, "Prediction of bottom-hole conditions for wet steam injection wells," *Journal of Canadian Petroleum Technology*, vol. 21, no. 2, 8 pages, 1982.

[9] S. M. F. Ali, "A comprehensive wellbore stream/water flow model for steam injection and geothermal applications," *Society of Petroleum Engineers Journal*, vol. 21, no. 5, pp. 527–534, 1981.

[10] Z. Wu, J. Xu, X. Wang, K. Chen, X. Li, and X. Zhao, "Predicting temperature and pressure in high-temperature-high-pressure gas wells," *Petroleum Science and Technology*, vol. 29, no. 2, pp. 132–148, 2011.

[11] J. Xu, M. Luo, S. Wang, B. Qi, and Z. Qiao, "Pressure and temperature prediction of transient flow in HTHP injection wells by Lax-Friedrichs method," *Petroleum Science and Technology*, vol. 31, no. 9, pp. 960–976, 2013.

[12] S. K. Godunov, "A difference method for numerical calculation of discontinuous solutions of the equations of hydrodynamics," *Matematicheskii Sbornik*, vol. 47, no. 89, pp. 271–306, 1959.

[13] J. Li and G. Chen, "The generalized Riemann problem method for the shallow water equations with bottom topography," *International Journal for Numerical Methods in Engineering*, vol. 65, no. 6, pp. 834–862, 2006.

[14] D. John and J. R. Anderson, *Computational Fluid Dynamics—The Basics with Applications*, McGraw-Hill, New York, NY, USA, 1995.

[15] X.-W. Liao and J.-L. Feng, "Pressure-temperature coupling calculation of transient wellbore heat transfer in deep geopressured gas reservoir," *Petroleum Exploration and Development*, vol. 32, no. 1, pp. 67–69, 2005.

[16] E. F. Toro, *Riemann Solvers and Numerical Methods for Fluid Dynamics: A Practical Introduction*, Springer, Berlin, Germany, 1997.

[17] J. Xu, J. Hu, M. Luo, S. Wang, B. Qi, and Z. Qiao, "Optimisation of perforation distribution in HTHP vertical wells," *Canadian Journal of Chemical Engineering*, vol. 91, pp. 332–343, 2011.

Hindawi Publishing Corporation
Abstract and Applied Analysis
Volume 2013, Article ID 840218, 6 pages
http://dx.doi.org/10.1155/2013/840218

Research Article

A New Method of Moments for the Bimodal Particle System in the Stokes Regime

Yan-hua Liu[1] and Zhao-qin Yin[2]

[1] *College of Mechanical and Electrical Engineering, Hohai University, Changzhou 213022, China*
[2] *China Jiliang University, Hangzhou 310018, China*

Correspondence should be addressed to Yan-hua Liu; liuyanhua@zju.edu.cn

Received 22 September 2013; Accepted 30 October 2013

Academic Editor: Jianzhong Lin

The current paper studied the particle system in the Stokes regime with a bimodal distribution. In such a system, the particles tend to congregate around two major sizes. In order to investigate this system, the conventional method of moments (MOM) should be extended to include the interaction between different particle clusters. The closure problem for MOM arises and can be solved by a multipoint Taylor-expansion technique. The exact expression is deduced to include the size effect between different particle clusters. The collision effects between different modals could also be modeled. The new model was simply tested and proved to be effective to treat the bimodal system. The results showed that, for single-modal particle system, the results from new model were the same as those from TEMOM. However, for the bimodal particle system, there was a distinct difference between the two models, especially for the zero-order moment. The current model generated fewer particles than TEMOM. The maximum deviation reached about 15% for m_0 and 4% for m_2. The detailed distribution of each submodal could also be investigated through current model.

1. Introduction

The particulate matter has become one of the most dangerous pollutants to the atmospheric environment and the health of human beings. It will reduce the visibility of the atmosphere and cause the traffic crowding and serious accidents. The fine particles (PM2.5) will also be breathed into the bronchus of human beings, followed by several kinds of respiratory diseases. The lungs will absorb the fine particles and cardiovascular disease will come into being [1]. However, the mechanism of the generation and evolution of the particulate matter still remains to be clarified. Hence, it has both theoretical and realistic senses to study the dynamics of the particulate matter.

Previous study on the aerosol dynamics usually supposes that the particle system is monodispersed (i.e., the system has only one scale) or multidispersed (i.e., the system has multiscales) but is in a log-normal distribution in size [2]. Such kinds of assumptions will greatly simplify the problems, and a series of approximate or precise solutions will be obtained. However, these assumptions are based on the experimental measurement and cannot be applied to all the cases. There is another type of particle size distribution, namely, bimodal or multimodal distribution. For example, the newborn particles together with the background particles compose the bimodal distribution system. Furthermore, the newborn particles may also exhibit a multimodal or bimodal distribution [3]. Pugatshova et al. [4] and Lonati et al. [5] measured the particulate matter in the urban on-road atmosphere in different cities and times. The multimodal distribution was observed. At this time, unacceptable error may appear using mono-dispersed or log-normal assumption.

Take the bimodal system, for example: the particles gather around two independent particle sizes. In order to study such a system, the particle size distribution should be separated into two sub-PSDs [6]. The dynamics of the system may be obtained according to the two subparticle clusters. Under this description, the governing equations of the particle system should be modified to represent the additional coagulation effect [7]; that is, the collision of particles is artificially separated into two kinds: internal coagulation and external

coagulation. Because the typical particle diameter of the bimodal system is 5 nm to 2.5 μm, which means that particles lie in different dynamic regimes (free molecular regime, transition regime and continuum regime), the coagulation in such a wide range should also be treated separately. The current study will focus on the continuum (Stokes) regime.

Generally, the particle balance equation (PBE) governs the detailed evolution process of PSD and can be numerically solved. However, because of its huge computation resource to solve the PBE directly, the method of moment (MOM) [2, 8, 9] is often taken into account as an alternation. It takes several moments of PSD in particle volume space and converts PBE into moment equations. Each moment has its physical meaning: zero-order moment represents the number concentration, first-order moment represents the volume concentration, and second-order moment is related to the polydispersity. Although MOM cannot directly give out the evolution of specific PSD, it can obtain the statistical characteristics of particle system and the calculation during this procedure reduces to an acceptable level. As a matter of fact, MOM is widely used in the research of aerosol dynamics for its simplicity and low computational cost.

One limitation of MOM is the closure problem due to the coagulation term in PBE. When PBE is converted into moment equations, the coagulation term will be transformed into fractional moments, which cannot be explicitly expressed and mathematical models should be introduced into MOM to solve this problem, the so-called closure problem. There are typically three kinds of methods: predetermined PSD [2], quadrature method of moment (QMOM) [10], and Taylor-expansion method of moment (TEMOM) [11]. The first class often supposes that the PSD is a log-normal distribution, and the coagulation term can be directly determined. It can only be applied to the log-normal distributed particle system. QMOM utilizes the Gaussian quadrature method to evaluate the coagulation term in the moment equations. The pre-determined PSD is not necessary, but the computation is easy to diverge. TEMOM expands the nonlinear term in the collision kernel using the Taylor expansion. Finally, the coagulation term can be expressed as a linear combination of different moments. TEMOM has its superiority on its easy expression, high precision, and low computational cost. It is widely used in the research of the aerosol dynamics [12–15].

However, using TEMOM to study the bimodal system has some problems. TEMOM expands the collision kernel function at the average diameter u_0. For the internal collision, there is no problem, but, for the external collision in bimodal system, this expansion should be extended. For a typical bimodal system, there are two clusters of particles with different diameters, and the total numbers of particles in each cluster are also different. This fact will contribute to the fact that the average diameter of the whole system may lie around the first mode or the second mode or even the mid place of the two modes. If the external collision term also expands at the average diameter of the system, additional error will decrease the accuracy of the simulation. In TEMOM, the convergent region is $(0, 2u_0)$ [16], while, for bimodal system, one mode may lie outside this region if both modes expand at the same point. This possibility may lead to the divergence of the calculation.

Hence, the Taylor-expansion method of moments should be developed to be applied to the bimodal particle system to improve the accuracy and the stability. The current research will focus on the multipoint Taylor-expansion method of moments, and the Stokes regime is preferred for ease.

2. Mathematical Theories

Considering the typical system with Brownian coagulation only, PSD satisfies the PBE as [2]

$$\frac{\partial N(v)}{\partial t} = \frac{1}{2}\int_0^v \beta(u, v-u)\, N(u)\, N(v-u)\, du - N(v,t)\int_0^\infty \beta(v,u)\, N(u)\, du, \tag{1}$$

where $N(v)$ is the size distribution function, which means the number of particles with a volume v, u and v are the particle volumes, and β is the Brownian coagulation coefficient.

In order to convert PBE into moment equations, the definition of moments is introduced

$$m_k(t) = \int_0^\infty N(v,t)\, v^k dva. \tag{2}$$

Applying (2) to (1), the moment equations are obtained:

$$\frac{\partial m_k}{\partial t} = \frac{1}{2}\iint_0^\infty \left\{\left[(v_1+v_2)^k - v_1^k - v_2^k\right] \times \beta(v_1, v_2)\, N(v_1)\, N(v_2)\right\} dv_1 dv_2. \tag{3}$$

In current paper, the Stokes regime is studied, and the collision kernel β may be rewritten as

$$\beta_c(v_1, v_2) = B\left[2 + \left(\frac{v_2}{v_1}\right)^{1/3} + \left(\frac{v_1}{v_2}\right)^{1/3}\right], \tag{4}$$

where $B = 2k_bT/\mu, k_b$ is the Boltzmann constant, T is the environment temperature, and μ is the molecular viscosity of gas.

When investigating the bimodal system, PSD can be expressed as $N(v,t) = N_i(v,t) + N_j(v,t)$. PBE for each sub-PSD can be established. Apply the definition equation (2) to the PBEs. The moment equations can be attained for both cluster i and cluster j listed as follows:

$$\frac{\partial m_k^i}{\partial t} = C_k^{ii} + D_k^{ij}, \qquad \frac{\partial m_k^j}{\partial t} = C_k^{jj} + E_k^{ij}, \tag{5}$$

where

$$C_k^{ii} = \frac{1}{2}\iint_0^\infty \left\{\left[(u+v)^k - u^k - v^k\right] \times \beta(u,v) N_i(u) N_i(v)\right\} du\, dv, \quad (6)$$

$$D_k^{ij} = -\iint_0^\infty u^k \beta(u,v) N_i(u) N_j(v)\, du\, dv, \quad (7)$$

$$E_k^{ij} = \iint_0^\infty \left\{\left[(u+v)^k - v^k\right] \times \beta(u,v) N_i(u) N_j(v)\right\} du\, dv. \quad (8)$$

Note that C_k^{ii} and C_k^{jj} are only related to N_i or N_j. These two terms represent the internal coagulation effect in the cluster i or j. As a result, the single point binary Taylor expansion is used to deal with these two terms (at u_1 or u_2). The results from the typical TEMOM can be directly used. In (9) m_k represents kth moment of PSD N_i or N_j. Consider

$$C_0^{ii} = \frac{Bm_0^{i2}}{81m_1^{i2}}\left(-151m_1^{i4} - 2m_2^{i2}m_0^{i2} - 13m_2^i m_1^{i2} m_0^i\right),$$
$$C_1^{ii} = 0, \quad (9)$$
$$C_2^{ii} = \frac{-2B_1}{81m_1^{i2}}\left(2m_2^{i2} - 13m_2^i m_1^{i2} m_0^i - 151m_1^{i4}\right).$$

The approximation of D_k^{ij} and E_k^{ij} will be deduced in the following part. Substitute (4) into (7) and (8). A lot of fractional moments will appear in the expression of D_k^{ij} and E_k^{ij}, which can be approximated through the Taylor expansion of v^p (p is fraction) at u_1 or u_2. Consider

$$m_p \approx \frac{u^{p-2}\left(p^2 - p\right)}{2} m_2 - u^{p-1}\left(p^2 - 2p\right) m_1 + \frac{u^p}{2}\left(p^2 - 3p + 2\right) m_0. \quad (10)$$

Making use of (10), D_k^{ij} and E_k^{ij} can be expressed as a linear combination of m_k^i and m_k^j. Moreover

$$D_0 = -\frac{\sum a_{mn} m_m^i m_n^j}{81}, \quad D_1 = \frac{\sum b_{mn} m_m^i m_n^j}{81},$$
$$D_2 = \frac{\sum c_{mn} m_m^i m_n^j}{81}, \quad E_0 = 0, \quad (11)$$
$$E_1 = \frac{\sum d_{mn} m_m^i m_n^j}{81}, \quad E_2 = -\frac{\sum e_{mn} m_m^i m_n^j}{81}.$$

The exact expressions of the coefficients in D_0, D_1, D_2, E_1, and E_2 are listed in the appendix.

3. Tests and Discussion

In order to verify the deduction, both theoretical and numerical validations are performed, respectively.

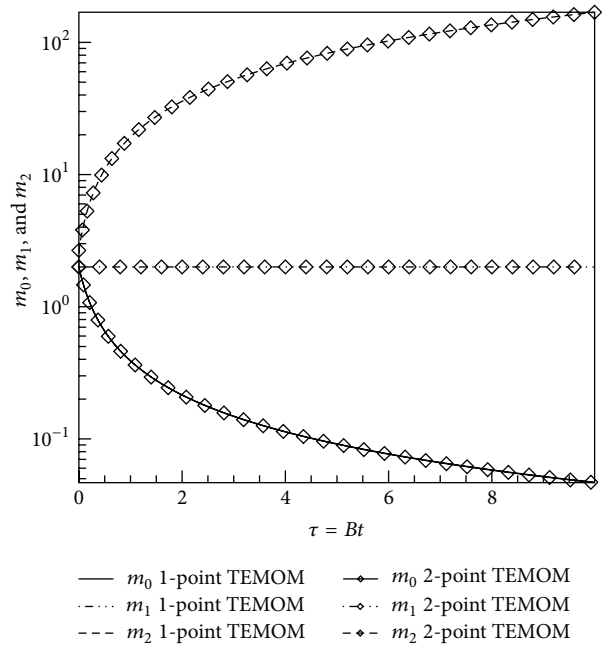

Figure 1: The evolution of moments for Case I using different expansion schemes.

Note that, if $N_i = N_j = N/2$, (5) turns into two sets of moment equations with monomodal distribution. If (5) and set $m_k = m_k^i + m_k^j$, the theoretical systematic moment equations are attained:

$$\frac{\partial m_k}{\partial t} = 4C_k^{ii}. \quad (12)$$

Substitute D_0, D_1, D_2, E_1, and E_2 into (5), and set $u_1 = u_2 = m_1/m_0$, $r = 1$. The right side of new equation just equals 4 times of (9), which is consistent with the theoretical equation (12).

Two simple bimodal systems are simulated to validate the current model. The single point and multipoint expansion methods are both taken into account and the results are compared with each other to show the validity and accuracy. The initial size distributions both satisfy the log-normal distribution as follows:

$$N(v,t) = N_0 \exp\frac{\left(-\left(\ln^2\left(v/v_g\right)\right)/\left(2w_g^2\right)\right)}{\left(\sqrt{2\pi} v w_g\right)}. \quad (13)$$

For Case I, $N_0^i = N_0^j = 1.0$, $v_g^i = v_g^j = \sqrt{3}/2$, and $w_g^i = w_g^j = \sqrt{\ln(4/3)}$ [8], which represents a monomodal system and the PSD is separated into two equal sub-PSDs. For Case II, $N_0^i = 1.0$, $v_g^i = \sqrt{3}/2$ and $w_g^i = \sqrt{\ln(4/3)}$ and $N_0^j = 0.1\, N_0^i$, $v_g^j = 1000 v_g^i$, and $w_g^j = 0.1 w_g^i$, which represents a bimodal system consisting of two log-normal sub-PSDs.

Figure 1 shows the results of Case I for both single point TEMOM and multipoint TEMOM. From the figure, a good agreement is obtained. This is because the particle system is, in the final analysis, a mono-modal system. The consistency

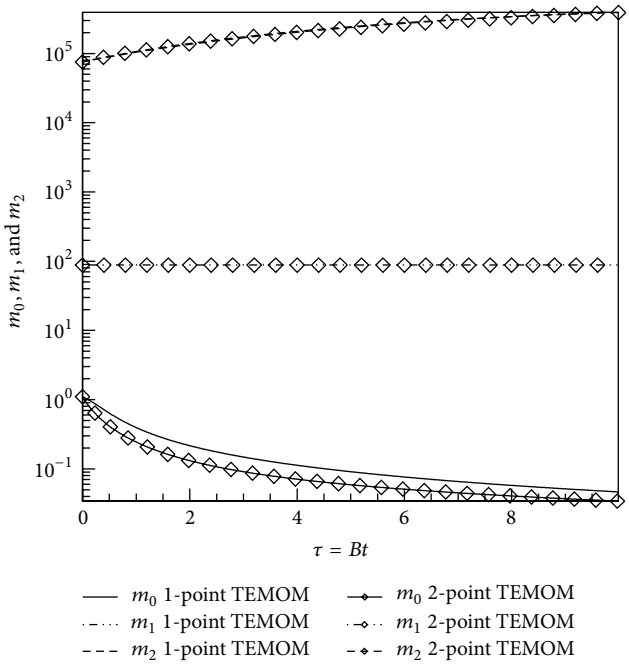

Figure 2: The evolution of moments for Case II using different expansion schemes.

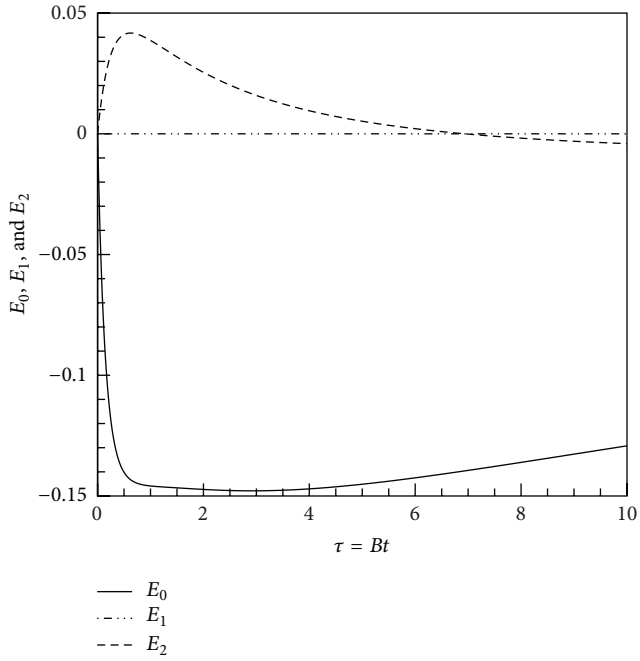

Figure 3: The variation of error function E_k versus dimensionless time τ.

between two methods is just as the same as the theoretical analysis at the beginning of this paragraph.

Figure 2 shows the results of Case II for both single point TEMOM and multi point TEMOM. From the figure, an obvious deviation is found. It shows that, for a typical bimodal system, the particle size difference between different models can not be neglected. The value for multipoint TEMOM is always smaller than that for TEMOM especially for m_0. This means that the original TEMOM model will underestimate the coagulation effect for the particle number concentration (m_0). Another interesting phenomenon is that m_1 is the same for both of the two models. The reason is that m_1 physically represents the volume fraction of particles. The particle collision (coagulation) will not change the total volume or the mass of particles. Hence, m_1 is a constant from the beginning to the end.

Define the error function as

$$E_k = \frac{m_k^{\mathrm{m}} - m_k^{\mathrm{s}}}{m_k^{\mathrm{s}}}, \tag{14}$$

Where m_k^{m} represents the moments in multi-point TEMOM and m_k^{s} represents the moments in original TEMOM. The exact tendency of E_k is shown in Figure 3. According to the figure, the maximum deviation for m_0 will be about 15% and 4% for m_2. For m_0, the error function E_0 will increase in a very short time, reach the maximum, and then decrease slowly. This phenomenon indicates that the difference in particle size will lead to a relatively large deviation at the very beginning of coagulation for bimodal particle system when the TEMOM is selected for the bimodal particle system.

Figure 4 shows the different moments in modes i and j using the technique proposed in current paper. According to

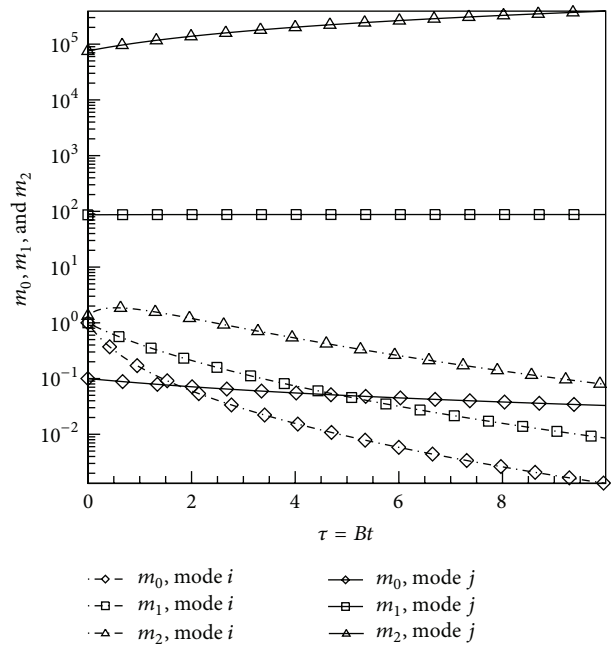

Figure 4: The evolution of moments for Case II with different modes.

the figure, an obvious reduction is found for each moment m_k in mode i, which means that the coagulation will lead to the decrease of m_0 (particle number concentration) and m_1 (particle volume fraction). Particularly the volume fraction of particles, m_1, no longer keeps a constant because of the external collision with particles in mode j and the new birth of bigger particles. For particles in mode j, the internal

coagulation in mode j will lead to the decrease of m_0, while the external coagulation between mode i and mode j will take no effect on m_0. As a result, the slope of curve is flatter than that in Figure 2. However, m_1 and m_2 are comparable with those in Figure 2, because these two parameters are related to the particle volume tightly. The average volume of particle in mode j is much bigger than that in mode i, according to the initial condition. In general, such a result indicates the importance of current technique, giving more accurate result and more detail for the complex bimodal particle system.

4. Conclusions

The current research showed a multipoint Taylor-expansion method of moments for the bimodal particle system in the Stokes regime. A theoretical deduction was performed and brief results are given. Both theoretical validation and numerical tests are implemented. The results show that, for a single-modal system, there is no difference between the two methods. However, for a bimodal system, although the evolution of moments has the same tendency, there is obvious deviation between the two methods. For the case investigated in current paper, the maximum deviation for m_0 is about 15% and 4% for m_2. Each moment m_k in mode i will decrease. The technique proposed in this paper will bring in the accuracy and details of particles. This method can be further extended to the multi-modal system

Appendix

The coefficients in (11) are listed with the definition $r = (u_1/u_2)^{1/3}$. Consider

$$a_{00} = 70r + 70r^{-1} + 162, \qquad a_{01} = 35u_1^{-1}\left(2r^2 - r^4\right),$$
$$a_{02} = u_1^{-2}\left(10r^7 - 14r^5\right), \qquad a_{10} = 35u_1^{-1}\left(2r - r^{-1}\right),$$
$$a_{11} = -35u_1^{-2}\left(r^4 + r^2\right), \qquad a_{12} = u_1^{-3}\left(10r^7 + 7r^5\right),$$
$$a_{20} = u_1^{-2}\left(10r^{-1} - 14r\right), \qquad a_{21} = u_1^{-3}\left(7r^4 + 10r^2\right),$$
$$a_{22} = -2u_1^{-4}\left(r^7 + r^5\right);$$
$$b_{00} = u_1\left(14r - 10r^{-1}\right), \qquad b_{01} = -7r^4 - 10r^2,$$
$$b_{02} = 2u_1^{-1}\left(r^7 + r^5\right), \qquad b_{10} = -112r - 40r^{-1} - 162,$$
$$b_{11} = u_1^{-1}\left(56r^4 - 40r^2\right), \qquad b_{12} = 8u_1^{-2}\left(r^5 - 2r^7\right),$$
$$b_{20} = u_1^{-1}\left(5r^{-1} - 28r\right), \qquad b_{21} = u_1^{-2}\left(14r^4 + 5r^2\right),$$
$$b_{22} = -u_1^{-3}\left(4r^7 + r^5\right);$$
$$c_{00} = u_1^2\left(5r^{-1} - 28\ r\right), \qquad c_{01} = u_1\left(14r^4 + 5\ r^2\right),$$
$$c_{02} = -4r^7 - r^5, \qquad c_{10} = u_1\left(98r - 25r^{-1}\right),$$
$$c_{11} = -49r^4 - 25r^2, \qquad c_{12} = u_1^{-1}\left(14r^7 + 5r^5\right),$$
$$c_{20} = -196r - 25r^{-1} - 162, \qquad c_{21} = u_1^{-1}\left(98r^4 - 25r^2\right),$$
$$c_{22} = u_1^{-2}\left(5r^5 - 28r^7\right);$$
$$d_{00} = u_1\left(10r^{-1} - 14r\right), \qquad d_{01} = 7r^4 + 10r^2,$$
$$d_{02} = -2u_1^{-1}\left(r^7 + r^5\right), \qquad d_{10} = 112r + 40r^{-1} + 162,$$
$$d_{11} = u_1^{-1}\left(40r^2 - 56r^4\right), \qquad d_{12} = 8u_1^{-2}\left(2r^7 - r^5\right),$$
$$d_{20} = u_1^{-1}\left(28r - 5r^{-1}\right), \qquad d_{21} = -u_1^{-2}\left(14r^4 + 5r^2\right),$$
$$d_{22} = u_1^{-3}\left(4r^7 + r^5\right);$$
$$e_{00} = u_1^2\left(-28r + 5r^{-1} + 4r^{-2} + 4r^{-4}\right),$$
$$e_{01} = u_1\left(14r^4 + 5r^2 + 16r - 32r^{-1}\right),$$
$$e_{02} = -4r^7 - r^5 - 2r^4 - 8r^2,$$
$$e_{10} = u_1\left(98r - 25r^{-1} - 32r^{-2} + 16r^{-4}\right),$$
$$e_{11} = -49r^4 - 25r^2 - 128r - 128r^{-1} - 324,$$
$$e_{12} = u_1^{-1}\left(14r^7 + 5r^5 + 16r^4 - 32r^2\right),$$
$$e_{20} = -196r - 25r^{-1} - 8r^{-2} - 2r^{-4} - 162,$$
$$e_{21} = u_1^{-1}\left(98r^4 - 25r^2 - 32r + 16r^{-1}\right),$$
$$e_{22} = u_1^{-2}\left(-28r^7 + 5r^5 + 4r^4 + 4r^2\right). \tag{A.1}$$

Conflict of Interests

The authors declare that there is no conflict of interests regarding the publication of this paper.

Acknowledgments

The authors gratefully acknowledges the financial support from the National Natural Science Foundation of China under Grant no. 11302070, the National Basic Research Program of China (973 Program) under Grant no. 2010CB-227102.

References

[1] T. L. Chan, Z. Ning, J. S. Wang, C. S. Cheung, C. W. Leung, and W. T. Hung, "Gaseous and particle emission factors from the selected on-road petrol/gasoline, diesel, and liquefied petroleum gas vehicles," *Energy and Fuels*, vol. 21, no. 5, pp. 2710–2718, 2007.

[2] R. B. Diemer and J. H. Olson, "A moment methodology for coagulation and breakage problems, part 2: moment models and distribution reconstruction," *Chemical Engineering Science*, vol. 57, no. 12, pp. 2211–2228, 2002.

[3] J. I. Jeong and M. Choi, "A bimodal moment model for the simulation of particle growth," *Journal of Aerosol Science*, vol. 35, no. 9, pp. 1071–1090, 2004.

[4] A. Pugatshova, A. Reinart, and E. Tamm, "Features of the multimodal aerosol size distribution depending on the air mass origin in the Baltic region," *Atmospheric Environment*, vol. 41, no. 21, pp. 4408–4422, 2007.

[5] G. Lonati, M. Crippa, V. Gianelle, and R. van Dingenen, "Daily patterns of the multi-modal structure of the particle number size distribution in Milan, Italy," *Atmospheric Environment*, vol. 45, no. 14, pp. 2434–2442, 2011.

[6] H. Tang and J. Lin, "Research on bimodal particle extinction coefficient during Brownian coagulation and condensation for the entire particle size regime," *Journal of Nanoparticle Research*, vol. 13, no. 12, pp. 7229–7245, 2011.

[7] A. S. Koziol and H. G. Leighton, "The moments method for multi-modal multi-component aerosols as applied to the coagulation-type equation," *Quarterly Journal of the Royal Meteorological Society*, vol. 133, no. 625, pp. 1057–1070, 2007.

[8] J. C. Barrett and J. S. Jheeta, "Improving the accuracy of the moments method for solving the aerosol general dynamic equation," *Journal of Aerosol Science*, vol. 27, no. 8, pp. 1135–1142, 1996.

[9] C. H. Jung and Y. P. Kim, "Numerical estimation of the effects of condensation and coagulation on visibility using the moment method," *Journal of Aerosol Science*, vol. 37, no. 2, pp. 143–161, 2006.

[10] R. McGraw, "Description of aerosol dynamics by the quadrature method of moments," *Aerosol Science and Technology*, vol. 27, no. 2, pp. 255–265, 1997.

[11] M. Yu, J. Lin, and T. Chan, "A new moment method for solving the coagulation equation for particles in Brownian motion," *Aerosol Science and Technology*, vol. 42, no. 9, pp. 705–713, 2008.

[12] M. Yu and J. Lin, "Taylor-expansion moment method for agglomerate coagulation due to Brownian motion in the entire size regime," *Journal of Aerosol Science*, vol. 40, no. 6, pp. 549–562, 2009.

[13] M. Yu and J. Lin, "Binary homogeneous nucleation and growth of water-sulfuric acid nanoparticles using a TEMOM model," *International Journal of Heat and Mass Transfer*, vol. 53, no. 4, pp. 635–644, 2010.

[14] M. Yu, J. Lin, and T. Chan, "Numerical simulation for nucleated vehicle exhaust particulate matters via the temom/les method," *International Journal of Modern Physics C*, vol. 20, no. 3, pp. 399–421, 2009.

[15] J. Lin, P. Lin, and H. Chen, "Research on the transport and deposition of nanoparticles in a rotating curved pipe," *Physics of Fluids*, vol. 21, no. 12, pp. 1–11, 2009.

[16] M. Yu, J. Lin, H. Jin, and Y. Jiang, "The verification of the Taylor-expansion moment method for the nanoparticle coagulation in the entire size regime due to Brownian motion," *Journal of Nanoparticle Research*, vol. 13, no. 5, pp. 2007–2020, 2011.

Hindawi Publishing Corporation
Abstract and Applied Analysis
Volume 2013, Article ID 131025, 7 pages
http://dx.doi.org/10.1155/2013/131025

Research Article

Lattice Boltzmann Simulation of Collision between 2D Circular Particles Suspension in Couette Flow

Li-Zhong Huang[1] and De-Ming Nie[2]

[1] *Institute of Fluid Engineering, Zhejiang University, Hangzhou 310027, China*
[2] *College of Metrology and Technology Engineering, China Jiliang University, Hangzhou 310018, China*

Correspondence should be addressed to De-Ming Nie; nieinhz@cjlu.edu.cn

Received 23 October 2013; Accepted 5 November 2013

Academic Editor: Jianzhong Lin

Collision between 2D circular particles suspension in Couette flow is simulated by using multiple-relaxation-time based lattice Boltzmann and direct forcing/fictitious domain method in this paper. The patterns of particle collisions are simulated and analyzed in detail by changing the velocity of top and bottom walls in the Couette flow. It can be seen from the simulation results that, while the velocity is large enough, the number of collisions between particles will change little as this velocity varies.

1. Introduction

Multiphase flow is a very important branch of fluid mechanics, while fluid-solid two-phase flow is the main part of such flow. And fluid-solid two-phase flow is very common in nature and industry, such as raindrop formation, material science, chemical industry, aerosol deposition, fluidized beds, and injection molding machine [1, 2]. Particle collisions, which will influence the performance of product, happen occasionally in those processes. So it is very meaningful to do some research to understand particle collisions and then take control to improve the performance of product.

Even with the help of the precise and advanced particle image velocity (PIV) instrument, it is very difficult to observe the phenomenon of particle collisions in detail. Comparing the experimental measurement, numerical simulation has great advantages to investigate particle collisions in fluid-solid two-phase flow, especially for direct numerical simulation (DNS) methods. The lattice Boltzmann method (LBM), one of the best DNS methods with several remarkable advantages, was first proposed by Ladd [3] and then improved by Aidun et al. [4] to simulate particles suspended in a viscous fluid. Feng and Michaelides [5] and Tian et al. [6] united immersed boundary method (IBM) into LBM to deal with fluid-solid interface problem. In the past several decades the LBM method was proved robust and efficient for particulate flows, especially in the case of large number of particles [7–12]. Nie and Lin [13] developed a single-relaxation-time (SRT) based lattice Boltzmann-direct forcing/fictitious domain (SRT LB-DF/FD) method to simulate particle suspensions and then improved to multiple-relaxation-time (MRT LB-DF/FD).

Several papers investigated particle collisions in three-dimensional homogeneous isotropic turbulence [14–18] but not by using DNS method. In this paper, DNS method is adopted to simulate particle collisions. Because the MRT model has better ability of computing pressure and more time saving than the SRT model, the MRT LB DF/FD method is utilized. Firstly, this method is introduced in detail in Section 2. Secondly, simulation problem is described in Section 3. And finally, several simulation results and conclusions are presented in Section 4.

2. Numerical Method

2.1. The MRT LB DF/FD Method. The lattice Boltzmann method based on the multiple-relaxation-time (MRT) collision model is adopted in this paper [13]. The discrete

equations can be written as follows:

$$f_i\left(\mathbf{x}+\mathbf{e}_i\Delta t, t+\Delta t\right) = f_i\left(\mathbf{x}, t\right) - M^{-1}S\left[\mathbf{m}-\mathbf{m}^{(\mathrm{eq})}\right] + \mathbf{F}\Delta t, \tag{1}$$

where S is the diagonal collision matrix, $S = \mathrm{diag}(0, s_e, s_\varepsilon, 0, s_q, 0, s_q, s_\nu, s_\nu)$, and M is the transform matrix,

$$M = \begin{bmatrix} 1 & 1 & 1 & 1 & 1 & 1 & 1 & 1 & 1 \\ -4 & -1 & -1 & -1 & -1 & 2 & 2 & 2 & 2 \\ 4 & -2 & -2 & -2 & -2 & 1 & 1 & 1 & 1 \\ 0 & 1 & 0 & -1 & 0 & 1 & -1 & -1 & 1 \\ 0 & -2 & 0 & 2 & 0 & 1 & -1 & -1 & 1 \\ 0 & 0 & 1 & 0 & -1 & 1 & 1 & -1 & 1 \\ 0 & 0 & -2 & 0 & 2 & 1 & 1 & -1 & -1 \\ 0 & 1 & -1 & 1 & -1 & 0 & 0 & 0 & 0 \\ 0 & 0 & 0 & 0 & 0 & 1 & -1 & 1 & -1 \end{bmatrix}. \tag{2}$$

The moment space spanned by $\mathbf{m}_i$ and the velocity space spanned by f_i are related by a linear mapping, $\mathbf{m} = Mf$; that is, $f = M^{-1}\mathbf{m}$. The D2Q9 model is used in 2D simulation, and the discrete velocities are listed as the follows:

$$\mathbf{c}_i = \begin{cases} (0,0) & i = 0, \\ (\pm 1, 0)\, c, (0, \pm 1)\, c & i = 1-4, \\ (\pm 1, \pm 1)\, c, (\pm 1, \pm 1)\, c & i = 5-8, \end{cases} \tag{3}$$

where $c = \Delta x/\Delta t$ is the lattice speed, among which Δx is the lattice spacing, and Δt *is* the time step. For D2Q9 model, the corresponding nine moments are given by [19]

$$\mathbf{m} = \left(\rho, e, \varepsilon, j_x, q_x, j_y, q_y, p_{xx}, p_{xy}\right)^\dagger, \tag{4}$$

where ρ is the mean density and $j_x = \rho u_x$, $j_y = \rho u_y$ are the conserved moments. Moreover, the other nonconserved moments are listed as follows:

$$e^{(\mathrm{eq})} = -2\rho + \frac{3\mathbf{j}\cdot\mathbf{j}}{\rho}, \qquad \varepsilon^{(\mathrm{eq})} = \rho - \frac{3\mathbf{j}\cdot\mathbf{j}}{\rho}, \qquad q_x^{(\mathrm{eq})} = -j_x,$$
$$q_y^{(\mathrm{eq})} = -j_y, \qquad p_{xx}^{(\mathrm{eq})} = \frac{\left(j_x^2 - j_y^2\right)}{\rho}, \qquad p_{xy}^{(\mathrm{eq})} = \frac{j_x j_y}{\rho}. \tag{5}$$

According to Guo et al. [20], the forcing term $\mathbf{F}$ is defined as follows:

$$\mathbf{F} = M^{-1}\left(I - \frac{1}{2}S\right)M\overline{\mathbf{F}},$$
$$\overline{F_i} = w_i\left[\frac{\mathbf{c}_i\cdot\boldsymbol{\alpha}}{c_s^2} + \frac{\mathbf{u}\boldsymbol{\alpha}:\mathbf{c}_i\mathbf{c}_i}{c_s^4} - \frac{\mathbf{u}\boldsymbol{\alpha}:c_s^2 I}{c_s^4}\right], \tag{6}$$

where $\boldsymbol{\alpha}$ is the acceleration due to the external force and w_i are weights related to the lattice model which are chosen as $w_0 = 4/9$; $w_i = 1/9$, $i = 1\sim4$; $w_i = 1/36$, $i = 5\sim8$. The speed of sound c_s is equal to $c/3^{1/2}$. By applying the Taylor expansion techniques and the Chapman-Enskog analysis, (1) leads to the hydrodynamic equations that are shown as follows:

$$\nabla\cdot\mathbf{u} = 0, \qquad \rho_f\left(\frac{\partial\mathbf{u}}{\partial t} + (\mathbf{u}\cdot\nabla)\,\mathbf{u}\right) = -\nabla p + \mu\nabla^2\mathbf{u} + \mathbf{a}. \tag{7}$$

The shear viscosity and the bulk viscosity can be defined as follows [21]:

$$\nu = \frac{1}{3}\left(\frac{1}{s_\nu} - \frac{1}{2}\right)c\Delta x, \qquad \zeta = \frac{1}{3}\left(\frac{1}{s_e} - \frac{1}{2}\right)c\Delta x. \tag{8}$$

2.2. Collisions Model. A collision model is needed to avoid particles overlapping. Then the short-range repulsive force developed by Wan and Turek [22] is utilized in this paper because it is easily carried out in the code. For particle-particle collisions, the short-range repulsive force is calculated by

$$F_{i,j}^P = \begin{cases} 0 & d_{i,j} > R_i + R_j + \xi, \\ \dfrac{1}{\varepsilon_P'}\left(\mathbf{X}_i - \mathbf{X}_j\right)\left(R_i + R_j - d_{i,j}\right) & \\ & d_{i,j} \le R_i + R_j, \\ \dfrac{1}{\varepsilon_P}\left(\mathbf{X}_i - \mathbf{X}_j\right)\left(R_i + R_j + \xi - d_{i,j}\right)^2 & \\ & R_i + R_j \le d_{i,j} \le R_i + R_j + \xi, \end{cases} \tag{9}$$

where $\mathbf{X}_i$ and $\mathbf{X}_j$ are the mass center coordinates of the ith and jth particle, R_i and R_j are their radius, $d_{i,j}$ is the distance between their mass centers which equals to $|\mathbf{X}_i - \mathbf{X}_j|$, ξ is the force range which is usually set to be one or two lattice spacing, and ε_p' and ε_p are two small positive stiffness parameters for particle-particle collisions.

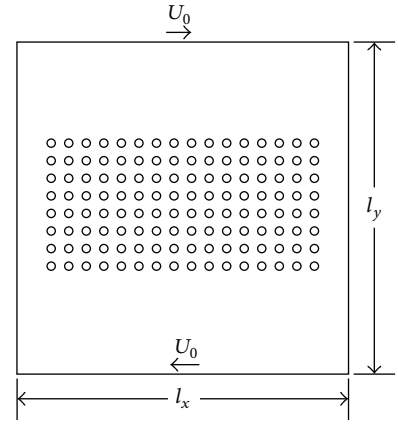

Figure 1: Schematic diagram of geometry.

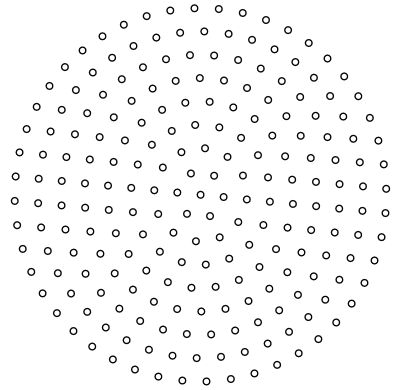

Figure 2: Arrangements of Lagrangian points.

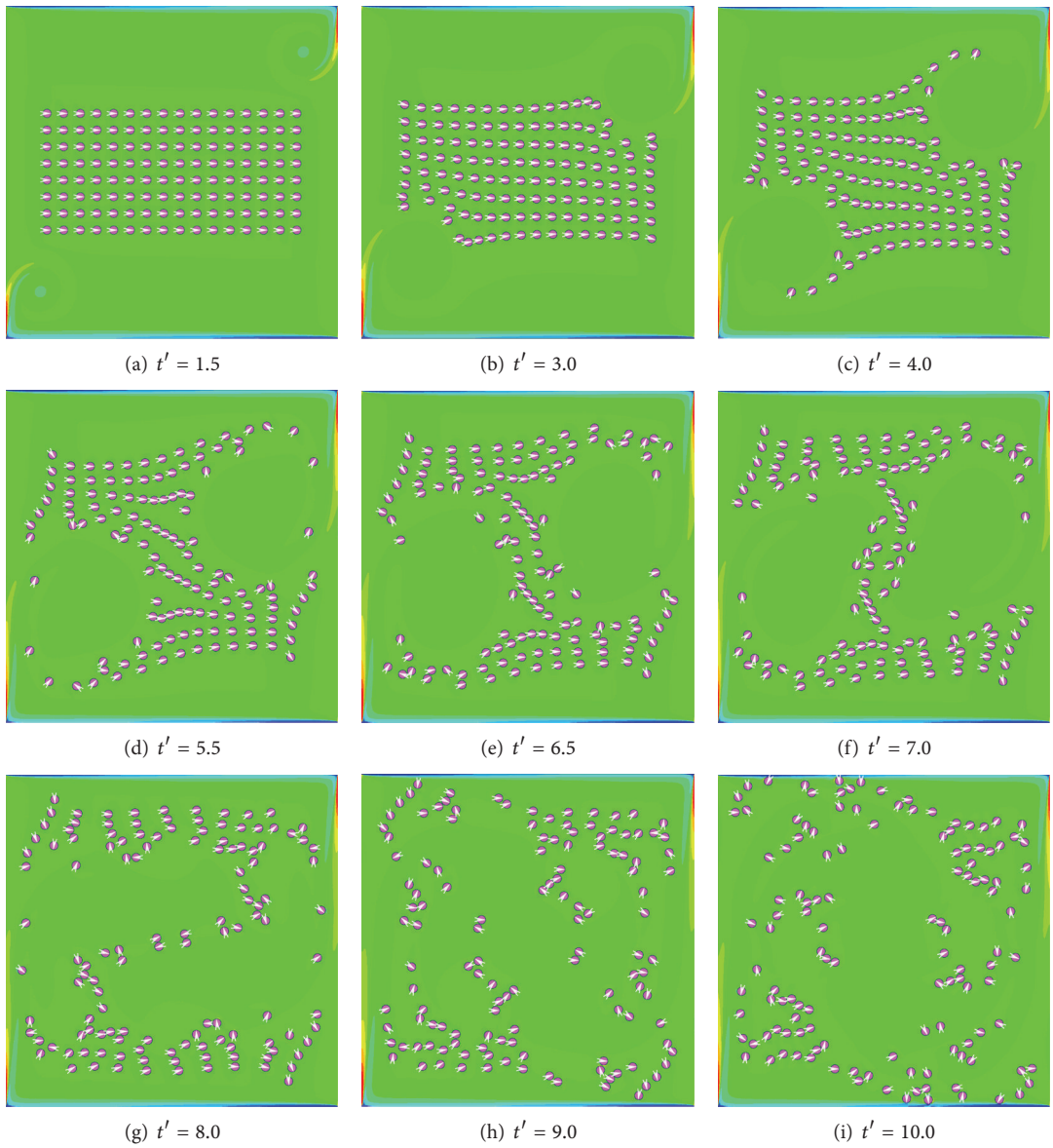

(a) $t' = 1.5$ (b) $t' = 3.0$ (c) $t' = 4.0$

(d) $t' = 5.5$ (e) $t' = 6.5$ (f) $t' = 7.0$

(g) $t' = 8.0$ (h) $t' = 9.0$ (i) $t' = 10.0$

Figure 3: Vorticity contours when $U_0 = 0.1$ m/s.

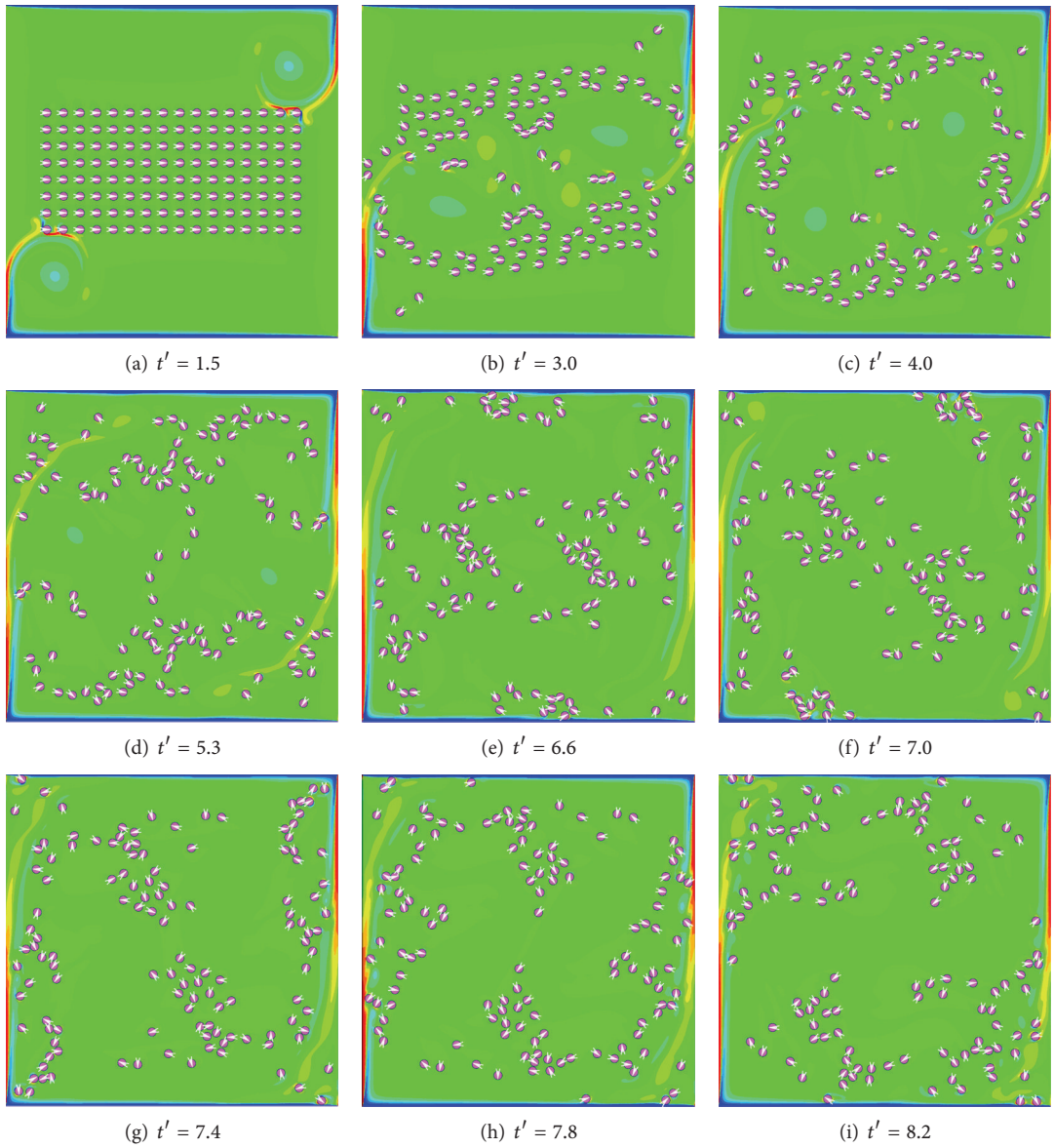

(a) $t' = 1.5$ (b) $t' = 3.0$ (c) $t' = 4.0$

(d) $t' = 5.3$ (e) $t' = 6.6$ (f) $t' = 7.0$

(g) $t' = 7.4$ (h) $t' = 7.8$ (i) $t' = 8.2$

FIGURE 4: Vorticity contours when $U_0 = 0.2$ m/s.

But for particle-wall collisions, the corresponding short-range repulsive force is determined as follows:

$$F_{i,j}^{W} = \begin{cases} 0 & d_i' > 2R_i + \xi, \\ \dfrac{1}{\varepsilon_W'}\left(\mathbf{X}_i - \mathbf{X}_i'\right)\left(2R_i - d_i'\right) & d_i' \le 2R_i, \\ \dfrac{1}{\varepsilon_W}\left(\mathbf{X}_i - \mathbf{X}_i'\right)\left(2R_i + \xi - d_i'\right)^2 & 2R_i \le d_i' \le 2R_i + \xi, \end{cases} \tag{10}$$

where $\mathbf{X}_i'$ is the coordinate of the nearest imaginary particle located on the boundary nearby the ith particle, d_i' is the distance between the imaginary particle and the real one which equals to $|\mathbf{X}_i - \mathbf{X}_i'|$, and ε_W' and ε_W are the other two small positive stiffness parameters for particle-wall collisions. In this paper, ε_p', ε_p, ε_W', and ε_W are all set to be 1e-7.

3. Problem Description

The main purpose of this paper is to study collisions between 2D circular particles suspension in Couette flow. The schematic diagram of geometry is shown in Figure 1 which is constructed by four solid walls, $lx = ly = 8$ cm, and mesh element is 640000. The left and right walls are fixed, while the top wall moves in the right direction with a velocity of U_0 and the bottom wall moves in the left direction at the same velocity. 128 circular particles (8 rows, 16 columns) are placed in the middle of this domain, and the distance of center of two neighborhood particles in horizontal and vertical direction is

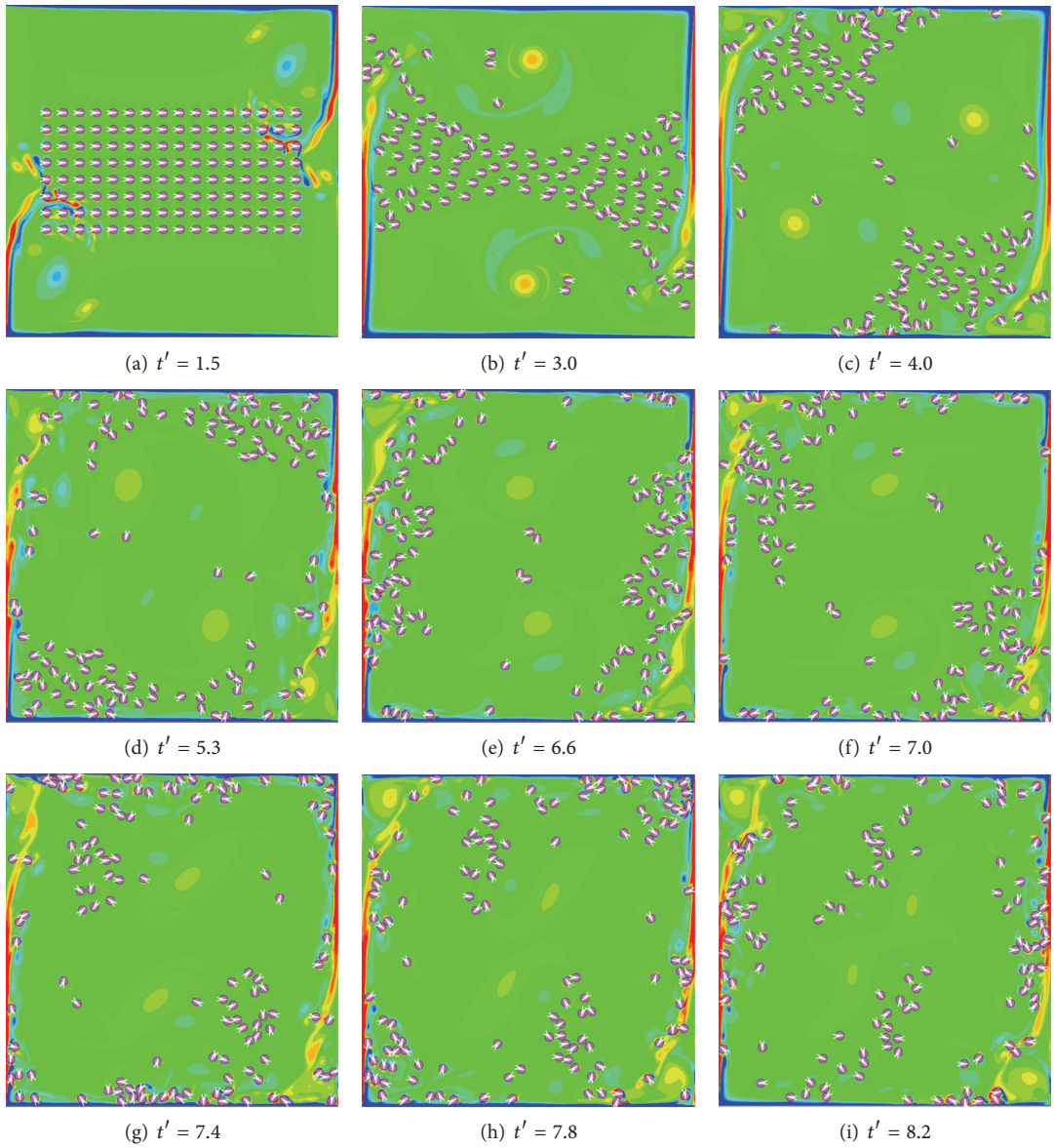

(a) $t' = 1.5$ (b) $t' = 3.0$ (c) $t' = 4.0$

(d) $t' = 5.3$ (e) $t' = 6.6$ (f) $t' = 7.0$

(g) $t' = 7.4$ (h) $t' = 7.8$ (i) $t' = 8.2$

FIGURE 5: Vorticity contours when $U_0 = 0.3$ m/s.

two times of the diameter of particle. In order to ignore the influence of gravity, the density of particles is set to be same as the suspension fluid, $\rho_p = \rho_f = 1.0\,\text{g/cm}^3$. The kinematic viscosity of the fluid is set to be $0.01\,\text{cm}^2\,\text{s}^{-1}$. For each particle, the diameter is 0.2 cm and the arrangement of Lagrangian points is shown in Figure 2.

4. Simulation Results and Conclusions

In this paper, when $t' = t/10^4\,\text{s} \leq 1.5$, the circular particles are fixed to generate a fully developed Couette flow which can be seen from Figures 3(a), 4(a), and 5(a). And when $t' > 1.5$, those particles begin to move in the suspension fluid. At first, U_0 is set to be very small which equals to 0.1 m/s and the instantaneous vorticity contours can be seen from Figures 3(a)–3(i). Obviously, the vorticity is not strong enough which makes the number of collisions very big.

Instantaneous vorticity contours for $U_0 = 0.2$ m/s at several interval times are shown in Figures 4(a)–4(i). It can be seen from those figures that the particles are moving by the influence of the two main symmetry vortices. Even when $t' = 8.2$, the vortex contour is rotational symmetry from the center of the simulation domain.

But when $U_0 = 0.3$ m/s, Figures 5(a)–5(i) show that the circular particles are agglomerated near the four sidewalls by the influence of the two main vortices. And when $t' > 7.8$, the particles are no longer rotational symmetry from the center of the simulation domain, distributed at completely random. The vortex patterns are totally different when U_0 varies from 0.1 m/s to 0.3 m/s; however, the number of particle collisions

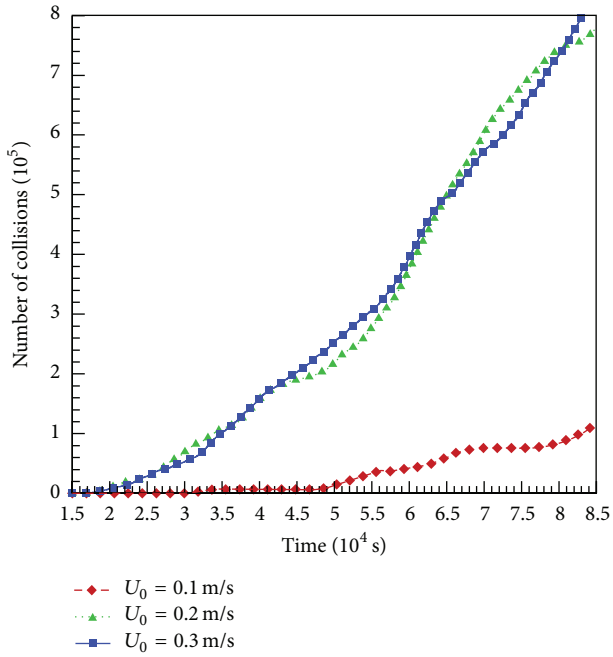

Figure 6: Comparison of collision number with different U_0.

varies little when U_0 is large enough which can be seen from Figure 6.

Acknowledgment

This work is supported by the National Natural Science Foundation of China with Grant 11132008.

References

[1] J. Lin, X. Shi, and Z. Yu, "The motion of fibers in an evolving mixing layer," *International Journal of Multiphase Flow*, vol. 29, no. 8, pp. 1355–1372, 2003.

[2] L. Jianzhong, Z. Weifeng, and Y. Zhaosheng, "Numerical research on the orientation distribution of fibers immersed in laminar and turbulent pipe flows," *Journal of Aerosol Science*, vol. 35, no. 1, pp. 63–82, 2004.

[3] A. J. C. Ladd, "Numerical simulations of particulate suspensions via a discretized Boltzmann equation. I. Theoretical foundation," *Journal of Fluid Mechanics*, vol. 271, pp. 285–309, 1994.

[4] C. K. Aidun, Y. Lu, and E.-J. Ding, "Direct analysis of particulate suspensions with inertia using the discrete Boltzmann equation," *Journal of Fluid Mechanics*, vol. 373, pp. 287–311, 1998.

[5] Z.-G. Feng and E. E. Michaelides, "The immersed boundary-lattice Boltzmann method for solving fluid-particles interaction problems," *Journal of Computational Physics*, vol. 195, no. 2, pp. 602–628, 2004.

[6] F.-B. Tian, H. Luo, L. Zhu, J. C. Liao, and X.-Y. Lu, "An efficient immersed boundary-lattice Boltzmann method for the hydrodynamic interaction of elastic filaments," *Journal of Computational Physics*, vol. 230, no. 19, pp. 7266–7283, 2011.

[7] L. Jianzhong, S. Xing, and Y. Zhenjiang, "Effects of the aspect ratio on the sedimentation of a fiber in Newtonian fluids," *Journal of Aerosol Science*, vol. 34, no. 7, pp. 909–921, 2003.

[8] X. Shi, J. Lin, and Z. Yu, "Discontinuous Galerkin spectral element lattice Boltzmann method on triangular element," *International Journal for Numerical Methods in Fluids*, vol. 42, no. 11, pp. 1249–1261, 2003.

[9] J.-Z. Lin, Y.-L. Wang, and J. A. Olsen, "Sedimentation of rigid cylindrical particles with mechanical contacts," *Chinese Physics Letters*, vol. 22, no. 3, pp. 628–631, 2005.

[10] L. Jianzhong and K. Xiaoke, "Fiber orientation distributions in a suspension flow through a parallel plate channel containing a cylinder," *Journal of Composite Materials*, vol. 43, no. 12, pp. 1373–1390, 2009.

[11] X. K. Ku and J. Z. Lin, "Inertial effects on the rotational motion of a fibre in simple shear flow between two bounding walls," *Physica Scripta*, vol. 80, no. 2, Article ID 025801, 2009.

[12] X. Ku and J. Lin, "Numerical simulation of the flows over two tandem cylinders by lattice Boltzmann method," *Modern Physics Letters B*, vol. 19, no. 28-29, pp. 1551–1554, 2005.

[13] D. Nie and J. Lin, "A LB-DF/FD method for particle suspensions," *Communications in Computational Physics*, vol. 7, no. 3, pp. 544–563, 2010.

[14] L. I. Zaichik, O. Simonin, and V. M. Alipchenkov, "Collision rates of bidisperse inertial particles in isotropic turbulence," *Physics of Fluids*, vol. 18, no. 3, Article ID 035110, 2006.

[15] L. I. Zaichik, O. Simonin, and V. M. Alipchenkov, "Two statistical models for predicting collision rates of inertial particles in homogeneous isotropic turbulence," *Physics of Fluids*, vol. 15, no. 10, pp. 2995–3005, 2003.

[16] L.-P. Wang, A. S. Wexler, and Y. Zhou, "On the collision rate of small particles in isotropic turbulence. I. Zero-inertia case," *Physics of Fluids*, vol. 10, no. 1, pp. 266–276, 1998.

[17] Y. Zhou, A. S. Wexler, and L.-P. Wang, "On the collision rate of small particles in isotropic turbulence. II. Finite inertia case," *Physics of Fluids*, vol. 10, no. 5, pp. 1206–1216, 1998.

[18] C. N. Franklin, P. A. Vaillancourt, M. K. Yau, and P. Bartello, "Collision rates of cloud droplets in turbulent flow," *Journal of the Atmospheric Sciences*, vol. 62, no. 7, pp. 2451–2466, 2005.

[19] L.-S. Luo, W. Liao, X. Chen, Y. Peng, and W. Zhang, "Numerics of the lattice Boltzmann method: effects of collision models on the lattice Boltzmann simulations," *Physical Review E*, vol. 83, no. 5, Article ID 056710, 2011.

[20] Z. Guo, C. Zheng, and B. Shi, "Discrete lattice effects on the forcing term in the lattice Boltzmann method," *Physical Review E*, vol. 65, no. 4, Article ID 046308, 6 pages, 2002.

[21] D. d'Humières, I. Ginzburg, M. Krafczyk, P. Lallemand, and L.-S. Luo, "Multiple-relaxation-time lattice Boltzmann models in three dimensions," *The Royal Society of London*, vol. 360, no. 1792, pp. 437–451, 2002.

[22] D. Wan and S. Turek, "An efficient multigrid-FEM method for the simulation of solid-liquid two phase flows," *Journal of Computational and Applied Mathematics*, vol. 203, no. 2, pp. 561–580, 2007.

Hindawi Publishing Corporation
Abstract and Applied Analysis
Volume 2013, Article ID 384640, 5 pages
http://dx.doi.org/10.1155/2013/384640

Research Article

Modeling and Simulation of Flow and Formation Damage of Asphalt-Paved Roads

M. H. Alawi,[1] M. M. El-Qadi,[2] and M. A. El-Ameen[3]

[1] *Civil Engineering Department, Collage of Engineering, Umm Al-Qura University, Saudi Arabia*
[2] *Mathematics Department, Faculty of Science, Helwan University, Egypt*
[3] *Preparing Year Department, Collage of Engineering, Umm Al-Qura University, Saudi Arabia*

Correspondence should be addressed to M. A. El-Ameen; mohamedmossa327@yahoo.com

Received 29 September 2013; Accepted 5 October 2013

Academic Editor: Mohamed Fathy El-Amin

Porous asphalt is a standard asphalt built on aggregate storage bed which allows water to drain through it and reduces stormwater runoff. However, porosity of the porous asphalt and the storage bed may be effectively reduced due to trapping suspended solids from the water or from the asphalt damage. In this paper, we present mathematical modeling and numerical simulation of flow and damage of porous asphalt-paved roads. A mathematical model to describe the fine-particles transport carried by a two-phase flow in a porous medium is presented. The buoyancy, capillarity, and mixed relative permeabilities correlations to fit with the mixed-wet system are considered. Throughout this investigation, we monitor the changing of the fluids properties such as water saturation and solid properties such as porosity and permeability due to trapping the fine-particles.

1. Introduction

The impervious asphalt-paved roads may store significant amounts of thermal energy during summer. The stored thermal energy may be transferred to stream waters during runoff events. Moreover, as a result of fluctuations in ambient air temperatures—diurnal and seasonal, intensity of solar radiation of the asphalt-paved, a significant deformation of asphalt-paved may occur due to the heat and mass transfer between asphalt and water. On the other hand porous (pervious, permeable, or open-graded) asphalt is standard asphalt with reduced sand or fines that allows water to drain through it. Pervious asphalt built on aggregate storage bed reduces stormwater runoff. In addition to reducing runoff, this effectively traps suspended solids and filters pollutants from the water. The stormwater flows through the asphalt to the layer of crushed stone aggregate bedding and base that supports the asphalt while providing storage and runoff treatment. The use of porous asphalt can potentially reduce additional expenditures and land consumption for conventional collection, conveyance, and detention stormwater infrastructure. Compared to the lifetime of dense graded asphalt concrete roads, the lifetime of porous asphalt concrete is less [1]. The loss of stones from the road surface, called raveling, is mostly reported as the dominant defect in porous asphalt wearing course [2, 3]. Raveling is the start of major defects like potholes, because once a stone is gone, the surrounding stones will follow for lacking support in at least one direction [4]. Raveling also has negative influence on the noise reduction function and skid resistance of porous asphalt pavement. During service life, the pores tend to be clogged by dirt, dust, or other clogging agents. The formulation of fine-particles transport in two-phase flow in porous media has been studied experimentally and numerically in [5–7]. Formation damage is a common problem in reservoir development. The particles migrate through the porous media, deposit on the pore surfaces, and become trapped at pore constrictions to reduce the rock porosity and permeability.

Researchers have done many attempts to predict these phenomena experimentally and numerically; however, there is no study that considers the possible porosity and permeability reduction. So, in order to keep porous asphalt and its storage bed efficient, considering these kinds of effects may

lead to interesting results. In the current work, we introduce modeling and numerical simulation of fine-particle transport in two-phase flow in porous asphalt-paved roads.

2. Mathematical Modeling

The basic equations that govern the flow of the two-phase flow in porous media are mass conservation equation and constitutive equation (Darcy's law). The two-dimensional governing equations may be written as

$$\frac{\partial(\varphi\rho_w S_w)}{\partial t} = -\nabla\cdot(\rho_w v_w), \tag{1a}$$

$$\frac{\partial(\varphi\rho_a S_a)}{\partial t} = -\nabla\cdot(\rho_a v_a), \tag{1b}$$

$$v_w = -\frac{Kk_{rw}}{\mu_w}(\nabla p_w - \rho_w \mathbf{g}), \tag{2a}$$

$$v_a = -\frac{Kk_{ra}}{\mu_a}(\nabla p_a - \rho_a \mathbf{g}), \tag{2b}$$

where S is the saturation and v [m/s] is the velocity. w stands for the wetting phase (water), and a stands for the nonwetting phase (air). φ is the porosity of the medium, and $\nabla = (\partial/\partial x, \partial/\partial z)$ is the divergence operator. K [m^2] is the absolute permeability, $k_{r\alpha}$ [dimensionless] is the relative permeability, ρ [$kg\,m^3$] is the density, p [Pa] is the pressure, and $\mathbf{g} = (0, -g)^T$ is the gravitational acceleration. μ is the viscosity. The fluid saturations for the two-phase flow are interrelated by

$$S_w + S_a = 1. \tag{3}$$

The total velocity is

$$v_t = v_w + v_a. \tag{4}$$

Summing the saturation equation for water phase and the oil phase, one obtains

$$\nabla\cdot v_t = 0. \tag{5}$$

Moreover, adding the constitutive equations for each phase, (1a)–(2b), and substituting into (5), we end up with

$$v_t = -K[\lambda_t(S)\nabla p_w + \lambda_a(S)\nabla p_c] + K\chi(S)g, \tag{6}$$

where $\lambda_\alpha(S) = k_{r\alpha}(S)/\mu_\alpha$ is the mobility, $\lambda_t(S) = \lambda_a(S)+\lambda_w(S)$ is the total mobility, and $\chi = \lambda_a(S)\rho_a + \lambda_w(S)\rho_w$. In order to derive the pressure equation, substitute (6) into (5). We obtain

$$\nabla\cdot[\lambda_t(S)\nabla p_w + \lambda_a(S)\nabla p_c(S) - \chi(S)g] = 0. \tag{7}$$

Substituting the constitutive equation of the water phase, (2a) and (2b), into (1a) and (1b) gives

$$\frac{\partial(\varphi S_w)}{\partial t} + \nabla\cdot v_w = 0. \tag{8}$$

Therefore, water velocity may be written as

$$v_w = f_a v_t + \lambda_w K[f_a \nabla p_c] + \lambda_w f_a K\Delta\rho g, \tag{9}$$

where $\Delta\rho = \rho_w - \rho_a$.

On the other hand, a mathematical model is developed to describe the fine-particles transport carried by two-phase flow in porous media. Assuming that we have a number m of size intervals of particles in the water phase, the transport equation for each size interval i of the particles in the water phase can be written as

$$\frac{\partial(\phi S_w C_i)}{\partial t} + v_w\cdot\nabla C_i = \nabla\cdot(\varphi S_w D_i \nabla C_i) + R_i, \tag{10}$$

where $i = 1, 2, \ldots, m$. D_i is the dispersion coefficients of particles in size interval i in the water phase. R_i is the net rate of loss of particles in size interval i in the water phase. The net rate of loss of particles may be written as [5–7] follows:

$$R_i = \frac{\partial(\delta\phi)_i}{\partial t}, \tag{11}$$

where $(\delta\phi)_i = v_i + v_i^*$ is the porosity change due to release or retention of particles of interval i in the water phase. v_i is the volume of the particles of interval size i in contact with the water phase available on the pore surfaces per unit bulk volume of sandstone. v_i^* is the volume of the particles of interval size i entrapped in pore throats from the water phase per unit bulk volume of sandstone due to plugging and bridging. At the critical velocity of the surface deposition only particle retention occurs while above it retention and entrainment of the particles take place simultaneously [8]. A modified Gruesbeck and Collins's model for the surface deposition is expressed by [5–7] the following:

$$\frac{\partial v_i}{\partial t} = \begin{cases} \alpha_{d,i}|v_w| C_i & \text{when } v_w \le v_c \\ \alpha_{d,i}|v_w| C_i - \alpha_{e,i} v_i |v_w - v_c| & \text{when } v_w > v_c, \end{cases} \tag{12}$$

where $\alpha_{d,i}$ is the rate coefficients for surface retention of the particles in interval i. $\alpha_{e,i}$ is the rate coefficients for entrainment of the particles in interval i. v_c is the critical velocity. Similarly, the rate of entrapment of the particles in interval i is

$$\frac{\partial v_i^*}{\partial t} = \alpha_{pt,i}|v_w| C_i, \tag{13}$$

where $\alpha_{pt,i}$ is the pore throat blocking constants. Porosity may be changed because of particles deposition on the pore surfaces or blocking of pore throats. The porosity variation may be expressed by [5–7] the following:

$$\phi = \phi_0 - (\delta\phi)_i, \tag{14}$$

where ϕ_0 is the initial porosity. Also, the permeability variation due to particles deposition on the pore surfaces or blocking of pore throats may be expressed as [5–7] follows:

$$K = K_0\left((1-f)k_f + \frac{f\phi}{\phi_0}\right)^l, \tag{15}$$

where K_0 is the initial permeability, k_f is a constant for fluid seepage allowed by the plugged pores, $f = 1 - \sum_i \alpha_{f,i} v_i^*$ is the fraction of the original cross-sectional area open to flow, and the value of the exponent l has range from 2.5 to 3.5. For the particles transport carried by fluid stream in the porous media, deposition on pore surfaces and blockage in pore throats may occur. The retained particles on pore surfaces may desorb for hydrodynamic forces and then possibly adsorb on other sites of the pore bodies or get entrapped at other pore throats.

3. Results and Discussion

In order to get physical insights for the problem under consideration, we consider that typical cross-section for pervious pavement system consists of six porous layers (Figure 1) that can be simplified to one-dimensional system for calculations. The porous asphalt layer taken is 15 cm, the choker course layer is 20 cm, the filter course is 30 cm, the filter blanket is 8 cm, the reservoir course is 10 cm, and finally the native material is optional that we consider it 20 cm. We consider the top boundary as inlet of water-particles suspension. So water imbibes into the porous asphalt and replaces the air that leaves the medium from the same boundary. This type of flow in porous media is called countercurrent imbibition [9–12]. In countercurrent imbibition both wetting and nonwetting phases flow through one inflow-outflow boundary. Therefore, the total velocity becomes zero, $v_t = 0$. Therefore, the flow equations may be written as

$$\frac{\partial P_w}{\partial z} = -f_w(S)\frac{\partial P_c(S)}{\partial z} - \chi(S)\, g,$$
$$v_w = K\lambda_w f_a\left(\frac{\partial P_c}{\partial z} + \Delta\rho g\right). \tag{16}$$

Therefore,

$$\frac{\partial(\varphi S_w)}{\partial t} + K\frac{\partial}{\partial z}\left[\lambda_w f_a\left(\frac{\partial P_c}{\partial z} - \Delta\rho g\right)\right] = 0. \tag{17}$$

The relative permeabilities are given in terms of the normalized wetting phase saturation S, given as

$$k_{rw} = k_{rw}^0 S^a,$$
$$k_{ra} = k_{ra}^0 (1-S)^b, \tag{18}$$

where a and b are positive numbers, $k_{rw}^0 = k_{rw}(S = 1)$ is the endpoint relative permeability to wetting phase, and $k_{ra}^0 = k_{ra}(S = 0)$ is the endpoint relative permeability to nonwetting phase. The normalized wetting phase saturation is given by

$$S = \frac{S_w - S_{iw}}{1 - S_{ra} - S_{iw}}, \quad 0 \le S \le 1, \tag{19}$$

where S_{iw} is the irreducible water saturation and S_{ra} is the residual air saturation.

Figure 1: Typical cross-section for pervious pavement system.

For the capillary pressure we used the general correlation

$$p_c = c_w\left(\frac{S_w - S_{wr}}{1 - S_{wr}}\right)^{-a_w} + c_a\left(\frac{S_a - S_{ar}}{1 - S_{ar}}\right)^{-a_a}, \tag{20}$$

where c_w and c_a are constants that represent the entry pressure for imbibition and drainage, respectively. The constants $1/a_w$ and $1/a_a$ are the pore size distribution indexex for imbibition and drainage, respectively.

The transport equation for the interval i of the particles can be written as

$$\frac{\partial(\varphi S_w C_i)}{\partial t} + v_w\frac{\partial C_i}{\partial z} = \frac{\partial}{\partial z}\left(\varphi S_w D_i\frac{\partial C_i}{\partial z}\right) + R_i,$$

$$R_i = \begin{cases} (\alpha_{d,i} + \alpha_{pt,i})\|v_w\| C_i, & \|u_w\| \le u_c \\ (\alpha_{d,i} + \alpha_{pt,i})\|v_w\| C_i - \alpha_{e,i} v_i \|v_w - v_c\| C_i, & \|u_w\| > u_c. \end{cases} \tag{21}$$

The surface deposition of the particles in the interval i is

$$\frac{\partial v_i}{\partial t} = \begin{cases} \alpha_{d,i}\|v_w\| C_i, & \|v_w\| \le u_c \\ \alpha_{d,i}\|v_w\| C_i - \alpha_{e,i} v_i \|v_w - v_c\| C_i, & \|v_w\| > u_c. \end{cases} \tag{22}$$

The rate of entrapment of the particles in interval i is

$$\frac{\partial v_i^*}{\partial t} = \alpha_{pt,i}\|v_w\| C_i. \tag{23}$$

The initial conditions are

$$S_w = S_{0w}, \qquad C_i = v_i = v_i^* = 0,$$
$$t = 0, \quad 0 \le z \le H, \tag{24}$$

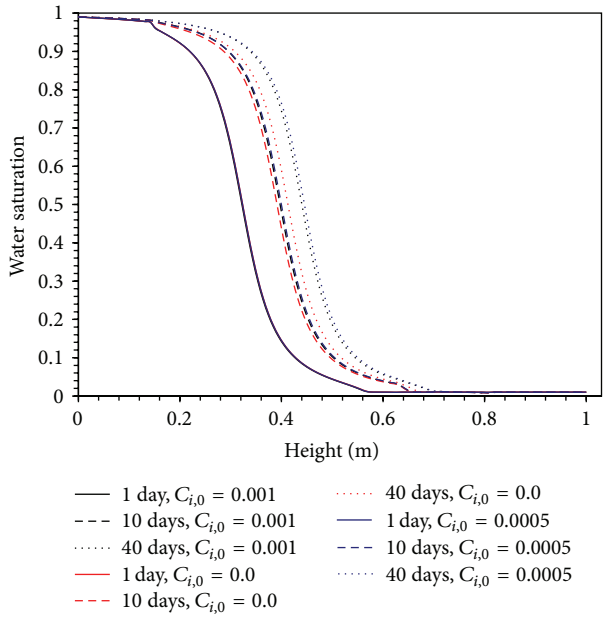

Figure 2: Water saturation against the height with various imbibition times and inlet concentrations.

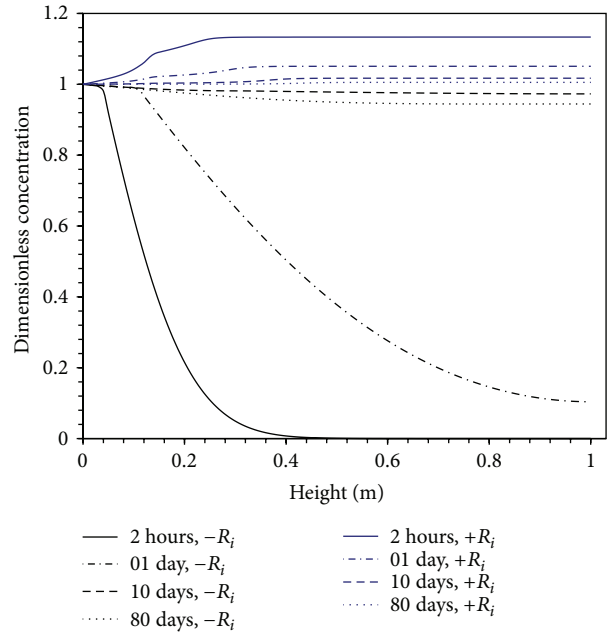

Figure 3: Normalized particles concentration against height with positive/minus R_i and various imbibition times.

where H is the depth and S_{0w} is the initial water saturation. The boundary conditions are

$$S_w = 1 - S_{or}, \qquad C_i = C_{i,0}, \qquad v_i = v_i^* = 0, \quad t \geq 0, \quad z = 0,$$
$$\frac{dS_w}{dz} = \frac{dC_i}{dz} = \frac{dv_i}{dz} = \frac{dv_i^*}{dz} = 0, \quad t \geq 0, \quad z = H, \tag{25}$$

where $C_{i,0}$ is the concentration of particles in the particles suspension at the inlet boundary. The governing equations (17)–(23) are solved numerically along with the initial and boundary conditions, (24)–(25). An efficient algorithm is used to solve the above high-nonlinear parabolic partial differential equation in one space variable z and time t. The Galerkin method is used for spatial discretization [13], while the time integration for the resulting ordinary differential equation is done with an adaptive time step. 100 points of the spatial grid were used during calculations and were enough to provide an acceptable accuracy. Now, we consider one-size particles suspension in the water phase at the inlet, with the following parameter [6, 7], $\alpha_{d,i} = 8\,\mathrm{m}^{-1}$, $\alpha_{pt,i} = 17\,\mathrm{m}^{-1}$, $\alpha_{e,i} = 400\,\mathrm{m}^{-1}$, $v_c = 4.6 \times 10^{-3}$ m/s, and $D_i = 5.6 \times 10^{-3}\,\mathrm{m}^2/\mathrm{s}$. The inlet particles concentration values are $C_{i,0} = 0.0$ (without particles), 0.0005, and 0.01. The remaining model parameters are $S_{wr} = S_{or} = 0.001$, $a_w = a_a = 0.5$, $c_w = 500$, $c_a = -500$, $\varphi_0 = 0.2$, $l = 3$, $k_f = 0.015$, $\gamma_f = 0.01$, $k_{rw0} = k_{ra0} = 1$, and $a = b = 4$.

Figure 2 shows the water saturation against the dimensionless distance with various imbibition times and inlet particles concentrations. It is notable that the concentration of particles increases the water saturation in particular after significant time of imbibition. Moreover, the saturation of water increases with the time imbibition.

The normalized particles concentration is plotted in Figure 3 against the dimensionless distance with various inlet concentrations and imbibition times. From this figure it can be seen that the concentration of particles increases as the concentration at the inlet increases for positive R_i. An interesting phenomenon can be observed from Figure 3 that the concentration increases with time but after a certain time of imbibition concentration of particles start to decrease with time. This may be interpreted by increasing the rate of particles precipitation on the pore surface of the porous medium. The opposite is true for minus R_i. It is noteworthy that, in Figure 3, the dimensionless concentration goes larger than 1 because the concentration of particles increases by erosion of more particles from the medium ($-R_i$). On the other hand, the reference concentration was the inlet concentration of the particles coming with water from outside.

Figures 4 and 5 illustrate the ratios of the permeability and porosity against the dimensionless distance with various imbibition times, respectively. Both the permeability and the porosity are reduced due to the precipitation of the particles on the pores walls. It is interesting to note that the reduction rates of the permeability and porosity depend on the layer permeability of the medium.

4. Conclusions

In this pape, we presented numerical modeling and simulation of particle transport in two-phase flow in porous asphalt-paved roads. Numerical experiments have been performed to explore these phenomena and to study the possible porosity and permeability variations. We found that both

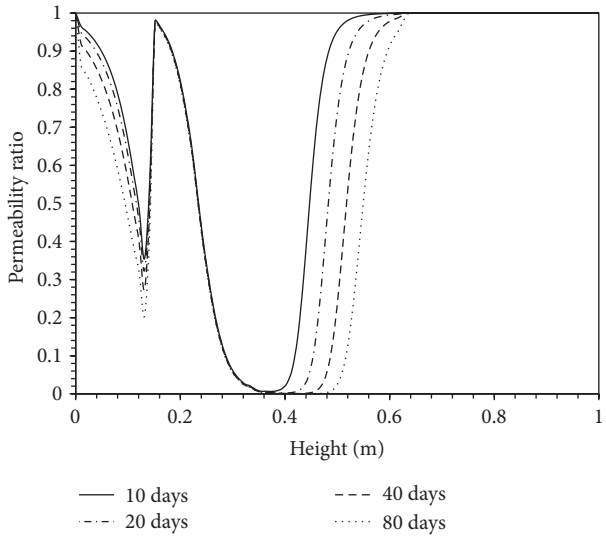

Figure 4: Permeability ratio against the height with various imbibition times.

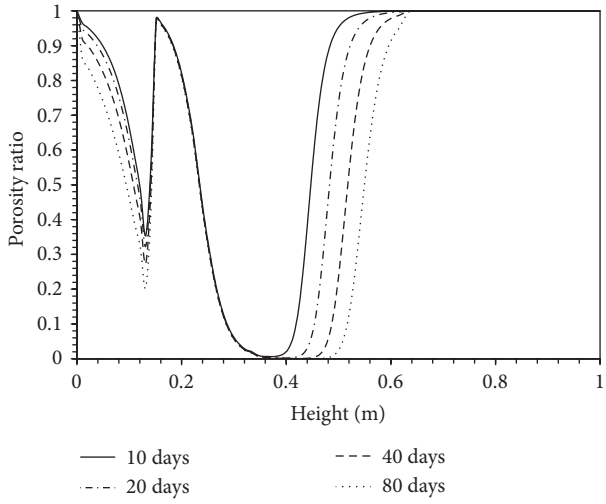

Figure 5: Porosity ratio against the height with various imbibition times.

the permeability and the porosity are reduced due to the precipitation of the particles on the pores walls. These results may help engineers to keep porous asphalt and its storage bed efficient by looking for cleaning methodologies to avoid media blocking.

Acknowledgment

The authors would like to thank the Institute of Scientific Research and Revival of Islamic Heritage, Umm Al-Qura University, for supporting the Project no. 43208015.

References

[1] J. L. M. Voskuilen and P. N. W. Verhoef, "Cause of premature ravelling failure of porous asphalt," in *Proceedings of the 6th International RILEM Symposium on Performance Testing and Evaluation of Bituminous Materials*, pp. 191–197, 2003.

[2] C. Padmos, "Over ten years experience with porous road surfaces," in *Proceedings of the ISAP 9th International Conference on Asphalt Pavements*, Copenhagen, Denmark, 2002.

[3] J. L. M. Voskuilen and M. Huurman, *Conversations, Centre For Transport and Navigation of the Dutch Ministry of Transport*, Public Wprks and Water Management, Delft, The Netherlands, 2009.

[4] A. Kneepkens, T. van Hoof, H. Schaefer, and W. van Keulen, *VIA-RAL for Porous Asphalt: A Result of research and Development, But Most of all of implementation*, Wegbouwkundige Werkdagen, Delft, The Netherlands, 2004.

[5] X. H. Liu and F. Civian, "Characterization and prediction of formation damage in two-phase flow systems," in *Proceedings of the SPE Production Operations Symposium*, Oklahoma City, Okla, USA, 1993.

[6] X. Liu and F. Civan, "Multiphase mud fluid infiltration and filter cake formation model," in *Proceedings of the SPE International Symposium on Oilfield Chemistry*, pp. 607–621, March 1989.

[7] X. Liu and C. Farouk, "Formation damage and skin factor due to filter cake formation and fines migration in the near-wellbore region," in *Proceedings of the International Symposium on Formation Damage Control*, pp. 259–273, Lafayette, Ind, USA, February 1994.

[8] C. Gruesbeck and R. E. Collins, "Entrainment and deposition of fines particles in porous media," *Society of Petroleum Engineers Journal*, vol. 22, no. 6, pp. 847–856, 1982.

[9] M. F. El-Amin, A. Salama, and S. Sun, "Numerical and dimensional investigation of two-phase countercurrent imbibition in porous media," *Journal of Computational and Applied Mathematics*, vol. 242, pp. 285–296, 2013.

[10] S. Sun, A. Salama, and M. F. El Amin, "Matrix-oriented implementation for the numerical solution of the partial differential equations governing flows and transport in porous media," *Computers & Fluids*, vol. 68, pp. 38–46, 2012.

[11] M. El-Amin, A. Salama, and S. Sun, "Effects of gravity and inlet location on a two-phase countercurrent imbibition in porous media," *International Journal of Chemical Engineering*, vol. 2012, Article ID 210128, 7 pages, 2012.

[12] M. F. El-Amin and S. Sun, "Effects of gravity and inlet/outlet location on a two-phase cocurrent imbibition in porous media," *Journal of Applied Mathematics*, vol. 2011, Article ID 673523, 18 pages, 2011.

[13] R. D. Skeel and M. Berzins, "A method for the spatial discretization of parabolic equations in one space variable," *SIAM Journal on Scientific and Statistical Computing*, vol. 11, no. 1, pp. 1–32, 1990.

Hindawi Publishing Corporation
Abstract and Applied Analysis
Volume 2013, Article ID 245074, 8 pages
http://dx.doi.org/10.1155/2013/245074

Research Article

Modeling and Numerical Analysis of the Solid Particle Erosion in Curved Ducts

Ke Sun,[1,2] Lin Lu,[1] and Hanhui Jin[2]

[1] *Faculty of Construction and Environment, The Hong Kong Polytechnic University, Hung Hom, Kowloon, Hong Kong*
[2] *School of Aeronautics and Astronautics, Zhejiang University, Hangzhou 310027, China*

Correspondence should be addressed to Lin Lu; vivien.lu@polyu.edu.hk and Hanhui Jin; enejhh@emb.zju.edu.cn

Received 9 September 2013; Accepted 18 October 2013

Academic Editor: Jianzhong Lin

This paper presents a modeling and computational study on particle erosion in curved ducts. It is found that the average erosion rates per impact range from 4.2×10^{-7} to 9.5×10^{-3} mm^3/g under current conditions. For each doubled inlet velocity, the increases of erosion rates per impact are 2–14 times. The erosion rate per impact varies with particle diameter with "$\surd$" shape through bends, which is similar to the particle deposition behavior in duct flows. The erosion rate curves per injected particle show the shapes of a 90-degree anticlockwise rotated "S" and a wide open "V," respectively, for three larger and smaller inlet velocities. The average erosion rates per injected particle are 1.4–18.9 times those rates per impact due to huge amounts of impacting, especially for those depositing particles. It is obvious that the erosion rate distribution per impact is similar to a "fingerprint" with five clear stripes and a lower "cloud" along the bend deflection angle for the three largest particles; yet, for other smaller particles, the erosion rate distributions are much like an entire "cloud."

1. Introduction

Particulate flow is a significant phenomenon in environmental, industrial, medical, and lifetime applications. For example, the conveying and ventilation system is severely affected by particle flow and its erosion [1–3]. The aerosol deposition, accumulation, and soiling on solar panels and glazing glass will erode their surfaces obviously [4]. These applications also include a large amount of straight and curved duct flow. However, the particle flow and erosion in bends have not been fully studied [5, 6].

El-Behery et al. [7] studied the penetration rate distribution for estimating solid particle erosion in curved 90° and 180° ducts. Sun et al. [8] studied the particle penetration and deposition in and behind bends. Chen et al. [9] proposed a comprehensive procedure to estimate the erosion in elbows mainly for bubbly or droplet flow. Zhang et al. [10] adopted Computational Fluid Dynamics (CFD) with near-wall and volume improvement to predict particle impact in a sharp bend. Macchini et al. [11] investigated the influence of particle size, density, and concentration on bend erosive wear under high particle concentrations. Although some studies have been conducted to investigate the particle erosion in bends, prediction research on the erosion distribution is limited.

Therefore, present study focuses on the erosion status modeling and analysis of curved walls. The airflow and particle flow are modeled and predicted to obtain the erosion information in typical 90-degree bends. The behaviors of erosion rates varying with particle diameter or Stokes number, inlet velocity, and deflection angles are analyzed in detail.

2. Method

2.1. Fluid and Particle Flow Model. Before solving the particle flow in a fluid, the fluid flow conservation equations were deducted and predicted by CFD tools [12]. Together with near-wall two-layer model, the Reynolds stress model (RSM)

was utilized to solve the fluid flow system in the curved duct due to its ability to predict the swirling, turbulent, and near-surface flow [8]. Details of the RSM model are given as follows:

$$\frac{\partial \overline{u}_i}{\partial x_i} = 0,$$
$$\frac{\partial \overline{u}_i}{\partial t} + \overline{u}_j \frac{\partial \overline{u}_i}{\partial x_j} = -\frac{1}{\rho}\frac{\partial \overline{p}}{\partial x_i} + \frac{1}{\rho}\frac{\partial}{\partial x_j}\left(\mu \frac{\partial \overline{u}_i}{\partial x_j} - \rho \overline{u_i' u_j'}\right), \tag{1}$$

where $\overline{u}_i$ is the mean velocity, r and m are the density and molecular viscosity of the fluid, respectively, $\overline{p}$ is the mean pressure, and $-\rho \overline{u_i' u_j'}$ is the Reynolds stress. The general transport equations for the Reynolds stresses could be estimated by

$$\begin{aligned}
&\frac{\partial}{\partial t}\left(\rho \overline{u_i' u_j'}\right) + \frac{\partial}{\partial x_k}\left(\rho \overline{u_k} \overline{u_i' u_j'}\right) \\
&\quad = -\frac{\partial}{\partial x_k}\left[\rho \overline{u_i' u_j' u_k'} + \overline{p\left(\delta_{kj} u_i' + \delta_{ik} u_j'\right)}\right] \\
&\qquad + \frac{\partial}{\partial x_k}\left[\mu \frac{\partial}{\partial x_k}\left(\overline{u_i' u_j'}\right)\right] - \rho\left(\overline{u_i' u_k'}\frac{\partial \overline{u_j}}{\partial x_k} + \overline{u_j' u_k'}\frac{\partial \overline{u_i}}{\partial x_k}\right) \\
&\qquad - \rho\beta\left(g_i \overline{u_j'\theta} + g_j \overline{u_i'\theta}\right) + \overline{p\left(\frac{\partial u_i'}{\partial x_j} + \frac{\partial u_j'}{\partial x_i}\right)} \\
&\qquad - 2\mu \overline{\frac{\partial u_i'}{\partial x_k}\frac{\partial u_j'}{\partial x_k}} \\
&\qquad - 2\rho\Omega_k\left(\overline{u_j' u_m'} E_{ikm} + \overline{u_i' u_m'} E_{jkm}\right) + S_{\text{user}},
\end{aligned} \tag{2}$$

where the 1st and 4th–6th terms on the right of this equation have detailed models to close this equation as that in [12]. Neumann outlet flow conditions were employed and the walls were set as smooth. Staggered numerical scheme was adopted for pressure equation and second-order discretization methods were applied for other variables. These variable convergences were achieved when their residuals were 10^{-5} or less.

Based on the modeling and computation of fluid flow field, the particle flow was determined by tracking the path of each particle with the Lagrangian method. When using this method, particles were assumed to be spherical solid ones with diluted flow. The Lagrangian equation can be expressed as

$$\frac{du_{pi}}{dt} = F_D\left(u_i - u_{pi}\right) + g_i\left(1 - \frac{\rho_a}{\rho_p}\right) + F_{ai}, \tag{3}$$

where u_{pi} is particle velocity in the ith direction (m/s) and u_i represents the air velocity. The 1st term on the formula right represents the particle drag force in the ith direction (m/s^2), and the 2nd one is the gravitational force. The 3rd term stands for other possible forces [13]. To simplify the modelling of particle forces, this article only adopts lift force to predict the particle flow through curved duct [14]. The random fluctuation effects of the fluid flow on particles were modeled by "Eddy lifetime" method [15].

2.2. Particle Wall Interaction and Erosion Models. When particles flow along constrained domains, they will interact with different surfaces. For present solid particles, they would deposit on, rebound from, or reimpact with wall surfaces. To model this process, an algebraic particle-wall impact model [16] was utilized to describe the interaction process between particle and wall as follows:

$$\begin{aligned}
e &= -\frac{v_{2,n}^p}{v_{1,n}^p} = R_{pw}\left(1 - \rho_{pw}\right), \\
v_{2,n}^p &= -e v_{1,n}^p, \\
v_{2,t}^p &= v_{1,t}^p - \mu_1 (1 + e)\, v_{1,n}^p,
\end{aligned} \tag{4}$$

where e is the restitution coefficient, $v_{1,n}^p$ and $v_{2,n}^p$ are particle normal incident and reflected velocities, respectively, R_{pw} stands for the coefficient of restitution without adhesion, ρ_{pw} is the coefficient of adhesion, and μ_1 is the ratio of tangential to normal impulse. This model was integrated into the main particle computation by in-house codes.

When particle-wall impact happens, the wall will be eroded by impacted particles gradually. The wall surface erosion rate or wastage rate is commonly defined as the ratio of wall eroded mass or volume to that of impacted particles. The erosion rate is usually determined by particle impacting velocity and angle, wall and particle materials, and their temperatures. In this paper, a convenient model developed by Menguturk et al. [17, 18] was introduced into the curved duct flow to analyse the wall erosion condition on the curved duct walls as follows:

$$\begin{aligned}
E_v &= 1.63 \times 10^{-6}\left(v_1^p \cos\alpha\right)^{2.5} \sin\left(\frac{\pi\alpha}{2\alpha_c}\right) \\
&\quad + 4.68 \times 10^{-7}\left(v_1^p \sin\alpha\right)^{2.5} \quad (\alpha \le \alpha_c), \\
E_v &= 1.63 \times 10^{-6}\left(v_1^p \cos\alpha\right)^{2.5} \\
&\quad + 4.68 \times 10^{-7}\left(v_1^p \sin\alpha\right)^{2.5} \quad (\alpha > \alpha_c),
\end{aligned} \tag{5}$$

where the unit of erosion rate E_v is mm^3/g, v_1^p is the incident impact velocity, α is the incident impact angle near the wall, and α_c is the critical incident angle with a constant value of 22.7°. In these formulas, the erosion rate E_v has a power relationship with index 2.5 with impact velocity v_1^p. This model was incorporated into the particle-wall interaction model and main particle flow model to obtain the impact and erosion information in the curved duct flow.

3. Results and Discussion

In this paper, the background fluid was selected as air, and the flow domain was formed in the typical curved two-dimensional duct with a 90-degree bend as shown in Figure 1. Since particles mainly deposit and impact on the outer bend wall, the erosions are also observed to happen at these places. The deflection angle θ is also demonstrated from 0° to 90° in this figure. Eight particle groups were injected into the duct flow from the duct inlet with even space distribution, which have the diameters $d_p = 1, 3, 7, 16, 30, 60, 100$, and 200 μm. At the duct inlet, 60000 particles were injected. The volume fraction is less than 1.02×10^{-6}. Six inlet velocity u_{in} conditions were adopted in this analysis, that is, 2.2, 5.3, 9, 15, 33, and 52 m/s. Totally, more than 48 different conditions were analyzed. The airflow and particle flow models were validated by experimental data through previous works [8, 19] in terms of the air and particle velocity profiles, and particle depositions and penetrations, which support the present investigations.

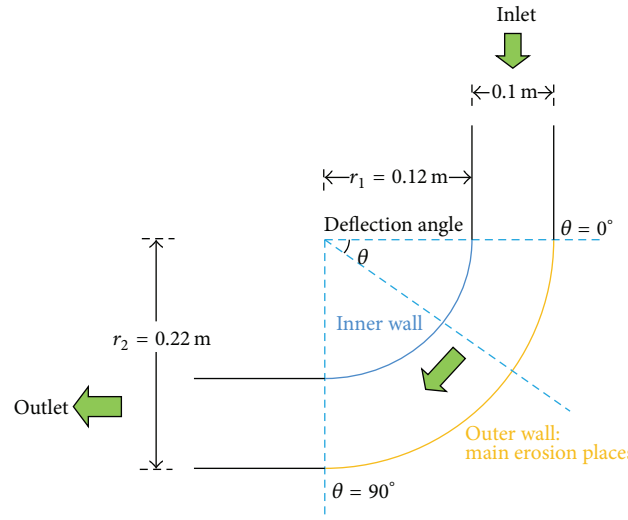

FIGURE 1: Schematic chart of the model geometry.

3.1. Erosion Rate per Impact on Curved Walls. Based on the airflow and particle flow modeling and prediction, statistic results of particle-wall impact and erosion status are given in Figure 1. This figure shows the average erosion rate per impacted particle on the curved wall for each inlet velocity and particle diameter conditions. Using the concept of erosion rate per impacted particle can have more physical meanings and higher application abilities.

Generally, the average erosion rates shown in Figure 2 range from 9.5×10^{-3} to 4.2×10^{-7} mm^3/g for the inlet velocity from 52 m/s to 2.2 m/s. Based on these erosion rate results, the wall wastage can be calculated out considering the injected particle mass. The erosion rate changes with inlet velocity sharply as demonstrated in the figure. The inlet velocity conditions are roughly set around 2-time increase from one smaller inlet velocity to another bigger one. However, the erosion rate generally increases nearly 2 to 14 times. This phenomenon can be explained from the erosion rate equation in (5). Although the erosion rate has a power relationship with impact velocity with index 2.5, the erosion rate has much more complicated nonlinear correlation with inlet velocity due to the complex curved duct flow conditions.

In terms of the changing with particle diameter, the general trend of erosion rate is similar for particle diameter from $d_p = 1$ to 200 μm for different inlet velocities. Firstly, the erosion rate decreases with particle diameter increase. When particle diameter d_p is 7 or 16 μm, the erosion rate gets to the lowest value. After that, it increases with the particle diameter increase. For very large flow inlet velocity and particle diameter, like $d_p = 200$ μm at $u_{\text{in}} = 33$ and 52 m/s, the erosion rate decreases a little due to the large inertia and gravity of these large particles with large Stokes number St. These phenomena are similar to that observed in the particle deposition behavior with "√" shape in duct flows [20, 21]. This phenomenon may be attributed to the similar impact mechanism during the deposition, rebounding, and reimpaction process. Smaller particles of $d_p = 1$ to 3 μm are affected more by diffusion, turbulence, and vortex in the bend and they may have higher impact angle, and thus higher erosion rates are observed. Coarse ones of $d_p = 30$ to 200 μm are controlled by inertia and gravity, and thus they would erode more wall masses.

3.2. Erosion Rate per Injected Particle on Curved Walls. Since particles may rebound and reimpact onto walls due to the near-wall forces or mechanism like turbulence and vortex, average erosion rate per impacted particle cannot give macroinformation about the injected particle erosion ability. Therefore, Figure 3 shows the average erosion rate per injected particles statistically against the particle Stokes number. The Stokes number St is a key parameter to describe the particle response to fluid flow in bends. This dimensionless number is determined by the following formula:

$$\text{St} = \frac{\tau_p}{\tau_b} = \frac{\tau_p u_{\text{in}}}{(D_h/2)} = \frac{C_c \rho_p d_p^2}{18\mu} \cdot \frac{u_{\text{in}}}{(D_h/2)}, \tag{6}$$

where τ_p is the particle relaxation time, τ_b is the time scale of the bend, u_{in} is the air velocity at the duct inlet, D_h is the hydraulic diameter of the duct, C_c is the Cunningham slip correction factor for microparticles, ρ_p and d_p are particle density and diameter, respectively, and μ is the air dynamic viscosity. The friction velocity, u^*, shown in Figure 3 could be calculated by

$$\begin{aligned} u^* &= u_{\text{in}}\sqrt{\frac{f}{2}} = \frac{u_{\text{in}}/\sqrt{2}}{-3.6\log\left[6.9/\text{Re} + \left(k'/3.7D_h\right)^{1.11}\right]} \\ &= -\frac{u_{\text{in}}}{5.1\log\left[6.9/\text{Re} + \left(k'/3.7D_h\right)^{1.11}\right]}, \end{aligned} \tag{7}$$

where f is the Fanning friction factor determined in straight duct by White [22], k' is the average microscale roughness height of the rough wall, which is zero in this work for smooth walls, and Re is the Reynolds number.

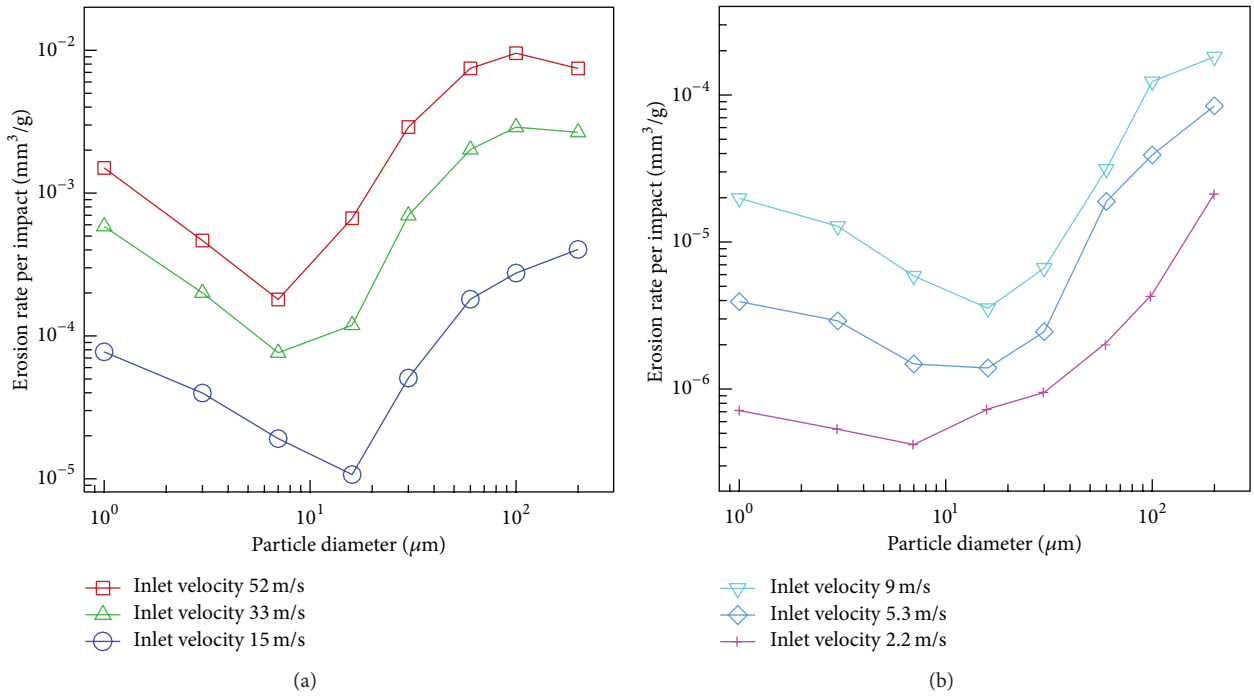

FIGURE 2: Comparison of the erosion rate E_v per impact particle against the particle diameter and inlet flow velocity: (a) larger inlet velocities of 15, 33, and 52 m/s and (b) smaller inlet velocities of 2.2, 5.3, and 9 m/s.

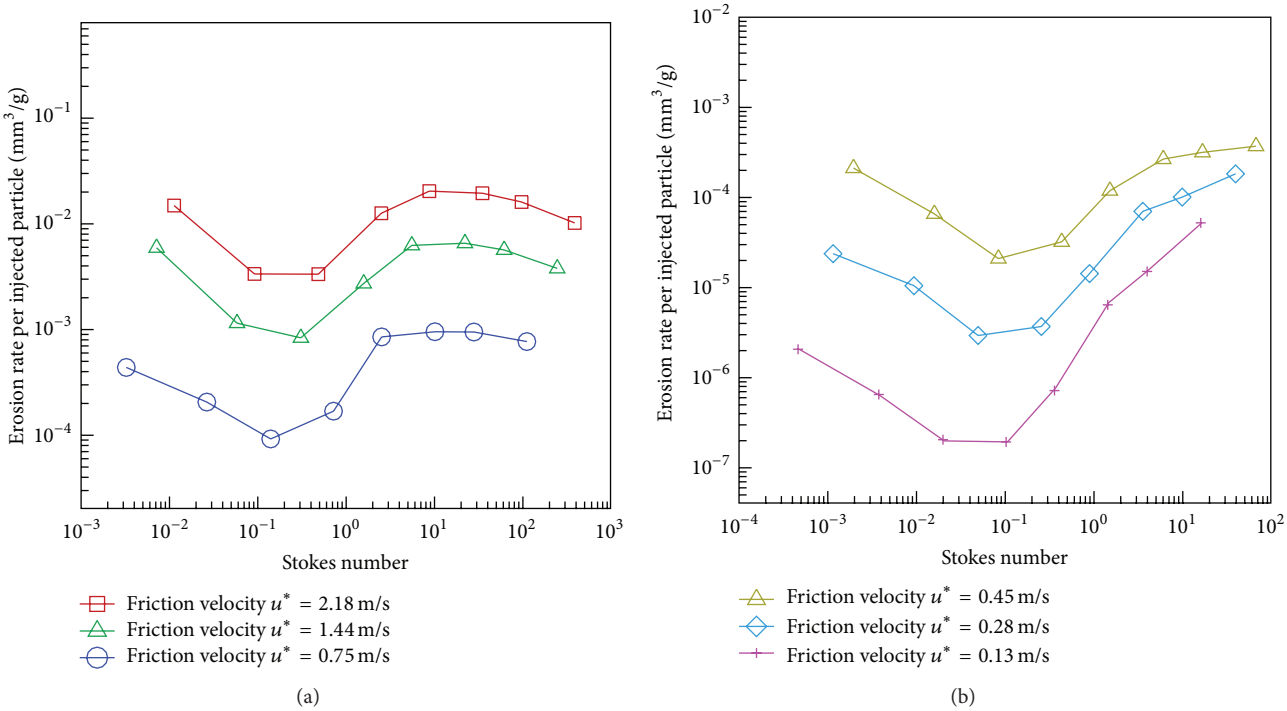

FIGURE 3: Comparison of the erosion rate E_v per injected particle against the particle diameter and inlet flow velocity: (a) larger inlet velocities of 15, 33, and 52 m/s and (b) smaller inlet velocities of 2.2, 5.3, and 9 m/s.

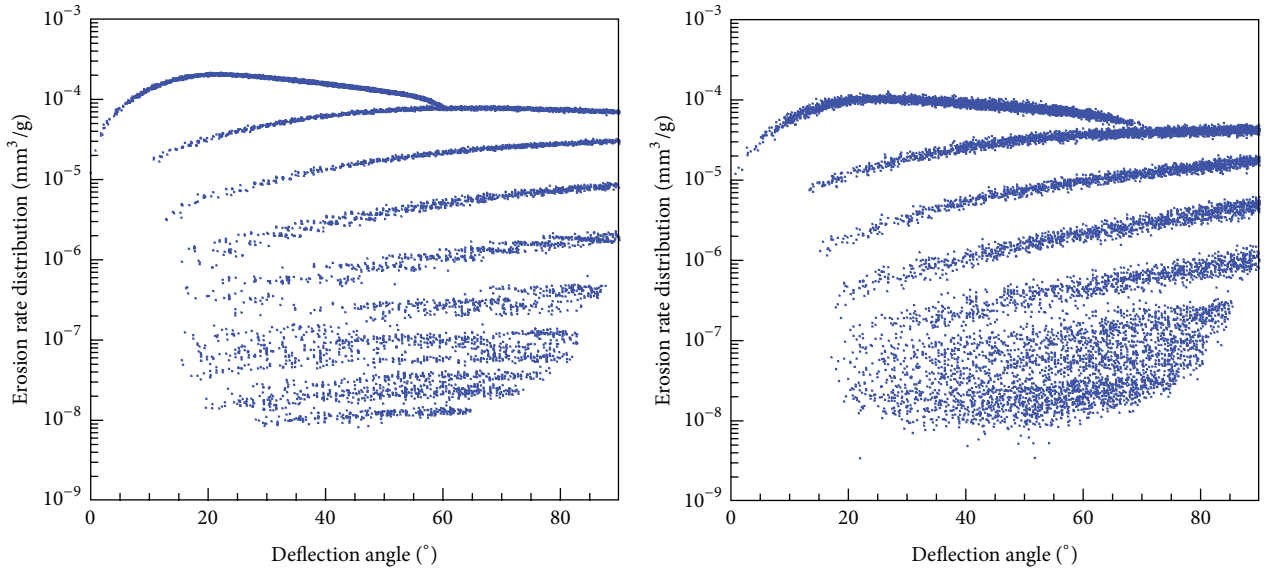

FIGURE 4: Erosion rate E_v distribution per impact particle against the deflection angle of curved duct at the inlet velocity 5.3 m/s: (a) particle diameter 200 μm and (b) particle diameter 100 μm.

The erosion rate curves shown in Figure 3 are generally smoother than those in Figure 2. The curve shapes in Figure 3(a) are much like a 90-degree anticlockwise rotated "S." The erosion rates range from 9.2×10^{-5} to 2.0×10^{-2} mm^3/g. The magnitudes of the values are generally much larger than those in Figure 2(a) due to huge amounts of impacting, especially for those depositing particles. For a similar condition, the erosion rates in Figure 3(a) are 1.4–18.9 times those in Figure 2(a). If the solid particles have high velocities and will deposit onto the bend surfaces, they may impact, rebound, and reimpact on the bend walls to gradually lower down its velocity for deposition. Furthermore, since particles will deposit more on ducts for larger inlet velocities or friction velocities as demonstrated in previous research [19, 20], the erosion rates in Figure 3(a) are generally high. In addition, smaller particles of Stokes number St = 3.3×10^{-3}–7.2×10^{-1} have higher impaction frequencies or amounts than the other larger ones as shown in the figure. This behavior may be due to their frequent interaction with airflows.

For lower inlet velocity cases shown in Figure 3(b), the erosion rate curves are much like wide open "V" shapes. If larger particles of $d_p > 200\,\mu$m are simulated, the curves may become the shapes demonstrated in Figure 3(a). The erosion rates range from 1.9×10^{-7} to 3.7×10^{-4} mm^3/g. Most of these erosion rates are still larger than those shown in Figure 2(b) due to multi-impaction of a single depositing particle. The increasing degrees in this figure are smaller than those in Figure 3(a). For friction velocity $u^* = 0.13$ m/s, the increase degree is the smallest. Furthermore, three erosion rates are smaller than those in Figure 2(b) for the particle groups of St = 0.02, 0.11, 0.37. This phenomenon may be attributed to the low particle impaction amount and low particle deposition for these particles with the smallest friction velocity.

3.3. Erosion Rate Distribution for Each Impact. Distribution of the erosion rate per impacted particle can further demonstrate the particle erosion picture on bend walls. Detailed erosion magnitude and locations can be interpreted. Particle depositions in bends mainly happen on the outer bend walls as shown in Figure 1 and previous research results [23]. Therefore, the following analysis primarily states the erosions on different locations of the outer bend wall.

Figures 4–7 show the distribution of erosion rate E_v per impacted particle against the deflection angle as demonstrated in Figure 1. The angles from 0° to 90° represent bend inlet to outlet. The case of the inlet velocity $u_{in} = 5.3$ m/s is selected as an example to explain the erosion rate distribution. Figure 4 presents the erosion rate for the largest particles with diameters $d_p = 100$ and $200\,\mu$m. It is very obvious that the erosion rate is like a "fingerprint" with clear stripes. These stripes are probably caused by the clear impactions of particles. The top stripe is the first impact of particles on the outer bend wall with the largest erosion rate. Following the airflow, the deflection angles with first impaction are from 0° to 60°, where the peak erosion rate appears at around 20°. After this impaction, four much clear impactions are observed but with lower erosion rate due to moment or velocity reduction after each impaction. The lowest unclear cloud-like areas are the lightest impactions close to particle depositions. They are more randomly distributed due to turbulence, impaction, and diffusion. Deeper color represents that the erosion rates have a large amount at these areas. It can be seen that the particles in this figure have very high erosion rates from $E_v = 1.0 \times 10^{-5}$ to 1.0×10^{-4} mm^3/g. Furthermore, the "fingerprint" phenomenon in this figure indicates that further impactions would happen after the bend because the

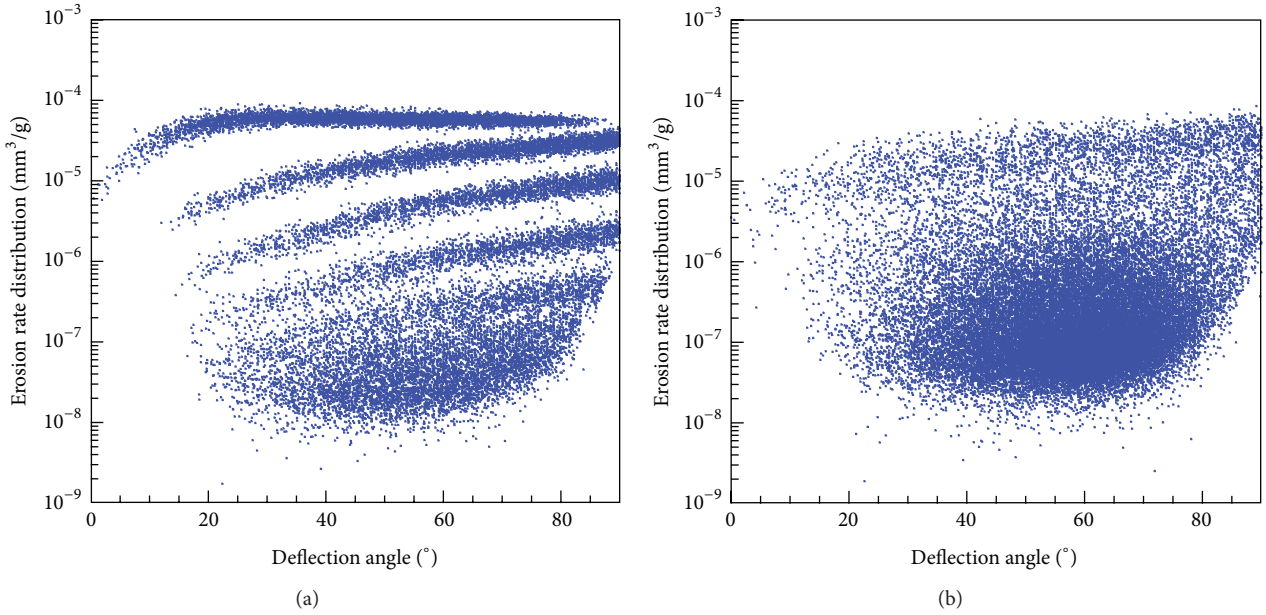

FIGURE 5: Erosion rate E_v distribution per impact particle against the deflection angle of curved duct at the inlet velocity 5.3 m/s: (a) particle diameter 60 μm and (b) particle diameter 30 μm.

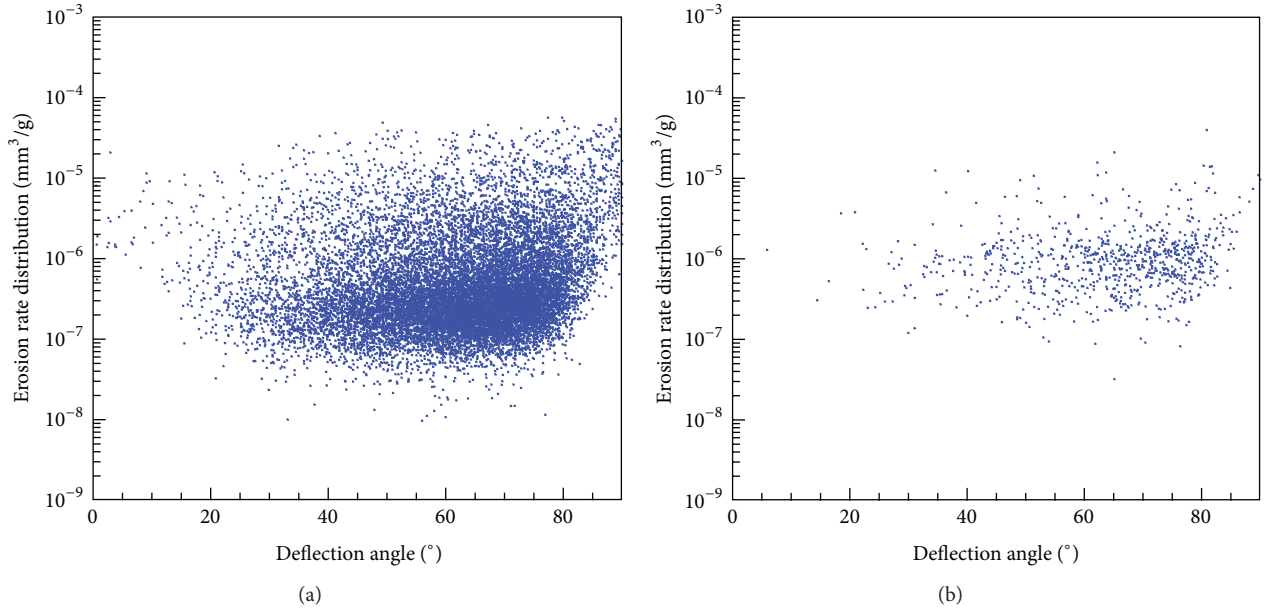

FIGURE 6: Erosion rate E_v distribution per impact particle against the deflection angle of curved duct at the inlet velocity 5.3 m/s: (a) particle diameter 16 μm and (b) particle diameter 7 μm.

stripes do not have end tails at 90° deflection angle or bend outlet.

Figure 5 demonstrates the erosion rates for particles with diameters $d_p = 60$ and 30 μm. From Figure 4 to Figure 5(a), the stripe boundaries are gradually obscure, and they begin to widen their widths. From Figure 5(a) to Figure 5(b), stripes have disappeared, and the general erosion rates decrease. In Figure 5(b), most of the erosions are from $E_v = 1.0 \times 10^{-8}$ to 1.0×10^{-6} mm^3/g. From Figures 5 to 6, erosions decrease with impaction and deposition decreases because particle diameter decreases. From Figures 6 to 7, erosion amounts increase again as seen in Figures 2 and 3 due to diffusion-induced impactions of smaller particles. In Figure 7(b), most of the erosions are from $E_v = 5.0 \times 10^{-7}$ to 1.0×10^{-5} mm^3/g. These larger erosion values and amounts may be caused by larger incident angle impactions due to diffusion and turbulent eddy mixing.

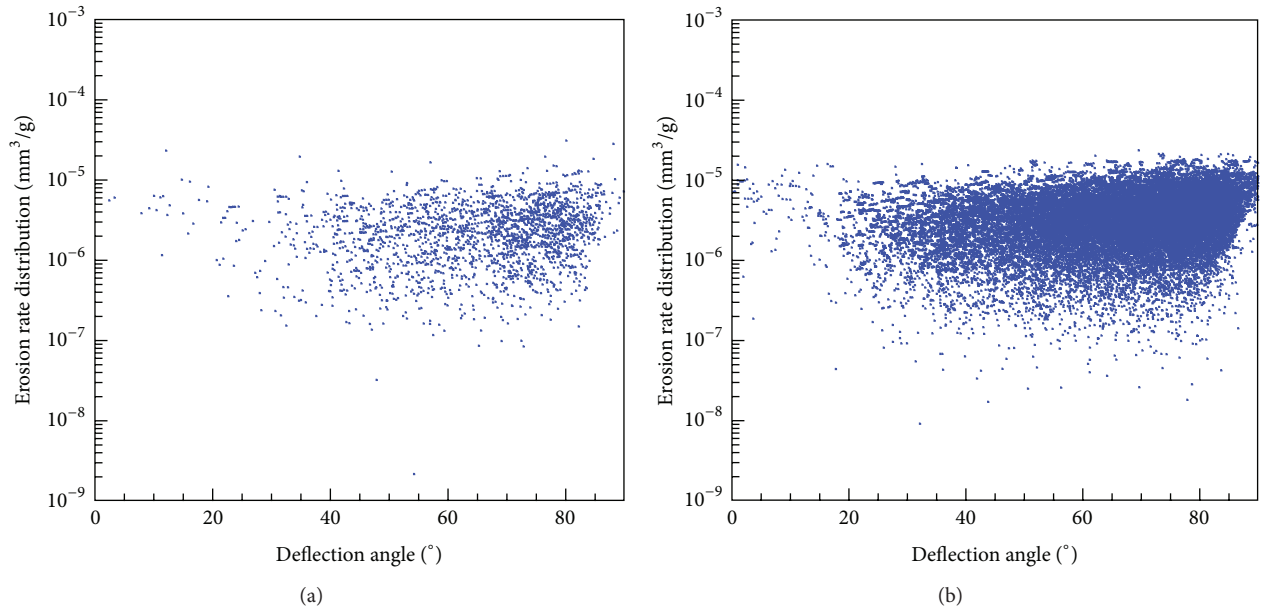

FIGURE 7: Erosion rate E_v distribution per impact particle against the deflection angle of curved duct at the inlet velocity 5.3 m/s: (a) particle diameter 3 μm and (b) particle diameter 1 μm.

4. Conclusions

This paper presented a modeling and computational study on particle erosion in curved ducts. An algebraic particle-wall impact model and a convenient erosion model were adopted in a typical 90-degree bend. The erosion rates per impacted particle and per injected particle were investigated against different particle diameter, inlet velocity, and Stokes number. The distribution of erosion rate was visualized and analyzed along bend deflection angles. The major findings are summarized as follows.

(1) Generally, the average erosion rates per impacted particles range from 4.2×10^{-7} to 9.5×10^{-3} mm^3/g for the inlet velocity from 2.2 m/s to 52 m/s. For each doubled inlet velocity, the increases of erosion rates per impact are 2–14 times. This phenomenon indicates a sharp enhancement of erosion rate due to inlet velocity increase.

(2) The erosion rate per impact changes with particle diameter with "$\surd$" shape in bend flows, which is similar to the particle deposition behavior in duct flows. When particle diameter d_p is 7 or 16 μm, the erosion rate gets to the lowest value. Other smaller ones have higher erosion rates due to diffusion, turbulence, and vortex. Higher erosion rates for larger particles are caused by inertia and gravity.

(3) The erosion rate curves per injected particle are much like a 90-degree anticlockwise rotated "S" for three larger inlet velocities of 15, 33, and 52 m/s. The erosion rates range from 9.2×10^{-5} to 2.0×10^{-2} mm^3/g. The magnitudes of the values are 0.4-to-17.9 times larger than those per impact due to huge amounts of impacting, especially for those depositing particles. For the lower three inlet velocities, the erosion rate curves are much like wide open "V" shapes. Their erosion rates range from 1.9×10^{-7} to 3.7×10^{-4} mm^3/g.

(4) It is obvious that the erosion rate is like a "fingerprint" with clear stripes for the three largest particles with diameters d_p = 60, 100, and 200 μm. The deflection angles with first impaction stripe are from 0° to 60°, where the peak erosion rate appears at around 20°. After this impaction, other four clear impaction stripes are observed but with lower value due to the velocity reduction after each impaction. The lowest cloud-like areas are the lightest impactions close to particle depositions.

(5) For other smaller particles, the erosion rate distribution is much like an entire "cloud" along the bend deflection angle. These "clouds" become smaller and then bigger when the particle diameter decreases. The deflection angles of "clouds" are mainly from 20° to 90°.

Conflict of Interests

The authors declare that there is no conflict of interests regarding the publication of this paper.

Acknowledgment

This work was financially supported by The Hong Kong Polytechnic University through research Grants 1-ZV6Z, A-PJ61, and A-PJ12.

References

[1] M. R. Sippola and W. W. Nazaroff, "Particle deposition in ventilation ducts: connectors, bends and developing turbulent flow," *Aerosol Science and Technology*, vol. 39, no. 2, pp. 139–150, 2005.

[2] L. Jianzhong, S. Xing, and Y. Zhenjiang, "Effects of the aspect ratio on the sedimentation of a fiber in Newtonian fluids," *Journal of Aerosol Science*, vol. 34, no. 7, pp. 909–921, 2003.

[3] M. Yu, A. J. Koivisto, K. Hämeri, and M. Seipenbusch, "Size dependence of the ratio of aerosol coagulation to deposition rates for indoor aerosols," *Aerosol Science and Technology*, vol. 47, no. 4, pp. 427–434, 2012.

[4] T. Sarver, A. Al-Qaraghuli, and L. L. Kazmerski, "A comprehensive review of the impact of dust on the use of solar energy: history, investigations, results, literature, and mitigation approaches," *Renewable and Sustainable Energy Reviews*, vol. 22, pp. 698–733, 2013.

[5] K. Sun and L. Lu, "Particle flow behavior of distribution and deposition throughout 90° bends: analysis of influencing factors," *Journal of Aerosol Science*, vol. 65, pp. 26–41, 2013.

[6] J. Z. Lin, P. F. Lin, and H. J. Chen, "Research on the transport and deposition of nanoparticles in a rotating curved pipe," *Physics of Fluids*, vol. 21, no. 12, Article ID 122001, 11 pages, 2009.

[7] S. M. El-Behery, M. H. Hamed, K. A. Ibrahim, and M. A. El-Kadi, "CFD evaluation of solid particles erosion in curved ducts," *Journal of Fluids Engineering*, vol. 132, no. 7, Article ID 071303, 10 pages, 2010.

[8] K. Sun, L. Lu, and H. Jiang, "A numerical study of bend-induced particle deposition in and behind duct bends," *Building and Environment*, vol. 52, pp. 77–87, 2012.

[9] X. H. Chen, B. S. McLaury, and S. A. Shirazi, "A comprehensive procedure to estimate erosion in elbows for gas/liquid/sand multiphase flow," *Journal of Energy Resources Technology*, vol. 128, no. 1, pp. 70–78, 2006.

[10] Y. L. Zhang, B. S. McLaury, and S. A. Shirazi, "Improvements of particle near-wall velocity and erosion predictions using a commercial CFD code," *Journal of Fluids Engineering*, vol. 131, no. 3, Article ID 031303, 9 pages, 2009.

[11] R. Macchini, M. S. A. Bradley, and T. Deng, "Influence of particle size, density, particle concentration on bend erosive wear in pneumatic conveyors," *Wear*, vol. 303, no. 1-2, pp. 21–29, 2013.

[12] ANSYS Inc., *ANSYS FLUENT 12.0 Users Guide*, ANSYS Inc., Lebanon, NH, USA, 2010.

[13] J. Z. Lin, J. Li, and W. F. Zhang, "The forces exerted on a cylindrical particle in the elongational-shear flows," *International Journal of Nonlinear Sciences and Numerical Simulation*, vol. 5, no. 1, pp. 9–16, 2004.

[14] B. Zhao, Y. Zhang, X. T. Li, X. D. Yang, and D. T. Huang, "Comparison of indoor aerosol particle concentration and deposition in different ventilated rooms by numerical method," *Building and Environment*, vol. 39, no. 1, pp. 1–8, 2004.

[15] D. I. Graham and P. W. James, "Turbulent dispersion of particles using eddy interaction models," *International Journal of Multiphase Flow*, vol. 22, no. 1, pp. 157–175, 1996.

[16] R. M. Brach and P. F. Dunn, "Models of rebound and capture for oblique microparticle impacts," *Aerosol Science and Technology*, vol. 29, no. 5, pp. 379–388, 1998.

[17] M. Menguturk and E. F. Sverdrup, "Calculated tolerance of a large electric utility gas turbine to erosion damage by coal gas ash particles," ASTM Special Technical Publications 664, ASTM, Philadelphia, Pa, USA, 1979.

[18] X. Q. Song, J. Z. Lin, J. F. Zhao, and T. Y. Shen, "Research on reducing erosion by adding ribs on the wall in particulate two-phase flows," *Wear*, vol. 193, no. 1, pp. 1–7, 1996.

[19] K. Sun, L. Lu, H. Jiang, and H. Jin, "Experimental study of solid particle deposition in 90° ventilated bends of rectangular cross section with turbulent flow," *Aerosol Science and Technology*, vol. 47, no. 2, pp. 115–124, 2013.

[20] M. R. Sippola, *Particle deposition in ventilation ducts [Ph.D. thesis]*, University of California, Berkeley, Berkeley, Calif, USA, 2002.

[21] A. C. K. Lai and W. W. Nazaroff, "Modeling indoor particle deposition from turbulent flow onto smooth surfaces," *Journal of Aerosol Science*, vol. 31, no. 4, pp. 463–476, 2000.

[22] F. M. White, *Fluid Mechanics*, McGraw-Hill, New York, NY, USA, 2nd edition, 1986.

[23] M. Breuer, H. T. Baytekin, and E. A. Matida, "Prediction of aerosol deposition in 90° bends using LES and an efficient Lagrangian tracking method," *Journal of Aerosol Science*, vol. 37, no. 11, pp. 1407–1428, 2006.

Hindawi Publishing Corporation
Abstract and Applied Analysis
Volume 2013, Article ID 845872, 8 pages
http://dx.doi.org/10.1155/2013/845872

Research Article

Direct Numerical Simulation of Concentration and Orientation Distribution of Fibers in a Mixing Layer

Kun Zhou,[1] Wei Yang,[2,3] Zhu He,[1] and Ming Xiao[1]

[1] *Key Laboratory for Ferrous Metallurgy and Resources Utilization of Ministry of Education, Wuhan University of Science and Technology, Wuhan 430081, China*
[2] *College of Aeronautics and Astronautics, Zhejiang University, Hangzhou 310027, China*
[3] *College of Mechanical Engineering, Ningbo University of Technology, Ningbo 315211, China*

Correspondence should be addressed to Kun Zhou; zhou.kun@wust.edu.cn

Received 5 September 2013; Accepted 12 October 2013

Academic Editor: Jianzhong Lin

The concentration and orientation of suspended fibers in a mixing layer are investigated numerically. Two cases (diffusive and nondiffusive) are investigated for the fiber concentration distribution. The fine structures of the instantaneous distributions under these two cases are very different due to molecular diffusion. Sharp front of concentration is observed in the nondiffusive case. However, there is no obvious difference in the mean concentration between the two cases. With regard to the orientation, a fiber may rotate periodically or approach an asymptotic orientation, which is determined by a determinant defined with the stain rate. The symmetric part of the strain rate tends to make a fiber align to an asymptotic orientation, while the antisymmetric part drives a fiber to rotate. When a fluid parcel passes through a region with relatively high shear rate, fibers carried by the fluid parcel are most likely to rotate incessantly. On the other hand, in the region of relatively high extension rate, fibers tend to align to some asymptotic orientation. Generally, fibers tend to align with the shear plane. This fact has significant implications in predicting the rheological properties of fiber suspension flows.

1. Introduction

Fiber suspension flows can be found in many processes, such as papermaking, polymer flows in melt-blowing extruders, and nanofibers in the respiratory system. Here, discussions are limited to rigid fibers, which are very slender bodies and can be treated as high aspect ratio cylinders or ellipsoids. The aspect ratio r_c is generally defined as the ratio of the maximum and the minimum characteristic sizes of a fiber. Because of the high aspect ratio, fiber suspensions generally exhibit anisotropic properties. From a macroscopic point of view, fiber suspension flows are generally nonNewtonian fluid, and the flows are described by the Navier-Stokes equation with appropriate constitutive equations for the strain rate and stress. In this scale, the effects of fiber additive are treated through ensemble average. In other words, continuous fields are used to describe the fibers states, most importantly fiber concentration and orientation distribution. From a microscopic point of view, the flow around a single fiber and the corresponding translational and rotational dynamics of a fiber are of concern. These two perspectives are integrated to provide a continuous constitutive equation for the strain rate and the stress through the statistical average on all the possible microscopic flow structures. This two-scale perspective leads the research in fiber suspension flow to focus on two main aspects.

One aspect is to investigate the movement of fibers in various flows. Since fibers are generally very small, the flow around a fiber can usually be seen as a creeping flow in the moving coordinates aligned with the fiber's mass center. Other than the translational movement, the rotation of a fiber has received investigation long ago [1]. Since then, a lot of research works have been done on the orientation of fibers in various flows [2–15]. The other aspect is to investigate the new properties of flows caused by the addition of fibers. Intrinsically, it is the additional stress induced by the fiber suspensions that makes the fiber suspensions flows exhibit special rheological properties [16, 17], such as the drag

reducing [18, 19], shear thinning [20]. In his serial works [21–23], Batchelor developed a well-accepted model about the additional stress, which closely relies on the fiber orientation distribution.

In this work, the translational and rotational movements of fibers in a canonical mixing layer are simulated. The mixing layer configuration is geometrically simple and is a very broadly used model to investigate the shear flow, which characterizes the most important fluid dynamics. A Lagrangian particles scheme is used to deal with the convection of fibers. The evolution of fiber orientation is tracked along Lagrangian trajectories. This new scheme provides insightful understanding of the fiber rotational dynamics, which helps understand and predict the rheological properties of fiber suspension flow. Meanwhile, it is computationally efficient and highly flexible in adjusting the discretization error on the orientation distribution. The paper is organized as follows. Models and methods are described in Section 2. The results on fiber concentration and orientation are presented in Section 3. Section 4 is the conclusion.

2. Models and Methods

2.1. Mixing Layer Configuration. This work is to simulate the concentration and orientation distribution of fibers in a canonical mixing layer. To save the computational time, the flow is assumed to be homogeneous in the spanwise direction. On the other hand, the feedback from the fiber additive is neglected; only one-way coupling is considered. Hence, a planar mixing is solved. The configuration is depicted in Figure 1. The spacial dimension is normalized by the momentum thickness of the mixing layer at the inlet. The computational methods for the fluid dynamics are the same as those in Zhou and He [24]. Finite difference scheme with structured grid is used. At the inlet, the streamwise velocity profile is imposed by combining two Blasius laminar boundary layers. The two streams have inlet velocities $u_1 = 15$ m/s and $u_2 = 5$ m/s, respectively. The Reynolds number at the inlet based on the velocity difference and the momentum thickness is 111. The normalized fiber concentrations at the two streams are $c_1 = 1$ and $c_2 = 0$, respectively.

2.2. Fiber Concentration. It is assumed that the fiber concentration c is a passive scalar which satisfies the convection diffusion equation

$$\frac{\partial c}{\partial t} + \nabla \cdot (\mathbf{u}c) = D_c \nabla^2 c. \tag{1}$$

The assumption is valid when the fiber is very small and follows the fluid flow very well; additionally, the fiber concentration is very low and the additional stress due to the fiber additive is negligible. The main purpose is to investigate the Schmidt number effect on the fiber concentration in the mixing layer configuration here. The Schmidt number is $\mathrm{Sc} = \nu/D_c$, where ν is the kinematic viscosity. Two cases $\mathrm{Sc} = 1$ and $\mathrm{Sc} = \infty$ (i.e., $D_c = 0$) are investigated. The concentrations in the two streams of the mixing layer at the inlet are assumed to be 0 and 1 (nondimensionalized). The absolute magnitude of the concentration is immaterial, since the fiber concentration has no impact on the fluid flow (one-way coupling).

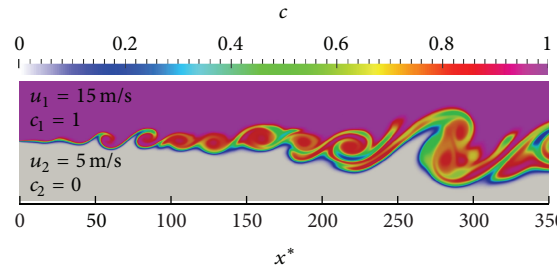

Figure 1: Schematic view of the mixing layer, with instantaneous fiber concentration c in the mixing layer for the case $\mathrm{Sc} = 1$.

2.3. Fiber Rotational Dynamics. The rotation of a fiber is described by the Jeffery [1] equation

$$\dot{\mathbf{p}} = \boldsymbol{\omega} \cdot \mathbf{p} + \lambda (\boldsymbol{\epsilon} \cdot \mathbf{p} - \boldsymbol{\epsilon} : \mathbf{ppp}), \tag{2}$$

where $\mathbf{p}$ is the unit vector aligned with the fiber axis (Figure 2), the dot over a variable denotes the time derivative, $\boldsymbol{\omega} = (\nabla \mathbf{u}^\dagger - \nabla \mathbf{u})/2$ is the vorticity tensor, $\boldsymbol{\epsilon} = (\nabla \mathbf{u}^\dagger + \nabla \mathbf{u})/2$ is the deformation rate tensor, and $\lambda = (r_c^2 - 1)/(r_c^2 + 1)$. The equation is originally derived for an ellipsoid in Stokes flows. It is found [1] that the force acting on the ellipsoid reduces to two couples, with one tending to make the ellipsoid adopt the same rotation as the surrounding fluid and the other tending to set the ellipsoid with its axes parallel to the principle axes of distortion of the surrounding fluid. This discovery was verified by the subsequent experiment of Taylor [25]. Furthermore, Bretherton [26] found that the same equation (2) also applies to a revolution body.

As discussed in Section 2.1, the mixing layer is assumed to be homogeneous along the spanwise direction (z in Figure 2). Hence, only components ω_{12} in the vorticity tensor and ϵ_{11}, ϵ_{12}, and ϵ_{22} in the deformation rate tensor are present to determine the rotation of a fiber. Under this condition, the Jeffery equation (2) is simplified to

$$\begin{aligned} \dot{p}_1 = {} & \omega_{12} p_2 + \lambda \left(\epsilon_{11} p_1 + \epsilon_{12} p_2 - \epsilon_{11} p_1^3 \right. \\ & \left. - 2\epsilon_{12} {p_1}^2 p_2 - \epsilon_{22} {p_2}^2 p_1 \right), \end{aligned} \tag{3a}$$

$$\begin{aligned} \dot{p}_2 = {} & -\omega_{12} p_1 + \lambda \left(\epsilon_{12} p_1 + \epsilon_{22} p_2 - \epsilon_{11} p_1^2 p_2 \right. \\ & \left. - 2\epsilon_{12} p_1 p_2^2 - \epsilon_{22} p_2^3 \right), \end{aligned} \tag{3b}$$

$$\dot{p}_3 = -\lambda p_3 \left(\epsilon_{11} p_1^2 + 2\epsilon_{12} p_1 p_2 + \epsilon_{22} p_2^2 \right). \tag{3c}$$

The orientation vector implicitly satisfies the condition $p_1^2 + p_2^2 + p_3^2 = 1$, since the fiber is rigid, which cannot extend or shrink.

The rotational dynamic equations (3a), (3b), and (3c) are integrated along a Lagrangian trajectory (discussed in the next section) with the local vorticity and deformation rate by

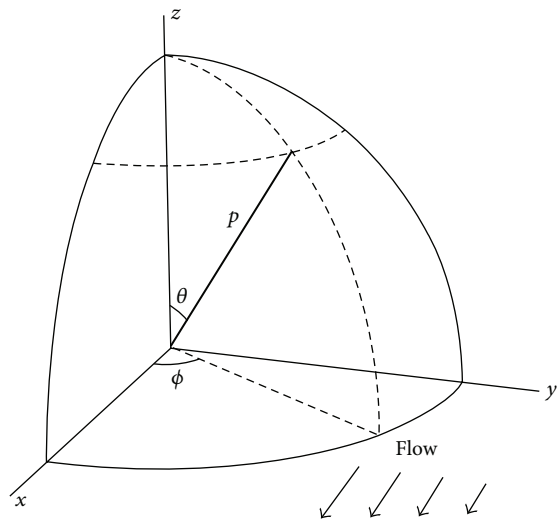

Figure 2: Schematics of fiber orientation. The bold line segment denotes the fiber orientation vector.

the solver DOPRI5 [27], which uses a fourth order Runge-Kutta method with adaptive time step based a fifth order error estimate.

2.4. Lagrangian Particles Scheme. For the translational movement of fibers, two cases Sc = 1 and Sc = ∞ are considered. For Sc = 1, the WENO scheme [28] is used to solved the convection diffusion equation (1). For the nondiffusive case Sc = ∞, the traditional schemes in Eulerian framework usually introduce numerical diffusion. To avoid the numerical diffusion, the Lagrangian particles scheme [29] is used for the case Sc = ∞. Under the conditions of no diffusion and negligible inertial, the movement of the mass center of a fiber follows the local fluid parcel. Hence, the transport of fibers can be described by the Lagrangian particles method. In the Lagrangian particles method, the trajectories of a large number of Lagrangian particles are tracked simultaneously. Meanwhile, the Lagrangian particles carry the fiber concentration and orientation, which evolve along the Lagrangian trajectories independently. The fiber concentration is a scalar, which is easy to deal with. When calculating the orientation distribution at a spatial position, which is a function on the unit sphere (Figure 2), statistics of fiber orientation at the position are required. A Monte Carlo scheme is used to simulate the orientation evolution along a trajectory. A Lagrangian particle carries many fibers, and these fibers all obey the rotational dynamics equation (2). The initial orientations of these fibers are generated randomly on the unit sphere. The orientation distribution is approximated through statistical averaging on the orientations of all these fibers. Thousands of fibers are used to obtain statistically convergent orientation distribution. The main advantage of the Lagrangian particles scheme is that the convection of all the fibers along a Lagrangian particle is solved simultaneous in the same way. The number of fibers along a trajectory can be adjusted conveniently to balance the computational cost and the statistical error.

The dynamic equations for the Lagrangian particles and the concentration and orientation of fibers are as follows:

$$\frac{d\mathbf{x}^p}{dt} = \mathbf{v}^p\left(\mathbf{x}^p\right), \quad \left(p = 1, 2, \ldots, N_p\right), \tag{4}$$

$$\frac{dc^p}{dt} = 0, \quad \left(p = 1, 2, \ldots, N_p\right), \tag{5}$$

in addition to (3a), (3b), and (3c), where the strain rate is obtained along the trajectories determined by (4). Here $\mathbf{x}^p$ and $\mathbf{v}^p$ denote the location and the velocity of a Lagrangian particle p, and N_p is the number of Lagrangian particles.

In this study, the flow velocity is solved in the traditional Eulerian framework. Fiber concentration and orientation are evolved along Lagrangian trajectories. The Eulerian and Lagrangian frameworks are coupled together. On the one hand, trilinear interpolation is used to convert variables from the Eulerian framework to the Lagrangian framework. To calculate the particle trajectories, the particle velocity $\mathbf{v}^p(\mathbf{x}^p)$ is obtained by interpolating the Eulerian velocity field at position $\mathbf{x}^p$. The strain rate is also obtained from the Eulerian field through interpolating it in a grid cell. On the other hand, the reconstruction of Eulerian fields from the Lagrangian particles uses

$$c\left(\mathbf{x}\right) = \frac{1}{N_\Omega}\sum_{p\in\Omega} c^p, \tag{6}$$

where Ω is the set of particles located in the cell $\mathbf{x}$ and N_Ω is the number of such particles. Similar treatment for the orientation is carried out.

Lagrangian particles are injected at the inlet of the mixing layer at a rate proportional to the inlet velocity, to make the number of particle 100 in a cell on average. The number of particles be in a cell controls the discretization error in evaluating the orientation distribution, which can be conveniently adjusted. Increasing the number of particles does not affect the cost of solving the fluid dynamics but only increases the cost to track the Lagrangian trajectories and the integration of fiber rotational dynamics along these trajectories. It is found that 100 particles in a cell are enough to produce statistically convergent results.

3. Results and Discussion

3.1. Fiber Concentration. The instantaneous fiber concentrations for Sc = 1 and Sc = ∞ are given in Figure 3. The concentration distribution for the two cases has similar large structure. For Sc = 1, the concentration changes smoothly from 0 to 1. However, for Sc = ∞, the concentration is either 0 or 1; no intermediate value is in-between, which is typical for nondiffusive mixing process. The Lagrangian particles scheme captures the sharp front quite well. The front separating $c = 0$ and 1 in Figure 3(b) is not smooth but exhibits staggered structure, which is related to the grid resolution. It is clear that high resolution is needed to resolve the fine scalar structure in high Schmidt numbers flows.

Although the instantaneous fine structures of the fiber concentration for Sc = 1 and Sc = ∞ are very different, the

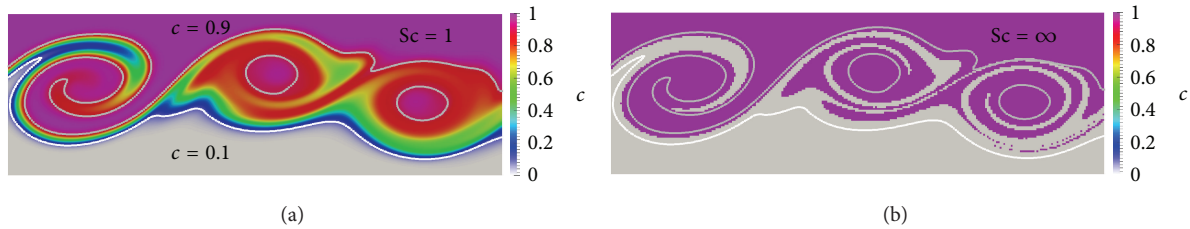

(a) (b)

FIGURE 3: Comparison of instantaneous fiber concentration distributions (clipped). (a) Sc = 1, (b) Sc = ∞. Same isocontours of $c = 0.9$ and $c = 0.1$ for Sc = 1 are also added in (b) for comparison purpose. The fiber concentration has a sharp front for Sc = ∞.

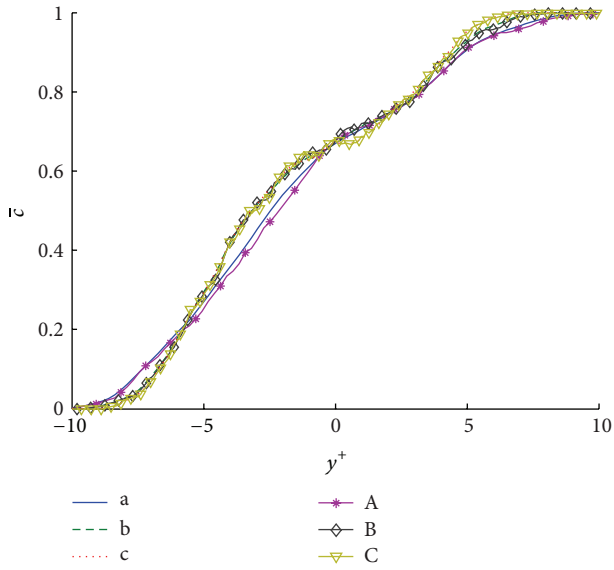

FIGURE 4: Mean concentration a cross profiles at various crosswise locations ($x^* = 137$, $x^* = 228$, and $x^* = 319$) for Sc = 1 (a, b, and c) and Sc = ∞ (A, B, and C).

mean values are almost the same. Figure 4 shows the mean concentration cross profiles at various streamwise locations, where $y^+ = y/\delta(x^*)$ is the normalized coordinate with the local momentum thickness ($\delta(x^*)$) of the mixing layer. The profiles a, b, and c are for Sc = 1 at $x^* = 137$, $x^* = 228$, and $x^* = 319$, respectively. The profiles A, B, and C are for Sc = ∞ at the same locations corresponding to a, b, and c. There is no significant difference between the diffusive and nondiffusive cases. Only minor difference between a and A is observed. It is clear that the molecular diffusion has negligible effect in determining the mean concentration in turbulent flows. Generally, the Schmidt number for the translational movement of a fiber is much larger than unity. Hence, the molecular diffusion can be neglected in determining the mean concentration.

3.2. Fiber Orientation. The orientation vector has three components in the Cartesian coordinates. However, only two of them are independent. The third one can be determined through the normalization condition $p_1^2 + p_2^2 + p_3^2 = 1$. Equivalently, the orientation vector can be described in the spherical coordinates with $\phi = \arctan(p_2/p_1)$ and $\theta = \arccos(p_3)$ (see Figure 2). For a given constant strain rate, Zhou et al. [30] have derived the analytical solution for the rotational movement of a fiber in a planar flow. They found that a fiber either rotates periodically or approaches an asymptotic orientation according to the sign of a determinant Δ, which is defined with the strain rate. The asymptotic orientation (if $\Delta > 0$) and the period (if $\Delta < 0$) are also given there. In their derivation the shear stain is normalized by the component u_y. Their formula cannot describe the case when $u_y = 0$. Here we extend their results slightly to present the results in a more general form (including the case for $u_y = 0$). The determinant is defined as

$$\Delta = \lambda^2 \left(\epsilon_{11}^2 + \epsilon_{12}^2 - \omega_{12}^2\right). \tag{7}$$

If $\Delta > 0$, the fiber approaches an asymptotic orientation with

$$\phi = \frac{-\lambda\epsilon_{11} \pm 2\Delta}{\lambda\epsilon_{11} - \omega_{12}}, \tag{8a}$$

$$\theta = \begin{cases} \dfrac{\pi}{2} & \text{if } \theta_0 = \dfrac{\pi}{2}, \\ 0 & \text{otherwise,} \end{cases} \tag{8b}$$

where θ_0 is the initial polar angle. The results state that except, for very special initial condition $\theta_0 = \pi/2$, a fiber will approach the shear plane ($\theta = \pi/2$) and the azimuthal angle given by (8a). If $\Delta < 0$, the fiber rotates periodically, with period

$$T = \frac{\pi}{\sqrt{|\Delta|}}. \tag{9}$$

It is worth pointing out that the results on the asymptotic angle (if $\Delta > 0$) and the period (if $\Delta < 0$) differ from those of Zhou et al. [30] due to the difference in the definition of Δ (a constant factor 4). The results here are slightly more general in applicable conditions and more compact in form.

In this simulation, a large number of Lagrangian trajectories (over one million) are tracked. The evolution of fiber concentration and orientation along these trajectories is simulated. The trajectories reveal how fluid parcels move in the mixing layer. Figure 5 shows the Lagrangian trajectories that pass through the same spatial cell (at various time instants). The cell is located at $x^* = 319$ and corresponds to the median of the mean concentration, $\bar{c} = 0.5$. The median $\bar{c} = 0.5$ does not lie in the center line of the mixing layer

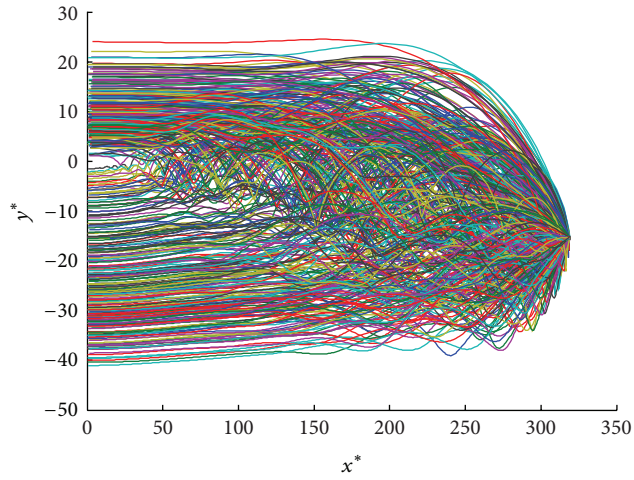

FIGURE 5: Lagrangian trajectories passing through a point at various time instants.

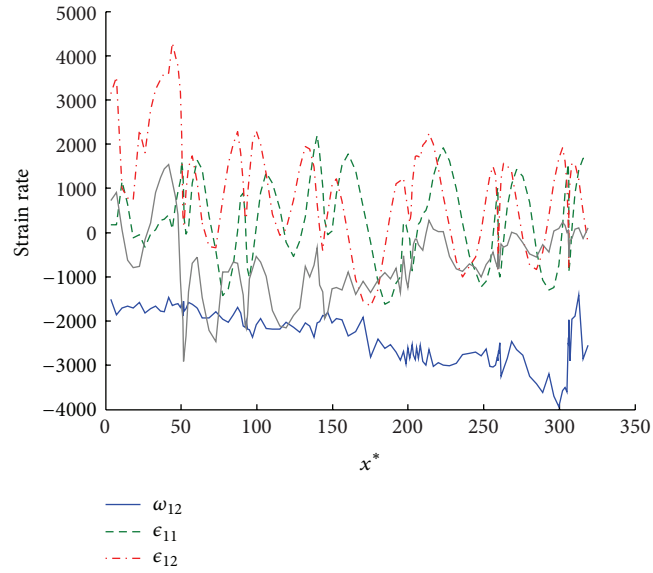

FIGURE 6: Profiles of the vorticity and deformation rate along a sample Lagrangian trajectory. The continuous gray is the corresponding determinant Δ evaluated from (7).

but shifts to the slow stream side (here negative y). From a Lagrangian point of view, this can be explained by the ensemble average of the concentration along the trajectories passing through the cell. Since there is no diffusion, the concentration along a Lagrangian trajectory is constant (see (5)); the constant is determined by the initial value at the inlet of the mixing layer. From Figure 5 it is obvious that a fluid parcel originating from the fast stream ($y > 0$) is more likely to travel down to the slow stream region than a fluid parcel originating from the slow stream ($y < 0$) to travel up to the fast stream region. That is why the median $\bar{c} = 0.5$ is located in the slow stream region. On another aspect, the fluctuation of the trajectories also quantitatively reflects the strength of the mixing.

The fiber orientation along a Lagrangian trajectory is determined by the vorticity and deformation rate that a fiber undergoes. Figure 6 shows the profiles of the vorticity and deformation rate along a sample Lagrangian trajectory. The profile of the determinant Δ from (7) is also given in the figure. Theoretical analysis demonstrates that a fiber will rotate periodically if $\Delta < 0$. From (7) it is clear that only ω_{12} contributes to the negative part of the determinant. In other words, the antisymmetric part of the strain rate (vorticity) drives a fiber to rotate, and the symmetric part (deformation rate) tends to push a fiber to a specific orientation. In fact, as Lipscomb et al. [31] pointed out, (2) may be interpreted physically as stating the $\mathbf{p}$ rotates with the fluid according to term "$\boldsymbol{\omega} \cdot \mathbf{p}$", and simultaneously partially stains with the fluid according to term "$\lambda \boldsymbol{\epsilon} \cdot \mathbf{p}$". The term, $-\lambda \boldsymbol{\epsilon} : \mathbf{p}$, compensates a change of length which resulted from the motion described by $\boldsymbol{\omega} \cdot \mathbf{p}$ and $\lambda \boldsymbol{\epsilon} \cdot \mathbf{p}$, because $\mathbf{p}$ is of unit length. This physical interpretation is very informative. However, it is far from being straightforward to directly derive the conclusion from (2) per se. Here, the determinant Δ (see (7)) has very simple form, and it is straightforward to draw the conclusion from the form of Δ. By comparing the components of the vorticity and deformation rate in Figure 6, it is clear that the profile of ω_{12} is more irregular than those of ϵ_{11} and ϵ_{12} (notice the zig-zag structures). Along this sample trajectory, most of the Δ profile in Figure 6 is negative, indicating that a fiber is of periodic rotation most of the time along the sample Lagrangian trajectory but with changing period.

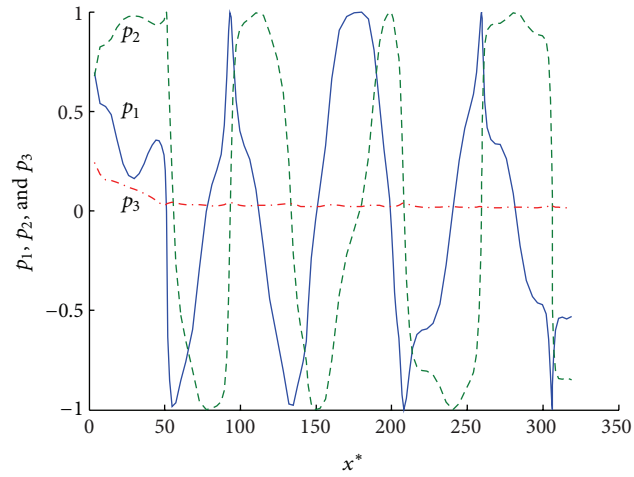

FIGURE 7: Components of the fiber orientation vector along the same sample Lagrangian trajectory as used in Figure 6.

Figure 7 shows the three components of the orientation vector for a fiber traveling along the same Lagrangian trajectory as discussed in Figure 6. Both p_1 and p_2 exhibit nearly periodic behavior. However, p_3 approaches 0. The initial values of p_1, p_2, and p_3 are not important; all will exhibit similar evolution behavior as shown in Figure 7; except that for a special initial value $p_3 = 1$ (and hence $p_1 = p_2 = 0$), the orientation vector will not change. The fact that p_3 approaches 0 shows that a fiber is very likely to align to the shear plane (x-y), insensitive to its initial orientation.

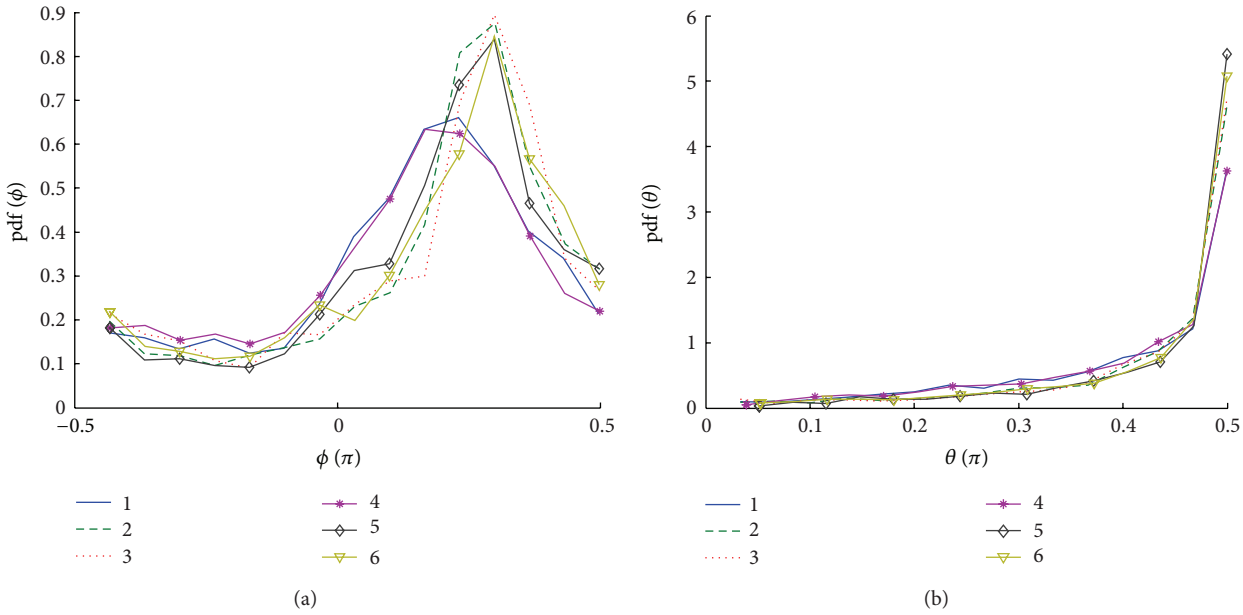

FIGURE 8: Orientation distribution at six positions: 1, 2, and 3 are at $x^* = 228$ and correspond to $\bar{c} = 0.3$, $\bar{c} = 0.5$, and $\bar{c} = 0.7$, respectively; 4, 5, and 6 are at $x^* = 319$ and correspond to $\bar{c} = 0.3$, $\bar{c} = 0.5$, and $\bar{c} = 0.7$, respectively. (a) Azimuthal angle ϕ; (b) polar angle θ.

Figures 6 and 7 show the strain rate and orientation along the same sample Lagrangian trajectory. Along this selected trajectory, the magnitude of vorticity ω_{12} is relatively high compared to ϵ_{11} and ϵ_{12}, most of the Δ value is negative, and hence a fiber mostly rotates periodically, with changing period predicted by (9). Investigation in a large number of Lagrangian trajectories shows that Δ is usually larger than zero, which means that fibers along these trajectories are most likely to approach an asymptotic orientation predicted by (8a) and (8b). However, since the strain rate is not constant along a trajectory, the asymptotic orientation also changes correspondingly. Hence, a fiber seems to swing incessantly when it tries to approach an evolving asymptotic orientation. Through averaging the orientation over a very large number of Lagrangian trajectories that pass through the same location (at various time instants), the orientation distribution at the location can be obtained. Figure 8 gives the orientation distribution probability density function (pdf(ϕ) and pdf(θ)) at various locations. It is worth pointing out that pdf(ϕ) is only shown in the range $[-0.5\pi, 0.5\pi]$, which has period π, since a fiber which orients at ϕ or $\phi + \pi$ is indistinguishable in its distribution, and pdf(θ) is given in the range $[0, 0.5\pi]$, which has period 0.5π, since the flow field is symmetric with respect to the plane $\theta = 0$. Distributions 1, 2, and 3 are at cross-section $x^* = 228$ and correspond to the mean concentration $\bar{c} = 0.3$, $\bar{c} = 0.5$, and $\bar{c} = 0.7$, respectively. Distributions 4, 5, and 6 are at cross section $x^* = 319$ and also correspond to $\bar{c} = 0.3$, $\bar{c} = 0.5$, and $\bar{c} = 0.7$, respectively. Through comparing the corresponding distributions at $x^* = 228$ and $x^* = 319$, no evident difference is found. It implies that the fiber orientation distribution (which is uniformly distributed at the inlet) has already reached a stable state, and it does not evolve along the streamwise direction any longer in the turbulent region. In Figure 8(a) the distributions pdf(ϕ) all have similar shape, a peak, and a valley. Under a simple shear flow, pdf(ϕ) will have a peak at $\phi = 0$ [30, 32]. Here, due to the synthetic effect of vorticity and deformation rate the peak is in between 0 and 0.5π, which is believed to be closely related to the steady asymptotic direction predicted by (8a) and (8b). On the other hand, the valley is believed to be related to the unsteady asymptotic direction in (8a) and (8b). For pdf(θ), it has a very high peak at $\theta = 0.5\pi$, which agrees with the analysis on the evolution of p_3 in Figure 7 that a fiber is very likely to turn to the shear plane ($\theta = 0$) and stays there. In Figure 8 the distributions 1 and 4 correspond to $\bar{c} = 0.3$. Both pdf(ϕ) and pdf(θ) are found to be flatter than the distributions corresponding to $\bar{c} = 0.5$ or $\bar{c} = 0.7$. This may be due to the position corresponding to $\bar{c} = 0.3$ is located in the slow stream of the mixing layer, and the magnitude of the strain rate is relatively smaller than those in the fast stream.

4. Conclusion

The concentration and orientation of suspended fibers in a mixing layer are investigated numerically. The flow is assumed to be homogeneous in the spanwise direction, and the effects of fiber additive on the flow are neglected (very dilute suspension). A Lagrangian particles scheme is used to deal with the convection of fibers. With this Lagrangian particles scheme, fiber concentration and orientation evolve along Lagrangian trajectories independently. Ensemble average over a large number of Lagrangian trajectories is used to obtain statistically steady values of concentration and orientation. This Lagrangian particles scheme is found to be very efficient to compute the fiber orientation, which is discretized by hundreds of points on the unit sphere to represent the fiber orientation distribution.

Two cases Sc = 1 (diffusive) and Sc = ∞ (nondiffusive) are investigated for the fiber concentration distribution. The fine structures of the instantaneous distributions under these two cases are very different due to the molecular diffusion. Sharp front of the concentration is observed in the nondiffusive case. However, there is no obvious difference in the mean concentration between the two cases. Molecular diffusion is negligible in determining the mean concentration of fibers in turbulent flows.

For the rotational dynamics of a fiber, the analytical solution of Zhou et al. [30] is slightly generalized, and the new solution is presented in a more compact and informative form. A fiber will rotate periodically if the determinant is negative, where the determinant is defined with the strain rate. A fiber will approach an asymptotic orientation if the determinant is positive. The sign of the determinant is determined by the relative magnitude of the deformation rate and the vorticity. The symmetric part of the strain rate tends to make a fiber align to an asymptotic orientation, while the antisymmetric part makes a fiber rotate. This general conclusion helps understand the evolution of the fiber orientation along Lagrangian trajectories. When a fluid parcel passes through a region with relatively high shear rate, fibers followed by the fluid parcel are most likely to rotate incessantly. On the other hand, in the region of relatively high extension rate, fibers tend to align to some asymptotic orientation. Analysis on the orientation distribution shows that the distribution is stable in the turbulent region, which does not change along the streamwise direction. It is also believed that the orientation is not sensitive to the initial distribution at the inlet of the mixing layer. The pdf of the azimuthal angle ϕ has the shape of a peak and a valley, which most likely correspond to the steady and unsteady asymptotic orientations predicted by the analytical solution. The pdf of the polar angle θ has a prominent peak at $\theta = 0.5\pi$, which shows that fibers are very likely to align with the shear plane. This fact has significant implications in predicting the rheology of fiber suspension flows.

Conflict of Interests

The authors declare that there is no conflict of interests regarding the publication of this paper.

Acknowledgment

Kun Zhou would like to thank the help from A. Attili and F. Bisetti. Wei Yang is supported by the National Natural Science Foundation of China (Grant no. 11302110). Zhu He is supported by the National Key Technology R&D Program of Chian (Grant no. 2011BAK06B02).

References

[1] G. B. Jeffery, "The motion of ellipsoidal particles immersed in a viscous fluid," *Proceedings of the Royal Society A*, vol. 102, no. 715, pp. 161–179, 1922.

[2] T. Nishimura, K. Yasuda, and K. Nakamura, "Orientation behaviour of fibers in suspension flow through a branching channel," *Journal of Non-Newtonian Fluid Mechanics*, vol. 73, no. 3, pp. 279–288, 1997.

[3] S. B. Chen and L. Jiang, "Orientation distribution in a dilute suspension of fibers subject to simple shear flow," *Physics of Fluids*, vol. 11, no. 10, pp. 2878–2890, 1999.

[4] J. Z. Lin, X. Shi, and Z. S. Yu, "The motion of fibers in an evolving mixing layer," *International Journal of Multiphase Flow*, vol. 29, no. 8, pp. 1355–1372, 2003.

[5] L. Jianzhong, S. Xing, and Y. Zhenjiang, "Effects of the aspect ratio on the sedimentation of a fiber in Newtonian fluids," *Journal of Aerosol Science*, vol. 34, no. 7, pp. 909–921, 2003.

[6] L. Jianzhong, Z. Weifeng, and Y. Zhaosheng, "Numerical research on the orientation distribution of fibers immersed in laminar and turbulent pipe flows," *Journal of Aerosol Science*, vol. 35, no. 1, pp. 63–82, 2004.

[7] J. A. Olson, I. Frigaard, C. Chan, and J. P. Hämäläinen, "Modeling a turbulent fibre suspension flowing in a planar contraction: the one-dimensional headbox," *International Journal of Multiphase Flow*, vol. 30, no. 1, pp. 51–66, 2004.

[8] M. Parsheh, M. L. Brown, and C. K. Aidun, "On the orientation of stiff fibres suspended in turbulent flow in a planar contraction," *Journal of Fluid Mechanics*, vol. 545, pp. 245–269, 2005.

[9] L.-X. Zhang, J.-Z. Lin, and T. L. Chan, "Orientation distribution of cylindrical particles suspended in a turbulent pipe flow," *Physics of Fluids*, vol. 17, no. 9, Article ID 093105, 2005.

[10] J.-Z. Lin, K. Sun, and J. Lin, "Distribution of orientations in fibre suspension flowing in a turbulent boundary layer," *Chinese Physics Letters*, vol. 22, no. 12, pp. 3111–3114, 2005.

[11] J. Lin, S. Zhang, and J. A. Olson, "Effect of fibers on the flow property of turbulent fiber suspensions in a contraction," *Fibers and Polymers*, vol. 8, no. 1, pp. 60–65, 2007.

[12] Z. Shanliang, L. Jianzhong, and Z. Weifeng, "Numerical research on the fiber suspensions in a turbulent T-shaped branching channel flow," *Chinese Journal of Chemical Engineering*, vol. 15, no. 1, pp. 30–38, 2007.

[13] L. Jianzhong and K. Xiaoke, "Fiber orientation distributions in a suspension flow through a parallel plate channel containing a cylinder," *Journal of Composite Materials*, vol. 43, no. 12, pp. 1373–1390, 2009.

[14] W. Yang and K. Zhou, "A new method of simulating fiber suspensions and applications to channel flows," *Chinese Physics Letters*, vol. 29, no. 6, Article ID 064702, 2012.

[15] J. Z. Lin, X. Y. Liang, and X. K. Ku, "A successive iteration method on predicting properties of turbulent fiber suspensions and its application to pipe flows," *Computers & Fluids*, vol. 71, pp. 461–468, 2013.

[16] R. B. Bird, R. C. Armstrong, and O. Hassager, *Dynamics of Polymeric Liquids*, vol. 1 of *Fluid Mechanics*, John Wiley & Sons, New York, NY, USA, 2nd edition, 1987.

[17] R. B. Bird, O. Hassager, R. C. Armstrong, and C. F. Curtiss, *Dynamics of Polymeric Liquids*, vol. 2 of *Kinetic Theory*, John Wiley & Sons, New York, NY, USA, 2nd edition, 1987.

[18] J. M. J. Den Toonder, M. A. Hülsen, G. D. C. Kuiken, and F. T. M. Nieuwstadt, "Drag reduction by polymer additives in a turbulent pipe flow: numerical and laboratory experiments," *Journal of Fluid Mechanics*, vol. 337, pp. 193–231, 1997.

[19] J. S. Paschkewitz, Y. Dubief, C. D. Dimitropoulos, E. S. G. Shaqfeh, and P. Moin, "Numerical simulation of turbulent drag reduction using rigid fibres," *Journal of Fluid Mechanics*, vol. 518, pp. 281–317, 2004.

[20] M. Manhart, "Rheology of suspensions of rigid-rod like particles in turbulent channel flow," *Journal of Non-Newtonian Fluid Mechanics*, vol. 112, no. 2-3, pp. 269–293, 2003.

[21] G. K. Batchelor, "The stress system in a suspension of force-free particles," *Journal of Fluid Mechanics*, vol. 41, no. 3, pp. 545–570, 1970.

[22] G. K. Batchelor, "Slender-body theory for particles of arbitrary cross-section in Stokes flow," *Journal of Fluid Mechanics*, vol. 44, pp. 419–440, 1970.

[23] G. K. Batchelor, "The stess generated in a non-dilute suspension of elongated particles by pure straining motion," *Journal of Fluid Mechanics*, vol. 46, pp. 813–829, 1971.

[24] K. Zhou and Z. He, "Monte Carlo simulation of aerosol evolution in a planar mixing layer," *International Journal of Numerical Methods for Heat & Fluid Flow*. In press.

[25] G. I. Taylor, "The motion of ellipsoidal particles in a viscous fluid," *Proceedings of the Royal Society A*, vol. 103, no. 720, pp. 58–61, 1923.

[26] F. P. Bretherton, "The motion of rigid particles in a shear flow at low Reynolds number," *Journal of Fluid Mechanics*, vol. 14, pp. 284–304, 1962.

[27] E. Hairer, S. P. Nørsett, and G. Wanner, *Solving Ordinary Differential Equations I. Nonstiff Problems*, vol. 8 of *Springer Series in Computational Mathematics*, Springer, 2nd edition, 1993.

[28] X.-D. Liu, S. Osher, and T. Chan, "Weighted essentially non-oscillatory schemes," *Journal of Computational Physics*, vol. 115, no. 1, pp. 200–212, 1994.

[29] A. Attili and F. Bisetti, "Application of a robust and efficient Lagrangian particle scheme to soot transport in turbulent flames," *Computers & Fluids*, vol. 84, pp. 164–175, 2013.

[30] K. Zhou, J. Z. Lin, and T. L. Chan, "Solution of three-dimensional fiber orientation in two-dimensional fiber suspension flows," *Physics of Fluids*, vol. 19, no. 11, Article ID 113309, 2007.

[31] G. G. Lipscomb II, M. M. Denn, D. U. Hur, and D. V. Boger, "The flow of fiber suspensions in complex geometries," *Journal of Non-Newtonian Fluid Mechanics*, vol. 26, no. 3, pp. 297–325, 1988.

[32] K. Zhou and J. Z. Lin, "Three dimensional fiber orientation distribution in two dimensional flows," *Fibers and Polymers*, vol. 9, no. 1, pp. 39–47, 2008.

Hindawi Publishing Corporation
Abstract and Applied Analysis
Volume 2013, Article ID 984894, 8 pages
http://dx.doi.org/10.1155/2013/984894

Research Article

Numerical Modeling of the Fluid Flow in Continuous Casting Tundish with Different Control Devices

Zhu He, Kun Zhou, Shuang Liu, Wei Xiong, and Baokuan Li

Key Laboratory for Ferrous Metallurgy and Resources Utilization, Ministry of Education, Wuhan University of Science and Technology, Wuhan 430081, China

Correspondence should be addressed to Zhu He; hezhu@wust.edu.cn

Received 23 August 2013; Accepted 16 September 2013

Academic Editor: Jianzhong Lin

Numerical simulations were conducted to study the melt flow under the influence of control devices in a T-type two-strand bloom caster tundish via the open source Computational Fluid Dynamics software OpenFOAM. Three different cases were studied: a bare tundish, a tundish with two pairs of baffles, and a tundish equipped with a turbulence inhibitor and a pair of baffles. Turbulence inhibitor and baffles arrangement showed an improvement of the fluid flow characteristics, yielding lower values of dead volume and higher values of plug flow. With a turbulence inhibitor, the velocity of metal which flows directly toward the tundish floor is smaller and the turbulence kinetic energy of the melt top surface is lower than the other two arrangements.

1. Introduction

In the steel production route, continuous casting of liquid steel is the most important process. Basically, the tundish in the continuous casting is an intermediate vessel between the ladle and the mold to distribute and supply liquid steel to different molds at an approximately constant rate (Figure 1). In recent years, tundish has become more of a continuous reactor than merely an intermediate buffer to distribute and supply liquid steel with an approximately constant rate [1]. Various metallurgical operations, such as alloy trimming of steel, thermal and chemical homogenization, inclusion separation and floatation, are carried out in steel making tundishes. The time available for these operations is very short, and therefore, it is necessary to have a good understanding of fluid flow behavior in the tundish. Generally, two research methods, physical modeling and mathematical simulation [2–5], are used for the tundish configurations optimization and flow control devices, such as weirs, dams, baffles with inclined holes, and turbulence inhibitors (TI), have been widely used to increase residence times and plug flow volume of liquid steel [6–8].

Since detailed knowledge of the molten steel flow is a prerequisite to any effective flow-control optimization, significant efforts have been made by researchers to investigate fluid flow phenomena in tundish systems. Estimation of the various residence time distribution (RTD) parameters via the pulse tracer addition technique has been widely used to study the fluid flow patterns in tundish system [9–11]. In such studies, a tracer (e.g., dye, acid, or salt) is injected through the incoming water stream and its concentration at the exit is recorded as a function of time. The plot of the exit concentration against time is known as the RTD curve. The RTD of the fluid in a tundish is analyzed to characterize the flow which, normally, includes the determination of the extent of mixing (plug and mixed volumes) and the dead volume in the tundish. And it has been generally considered that the mathematical model is able to simulate RTD phenomena realistically [12–14].

In the present, work fluid flow in a 30 t tundish with different flow control devices was investigated by mathematical models. In each case of study, flow characteristics, velocity patterns, RTD curves, and inclusion distribution were obtained. The objective in this work was to study the effects of the flow control devices on the fluid flow pattern and RTD curves in a T-type two-strand tundish of a bloom caster.

Figure 2 shows the physical dimensions of this problem. Design of the baffles and the turbulence inhibitor as well as the positions of the TI and baffles inside the tundish is also indicated in Figure 2. Three types of the tundishes were studied as follows: the bare tundish (Case I), a tundish with a pair of baffles (Case II), and a tundish with a TI

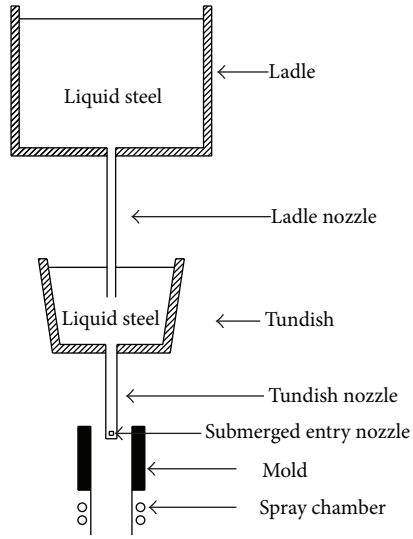

Figure 1: Schematic diagram of a continuous casting setup.

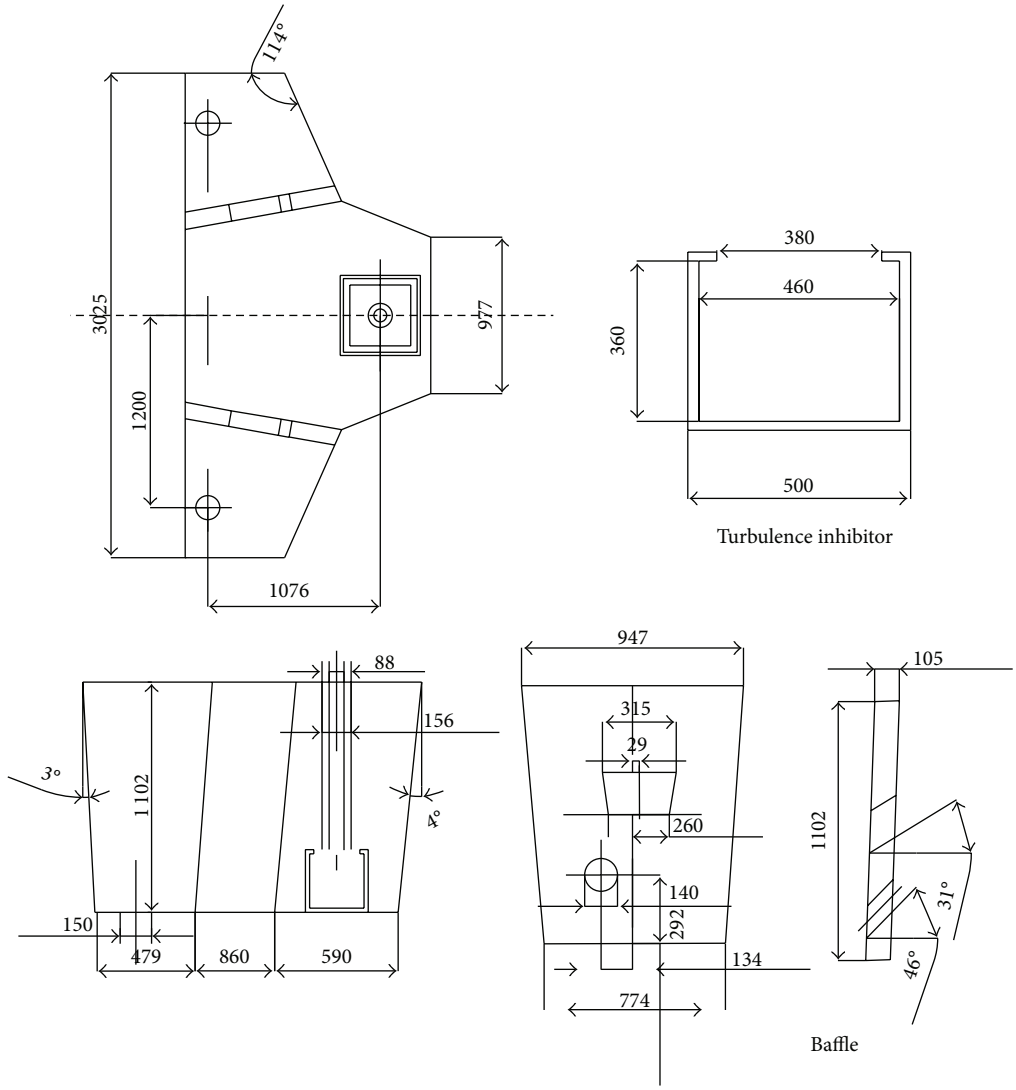

Figure 2: Physical dimensions of the tundish and the control devices.

and a pair of baffles (Case III). The cross-section of slab is 1600 mm × 200 mm and the casting speed is 1.2 m/min, so the corresponding flow rate is 0.768 m^3/min.

2. Mathematic Formulation

2.1. Fundamental Equations. The liquid steel flow in the continuous casting tundish can be considered to be three-dimensional, Newtonian, and incompressible turbulence. A layer of slag at the top of liquid is neglected and the melt surface is assumed to be flat. The mathematical model, which is used to simulate the melt flow inside the tundish as well as the chemical mixing process of the tracer injected by a pulse in the incoming stream, was formulated based on the solution of the three-dimensional Navier-Stokes equations, the mass transfer equation, and two equations for the k-ε model chosen to represent turbulent viscosity.

Continuity equation:

$$\frac{\partial\left(\rho u_j\right)}{\partial x_j} = 0. \tag{1}$$

Momentum equation:

$$\rho u_j \frac{\partial u_i}{\partial x_j} = -\frac{\partial p}{\partial x_i} + \frac{\partial}{\partial x_j}\left(\mu_{\text{eff}}\left(\frac{\partial u_i}{\partial x_j} + \frac{\partial u_j}{\partial x_i}\right)\right) + \rho g_i, \tag{2}$$

where $u_{i,j}$ are the time-averaged fluid velocities in the ith and jth directions, respectively, ρ is the liquid density, p is the pressure in the fluid, μ_{eff} is the effective turbulent viscosity, g_i is the gravitational acceleration in the ith direction, x_i, x_j are the spatial coordinates in the ith and jth directions, respectively, and i, j denote the three directions in the global Cartesian coordinate system.

Effective viscosity μ_{eff} is the sum of laminar viscosity μ and turbulent viscosity μ_t:

$$\mu_{\text{eff}} = \mu + \mu_t = \mu + \rho c_\mu \frac{k^2}{\varepsilon}. \tag{3}$$

The following equation describes the turbulent kinetic energy:

$$\rho u_j \frac{\partial k}{\partial x_j} = \frac{\partial}{\partial x_j}\left(\frac{\mu_{\text{eff}}}{\sigma_k} \times \frac{\partial k}{\partial x_j}\right) + G - \rho\varepsilon. \tag{4}$$

The following equation describes the dissipation rate of turbulence energy:

$$\rho u_j \frac{\partial \varepsilon}{\partial x_j} = \frac{\partial}{\partial x_j}\left(\frac{\mu_{\text{eff}}}{\sigma_\varepsilon} \times \frac{\partial \varepsilon}{\partial x_j}\right) + \frac{\left(c_1 G\varepsilon - c_2\rho\varepsilon^2\right)}{k}, \tag{5}$$

where G is the generation of turbulence kinetic energy caused by the mean velocity gradients:

$$G = \mu_t \frac{\partial u_j}{\partial x_i}\left(\frac{\partial u_i}{\partial x_j} + \frac{\partial u_j}{\partial x_i}\right). \tag{6}$$

The values for the constants in this k-ε model c_1, c_2, c_μ, σ_k, and σ_ε are 1.44, 1.92, 0.09, 1.00, and 1.30, respectively [15].

Mass transfer equation:

$$\frac{\partial C}{\partial t} + u_i \frac{\partial C}{\partial x_i} = -D_{\text{eff}} \frac{\partial}{\partial x_j}\left(\frac{\partial C}{\partial x_j}\right). \tag{7}$$

In the mass transfer equations, C is the tracer concentration. $D_{\text{eff}} = D_m + D_t$ is the effective mass transfer diffusivity, which is the summation of molecular and turbulent diffusivities, respectively. The turbulent diffusivity D_t is related to the turbulent viscosity μ_t by

$$D_t = \frac{\mu_t}{\rho} \tag{8}$$

which means that the turbulent Schmidt number is equal to one.

2.2. Boundary and Initial Conditions. Due to symmetry, only a half tundish from the symmetric central-longitudinal plane was chosen for this mathematical simulation. On the top surface of the bath and in symmetry planes, the fluxes of all variables were set equal to zero. No slip conditions were applied to all solid surfaces of the tundish including baffles, and interior walls of the tundish and standard wall functions were applied. The tundish exit is computationally treated as a plane, at which flow occurs at an ambient pressure. The vertical velocity profiles of the liquid steel at the inlet of the tundish were assumed to be uniform through the cross-sections and the other two velocity components were assumed to be zero. The values of k and ε at the inlet were calculated from the inlet average velocity through the following equations:

$$\begin{aligned} U_{\text{in}} &= \frac{Q}{A_{\text{nozzle}}}, \\ k_{\text{in}} &= 0.01 U_{\text{in}}^2, \\ \varepsilon_{\text{in}} &= \frac{2k_{\text{in}}^{2/3}}{D_{\text{nozzle}}}. \end{aligned} \tag{9}$$

The initial condition for (5) is that the tracer concentration is zero except in the ladle nozzle from the injection point to the nozzle tip.

2.3. Geometry and Numerical Methods. A control volume-based technique was used to convert the nonlinear governing equations to algebraic equations that can be solved numerically using the 3D mesh (Figure 3). A dense mesh was employed near the wall of the tundish. SIMPLE algorithm [16] was applied for the pressure-velocity coupling. A segregated and implicit solver was used to solve the governing equations and the second-order accuracy upwind differencing scheme was adopted to improve the accuracy of the solution. The open source Computational Fluid Dynamics software OpenFOAM [17] was used to compute the velocity and concentration fields. OpenFOAM is an open source code which is designed for continuum mechanics applications and has attracted much attention recently. It is an object oriented

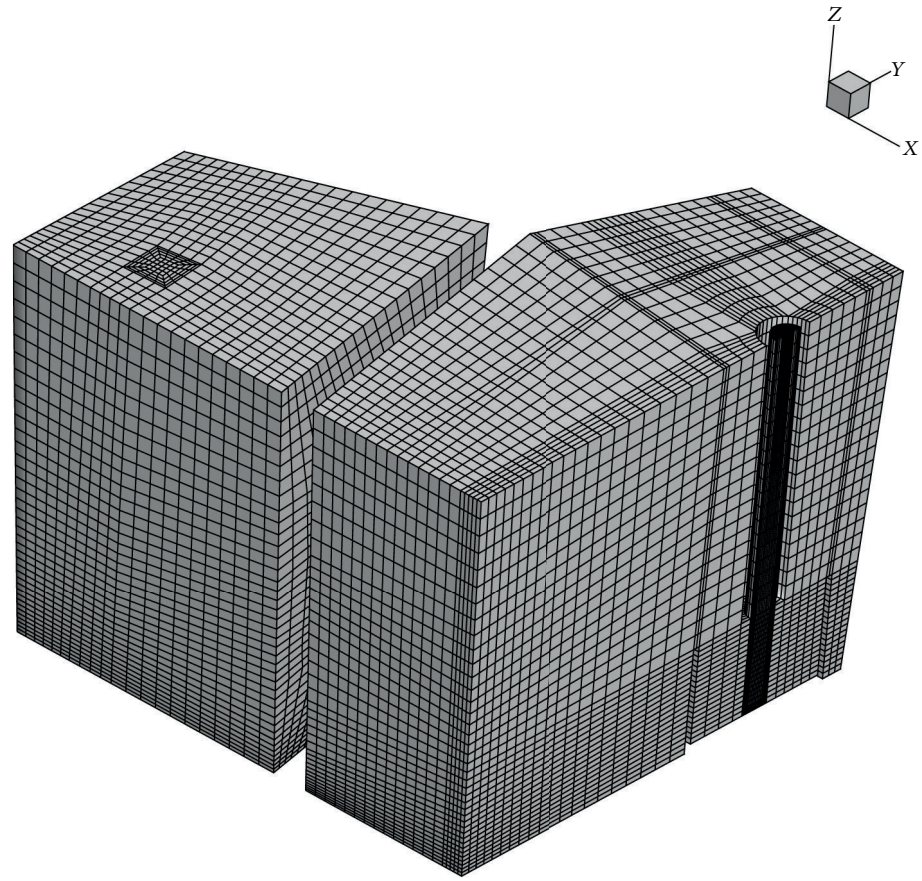

Figure 3: 3D computational mesh employed in the present model.

programming based toolbox which makes it sustainable in terms of reuse and development by users all around the world. OpenFOAM gives a flexible framework which combined almost all the required tools for solving CFD problem. Firstly, (1)–(4) were solved together with their boundary conditions until the steady state of the fluid flow was reached. Then the velocity field was employed to solve (7) for the tracer concentration under unsteady state conditions. Here, the tracer was treated as a passive scalar; that is, the presence of the tracer does not affect the melt flow. A criterion for convergence was set to be less than 10^{-5} on all variables and computations were carried out until the relative sum of residuals on all variables fell below the stipulated value.

3. Results and Discussion

3.1. Model Validation. In this section, the fluid flow model was validated against the experimental data [18] in the water model for a single inlet, single outlet tundish in which the tracer concentrations with time at the outlet were measured. The bath height was kept at 260 mm in the experiment and the same height was used for the model accordingly. Figure 4 shows the temporal variation of the tracer concentration (nondimensional) with nondimensional time and its comparison with the experiment. It can be seen that the overall characteristics of the RTD curve predicted by the present mathematical model match quite well with the experimental data although some delays existed.

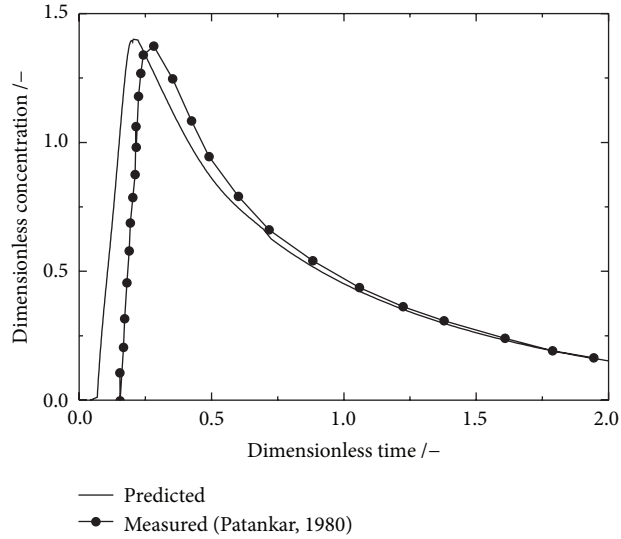

Figure 4: Comparison of the predicted and measured RTD curves.

A typical grid independence test (i.e., 51 × 58 × 34, 63 × 79 × 40, and 76 × 96 × 48) of the present numerical calculation was evaluated in Figure 5 which shows the profiles

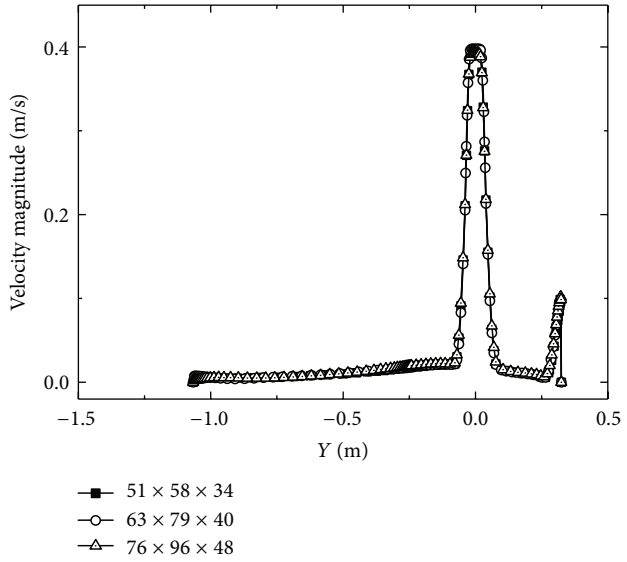

Figure 5: Grid independence check of solutions in a bare tundish.

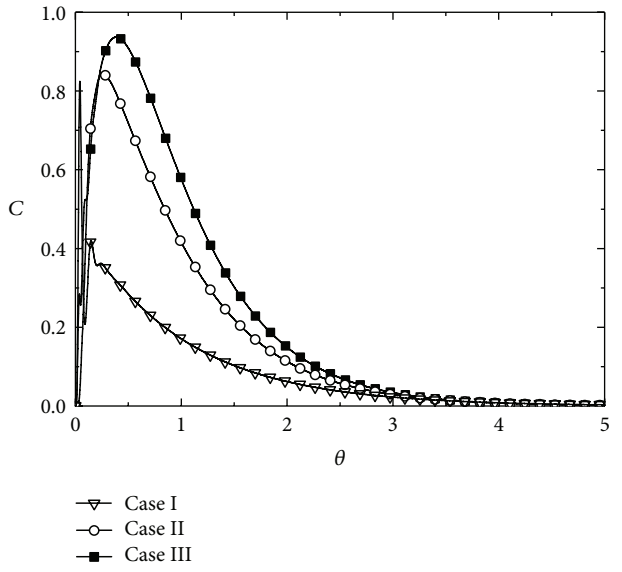

Figure 6: RTD curves for the three cases studied.

of the velocity at various transverse positions in the symmetry plane of the bare tundish ($x = 0$, $-1.066 \leq y \leq 0.324$, $z = 0.1$). According to the results, the grid size schemes of $63 \times 79 \times 40$ and $76 \times 96 \times 48$ have almost the same velocity magnitude distribution, which demonstrates that the grid size scheme of $63 \times 79 \times 40$ is accurate enough for the present numerical calculation.

3.2. Effects of the Control Devices on the RTD Curve. Figure 6 shows the comparison of the RTD for the three studied cases. The curve for Case I is characterized by two peak values of concentrations, one soon after the tracer injection and then the second. After then, the tracer concentration decreases continuously with time. This is because a portion of the liquid moves on the horizontal plane straight towards the exit [19]. The existence of the two peak values of concentration may

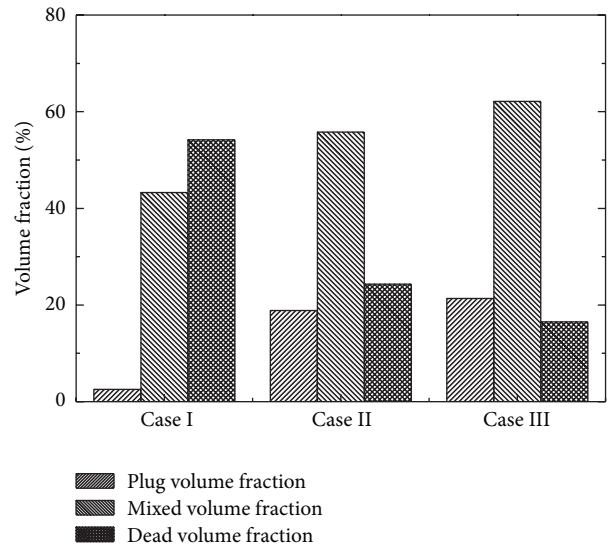

Figure 7: Volume fraction of flow for the studied cases.

Table 1: RTD parameters in the tundish system.

Tundish configuration	t_{min} (s)	t_{max} (s)	t_{av} (s)
Case I	17	28	288
Case II	65	118.8	259.6
Case III	70	164.2	325.5

suggest that the flow field in the tundish is short circuited and that is undesirable in tundish fluid system. Thus the bare tundish is associated with considerable short-circuiting and large dead volumes, which are potentially detrimental to the floatation of nonmetallic inclusions. As seen from Figure 6, the RTD parameters in Case II and III are improved considerably and only one peak value appeared.

From the RTD curves, minimum residence time, t_{min}, peak concentration time, t_{max}, and mean residence time, t_{av}, can be obtained for each case. Considering that there is fluid exchange between the fluids in the dead zone and in the active zone, the flow model proposed by Sahai and Emi [20] was employed in this work to calculate dead volume fraction, the fractions of plug flow and well-mixed volumes.

Table 1 shows a summary of the flow characteristics in the tundish with different flow control devices. Each volume fraction of flow for the studied cases is shown in Figure 7. It can be seen that the associated dead volume is significantly high for the bare tundish. The application of baffles brings down the dead volume from 54% to 24% and it is further decreased to 16% with the TI+baffle configuration as is clearly mentioned in Table 1. The better mixing in the tundish occurs corresponding to higher well-mixed along with lower dead volume and therefore it is also expected for better temperature homogenization. At the same time, higher plug volume with minimum dead region shows the better inclusion removal in the tundish.

3.3. Analysis of Velocity Fields. Figure 8 shows the predicted flow fields in one half of the two-strand bare tundish system

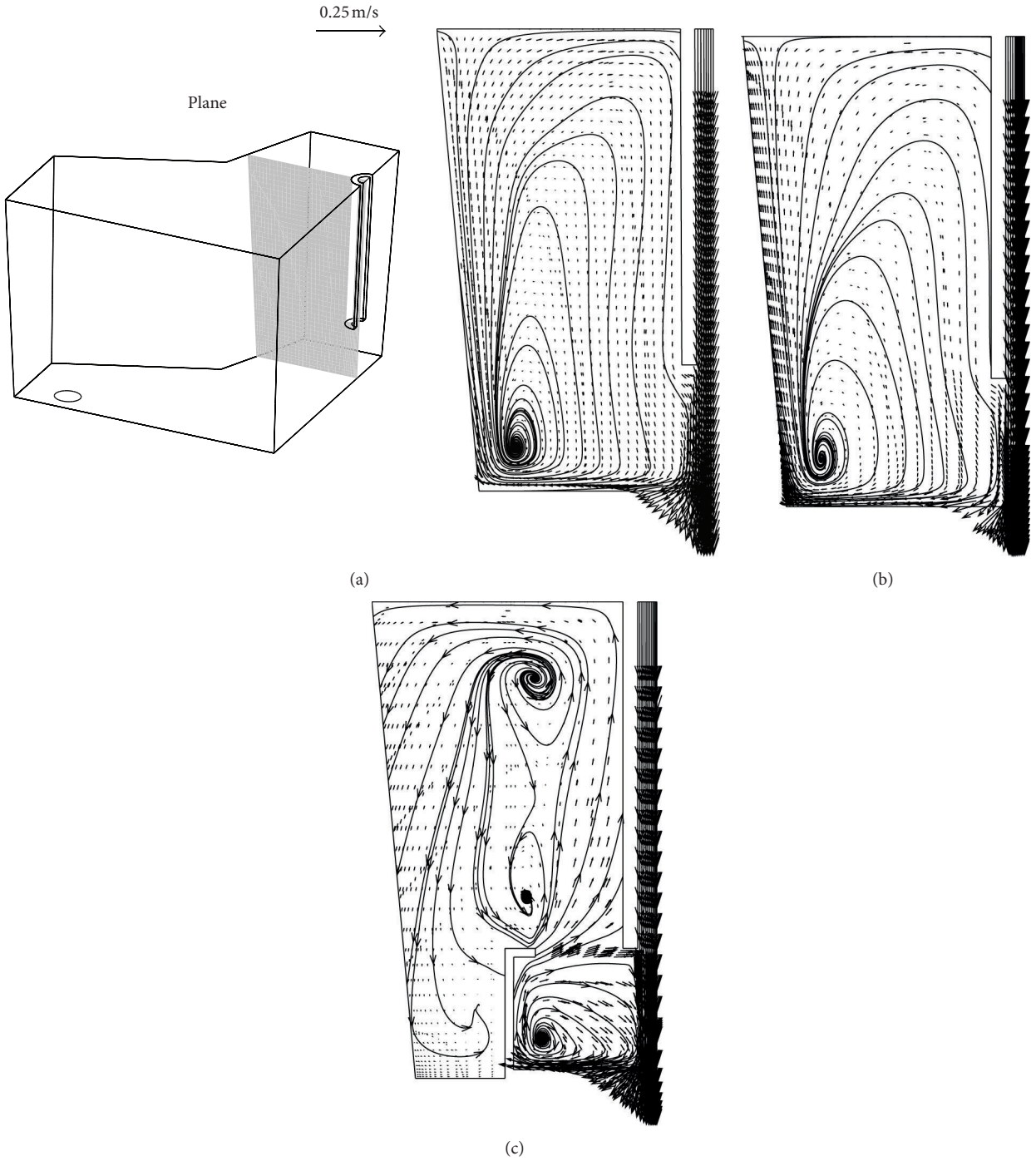

Figure 8: Predicted metal flow field in tundish for all cases: (a) Case I, (b) Case II, and (c) Case III.

which represent the velocity fields in YZ plane (central longitudinal vertical plane) at $X = 0$ (inlet stream). Highly turbulent flow can be clearly seen near the inlet region of the tundish. The incoming jet hits the tundish bottom with very high velocity, which is evidently shown in Figure 8(a). After striking the tundish bottom, the melt partly moves up along the tundish side walls to the free surface, partly moving downstream to the exit and the rest recirculating back toward the incoming jet. The strong velocity fields thus created are responsible for reversal of flow towards the inlet stream and generated clockwise recirculatory flow. The impact of the melt flow on the walls will result in high refractory wear in the entry zone and the wall refractory wear will increase the exogenous inclusion count of the steel supplied to the molds. Figure 8(b) shows the flow fields for Case II, which is very similar to Case I. With the aid of the TI in Case III, though the recirculating flow remains, it is directed toward the tundish floor and the turbulent flow with smaller velocity vectors is well controlled, as shown in Figure 8(c). At the same time, due to the high turbulence level in the TI area, it would be the best

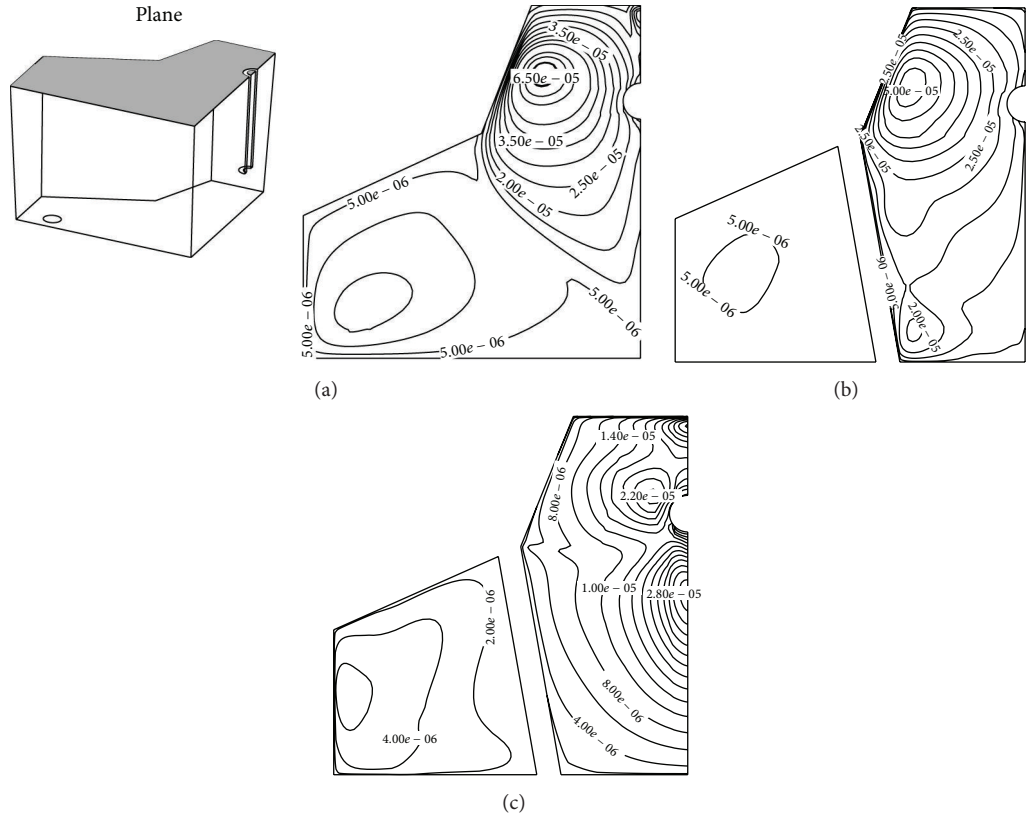

Figure 9: Predicted turbulent kinetic energy field in tundish for all cases: (a) Case I, (b) Case II, and (c) Case III.

region to make any alloy additions in the tundish. And along with the higher convective and diffusive mixing in this region, the alloy will get uniformly distributed in the rest of the tundish, which results in homogeneity during the casting.

Figure 9(a) through Figure 9(c) shows the predicted turbulence kinetic energy contours along the top surface of one half of the tundish for Cases I, II, and III, respectively. The high turbulence kinetic energy is associated with the liquid steel top surface instability and the entrainment of the slag. As seen from Figure 9(a), the highest value of the turbulence kinetic energy is found in the region just above the inlet stream and it is $6.5e-5\ m^2/s^2$ per kg of the liquid. With a pair of baffles, the highest value is lowered to $5.0e-5\ m^2/s^2$ per kg of the liquid (Figure 9(b)). For Case III as shown in Figure 9(c), the turbulence kinetic energy is greatly decreased and the highest value is $2.8e-5\ m^2/s^2$ per kg of the liquid.

4. Conclusions

A numerical study was conducted to investigate the fluid flow and residence time distribution of the T-type two-strand continuous casting tundish with and without flow control devices. The following conclusions have been drawn from the present study.

(i) The application of a pair of baffles eliminates the short circuiting phenomena in the tundish and brings down the dead volume from 54% to 24%.

(ii) The employment of a TI and a pair of baffles is more effective to increase the plug fraction than a bare tundish or a tundish with just a pair of baffles, and it was found to be an optimum configuration of the two-strand tundish in the present study.

(iii) With a TI, the velocity vectors directed toward the tundish floor are smaller and the turbulence kinetic energy of the liquid steel top surface is lower than the other two arrangements, which means a more stable slag-metal interface.

Acknowledgments

This work was supported by the Natural Science Foundation of China (51210007) and the National Key Technology R&D Program of China (2011BAK06B02).

References

[1] D. Mazumdar and R. I. L. Guthrie, "Physical and mathematical modelling of continuous casting tundish systems," *ISIJ International*, vol. 39, no. 6, pp. 524–547, 1999.

[2] L. Zhong, B. Li, Y. Zhu, R. Wang, W. Wang, and X. Zhang, "Fluid flow in a four-strand bloom continuous casting tundish with different flow modifiers," *ISIJ International*, vol. 47, no. 1, pp. 88–94, 2007.

[3] A. Braun, M. Warzecha, and H. Pfeifer, "Numerical and physical modeling of steel flow in a two-strand tundish for different

casting conditions," *Metallurgical and Materials Transactions B*, vol. 41, no. 3, pp. 549–559, 2010.

[4] T. Merder and J. Pieprzyca, "Numerical modeling of the influence subflux controller of turbulence on steel flow in the tundish," *Metalurgija*, vol. 50, no. 4, pp. 223–226, 2011.

[5] M. Warzecha and T. Merder, "Numerical analysis of the nonmetallic inclusions distribution and separation in a two-strand Tundish," *Metalurgija*, vol. 52, no. 2, pp. 153–156, 2013.

[6] R. D. Morales, J. J. de Barreto, S. López-Ramirez, J. Palafox-Ramos, and D. Zacharias, "Melt flow control in a multistrand tundish using a turbulence inhibitor," *Metallurgical and Materials Transactions B*, vol. 31, no. 6, pp. 1505–1515, 2000.

[7] S. López-Ramirez, J. D. J. Barreto, J. Palafox-Ramos, R. D. Morales, and D. Zacharias, "Modeling study of the influence of turbulence inhibitors on the molten steel flow, tracer dispersion, and inclusion trajectories in tundishes," *Metallurgical and Materials Transactions B*, vol. 32, no. 4, pp. 615–627, 2001.

[8] B. Moumtez, A. Bellaouar, and K. Talbi, "Numerical investigation of the fluid flow in continuous casting Tundish using analysis of RTD curves," *Journal of Iron and Steel Research International*, vol. 16, no. 2, pp. 22–29, 2009.

[9] P. K. Jha and S. K. Dash, "Effect of outlet positions and various turbulence models on mixing in a single and multi strand tundish," *International Journal of Numerical Methods for Heat and Fluid Flow*, vol. 12, no. 5, pp. 560–584, 2002.

[10] A. Kumar, S. C. Koria, and D. Mazumdar, "An assessment of fluid flow modelling and residence time distribution phenomena in steelmaking tundish systems," *ISIJ International*, vol. 44, no. 8, pp. 1334–1341, 2004.

[11] T. Merder, "Effect of casting flow rate on steel flow phenomenna in Tundish," *Metalurgija*, vol. 52, no. 2, pp. 161–164, 2013.

[12] A. Kumar, D. Mazumdar, and S. C. Koria, "Experimental validation of flow and tracer-dispersion models in a four-strand billet-casting tundish," *Metallurgical and Materials Transactions B*, vol. 36, no. 6, pp. 777–785, 2005.

[13] K. J. Craig, D. J. de Kock, K. W. Makgata, and G. J. de Wet, "Design optimization of a single-strand continuous caster tundish using residence time distribution data," *ISIJ International*, vol. 41, no. 10, pp. 1194–1200, 2001.

[14] K. Chattopadhyay, M. Isac, and R. I. L. Guthrie, "Physical and mathematical modelling of steelmaking tundish operations: a review of the last decade (1999–2009)," *ISIJ International*, vol. 50, no. 3, pp. 331–348, 2010.

[15] B. E. Launder and D. B. Spalding, "The numerical computation of turbulent flows," *Computer Methods in Applied Mechanics and Engineering*, vol. 3, no. 2, pp. 269–289, 1974.

[16] S. V. Patankar, "Numerical heat transfer and fluid flow," McGraw-Hill, New York, NY, USA, 1980.

[17] H. Weller, G. Tabor, and H. C. Jasak, "Fureby A tensorial approach to computational continuum mechanics using object-oriented techniques," *Computers in Physics*, vol. 12, no. 6, pp. 620–631, 1998.

[18] S. Singh and S. C. Koria, "Model study of the dynamics of flow of steel melt in the tundish," *ISIJ International*, vol. 33, no. 12, pp. 1228–1237, 1993.

[19] J. Szekely and N. Themelis, *Rate Phenomena in Process Metallurgy*, Wiley Interscience, New York, NY, USA, 1972.

[20] Y. Sahai and T. Emi, "Melt flow characterization in continuous casting tundishes," *ISIJ International*, vol. 36, no. 6, pp. 667–672, 1996.

Hindawi Publishing Corporation
Abstract and Applied Analysis
Volume 2013, Article ID 386085, 5 pages
http://dx.doi.org/10.1155/2013/386085

Research Article

Design of T-Shaped Micropump Based on Induced Charge Electroosmotic

Kai Zhang, Xiaojing Mi, and Bingying Sheng

Department of Mechanics, China Jiliang University, Hangzhou, Zhejiang 310018, China

Correspondence should be addressed to Kai Zhang; zkzb3026@gmail.com

Received 1 September 2013; Accepted 23 September 2013

Academic Editor: Jianzhong Lin

The fluid-driven efficiency of the micropump based on induced charge electroosmotic was studied by numerical simulation method. In this paper, we propose to make some improvement against the T-shaped piping design of micropump, and we embed a janus cylinder in the junction of the T-shaped pipe for the micropump design. We offer different voltage to the inlet of the pipe and carry out the numerical study of the fluid field induced by the cylinder, and the comparison of the velocity and flux of the outlet in different voltage as carried out. It is found that there are two symmetrical circulations around the polarizable side of the cylinder. And the comparison results show that the flow and the velocity of the outlet were increased with the increasing voltage of the entrance.

1. Introduction

The development of microfluidic system raises the fundamental question of how to achieve good microfluid transmission and drive results [1]. However, the phenomena of flow in microfluidic system are very different from that in the macroscopic system, which is caused by the scale effect of flow, the electric field force at the liquid/solid interface, and the coupled physics field of electric field-flow field-temperature field-ion movement field in the pipeline at the micron level [2]. The regular volume force (such as gravity and inertial force) is not generally important, and the electric field force becomes the leading driver of the liquid flow in microfluidic system. And the electroosmotic flow has become one of the most important ways of fluid transmission in the microfluidic chip, which does not require the machinery unit and provide the piston flow cross section.

However, there are some shortcomings for electroosmosi. For example, (1) strong electric field must be applied to the whole system to achieve the necessary field strength, generating Joule heating and raising the solution temperature, and temperature field will make feedback effect on electric field and flow field [3–5]. (2) Ac fields, which can reduce undesirable Faradaic reactions and Joule heating, produce zero time-averaged flow. Fortunately, these drawbacks do not apply to inducedcharge electroosmosis (Ramose et al. and Ajdari). Different from electroosmosis (EOF), ICEOF results from the interaction of the applied electric field and its own induced diffuse charge around immobile polarizable surfaces. The prototypical scenario involves a perfectly conducting ion-impermeable cylinder which is placed in an electrolyte solution. When an external electric field is applied, Faraday currents charge the region adjacent to its surface, thereby generating a polarized Debye layer. Simultaneously, the particle itself polarizes. The electric field exerts Lorentz body forces on its self-induced Debye cloud, thereby generating a velocity field [6].

In comparison with EOF, the velocity of ICEOF may be higher because of its nonlinear dependence on the applied electric field. Those unique characteristics may lead to new applications in microfluidics and nanofluidics. Recent research includes using ICEOF for mixing [7, 8] and flow regulating [9, 10] and promoting stirring and chaotic advection [11], the particles in Brownian motion [12], particle-wall interaction [13] and particle-particle interaction [14], nonspherical particles [15], and suspension dynamics [16].

In general, the induced charge electroosmosis (ICEOF) could be used for the design of micro-pump in microfluidic system. The impetus of this paper is to advance the understanding of induced charge electroosmosis (ICEOF) around

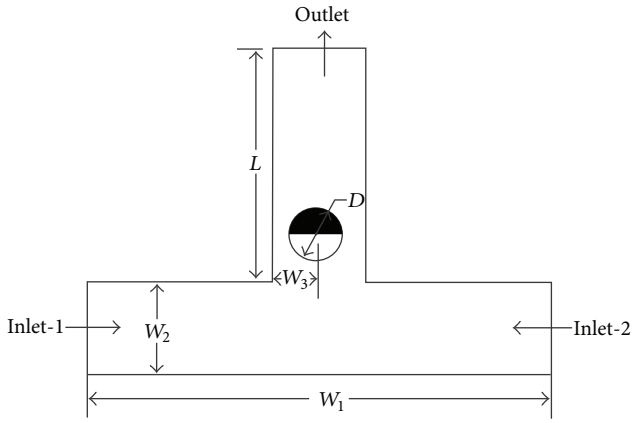

Figure 1: Schematic diagram of the T-shaped microchannel with Janus cylinder.

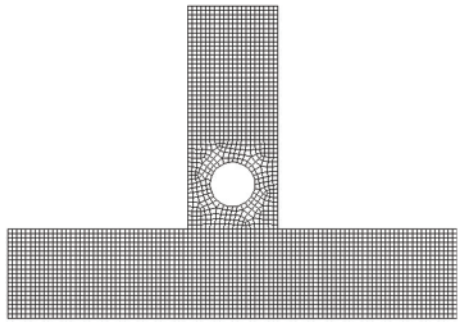

Figure 2: The mesh used in numerical simulation.

a Janus cylinder in a confined T-shaped microchannel, and it is mostly concerned with the design of a super efficient T-shaped micro-pump. The relationship between fluid field and extra electric field is also studied in this research.

2. Mathematical Model and Boundary Conditions

2.1. Mathematical Model. The design of the T-shaped micro-pump with a Janus cylinder is shown in Figure 1, and the black side of the cylinder is nonpolarizable and the white side is polarizable, and Figure 2 is the mesh of the computational domain.

For the design of the T-shaped micro-pump, we study the ICEOF around the Janus cylinder, and the model parameters are shown in Table 1.

Assuming the flow is incompressible and steady and driven by the ICEOF, the momentum equation of flow can be given as

$$\rho\left(\overrightarrow{V}\bullet\nabla\right)\overrightarrow{V}=-\nabla p+\mu\nabla^2\overrightarrow{V}+\overrightarrow{F}, \tag{1}$$

where $\overrightarrow{V}$ is velocity vector, p is pressure, and ρ and μ denote the density and the viscosity of the solution, respectively.

Based on the property of flow field, two velocity components are described by $u = u(x, y)$, $v = v(x, y)$. In addition, the flow is driven by electroosmosis, and then (1) can be expressed as

$$\rho\left(\overrightarrow{V}\cdot\nabla\right)\overrightarrow{V}=-\nabla p+\mu\nabla^2\overrightarrow{V}+\rho_e\overrightarrow{E}, \tag{2}$$

where $\overrightarrow{E}$ is the electric field, which is given by $\overrightarrow{E} = \nabla\Psi$, Ψ is the electric potential, and ρ_e is the charge density. The relation between the net charge density ρ_e and the electrical potential Ψ is shown as follows

$$\frac{\partial^2\Psi}{\partial x^2}+\frac{\partial^2\Psi}{\partial y^2}=-\frac{\rho_e}{\varepsilon\varepsilon_0}, \tag{3}$$

where ε is the dielectric constant of the electrolyte solution and ε_0 is the permittivity of vacuum.

In general, ion concentration is affected by both the distribution of the externally applied potential, φ, and the distribution of the potential, ψ, associated with the electrical double layer (with surface potential, ζ). The overall electric potential, Ψ, is composed of both φ and ψ. However, in general, the EDL potential distribution ψ is only a small fraction of Ψ. Since the Debye length (λ_d) is typically very small compared to the microchannel height, the ion distribution is influenced primarily by the ζ potential. It is reasonable to assume that the electric potential Ψ is given by the linear superposition of the electrical double layer potential and the externally applied potential, that is, $\Psi = \psi + \varphi$. Therefore, (3) can be represented as

$$\begin{gathered}\frac{\partial^2\psi}{\partial x^2}+\frac{\partial^2\psi}{\partial y^2}=-\frac{\rho_e}{\varepsilon\varepsilon_0},\\ \nabla^2\phi=0,\end{gathered} \tag{4}$$

where,

$$\rho_e=-2n_\infty ze\sinh\left(\frac{ze\psi}{k_bT}\right), \tag{5}$$

where z is the valence of ions, e is the fundamental electric charge, n_∞ is the ionic number concentration in the bulk solution, T is the absolute temperature of the solution, and k_b is Boltzmann's constant. Taking (5) into (2) results in

$$\rho\left(\overrightarrow{V}\cdot\nabla\right)\overrightarrow{V}=-\nabla p+\mu\nabla^2\overrightarrow{V}+2n_\infty ze\sinh\left(\frac{ze\psi}{k_bT}\right)\nabla(\psi+\phi). \tag{6}$$

2.2. Boundary Conditions. For fluid flow, atmospheric pressure is specified at the inlet and outlet, and there is no slip boundary condition on the wall. For external potential, a constant value for potential is specified at the inlet and outlet, and its normal-differential value on the wall is zero. For EDL potential, its normal-differential value on the inlet and outlet is zero. Now, we will discuss the surface electric potential in detail.

Standard electric flow contains the interaction between the external electric potential and the fixed electric double layer. Thus, the electroosmotic flow velocity is linearly

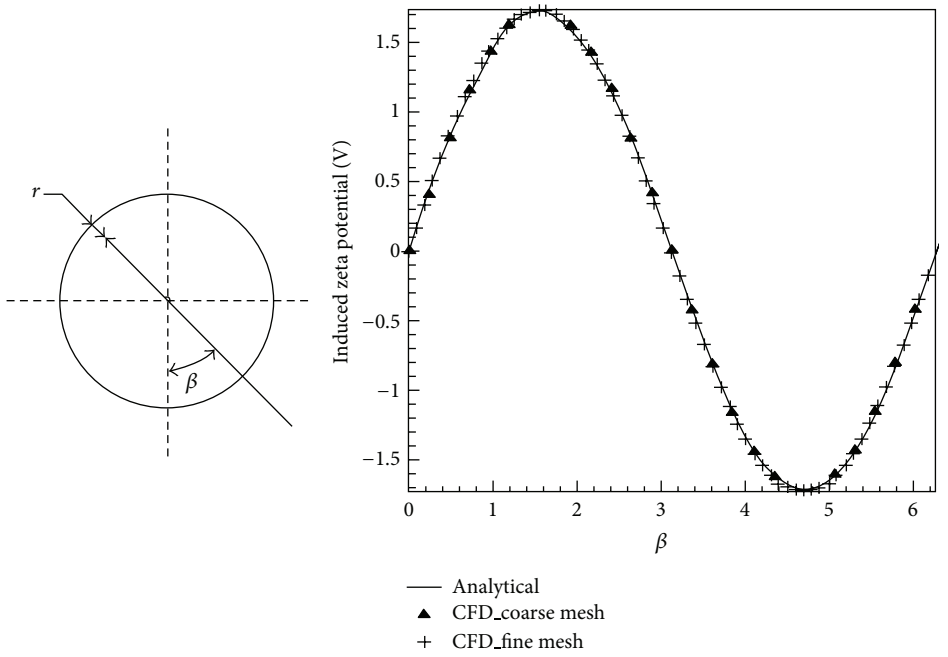

Figure 3: Schematic diagrams of induced zeta potential distribution on the polarizable particle's surface. $E_0 = 42.76$ KV/m, $r = 20\,\mu$m.

Table 1: Model parameters.

Parameter	Value	Description
W_1	100 μm	The distance between inlet-1 and inlet-2
W_2	20 μm	The width of the microchannel
W_3	10 μm	The distance between cylinder center and side wall
L	50 μm	The length of vertical pipe of T-shaped microchannel
D	10 μm	The diameter of the Janus cylinder

dependent with the external electric field strength. However, when the solid surface is polarizable and conductive, the interrelation between the two will be very different. In this case, the induced zeta potential ζ_i is dependent with the local electric field strength E and differs depending on the location of the conductive surface. In the early study, an easy correction method was proposed to achieve the numerical simulation of the zeta potential of the conductive surface induced by the local external electric potential φ_e. The induced zeta potential ζ_i is shown as

$$\zeta_i = -\phi_e + \phi_c, \tag{7}$$

where

$$\phi_c = \frac{\int_S \phi_e dA}{A} \tag{8}$$

is an electric potential constant revision. Obviously, now, the induced zeta potential ζ_i is no longer a constant but will change with the local external electric potential.

We choose the control-volume-based method to solve the equations, and a specific discrete method is used to get the second-order accuracy. Firstly, we solve (7) and (4) to get the zeta potential and the external electric potential distribution in microchannel. Then, we solve (6) to get the flow field situation. In addition, in numerical situation, we should certificate the grid-independent to ensure the statistical independence of the calculations. As shown in Figure 2, the difference caused by the further mesh optimization above this number of grid is less than 1%.

2.3. Validation. Evaluating the induced zeta potential around conducting surface is critical to calculate ICEOF, and for 2D circular cylinder, our numerical scheme has been validated by the comparison with the analytical formulation that has been derived (Bazant & Squires [6]) as shown in

$$\zeta = 2E_0 r \cos\beta, \tag{9}$$

where r is the radius of cylinder, E_0 is the averaged electric field around cylinder, and β is the angle as shown in Figure 3. The results show a good matching between the numerical and the analytical formulations.

3. Results and Discussion

The present simulation assumes that the T-shaped microchannel is made of silica glass. And it is assumed

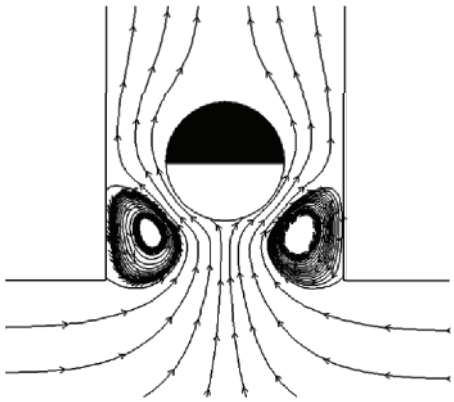

Figure 4: The flow diagram around the Janus cylinder when $E = 2e5\,\mathrm{V/m}$.

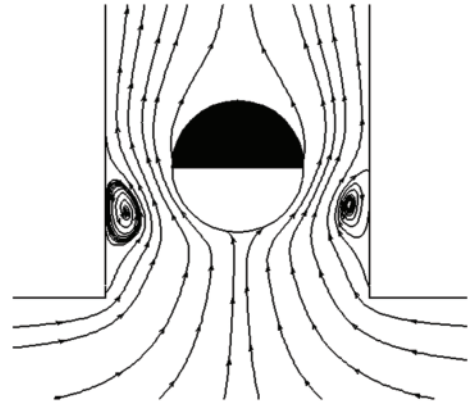

Figure 5: The flow diagram around the Janus cylinder when $E = 2e5\,\mathrm{V/m}$.

that water-liquid is used as the working fluid and its physical properties are given by $\varepsilon = 80$, $\varepsilon_0 = 8.85e-12\,\mathrm{CV^{-1}m^{-1}}$, $\mu = 1.003e-3\,\mathrm{kgm^{-1}s^{-1}}$, $\rho = 998.2\,\mathrm{kg/m^3}$. All the numerical solutions presented in the following have been carefully studied such that grid-independent solutions are obtained.

In this investigation, the microchannel has an external electric potential of $\phi_{\mathrm{out}} = 0\,\mathrm{V}$, while ϕ_{in} is changeable from 10 V to 50 V; accordingly, the electric field strength varies from $E = 2e5\,\mathrm{V/m}$ to $E = 1e6\,\mathrm{V/m}$. The zeta potential at the microchannel wall is zero, and that of the conductive surface can be obtained from (3).

As previously stated, when the conducting cylinders are immersed in the electric field, a nonuniform distribution of zeta potential will be induced on the conducting surfaces, causing a varying driving force of the electroosmotic flow. Consequently, the slipping velocity on the conducting surfaces changes with position, resulting in a nonuniform flow field. Due to the oppositely charged surfaces, flow circulations are generated near the conductive side of the embedded cylinder.

Here, we offer the flow diagram around the Janus cylinder when $E = 2e5\,\mathrm{V/m}$ and $E = 1e6\,\mathrm{V/m}$, as shown in Figures 4 and 5, respectively. We can see that consistent with the theoretical analysis, there exist 2 symmetrical flow circulations around the conductive side of the cylinder. In addition, we can find that the flow circulations will become smaller significantly and approach to the pipe wall but still be symmetrical.

For better study of the relationship between external electric field strength and the T-shaped pump driven efficacy, we make numerical simulation when $\phi_{\mathrm{in}} = 10\,\mathrm{V}$, 20 V, 30 V, 40 V, and 50 V, respectively. As shown in Figure 6, at the outlet of the microchannel, the velocity gradient increases with the increasing of the electrical field strength, which means that the driven efficacy of the T-shaped micro-pump increases with the increasing of the electrical field. For better description of the driven efficiency, we figure out the average velocity magnitude $\overline{V}$ at the outlet and offer the corresponding flux $Q = \overline{V} * W_3$. As shown in Figure 7, we

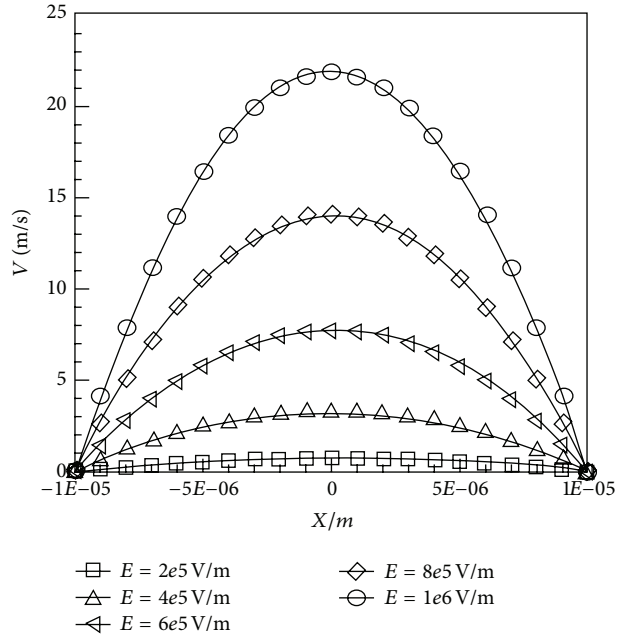

Figure 6: The velocity magnitude profiles under different applied electric field.

can quantitatively see that the variation range of the T-shaped micro-pump flux is from 12.41 mL/s to 348 mL/s.

In summary, the T-shaped micro pump embedded a Janus cylinder, and we propose in this paper that good fluid-driven efficiency can be obtained under small external electric potential, which is of practical value.

4. Conclusions

In this paper, we offer a design of T-shaped micro-pump that embedded a Janus cylinder. We carry out the numerical study of the fluid field induced by the cylinder and make comparison between the velocity magnitude and flux of the outlet in different voltage. It is found that there are two symmetrical flow circulations around the polarizable side

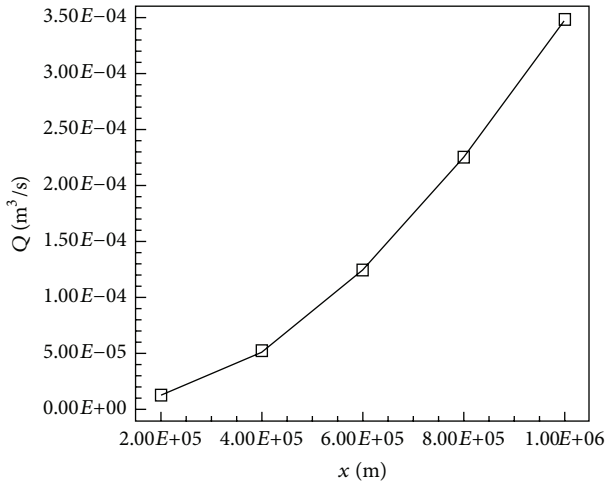

Figure 7: The flux at the outlet of the microchannel under different applied electric field.

of the Janus cylinder, and they can be used to improve the driven efficiency of the pump. The dependence of the driven efficiency on the electric field is also predicted. The conclusions above can be utilized for the optimization of the design of microfluidic devices.

Acknowledgments

The authors are extremely grateful to the editor and the anonymous reviewers for their constructive and valuable comments, which have contributed much to the improvement of this paper. Also, the authors gratefully acknowledge the financial support from the National Natural Science Foundation of China with Grant no. 10902105 and the Natural Science Foundation of Zhejiang Province with Grant no. Y6090406/2010R10014.

References

[1] J. Clayton, "Go with the microflow," *Nature Methods*, vol. 2, no. 8, pp. 621–627, 2005.

[2] G. H. Mohamed, *The MEMS Handbook*, CRC Press, New York, NY, USA, 1999.

[3] K. Zhang and J. Lin, "The effect of temperature distribution on the mass species transport in micro-channels driven by electroosmosis," in *Proceedings of the Coference of Global Chinese Scholars on Hydynamics (CCSH '06)*, pp. 65–70, 2006.

[4] E. Grushka, R. M. McCormick, and J. J. Kirkland, "Effect of temperature gradients on the efficiency of capillary zone electrophoresis separations," *Analytical Chemistry*, vol. 61, no. 3, pp. 241–246, 1989.

[5] A. E. Jones and E. Grushka, "Nature of temperature gradients in capillary zone electrophoresis," *Journal of Chromatography A*, vol. 466, pp. 219–225, 1989.

[6] M. Z. Bazant and T. M. Squires, "Induced-charge electrokinetic phenomena: theory and microfluidic applications," *Physical Review Letters*, vol. 92, no. 6, Article ID 066101, 2004.

[7] Z. Wu and D. Li, "Mixing and flow regulating by induced-charge electrokinetic flow in a microchannel with a pair of conducting triangle hurdles," *Microfluidics and Nanofluidics*, vol. 5, no. 1, pp. 65–76, 2008.

[8] J.-Z. Lin, K. Zhang, and H.-J. Li, "Study on the mixing of fluid in curved microchannels with heterogeneous surface potentials," *Chinese Physics*, vol. 15, no. 11, pp. 2688–2696, 2006.

[9] K. Zhang, J.-Z. Lin, and Z.-H. Li, "Research on diffusion in micro-channel flow driven by electroosmosis," *Applied Mathematics and Mechanics (English Edition)*, vol. 27, no. 5, pp. 575–582, 2006.

[10] Z.-H. Li, J.-Z. Lin, and D.-M. Nie, "New approach to minimize dispersion induced by turn in capillary electrophoresis channel flows," *Applied Mathematics and Mechanics (English Edition)*, vol. 26, no. 6, pp. 685–690, 2005.

[11] H. Zhao and H. H. Bau, "Microfluidic chaotic stirrer utilizing induced-charge electro-osmosis," *Physical Review E*, vol. 75, no. 6, Article ID 066217, 2007.

[12] M. Yu, J. Lin, and T. Chan, "A new moment method for solving the coagulation equation for particles in Brownian motion," *Aerosol Science and Technology*, vol. 42, no. 9, pp. 705–713, 2008.

[13] Z. Wu and D. Li, "Induced-charge electrophoretic motion of ideally polarizable particles," *Electrochimica Acta*, vol. 54, no. 15, pp. 3960–3967, 2009.

[14] D. Saintillan, "Nonlinear interactions in electrophoresis of ideally polarizable particles," *Physics of Fluids*, vol. 20, no. 6, Article ID 067104, 10 pages, 2008.

[15] D. Saintillan, E. S. G. Shaqfeh, and E. Darve, "The growth of concentration fluctuations in dilute dispersions of orientable and deformable particles under sedimentation," *Journal of Fluid Mechanics*, vol. 553, pp. 347–388, 2006.

[16] E. Yariv, "Slender-body approximations for electro-phoresis and electro-rotation of polarizable particles," *Journal of Fluid Mechanics*, vol. 613, pp. 85–94, 2008.

Hindawi Publishing Corporation
Abstract and Applied Analysis
Volume 2013, Article ID 721578, 14 pages
http://dx.doi.org/10.1155/2013/721578

Research Article

Exact Analytical Solution for Suction and Injection Flow with Thermal Enhancement of Five Nanofluids over an Isothermal Stretching Sheet with Effect of the Slip Model: A Comparative Study

Emad H. Aly[1,2] and Abdelhalim Ebaid[3]

[1] *Department of Mathematics, Faculty of Science, King Abdulaziz University, Jeddah 21589, Saudi Arabia*
[2] *Department of Mathematics, Faculty of Education, Ain Shams University, Roxy, Cairo 11757, Egypt*
[3] *Department of Mathematics, Faculty of Science, University of Tabuk, Tabuk 71491, Saudi Arabia*

Correspondence should be addressed to Emad H. Aly; emad-aly@hotmail.com

Received 8 August 2013; Revised 29 August 2013; Accepted 30 August 2013

Academic Editor: Mohamed Fathy El-Amin

We introduced a direct and effective approach to obtain the exact analytical solution for the nanoparticles-water flow over an isothermal stretching sheet with the effect of the slip model. In particular, we examined and compared the effect of the existence of five metallic and nonmetallic nanoparticles, namely, Silver, Copper, Alumina, Titania, and Silicon Dioxide, in a base of water. The most interesting physical parameters were then discussed in the presence of no-slip model, first order slip, and second order slip parameters. It is found that, with no-slip effect, the present exact solutions are in a very good agreement with the previous published results. On the other hand, with the effect of the slip model, increase in the nanoparticle volume friction decreases the velocity for the high density of nanoparticles, increases it for the low density of them, and increases the temperature for all investigated nanoparticles. Further, increase in the wall mass decreases the velocity and temperature; however, it increases the local skin friction. Furthermore, increase in the slips slows down the velocity, increases the temperature with an impressive effect in the injection case, and decreases the local skin friction and the reduced Nusselt number. It was also demonstrated that, as the nanoparticle becomes heavier, this results in increase and decrease in reduced skin friction coefficient and reduced Nusselt number, respectively, with significant effect in the presence of the second slip. Finally, Silver is the suitable nanoparticle if slowing down the velocity and increasing the temperature are needed; Silicon Dioxide is the appropriate nanoparticle if different behavior is to be considered.

1. Introduction

Because of its numerous applications, the problem of flow and heat transfer in boundary-layer over a stretching surface has attracted many researchers. Examples of these applications are metallurgical processes, such as drawing of continuous filaments through quiescent fluids, annealing and tinning of copper wires, glass blowing, manufacturing of plastic and rubber sheets, crystal growing, and continuous cooling and fiber spinning [1]. Further, there are wide range of applications in many engineering processes, such as polymer extrusion, wire drawing, continuous casting, manufacturing of foods and paper, glass fiber production, stretching of plastic films, and many others. In particular, during the manufacture of these sheets, the melt issues from a slit and is subsequently stretched to achieve the desired thickness. Hence, the final product with the desired characteristics strictly depends upon the stretching rate, the rate of cooling in the process, and the process of stretching [2]. Therefore, the choice of a proper cooling/heating liquid is essential as it has a direct impact on the rate of heat transfer.

The pioneer studies of stretching sheets were done by Sakiadis [3, 4] for a moving, inextensible sheet and later extended by Crane [5] to a fluid flow over a linearly stretched

sheet. Following the classical boundary-layer theory, many properties were later investigated using the no-slip condition on the wall. However, when the fluid is particulate such as emulsions, suspensions, foams, and polymer solutions, the no-slip condition is inadequate [6]. In such cases, investigations show that the no-slip condition is no longer valid, specially at the micro- and nanoscale, and instead, a certain degree of tangential slip must be allowed [7]. In particular, the fluid flow behaviour deviates significantly from the traditional no-slip flow. Therefore, in the recent years, the interest has been given to the study of this type of flow and some useful results have been recently introduced by many authors, as mentioned in the next paragraphs.

Convective heat transfer in nanofluids is a topic of major contemporary interest both in applied sciences and engineering, where a very good review was presented by Wang and Mujumdar [8, 9] and Saidur et al. [10]. Choi [11] may be the first author to introduce the word "nanofluid" that represents the fluid in which nanoscale particles (diameter < 50 nm) are suspended in the base fluid. With the rapid advances in nanotechnology, many inexpensive combinations of liquid/particles are now available. The base fluids used are usually water, ethylene glycol, toluene, and oil. Recent research on nanofluids showed that nanoparticles changed the fluid characteristics because thermal conductivity of these particles was higher than convectional fluids. Nanoparticles are of great scientific interest as they are effectively a bridge between bulk materials and atomic or molecular structures. The common nanoparticles that have been used are Aluminum, Copper, Silver, and Titanium or their oxides. Experimental studies by Eastman et al. [12] and Xuan and Li [13] showed that even with the small volumetric fraction of nanoparticles (usually <5%), the thermal conductivity of the base liquid can be enhanced by 10–20%. The enhanced thermal conductivity of nanofluids together with the thermal conductivity of the base liquid and turbulence induced by their motion contributes to a remarkable improvement in the convective heat transfer coefficient. Further, Majumder et al. [14] showed experimentally that nanofluidic flow usually exhibits partial slip against the solid surface, which can be characterized by the so-called slip length (around 3.4–68 micrometers for different liquids). Therefore, the no-slip condition is no longer valid for fluid flows at the micro- and nanoscale.

In addition to the above discussion about the slip model, Noghrehabadi et al. [15] discussed the effect of partial slip boundary condition on the flow and heat transfer of nanofluids past stretching sheet at constant wall temperature to extend the work done by Khan and Pop [16]. Nandeppanavar et al. [17] have tabulated the literature of the first order slip; consequently Fang et al. [18] only considered the effect of the second order slip on the flow on a shrinking sheet. Hence, the paper by Nandeppanavar et al. [17] may be the first work to investigate the analysis of second order slip flow and heat transfer over a stretching sheet. Recently, Turkyilmazoglu [19] has analytically studied the heat and mass transfer of magnetohydrodynamic second order slip flow. He has mentioned that there exists a unique solution for any combination of the considered parameters if the stretching sheet is considered. Very recently, Roşca and Pop [20] investigated the steady flow and heat transfer over a vertical permeable stretching/shrinking sheet with a second order slip being investigated using a second order slip flow model. This very important study showed clearly that the second order slip flow model is necessary to predict the flow characteristics accurately.

To show the enhancement of using nanofluids in comparison with pure base fluid, Yacob et al. [21] compared numerically the thermal enhancement of two types of nanofluids, namely, Ag-water and Cu-water, over an impermeable stretching sheet. In addition, with the effect of magnetic field, Hamad [22] studied boundary layer and heat transfer of nanofluids over impermeable isothermal stretching sheet for the metallic and metallic oxide nanoparticles. Further, Noghrehabadi et al. [23] examined theoretically the flow and heat transfer of two types of nanofluids, namely, Silver water and Silicon Dioxide water. They solved the governing equations by applying a combination of a symbolic power series and Padé approximation method. Very recently, Vajravelu et al. [24] studied the effect of variable viscosity on the flow and heat transfer of viscous Ag-water and Cu-water nanofluids. They indicated that nanoparticle volume fraction is to increase the heat transfer and hence enhance the thermal boundary-layer thickness.

The aim of this work is to introduce a direct and effective approach to analytically obtain the exact solution for the flow over an isothermal stretching sheet with effect of no-slip, first order slip parameter, and second order slip parameter. In addition, it is to examine the effect of the existence of the most five common nanoparticles, namely, Silver, Copper, Alumina, Titania, and Silicon Dioxide, in a base of water. Further, we discuss the interested physical parameters, that is, the velocity, temperature, reduced skin friction coefficient, and reduced Nusselt number. The structure of the paper is as follows. Description of the problem, basic equations, and similarity solution are presented in Section 2. In Section 3, second, third, and fourth degree algebraic equations, including the investigated parameters, are governed on deducing the exact solution of the flow with no, first order, and second order slips, respectively. In addition, exact analytical solution of the temperature equation, represented in a simple gamma function, is proposed in the same section. This research is to be considered as an extension to the work done by Hamad [22] and Noghrehabadi et al. [23], besides the comparison with Wang [25] and Reddy Gorla and Sidawi [26] in the special cases.

2. Governing System of Equations

2.1. Description of the Problem. Consider a two-dimensional incompressible, laminar, and steady boundary-layer flow past an isothermal stretching sheet coinciding with the plane $y = 0$, with the flow being confined to $y > 0$. This sheet is in a water-based nanofluids, which can contain different volume fractions of nanofluids, such as Silver (Ag), Silicon Dioxide (SiO_2), Copper (Cu), Alumina (Al_2O_3), and Titania (TiO_2). In addition, we assume that the [15, 17]

(i) sheet surface has temperature at the wall T_w and at ambient fluid T_∞, where $T_w > T_\infty$;

(ii) base fluid (i.e., water) and the nanoparticles are in a thermal equilibrium;

(iii) fluid outside the boundary layer is quiescent and stretching sheet velocity is linear;

(iv) velocity of the sheet is $U_w(x) = cx$, where $c > 0$ is the stretching constant and x is the coordinate measured along the stretching surface.

The thermophysical properties of the base fluid and nanoparticles are given in Table 1.

2.2. Basic Equations. Under the above assumptions, the governing boundary-layer equations of the considered nanofluid (continuity, momentum, and energy) can be written, respectively, in the dimensional form as

$$\frac{\partial u}{\partial x} + \frac{\partial v}{\partial y} = 0, \tag{1}$$

$$u\frac{\partial u}{\partial x} + v\frac{\partial u}{\partial y} = \frac{\mu_{nf}}{\rho_{nf}}\frac{\partial^2 u}{\partial y^2}, \tag{2}$$

$$u\frac{\partial T}{\partial x} + v\frac{\partial T}{\partial y} = \frac{k_{nf}}{\left(\rho C_p\right)_{nf}}\frac{\partial^2 T}{\partial y^2}, \tag{3}$$

where (x, y) denotes the Cartesian coordinates along the sheet and normal to it, u and v are the velocity components of the nanofluid in the x- and y-directions, respectively, p is the pressure of the nanofluid, T is the temperature of the nanofluid, C_p is the specific heat at constant pressure, ρ_{nf} is the effective density, μ_{nf} is the effective dynamic viscosity, $(\rho C_p)_{nf}$ is the heat capacitance, and k_{nf} is the thermal conductivity, where $(\sim)_{nf}$ denotes the nanofluid and is defined as follows [28, 29]:

$$\rho_{nf} = (1-\phi)\rho_f + \phi\rho_s, \tag{4a}$$

$$\mu_{nf} = \frac{\mu_f}{(1-\phi)^{2.5}}, \tag{4b}$$

$$\left(\rho C_p\right)_{nf} = (1-\phi)\left(\rho C_p\right)_f + \phi\left(\rho C_p\right)_s, \tag{4c}$$

$$k_{nf} = \frac{\left(k_s + 2k_f\right) - 2\phi\left(k_f - k_s\right)}{\left(k_s + 2k_f\right) + \phi\left(k_f - k_s\right)}k_f, \tag{4d}$$

where ϕ is the solid volume fraction, μ_f is the dynamic viscosity, ρ_f and ρ_s are the densities, $(\rho C_p)_f$ and $(\rho C_p)_s$ are the heat capacitances, and k_f and k_s are the thermal conductivities, where $(\sim)_f$ and $(\sim)_s$ denote the basic fluid and solid fractions, respectively. The appropriate boundary conditions of (1)–(3) are as follows:

$$\begin{gathered} u = U_w(x) + U_{\text{slip}}, \qquad v = v_w(x), \\ T = T_w(x) \quad \text{at } y = 0, \\ u = v = 0, \qquad T \longrightarrow T_\infty, \quad \text{as } y \longrightarrow \infty, \end{gathered} \tag{5}$$

where U_{slip} is the slip velocity introduced in the next section.

2.3. Slip Model. In the present work, we consider Wu's slip model [30] (valid for arbitrary Knudsen number, K_n) which is given by

$$\begin{aligned} U_{\text{slip}} = {} & \frac{2}{3}\left(\frac{3-\alpha_m l^3}{\alpha_m} - \frac{3}{2}\frac{1-l^2}{K_n}\right)\lambda_m\frac{\partial u}{\partial y} \\ & - \frac{1}{4}\left[l^4 + \frac{2}{K_n^2}\left(1-l^2\right)\right]\lambda_m^2\frac{\partial^2 u}{\partial y^2} = A\frac{\partial u}{\partial y} + B\frac{\partial^2 u}{\partial y^2}, \end{aligned} \tag{6}$$

where $l = \min[1/K_n, 1]$ and $0 \le \alpha_m \le 1$ and λ_m are the momentum accommodation and molecular mean free path, respectively. Based on the definition of l, it is noticed that for any given value of K_n, we have $0 \le l \le 1$. Therefore, the molecular mean free path is always positive. Therefore, we know that $B < 0$, and hence the second term in the right hand side of (6) is a positive number.

2.4. Similarity Solution. The dimensionless variables can be introduced as follows [22, 31]:

$$\eta = y\sqrt{\frac{c}{\nu}}, \qquad f(\eta) = \frac{\psi}{x\sqrt{c\nu}}, \qquad \theta(\eta) = \frac{T - T_\infty}{T_w - T_\infty}, \tag{7}$$

where η is the similarity variable, $f(\eta)$ is the dimensionless stream function, and $\theta(\eta)$ is the dimensionless temperature. Further, ψ is the stream function which is defined in the usual way as $u = \partial\psi/\partial y$ and $v = -\partial\psi/\partial x$ to identically satisfy (1). From (7), we therefore obtain

$$u = cxf'(\eta), \qquad v = -\sqrt{c\nu}f(\eta), \tag{8}$$

where the prime denotes differentiation with respect to η. Hence, the mass transfer velocity at the wall becomes

$$v_w = -\sqrt{c\nu}f(0). \tag{9}$$

Now on substituting (7) and (8) into (2) and (3), we obtain the following nonlinear ordinary differential equations:

$$\begin{aligned} & \frac{1}{(1-\phi)^{2.5}\left[(1-\phi) + \left(\phi\rho_s/\rho_f\right)\right]}f'''(\eta) \\ & \quad + f(\eta)f''(\eta) - f'^2(\eta) = 0, \\ & \frac{1}{Pr}\frac{k_{nf}/k_f}{(1-\phi) + \phi\left(\rho C_p\right)_s/\left(\rho C_p\right)_f}\theta''(\eta) + f(\eta)\theta'(\eta) = 0, \end{aligned} \tag{10}$$

where $Pr = \nu(\rho C_p)_f/k_f$ is the Prandtl number. The boundary conditions (5) then turn into

$$\begin{gathered} f(0) = s, \qquad f'(0) = 1 + \delta_1 f''(0) + \delta_2 f'''(0), \\ \theta(0) = 1, \qquad f'(\eta) \longrightarrow 0, \\ \theta(\eta) \longrightarrow 0 \quad \text{as } \eta \longrightarrow \infty, \end{gathered} \tag{11}$$

where s $(= -v_w/\sqrt{c\nu})$ is the wall mass transfer parameter, which refers to the suction and injection when $s > 0$ and $s < 0$, respectively, and $0 < \delta_1$ $(= A\sqrt{c/\nu})$ and $0 > \delta_2$ $(= Bc/\nu)$ are the first order slip and second order slip parameters, respectively.

Table 1: Thermophysical properties of the base fluid and nanoparticles [27].

Physical properties	Fluid phase (water)	Ag	Cu	TiO_2	Al_2O_3	SiO_2
C_p (J/kg K)	4179	235	385	686.2	765	765
ρ (kg/m^3)	997.1	10500	8933	4250	3970	3970
k (W/m K)	0.613	429	401	8.9538	40	36

2.5. The Quantities of Practical Interest. In this type of study, it should be noted that the quantities of practical interest are the skin friction coefficient C_f and local Nusselt number Nu, which are defined as

$$C_f = \frac{\tau_w}{\rho_f U_w^2}, \qquad \mathrm{Nu} = \frac{x q_w}{k_f (T_w - T_\infty)}, \tag{12}$$

where τ_w and q_w are the skin friction, or the shear stress, and heat flux from the surface, respectively, which are given by

$$\tau_w = -\mu_{nf}\left(\frac{\partial u}{\partial y}\right)_{y=0}, \qquad q_w = -k_{nf}\left(\frac{\partial T}{\partial y}\right)_{y=0}. \tag{13}$$

Therefore, on using (7) and (8) in (12) and (13), the reduced skin friction coefficient and reduced Nusselt number [22, 31] are

$$\begin{aligned} C_f (\mathrm{Re}_x)^{1/2} &= \frac{1}{(1-\phi)^{2.5}} f''(0), \\ \mathrm{Nu}(\mathrm{Re}_x)^{-1/2} &= -\frac{k_{nf}}{k_f}\theta'(0), \end{aligned} \tag{14}$$

where $\mathrm{Re}_x = cx^2/\nu$ is the local Reynolds number based on the stretching velocity.

3. Exact Solution

Equations (2) and (3) can be rewritten as

$$\lambda f''' + f f'' - f'^2 = 0, \tag{15}$$

$$\tau\theta'' + f\theta' = 0, \tag{16}$$

where

$$\lambda = \frac{(1-\phi)^{-2.5}}{1 - \phi + \phi\left(\rho_s/\rho_f\right)},$$

$$\tau = \frac{\left(\left(k_s + 2k_f\right) - 2\phi\left(k_f - k_s\right)\right)/\left(\left(k_s + 2k_f\right) + \phi\left(k_f - k_s\right)\right)}{Pr\left(1 - \phi + \phi\left(\left(\rho C_p\right)_s/\left(\rho C_p\right)_f\right)\right)}, \tag{17}$$

which is exactly solved, subject to the boundary conditions (11) in the next sections.

3.1. Exact Solution of the Flow: $f(\eta)$. Following the spirit analysis as introduced by Wang [32] and, Aly and Ebaid [33, 34], the exact solution of f equation can be deduced as follows:

$$f(\eta) = a + be^{-\beta\eta}, \quad \text{where } a = \lambda\beta,\ b = s - a, \tag{18}$$

which satisfies (15) and the first condition in (11). Further, from the second condition in (11), the parameter β satisfies algebraic equations for three models discussed in the next three subsections.

3.1.1. No Slips: δ_1=δ_2=0. When there is no slip between the base fluid and nanoparticles, that is, $\delta_1 = \delta_2 = 0$, then β satisfies the following second degree algebraic equation:

$$\lambda\beta^2 - s\beta - 1 = 0 \Longrightarrow \beta = \frac{s \pm \sqrt{s^2 + 4\lambda}}{2\lambda}. \tag{19}$$

This expressions is more easier than those given in [17–19, 23].

3.1.2. Effect of the First Slip Only: δ_2=0. If the first order slip is only to be considered, then β has to achieve the following third degree algebraic equation:

$$\delta_1\lambda\beta^3 + (\lambda - \delta_1 s)\beta^2 - s\beta - 1 = 0. \tag{20}$$

By solving (20) and taking into account Descartes' rule of signs and from the fact that $\delta_1 > 0$ and $\lambda > 0$, there is only one positive root; see Van Gorder et al. [35].

3.1.3. Effect of the Second Slip: $\delta_1 \neq 0$, $\delta_2 \neq 0$. In this case, β satisfies the following fourth degree algebraic equation:

$$\delta_2\lambda\beta^4 - (\delta_1\lambda + \delta_2 s)\beta^3 + (\delta_1 s - \lambda)\beta^2 + s\beta + 1 = 0. \tag{21}$$

Following the analysis in [19], the corresponding four roots of (21) are given by

$$\beta = \begin{cases} \dfrac{1}{4\delta_2\lambda}\left[\delta_1 + \delta_2\lambda\left(s \mp \sqrt{12\beta_3 - \dfrac{\beta_4}{\sqrt{\beta_6}} - 4\beta_6}\right) - 2\delta_2\lambda\sqrt{\beta_6}\right], \\ \dfrac{1}{4\delta_2\lambda}\left[\delta_1 + \delta_2\lambda\left(s \mp \sqrt{12\beta_3 + \dfrac{\beta_4}{\sqrt{\beta_6}} - 4\beta_6}\right) + 2\delta_2\lambda\sqrt{\beta_6}\right], \end{cases} \tag{22}$$

with the following dummy variables:

$$\beta_1 = 27s^2\delta_2\lambda - 72\delta_2\lambda(\delta_1 s - \lambda) + 2(\delta_1 s - \lambda)^3 + 9s(\delta_1 s - \lambda)(\delta_1\lambda + \delta_2 s) + 27(\delta_1\lambda + \delta_2 s)^2,$$

$$\beta_2 = \frac{\sqrt[3]{2}}{3\delta_2\lambda}\left[12\delta_2\lambda + (\delta_1 s - \lambda)^2 + 3s(\delta_1\lambda + \delta_2 s)\right],$$

$$\beta_3 = -\frac{2(\delta_1 s - \lambda)}{3\delta_2\lambda} + \frac{(\delta_1\lambda + \delta_2 s)^2}{4\delta_2^2\lambda^2},$$

$$\beta_4 = -\frac{8s}{\delta_2\lambda} + \frac{4(\delta_1 s - \lambda)(-\delta_1\lambda - \delta_2 s)}{\delta_2^2\lambda^2} - \frac{(-\delta_1\lambda - \delta_2 s)^3}{\delta_2^3\lambda^3},$$

$$\beta_5 = \beta_1 + \sqrt{\beta_1^2 - 54\delta_2^2\lambda^2\beta_2^2},$$

$$\beta_6 = \beta_3 + \frac{\beta_2}{\sqrt[3]{\beta_5}} + \frac{\sqrt[3]{\beta_5}}{\sqrt[3]{32}\delta_2\lambda}. \tag{23}$$

3.1.4. Important Note. Solutions exist for all values of s (suction and injection), $\delta_1 \geq 0$ (first slip), and $\delta_2 \leq 0$ (second slip). It should be noted that any number of decimal places can be therefore obtained in a direct way on applying any software package, like Mathematica, Maple, or Matlab. Mathematica 6 has been used in the current analysis, where the positive root of (19), (20), and (21) gives the physically meaningful and therefore this is only the root to be considered. In addition, Turkyilmazoglu [19] has recently proved that there exists a unique solution for any combination of the considered parameters if the stretching sheet is considered (which was also spotted in [17]). Therefore, on obtaining the roots, skin friction coefficient of the physical significance is easily given by

$$f''(0) = \beta^2(s - \lambda\beta). \tag{24}$$

In an indirect and difficult analysis, this was the same result obtained by Fang et al. [18] and Nandeppanavar et al. [17], in the special case when $\lambda = 1$ (i.e., when $\phi = 0$).

3.2. Exact Solution of the Heat Transfer: $\theta(\eta)$. Substituting (18) into (16), we obtain

$$\frac{\theta''}{\theta'} = -\frac{1}{\tau}\left(a + be^{-\beta\eta}\right); \tag{25}$$

then by the integration of this equation, we get

$$\theta'(\eta) = \theta'(0)\exp\left[-\frac{b}{\tau\beta}\left(1 - e^{-\beta\eta}\right) - \frac{a}{\tau}\eta\right]. \tag{26}$$

Further, on integrating the last equation again, we obtain

$$\theta(\eta) = 1 + \theta'(0)e^{-(b/\tau\beta)}\Omega(\eta), \tag{27}$$

where $\theta(0) = 1$, and

$$\Omega(\eta) = \int_0^\eta e^{-(a/\tau)\sigma} \times e^{(b/\tau\beta)e^{-\beta\sigma}}\, d\sigma. \tag{28}$$

On supposing that

$$z = -\frac{b}{\tau\beta}e^{-\beta\sigma}, \tag{29}$$

then (28) becomes

$$\Omega = \frac{1}{\beta}\left(-\frac{\tau\beta}{b}\right)^{a/\tau\beta}\int_{(-b/\tau\beta)e^{-\tau\beta}}^{-b/\tau\beta} z^{(a/\tau\beta)-1}e^{-z}\, dz. \tag{30}$$

On substituting (30) into (27), taking into account the definition of Γ function, we obtain

$$\theta(\eta) = 1 + \theta'(0)e^{-b/\tau\beta}\frac{1}{\beta}\left(-\frac{\tau\beta}{b}\right)^{a/\tau\beta}\Gamma\left(\frac{a}{\tau\beta}, \frac{-b}{\tau\beta}e^{-\tau\beta}, \frac{-b}{\tau\beta}\right). \tag{31}$$

Applying the condition $\theta(\infty) = 0$, we get

$$\theta'(0)e^{-b/\tau\beta}\frac{1}{\beta}\left(-\frac{\tau\beta}{b}\right)^{a/\tau\beta} = \frac{-1}{\Gamma(a/\tau\beta, 0, -b/\tau\beta)}. \tag{32}$$

Hence with the help of Γ properties, (31) is given in the final exact form as

$$\theta(\eta) = \frac{\Gamma\left(\lambda/\tau, 0, \left((\lambda\beta - s)/\tau\beta\right)e^{-\beta\eta}\right)}{\Gamma\left(\lambda/\tau, 0, (\lambda\beta - s)/\tau\beta\right)}, \tag{33}$$

where Γ here is the generalized incomplete gamma function, and λ, τ, and β are well defined in (17) and (19), respectively. It should be noted here that $\theta'(0)$, which is the importance term as mentioned in Section 2, can be easily formulated from (32) and also by differentiating (33), as

$$\theta'(0) = -\frac{\beta e^{((s-\lambda\beta)/\tau\beta)}\left((\lambda\beta - s)/\tau\beta\right)^{(\lambda/\tau)}}{\Gamma\left((\lambda/\tau), 0, (\lambda\beta - s)/\tau\beta\right)}. \tag{34}$$

4. Results and Discussion

In this paper, the flow and heat equations of nanofluids over an isothermal stretching sheet with effect of the slip model were analytically solved. Exact solutions were obtained for stream function, in the presence of first order and second order slips, and temperature, in a direct and very effective way using gamma function. In addition, five metallic and nonmetallic nanoparticles have been considered in this analysis, namely, Silver (Ag), Copper (Cu), Alumina (Al_2O_3), Titania (TiO_2), and Silicon Dioxide (SiO_2). Comparison with the published results via four tables was presented considering the no-slip model. The two types of slip model are then considered; these cases are to be discussed in the next sections with the effect of the various physical parameters, where the Prandtl number of the base fluid (water) is kept at 6.2.

4.1. Case 1: When $\delta_1 = \delta_2 = 0$. In the case of $\delta_1 = \delta_2 = 0$, that is, no-slip model effects, (24) and (32) with (19) have been programmed. The results of $-f''(0)$ and $-\theta'(0)$ for variation of Pr, different nanoparticles, and Ag-water nanoparticles are compared with Hamad [22], Wang [25],

Table 2: Comparison of results for $-\theta'(0)$ when $\phi = 0$, $s = 0$, and $\delta_1 = \delta_2 = 0$.

	$-\theta'(0)$			
Pr	Present results	Hamad [22]	Wang [25]	Reddy Gorla and Sidawi [26]
0.07	0.0655625	0.06556	0.0656	0.0656
0.02	0.1690886	0.16909	0.1691	0.1691
0.70	0.4539162	0.45391	0.4539	0.4539
2.00	0.9113577	0.91136	0.9114	0.9114
7.00	1.8954033	1.89540	1.8954	1.8905
20.0	3.3539041	3.35390	3.3539	3.3539
70.0	6.4621995	6.46220	6.4622	6.4622

Table 3: Comparison between the results of $-f''(0)$ and $-\theta'(0)$ for different nanoparticles when Pr = 6.2, $s = 0$, and $\delta_1 = \delta_2 = 0$.

ϕ	Cu-water		Ag-water		Al_2O_3-water		TiO_2-water	
	Present results	Hamad [22]	Present results	Hamad [22]	Present results	Hamad [22]	Present results	Hamad [22]
				$-f''(0)$				
0.05	1.1089199	1.10892	1.1396597	1.13966	1.0053774	1.00538	1.0115012	1.01150
0.10	1.1747460	1.17475	1.2250681	1.22507	0.9987720	0.99877	1.0095168	1.00952
0.15	1.2088623	1.20886	1.2721529	1.27215	0.9818445	0.98185	0.9960305	0.99603
0.20	1.2180438	1.21804	1.2897880	1.28979	0.9559188	0.95592	0.9725895	0.97259
				$-\theta'(0)$				
0.05	1.5989923	1.59899	1.5813558	1.58136	1.6224626	1.62246	1.6379138	1.63791
0.10	1.4520723	1.45207	1.4205773	1.42058	1.4916979	1.49170	1.5195895	1.51959
0.15	1.3246459	1.32465	1.2819255	1.28193	1.3754278	1.37543	1.4135927	1.41359
0.20	1.2128974	1.21290	1.1609900	1.16100	1.2711811	1.27118	1.3180499	1.31805

Table 4: Comparison between the results of $-f''(0)$ and $-\theta'(0)$ for Ag-water nanoparticles when Pr = 6.2 and $\delta_1 = \delta_2 = 0$.

ϕ	$s = -0.5$		$s = 0.5$		$s = 3$		$s = 10$	
	Present results	Noghrehabadi et al. [23]	Present results	Noghrehabadi et al. [23]	Present results	Noghrehabadi et al. [23]	Present results	Noghrehabadi et al. [23]
					$-f''(0)$			
0.00	0.7807764	0.78078	1.2807764	1.28078	3.3027756	3.30278	10.099020	10.09902
0.05	0.8603080	0.86031	1.5097201	1.50972	4.2053250	4.20532	13.087484	13.08748
0.10	0.9060379	0.90604	1.6564339	1.65643	4.8141236	4.81412	15.107262	15.10726
0.15	0.9303482	0.93035	1.7395348	1.73953	5.1682565	5.16826	16.283121	16.28312
0.20	0.9392930	0.93929	1.7710695	1.77107	5.3042838	5.30428	16.734937	16.73494
					$-\theta'(0)$			
0.00	0.3341463	0.33415	4.1338760	4.13375	18.877000	18.87699	62.085783	62.08581
0.05	0.3374948	0.33750	3.5686858	3.56861	16.003319	16.00329	52.565657	52.56564
0.10	0.3412474	0.34125	3.0990601	3.00902	13.637179	13.63716	44.731160	44.73115
0.15	0.3441451	0.34415	2.7036778	2.70365	11.662391	11.66238	38.194788	38.19476
0.20	0.3458192	0.34582	2.3673248	2.36732	9.995764	9.99572	32.679360	32.67934

Reddy Gorla and Sidawi [26], and Noghrehabadi et al. [23] in Tables 2, 3, and 4, respectively. These tables indicate an excellent agreement between the present exact solutions and the previous results but in a simple and direct analysis rather than the long analytical presentation in [22] and even the difficult combination of a symbolic power series and Padé approximation method in [23].

4.2. Case 2: When $\delta_1 \neq 0$ and δ_2=0. Figures 1 and 2 show the effect of the volume friction ϕ of Cu-water and Al_2O_3-water nanoparticles, respectively, on velocity distribution $f'(\eta)$ at different values of s when $Pr = 6.2$ and $\delta_1 = 1$. These figures indicate that the increase in nanoparticle volume friction decreases the velocity magnitude in the case of Cu-water nanofluid; however it increases the velocity magnitude in

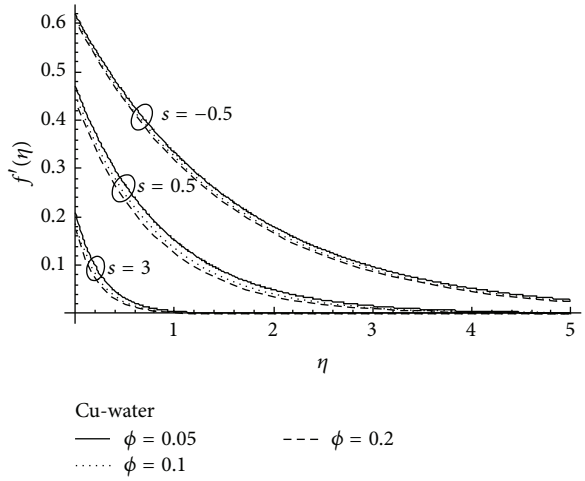

FIGURE 1: Effect of the volume friction ϕ of Cu-water nanoparticles on velocity distribution $f'(\eta)$ at different values of s when $Pr = 6.2$, $\delta_1 = 1$, and $\delta_2 = 0$.

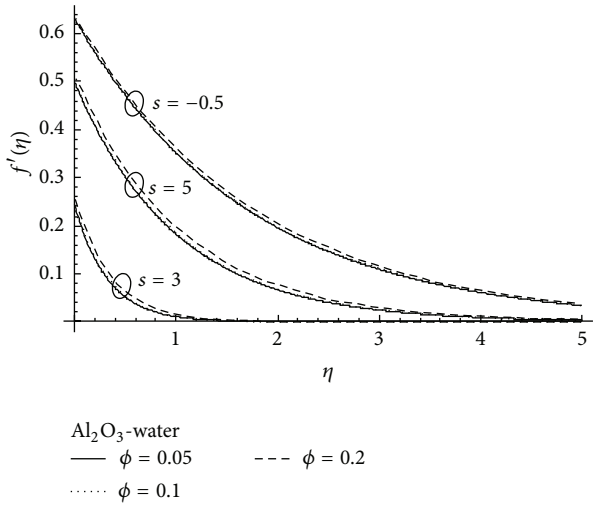

FIGURE 2: Effect of the volume friction ϕ of Al_2O_3-water nanoparticles on velocity distribution $f'(\eta)$ at different values of s when $Pr = 6.2$, $\delta_1 = 1$, and $\delta_2 = 0$.

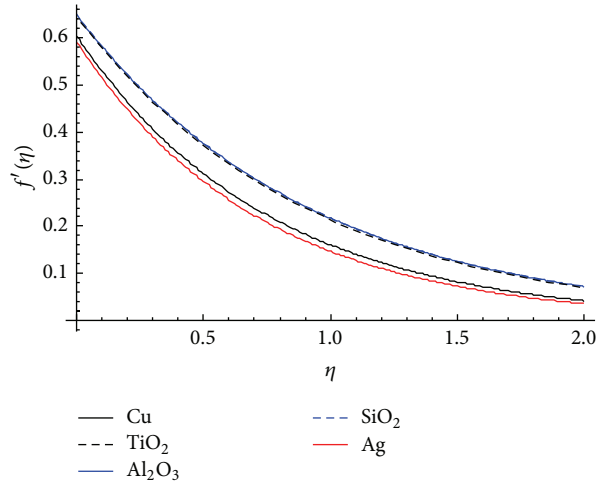

FIGURE 3: Comparing the variation of velocity distribution $f'(\eta)$ for the investigated nanoparticles when $Pr = 6.2$, $\delta_1 = 0.5$, $\delta_2 = 0$, $s = 0.5$, and $\phi = 0.1$.

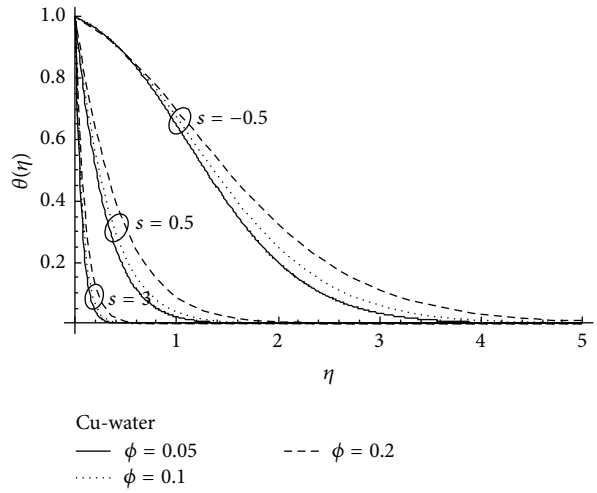

FIGURE 4: Effect of the volume friction ϕ of Cu-water nanoparticles on temperature distribution $\theta(\eta)$ at different values of s when $Pr = 6.2$, $\delta_1 = 1$, and $\delta_2 = 0$.

the case of Al_2O_3-water nanofluid. The difference between their behaviour is because of the difference between density ratios of the proposed nanoparticles to the density of water, which affects the momentum equation. Further, in both cases of Cu-water and Al_2O_3-water nanofluids, the increase in s decreases the magnitude of $f'(\eta)$ and hydrodynamic boundary layer. It should be mentioned here that the other nanoparticles have been also examined and it was found that Ag-water nanofluid behaves like Cu-water nanofluid, while TiO_2-water and SiO_2-water nanofluids behave as Al_2O_3-water nanofluid. However, the velocity distribution $f'(\eta)$ of these nanoparticles is as follows: $f'|_{Ag} < f'|_{Cu} < f'|_{TiO_2} < f'|_{Al_2O_3} \cong f'|_{SiO_2}$. This is presented in Figure 3, which shows a comparison of the variation of the velocity profiles for all the studied nanoparticles at specific values of the physical parameters.

The effect of the volume friction ϕ of Cu-water nanoparticles on temperature distribution $\theta(\eta)$ at different values of s when $Pr = 6.2$ and $\delta_1 = 1$ is plotted in Figure 4. This figure indicates that the increase in ϕ increases $\theta(\eta)$ and hence the thermal boundary-layer thickness. This result is compatible with those obtained very recently by Vajravelu et al. [24] and also agrees with the physical behaviour as addition of ϕ increases the thermal conductivity of the pure fluid and this results in increasing the thermal diffusion in the boundary layer. Further, increase in s decreases $\theta(\eta)$ as well as the thermal boundary-layer thickness. All of the other investigated nanoparticles behave like Cu-water nanofluid with $\theta|_{Ag} > \theta|_{Cu} > \theta|_{Al_2O_3} \cong \theta|_{SiO_2} > \theta|_{TiO_2}$, as illustrated

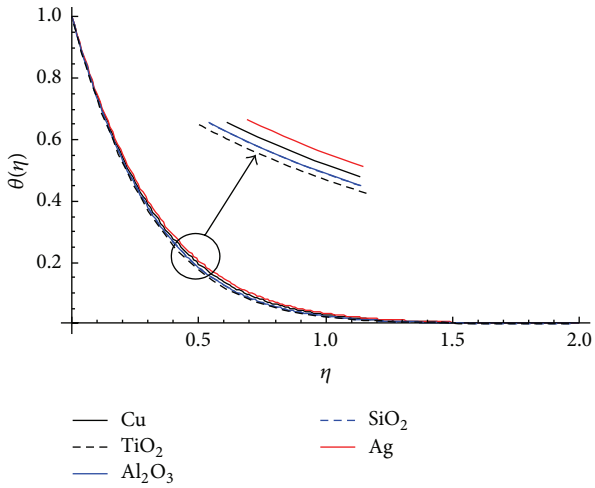

FIGURE 5: Comparing the variation of temperature distribution $\theta(\eta)$ for the investigated nanoparticles when $Pr = 6.2$, $\delta_1 = 0.5$, $\delta_2 = 0$, $s = 0.5$, and $\phi = 0.1$.

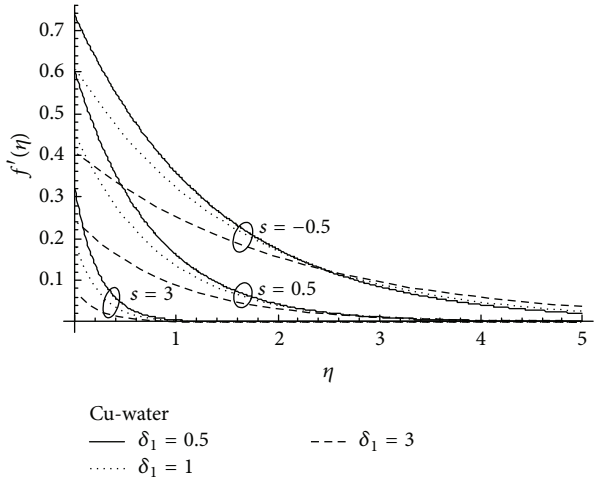

FIGURE 6: Effect of the first slip δ_1 on velocity distribution $f'(\eta)$ at different values of s for Cu-water nanoparticles when $Pr = 6.2$, $\phi = 0.1$, and $\delta_2 = 0$.

in Figure 5, which presents a comparison of the variation of temperature distribution for all the studied nanoparticles at specific values of the physical parameters.

Figures 6 and 7 present the effect of the first slip δ_1 on the velocity f' and temperature θ distributions at different values of s for Cu-water nanoparticles when $Pr = 6.2$, and $\phi = 0.1$, respectively. Figure 6 shows that the increase in δ_1 significantly decreases the velocity near $\eta = 0$ and then slightly increases it as $\eta \to \eta_\infty$. However, the increase in δ_1 increases significantly the temperature and thermal boundary-layer thickness in the injection case, that is, when $s < 0$, with a little increasing in the suction case when $s > 0$, and no effect when $s \gg 1$. From these figures, one can also notice that increase in s decreases $f'(\eta)$ and $\theta(\eta)$, as well as the hydrodynamic and thermal boundary-layer thickness, respectively. This means that, although the increase in the first

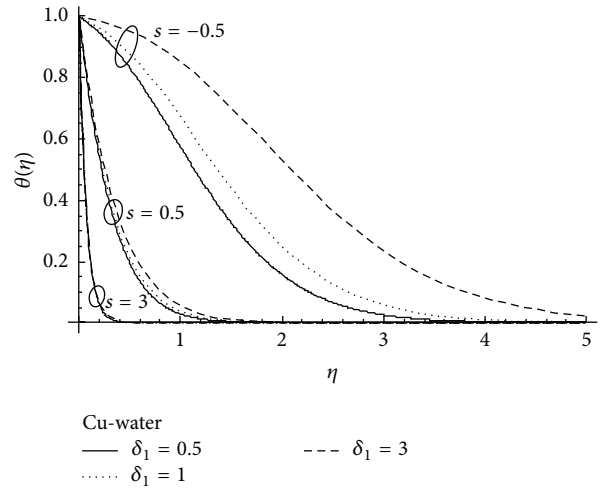

FIGURE 7: Effect of the first slip δ_1 on temperature distribution $\theta(\eta)$ at different values of s for Cu-water nanoparticles when $Pr = 6.2$, $\phi = 0.1$, and $\delta_2 = 0$.

slip slows down the velocity, it increases the temperature with impressive effect in the injection case.

The most important parameters of hydrodynamic and thermal boundary layer, namely, reduced skin friction coefficient and reduced Nusselt number, have been indicated in Figures 8–11. In particular, Figures 8 and 9 present the effect of the first slip δ_1 and s, respectively, for reduced skin friction coefficient as a function of $0 \le \phi \le 0.2$ for Cu-water nanofluid, as a representative for the behaviour of all investigated nanoparticles, when $Pr = 6.2$ and $s = 0.5$, while Figures 10 and 11 show also the effect of δ_1 and s on reduced Nusselt number at the same specific values. Figures 8 and 9 show that increase in δ_1 and s decreases and increases, respectively, the local skin friction. With significant effects, the same result is also observed in Figures 10 and 11 for the reduced Nusselt number.

Comparison of the variation of reduced skin friction coefficient and reduced Nusselt number for the studied nanoparticles, at selected values of the physical parameters, is plotted in Figures 12 and 13. These figures show that the reduced skin friction coefficient (RSFC) of these nanoparticles is as follows: $\text{RSFC}|_{\text{Ag}} > \text{RSFC}|_{\text{Cu}} > \text{RSFC}|_{\text{TiO}_2} > \text{RSFC}|_{\text{Al}_2\text{O}_3} \cong \text{RSFC}|_{\text{SiO}_2}$. However, vise versa behaviour is noticed in Figure 13. The difference between these types of nanoparticles is because the difference between their densities. Observing Table 1 and (15)–(17), as the nanoparticle becomes heavy, this results in increase and decrease in reduced skin friction coefficient and reduced Nusselt number, respectively.

4.3. Case 3: When $\delta_1 \neq 0$, and $\delta_2 \neq 0$. In the presence of second order slip, as shown in Figures 14, 15, 16, and 17, behaviour of the velocity and temperature is similar to those in 1, 3, 4, and 5, respectively. However, for Ag-water and Cu-water nanoparticles, a decreasing difference is noticed on comparing Figures 15 and 3. This means that the second slip affects significantly the heaviest nanoparticles. Figures 18 and

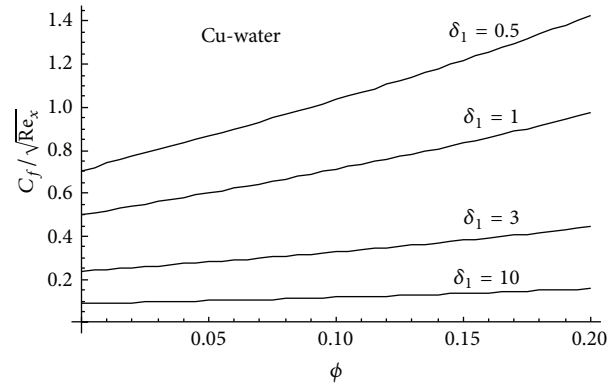

Figure 8: Effect of the first slip δ_1 on reduced skin friction coefficient as a function of $0 \le \phi \le 0.2$ for Cu-water nanoparticles when $Pr = 6.2$, $s = 0.5$, and $\delta_2 = 0$.

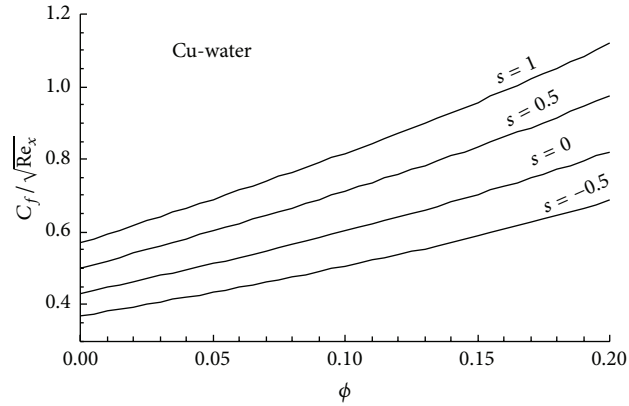

Figure 9: Effect of s on reduced skin friction coefficient as a function of $0 \le \phi \le 0.2$ for Cu-water nanoparticles when $Pr = 6.2$, $\delta_1 = 1$, and $\delta_2 = 0$.

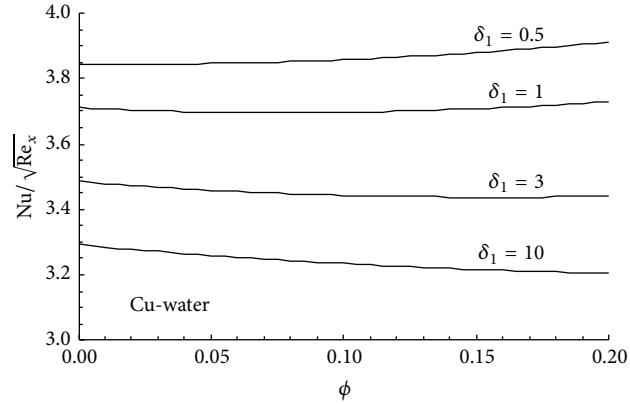

Figure 10: Effect of the first slip δ_1 on reduced Nusselt number as a function of $0 \le \phi \le 0.2$ for Cu-water nanoparticles when $Pr = 6.2$, $s = 0.5$, and $\delta_2 = 0$.

19 compare the variation of reduced skin friction coefficient and reduced Nusselt number, respectively, for the studied nanoparticles, at selected values of the physical parameters. These figures show that the RSFC of these nanoparticles is as follows: $\mathrm{RSFC}|_{\mathrm{Ag}} < \mathrm{RSFC}|_{\mathrm{Cu}} < \mathrm{RSFC}|_{\mathrm{TiO_2}} < \mathrm{RSFC}|_{\mathrm{Al_2O_3}} \cong \mathrm{RSFC}|_{\mathrm{SiO_2}}$. This is vise versa behaviour comparing with Figure 12 with significant change in the Ag-water and Cu-water nanoparticles, as stated before. Although the same behaviour is observed in Figures 13 and 19, the nanoparticles with highest density are more affected in the presence of the second slip. The results of this section demonstrate clearly that the second order slip flow model is necessary to predict

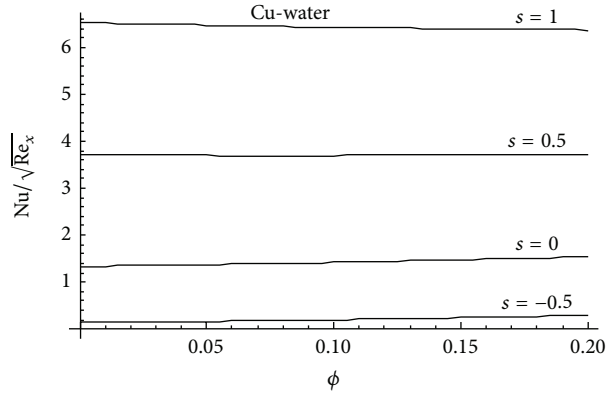

Figure 11: Effect of s on reduced Nusselt number as a function of $0 \le \phi \le 0.2$ for Cu nanoparticles when $Pr = 6.2$, $\delta_1 = 1$, and $\delta_2 = 0$.

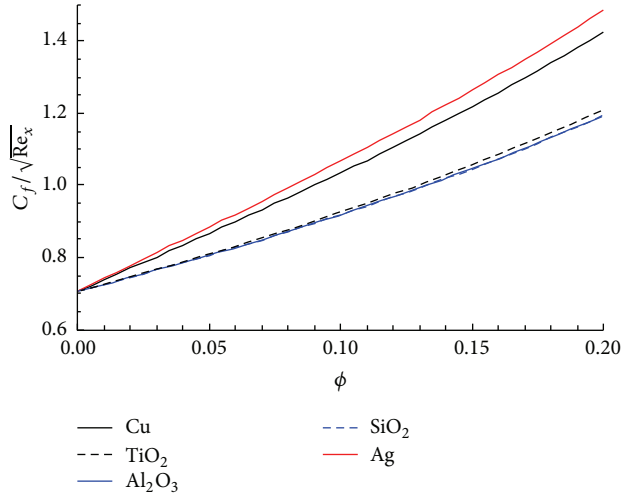

Figure 12: Comparing the variation of reduced skin friction coefficient as a function of $0 \le \phi \le 0.2$ for the investigated nanoparticles $Pr = 6.2$, $\delta_1 = 0.5$, $\delta_2 = 0$, and $s = 0.5$.

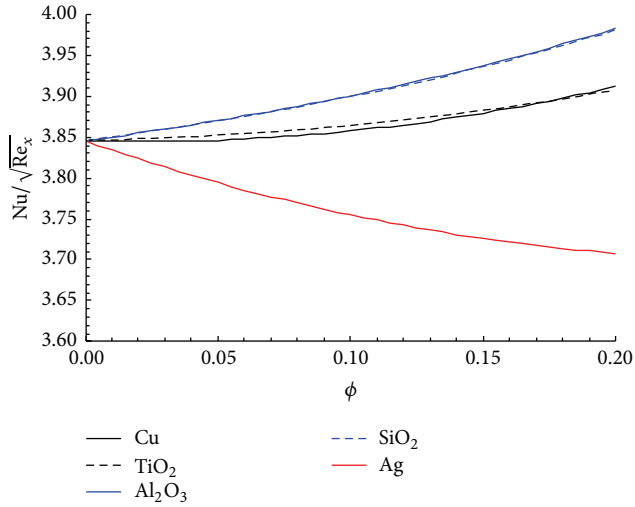

Figure 13: Comparing the variation of reduced Nusselt number as a function of $0 \le \phi \le 0.2$ for the investigated nanoparticles $Pr = 6.2$, $\delta_1 = 0.5$, $\delta_2 = 0$, and $s = 0.5$.

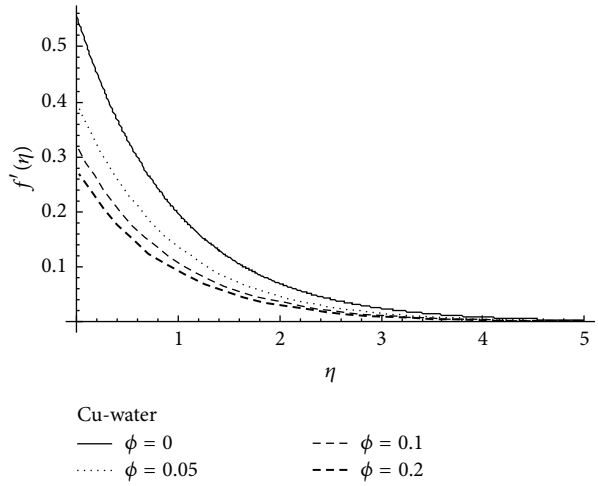

FIGURE 14: Effect of the volume friction ϕ of Cu-water nanoparticles on velocity distribution $f'(\eta)$ when $Pr = 6.2$, $s = 0.5$, $\delta_1 = 1$, and $\delta_2 = -1$.

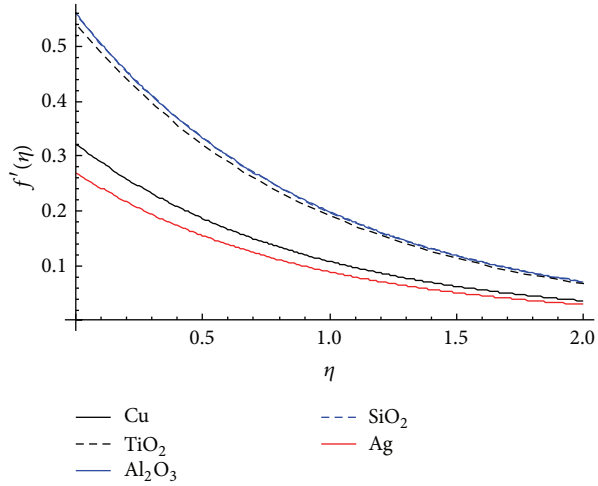

FIGURE 15: Comparing the variation of velocity distribution $f'(\eta)$ for the investigated nanoparticles when $Pr = 6.2$, $\delta_1 = 1$, $\delta_2 = -1$, $s = 0.5$, and $\phi = 0.1$.

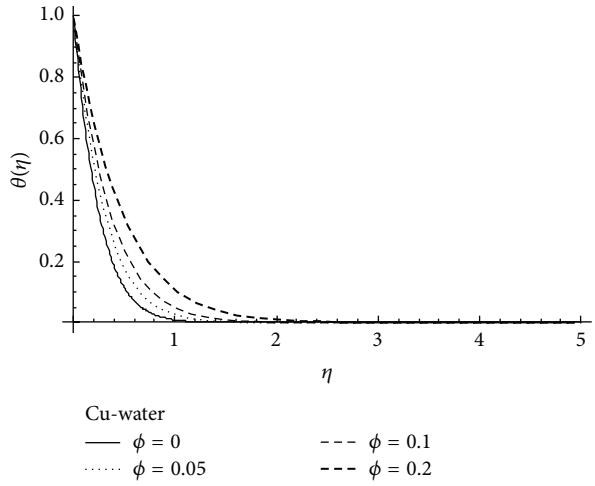

FIGURE 16: Effect of the volume friction ϕ of Cu-water nanoparticles on temperature distribution $\theta(\eta)$ when $Pr = 6.2$, $s = 0.5$, $\delta_1 = 1$, and $\delta_2 = -1$.

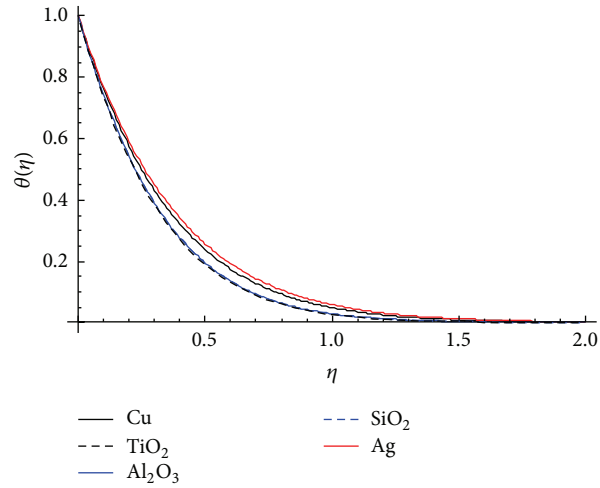

FIGURE 17: Comparing the variation of temperature distribution $\theta(\eta)$ for the investigated nanoparticles when $Pr = 6.2$, $\delta_1 = 1$, $\delta_2 = -1$, $s = 0.5$, and $\phi = 0.1$.

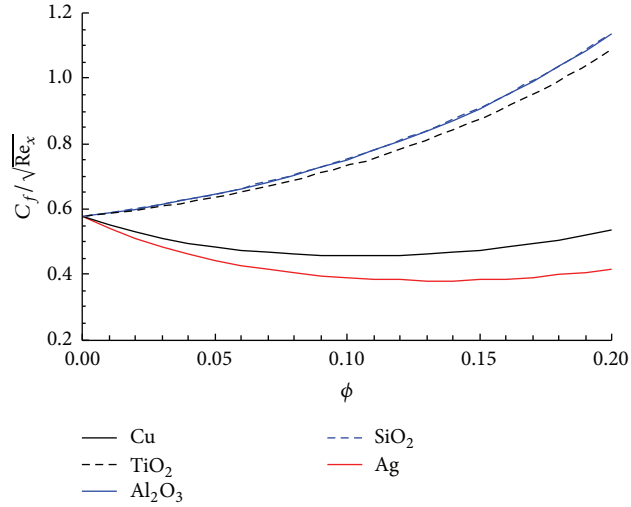

FIGURE 18: Comparing the variation of reduced skin friction coefficient as a function of $0 \le \phi \le 0.2$ for the investigated nanoparticles $Pr = 6.2$, $\delta_1 = 1$, $\delta_2 = -1$, and $s = 0.5$.

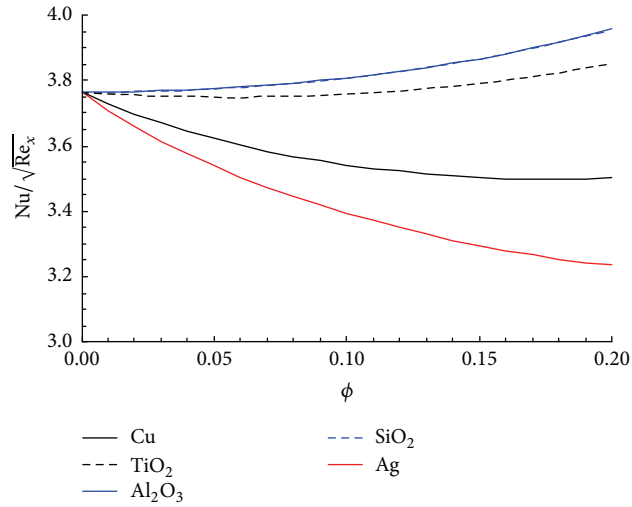

FIGURE 19: Comparing the variation of reduced Nusselt number as a function of $0 \le \phi \le 0.2$ for the investigated nanoparticles $Pr = 6.2$, $\delta_1 = 1$, $\delta_2 = -1$, and $s = 0.5$.

the flow characteristics accurately. This agrees with the result obtained recently by Roşca and Pop [20].

5. Conclusion

The governing equations for nanofluids flow over an isothermal stretching sheet with the effect of the slip model were examined in this paper. In a direct and very effective manner, we analytically obtained the exact solutions for the flow and temperature equations. Further, five nanoparticles were considered and compared in the present analysis. Therefore, the most interesting physical parameters were discussed in the presence of no slip, first order slip, and second order slip, parameters.

With no-slip effect, the present exact solutions are in a very good agreement with the results presented in [22, 23, 25, 26]. Some of the interesting results of applying the slip model are as follows:

(1) increase in the nanoparticle volume friction decreases the velocity of Cu/Ag-water nanoparticles, increases it for $Al_2O_3/TiO_2/SiO_2$-water nanoparticles, and increases the temperature, and hence the thermal boundary-layer thickness, for the whole five investigated nanoparticles;

(2) increase in the wall mass decreases the velocity and temperature, as well as the thermal and hydrodynamic boundary-layer thickness, and increases the local skin friction;

(3) increase in the slips slows down the velocity, increases the temperature with an impressive effect in the injection case, and decreases the local skin friction and the reduced Nusselt number, with significate effects;

(4) as the nanoparticle becomes heavier, this results in increase and decrease in the reduced skin friction coefficient and reduced Nusselt number, respectively;

(5) the second order slip parameter affects considerably the flow characteristics, specially for the heaviest nanoparticles.

The final note is for practical and industrial applications; Silver is the suitable nanoparticle if slowing down the velocity and increasing the temperature are needed; on the other hand, Silicon Dioxide is the appropriate nanoparticle if vise versa behaviour is to be considered.

Conflict of Interests

The authors declare that there is no conflict of interests regarding the publication of this paper.

Acknowledgment

This paper was funded by the Deanship of Scientific Research (DSR), King Abdulaziz University, Jeddah, under grant no. (130-011-D1433). The authors, therefore, acknowledge with thanks DSR technical and financial support.

References

[1] T. Metal, S. Oh, and H. Gegel, *Metal Forming Fundamentals and Applications*, American Society of Metals, Metals Park, Ohio, USA, 1979.

[2] M. V. Karwe and Y. Jaluria, "Numerical simulation of thermal transport associated with a continuously moving flat sheet in materials processing," *Journal of Heat Transfer*, vol. 113, no. 3, pp. 612–619, 1991.

[3] B. C. Sakiadis, "Boundary layer behaviour on continuous solid surfaces—I. Boundary layer equations for two-dimensional and axisymmetric flow," *AIChE Journal*, vol. 7, pp. 26–28, 1961.

[4] B. C. Sakiadis, "Boundary layer behaviour on continuous solid surfaces—II. The boundary layer on a continuous flat surface," *AIChE Journal*, vol. 7, pp. 221–225, 1961.

[5] L. J. Crane, "Flow past a stretching plate," *Zeitschrift für Angewandte Mathematik und Physik*, vol. 21, no. 4, pp. 645–647, 1970.

[6] A. Yoshimura and R. K. Prud'homme, "Wall slip corrections for Couette and parallel disk viscometers," *Journal of Rheology*, vol. 32, no. 1, pp. 53–67, 1988.

[7] M. Gad-el-Hak, "Fluid mechanics of microdevices-the freeman scholar lecture," *Journal of Fluids Engineering, Transactions of the ASME*, vol. 121, no. 1, pp. 5–33, 1999.

[8] X.-Q. Wang and A. S. Mujumdar, "Heat transfer characteristics of nanofluids: a review," *International Journal of Thermal Sciences*, vol. 46, no. 1, pp. 1–19, 2007.

[9] X.-Q. Wang and A. S. Mujumdar, "A review on nanofluids—part II: experiments and applications," *Brazilian Journal of Chemical Engineering*, vol. 25, no. 4, pp. 631–648, 2008.

[10] R. Saidur, K. Y. Leong, and H. A. Mohammad, "A review on applications and challenges of nanofluids," *Renewable and Sustainable Energy Reviews*, vol. 15, no. 3, pp. 1646–1668, 2011.

[11] S. U. S. Choi, "Enhancing thermal conductivity of fluids with nanoparticles," *Developments and Applications of Non-Newtonian Flows*, vol. 66, pp. 99–105, 1995.

[12] J. A. Eastman, S. U. S. Choi, S. Li, W. Yu, and L. J. Thompson, "Anomalously increased effective thermal conductivities of ethylene glycol-based nanofluids containing copper nanoparticles," *Applied Physics Letters*, vol. 78, no. 6, pp. 718–720, 2001.

[13] Y. Xuan and Q. Li, "Investigation on convective heat transfer and flow features of nanofluids," *Journal of Heat Transfer*, vol. 125, no. 1, pp. 151–155, 2003.

[14] M. Majumder, N. Chopra, R. Andrews, and B. J. Hinds, "Nanoscale hydrodynamics: enhanced flow in carbon nanotubes," *Nature*, vol. 438, no. 7064, article 44, 2005.

[15] A. Noghrehabadi, R. Pourrajab, and M. Ghalambaz, "Effect of partial slip boundary condition on the flow and heat transfer of nanofluids past stretching sheet prescribed constant wall temperature," *International Journal of Thermal Sciences*, vol. 54, pp. 253–261, 2012.

[16] W. A. Khan and I. Pop, "Boundary-layer flow of a nanofluid past a stretching sheet," *International Journal of Heat and Mass Transfer*, vol. 53, no. 11-12, pp. 2477–2483, 2010.

[17] M. M. Nandeppanavar, K. Vajravelu, M. S. Abel, and M. N. Siddalingappa, "Second order slip flow and heat transfer over a stretching sheet with non-linear Navier boundary condition," *International Journal of Thermal Sciences*, vol. 58, pp. 143–150, 2012.

[18] T. Fang, S. Yao, J. Zhang, and A. Aziz, "Viscous flow over a shrinking sheet with a second order slip flow model," *Communications in Nonlinear Science and Numerical Simulation*, vol. 15, no. 7, pp. 1831–1842, 2010.

[19] M. Turkyilmazoglu, "Heat and mass transfer of MHD second order slip flow," *Computers & Fluids*, vol. 71, pp. 426–434, 2013.

[20] A. V. Roşca and I. Pop, "Flow and heat transfer over a vertical permeable stretching/shrinking sheet with a second order slip," *International Journal of Heat and Mass Transfer*, vol. 60, pp. 355–364, 2013.

[21] N. A. Yacob, A. Ishak, I. Pop, and K. Vajravelu, "Boundary layer flow past a stretching/shrinking surface beneath an external uniform shear flow with a convective surface boundary condition in a nanofluid," *Nanoscale Research Letters*, vol. 6, pp. 314–321, 2011.

[22] M. A. A. Hamad, "Analytical solution of natural convection flow of a nanofluid over a linearly stretching sheet in the presence of magnetic field," *International Communications in Heat and Mass Transfer*, vol. 38, no. 4, pp. 487–492, 2011.

[23] A. Noghrehabadi, M. Ghalambaz, M. Ghalambaz, and A. Ghanbarzadeh, "Comparing thermal enhancement of Ag-water and SiO_2-water nanofluids over an isothermal stretching sheet with suction or injection," *Journal of Computational and Applied Research in Mechanical Engineering*, vol. 2, pp. 35–47, 2012.

[24] K. Vajravelu, K. V. Prasad, and C.-O. Ng, "The effect of variable viscosity on the flow and heat transfer of a viscous Ag-water and Cu-water nanofluids," *Journal of Hydrodynamics*, vol. 25, pp. 1–9, 2013.

[25] C. Y. Wang, "Free convection on a vertical stretching surface," *Journal of Applied Mathematics and Mechanics*, vol. 69, pp. 418–420, 1989.

[26] R. S. Reddy Gorla and I. Sidawi, "Free convection on a vertical stretching surface with suction and blowing," *Applied Scientific Research*, vol. 52, no. 3, pp. 247–257, 1994.

[27] H. F. Oztop and E. Abu-Nada, "Numerical study of natural convection in partially heated rectangular enclosures filled with nanofluids," *International Journal of Heat and Fluid Flow*, vol. 29, no. 5, pp. 1326–1336, 2008.

[28] K. Khanafer, K. Vafai, and M. Lightstone, "Buoyancy-driven heat transfer enhancement in a two-dimensional enclosure utilizing nanofluids," *International Journal of Heat and Mass Transfer*, vol. 46, no. 19, pp. 3639–3653, 2003.

[29] K. Khanafer and K. Vafai, "A critical synthesis of thermophysical characteristics of nanofluids," *International Journal of Heat and Mass Transfer*, vol. 54, no. 19-20, pp. 4410–4428, 2011.

[30] L. Wu, "A slip model for rarefied gas flows at arbitrary Knudsen number," *Applied Physics Letters*, vol. 93, no. 25, Article ID 253103, 2008.

[31] K. Vajravelu, K. V. Prasad, J. Lee, C. Lee, I. Pop, and R. A. Van Gorder, "Convective heat transfer in the flow of viscous Ag-water and Cu-water nanofluids over a stretching surface," *International Journal of Thermal Sciences*, vol. 50, no. 5, pp. 843–851, 2011.

[32] C. Y. Wang, "Analysis of viscous flow due to a stretching sheet with surface slip and suction," *Nonlinear Analysis. Real World Applications*, vol. 10, no. 1, pp. 375–380, 2009.

[33] E. H. Aly and A. Ebaid, "On the exact analytical and numerical solutions of nano boundary-layer fluid flows," *Abstract and Applied Analysis*, vol. 2012, Article ID 415431, 22 pages, 2012.

[34] E. H. Aly and A. Ebaid, "New exact solutions for boundary-layer flow of a nanofluid past a stretching sheet," *Journal of Computational and Theoretical Nanoscience*, vol. 10, pp. 2591–2595, 2013.

[35] R. A. Van Gorder, E. Sweet, and K. Vajravelu, "Nano boundary layers over stretching surfaces," *Communications in Nonlinear Science and Numerical Simulation*, vol. 15, no. 6, pp. 1494–1500, 2010.

Hindawi Publishing Corporation
Abstract and Applied Analysis
Volume 2013, Article ID 350647, 9 pages
http://dx.doi.org/10.1155/2013/350647

Research Article

The Flow and Heat Transfer of a Nanofluid Past a Stretching/Shrinking Sheet with a Convective Boundary Condition

Syahira Mansur[1] and Anuar Ishak[2]

[1] *Department of Mathematics and Statistics, Faculty of Science, Technology and Human Development, Universiti Tun Hussein Onn Malaysia, Batu Pahat, 86400 Parit Raja, Johor, Malaysia*
[2] *School of Mathematical Sciences, Faculty of Science and Technology, Universiti Kebangsaan Malaysia (UKM), 43600 Bangi, Selangor, Malaysia*

Correspondence should be addressed to Anuar Ishak; anuarishak@yahoo.com

Received 26 June 2013; Revised 2 September 2013; Accepted 3 September 2013

Academic Editor: Jianzhong Lin

The boundary layer flow of a nanofluid past a stretching/shrinking sheet with a convective boundary condition is studied. Numerical solutions to the governing equations are obtained using a shooting method. The results are found for the local Nusselt number and the local Sherwood number as well as the temperature and concentration profiles for some values of the convective parameter, stretching/shrinking parameter, Brownian motion parameter, and thermophoresis parameter. The results indicate that the local Nusselt number is consistently higher for higher values of the convective parameter. However, the local Nusselt number decreases with increasing values of the Brownian motion parameter as well as the thermophoresis parameter. In addition, the local Sherwood number increases with increasing Brownian motion parameter and decreases with increasing convective parameter and thermophoresis parameter.

1. Introduction

The boundary layer flow over a stretching sheet is important in applications such as extrusion, wire drawing, metal spinning, and hot rolling [1]. Crane [2] pioneered the study of stretching sheet by presenting an exact analytical solution for the steady two-dimensional stretching of a plate in a quiescent fluid. Since then, many authors have considered various aspects of this problem. Wang [3] extended Crane's study to include both suction and slip effects at the boundary. Sahoo [4] considered non-Newtonian fluid in his research.

Recently, the study on the flow over a shrinking sheet has garnered considerable attention. Miklavčič and Wang [5] initiated the study of flow over a shrinking sheet. They found that the vorticity is not confined within a boundary layer, and a steady flow cannot exist without exerting adequate suction at the boundary. Ever since, numerous studies emerge, investigating different aspects of this problem. Fang et al. [6] used a second-order slip flow in their research. Bhattacharyya et al. [7] analyzed the effects of partial slip on laminar boundary layer stagnation-point flow and heat transfer towards a shrinking sheet.

Inclusion of nanoparticles into the base fluid such as water is known to increase the heat transfer capability of the fluid. Choi and Eastman [8] discovered that the addition of less than 1% of nanoparticles into the base fluid doubles the heat conductivity of the fluid. Other characteristics of nanofluid include minimal clogging of tube and long term stability as compared to other fluids containing micro- and millimeter sized particles (see [9–13]). Two models have been constantly used by researchers to study the behaviour of nanofluid, namely, the Tiwari-Das model [14] and Buongiorno model [15]. Contrary to the Tiwari-Das model [14] that focuses on volumetric fraction of nanoparticles, Buongiorno model [15] pays more attention to Brownian motion

and thermophoresis effects. Furthermore, instead of focusing on the thermophysical properties of the nanofluid, Buongiorno model shifted the focus to explaining the further heat transfer enhancement observed in convective situations. Buongiorno model was used in many recent papers, for example, Nield and Kuznetsov [16–18], Kuznetsov and Neild [19, 20], Khan and Pop [21], Bachok et al. [22, 23], and Khan and Aziz [24], among others.

In the boundary layer flow and heat transfer analysis, constant surface temperature and heat flux are customarily used. However, there are times when heat transfer at the surface relies on the surface temperature, as what mostly occurs in heat exchangers. In this situation, convective boundary condition is used to replace the condition of prescribed surface temperature or prescribed surface heat flux. Aziz [25] employed the convective boundary condition in his research to study the heat transfer characteristics for the Blasius flow. Ishak [26] introduced the effects of suction and injection at the boundary. Makinde and Aziz [27] investigated the boundary layer flow of a nanofluid past a stretching sheet with a convective surface boundary condition.

Motivated by the above-mentioned investigations and applications, we extend the study of Makinde and Aziz [27] to include both stretching and shrinking cases, in addition to the suction effect. Although there are many studies conducted on the shrinking or stretching sheet, little work has been done to include both the stretching and shrinking cases. For the shrinking case which was not considered by Makinde and Aziz [27], the solutions do not exist since vorticity could not be confined within the boundary layer. However, with an added suction effect to confine the vorticity, the solution may exist. The dependency of the local Nusselt number and the local Sherwood number on four parameters, namely, the stretching/shrinking, convective, Brownian motion, and thermophoresis parameters, is the main focus of the present investigation. Numerical solutions are presented graphically and in tabular forms to show the effects of these parameters on the local Nusselt number and the local Sherwood number.

2. Mathematical Formulation

Consider a steady, two-dimensional (x, y) boundary layer flow of a viscous and incompressible fluid over a stretching/shrinking sheet immersed in a nanofluid. It is assumed that the stretching/shrinking velocity is in the form $U_w = ax$, where a is a positive constant and x is the coordinate measured along the stretching/shrinking surface. It is also assumed that the constant mass flux velocity is v_0 with $v_0 < 0$ for suction and $v_0 > 0$ for injection or withdrawal of the fluid. The nanofluid is confined to $y > 0$, where y is the coordinate measured normal to the stretching/shrinking surface, as shown in Figure 1. It is further assumed that the bottom surface of the sheet is heated by convection from a hot fluid at temperature T_f which provides a heat transfer coefficient h. The surface temperature T_w is the result of a convective heating process characterized by the hot fluid.

The governing equations for the steady conservation of mass, momentum, thermal energy, and nanoparticle volume fraction equations can be written as [15–24]

$$\frac{\partial u}{\partial x} + \frac{\partial v}{\partial y} = 0, \tag{1}$$

$$u\frac{\partial u}{\partial x} + v\frac{\partial u}{\partial y} = -\frac{1}{\rho_f}\frac{\partial P}{\partial x} + \nu\left(\frac{\partial^2 u}{\partial x^2} + \frac{\partial^2 u}{\partial y^2}\right), \tag{2}$$

$$u\frac{\partial v}{\partial x} + v\frac{\partial v}{\partial y} = -\frac{1}{\rho_f}\frac{\partial P}{\partial y} + \nu\left(\frac{\partial^2 v}{\partial x^2} + \frac{\partial^2 v}{\partial y^2}\right), \tag{3}$$

$$\begin{aligned} u\frac{\partial T}{\partial x} + v\frac{\partial T}{\partial y} &= \alpha\left(\frac{\partial^2 T}{\partial x^2} + \frac{\partial^2 T}{\partial y^2}\right) \\ &\quad + \tau\left\{D_B\left(\frac{\partial \varphi}{\partial x}\frac{\partial T}{\partial x} + \frac{\partial \varphi}{\partial y}\frac{\partial T}{\partial y}\right)\right. \\ &\quad \left. + \frac{D_T}{T_\infty}\left[\left(\frac{\partial T}{\partial x}\right)^2 + \left(\frac{\partial T}{\partial y}\right)^2\right]\right\}, \end{aligned} \tag{4}$$

$$u\frac{\partial \varphi}{\partial x} + v\frac{\partial \varphi}{\partial y} = D_B\left(\frac{\partial^2 \varphi}{\partial x^2} + \frac{\partial^2 \varphi}{\partial y^2}\right) + \frac{D_T}{T_\infty}\left(\frac{\partial^2 T}{\partial x^2} + \frac{\partial^2 T}{\partial y^2}\right), \tag{5}$$

where u and v are the velocity components along the x- and y-axis, respectively, P is the fluid pressure, T is the fluid temperature, α is the thermal diffusivity, ν is the kinematic viscosity, D_B is the Brownian diffusion coefficient, D_T is the thermophoresis diffusion coefficient, and φ is the nanoparticle volume fraction. Furthermore, $\tau = (\rho c)_p/(\rho c)_f$ is the ratio between the effective heat capacity of the fluid with ρ_f and ρ_p being the density of the fluid and the density of the particles, respectively, and c_f and c_p denote the specific heat of the fluid and the particle at constant pressure, respectively. The subscript ∞ represents the values at large values of y (outside the boundary layer). Details of the derivation of (4) and (5) are given in the papers by Buongiorno [15] and Nield and Kuznetsov [17].

Equations (1)–(5) are subjected to the following boundary conditions [25–27]:

$$\begin{aligned} &v = v_0, \quad u = \sigma\, U_w(x), \\ &-k\frac{\partial T}{\partial y} = h\left(T_f - T\right), \quad \varphi = \varphi_w \quad \text{at } y = 0, \\ &u \longrightarrow 0, \quad v \longrightarrow 0, \quad T \longrightarrow T_\infty, \\ &\varphi \longrightarrow \varphi_\infty \quad \text{as } y \longrightarrow \infty, \end{aligned} \tag{6}$$

where σ is a constant with $\sigma > 0$ for stretching and $\sigma < 0$ for shrinking and k is the thermal conductivity of the base fluid. The subscript w denotes the values at the solid surface. The governing equations (1)–(5) subjected to the

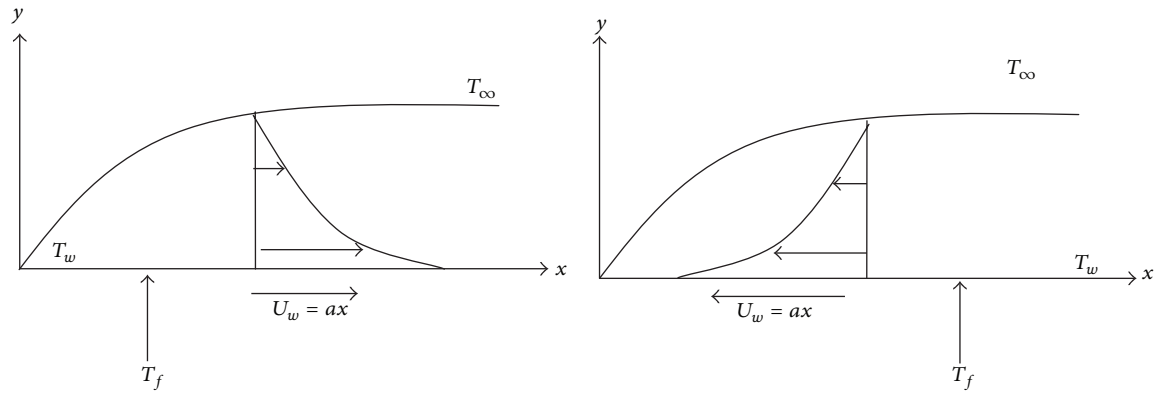

FIGURE 1: Geometry of the problem for (a) stretching and (b) shrinking sheets.

boundary conditions (6) can be expressed in a simpler form by introducing the following transformation:

$$\psi = \left(U_w \nu x\right)^{1/2} f(\eta), \qquad \eta = \left(\frac{U_w}{\nu x}\right)^{1/2} y,$$
$$\theta(\eta) = \frac{T - T_\infty}{T_f - T_\infty}, \qquad \beta(\eta) = \frac{\varphi - \varphi_\infty}{\varphi_w - \varphi_\infty}, \tag{7}$$

where η is the similarity variable and ψ is the stream function defined as $u = \partial\psi/\partial y$ and $v = -\partial\psi/\partial x$, which identically satisfies (1). By employing the boundary layer approximations and the similarity variables (7), (2)–(5) reduce to the following nonlinear ordinary differential equations:

$$f''' + ff'' - f'^2 = 0, \tag{8}$$

$$\frac{1}{\mathrm{Pr}}\theta'' + f\theta' + \mathrm{Nb}\beta'\theta' + \mathrm{Nt}\theta'^2 = 0, \tag{9}$$

$$\beta'' + \frac{\mathrm{Nt}}{\mathrm{Nb}}\theta'' + \mathrm{Le} f\beta' = 0, \tag{10}$$

and the boundary conditions (6) become

$$f(0) = S, \qquad f'(0) = \sigma,$$
$$\theta'(0) = -\gamma\left[1 - \theta(0)\right], \qquad \beta(0) = 1, \tag{11}$$

$$f' = 0, \qquad \theta = 0, \qquad \beta = 0 \quad \text{as } \eta \longrightarrow \infty, \tag{12}$$

where primes denote differentiation with respect to η. Further, Pr is the Prandtl number, Nb is the Brownian motion parameter, Nt is the thermophoresis parameter, Le is the Lewis number, S is the mass flux parameter with $S > 0$ for suction and $S < 0$ for injection, and γ is the Biot number (convective parameter), which are defined as

$$\mathrm{Pr} = \frac{\nu}{\alpha}, \qquad \mathrm{Nb} = \frac{\tau D_B\left(\varphi_w - \varphi_\infty\right)}{\nu},$$
$$\mathrm{Nt} = \frac{\tau D_T\left(T_w - T_\infty\right)}{\nu T_\infty},$$
$$\mathrm{Le} = \frac{\nu}{D_B}, \qquad S = -\frac{v_0}{\sqrt{a\nu}}, \qquad \gamma = \frac{h}{k}\sqrt{\frac{\nu}{a}}. \tag{13}$$

When Nb = Nt = 0, the present problem reduces to a regular viscous fluid, and the nanoparticle volume fraction equation (10) becomes ill-posed and is of no physical significance.

The physical quantities of interest are the skin friction coefficient C_f, the local Nusselt number Nu_x, and the local Sherwood number Sh_x which are defined as

$$C_f = \frac{\tau_w}{\rho U_w^2}, \qquad \mathrm{Nu}_x = \frac{x q_w}{k\left(T_f - T_\infty\right)},$$
$$\mathrm{Sh}_x = \frac{x q_m}{D_B\left(\varphi_w - \varphi_\infty\right)}, \tag{14}$$

where τ_w, q_w, and q_m are the surface shear stress, the heat, and mass fluxes, respectively, which are given by [23]

$$\tau_w = \mu\left(\frac{\partial u}{\partial y}\right)_{y=0}, \qquad q_w = -k\left(\frac{\partial T}{\partial y}\right)_{y=0},$$
$$q_m = -D_B\left(\frac{\partial \varphi}{\partial y}\right)_{y=0}. \tag{15}$$

Using the similarity variables (7), we obtain

$$C_f \mathrm{Re}_x^{1/2} = f''(0), \qquad \mathrm{Nu}_x \mathrm{Re}_x^{-1/2} = -\theta'(0),$$
$$\mathrm{Sh}_x \mathrm{Re}_x^{-1/2} = -\beta'(0), \tag{16}$$

where $\mathrm{Re}_x = U_w x/\nu$ is the local Reynolds number.

3. Results and Discussion

The set of ordinary differential equations (8)–(10) with the boundary conditions (11) and (12) were solved numerically using a shooting method. In this method, the dual solutions are obtained by setting different initial guesses for the values of $f''(0)$, $-\theta'(0)$, and $-\beta'(0)$, where all profiles satisfy the far field boundary conditions (12) asymptotically but with different boundary layer thicknesses. The problem for a regular (viscous) fluid involves five parameters: Prandtl number, stretching/shrinking, suction/injection, and convective parameters. In this study, three parameters are added, namely, the Lewis number, Brownian motion, and thermophoresis parameters. The asymptotic boundary conditions (12) at $\eta = \infty$ are replaced by $\eta = 15$ as customary in the boundary layer analysis. This choice is adequate for the velocity, temperature, and concentration profiles to reach the far field boundary conditions asymptotically. We note that when $\sigma = 1$, the closed-form solution for (8) was reported by P. S. Gupta and A. S. Gupta [28] and Ishak et al. [29], which is given by $f(\eta) = \zeta - (1/\zeta)e^{-\zeta\eta}$, where $\zeta - (1/\zeta) = S$ and $\zeta > 0$. Consequently, this expression leads to $f''(\eta) = -\zeta e^{-\zeta\eta}$. Numerical results for $f''(0)$ are compared with the analytical results obtained and shown in Table 1 where they are found to be in excellent agreement, cementing the validity of the numerical results in this study. From Table 1, it is obvious that the skin friction coefficient $f''(0)$ decreases with the increasing of σ.

Table 1: Values of $f''(0)$ for different values of S.

S	σ	$f''(0)$ P. S. Gupta and A. S. Gupta [28] Ishak et al. [29]	$f''(0)$ Present study
2	−0.2	—	0.3789
	−0.1	—	0.1949
	0.1	—	−0.2049
	0.5	—	−1.1124
	1	−2.4142	−2.4142
2.5	−0.2	—	0.4834
	−0.1	—	0.2489
	0.1	—	−0.2539
	0.5	—	−1.3431
	1	−2.8508	−2.8508
3	−0.2	—	0.5864
	−0.1	—	0.2966
	0.1	—	−0.3033
	0.5	—	−1.5792
	1	−3.3028	−3.3028

Variations with σ of the local Nusselt number $\mathrm{Nu}_x\mathrm{Re}_x^{-1/2}$ (heat transfer rates) and the local Sherwood number $\mathrm{Sh}_x\mathrm{Re}_x^{-1/2}$ (concentration rates) for different values of parameters are presented in Figures 2–7. As can be seen in these figures, there are more than one solution obtained for a fixed value of σ. When σ is equal to a certain value $\sigma = \sigma_c$ where σ_c (<0) is the critical value of σ, there is only one solution, and when $\sigma < \sigma_c$, there is no solution. From these figures, it is seen that the values of $|\sigma_c|$ remain unchanged for different values of γ, Nt, and Nb. This is clear from (8)–(12) where the thermal field does not affect the flow field. However, based on our computations, we found that by increasing the mass flux parameter S, the range of solutions widens where $\sigma_c = -1.0000$, -1.5625, and -2.2500 for $S = 2$, 2.5, and 3, respectively.

From Figures 2–7, the local Nusselt number and the local Sherwood number for a nanofluid change with the variations of γ, Nt, and Nb. It can be seen that the surface heat transfer from Figures 2–4 generally decreases as σ increases. From these figures, it is shown that the local Nusselt number (Figure 2) is consistently higher for a nanofluid with higher values of convective parameter γ. As γ is directly proportional to the heat transfer coefficient h, it is inversely proportional to the thermal resistance [25]. Thus, as γ increases, the heat resistance decreases and hence increases the heat transfer rate at the surface. Figures 3 and 4 show the effects of thermophoresis and Brownian motion parameter (Nt and Nb, resp.) on the local Nusselt number. The figures show that by increasing both parameters, the heat transfer rate at the surface reduces. To further test this observation, we construct Tables 2(a) and 3(a) where we compute variations of the local Nusselt number with Nt and Nb, and Nt and γ. Again, we can see that the surface heat transfer is lower for higher values of Nt and Nb. These results concur with previous results obtained by Nield and Kuznetsov (see [16–18]). Increasing Brownian motion and thermophoresis parameters causes the thermal boundary layer to thicken, thus decreasing the local Nusselt number. This phenomenon is explained by Rasekh et al. [30] where they claimed that the increased Brownian motion impacts a larger extent of the fluid and the thermophoresis diffusion penetrates deeper into the fluid. On the other hand, to further attest to the results shown in Figure 2, Table 3(a) shows that for every value of Nt, the local Nusselt number increases with the increment of γ. From Figures 3 and 4 and Table 2(a), it is interesting to note that while the local Nusselt number changes by approximately 0.4% when Nb is increased, the local Nusselt number decreases by only 0.006% when Nt is increased. From this observation, it seems that Brownian motion parameter Nb affects the surface heat transfer more than the thermophoresis parameter Nt does.

As opposed to the local Nusselt number, the local Sherwood number increases with increasing σ. However, Figure 5 shows that increasing γ does not favour mass exchange efficiency, and thus the local Sherwood number drops. Table 3(b) supports this claim where we compute the variations of the local Sherwood number with Nt and γ. Figures 6 and 7 depict the variations of mass transfer rates with different Nt and Nb. Similar to the local Nusselt number, increasing the thermophoresis parameter Nt will cause the local Sherwood number to drop. Nevertheless, the latter increases with increasing Nb. These observations are also shown in Table 2(b). From the table, it is noted that although the increment of Nb increases the local Sherwood number, higher values of Nt lower the mass transfer rates. Through

Table 2: (a) Variation of the local Nusselt number Nu_x with Nb and Nt and (b) variation of the local Sherwood number Sh_x with Nb and Nt for $\gamma = 0.1$, Le = 2, and Pr = 6.8.

(a)

Nb = 0.1		Nb = 0.2		Nb = 0.3		Nb = 0.4		Nb = 0.5	
Nt	Nu_x	Nt	Nu_x	Nt	Nu_x	Nt	Nu_x	Nt	Nu_x
0.1	0.099140	0.1	0.098973	0.1	0.098752	0.1	0.098453	0.1	0.098043
0.2	0.099139	0.2	0.098972	0.2	0.098750	0.2	0.098451	0.2	0.098039
0.3	0.099138	0.3	0.098971	0.3	0.098749	0.3	0.098448	0.3	0.098035
0.4	0.099137	0.4	0.098970	0.4	0.098747	0.4	0.098446	0.4	0.098031
0.5	0.099136	0.5	0.098969	0.5	0.098746	0.5	0.098443	0.5	0.098026

(b)

Nb = 0.1		Nb = 0.2		Nb = 0.3		Nb = 0.4		Nb = 0.5	
Nt	Sh_x	Nt	Sh_x	Nt	Sh_x	Nt	Sh_x	Nt	Sh_x
0.1	3.866697	0.1	3.916454	0.1	3.933054	0.1	3.941369	0.1	3.946375
0.2	3.767307	0.2	3.866821	0.2	3.900021	0.2	3.916650	0.2	3.926663
0.3	3.667917	0.3	3.817189	0.3	3.866988	0.3	3.891933	0.3	3.906953
0.4	3.568529	0.4	3.767557	0.4	3.833956	0.4	3.867217	0.4	3.887244
0.5	3.469141	0.5	3.717926	0.5	3.800925	0.5	3.842501	0.5	3.867536

Table 3: (a) Variation of the local Nusselt number Nu_x with γ and Nt and (b) variation of the local Sherwood number Sh_x with γ and Nt for Nb = 0.5, Le = 2, and Pr = 6.8.

(a)

Nt = 0.1		Nt = 0.2		Nt = 0.3		Nt = 0.4		Nt = 0.5	
γ	Nu_x	γ	Nu_x	γ	Nu_x	γ	Nu_x	γ	Nu_x
0.1	0.098043	0.1	0.098039	0.1	0.098035	0.1	0.098031	0.1	0.098026
0.2	0.192308	0.2	0.192276	0.2	0.192243	0.2	0.192211	0.2	0.192178
0.3	0.282986	0.3	0.282884	0.3	0.282779	0.3	0.282673	0.3	0.282565
0.4	0.370261	0.4	0.370029	0.4	0.369792	0.4	0.369549	0.4	0.369301
0.5	0.454302	0.5	0.453870	0.5	0.453427	0.5	0.452972	0.5	0.452503

(b)

Nt = 0.1		Nt = 0.2		Nt = 0.3		Nt = 0.4		Nt = 0.5	
γ	Sh_x	γ	Sh_x	γ	Sh_x	γ	Sh_x	γ	Sh_x
0.1	3.946375	0.1	3.926663	0.1	3.906953	0.1	3.887244	0.1	3.867536
0.2	3.927421	0.2	3.888766	0.2	3.850122	0.2	3.811491	0.2	3.772871
0.3	3.909188	0.3	3.852327	0.3	3.795505	0.3	3.738723	0.3	3.681982
0.4	3.891640	0.4	3.817279	0.4	3.743010	0.4	3.668834	0.4	3.594756
0.5	3.874741	0.5	3.783559	0.5	3.692549	0.5	3.601719	0.5	3.511676

Figures 5–7, it is interesting to see that the change occurring in the mass transfer rates is almost monotonous for all values of Nt. However, the difference in the local Sherwood number increases as γ increases and decreases as Nb increases.

Figures 8–11 show the samples of temperature and concentration profiles for different values of γ and Nt. These profiles satisfy the far field boundary conditions (12) asymptotically which support the validity of the numerical results obtained, as well as supporting the existence of the dual solutions shown in Figures 2–7. For a similar problem where dual solutions exist, Merkin [31], Weidman et al. [32], and Postelnicu and Pop [33] have shown that the first solution is linearly stable and physically realizable, while the second solution is not. Thus for the present problem, it is expected that only the first solution is physically relevant. The generated temperature profiles shown in Figure 8 are qualitatively similar to those of Aziz [25] and Ishak [26]. From the figure, it is seen that the temperature increases as γ increases. As mentioned earlier, the surface temperature T_w depends on the convective parameter γ. As γ reaches ∞, the surface temperature will approach 1, which conforms to the boundary condition (11). Figure 9 shows the temperature profiles for different values of Nt. It is observed that the change in temperature occurs only slightly for every change in Nt. This phenomenon supports the results obtained in Figure 3 and Table 2(a). Figures 8 and 9 agree with the observation of

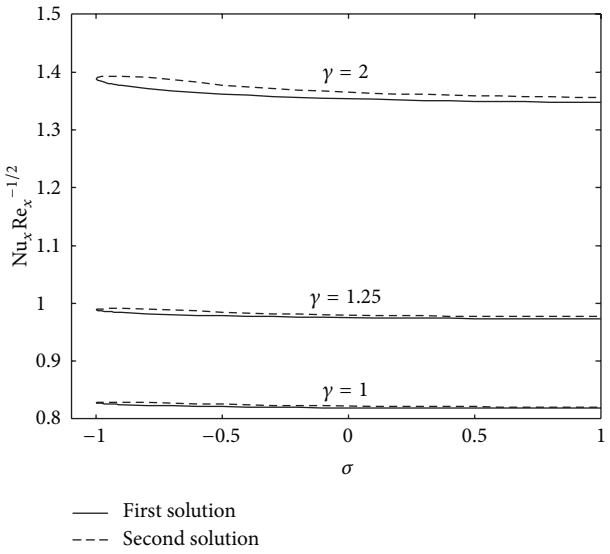

Figure 2: Variations of the local Nusselt number (heat transfer rate) with σ for different values of γ when Nb = Nt = 0.5, Le = 2, Pr = 6.8, and $S = 2$.

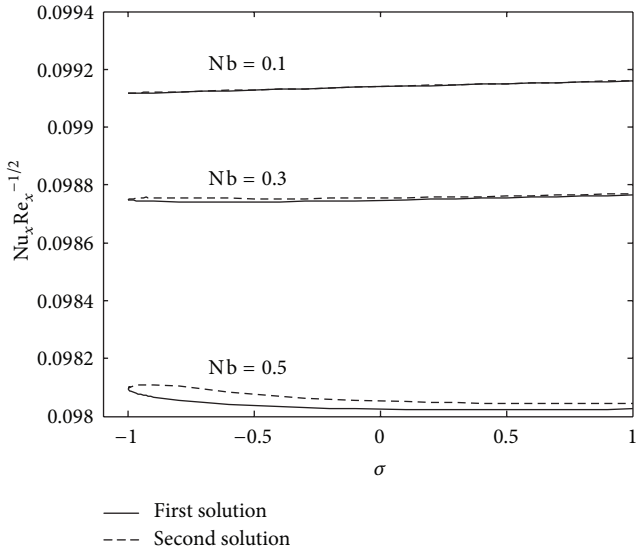

Figure 4: Variations of the local Nusselt number (heat transfer rate) with σ for different values of Nb when Nt = 0.5, Le = 2, Pr = 6.8, γ = 0.1, and $S = 2$.

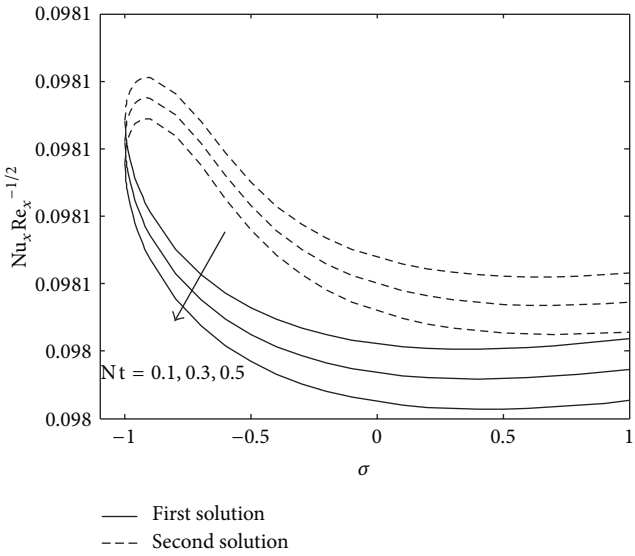

Figure 3: Variations of the local Nusselt number (heat transfer rate) with σ for different values of Nt when Nb = 0.5, Le = 2, Pr = 6.8, γ = 0.1, and $S = 2$.

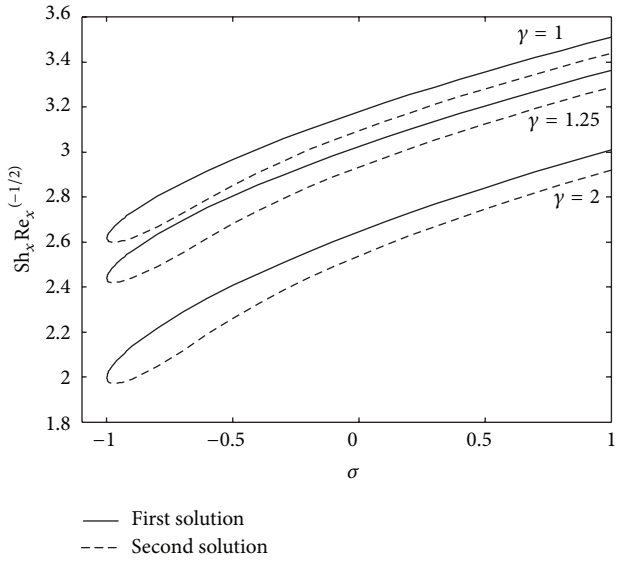

Figure 5: Variations of the local Sherwood number (concentration rates) with σ for different values of γ when Nb = Nt = 0.5, Le = 2, Pr = 6.8, and $S = 2$.

Makinde and Aziz [27] where the thermal boundary layer thickens with the rise in temperature as convective parameter and thermophoresis parameter intensify.

The concentration profiles corresponding to the temperature profiles in Figures 8 and 9 are shown in Figures 10 and 11. In Figures 8 and 9, it is observed that the temperature increases as the convective parameter γ and thermophoresis parameter Nt increase. Due to the dependency of the concentration on the temperature field, we expect that higher convective and thermophoresis parameters would allow a deeper penetration of the concentration [27]. Hence, it is seen that in Figures 10 and 11, the concentration increases with the increasing of convective parameter γ and thermophoresis parameter Nt.

4. Conclusions

The boundary layer flow of a nanofluid past a stretching/shrinking sheet with a convective boundary condition was studied. The effects of stretching/shrinking parameter, convective parameter, Brownian motion parameter and thermophoresis parameter on the local Nusselt number and local

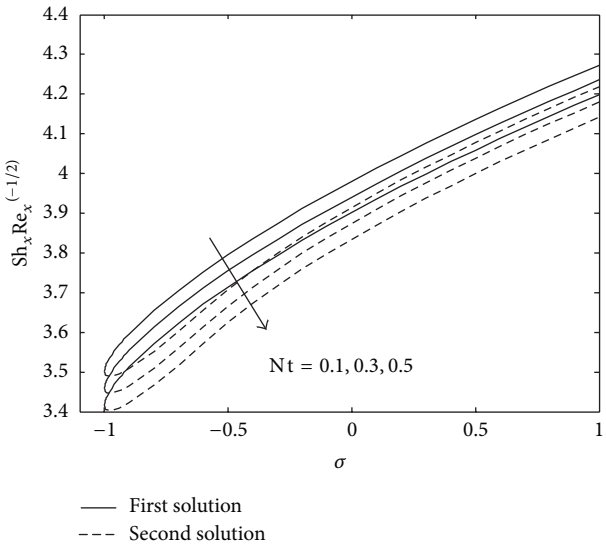

Figure 6: Variations of the local Sherwood number (concentration rates) with σ for different values of Nt when Nb = 0.5, Le = 2, Pr = 6.8, $\gamma = 0.1$, and $S = 2$.

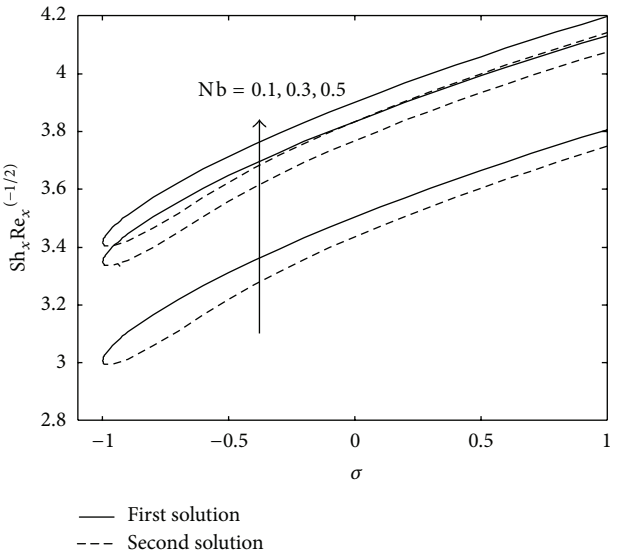

Figure 7: Variations of the local Sherwood number (concentration rates) with σ for different values of Nb when Nt = 0.5, Le = 2, Pr = 6.8, $\gamma = 0.1$, and $S = 2$.

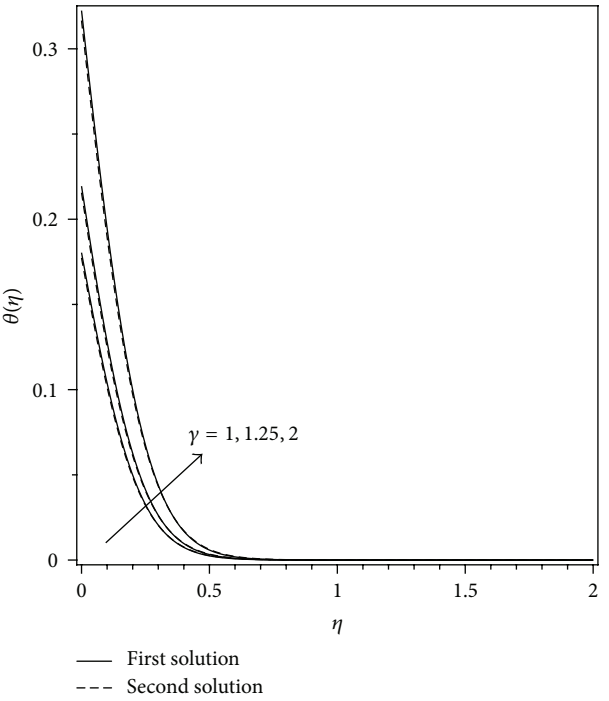

Figure 8: Temperature profiles for different values of γ when Nb = Nt = 0.5, Le = 2, Pr = 6.8, $\sigma = -0.1$, and $S = 2$.

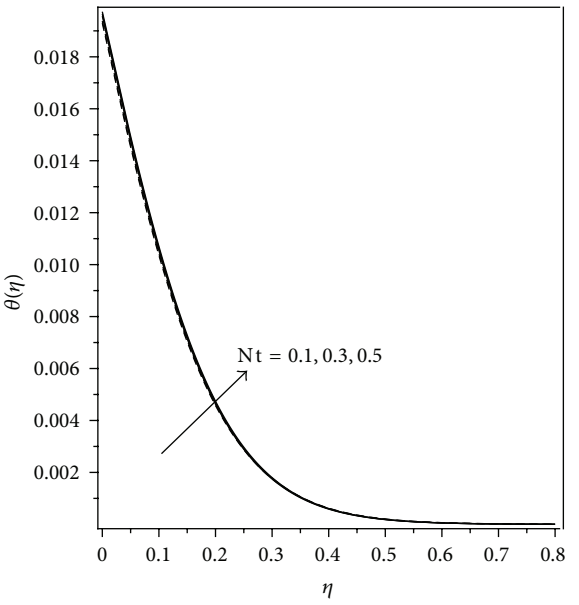

Figure 9: Temperature profiles for different values of Nt when Nb = 0.5, Le = 2, Pr = 6.8, $\gamma = 0.1$, $\sigma = -0.1$, and $S = 2$.

Sherwood number were studied. Numerical solutions to the governing equations were obtained using a shooting method. The results for the local Nusselt number and the local Sherwood number are presented for different values of the governing parameters. The local Nusselt number decreases as the stretching/shrinking parameter increases. On the other hand, the local Sherwood number increases with the increasing of stretching/shrinking parameter. The local Nusselt number is consistently higher for higher values of the convective parameter but lower for higher values of the Brownian motion parameter and thermophoresis parameter. From the results, Brownian motion parameter affects the surface heat transfer rate more than the thermophoresis parameter. The local Sherwood number increases with increasing Brownian motion parameter and decreases with increasing convective parameter and thermophoresis parameter. The results also indicate the existence of dual solutions for both stretching and shrinking cases.

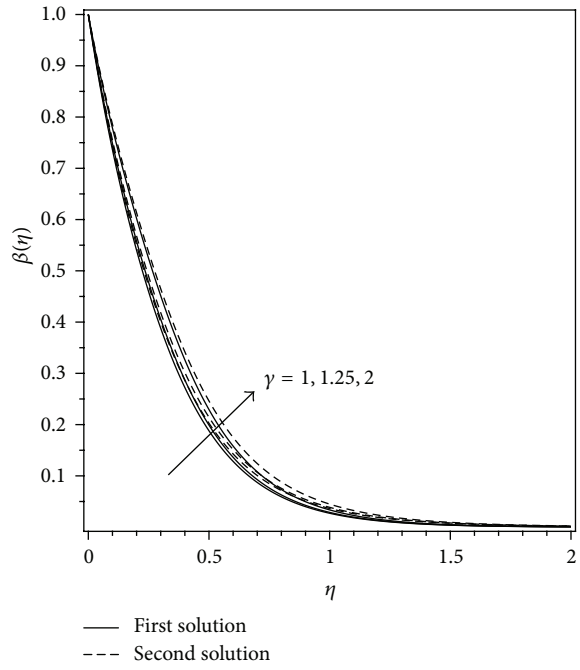

Figure 10: Concentration profiles for different values of γ when Nb = Nt = 0.5, Le = 2, Pr = 6.8, $\sigma = -0.1$, and $S = 2$.

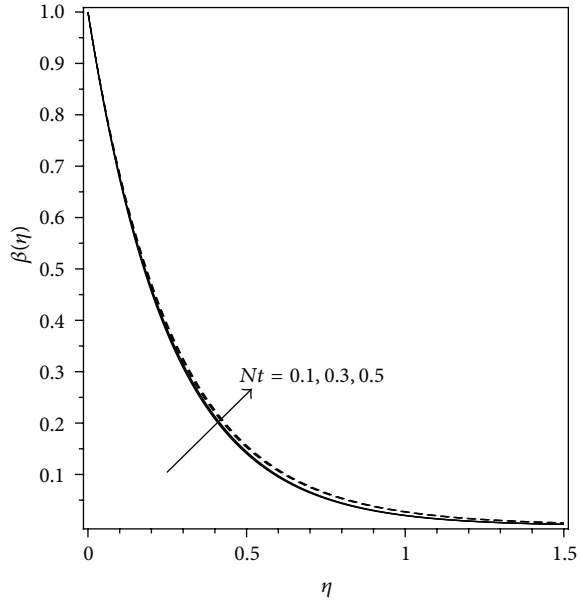

Figure 11: Concentration profiles for different values of Nt when Nb = 0.5, Le = 2, Pr = 6.8, $\gamma = 0.1$, $\sigma = -0.1$, and $S = 2$.

Conflict of Interests

The authors declare that there is no conflict of interests regarding the publication of this paper.

Acknowledgments

The authors wish to express their thanks to the anonymous referees for their valuable comments and suggestions. The financial supports received from the Ministry of Higher Education, Malaysia (Project code: FRGS/1/2012/SG04/UKM/01/1), and the Universiti Kebangsaan Malaysia (Project code: DIP-2012-31) are gratefully acknowledged.

References

[1] E. G. Fischer, *Extrusion of Plastics*, Wiley, New York, NY, USA, 1976.

[2] L. J. Crane, "Flow past a stretching plate," *Journal of Applied Mathematics and Physics* , vol. 21, no. 4, pp. 645–647, 1970.

[3] C. Y. Wang, "Analysis of viscous flow due to a stretching sheet with surface slip and suction," *Nonlinear Analysis: Real World Applications*, vol. 10, no. 1, pp. 375–380, 2009.

[4] B. Sahoo, "Flow and heat transfer of a non-Newtonian fluid past a stretching sheet with partial slip," *Communications in Nonlinear Science and Numerical Simulation*, vol. 15, no. 3, pp. 602–615, 2010.

[5] M. Miklavčič and C. Y. Wang, "Viscous flow due to a shrinking sheet," *Quarterly of Applied Mathematics*, vol. 64, no. 2, pp. 283–290, 2006.

[6] T. Fang, S. Yao, J. Zhang, and A. Aziz, "Viscous flow over a shrinking sheet with a second order slip flow model," *Communications in Nonlinear Science and Numerical Simulation*, vol. 15, no. 7, pp. 1831–1842, 2010.

[7] K. Bhattacharyya, S. Mukhopadhyay, and G. C. Layek, "Slip effects on boundary layer stagnation-point flow and heat transfer towards a shrinking sheet," *International Journal of Heat and Mass Transfer*, vol. 54, no. 1–3, pp. 308–313, 2011.

[8] S. U. S. Choi and J. A. Eastman, "Enhancing thermal conductivities of fluids with nanoparticles," in *Proceedings of the ASME International Mechanical Engineering Congress and Exposition*, San Francisco, Calif, USA, 1995.

[9] H. Masuda, A. Ebata, K. Teramae, and N. Hishinuma, "Alteration of thermal conductivity and viscosity of liquid by dispersing ultra-fine particles," *Netsu Bussei*, vol. 7, pp. 227–233, 1993.

[10] M. M. Rahman, M. A. Al-Lawatia, I. A. Eltayeb, and N. Al-Salti, "Hydromagnetic slip flow of water based nanofluids past a wedge with convective surface in the presence of heat generation (or) absorption," *International Journal of Thermal Sciences*, vol. 57, pp. 172–182, 2012.

[11] Y. Xuan and Q. Li, "Heat transfer enhancement of nanofluids," *International Journal of Heat and Fluid Flow*, vol. 21, no. 1, pp. 58–64, 2000.

[12] Y. Xuan and W. Roetzel, "Conceptions for heat transfer correlation of nanofluids," *International Journal of Heat and Mass Transfer*, vol. 43, no. 19, pp. 3701–3707, 2000.

[13] S. Lee, S. U. S. Choi, S. Li, and J. A. Eastman, "Measuring thermal conductivity of fluids containing oxide nanoparticles," *Journal of Heat Transfer*, vol. 121, no. 2, pp. 280–288, 1999.

[14] R. K. Tiwari and M. K. Das, "Heat transfer augmentation in a two-sided lid-driven differentially heated square cavity utilizing nanofluids," *International Journal of Heat and Mass Transfer*, vol. 50, no. 9-10, pp. 2002–2018, 2007.

[15] J. Buongiorno, "Convective transport in nanofluids," *Journal of Heat Transfer*, vol. 128, no. 3, pp. 240–250, 2006.

[16] D. A. Nield and A. V. Kuznetsov, "The Cheng-Minkowycz problem for natural convective boundary-layer flow in a porous medium saturated by a nanofluid," *International Journal of Heat and Mass Transfer*, vol. 52, no. 25-26, pp. 5792–5795, 2009.

[17] D. A. Nield and A. V. Kuznetsov, "Thermal instability in a porous medium layer saturated by a nanofluid," *International Journal of Heat and Mass Transfer*, vol. 52, no. 25-26, pp. 5796–5801, 2009.

[18] D. A. Nield and A. V. Kuznetsov, "The Cheng-Minkowycz problem for the double-diffusive natural convective boundary layer flow in a porous medium saturated by a nanofluid," *International Journal of Heat and Mass Transfer*, vol. 54, no. 1–3, pp. 374–378, 2011.

[19] A. V. Kuznetsov and D. A. Nield, "Natural convective boundary-layer flow of a nanofluid past a vertical plate," *International Journal of Thermal Sciences*, vol. 49, no. 2, pp. 243–247, 2010.

[20] A. V. Kuznetsov and D. A. Nield, "Double-diffusive natural convective boundary-layer flow of a nanofluid past a vertical plate," *International Journal of Thermal Sciences*, vol. 50, no. 5, pp. 712–717, 2011.

[21] W. A. Khan and I. Pop, "Boundary-layer flow of a nanofluid past a stretching sheet," *International Journal of Heat and Mass Transfer*, vol. 53, no. 11-12, pp. 2477–2483, 2010.

[22] N. Bachok, A. Ishak, and I. Pop, "Boundary-layer flow of nanofluids over a moving surface in a flowing fluid," *International Journal of Thermal Sciences*, vol. 49, no. 9, pp. 1663–1668, 2010.

[23] N. Bachok, A. Ishak, and I. Pop, "Unsteady boundary-layer flow and heat transfer of a nanofluid over a permeable stretching/shrinking sheet," *International Journal of Heat and Mass Transfer*, vol. 55, no. 7-8, pp. 2102–2109, 2012.

[24] W. A. Khan and A. Aziz, "Natural convection flow of a nanofluid over a vertical plate with uniform surface heat flux," *International Journal of Thermal Sciences*, vol. 50, no. 7, pp. 1207–1214, 2011.

[25] A. Aziz, "A similarity solution for laminar thermal boundary layer over a flat plate with a convective surface boundary condition," *Communications in Nonlinear Science and Numerical Simulation*, vol. 14, no. 4, pp. 1064–1068, 2009.

[26] A. Ishak, "Similarity solutions for flow and heat transfer over a permeable surface with convective boundary condition," *Applied Mathematics and Computation*, vol. 217, no. 2, pp. 837–842, 2010.

[27] O. D. Makinde and A. Aziz, "Boundary layer flow of a nanofluid past a stretching sheet with a convective boundary condition," *International Journal of Thermal Sciences*, vol. 50, no. 7, pp. 1326–1332, 2011.

[28] P. S. Gupta and A. S. Gupta, "Heat and mass transfer on a stretching sheet with suction or blowing," *The Canadian Journal of Chemical Engineering*, vol. 55, no. 6, pp. 744–746, 1977.

[29] A. Ishak, R. Nazar, and I. Pop, "Heat transfer over an unsteady stretching permeable surface with prescribed wall temperature," *Nonlinear Analysis: Real World Applications*, vol. 10, no. 5, pp. 2909–2913, 2009.

[30] A. Rasekh, D. D. Ganji, and S. Tavakoli, "Numerical solutions for a nanofluid past over a stretching circular cylinder with non-uniform heat source," *Frontiers in Heat and Mass Transfer*, vol. 3, pp. 1–6, 2012.

[31] J. H. Merkin, "On dual solutions occurring in mixed convection in a porous medium," *Journal of Engineering Mathematics*, vol. 20, no. 2, pp. 171–179, 1986.

[32] P. D. Weidman, D. G. Kubitschek, and A. M. J. Davis, "The effect of transpiration on self-similar boundary layer flow over moving surfaces," *International Journal of Engineering Science*, vol. 44, no. 11-12, pp. 730–737, 2006.

[33] A. Postelnicu and I. Pop, "Falkner-Skan boundary layer flow of a power-law fluid past a stretching wedge," *Applied Mathematics and Computation*, vol. 217, no. 9, pp. 4359–4368, 2011.

Hindawi Publishing Corporation
Abstract and Applied Analysis
Volume 2013, Article ID 709497, 7 pages
http://dx.doi.org/10.1155/2013/709497

Research Article

Evolution of Aerosol Particles in the Rainfall Process via Method of Moments

Fangyang Yuan and Fujun Gan

School of Aeronautics and Astronautics, Zhejiang University, Hangzhou 310027, China

Correspondence should be addressed to Fangyang Yuan; fyyuan.vip@gmail.com

Received 20 July 2013; Accepted 13 August 2013

Academic Editor: Jianzhong Lin

The method of moments is employed to predict the evolution of aerosol particles in the rainfall process. To describe the dynamic properties of particle size distribution, the population balance equation is converted to moment equations by the method of moments and the converted equations are solved numerically. The variations of particle number concentration, geometric mean diameter, and geometric standard deviation are given in the cases that the Brownian diffusion and inertial impaction of particles dominate, respectively. The effects of raindrop size distribution on particle size distribution are analyzed in nine cases. The results show that the particle number concentration decreases as time goes by, and particles dominated by Brownian diffusion are removed more significantly. The particle number concentration decreases much more rapidly when particle geometric mean diameter is smaller, and the particle size distribution tends to be monodisperse. For the same water content, the raindrops with small geometric mean diameters can remove particles with much higher efficiency than those with large geometric mean diameters. Particles in the "Greenfield gap" are relatively difficult to scavenge, and a new method is needed to remove it from the air.

1. Introduction

Our surroundings are filled with aerosol particles which not only affect the environment such as the air visibility, weather, and climate, but also cause respiratory diseases. Available researches show that the respiratory diseases are not only related to the particle mass concentration but also to the particle size and number concentration [1]. Therefore, it is necessary to remove aerosols from air. In nature, precipitation is one of the most effective approaches to remove aerosols in air, in which raindrops collide with aerosols and then collect them. The removing process is affected by external factors including aerosol size distribution [2], raindrop size distribution (RSD) [3], rainfall intensity [4], and physical and chemical properties [5] and internal factors including collision mechanisms between raindrops and aerosols and condensation/evaporation of raindrops and aerosols [6]. The mechanisms involved in the above processes include particle Brownian diffusion, direction interception, inertial impaction, thermo- and diffusiophoresis forces, and electrical forces [2, 7]. Although these forces are coupled, one or more of them may dominate for various regions of particle size, drop size, particle density and hydrodynamic temperature, and diffusion fields.

In the rainfall process, the most interesting thing is how the particle size distribution (PSD) changes as time progresses and how PSD is affected by different RSD. In order to answer the questions, the population balance equation (PBE) for particles is introduced [8]. The kernel of PBE is how to express the scavenging coefficient which represents the removing rate of aerosols by raindrops and is a function of collision efficiency of raindrops, terminal velocity of raindrops, and PSD [4]. In the pioneering work, Slinn [9] obtained a semiempirical formula of collision efficiency according to the Navier-Stokes equation using the dimensionless analysis coupled with the experimental data, which has been widely used when referring to the below-cloud scavenging process. Chate and Kamra [6] showed that the collision efficiency of water drops increases with the increasing impaction parameter. Chate et al. [5] evaluated the scavenging coefficient for aerosols of diameters in the range of 0.02–10 μm with various densities in accordance with their chemical compositions for heavy rain regime. They found that the inertial impaction mechanism is the dominant

one in removing particles of all sizes for the heavy rain regime, and the scavenging coefficient is highly dependent on relative humidity for hygroscopic particles. Mircea and Stefan [4] obtained an exponential expression of the scavenging coefficient as a function of rainfall intensity and collision efficiency between raindrops and aerosol particles. In their later work, Mircea et al. [8] got the linear relations between the scavenging coefficient and the rainfall intensity via numerical analysis. Andronache [10, 11] concluded that the below-cloud scavenging (BCS) coefficients of aerosols by rainfall depend mainly on the aerosol size distribution parameters and on rainfall intensity, decreasing significantly with aerosol diameter, increasing with rainfall rate, and average raindrop and aerosol electric charge. Later, Andronache et al. [12] developed a more complicated model to predict the scavenging coefficient, finding it sensitive to the choice of representation of mixing processes, raindrop size distribution, phoretic effects in aerosol-raindrop collisions, and cloud droplet activation.

The research mentioned above was focused on getting the relation between the scavenging coefficient and the external factors. Jung et al. [13] expressed the collision efficiency as polynomial expression of particle diameter and applied the method of moments (MOM) to get analytical solutions of PBE. In their following work [3], they employed the collision efficiency proposed by Slinn [9] and applied the MOM to study the evolution of PSD when the RSD obeys the Marshall-Palmer (MP) and Krigian-Mazin (KM) distributions, and they got relatively good results. Besides, Bae et al. [14] developed a good analytical expression for scavenging coefficient. The value of scavenging coefficient can be calculated when the initial three key parameters of PSD and rainfall intensity are given. While in the scavenging process, these parameters evolve as time goes by and the initially calculated scavenging coefficient will be inaccurate due to the evolution of the PSD, even if the rainfall intensity remains the same. In fact, the three parameters of PSD and the scavenging coefficient couple together. Thus, we suggest that more attention should be paid to the dynamic evolution of PSD before getting the value of the scavenging coefficient.

The method of moments has been extensively used to deal with the PBE when referring to physical/chemical changes of particles, including aggregation/breakage [15], condensation/evaporation [16], coagulation [17, 18], deposition/removal [19–21], and chemical reaction [22, 23]. The periodic moment method (PMM), proposed by Pratsinis [24], can be used to solve the evolution of PSD for simultaneous nucleation, condensation, and coagulation in the entire particle size spectrum through approximating the size distribution by a unimodal log-normal function.

In the present study, the PMM is adopted to deal with the PBE when referring to the wet scavenging process, and the scavenging coefficient is expressed as a polynomial function of aerosol diameter, raindrop diameter, and raindrop velocity. The evolutions of PSD are simulated numerically and the effects of RSD on PSD are studied. The variations of particle number concentration, geometric mean diameter, and geometric standard deviation are given when Brownian diffusion and inertial impaction of particles dominate, respectively.

2. Theory

2.1. Basic Theory of Wet Removal. The governing equation describing the time-dependent removal of particles in air by collision with raindrops [8] is as follows:

$$-\frac{\partial n\left(d_p,t\right)}{\partial t} = \Lambda\left(d_p\right)\cdot n\left(d_p,t\right), \tag{1}$$

where $n(d_p,t)$ is the particle size distribution in air and $\Lambda(d_p)$ is the scavenging coefficient representing the rate of scavenged particles by raindrop; consider

$$\Lambda\left(d_p\right) = \int_0^\infty K\left(d_p,D_d\right)E\left(d_p,D_d\right)dD_d, \tag{2}$$

where $K(d_p,D_d)$ is the collision kernel (or collection kernel) which describes the probability of collisions between particles with diameter d_p and raindrops with diameter D_d [3, 13]; consider

$$K\left(d_p,D_d\right) = \frac{\pi D_d^2}{4}U\left(D_d\right)n\left(D_d\right), \tag{3}$$

where $E(d_p,D_d)$ is the collision efficiency which will be discussed below. $U(D_d)$ is the velocity of a falling raindrop with diameter D_d and can be expressed as follows:

$$\begin{aligned} U\left(D_d\right) &= 30.75D_d^2\times 10^6, \quad D_d < 100\,\mu\text{m},\\ U\left(D_d\right) &= 38D_d^2\times 10^3, \quad 100\,\mu\text{m} < D_d < 1000\,\mu\text{m},\\ U\left(D_d\right) &= 133.046D_d^{0.5}, \quad D_d > 1000\,\mu\text{m}. \end{aligned} \tag{4}$$

The collision efficiency, $E(d_p,D_d)$, represents the ratio of the actual frequency of collisions to the theoretical frequency and is affected by turbulent diffusion, Brownian diffusion, van der Waals force, thermophoresis, electrostatic adsorption, and so on. Mircea et al. [4, 8] suggested the collision efficiency to be a constant or a function of rainfall intensity (including linear and power law functions). Jung et al. [13] got a set of analytical solutions for polydispersed particles by a wet removal process for submicrometer particles. Slinn [9] obtained the following semiempirical formula according to the Navier-Stokes equation using the dimensionless analysis coupled with the experimental data:

$$\begin{aligned} E\left(d_p,D_d\right) = {} & \frac{1}{\text{Re}\cdot\text{Sc}}\left[1+0.4\text{Re}^{1/2}\text{Sc}^{1/3}+0.16\text{Re}^{1/2}\text{Sc}^{1/2}\right]\\ & + 4\frac{d_p}{D_d}\left[\frac{\mu_a}{\mu_w}+\left(1+\text{Re}^{1/2}\right)\frac{d_p}{D_d}\right]\\ & + \left(\frac{\text{St}-S^*}{\text{St}-S^*+2/3}\right)^{3/2}, \end{aligned} \tag{5}$$

where $\text{Re} = D_d U(D_d)\rho_a/(2\,\mu_a)$ is the Reynolds number based on the raindrop diameter, $\text{Sc} = \mu_a/(\rho_a D_{\text{diff}})$ is the Schmidt number of particles with the diffusion coefficient $D_{\text{diff}} = k_b T C_c/(3\pi\mu_a d_p)$, $\text{St} = 2\tau U(D_d)/D_d$ is the Stokes number of

particles with relaxation time $\tau = \rho_p d_p^2/(18\mu_a)$, and $S^* = [1.2 + \ln(1 + \mathrm{Re})/12]/[1 + \ln(1 + \mathrm{Re})]$ is a dimensionless parameter. Here, ρ_a and μ_a are the density and the viscosity of air, respectively, μ_w is the viscosity of a water drop, k_b is Boltzmann's constant, T is the absolute temperature of air, and C_c is the Cunningham slip correction factor and can be approximated as follows [25]:

$$C_c = 1 + 2.493\frac{\lambda}{d_p} + 0.84\frac{\lambda}{d_p}\exp\left(-0.435\frac{d_p}{\lambda}\right) \cong 1 + 3.34\frac{\lambda}{d_p}, \tag{6}$$

where λ is the molecular mean free path.

The terms on the right-hand side (RHS) of (5) represent the effects of Brownian diffusion, interception, and inertial impaction, respectively.

2.2. Application of the Method of Moments. According to (2)-(3), the scavenging coefficient, $\Lambda(d_p)$, is related to the collision kernel between particles and raindrops, collision efficiency $E(d_p, D_d)$, and RSD $n(D_d)$. The RSD based on particle diameter can be described with the log-normal distribution [26], and the particle size distribution can also be approximated by the log-normal distribution [27] as follows:

$$\begin{aligned} n(D_d) &= \frac{N_d}{\sqrt{2\pi}\ln\sigma_{dg}}\exp\left[-\frac{\ln^2\left(D_d/D_{dg}\right)}{2\ln^2\left(\sigma_{dg}\right)}\right]\frac{1}{D_d}, \\ n\left(d_p\right) &= \frac{N_p}{\sqrt{2\pi}\ln\sigma_{pg}}\exp\left[-\frac{\ln^2\left(d_p/d_{pg}\right)}{2\ln^2\left(\sigma_{pg}\right)}\right]\frac{1}{d_p}, \end{aligned} \tag{7}$$

where N_d, D_{dg}, and σ_{dg} are the number concentration, geometric mean diameter, and geometric standard deviation of raindrop, respectively. Definitions of the kth moment of raindrops and particles are ξ_k and m_k, respectively [24]; consider

$$\begin{aligned} \xi_k &= \int_0^\infty D_d^k n(D_d)\, dD_d = \xi_0 D_{dg}^k \exp\left[\frac{k^2}{2}\ln^2\sigma_{dg}\right], \\ m_k &= \int_0^\infty d_p^k n\left(d_p\right) dd_p = m_0 d_{pg}^k \exp\left[\frac{k^2}{2}\ln^2\sigma_{dp}\right]. \end{aligned} \tag{8}$$

The last term on RHS of (5) is difficult to deal with when applying the moment method to (1). Thus, the approximate expression proposed by Jung et al. [3] is adopted as follows:

$$\left(\frac{\mathrm{St} - S^*}{\mathrm{St} - S^* + 2/3}\right)^{3/2} \cong 1 - 0.9\mathrm{St}^{-0.5}. \tag{9}$$

The final expression of scavenging coefficient and governing moment equation are as follows [3, 14, 28]:

$$\begin{aligned} \Lambda\left(d_p\right) &= \gamma_1\xi_1\left(d_p^{-1} + Ad_p^{-2}\right) + \gamma_2\xi_{7/4}\left(d_p^{-2/3} + 2Ad_p^{-5/3}/3\right) \\ &\quad + \gamma_3\xi_{7/4}\left(d_p^{-1/2} + Ad_p^{-3/2}/2\right) + \gamma_4\xi_{3/2}d_p + \gamma_5\xi_{1/2}d_p^2 \\ &\quad + \gamma_6\xi_{5/4}d_p^2 + \gamma_7\xi_{5/2} + \gamma_8\xi_{11/4}d_p^{-1}, \end{aligned} \tag{10}$$

$$\begin{aligned} -\frac{\partial m_k}{\partial t} &= \gamma_1\xi_1\left(m_{k-1} + Am_{k-2}\right) + \gamma_2\xi_{7/4} \\ &\quad \times \left[m_{k-2/3} + 2Am_{k-5/3}/3\right] + \gamma_3\xi_{7/4} \\ &\quad \times \left[m_{k-1/2} + Am_{k-3/2}/2\right] + \gamma_4\xi_{3/2}m_{k+1} \\ &\quad + \gamma_5\xi_{1/2}m_{k+2} + \gamma_6\xi_{5/4}m_{k+2} \\ &\quad + \gamma_7\xi_{5/2}m_k + \gamma_8\xi_{11/4}m_{k-1}, \end{aligned} \tag{11}$$

where

$$\begin{aligned} &\gamma_1 = \frac{k_bT}{6\,\mu_a}, \qquad \gamma_2 = \left(\frac{0.4\times 130\pi}{4}\right)\left(\frac{2\,\mu_a}{130\rho_a}\right)^{1/2}\left(\frac{k_b\rho_aT}{3\pi\mu_a^2}\right)^{2/3}, \\ &\gamma_3 = \left(\frac{0.16\times 130\pi}{4}\right)\left(\frac{2k_bT}{3\times 130\pi\mu_a}\right)^{1/2}, \qquad \gamma_4 = \frac{130\,\pi\mu_a}{\mu_w}, \\ &\gamma_5 = 130\pi, \qquad \gamma_6 = 130\pi\left(\frac{130\rho_a}{2\,\mu_a}\right)^{1/2}, \qquad \gamma_7 = \frac{130\pi}{4}, \\ &\gamma_8 = -\left(\frac{0.9\times 130\pi}{4}\right)\left(\frac{18\,\mu_a}{2\times 130\rho_p}\right)^{1/2}, \qquad A = 3.34\lambda. \end{aligned} \tag{12}$$

According to the definition of m_k, m_0 is the total particle number concentration, and $(\pi/6)m_3$ is the total volume of particles. In the following calculation, we solve the first three moment equations, that is, $k = 0$, 1, and 2. The geometric mean particle diameter, d_{pg}, and the geometric standard deviation, σ_{pg}, can be expressed as the function of the first three moments as follows:

$$d_{pg} = \frac{m_1^2}{m_0^{3/2}m_2^{1/2}}, \qquad \sigma_{pg} = \exp\left[\ln\left(\frac{m_2m_0}{m_1^2}\right)\right]^{1/2}. \tag{13}$$

3. Results and Discussions

3.1. Numerical Specifications. The 4th-order Runge-Kutta method with fixed time step is employed to solve (11) with $k = 0$, 1, and 2. The evolutions of PSD are simulated numerically and the effects of RSD on PSD are studied in nine cases. The values of the initialization parameter are listed in Table 1. Case 1 and Case 4 with initial geometric standard deviation $\sigma_{pg0} = 1.5$ are selected to validate the computation codes. Cases 2–5 are selected to obtain the evolution of PSD for clarifying the function by different mechanisms (i.e., Brownian diffusion is dominant for d_{pg0} = 1–10 nm; both Brownian diffusion and interception are dominant for d_{pg0} = 0.1–0.5 μm; and inertial impaction is dominant for d_{pg0} = 5–8 μm). Cases 6–9 are selected to study the effect of RSD on PSD for a given water content defined by (14) [4], and the corresponding raindrop number concentration, N_d, is calculated via (15). The computational programs are written

Table 1: The values of the initialization parameter for Cases 1–9.

Case	N_d/m^{-3}	D_{dg}/mm	σ_{dg}	N_{p0}/m^{-3}	d_{pg0}/μm	σ_{pg0}
1	1.0×10^5	0.1	1.2	1.0×10^6	0.001	1.2/1.5/1.8
2	1.0×10^5	0.1	1.2	1.0×10^6	0.01	1.2/1.5/1.8
3	1.0×10^5	0.1	1.2	1.0×10^6	0.1	1.2/1.5/1.8
4	1.0×10^5	0.1	1.2	1.0×10^6	5.0	1.2/1.5/1.8
5	1.031×10^7	0.2	1.1	1.0×10^6	0.01/0.5/8.0	1.3
6	9.569×10^4	0.2	1.5	1.0×10^6	0.01/0.5/8.0	1.3
7	6.601×10^5	0.5	1.1	1.0×10^6	0.01/0.5/8.0	1.3
8	6.124×10^3	0.5	1.5	1.0×10^6	0.01/0.5/8.0	1.3
9	6.786×10^4	0.5	1.5	1.0×10^6	0.01/0.5/8.0	1.3

using the C Programming Language and are performed on Microsoft Visual C++ 6.0 complier. Consider

$$w = \frac{\pi}{6}\int_{D_d}\rho_w D_d^3 n\left(D_d\right)dD_d, \tag{14}$$

$$N_d = \frac{6w}{\pi\rho_w D_{dg}^3\exp\left(9\sigma_{dg}^2/2\right)}. \tag{15}$$

3.2. Validation of Computation Codes. Particles with diameter d_{pg0} = 1 nm and 0.5 μm are selected to validate the computation codes. Figure 1 shows the numerical results of particle number concentration based on different collision efficiencies proposed by Slinn [9] and Jung and Lee [29], respectively. The collision efficiency proposed by Slinn is given with a semiempirical formula based on the Navier-Stokes equation using dimensionless analysis combined with experimental data. While the collision efficiency proposed by Jung and Lee, as shown in (16), is valid for $d_{pg0} < 1\,\mu$m,

$$E\left(d_p, D_d\right) = 2\left(\frac{\sqrt{3}\pi}{4Pe}\right)^{2/3}\left[\frac{(1-\alpha)(3\sigma+4)}{J+\sigma K}\right]. \tag{16}$$

3.3. Evolution of Particle Geometric Mean Diameter and Geometric Standard Deviation. Figures 2 and 3 show the evolution of particle geometric mean diameter, d_{pg}, and geometric standard deviation, σ_{pg}, in the rainfall process, respectively. From Figure 2 we can see that d_{pg} increases when the initial geometric mean diameter d_{pg0} is equal to 1 nm, 10 nm, and 0.1 μm, and it decreases when d_{pg0} is equal to 5 μm. Thus, we can deduce that there exists one kind of particle diameter, for which d_{pg} never changes in the whole scavenging process. For particles with d_{pg0} = 1 nm and 10 nm, d_{pg} grows much faster when the value of σ_{pg0} is larger. And for particles with d_{pg0} = 5 μm, d_{pg} decreases much more rapidly when σ_{pg0} is larger. The region that particle diameter locates between 0.01 μm and 2 μm is called "Greenfield gap" [30] because the collision efficiency of particles in this region and raindrops is relatively low. While for particles in the "Greenfield gap" (e.g., d_{pg0} = 0.1 μm), d_{pg} hardly changes in the whole process. The evolution of d_{pg} in the present study is qualitatively consistent with the result given by Jung et al. [13].

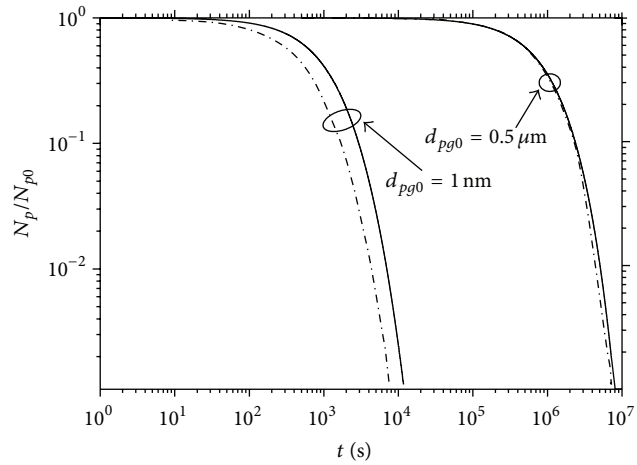

Figure 1: Comparison of particle number concentrations based on different collision efficiencies.

In Figure 3, the geometric standard deviation of particle diameter, σ_{pg}, converges to 1.0 as time goes by in the rainfall process for all particle sizes, which means that the particle size distribution tends to be monodisperse. For particles with the same value of d_{pg0}, σ_{pg} decays much faster when the value of σ_{pg0} is larger. For particles with the same initial value of σ_{pg0}, σ_{pg} decreases at an early stage for small particles dominated by the Brownian diffusion, and at a later stage for large particles controlled by the inertial impaction. σ_{pg} hardly changes for particles in the "Greenfield gap".

3.4. Effect of Raindrop Size Distribution on Particle Size Distribution. The effect of raindrop size distribution (RSD) on the particle size distribution (PSD) is studied using the values of initialization parameter for Cases 6–9 with the given water content (10 g/m^3). Figure 4 shows the evolution of particle number concentration. For Cases 6 and 8 the geometric standard deviation of raindrop diameter, σ_{dg}, is the same but the geometric mean raindrop diameter, D_{dg}, is different. The particle number concentration decreases faster in Case 6 than in Case 8 as shown in Figure 4. For particles

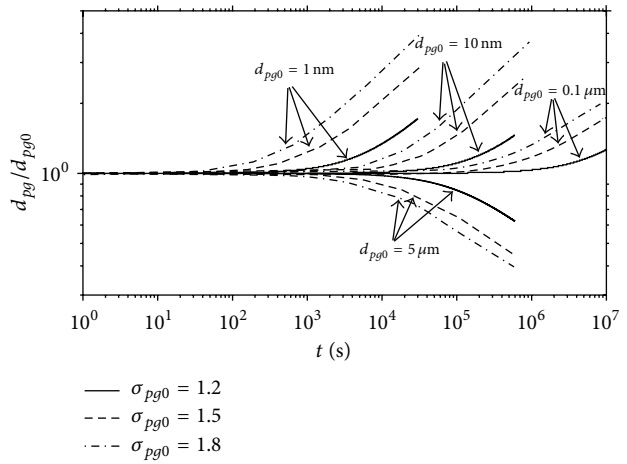

Figure 2: Evolution of particle geometric mean diameter as time progresses for Cases 2–5.

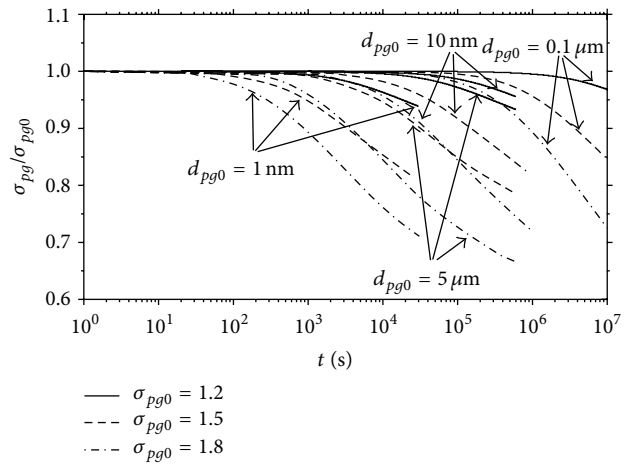

Figure 3: Evolution of geometric standard deviation of particle diameter for Cases 2–5.

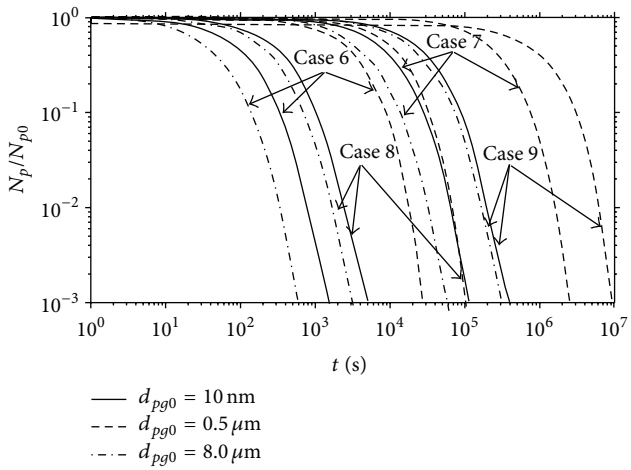

Figure 4: Effect of RSD on particle number concentration for Cases 6–9.

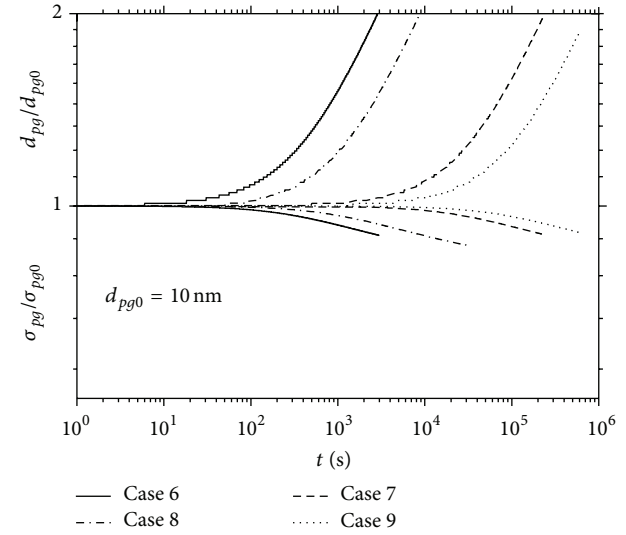

Figure 5: Effect of RSD on particle geometric mean diameter and geometric standard deviation (d_{pg0} = 10 nm).

with d_{pg0} = 0.5 μm and d_{pg0} = 8 μm in Cases 6 and 8, the same tendency can be observed, which demonstrates that the RSD in Case 6 can scavenge particles with a much higher efficiency than that in Case 8.

For Cases 8 and 9, the geometric mean raindrop diameter, D_{dg}, is the same but the geometric standard deviation of raindrop diameter, σ_{dg}, is different. It can be seen that the RSD in Case 8 can remove particles with a much higher efficiency than that in Case 9 for any kind of particles. Meanwhile, it takes a much longer time to scavenge particles when d_{pg0} = 0.5 μm in Case 9 than that for any other kind of particle diameters in any case.

Figure 5 shows the effect of RSD on d_{pg} and σ_{pg} for particles with d_{pg0} = 10 nm. It can be seen that d_{pg} increases and σ_{pg} decreases in all cases, which is consistent with the results given in Figures 2 and 3. It takes the longest time for d_{pg}/d_{pg0} and σ_{pg}/σ_{pg0} to get the same values in Case 9, and the shortest time in Case 6. The overall tendency of the effect of RSD on d_{pg} and σ_{pg} for particles with d_{pg0} = 0.5 μm and d_{pg0} = 8 μm, which is not shown in Figure 5, is the same as that for particles with d_{pg0} = 10 nm.

From the above numerical results and analysis, we can see that, for the same water content, the RSD with small D_{dg} can remove the particles more easily than with large D_{dg}. The RSD with small σ_{dg}, that is, a narrow distribution of particle diameter, can collect particles more easily than with large σ_{dg}. Thus, the RSD in Case 6 is the most efficient in scavenging particles, the RSD in Case 8 takes second place, the RSD in Case 7 the third, and the RSD in Case 9 is the worst, which is consistent with the experimental result [31]. This can be explained in the following way. The raindrop number concentration, N_d, increases as D_{dg} and σ_{dg} decrease with a given water content according to (15), leading to the increase of the total surface area of raindrops, which enhances the probability of capturing small particles dominated by the Brownian diffusion. The intermediate size

particles controlled by the combined effect of Brownian diffusion and interception depend on the value of d_p/D_d. For the particles with smaller D_{dg} and σ_{dg}, d_p/D_d is larger; that is, the RSD is more monodisperse, which makes the collision efficiency become large as shown in the second term on the right-hand side of (5). Thus, the RSD with smaller D_{dg} and σ_{dg} can scavenge intermediate size particles with a much higher efficiency. While for particles with a relatively large size, the scavenging coefficient becomes smaller with larger D_{dg} and σ_{dg}.

4. Conclusions

The removal of aerosol particles in the rainfall process is studied with the periodic moment method. Both the aerosol particle size distribution and raindrop size distribution are assumed to be log-normal. The effects on the collision efficiency of the mechanisms of Brownian diffusion, interception, and inertial impaction have been investigated. The binomial formulas are reexpanded to get a more accurate expression of scavenging coefficient. The first three moments of particle size distribution are simulated and the effects of raindrop size distribution on particle size distribution are studied in nine cases.

The results show that the particle number concentration decreases as time goes by. Particles dominated by Brownian diffusion are removed more easily. The particles in the "Greenfield gap" are the most difficult to be removed. The particle number concentration decreases much more rapidly when particle geometric mean diameter is smaller. In the scavenging process, the particle geometric mean diameter increases when $d_{pg0} < 10\,\text{nm}$, and decreases when $d_{pg0} \geq 1\,\mu\text{m}$, but changes a little when $10\,\text{nm} < d_{pg0} < 1\,\mu\text{m}$. The geometric standard deviation of particle diameter converges to 1.0 as time progresses for any kind of particles, which means that the particle size distribution tends to be monodisperse, and it decays much faster for particles with large σ_{pg0}.

For the same water content, the raindrop size distribution with small D_{dg} can remove particles with a much higher efficiency than that with large D_{dg}, and the raindrop size distribution with small σ_{dg} can collect particles more easily than with large σ_{dg}. Particles in the "Greenfield gap" are relatively difficult to scavenge, and a new method is needed to remove it from the air.

Conflict of Interests

The authors declare that there is no conflict of interests regarding the publication of this paper.

Acknowledgment

This work was supported by the Major Program of the National Natural Science Foundation of China (11132008).

References

[1] P. Penttinen, K. L. Timonen, P. Tiittanen, A. Mirme, J. Ruuskanen, and J. Pekkanen, "Number concentration and size of particles in urban air: effects on spirometric lung function in adult asthmatic subjects," *Environmental Health Perspectives*, vol. 109, no. 4, pp. 319–323, 2001.

[2] J. H. Seinfeld and S. N. Pandis, *Atmospheric Chemistry and Physics*, Wiley, New York, NY, USA, 1998.

[3] C. H. Jung, Y. P. Kim, and K. W. Lee, "A moment model for simulating raindrop scavenging of aerosols," *Journal of Aerosol Science*, vol. 34, no. 9, pp. 1217–1233, 2003.

[4] M. Mircea and S. Stefan, "A theoretical study of the microphysical parameterization of the scavenging coefficient as a function of precipitation type and rate," *Atmospheric Environment*, vol. 32, no. 17, pp. 2931–2938, 1998.

[5] D. M. Chate, P. S. P. Rao, M. S. Naik, G. A. Momin, P. D. Safai, and K. Ali, "Scavenging of aerosols and their chemical species by rain," *Atmospheric Environment*, vol. 37, no. 18, pp. 2477–2484, 2003.

[6] D. M. Chate and A. K. Kamra, "Collection efficiencies of large water drops collecting aerosol particles of various densities," *Atmospheric Environment*, vol. 31, no. 11, pp. 1631–1635, 1997.

[7] H. M. Davenport and L. K. Peters, "Field studies of atmospheric particulate concentration changes during precipitation," *Atmospheric Environment*, vol. 12, no. 5, pp. 997–1008, 1978.

[8] M. Mircea, S. Stefan, and S. Fuzzi, "Precipitation scavenging coefficient: influence of measured aerosol and raindrop size distributions," *Atmospheric Environment*, vol. 34, no. 29-30, pp. 5169–5174, 2000.

[9] W. G. N. Slinn, "Precipitation scavenging," in *Atmospheric Sciences and Power Production*, Division of Biomedical Environmental Research, US Department of Energy, Washington, DC, USA, 1983.

[10] C. Andronache, "Estimated variability of below-cloud aerosol removal by rainfall for observed aerosol size distributions," *Atmospheric Chemistry and Physics*, vol. 3, no. 1, pp. 131–143, 2003.

[11] C. Andronache, "Diffusion and electric charge contributions to below-cloud wet removal of atmospheric ultra-fine aerosol particles," *Journal of Aerosol Science*, vol. 35, no. 12, pp. 1467–1482, 2004.

[12] C. Andronache, T. Grönholm, L. Laakso, Y. Phillips, and A. Venäläinen, "Scavenging of ultrafine particles by rainfall at a boreal site: observations and model estimations," *Atmospheric Chemistry and Physics*, vol. 6, no. 12, pp. 4739–4754, 2006.

[13] C. H. Jung, Y. P. Kim, and K. W. Lee, "Analytic solution for polydispersed aerosol dynamics by a wet removal process," *Journal of Aerosol Science*, vol. 33, no. 5, pp. 753–767, 2002.

[14] S. Y. Bae, C. H. Jung, and Y. Pyo Kim, "Development and evaluation of an expression for polydisperse particle scavenging coefficient for the below-cloud scavenging as a function of rain intensity using the moment method," *Journal of Aerosol Science*, vol. 37, no. 11, pp. 1507–1519, 2006.

[15] D. L. Marchisio, R. D. Vigil, and R. O. Fox, "Implementation of the quadrature method of moments in CFD codes for aggregation-breakage problems," *Chemical Engineering Science*, vol. 58, no. 15, pp. 3337–3351, 2003.

[16] R. E. Sampson and G. S. Springer, "Condensation on and evaporation from droplets by a moment method," *Journal of Fluid Mechanics*, vol. 36, no. 3, pp. 577–584, 1969.

[17] M. Yu, J. Lin, and T. Chan, "A new moment method for solving the coagulation equation for particles in Brownian motion," *Aerosol Science and Technology*, vol. 42, no. 9, pp. 705–713, 2008.

[18] M. Yu and J. Lin, "Taylor-expansion moment method for agglomerate coagulation due to Brownian motion in the entire size regime," *Journal of Aerosol Science*, vol. 40, no. 6, pp. 549–562, 2009.

[19] S. H. Park and K. W. Lee, "Analytical solution to change in size distribution of polydisperse particles in closed chamber due to diffusion and sedimentation," *Atmospheric Environment*, vol. 36, no. 35, pp. 5459–5467, 2002.

[20] L. Jianzhong, S. Xing, and Y. Zhenjiang, "Effects of the aspect ratio on the sedimentation of a fiber in Newtonian fluids," *Journal of Aerosol Science*, vol. 34, no. 7, pp. 909–921, 2003.

[21] J. Lin, P. Lin, and H. Chen, "Research on the transport and deposition of nanoparticles in a rotating curved pipe," *Physics of Fluids*, vol. 21, no. 12, Article ID 122001, 11 pages, 2009.

[22] M. Yu, J. Lin, and T. Chan, "Numerical simulation of nanoparticle synthesis in diffusion flame reactor," *Powder Technology*, vol. 181, no. 1, pp. 9–20, 2008.

[23] M. Z. Yu, J. Z. Lin, and T. L. Chan, "Effect of precursor loading on non-spherical TiO2 nanoparticle synthesis in a diffusion flame reactor," *Chemical Engineering Science*, vol. 63, no. 9, pp. 2317–2329, 2008.

[24] S. E. Pratsinis, "Simultaneous nucleation, condensation, and coagulation in aerosol reactors," *Journal of Colloid and Interface Science*, vol. 124, no. 2, pp. 416–427, 1988.

[25] K. W. Lee and B. Y. H. Liu, "Theoretical study of aerosol filtration by fibrous filters," *Aerosol Science and Technology*, vol. 1, no. 2, pp. 147–161, 1982.

[26] G. Feingold and Z. Levin, "The lognormal fit to raindrop spectra from frontal convective clouds in Israel," *Journal of Climate and Applied Meteorology*, vol. 25, no. 10, pp. 1346–1363, 1986.

[27] E. R. Whitby and P. H. McMurry, "Modal aerosol dynamics modeling," *Aerosol Science and Technology*, vol. 27, no. 6, pp. 673–688, 1997.

[28] S. Y. Bae, C. H. Jung, and Y. P. Kim, "Derivation and verification of an aerosol dynamics expression for the below-cloud scavenging process using the moment method," *Journal of Aerosol Science*, vol. 41, no. 3, pp. 266–280, 2010.

[29] C. H. Jung and K. W. Lee, "Filtration of fine particles by multiple liquid droplet and gas bubble systems," *Aerosol Science and Technology*, vol. 29, no. 5, pp. 389–401, 1998.

[30] S. Greenfield, "Rain scavenging of radioactive particulate matter from the atmosphere," *Journal of Meteorology*, vol. 14, no. 2, pp. 115–125, 1957.

[31] K. W. Lai, N. Dayan, and M. Kerker, "Scavenging of aerosol particles by a falling water drop," *Journal of Atmospheric Science*, vol. 35, no. 4, pp. 674–682, 1978.